Matematisk-fysiske Meddelelser
udgivet af
Det Kongelige Danske Videnskabernes Selskab
Bind **34,** nr. 1

Mat. Fys. Medd. Dan. Vid. Selsk. **34,** no. 1 (1963)

THE AARHUS METEORITES

BY

KAREN CALLISEN AND HANS PAULY

Chemical Analysis by
ME MOURITZEN

København 1963
Kommissionær: Ejnar Munksgaard

Synopsis

The stony meteorite Aarhus I was observed falling on October the second, 1951. A few days later another stone, Aarhus II, was found. It is supposed to belong to the same fall. The first part of the following paper contains a short revue of the fall and the circumstances about the observations of the meteorpath. (This introduction has been written by Professor, Ph. D., A. Noe-Nygaard who handed the material over to the present authors).

The second part deals with the shape and size of the stones, the components and structure of Aarhus I, its non-opaque minerals of which bronzite and olivine are predominant, and the chondrules. The mineral composition is calculated from the analysis. The stone is to be classed as a veined brecciated gray bronzite-olivine chondrite, (by K. C.).

The latter part of the paper gives an account of an ore microscopic examination of the meteorite. Besides the well-known kamacite-taenite-troilite-chromite assemblage the examination revealed the presence of native copper in tiny specks mainly in the nickel-iron grains; pentlandite was seen as minute inclusions in the troilite both in this stone and in samples from the Mern and the Holbrook stones, used for comparison in the study of the Aarhus stone. The pentlandite was analyzed using the Castaing microprobe analyzer.

Two unidentified sulphides from the transition zone between crust and interior of the meteorite are mentioned. Some structural features are dealt with among which are the black veins which together with other phenomena seem to indicate extraterrestrial brecciation, (by H. P.).

PRINTED IN DENMARK
BIANCO LUNOS BOGTRYKKERI A-S

Introduction

"On the 2'nd of October 1951, at $17^h 13^m 5$ U.T. a bright fireball was seen from all parts of Denmark, southern Norway, and southern Sweden, and from Holstein almost as far south as Hamburg. The area of visibility may be estimated to amount to at least 250.000 km^2. The fireball left a persistent train, which at the endpoint of the path developed into a bright irregular cloud. Detonations were heard and a meteorite was seen falling to the Earth"; . . . "another meteorite was found later". (NIELSEN, 1953, p. 305) (5).

The meteorological conditions were favourable, the sky was bright and the fall took place a quarter of an hour after sunset, consequently the fireball was observed by many eye-witnesses. An appeal in newspapers and over the broadcasting service as a collaboration between the Ole Rømer Observatory in Aarhus and the Mineralogical Institute of the University of Copenhagen gave us about 400 eye-witnesses reports. Further, observator AXEL V. NIELSEN travelled round Denmark during a week of October, 8–14th, partly to interview observers personally, partly to measure the coordinates of the apparent path under the direction of the observer in question. In this way he succeeded in obtaining a large amount of observational material, "and the true path of the meteor may be said to have been more accurately determined than most paths hitherto recorded" (NIELSEN, 1953, p. 305) (5).

The point of the path at which the meteor was first seen was 143 km over a point on the Earth 50 km SSE of Warnemünde in Germany and 304 km from the endpoint of the path. The meteor flew over the western Baltic, over the Danish island Lolland, over the Great Belt, cutting across the island of Samsø in Kattegat and finally reaching the bay of Aarhus where it exploded at a height of 31.4 km. The two meteorites fell on the prolongation of the path at an interval of 1.3 km. (NIELSEN, 1953, p. 323–24) (5).

The meteorite, the fall of which was observed, fell into the small wood

Riisskov just north of the town of Aarhus, the second meteorite, which was found a few days later, fell into a timberyard in the northern outskirts of the town. The first stone, Aarhus I, broke into four pieces on falling, these were picked up by P. W. Holm, engineer and K. Hansen, mecanic. Aarhus II was found later by mr. H. Elgaard, it was unbroken. The exact locality for Aarhus I, Riisskov is 56°11′ N, 10°14′ E.

The present investigation has been carried out on Aarhus I, while Aarhus II is kept as a monolith. The weight of Aarhus I, of which a little is missing along the fractures, is ca. 300 g, the weight of Aarhus II is 420 g. The biggest fragment of Aarhus I is kept in the Museum of Natural History in Aarhus (upper fourth of fig. 1), the rest in the Mineralogical Museum of the University of Copenhagen.

Fig. 1. Aarhus Meteorite I. The four fragments.

Fig. 2. Aarhus Meteorite I. Reconstruction, the cast.

Shape and Size of the Meteorites

The four fragments of Aarhus I (fig. 1) corresponded exactly to each other; each of them had preserved a part of the primary black crust which to all appearance covered the whole stone before it broke up. H. Brorson Christensen from National Museum, Copenhagen, with his great ability could join the fragments perfectly in their original positions and make a plaster cast which in all essentials shows the original form of the meteorite and the size slightly diminished due to loss of material by the fracturing. On the cast (fig. 2) a fracture is faintly seen across the left face.

The cast shows that the original shape of the whole stone was an irregular, almost triangular flat pyramid. While photographed it was lying on the largest face which is almost flat with only a few, comparatively large,

shallow depressions. The other faces and all the edges are more or less rounded. The lower left corner (fig. 2) corresponds to the lower left fragment in fig. 1. On this fragment a great many quite small flow-lines are seen, indicating that this corner is a part of the leading surface, the "Brustseite". The opposite part of the pyramid, corresponding to the rear, is uneven and rugged and shows a number of pittings; it probably belongs to the "Rückenseite".

Fig. 3 a. Aarhus Meteorite II. The front surface.

The stone Aarhus II (fig. 3a–b) has a more indeterminate shape; edges and faces are rounded. Fig. 3a shows some rather weak flow-lines ("Brustseite") and on the opposite part of the stone (fig. 3b), probably the "Rückenseite", several shallow depressions are seen.

Aarhus II is a nearly complete stone except for two small scars at the corners (fig. 3b). A minor face on the left corner shows a secondary crust (fig. 3b).

The surface crust of the freshly fallen stones was shiny black, but few days later it became dull and a little grayish. Later on it became somewhat

cracked. In about the same time the originally whitish fracture-surface of the fragments changed to a slightly darker, grayish shade.

Fig. 3 b. Aarhus Meteorite II. The rear side.

Microscopical Investigations

Components and Structure

The light gray main mass of the meteorite is made up of a fine-grained crystalline aggregate predominantly consisting of *silicate minerals. Ore minerals,* however, occur rather abundantly and often as relatively large grains. Macroscopically a few *chondrules* are seen, or holes where chondrules have fallen out, the diameter of which does not exceed ca. 1 mm.

The stone is traversed by numerous dark or black *veins* (see fig. 1 and 4). They consist essentially of ore grains and small opaque particles, further some brown or black glass is seen. Very often the veins branch into crevices in the stone and enclose parts of the groundmass (fig. 4).

The dark veins are certainly due to a fracturing of the stone, and several microscopic features indicate that the texture of the meteorite before fracturing was considerably coarser than at present.

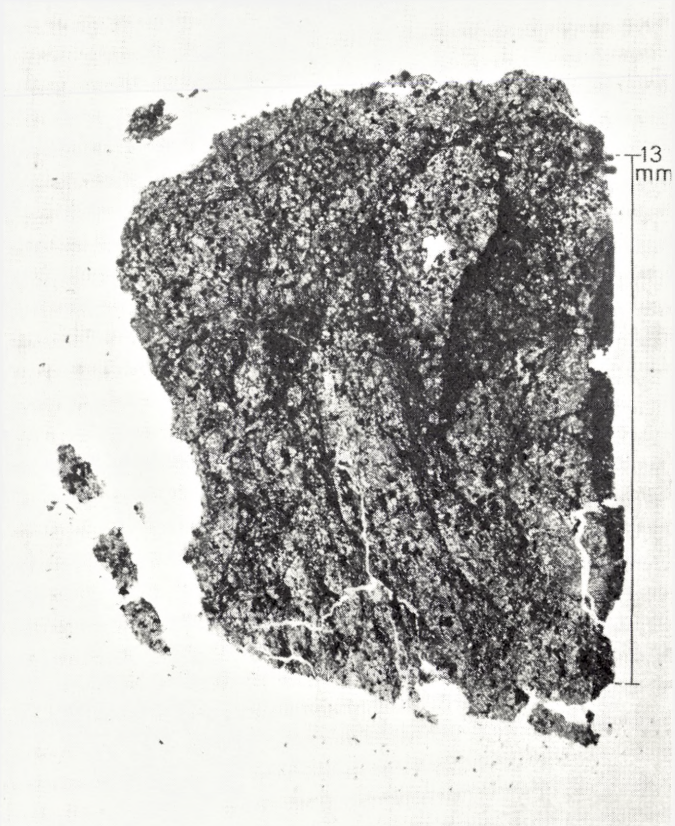

Fig. 4. Aarhus Meteorite I. Thin section in transmitted light showing dark veins.

Apart from the opaque minerals the Aarhus meteorite essentially consists of *pyroxene* and *olivine*, the pyroxenes being *bronzite* and *clinoenstatite*, more rarely *hypersthene*. *Feldspar* (oligoclase), and *maskelynite* occur frequently as quite small grains filling out interstices between the main minerals. In all probability *merrillite* and *oldhamite* are present though not proved with absolute certainty.

The shape of the silicate minerals is irregular and fragmental (see fig. 5). The pyroxenes are split up into fragments along the cleavage planes or into quite irregular splinters. Usually the fragments from one crystal show a more or less different extinction and sometimes they are a little displaced. But not infrequently the original size of a crystal may be judged from the fractures along parallel cleavage cracks, the simultaneous extinction and a

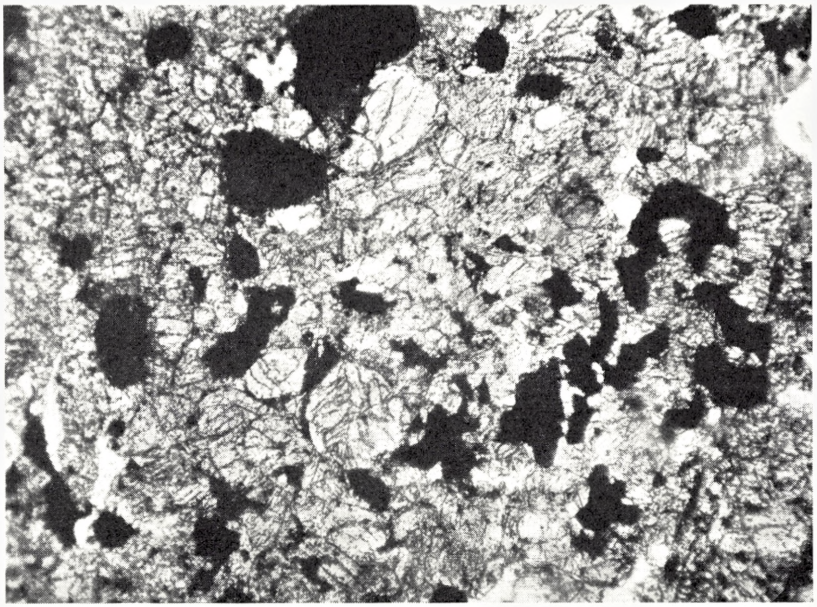

Fig. 5. Aarhus Meteorite I. Thin section in transmitted light showing the structure of the interior; in the lower part three small bronzite chondrules. Enlargement 70×.

crystallographically parallel position of the fragments, f. i. in one case where all the fragments were cut perpendicular to an optic axis. The original dimensions of several such pyroxenes were measured to about 0.3 à 0.4 mm whereas now the grain size of the silicates is generally below 0.1 mm varying down to that of dust.

The olivine is broken into irregular fragments which due to the less perfect cleavage of this mineral are sometimes of larger size than the pyroxenes. In fig. 5, upper part, a conspicuous crystal with characteristic conchoidal olivine cracks is seen; it is 0.22 mm long. On the left side it borders on a nickel-iron grain, on the other side it is surrounded by an extremely fine, crushed aggregate in which two small olivine fragments are observed; they are crystallographically parallel to the main olivine and were evidently separated by fracturing. Some other olivines are still larger, up to 0.52 mm in length.

The material filling in the fractures and cleavage cracks is usually an opaque black mass but not infrequently it also contains a brown or colourless, isotropic *glass* with refractive index a little above that of Canada balsam. Glass furthermore occurs in the silicate minerals as inclusions together with smaller amounts of opaque particles. In some small areas around the

nickel-iron the stone is coloured brown by limonite, seen especially in the cracks.

No fragments of other rock types are seen in the meteorite.

The rock of the Aarhus meteorite is extremely friable and crumbling so that ordinary good thin sections could not be prepared. The slices obtained are uneven and fragmental; it is impossible to estimate the relative amounts of the main minerals by their microscopical features. The probable quantitative mineralogical composition of the stone must therefore be deduced by calculation from the analysis (see p. 13).

For the microscopical determination of the minerals a number of preparations of finely crushed rock were used in addition to the thin sections. In these preparations individual colours, smaller inclusions and cleavage cracks usually appear more clearly than in the thin sections.

The Non-Opaque Minerals

Pyroxenes

Bronzite. In accordance with the immediate impression pyroxene is the prevalent mineral, and among the pyroxenes again bronzite is dominant in the groundmass as well as in the chondrules. Neither pyroxenes nor other minerals occur in good crystal form.

The colour is slightly brownish; thin splinters are colourless. Cleavage cracks and irregular cracks are abundant and because they are usually filled with dark material they may give the impression that the pyroxene is generally rather dark coloured, as seen for example in fig. 5 (the upper left corner). Otherwise ore-inclusions are not very common. In chondrules the pyroxene is lamellar, elongation positive. Parting on (001) is common. The optic axial angle 2V is nearly 90° and the average refractive index n: $1.709 > n > 1.679$.

Hypersthene is found as sporadic fragments or splinters in immersion preparations but its presence is not proved in thin sections. It shows pyroxene cleavage and distinct pleochroism: α' colourless, γ' yellow-brown. The average refractive index n: $1.731 > n > 1.699$.

Diopsidic monoclinic pyroxene. Some few individuals distinctly twinned on (100), are observed; sometimes they show a thin penetrating twin-lamella. Refractive index $1.661 > n$.

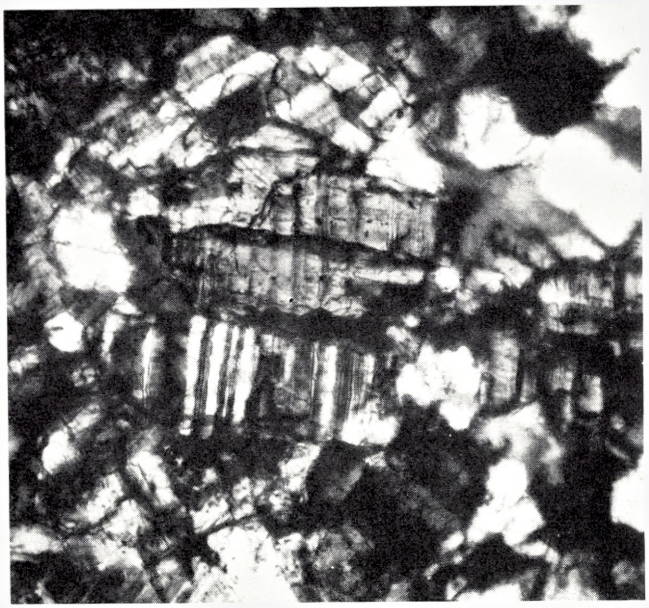

Fig. 6. Aarhus Meteorite I. Clinoenstatite in transmitted light. Nicols +. Enlargement 450×.

Clinoenstatite is found as an ordinary constituent of the groundmass. With a magnification of above 200× it is conspicuous by its polysynthetic twinning with lamellae parallel to (001), elongation negative (fig. 6). Sometimes it is found between the bronzite chondrule lamellae in a crystallographic orientation different to that of the bronzite. Observations in immersion preparations were: $\gamma' > 1.689 > \alpha'$; α' iridescent.

Olivine appears in thin sections as relatively large rounded grains with conchoidal fracture and irregular cracks. It differs from the darker, more strongly cracked pyroxene by being almost clear and colourless. Sections perpendicular to an optic axis are found in immersion preparations; they show two systems of cleavage cracks perpendicular to each other, the most distinct of them is parallel to (010). Other properties include $2V$ = ca. 90°; dispersion slight; β = ca. 1.7, $\gamma' = 1.71$, iridescent; these properties indicate an olivine with about 20 Mol% Fe_2SiO_4.

Feldspar, oligoclase occurs rather commonly but only as quite small colourless grains in the interstices of the other minerals (see fig. 7). Crystal form is not seen. More rarely the oligoclase is found between the bronzite lamellae in the chondrules or inclosed in pyroxene and olivine. Its refractive

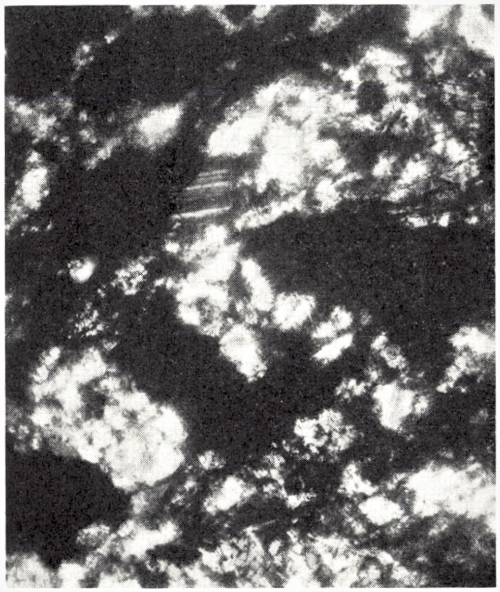

Fig. 7. Aarhus Meteorite I. Plagioclase, oligoclase, in transmitted light. Nicols +. Enlargement 200×.

indices are a little above that of Canada balsam. Twinning on the albite law is common, extinction angles small. Usually the oligoclase contains numerous small black particles besides some other brown and isotropic inclusions with high refractive index.

Several small grains are considered to be *maskelynite*. These occur in interstices and are much like oligoclase with regard to form and refractive indices but they are isotropic or have a very low double refraction and no twin lamellae.

Merrillite is not easily proved but seems to be present. In powder embedded in acethylene tetrabromide with refractive index 1.635 small colourless fragments are seen with a relief so low that some of them were almost invisible, that is: $n \leq 1.635$. The double refraction is very low. Probably these fragments consist of merrillite.

Oldhamite is probably present. In thin sections small brown isotropic inclusions in pyroxene are frequently seen; most of them consist of glass with low refraction index. But some others have a refractive index much above that of pyroxene. In immersion preparations the same brown grains

are conspicuous by their high relief and marked outlines; their refractive index is much above 1.74 (methylene iodide). Cubic cleavage is not seen.

The Mineralogical Composition

as calculated from the analysis (see p. 17)

$KAlSi_3O_8$	1.06 %	
$NaAlSi_3O_8$	4.15 -	.... 6.66 % Feldspar silicates
$CaAl_2Si_2O_8$	1.45 -	
$FeSiO_3$	6.34 -	
$FeTiO_3$	0.30 -	
$MnSiO_3$	0.63 -	
$MgSiO_3$	29.52 -	.... 40.31 % Pyroxene silicates
$CaSiO_3$	2.50 -	
Na_2SiO_3	1.02 -	
Fe_2SiO_4	5.09 -	... 26.47 % Olivine silicates
Mg_2SiO_4	21.38 -	
$3CaO.Na_2O.P_2O_5$	0.41 -	.....Merrillite
$FeCr_2O_4$	0.63 -	..... Chromite
Fe,Ni	19.23 -	..... Metal
FeS	5.64 -	..... Troilite etc.
	99.35 %	

Ilmenite has not been observed in this stone wherefore $FeTiO_3$ has been computed together with the pyroxene components of the analysis.

The glass component has not been accounted for.

The Chondrules

Chondrules are, on the whole, not numerous in the meteorite Aarhus I. They are irregularly distributed in the stone; in one thin section they may appear rather frequently, in another but sparingly.

Most of the chondrules consist mainly of bronzite, some few of olivine. The largest of them scarcely reach 1 mm in diameter. Usually they merge into the granular groundmass; only some quite small chondrules are well rimmed.

Only the following few types were found.

Pyroxene chondrules

The predominating chondrules consist of bronzite lamellae, some of them with a more or less fan-shaped radiating structure. The best developed are rounded and roughly ellipsoidal.

Fig. 8 shows a lamellar bronzite chondrum about 1 mm across. The longer direction of the lamellae is parallel to the crystallographic c-axis; the elongation is positive and 2V ca. 90°. The lamellae are all optically

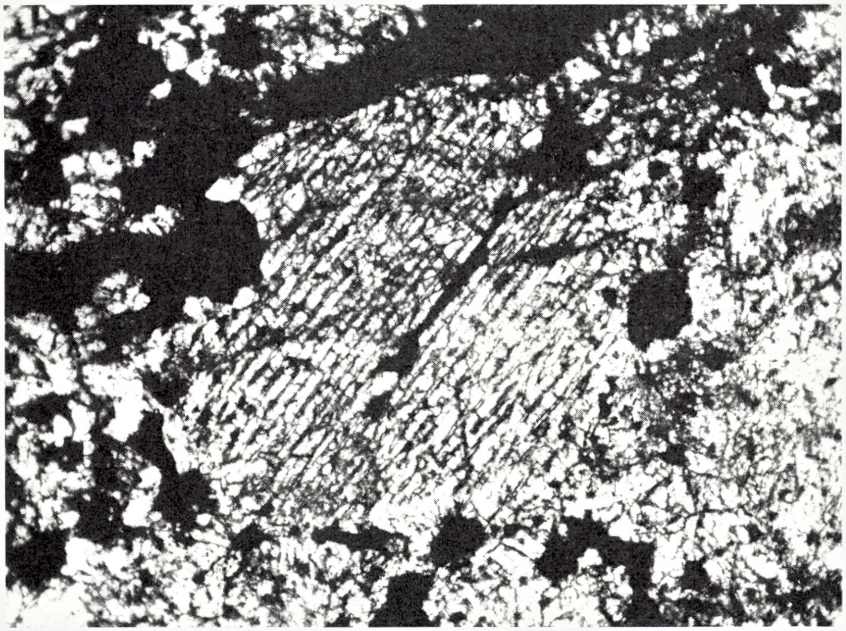

Fig. 8. Aarhus Meteorite I. Bronzite chondrum in transmitted light. Enlargement 85×.

parallel and show simultaneous straight extinction; they all belong to one individual. A parting across the lamellae is clearly seen besides irregular cracks which do not seem to have caused any displacement.

Between the lamellae are interposed quite thin colourless feldspar plates, feebly double refracting, and brown or black glass with refractive index a little above that of Canada balsam, and furthermore dark opaque inclusions of vein substance containing relatively large grains of nickel-iron and rarely yellow iron sulphide.

The upper part of the chondrum is bordered by a thick dark vein containing numerous grains of nickel-iron. From the surrounding vein an offshoot has penetrated into the chondrum along the lamellae. On the other

sides the chondrum is bordered by close-lying grains of nickel-iron. It seems probable that some resorption may have taken place with the vein formation.

In fig. 9 is seen a complex of two bronzite chondrules (1 and 2) together with one olivine chondrum (3); they are situated near the surface

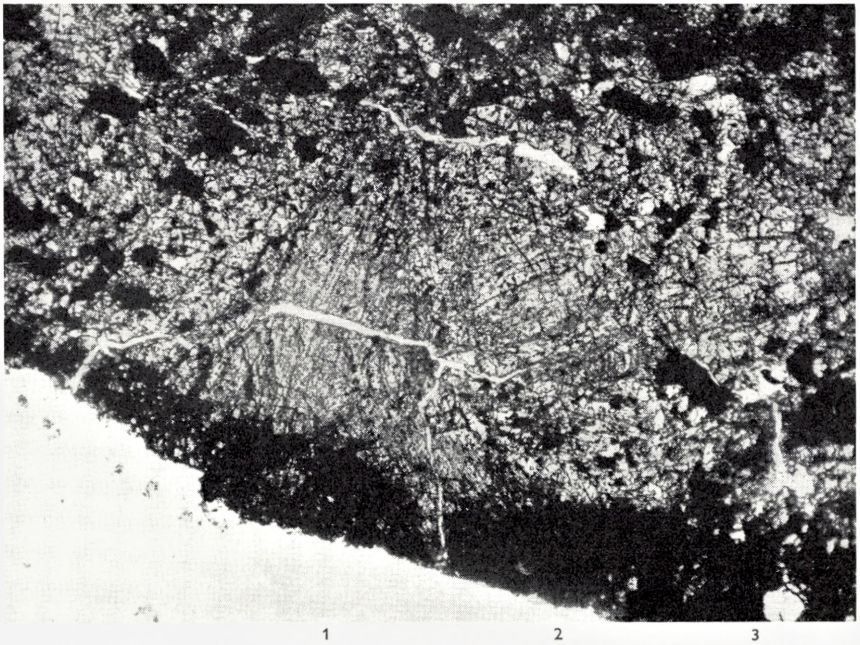

Fig. 9. Aarhus Meteorite I. Two bronzite chondrules (1–2) and one olivine chondrum (3) in transmitted light. Enlargement 30×.

crust. The left chondrum (1) has an elongate form, the other (2) is merely rounded; the borders are but slightly marked.

Mineralogically they resemble the above mentioned chondrum very much and show the same properties. In the greater part of each chondrum the lamellae are in crystallographically parallel position, only in the lower part of the left chondrum the lamellae are slightly radiating and here they penetrate into the surface crust.

In the lower part of fig. 5 are seen three small chondrules, only ca. 0.1–0.2 mm in diameter. They are perfectly spherical or oval and are surrounded by black rims containing small troilite grains. They consist of bronzite crystals with $2V$ = ca. 90°. Each chondrum contains 2–3 bronzite

individuals besides one or two quite small plagioclase grains. In the chondrum to the right a clear white plagioclase is seen at the periphery of the left side. The left chondrum is a double chondrum.

Several small pyroxene chondrules of this type are seen, especially in that part of the meteorite which surrounds the area illustrated in fig. 5.

Olivine chondrules

Only one small olivine chondrum of about the same size as the last mentioned bronzite chondrules is found. It has a slender oval form, 0.5 mm in the longest direction. This chondrum consists of two olivine grains, one of them quite small, and it is bordered by a number of very small olivine grains in parallel crystallographic position to the main individual. On the outside it is fringed with a thin black rim.

The chondrum (3) in fig. 9 is a polysomatic olivine chondrum. Its form is rounded and on the left side marked by an incomplete collar of nickel-iron grains; on the right side the border is faintly indicated by brown pigmented cracks. Between crossed nicols it is seen that the chondrum consists of a number of olivine grains, different in both size and optical orientation. As minor constituents a few ore grains occur besides plagioclase which as usual contains small dark particles. Interstices and cracks are filled with dark brown glass with refractive index a little above that of Canada balsam. Pyroxene is not found. Around the outer bordering grains of nickel-iron the stone is somewhat discoloured by limonite derived from oxydation of the ore.

Chemical Analysis

(by Miss Me Mouritzen)

The Aarhus meteorite was first analysed under the instruction of Dr. H. B. Wiik of the laboratory of the Geological Survey of Finland, Helsingfors (see Wiik (7)). At a later date part of the results were checked by different methods at the Mineralogical Institute, Copenhagen. There was a general agreement of results.

SiO_2, Al_2O_3, TiO_2, CaO, MgO, total iron and water were determined by the methods of the classical analysis. In this way the aluminia content is calculated as a difference, and is therefore apt to be incorrect; a control is made using the titration method for aluminia determination by H. L. Watts (Anal. Chem. vol. 30, p. 967, May 1958); an automatic titrator TTTl from

Fe	17.30 %
Ni	1.93 -
FeS	5.64 -
SiO_2	37.49 -
TiO_2	0.16 -
Al_2O_3	1.53 -
FeO	7.39 -
MnO	0.34 -
MgO	24.03 -
CaO	1.69 -
Na_2O	1.08 -
K_2O	0.18 -
P_2O_5	0.15 -
H_2O^+	0.11 -
H_2O^-	0.05 -
Cr_2O_3	0.43 -
	99.50 %

"Radiometer" was used for the titration. Further it was tried to isolate aluminia from the sesquioxides by use of the solubility of aluminium hydroxide in excess of sodium hydroxide. By these different methods of aluminia determination corresponding results were found.

Phosphorus and manganese were determined by decomposition with $HF + HNO_3$. The phosporus was weighed as ammonium phosphomolybdate and the manganese was colorimetrically determined.

Sodium and potassium were obtained using both the Lawrence Smith's and the flame photometer method (A Beckman DU flame photometer was used). The latter method gave slightly lower results than the Lawrence Smith's method.

Metallic iron was determined by treating a specimen with $HgCl_2$ and NH_4Cl in a water solution and a CO_2-environment, subsequently titrating with potassium permanganate. A part of the same solution was used for a control of the nickel determination; citric acid was added to prevent the precipitation of iron hydroxide, when ammonia is added before the precipitation of nickel with dimethylglyoxime. A check on nickel was moreover made on the main analysis as well as on a fusion of sodium carbonate and potassium nitrate. From this fusion chromium was determined colorimetrically, and sulphur was precipitated as barium sulfate.

A treatment with dilute acetic acid gave no calcium content to establish an amount of CaS (Wahl 1950); therefore all of the sulphur is calculated as belonging to iron in FeS. The value for ferrous iron is not determined directly, but is calculated as a difference between total iron minus that found in FeS and metallic iron.

Ore Microscope Examination

The ore microscope examination of the Aarhus stony meteorite was carried out on several small pieces – 5 mm in diameter or less. These pieces were obtained when the material for the chemical analysis was being prepared. Among the pieces are samples from the interior as well as from the outer part of the stone, a few of them showing the molten crust of the meteorite.

Interior

Silicates

Fig. 1* gives a characteristic picture of the mineralogical components of the meteorite as seen in the ore microscope. The non-opaque silicates show distinctive reflection properties due to which the distribution of the two main groups of silicate minerals can be studied.

A rough estimate of 1:9 as the proportion of silicates with low refractive index (about 1.5) to silicates with high refractive index (about 1.7). Non-opaque phases other than these have not been observed.

Oxides

Of the usually observed oxides chromite has been found throughout the meteorite, magnetite occurs only in the outermost, molten crust.

Chromite mostly appears as rounded grains somewhat smaller that the sulphidic and metallic grains (see fig. 1). Very characteristic of these grains are the numerous cracks; the grains seem to have been shattered through some mechanical action. The mineral is always found in the silicate with low RI and the same silicate fills the cracks.

Sulphides: *Troilite and Pentlandite*

The chemical analysis indicates the presence of 5.64 % of FeS. The amounts of metallic iron and nickel have been found to make up 19.23 %. Recalculated to volume percentages this means about 5 % of sulphide and

* For the following figures see PLATES I-IV.

10 % of metal, and this seems to be in accordance with the observed proportions.

The grain size of the sulphides is about .2 mm. A few grains over one mm in diameter have been seen. Sulphide grains less than 10 μ seem to be rare.

Troilite grains mostly occur as individual optic units. Now and then adjoining grains can be seen with the same optical orientation indicating that they belong to the same individual. Such an assumption may be supported by the lobate form of the troilite.

Now and then troilite grains can be built up of two or more individuals. In these the single individuals have irregular polygonal outlines. Single grains of troilite composed of numerous individuals seem to be very rare in this stone. Another phenomenon, however, is rather frequently met with. One-individual-grains often show wavy extinction between crossed nicols. This is illustrated on fig. 2a and b. Even though this is from the Holbrook stone it very accurately shows what can be observed in Aarhus I too. Such an extinction indicates that the mineral has been subject to dynamic forces giving rise to some recrystallisation through which lamellae were formed. On closer inspection these lamellae are seen to be subdivided into even smaller areas perpendicular to their length. There is a possibility that grains showing wavy extinction to a varying degree occur regularly distributed in the meteorite. Thus an examination of the situation of such grains within the meteorite could give information as to how and when the dynamic forces created this pattern. Due to lac of material it was not possible to investigate this question in the study of the Aarhus I stone.

Dr. V. Buchwald of the Technical University of Denmark has kindly determined the Vicker hardness of the troilite and found 310 ± 25, in fairly good agreement with the hardness of pyrrhotite.

A yellow-cream coloured sulphide has been observed enclosed in the troilite, in most cases only as areas less than 10–20 μ across. The reflectivity of this mineral is slightly higher than that of troilite, the hardness is near to or a little higher than that of troilite and the mineral appears isotropic between crossed nicols. Fig. 3 gives an impression of the mineral.

Based on the properties mentioned it has been possible to recognize this mineral in two other stony meteorites (Mern and Holbrook) and likewise in two irons, those from Savik and Thule. Concerning the latter see V. Buchwald (2).

Analysis carried out by means of the Castaing electron-probe microanalyzer on the yellowcream mineral in samples from Aarhus I and the Holbrook

stone gave the following results. In the same runs it was possible to analyze troilite in both mentioned stones and a valleriite-like mineral found in Holbrook. Native copper and taenite in Aarhus I was also examined in this way:

	Cu %	Fe %	Ni %	S* %
Aarhus I				
Troilite	0.1	62	–	–
Pentlandite	0.2	43	21	34
Taenite	0.4	41	58	–
Copper	80.–	–	–	–
Holbrook				
Troilite	–	62	–	38
Pentlandite	–	43	21	34
Valleriite-like sulphide	–	59	1–3	38

The analyses were carried out by civil engineer N. Lange at Metallografiska Institutet in Stockholm.

The analyzed sulphide phases are shown in fig. 2a and 3. In order to establish a basis for comparison the surrounding troilite was also analyzed.

As is seen from fig. 3, a small metallic grain occurs inside the pentlandite. It was assumed to be taenite and the analysis came out in agreement with the assumption. The high Ni should be noted.

The troilite in fig. 2 – of the Holbrook stone – was found to contain not only pentlandite but also in a tiny area in the one corner a vividly anisotropic sulphide resembling valleriite. With one nicol the mineral shows strong bireflection–in one position it has a colour near that of troilite and in another it is much like sphalerite. The analysis shows it has a composition very near to troilite. Whether the small nickel content has some influence on the structure of the phase or not is not clear but so far it seems reasonable to regard this mineral a variety of FeS and perhaps identical with some earlier described minerals, see f. i. Kouvo and Vuorelainen (4).

The copper grains shown in fig. 12 were tested for Cu. Unfortunately it was not possible to undertake analyses for Au, Ag etc., due to lack of material.

* Due to lack of a good FeS-standard the S-determinations are not completely reliable.

Shape and relation of troilite to the other minerals

The outlines of troilite grains are dominated by concave forms as is evident from fig. 1. Even grains which at the first glance seem to show rounded forms can be seen by closer study to have their boundaries built up of concave lines where they border silicates. Troilite grains may show pointing branches but such branches never seem to attain noticeable lengths. As a matter of fact the troilite seems to have its forms determined by its surroundings – the silicates – but, contrary to terrestrial occurrences where its intergranular position often gives rise to pronounced amoeboid forms, elongate branches seem rare.

Chromite has been seen in a few cases with idiomorphic borderlines against troilite.

Sulphide and nickel-iron show "mutual boundaries" relations, the borderlines are convex-concave. In a few cases advanced islands of troilite can be observed in the nickeliron. Whether these represent corrosion remnants, replacements or merely parts of the sulphide left over in the solidification can hardly be decided.

Cracks in the troilite, as for instance shown in fig. 2a and fig. 4, are rather often met with. In all cases they seem to contain the same substance, namely the silicate with low refractive index (about 1.5), feldspar or the glass component. The crack pictured in fig. 4 illustrates this and in addition it shows a displacement of the troilite without any corrosion. Even though this picture illustrates Holbrook material this observation is also valid for the Aarhus I stone.

Metal phases: *Taenite, Kamacite and Copper*

The analysis indicates the presence of 17.30 % Fe, 1.93 % Ni and to these can certainly be added small amounts of Cu, Co etc.

As is already known from some newer papers (3,6) on stony meteorites both taenite and kamacite occur in these. Both minerals may constitute single grains and they can be found together in a variety of intergrowth structures. Examples of this for the Aarhus I meteorite are given in fig. 5–11.

Kamacite in stony meteorites sometimes exhibits nicely developed Neumann bands. The examination of Aarhus I has, however, not revealed the existence of these bands, but a polygonal structure of the kamacite has been observed in several grains, see fig. 8 and 11.

In Aarhus I as well as in the earlier mentioned stones from Mern, Holbrook and Alfianello, metallic copper has been found as tiny particles mostly included in the nickel-iron, see fig. 12. Rather often copper occurs

on the borderline between troilite and nickel-iron and in a few cases the author has found copper grains in troilite. Due to the small dimensions of the copper grains – only a few μ in diameter – the mineral can be regarded as a sparse constituent of the meteorites but in spite of this remarkably many copper grains can be found in the samples. So in this sense it does not seem to be rare. This also appears from YUDINS observations, YUDIN (8).

Transition Zone

Fig. 13 shows a typical view of that part of the meteorite which constitutes the zone between the outer molten crust and the interior. The appearance is quite the same in the other meteorites mentioned which the author has had an opportunity to examine, and it corresponds closely to figures published by other authors (see HENTSCHEL (3)).

The width of the zone averages a few tenths of a mm and it is rarely more than .5 mm. It is characterized by the presence of numerous veins often, but not invariably, starting from larger grains of metal or sulphide. Both in their way of occurrence and in their constituents the veins clearly demonstrate the melting processes which led to their formation.

Fig. 14 illustrates the compound nature of this material which is an emulsion of metal – nickel-iron – in sulphide. Fig. 15 shows that the same structure is found in the thin veins. The metal always occurs with convex borders against the sulphide. In larger grains where both sulphide and metal are present the border between the two components appears as a serrate line and as a rule the sulphide area is seen to hold small droplets of metal. Sometimes a thin lining of sulphide can be observed along metal grains in this zone.

Veins with this emulsion structure can be seen veining both silicates and chromite grains.

In consequence of the clearly demonstrated melting processes one could expect the occurrence of sulphides other than FeS, such as compounds containing Ni. If copper happened to be present also sulphides of this element could have been formed. With these ideas in mind it was rather interesting to find at least two kinds of sulphides in the Aarhus meteorite different from troilite and pentlandite (and the mentioned valleriite resembling sulphide). Fig. 16 is a picture of a composite sulphide grain where the main part – a little darker than the rest – seems to be troilite and the rest is a lighter pentlandite resembling sulphide. Its optical properties seems to differ from those of pentlandite. Also another sulphide of a rather intense yellow cream colour much like chalcopyrite, but not as yellow as this mi-

neral(?), was found in the transition zone. Both of these unidentified minerals were so small that nothing else could be done in order to identify them.

Molten Crust

The outermost zone of the stony meteorite is .1 to hardly .2 mm in width. It is characterized by its content of numerous tiny crystallites of magnetite. When in a few cases it is possible to observe the magnetite in areas the mineral is seen to be built up of two zones of different shades of grey as seen in the ore microscope.

Black Veins of the Interior

These veins, so conspicuous in thin sections and characteristic of the macro appearance of the Aarhus I stone, are easily overlooked in the ore microscope. But when the polished samples are viewed between crossed nicols, all the non-opaque minerals are brightly lit up through internal reflexes. This view is more or less comparable to the ordinary appearance of a thin section and in this way the black veins can easily be observed. In ordinary light in the ore microscope these veins are seen to carry rows of elongated grains mostly of troilite; a few nickel-iron grains are present.

The most conspicuous thing about this feature of the stone is seen where the veins border on troilite of normal grain size. The outline of the troilite grain gives the impression that the grain was cut along a line at the side where it borders the vein, and often a tail of troilite is seen stretching in the direction of the vein. This no doubt indicates mechanical action, i. e. brecciation. The tail extending from after a troilite grain in such a position may attain a length of some hundredths of a mm, but this does not indicate more than the minimum distance of movement. Whether the total movement has been a few or many times this distance can hardly be said.

The general appearance of these veins in the ore microscope gives an impression of the veins being composed of many small more or less continuous parallel pieces. Thus, in a sense, each vein is a narrow zone (often only a few hundreths of a mm thick) of veinlets. They are marked by the presence of sulphides, and only small amounts of "glass" are seen. In places where veins branche larger amounts of "glass" can be seen and sulphides often form a pigmentation here.

The author's examination of Alfianello, however, provided an opportunity to see corresponding veins in another development.

From the ore microscopic examination of the veins seen in material from Alfianello it was found that the sulphides in the veins contained many

tiny drops of metal, and grains of clear emulsion structure were also found. This seems to indicate that the material has been subject to high temperatures causing the formation of sulphide-metal emulsion. The emulsion-veins characteristic of the transition zone do not occur here and no magnetite was seen. It is therefore possible that the material filling the fracture has been placed there before the stone entered the atmosphere, and this seems to be supported by the observation of such veins with no visible connection to the surface of the stone.

In the case of the veins in the Aarhus I stone no indications of temperature could be found. The author would, however, be inclined to ascribe to these veins the same extraterrestrial mode of formation as that of the veins observed in Alfianello, only the temperature of the environment at the time of brecciation has been different in the two cases.

Atmospheric Heating's Penetration into the Stone

It is interesting to note the different zones into which the meteorite can be subdivided. The outermost zone, the molten crust, corresponds to temperatures exceeding 1500°C, because silicates and all other components of the stone here underwent melting and for a large part were blown off the surface of the stone, only leaving the thin crust which we now find sprinkled with magnetite crystallites.

In the transition zone the emulsion structure formed by sulphidic and metallic material must indicate temperatures from 1100°C to, say, 900°C in the inner part of the zone. This indicate a fall in temperature from 1500°C to 900°C within only about .5 mm. In other words a gradient of about 120°C per .1 mm. If this gradient persisted, the temperature only a few mm inside the meteor would have been very low.

Acknowledgements

Mr. H. Brorson Christensen of the National Museum has given valuable help to the present study in making the excellent plaster casts of the meteorites.

Dr. Vagn Buchwald of the Technical University of Denmark has kindly assisted in etching samples of the meteorite and in helping to identify the metallic components. For this and his many suggestions we are most grateful.

Polishing and photographic facilities at the Mineralogical Department of the Kryolitselskabet Øresund A/S have been at our disposal for which we feel much obliged. We are grateful to Mr. Chr. Halkier, photographer at the Mineralogical Museum of the University of Copenhagen for part of the photographic works (the first nine textfigures).

Financial support for the analytical examination by means of the Castaing electron-probe microanalyzer has been procured by the Mineralogical Museum of the University of Copenhagen. Warm thanks are given to Metallografiska Institutet in Stockholm, and to civil engineer N. Lange who carried out the analyses not least on account of the rapidity with which these analyses were carried out.

Mr. V. Pulvertaft and Mr. John Ferguson have kindly assisted in correcting the English of the manuscript.

Literature

(1) Leon H. Borgström, Die Meteoriten von Hvittis und Marjalathi. Bull. de la Commission Géologique de Finlande, No. 14. Helsingfors 1903.

(2) Vagn Buchwald, The Iron Meteorite "Thule", North Greenland. Geochimica et Cosmochimica Acta, vol. 25, no. 2, p. 95, 1961.

(3) H. Hentschel, Der Meteorit von Breitscheid III – Petrografische Untersuchung. Geochimica et Cosmochimica Acta, vol. 17, no. 3/4, p. 323–338, 1959.

(4) Olavi Kouvo & Yrjö Vuorelainen, Valleriitista. Geologi, no. 3–4, Helsinki 1959.

(5) Axel V. Nielsen, The Path and Orbit of the Aarhus Meteorites. Medd. fra Ole Rømer observatoriet i Aarhus, no. 23, Marts 1963.

(6) H. C. Urey & Toshiko Mayeda, The Metallic Particles of some Condrites. Geochimica et Cosmochimica Acta, vol. 17, no. 1/2, p. 113–124, 1959.

(7) H. B. Wiik, The Chemical Composition of some Stony Meteorites. Geochimica et Cosmochimica Acta, vol. 9, p. 279–289. 1956.

(8) J. A. Yudin, Opaque Minerals of Stony Meteorites. cited from: Meteoritica, Issue XVL, Summaries, Moscow – 1958.

Indleveret til Selskabet den 28. juni 1963.
Færdig fra trykkeriet den 31. december 1963.

PLATES

PLATE I

Fig. 1. Pol. prep. 200×, Aarhus.
General view illustrating the different components: chromite (grey), troilite (light grey), nickel-iron (white), and silicates, one darker grey (RI ca. 1.5) than the other (RI ca. 1.7). Part of the largest troilite grain is reproduced in fig. 3.

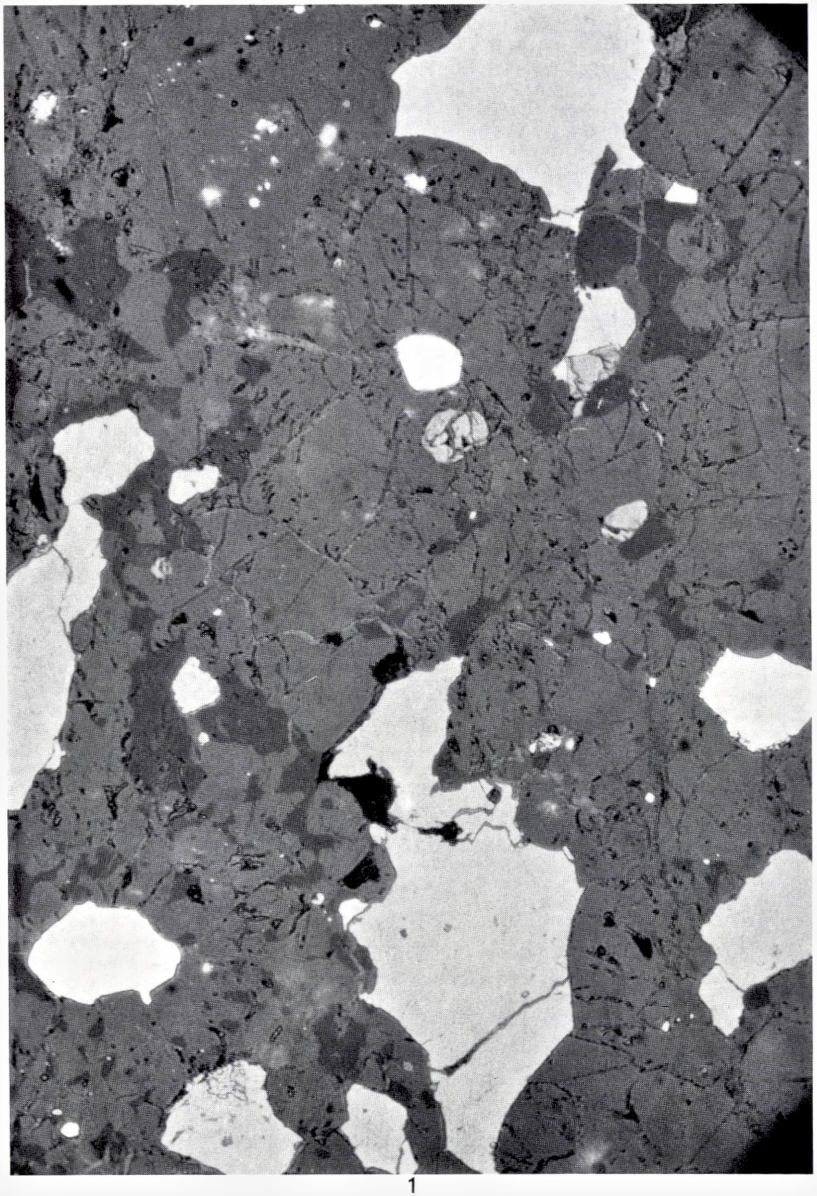

1

PLATE II

Fig. 2 a & b. Pol. prep. 160×, Holbrook.

a. With one nicol, showing troilite transected by fine cracks. The marginal area between the tips of the inverted V is pentlandite. The area at arrow consists of the valleriite resembling mineral.

b. The same, but with nearly crossed nicols, showing the troilite grain built up by wedgeshaped lamellae, giving rise to wavy extinction between crossed nicols.

Fig. 3. Pol. prep. 750×, Aarhus.
Inclusion of pentlandite in troilite. Taenite inside pentlandite appears white.

Fig. 4. Pol. prep. 333×, Holbrook.
Troilite with a crack cemented by "glass" or at least silicate with RI about 1.5. The rounded silicate has a RI about 1.7.

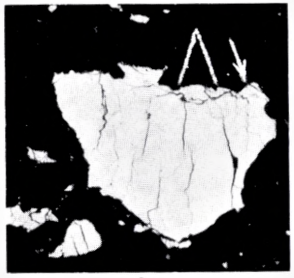

2a

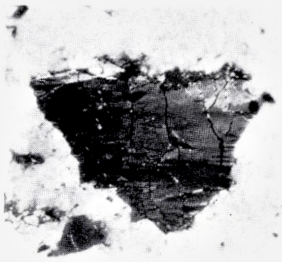

2b

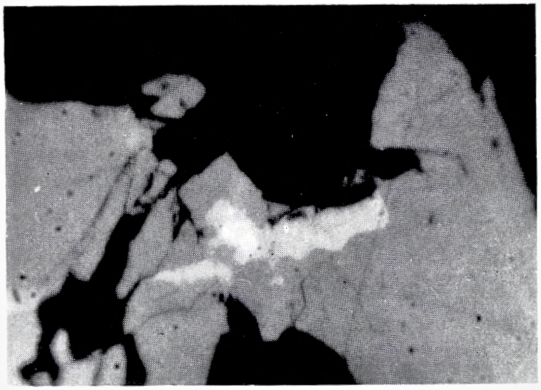

3

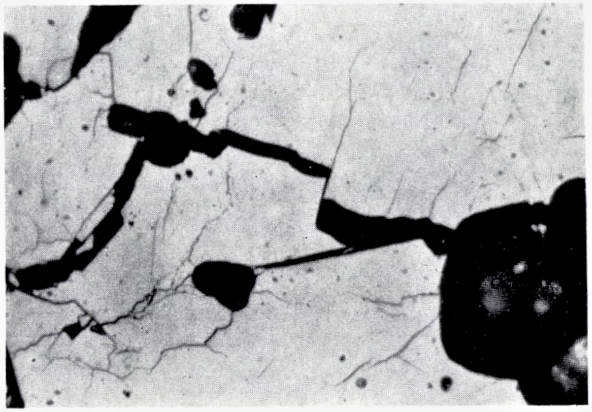

4

Plate III

Fig. 5. Pol. prep. 700×, etched, Aarhus.
Taenite with a non-etching borderzone and a weakly etching central zone. Part of a troilite grain is also seen.

Fig. 6. Pol. prep. 600×, etched, Aarhus.
Taenite with non-etching border and central zone; grey and blue (against central zone) etching intermediate zone.

Fig. 7. Pol. prep. 750×, etched, Aarhus.
Kamacite with taenite border and oriented bodies of taenite.

Fig. 8. Pol. prep. 400×, etched, Aarhus.
Kamacite with lamella-structure and faint polygonal division. Besides six taenite grains along the border small elongated taenite grains occur oriented in the kamacite.

Fig. 9. Pol. prep. 600×, etched, Aarhus.
Kamacite with oriented taenite grains. Two larger taenite grains are also present.

Fig. 10. Pol. prep. 700×, etched, Aarhus.
Kamacite with inclusions of irregular rounded taenite grains.

Fig. 11. Pol. prep. 500×, etched, Aarhus.
Kamacite showing polygonal structure. Troilite bottom left.

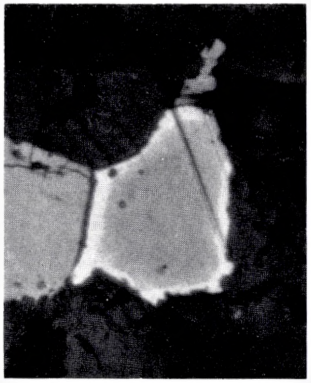

5

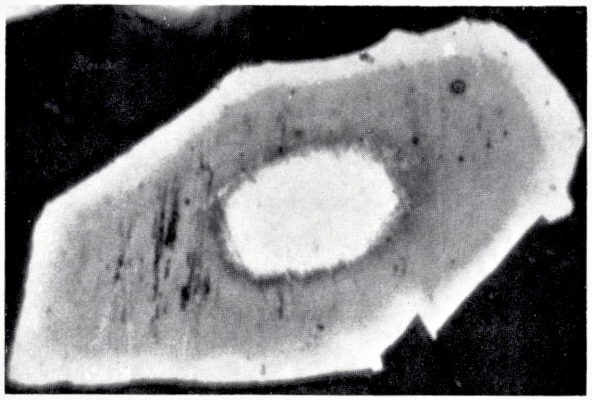

6

7

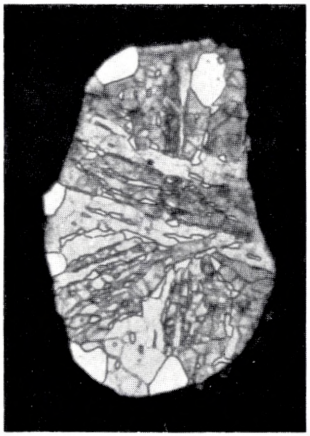

8

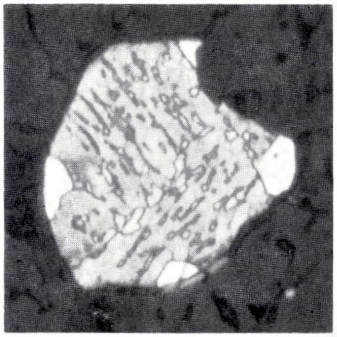

9

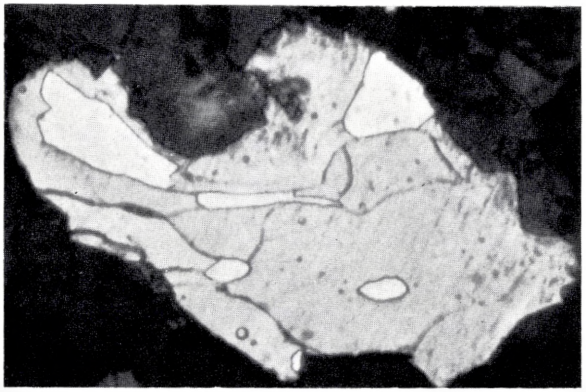

10

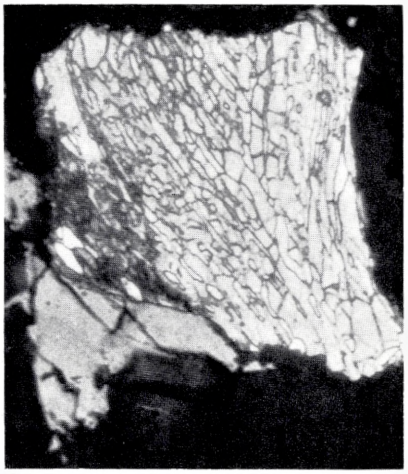

11

Plate IV

Fig. 12. Pol. prep. 650×, etched, Aarhus.
Taenite (nearly white) with inclusions. Kamacite (light grey) and troilite (grey). In the taenite irregular inclusions of troilite and tiny kamacite grains together with two grains of metallic copper (white, but this is caused by retouching).

Fig. 13. Pol. prep. 175×, Mern.
General view illustrating the zone between the interior of the meteorite and its molten crust. White grains and veins are metals and sulphides. Black are holes.

Fig. 14. Pol. prep. 800×, Aarhus.
Metal-sulphide emulsion. Grain from the transition zone.

Fig. 15. Pol. prep. 800×, Mern.
Metal-sulphide emulsion. The picture illustrates that this structure also exists in the narrow veins.

Fig. 16. Pol. prep. 750×, Aarhus.
Sulphide grain mainly consisting of troilite containing a lighter pentlandite coloured sulphide having serrate borderline against the troilite. Two tiny metal grains occur in the surrounding silicates, grey is cromite.

12

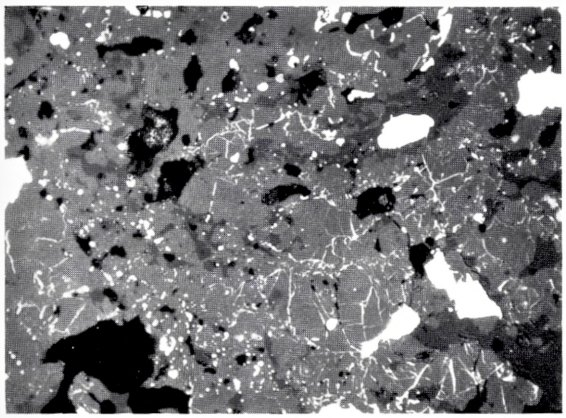

13

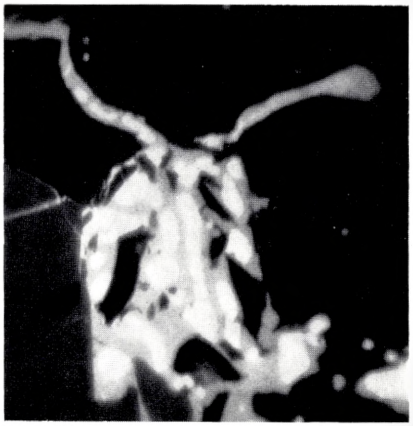

15

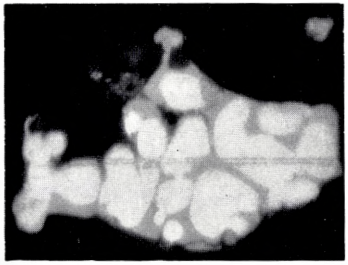

14

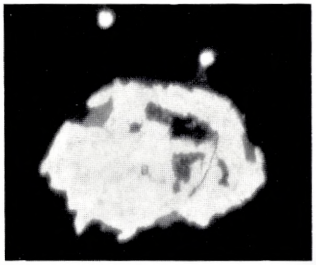

16

Matematisk-fysiske Meddelelser
udgivet af
Det Kongelige Danske Videnskabernes Selskab
Bind **34,** nr. 2

Mat. Fys. Medd. Dan. Vid. Selsk. **34,** no. 2 (1964)

CONJUGATE CONVEX FUNCTIONS IN TOPOLOGICAL VECTOR SPACES

BY

ARNE BRØNDSTED

København 1964
Kommissionær: Ejnar Munksgaard

Synopsis

Continuing investigations by W. L. JONES (Thesis, Columbia University, 1960), the theory of conjugate convex functions in finite-dimensional Euclidean spaces, as developed by W. FENCHEL (Canadian J. Math. 1 (1949) and Lecture Notes, Princeton University, 1953), is generalized to functions in locally convex topological vector spaces.

PRINTED IN DENMARK
BIANCO LUNOS BOGTRYKKERI A-S

Introduction

The purpose of the present paper is to generalize the theory of conjugate convex functions in finite-dimensional Euclidean spaces, as initiated by Z. BIRNBAUM and W. ORLICZ [1] and S. MANDELBROJT [8] and developed by W. FENCHEL [3], [4] (cf. also S. KARLIN [6]), to infinite-dimensional spaces. To a certain extent this has been done previously by W. L. JONES in his Thesis [5]. His principal results concerning the conjugates of real functions in topological vector spaces have been included here with some improvements and simplified proofs (Section 3). After the present paper had been written, the author's attention was called to papers by J. J. MOREAU [9], [10], [11] in which, by a different approach and independently of JONES, results equivalent to many of those contained in this paper (Sections 3 and 4) are obtained.

Section 1 contains a summary, based on [7], of notions and results from the theory of topological vector spaces applied in the following. Section 2 deals with real functions f defined on subsets D of a locally convex topological vector space. In particular convex functions are considered. In Sections 3 and 4 the theory of conjugate functions is developed. The starting point is a pair of locally convex topological vector spaces E_1, E_2 which are (topological) duals of each other. For a function f with domain $D \subseteq E_1$, briefly denoted by (D, f), we define

$$D' = \left\{ \xi \in E_2 \,\middle|\, \sup_{x \in D} (\xi\, x - f(x)) < \infty \right\}.$$

If D' is non-empty, the function (D', f'), where

$$f'(\xi) = \sup_{x \in D} (\xi\, x - f(x)) \qquad \text{for } \xi \in D',$$

is called the conjugate of (D, f). Analogously the conjugate of a function in E_2, in particular the second conjugate (D'', f'') of (D, f), that is, the conjugate of (D', f'), is defined. In Section 3 elementary properties of (D', f') and (D'', f'') are studied, and necessary and sufficient conditions in order that a convex function (D, f) have a conjugate and that it coincide with its second

conjugate are given. In Section 4 the conjugates of functions derived from others in various ways are determined. Finally, in Section 5 the class of convex functions (D, f) in E_1 which coincide with their second conjugates and have the property that their domains D as well as the domains D' of their conjugates have relative interior points is characterized in the case of Banach spaces E_1 and E_2.

1. Topological vector spaces

In the following R denotes the set of reals, R_+ the set of positive reals and Z_+ the set of positive intergers. When R is considered as a topological space, the topology is the usual one. All the vector spaces considered are vector spaces over R.

Let E be a vector space over R with elements $\boldsymbol{o}, \boldsymbol{x}, \boldsymbol{y}, \ldots, \boldsymbol{o}$ being the zero element, and let $\mathfrak{T}$ be a Hausdorff topology on E. If the mappings $E \times E \to E$ defined by $(\boldsymbol{x}, \boldsymbol{y}) \to \boldsymbol{x}+\boldsymbol{y}$ and $R \times E \to E$ defined by $(a, \boldsymbol{x}) \to a\boldsymbol{x}$ are continuous, E is said to be a topological vector space. $\mathfrak{T}$ is then called a vector space topology, and E is denoted $E\,[\mathfrak{T}]$.

If F is an algebraic subspace of $E\,[\mathfrak{T}]$, then F is a topological vector space in the induced topology.

If $\mathfrak{V} = \{V\}$ is a basis for the neighbourhood system of $\boldsymbol{o}$ in $E\,[\mathfrak{T}]$, then $\{\boldsymbol{x}+V \mid V \in \mathfrak{V}\}$ is a basis for the neighbourhood system of the point $\boldsymbol{x}$. There exists a basis $\mathfrak{V}$ such that all $V \in \mathfrak{V}$ are symmetric, in the sense that $\boldsymbol{x} \in V$ and $|a| \leq 1$ imply $a\boldsymbol{x} \in V$. If $b \neq 0$ and $V \in \mathfrak{V}$, then $bV \in \mathfrak{V}$. A subset M of $E\,[\mathfrak{T}]$ is said to be bounded if for all $V \in \mathfrak{V}$ there exists a $c \in R$ such that $M \subseteq cV$. Any set consisting of only one point is bounded.

The dual space of $E\,[\mathfrak{T}]$, denoted $(E\,[\mathfrak{T}])'$, is the set of continuous linear functions on $E\,[\mathfrak{T}]$, organized as a vector space in the well-known manner. For $\xi \in (E\,[\mathfrak{T}])'$ the value of ξ at $\boldsymbol{x} \in E\,[\mathfrak{T}]$ is denoted $\xi\,\boldsymbol{x} = \boldsymbol{x}\,\xi$.

A set $M \subseteq E\,[\mathfrak{T}]$ is called convex if $(1-t)\boldsymbol{x}+t\boldsymbol{y} \in M$ for all $\boldsymbol{x}, \boldsymbol{y} \in M$, $0 \leq t \leq 1$. The set $a_1M_1 + a_2M_2 + \ldots + a_nM_n$ is convex for M_i convex, $a_i \in R$, $i = 1, 2, \ldots n$. The intersection of convex sets is convex. The smallest convex set containing a set M, i.e. the intersection of all convex sets containing M, is denoted $\operatorname{conv} M$. It consists of all points $\boldsymbol{x} = \sum_{i=1}^{i=n} a_i \boldsymbol{x}_i$, where $a_i \in R$, $\boldsymbol{x}_i \in M$, $n \in Z_+$ and $\sum_{i=1}^{i=n} a_i = 1$. The set $\overline{\operatorname{conv} M}$ is the intersection of all closed convex sets containing M, and $\overline{\operatorname{conv} M} = \overline{\operatorname{conv} \overline{M}}$. If M is convex, then also the closure $\overline{M}$ of M and the interior $\mathring{M}$ of M are convex sets. If $\mathring{M}$ is not empty, then $(1-t)\boldsymbol{x}+t\boldsymbol{y} \in \mathring{M}$ for all $\boldsymbol{y} \in \mathring{M}$, $\boldsymbol{x} \in \overline{M}$ and $0 < t \leq 1$. We

express this by saying that all points in $\overline{M}$ can be reached from $\mathring{M}$. Further $\mathring{M} = \overline{\mathring{M}}$ and $\overline{M} = \overline{\mathring{M}}$.

A topological vector space is said to be locally convex if there exists a basis for the neighbourhood system of $\boldsymbol{o}$ consisting of convex sets. Normed spaces are locally convex topological vector spaces. A subspace of a locally convex space is itself locally convex.

Let E_1 and E_2 be vector spaces over R, and suppose that there exists a bilinear mapping $\mathfrak{B} : E_2 \times E_1 \to R$ with the following two properties:

(i) For all $\boldsymbol{x} \in E_1$, $\boldsymbol{x} \neq \boldsymbol{o}$, there exists a $\xi \in E_2$ such that $\mathfrak{B}(\xi, \boldsymbol{x}) \neq 0$.

(ii) For all $\xi \in E_2$, $\xi \neq \boldsymbol{o}$, there exists an $\boldsymbol{x} \in E_1$ such that $\mathfrak{B}(\xi, \boldsymbol{x}) \neq 0$.

We then say that E_1 and E_2 are in duality under $\mathfrak{B}$.

Let E_1 and E_2 be in duality under $\mathfrak{B}$. Then every $\xi \in E_2$ is a linear function on E_1, and every $\boldsymbol{x} \in E_1$ is a linear function on E_2, namely $\xi\boldsymbol{x} = \boldsymbol{x}\xi = \mathfrak{B}(\xi, \boldsymbol{x})$. There exist at least one locally convex topology $\mathfrak{T}_1$ on E_1 and at least one locally convex topology $\mathfrak{T}_2$ on E_2 such that E_2 is the set of continuous linear functions on $E_1[\mathfrak{T}_1]$ and E_1 is the set of continuous linear functions on $E_2[\mathfrak{T}_2]$, that is, $(E_1[\mathfrak{T}_1])' = E_2$ and $(E_2[\mathfrak{T}_2])' = E_1$. Such topologies are called admissible.

If $E[\mathfrak{T}]$ is locally convex, and E' is the dual space, then E and E' are in duality under $\mathfrak{B}(\xi, \boldsymbol{x}) = \xi\boldsymbol{x}$, and $\mathfrak{T}$ is an admissible topology on E.

Let $E[\mathfrak{T}]$ be a normed vector space, $\mathfrak{T}$ denoting the topology induced by the norm, and let E' be the dual space. It is well-known that $\| \xi \| = \sup_{\|\boldsymbol{x}\| \leq 1} | \xi\boldsymbol{x} |$ is a norm in E'. The topology $\mathfrak{T}'$ induced by this norm is admissible if and only if $E[\mathfrak{T}]$ is a reflexive Banach space. In that case $E'[\mathfrak{T}']$ is also a reflexive Banach space.

Let E_1 and E_2 be in duality under $\mathfrak{B}$. Defining $a(\boldsymbol{x}, x) = (a\boldsymbol{x}, ax)$ and $(\boldsymbol{x}, x) + (\boldsymbol{y}, y) = (\boldsymbol{x} + \boldsymbol{y}, x + y)$, $E_1 \times R$ is a vector space over R. Likewise for $E_2 \times R$. Further, $E_1 \times R$ and $E_2 \times R$ are in duality under $\tilde{\mathfrak{B}}((\xi, \xi), (\boldsymbol{x}, x)) = \mathfrak{B}(\xi, \boldsymbol{x}) + \xi x$. If $\mathfrak{T}_1$ is a locally convex topology on E_1, then $E_1[\mathfrak{T}_1] \times R$, that is, $E_1 \times R$ supplied with the product space topology, is a locally convex space. If $\mathfrak{T}_1$ is admissible, then the topology on $E_1[\mathfrak{T}_1] \times R$ is also admissible. A basis for the neighbourhood system of the zero element $(\boldsymbol{o}, 0)$ in $E_1[\mathfrak{T}_1] \times R$ consists of all sets of the form $V \times R_\varepsilon$, where V is in a basis for the neighbourhood system of $\boldsymbol{o}$ in $E_1[\mathfrak{T}_1]$, $\varepsilon \in R_+$ and $R_\varepsilon = \{ a \in R \mid |a| \leq \varepsilon \}$. Likewise for E_2.

Let E_1 and E_2 be in duality. For a subset M of E_1 we define

$$M^\perp = \{ \xi \in E_2 \mid \xi\boldsymbol{x} = 0 \text{ for all } \boldsymbol{x} \in M \}.$$

Likewise for $M \subseteq E_2$. Putting $(M^\perp)^\perp = M^{\perp\perp}$ and $(M^{\perp\perp})^\perp = M^{\perp\perp\perp}$, we have

$M \subseteq M^{\perp\perp}$ and $M^{\perp} = M^{\perp\perp\perp}$ for any subset M. Further, $M^{\perp}$ and $M^{\perp\perp}$ are subspaces which are closed in every admissible topology, and $M = M^{\perp\perp}$ if and only if M is a subspace which is closed in every admissible topology.

A linear manifold in a vector space E is a set of the form $\boldsymbol{y}+H$, where H is a subspace in E. The intersection of closed linear manifolds is a closed linear manifold. The intersection of all closed linear manifolds containing a subset M of $E\,[\mathfrak{T}]$ is denoted $m(M)$. An interior point of M in $m(M)$ is called a relative interior point of M.

If $\boldsymbol{y}+H$ is a linear manifold in E, and H has codimension one, then $\boldsymbol{y}+H$ is called a hyperplane. For every hyperplane $\boldsymbol{y}+H$ in E there exists a linear function ξ on E and a $c \in R$ such that $\boldsymbol{y}+H = \{\boldsymbol{x} \in E \mid \xi\boldsymbol{x} = c\}$. Conversely, if ξ is a linear function on E and c is in R, then the set $\{\boldsymbol{x} \in E \mid \xi\boldsymbol{x} = c\}$ is a hyperplane in E. Let $E\,[\mathfrak{T}]$ be a topological vector space. Then the hyperplane $\boldsymbol{y}+H$ is closed if and only if a corresponding linear function ξ is continuous. A non-closed hyperplane is dense in $E\,[\mathfrak{T}]$.

For $\xi \in (E\,[\mathfrak{T}])'$ and $c \in R$, the sets $\{\boldsymbol{x} \in E \mid \xi\boldsymbol{x} \leq c\}$ and $\{\boldsymbol{x} \in E \mid \xi\boldsymbol{x} \geq c\}$ are called the closed halfspaces determined by the hyperplane. They are closed convex sets. The sets $\{\boldsymbol{x} \in E \mid \xi\boldsymbol{x} < c\}$ and $\{\boldsymbol{x} \in E \mid \xi\boldsymbol{x} > c\}$ are called the open halfspaces determined by the hyperplane. They are open convex sets. A closed hyperplane in $E\,[\mathfrak{T}]$ is said to separate the sets A and B if A is contained in one of the two closed halfspaces determined by the hyperplane and B is contained in the other one. If A is contained in one of the open halfspaces and B in the other one, then the hyperplane is said to separate strictly. In that case A and B have no common points.

In locally convex spaces we have the following theorems:

1.1 If A is a closed convex set and $\boldsymbol{x}$ is a point not contained in A, then there exists a closed hyperplane which separates A and $\{\boldsymbol{x}\}$ strictly ([7] p. 245).

1.2. Every closed convex set A is the intersection of all closed halfspaces containing it ([7] p. 246).

2. Functions (D, f)

Let $E\,[\mathfrak{T}]$ be a locally convex topological vector space. Then also $E\,[\mathfrak{T}]\times R$ is a locally convex topological vector space.

The functions considered in the following are real functions defined on non-empty subsets of E. A pair consisting of a function f and its domain D will be denoted (D, f) and called a function in E.

If $\boldsymbol{x} \in D$ has a neighbourhood $\boldsymbol{x}+V$ such that $(\boldsymbol{x}+V) \cap (D \setminus \{\boldsymbol{x}\})$ is empty, then $\boldsymbol{x}$ is called an isolated point of D. Convex sets consisting of more than one point have no isolated points.

If (D, f) is a function in E, we define for a non-isolated point $\boldsymbol{x} \in \overline{D}$

$$\liminf_{z \to x} f(z) = \sup_{V \in \mathfrak{V}} \{\inf \{ f(z) \mid z \in (x+V) \cap (D \setminus \{x\}) \}\},$$

where $\mathfrak{V}$ is a basis for the neighbourhood system of $\boldsymbol{o}$ in E. If $\boldsymbol{x} \in D$ is isolated, we put

$$\liminf_{z \to x} f(z) = f(x).$$

Let (D, f) be a function in E. We say that f is *lower semi-continuous* at a point $\boldsymbol{x} \in D$ if

$$f(x) \leqq \liminf_{z \to x} f(z).$$

If f is lower semi-continuous at every point of D, (D, f) is said to be lower semi-continuous.

If (D, f) is a lower semi-continuous function such that for all $\boldsymbol{x} \in \overline{D}$

$$\liminf_{z \to x} f(z) < \infty \qquad \text{implies} \qquad x \in D,$$

then (D, f) is said to be *closed*. Theorem 2.2 below motivates this definition.

A function (D, f) is said to be *convex* if D is a convex set and

$$f((1-t)x + ty) \leqq (1-t) f(x) + t f(y)$$

for all $\boldsymbol{x}, \boldsymbol{y} \in D$ and $0 \leqq t \leqq 1$.

For any function (D, f) we define

$$[D, f] = \{(x, x) \in E \times R \mid x \in D, x \geqq f(x)\}.$$

Then the following statement obviously holds.

2.1. *A function (D, f) is convex if and only if $[D, f]$ is a convex set.*

Further, we have

2.2. *A function (D, f) is closed if and only if $[D, f]$ is a closed set.*

Proof. For $a \in R$ we define

$$T_a = \{x \in D \mid f(x) \leqq a\}.$$

If (D, f) is a closed function, then T_a is closed for every $a \in R$. For, $\boldsymbol{x}$ not in T_a implies $\boldsymbol{x}$ not in $\overline{D}$ or

$$\liminf_{z \to x} f(z) > a.$$

Thus there exists a $V \in \mathfrak{V}$ such that $(\boldsymbol{x}+V) \cap T_a$ is empty, which proves that the complement of T_a is open. Now let $(\boldsymbol{y}, b) \in \overline{[D, f]}$. Then $\boldsymbol{y} \in \overline{T}_a = T_a$ for every $a > b$, whence $\boldsymbol{y} \in D$ and $f(\boldsymbol{y}) \leqq b$. Consequently $(\boldsymbol{y}, b) \in [D, f]$, and so $[D, f]$ is closed.

Conversely, let $[D, f]$ be closed. Obviously the set

$$\{(\boldsymbol{x}, a) \in E \times R \mid \boldsymbol{x} \in E\}$$

is closed for every $a \in R$. Thus,

$$[D, f] \cap \{(\boldsymbol{x}, a) \mid \boldsymbol{x} \in E\}$$

is closed for every $a \in R$. This implies that T_a is closed for every $a \in R$. To prove that (D, f) is closed we consider an $\boldsymbol{x} \in \bar{D}$ such that

$$b = \liminf_{\boldsymbol{z} \to \boldsymbol{x}} f(\boldsymbol{z}) < \infty .$$

Now $b = -\infty$ would imply $\boldsymbol{x} \in \overline{T}_a = T_a$ for every $a \in R$ which is impossible. Hence $b \in R$, and clearly $\boldsymbol{x} \in \overline{T}_b = T_b$. So $\boldsymbol{x} \in D$ and $f(\boldsymbol{x}) \leqq b$ which proves that (D, f) is closed.

As a consequence of 1.2, 2.1 and 2.2 we have

2.3. *If $\mathfrak{T}_1$ and $\mathfrak{T}_2$ are locally convex vector space topologies on E such that $(E[\mathfrak{T}_1])' = (E[\mathfrak{T}_2])'$, then $\mathfrak{T}_1$ and $\mathfrak{T}_2$ determine the same closed convex functions in E.*

2.4. *If (D, f) is a convex function, then $f(\boldsymbol{x}) \geqq \liminf_{\boldsymbol{z} \to \boldsymbol{x}} f(\boldsymbol{z})$ for all $\boldsymbol{x} \in D$.*

Proof. If $D = \{\boldsymbol{x}\}$, there is nothing to prove. Otherwise consider a $\boldsymbol{y} \in D$, $\boldsymbol{y} \neq \boldsymbol{x}$. For $0 < t \leqq 1$ we have $(1-t)\boldsymbol{x} + t\boldsymbol{y} \in D \setminus \{\boldsymbol{x}\}$. Then

$$\liminf_{\boldsymbol{z} \to \boldsymbol{x}} f(\boldsymbol{z}) \leqq \liminf_{t \to 0} ((1-t) f(\boldsymbol{x}) + t f(\boldsymbol{y})) = f(\boldsymbol{x}).$$

From 2.4 we deduce

2.5. *A convex function (D, f) is closed if and only if*

$$D = \{\boldsymbol{x} \in \bar{D} \mid \liminf_{\boldsymbol{z} \to \boldsymbol{x}} f(\boldsymbol{z}) < \infty\}$$

and

$$f(\boldsymbol{x}) = \liminf_{\boldsymbol{z} \to \boldsymbol{x}} f(\boldsymbol{z}) \qquad \text{for } \boldsymbol{x} \in D.$$

The following four propositions are valid for arbitrary topological vector spaces.

2.6. *If (D, f) is a convex function, and there exists an $\boldsymbol{x} \in \overline{D}$ such that f is bounded below in some neighbourhood of $\boldsymbol{x}$ in D, then we have:*

(i) *f is bounded below on every bounded subset of D.*

(ii) *Every point of $\overline{D}$ has a neighbourhood in D in which f is bounded below.*

PROOF. We may assume that $\boldsymbol{x} = \boldsymbol{o} \in D$ and $f(\boldsymbol{o}) = 0$. Let $b \in R$ and $V \in \mathfrak{V}$, V open and symmetric, be such that $f(\boldsymbol{z}) \geqq b$ for all $\boldsymbol{z} \in V \cap D$. Let $0 < t \leqq 1$. For every $\boldsymbol{z} \in t^{-1}V \cap D$ we have

$$(1-t)\,\boldsymbol{o} + t\boldsymbol{z} \in V \cap D,$$

whence

$$b \leqq f((1-t)\,\boldsymbol{o} + t\boldsymbol{z}) \leqq (1-t)\,f(\boldsymbol{o}) + tf(\boldsymbol{z}),$$

that is

$$f(\boldsymbol{z}) \geqq t^{-1}b.$$

If M is a bounded set, then $M \subseteq t^{-1}V$ for some t, where $0 < t \leqq 1$. In particular, for every $\boldsymbol{y} \in \overline{D}$ there exists a t, where $0 < t \leqq 1$. such that $\boldsymbol{y} \in t^{-1}V$. And $t^{-1}V$ is a neighbourhood of $\boldsymbol{y}$. Hence, the assertions (i) and (ii) follow from what has been proved above.

Obviously 2.6 (ii) is equivalent to

2.6. (iii) *If (D, f) is a convex function, then either*

$$\liminf_{\boldsymbol{z} \to \boldsymbol{x}} f(\boldsymbol{z}) > -\infty \qquad \textit{for all } \boldsymbol{x} \in \overline{D}$$

or

$$\liminf_{\boldsymbol{z} \to \boldsymbol{x}} f(\boldsymbol{z}) = -\infty \qquad \textit{for all } \boldsymbol{x} \in \overline{D}.$$

REMARK TO 2.6 (iii). In finite-dimensional spaces we always have the first alternative, whereas in infinite-dimensional spaces the second one may occur. Every non-continuous linear function ξ in a topological vector space $E[\mathfrak{T}]$ provides an example, since for all $c \in R$ the set $\{\boldsymbol{x} \mid \xi\boldsymbol{x} = c\}$ is dense in $E[\mathfrak{T}]$.

Next we prove (cf. [2] p. 92).

2.7. *Let (D, f) be a convex function, and let D be open. If there exists a point $\boldsymbol{x} \in D$ such that f is bounded above in some neighbourhood of $\boldsymbol{x}$, then f is continuous on D.*

PROOF. Obviously we may assume that $\boldsymbol{x} = \boldsymbol{o}$ and $f(\boldsymbol{o}) = 0$. Let $a \in R$ and $V \in \mathfrak{V}$, V symmetric, be such that $f(\boldsymbol{z}) \leq a$ for all $\boldsymbol{z} \in V$. Consider an ε such that $0 < \varepsilon < 1$. If $\boldsymbol{z} \in \varepsilon V$, then

$$f(\boldsymbol{z}) = f\left((1-\varepsilon)\,\boldsymbol{o} + \varepsilon\left(\frac{1}{\varepsilon}\,\boldsymbol{z}\right)\right) \leqq (1-\varepsilon)\,f(\boldsymbol{o}) + \varepsilon\, f\left(\frac{1}{\varepsilon}\,\boldsymbol{z}\right) \leqq \varepsilon a,$$

since $\varepsilon^{-1}\boldsymbol{z} \in V$. Further

$$0 = f(\boldsymbol{o}) = f\left(\frac{1}{1+\varepsilon}\,\boldsymbol{z} + \left(1 - \frac{1}{1+\varepsilon}\right)\left(-\frac{1}{\varepsilon}\,\boldsymbol{z}\right)\right) \leqq \frac{1}{1+\varepsilon}\, f(\boldsymbol{z}) + \left(1 - \frac{1}{1+\varepsilon}\right) f\left(-\frac{1}{\varepsilon}\,\boldsymbol{z}\right),$$

that is,

$$f(\boldsymbol{z}) \geqq -\varepsilon\, f\left(-\frac{1}{\varepsilon}\,\boldsymbol{z}\right) \geqq -\varepsilon a,$$

since $-\varepsilon^{-1}\boldsymbol{z} \in V$. Hence we have proved that $\boldsymbol{z} \in \varepsilon V$ implies $|f(\boldsymbol{z})| \leqq \varepsilon a$. This shows that f is continuous at $\boldsymbol{x}$.

Let $\boldsymbol{y}$ be in D. We shall prove that $\boldsymbol{y}$ has a neighbourhood in which f is bounded above. This will complete the proof of 2.7. Since D is open, there exists a $\varrho > 1$ such that $\varrho\boldsymbol{y} \in D$. Let $\boldsymbol{z}$ be in $\boldsymbol{y} + (1-\varrho^{-1})\,V$, where V has the same meaning as above. Then

$$\boldsymbol{z} = \boldsymbol{y} + \left(1 - \frac{1}{\varrho}\right)\boldsymbol{y}_0 = \frac{1}{\varrho}\,(\varrho\boldsymbol{y}) + \left(1 - \frac{1}{\varrho}\right)\boldsymbol{y}_0$$

with $\boldsymbol{y}_0 \in V \subseteq D$. Since $0 < \varrho^{-1} < 1$, this implies $\boldsymbol{z} \in D$. Hence $\boldsymbol{y} + (1-\varrho^{-1})\,V \subseteq D$. Further

$$f(\boldsymbol{z}) \leqq \frac{1}{\varrho}\, f(\varrho\boldsymbol{y}) + \left(1 - \frac{1}{\varrho}\right) f(\boldsymbol{y}_0) \leqq \frac{1}{\varrho}\, f(\varrho\boldsymbol{y}) + \left(1 - \frac{1}{\varrho}\right) a,$$

which proves that f is bounded above in $\boldsymbol{y} + (1-\varrho^{-1})V$.

2.8. *If (D, f) is a convex function, and D has a non-empty relative interior $\mathring{D}$, then the following statements are equivalent*:

a) *At least one $\boldsymbol{x} \in \mathring{D}$ has a neighbourhood in D in which f is bounded above.*

b) *Every $\boldsymbol{x} \in \mathring{D}$ has a neighbourhood in D in which f is bounded above.*

c) *f is continuous at at least one $\boldsymbol{x} \in \mathring{D}$.*

d) *f is continuous on $\mathring{D}$.*

e) *$[D, f]$ has a non-empty relative interior.*

Proof. We may assume that $m(D)$ is a subspace. Since $\mathring{D}$ is open and convex in $m(D)$, we may apply 2.7 to the function $(\mathring{D}, f)$, i.e. the restriction of f to $\mathring{D}$. This yields the equivalence of the statements a), b), c) and d). Since $m([D, f]) = m(D) \times R$, the statements a) and e) are obviously equivalent. Thus 2.8 is proved.

2.9. *If (D, f) is a convex function, and $[D, f]$ has a non-empty relative interior $[D, \overset{\circ}{f}]$, then D has a non-empty relative interior $\mathring{D}$, and the projection mapping $E \times R \to E$ maps $[D, \overset{\circ}{f}]$ onto $\mathring{D}$.*

PROOF. This is an immediate consequence of 2.8.

Finally, we shall prove a result concerning convex functions in Banach spaces.

2.10. *Let (D, f) be a lower semi-continuous convex function in a Banach space, and let D have a non-empty relative interior $\mathring{D}$. Then f is continuous on $\mathring{D}$.*

PROOF. We shall use the following lemma (cf. [7] p. 45):

Let S be a complete metric space and φ a lower semi-continuous function on S. Further, let T denote the set of points in S having a neighbourhood in which φ is bounded above. Then T is dense in S.

There exists a closed set $S \subseteq \mathring{D}$ with a non-empty interior $\mathring{S}$ in $m(D)$. Applying the lemma to the restriction of f to S, we obtain that $\mathring{S}$ contains a point $\boldsymbol{x}$ such that f is bounded above in a neighbourhood $(\boldsymbol{x}+V) \cap S$ of $\boldsymbol{x}$ in S. But $(\boldsymbol{x}+V) \cap S$ is also a neighbourhood of $\boldsymbol{x}$ in D. Hence the assertion follows from 2.8.

3. Conjugate functions

Let E_1 and E_2 be two vector spaces in duality under $\mathfrak{B}$, and let $\mathfrak{T}_1$ and $\mathfrak{T}_2$ be admissible topologies on E_1 and E_2. Then $E_2 = (E_1[\mathfrak{T}_1])'$ and $E_1 = (E_2[\mathfrak{T}_2])'$. Further $E_1 \times R$ and $E_2 \times R$ are in duality under $\tilde{\mathfrak{B}}((\xi, \xi), (\boldsymbol{x}, x)) = \mathfrak{B}(\xi, \boldsymbol{x}) + \xi x = \xi \boldsymbol{x} + \xi x$, and the product space topologies are admissible. So $(E_1[\mathfrak{T}_1] \times R)' = E_2 \times R$ and $(E_2[\mathfrak{T}_2] \times R)' = E_1 \times R$.

For a function (D, f) in E_1 we define

$$D' = \left\{ \xi \in E_2 \,\middle|\, \sup_{\boldsymbol{x} \in D} (\xi \boldsymbol{x} - f(\boldsymbol{x})) < \infty \right\},$$

$$f'(\xi) = \sup_{\boldsymbol{x} \in D} (\xi \boldsymbol{x} - f(\boldsymbol{x})) \qquad \text{for } \xi \in D'.$$

The set D' may be empty. If D' is not empty, the function $(D, f)' = (D', f')$ in E_2 is called *the conjugate of* (D, f).

If (Γ, φ) is a function in E_2, the conjugate (Γ', φ') in E_1 is defined analogously. In particular we have a *second conjugate* $(D, f)''$ of a function (D, f) in E_1, namely the conjugate of (D', f'). Setting $(D')' = D''$, $(f')' = f''$, we have for the second conjugate $(D, f)'' = ((D')', (f')') = (D'', f'')$

$$D'' = \left\{ \boldsymbol{x} \in E_1 \,\middle|\, \sup_{\xi \in D'} (\xi \boldsymbol{x} - f'(\xi)) < \infty \right\},$$

$$f''(\boldsymbol{x}) = \sup_{\xi \in D'} (\xi \boldsymbol{x} - f'(\xi)) \qquad \text{for } \boldsymbol{x} \in D''.$$

Hereafter the meaning of $(D^{(n)}, f^{(n)})$, $n \in Z_+$, is clear.

In the set of functions in a vector space a partial order relation is defined by

$$(D_1, f_1) \leqq (D_2, f_2) \text{ if and only if } [D_2, f_2] \subseteq [D_1, f_1].$$

Then $(D_1, f_1) \leqq (D_2, f_2)$ holds if and only if $D_2 \subseteq D_1$ and $f_1(\boldsymbol{x}) \leq f_2(\boldsymbol{x})$ for all $\boldsymbol{x} \in D_2$. Accordingly, (D_1, f_1) is called a *minorant* of (D_2, f_2), and (D_2, f_2) a *majorant* of (D_1, f_1), when $(D_1, f_1) \leq (D_2, f_2)$.

3.1. *If (D, f) has a conjugate, and $(D, f) \leqq (D_1, f_1)$, then (D_1, f_1) has a conjugate, and $(D_1', f_1') \leqq (D', f')$.*

Proof. Let ξ be in D'. Then

$$f'(\xi) = \sup_{\boldsymbol{x} \in D} (\xi \boldsymbol{x} - f(\boldsymbol{x})) \geqq \sup_{\boldsymbol{x} \in D_1} (\xi \boldsymbol{x} - f_1(\boldsymbol{x})),$$

which implies $\xi \in D_1'$ and $f_1'(\xi) \leqq f'(\xi)$. This proves 3.1.

3.2. *If (D, f) has a conjugate, then it has a conjugate of any order $n \in Z_+$. Further $(D'', f'') \leqq (D, f)$, and $(D^{(n)}, f^{(n)})$ equals (D', f') for n odd, (D'', f'') for n even.*

Proof. Let $\boldsymbol{x}$ be in D. Then we have $f(\boldsymbol{x}) \geqq \xi \boldsymbol{x} - f'(\xi)$ for all $\xi \in D'$, which implies $\boldsymbol{x} \in D''$ and $f(\boldsymbol{x}) \geqq f''(\boldsymbol{x})$. Hence, (D, f) has a second conjugate, and $(D'', f'') \leqq (D, f)$. Since (D'', f'') is the conjugate of (D', f'), the same argument applied to (D', f') shows that (D, f) has a third conjugate, and $(D''', f''') \leqq (D', f')$. In particular, (D'', f'') has a conjugate, and since $(D'', f'') \leqq (D, f)$, 3.1 yields $(D', f') \leqq (D''', f''')$. Hence $(D''', f''') = (D', f')$. Hereafter, the unproved part of 3.2 follows by induction.

A closed hyperplane in $E_1[\mathfrak{T}_1] \times R$ is a set of the form

$$\{(\boldsymbol{x}, x) \in E_1 \times R \mid \eta \boldsymbol{x} + \eta x = c\},$$

where $(\eta, \eta) \in (E_1[\mathfrak{T}_1] \times R)' = E_2 \times R$ and $c \in R$, that is the set of those points $(\boldsymbol{x}, x)$ at which a continuous linear function (η, η) takes the value c. For the sake of convenience we specify the hyperplane by its equation $\eta \boldsymbol{x} + \eta x = c$. A hyperplane $\eta \boldsymbol{x} + \eta x = c$ in $E_1[\mathfrak{T}_1] \times R$ is called vertical if $\eta = 0$, non-vertical if $\eta \neq 0$.

Let M be a non-empty subset of $E_1[\mathfrak{T}_1] \times R$. By a *barrier* of M we mean a non-vertical closed hyperplane such that M is contained in one of the two closed halfspaces determined by the hyperplane. This means that if $\eta \boldsymbol{x} + \eta x = c$ is a barrier of M, we have either $\eta \boldsymbol{x} + \eta x \geqq c$ or $\eta \boldsymbol{x} + \eta x \leqq c$ for all

$(\boldsymbol{x}, x) \in M$. If M is of the form $[D, f]$, the equation of a barrier $\eta \boldsymbol{x} + \eta x = c$ can always be written in the form $\xi \boldsymbol{x} - x = \xi$, $(\xi, -1) \in E_2 \times R$, $\xi \in R$, and such that $\xi \boldsymbol{x} - x \leq \xi$ for all $(\boldsymbol{x}, x) \in M = [D, f]$. For, division by $-\eta$ gives an equation of the form $\xi \boldsymbol{x} - x = \xi$, and $\xi \boldsymbol{x} - x \geqq \xi$ for all $(\boldsymbol{x}, x) \in [D, f]$ is impossible, since $(\boldsymbol{x}, x) \in [D, f]$ and $k \in R_+$ implies $(\boldsymbol{x}, x + k) \in [D, f]$.

A barrier of the set $[D, f]$ will also be referred to as a barrier of (D, f).

The previously defined barriers of a function (D, f) have a close relation to the conjugate of (D, f). Let (D, f) be a function in E_1, and let $\xi \boldsymbol{x} - x = \xi$, where $(\xi, -1) \in E_2 \times R$, $\xi \in R$, be a barrier of (D, f). Then $\xi \geq \xi \boldsymbol{x} - x$ for all $(\boldsymbol{x}, x) \in [D, f]$. In particular, $\xi \geqq \xi \boldsymbol{x} - f(\boldsymbol{x})$ for all $\boldsymbol{x} \in D$. Hence $\xi \in D'$ and $\xi \geqq f'(\xi)$, and so $(\xi, \xi) \in [D', f']$. Conversely, let (D, f) have a conjugate, and let (ξ, ξ) be in $[D', f']$. Then we have

$$\xi \geqq f'(\xi) \geqq \xi \boldsymbol{x} - f(\boldsymbol{x}) \geqq \xi \boldsymbol{x} - x$$

for all $(\boldsymbol{x}, x) \in [D, f]$, which shows that $\xi \boldsymbol{x} - x = \xi$ is a barrier of (D, f). Hence, we have proved

3.3. *A function (D, f) has a conjugate if and only if it has a barrier. If (D, f) has a conjugate, then the point (ξ, ξ) is in $[D', f']$ if and only if the hyperplane $\{(\boldsymbol{x}, x) \mid \xi \boldsymbol{x} - x = \xi\}$ is a barrier of (D, f).*

Because of the duality, 3.3 is also valid for functions in E_2, in particular for (D', f'). This gives

3.4. *If (D, f) has a conjugate, then the point $(\boldsymbol{x}, x)$ is in $[D'', f'']$ if and only if the hyperplane $\{(\xi, \xi) \mid \xi \boldsymbol{x} - \xi = x\}$ is a barrier of (D', f').*

From 3.3 and 3.4 follows immediately

3.5. *If (D, f) has a conjugate, then*

$$\text{(i)} \quad [D', f'] = \bigcap_{(\boldsymbol{x}, x) \in [D, f]} \{(\xi, \xi) \mid \xi \boldsymbol{x} - \xi \leq x\}.$$

$$\text{(ii)} \quad [D'', f''] = \bigcap_{(\xi, \xi) \in [D', f']} \{(\boldsymbol{x}, x) \mid \xi \boldsymbol{x} - x \leq \xi\}.$$

Consequently the sets $[D', f']$ and $[D'', f'']$ are both intersections of closed halfspaces, and thus convex and closed. Thus, by 2.1 and 2.2, we have

3.6. THEOREM. *If (D, f) has a conjugate, then (D', f') and (D'', f'') are closed convex functions.*

Concerning the existence of conjugates we have

3.7. THEOREM. *If (D, f) is a closed convex function, then it has a conjugate.*

PROOF. For $\boldsymbol{y} \in D$ and $k \in R_+$ the point $(\boldsymbol{y}, f(\boldsymbol{y}) - k)$ is not in $[D, f]$. Consequently (cf. theorem 1.1) there exists a closed hyperplane $\eta \boldsymbol{x} + \eta x = c$, $(\eta, \eta) \in E_2 \times R$, $c \in R$, that strictly separates $[D, f]$ and the point $(\boldsymbol{y}, f(\boldsymbol{y}) - k)$. We can assume $\eta \boldsymbol{x} + \eta x < c$ for all $(\boldsymbol{x}, x) \in [D, f]$ and $\eta \boldsymbol{y} + \eta (f(\boldsymbol{y}) - k) > c$. Since $\boldsymbol{y} \in D$, it follows that $\eta \neq 0$. Hence $\eta \boldsymbol{x} + \eta x = c$ is a barrier of (D, f).

In 3.2 we showed that $(D'', f'') \leq (D, f)$. A fundamental question is under which conditions $(D'', f'') = (D, f)$ holds. By 3.6, it is necessary that (D, f) be convex and closed. Theorem 3.10 below states that this is also sufficient. In the proof we shall use

3.8. *Let M be a closed convex subset of $E_1 \times R$. If M has at least one barrier, then M is the intersection of all closed halfspaces containing M and bounded by barriers of M.*

PROOF. Being convex and closed, M is the intersection of all closed halfspaces containing it (cf. theorem 1.2). Thus we have to show that if there exists a vertical closed hyperplane separating M and the point $(\boldsymbol{y}, y)$, and not containing $(\boldsymbol{y}, y)$, then there exists a non-vertical closed hyperplane with the same property. Let $\zeta \boldsymbol{x} = c$, $(\zeta, 0) \in E_2 \times R$, $c \in R$, be a vertical closed hyperplane in $E_1 \times R$ such that $\zeta \boldsymbol{y} > c$ and $\zeta \boldsymbol{x} \leq c$ for all $\boldsymbol{x} \in p(M)$, p denoting the projection mapping $E_1 \times R \to E_1$. Further let $\eta \boldsymbol{x} + \eta x = \gamma$, $(\eta, \eta) \in E_2 \times R$, $\eta \neq 0$, $\gamma \in R$, be a barrier of M. We may assume $\eta \boldsymbol{x} + \eta x \leq \gamma$ for all $(\boldsymbol{x}, x) \in M$. Now, for every $t \in R_+$

$$\{ (\boldsymbol{x}, x) \in E_1 \times R \mid (\eta + t\zeta)\, \boldsymbol{x} + \eta x = \gamma + tc \}$$

is a closed non-vertical hyperplane such that

$$(\eta + t\zeta)\, \boldsymbol{x} + \eta x \leq \gamma + tc$$

for all $(\boldsymbol{x}, x) \in M$. If

$$(\eta + t\zeta)\, \boldsymbol{y} + \eta y \leq \gamma + tc,$$

then

$$t(\zeta \boldsymbol{y} - c) \leq \gamma - \eta \boldsymbol{y} - \eta y.$$

But this cannot be true for all $t \in R_+$ since $\zeta \boldsymbol{y} > c$. Consequently, there exists a t_0 such that

$$(\eta + t_0 \zeta)\, \boldsymbol{y} + \eta y > \gamma + t_0 c,$$

and so the non-vertical hyperplane

$$\{ (\boldsymbol{x}, x) \in E_1 \times R \mid (\eta + t_0 \zeta)\, \boldsymbol{x} + \eta x = \gamma + t_0 c \}$$

separates M and the point $(\boldsymbol{y}, y)$, and does not contain $(\boldsymbol{y}, y)$.

3.9. THEOREM. *If (D, f) has a conjugate, then*

$$[D'', f''] = \overline{\text{conv}}\,[D, f].$$

PROOF. By 3.3 and 3.5 (ii), $[D'', f'']$ is the intersection of all closed halfspaces containing $[D, f]$ and bounded by barriers of $[D, f]$. Since the barriers of $[D, f]$ are identical with the barriers of $\overline{\text{conv}}\,[D, f]$, it follows from 3.8 that $\overline{\text{conv}}\,[D, f]$ is the intersection of the same closed halfspaces as $[D'', f'']$, which proves the statement.

Since for a closed convex function (D, f)

$$[D, f] = \overline{\text{conv}}\,[D, f],$$

3.9 yields the theorem previously mentioned:

3.10. THEOREM. *If (D, f) is convex and closed, then $(D, f) = (D'', f'')$.*

We note that, under the assumptions of 3.10, the existence of (D'', f'') is ensured by 3.7.

As easily seen, there exists a closed convex minorant of the function (D, f) if and only if (D, f) has a conjugate. In that case there even exists a greatest closed convex minorant of (D, f) namely (D'', f''). For, let (D_1, f_1) be a closed convex minorant. Then $[D_1, f_1]$ is a closed convex set, and $[D, f] \subseteq [D_1, f_1]$. By 3.9, this implies $[D'', f''] \subseteq [D_1, f_1]$. So we have proved

3.11. THEOREM. *If (D, f) has a conjugate, then (D'', f'') is its greatest closed convex minorant.*

The question arises which functions do have conjugates. A necessary condition is that

$$\liminf_{z \to x} f(z) > -\infty \text{ for all } x \in \bar{D}.$$

For, let $\xi x - \alpha = \xi$ be a barrier. Since ξ is continuous, it is possible for every $x \in E$ to find a $V \in \mathfrak{V}$ such that $\xi z \geq \xi x - 1$ for all $z \in x + V$. From this we deduce

$$\begin{aligned} \liminf_{z \to x} f(z) &\geq \inf \{ f(z) \mid z \in (x+V) \cap (D \setminus \{x\}) \} \\ &\geq \inf \{ \xi z - \xi \mid z \in x + V \} \geq \xi x - 1 - \xi > -\infty. \end{aligned}$$

We shall prove that, for convex functions, this is also sufficient.

3.12. THEOREM. (i) *Let (D, f) be a convex function. Then (D, f) has a conjugate if (and only if)*

$$\liminf_{z \to x} f(z) > -\infty \qquad \text{for all } x \in \bar{D}.$$

In view of 2.6. (iii), we may also formulate the theorem in the following way:

3.12. THEOREM. (ii) *Let (D, f) be a convex function, and let $\boldsymbol{x}$ be an arbitrary point in $\overline{D}$. Then (D, f) has a conjugate if (and only if)*

$$\liminf_{\boldsymbol{z}\to\boldsymbol{x}} f(\boldsymbol{z}) > -\infty .$$

PROOF. Let (D, f) be a convex function such that for all $\boldsymbol{x} \in \overline{D}$

$$\liminf_{\boldsymbol{z}\to\boldsymbol{x}} f(\boldsymbol{z}) > -\infty .$$

Then the function

$$\hat{f}(\boldsymbol{x}) = \liminf_{\boldsymbol{z}\to\boldsymbol{x}} f(\boldsymbol{z})$$

is well-defined on the set

$$\hat{D} = \left\{ \boldsymbol{x} \in \overline{D} \mid \liminf_{\boldsymbol{z}\to\boldsymbol{x}} f(\boldsymbol{z}) < \infty \right\}.$$

a) *$(\hat{D}, \hat{f})$ is a convex function.*

Proof of a). Let $\boldsymbol{y}_0$ and $\boldsymbol{y}_1$ be in $\hat{D}$, and consider $\boldsymbol{y}_t = (1-t)\,\boldsymbol{y}_0 + t\boldsymbol{y}_1$, where $0 \leq t \leq 1$. Let $\boldsymbol{y}_t + V$ be a convex neighbourhood of $\boldsymbol{y}_t$. From the definition of $(\hat{D}, \hat{f})$ it follows that for every $\varepsilon \in R_+$ there exist a $\boldsymbol{z}_0 \in (\boldsymbol{y}_0 + V) \cap (D \setminus \{\boldsymbol{y}_0\})$ and a $\boldsymbol{z}_1 \in (\boldsymbol{y}_1 + V) \cap (D \setminus \{\boldsymbol{y}_1\})$ such that $f(\boldsymbol{z}_0) \leq \hat{f}(\boldsymbol{y}_0) + \varepsilon$ and $f(\boldsymbol{z}_1) \leq \hat{f}(\boldsymbol{y}_1) + \varepsilon$.

Since $\boldsymbol{z}_0$ and $\boldsymbol{z}_1$ are in D, the point $\boldsymbol{z}_t = (1-t)\,\boldsymbol{z}_0 + t\boldsymbol{z}_1$ is in D, and

$$f(\boldsymbol{z}_t) \leq (1-t)\,f(\boldsymbol{z}_0) + t f(\boldsymbol{z}_1) \leq (1-t)\,\hat{f}(\boldsymbol{y}_0) + t\hat{f}(\boldsymbol{y}_1) + \varepsilon .$$

Further $\boldsymbol{z}_t \in (1-t)\,(\boldsymbol{y}_0 + V) + t\,(\boldsymbol{y}_1 + V) = \boldsymbol{y}_t + V$. Hence

$$\inf \left\{ f(\boldsymbol{z}) \mid \boldsymbol{z} \in (\boldsymbol{y}_t + V) \cap D \right\} \leq (1-t)\,\hat{f}(\boldsymbol{y}_0) + t\hat{f}(\boldsymbol{y}_1) .$$

This implies

$$\inf \left\{ f(\boldsymbol{z}) \mid \boldsymbol{z} \in (\boldsymbol{y}_t + V) \cap (D \setminus \{\boldsymbol{y}_t\}) \right\} \leq (1-t)\,\hat{f}(\boldsymbol{y}_0) + t\hat{f}(\boldsymbol{y}_1),$$

since, if $\boldsymbol{y}_t \in D$,

$$f(\boldsymbol{y}_t) \geq \liminf_{\boldsymbol{z}\to\boldsymbol{y}_t} f(\boldsymbol{z}) \geq \inf \left\{ f(\boldsymbol{z}) \mid \boldsymbol{z} \in (\boldsymbol{y}_t + V) \cap (D \setminus \{\boldsymbol{y}_t\}) \right\}.$$

Consequently

$$\liminf_{\boldsymbol{z}\to\boldsymbol{y}_t} f(\boldsymbol{z}) \leq (1-t)\,\hat{f}(\boldsymbol{y}_0) + t\hat{f}(\boldsymbol{y}_1),$$

which shows that $(\hat{D}, \hat{f})$ is convex.

b) *$(\hat{D}, \hat{f})$ is a minorant of (D, f).*

Proof of b). From the convexity of (D, f) it follows that $\liminf_{\boldsymbol{z}\to\boldsymbol{x}} f(\boldsymbol{z})$

$\leqq f(\boldsymbol{x})$ for all $\boldsymbol{x} \in D$. This implies $D \subseteq \hat{D}$ and $f(\boldsymbol{x}) \geqq \hat{f}(\boldsymbol{x})$ for all $\boldsymbol{x} \in D$. Hence $(\hat{D}, \hat{f})$ is a minorant of (D, f).

c) *For all* $\boldsymbol{x} \in \overline{D}$ *we have* $\liminf_{\boldsymbol{z} \to \boldsymbol{x}} \hat{f}(\boldsymbol{z}) = \liminf_{\boldsymbol{z} \to \boldsymbol{x}} f(\boldsymbol{z})$.

Proof of c). Let $\boldsymbol{x}$ be in $\overline{D}$. Since $(\hat{D}, \hat{f})$ is a minorant of (D, f), we have

$$\inf \{ \hat{f}(\boldsymbol{z}) \mid \boldsymbol{z} \in (\boldsymbol{x}+V) \cap (\hat{D} \backslash \{\boldsymbol{x}\}) \}$$

$$\leqq \inf \{ f(\boldsymbol{z}) \mid \boldsymbol{z} \in (\boldsymbol{x}+V) \cap (D \backslash \{\boldsymbol{x}\}) \}$$

for all $V \in \mathfrak{V}$. This implies

$$\liminf_{\boldsymbol{z} \to \boldsymbol{x}} \hat{f}(\boldsymbol{z}) \leqq \liminf_{\boldsymbol{z} \to \boldsymbol{x}} f(\boldsymbol{z}).$$

To prove the reversed inequality we consider an arbitrary $\boldsymbol{z}_0 \in (\boldsymbol{x}+V) \cap (\hat{D} \backslash \{\boldsymbol{x}\})$, where $V \in \mathfrak{V}$ is assumed to be open. As the topology $\mathfrak{T}_1$ on E_1 is Hausdorff, and V is open, $(\boldsymbol{x}+V) \backslash \{\boldsymbol{x}\}$ is a neighbourhood of $\boldsymbol{z}_0$. Let $\varepsilon \in R_+$ be given. Since $\hat{f}(\boldsymbol{z}_0) = \liminf_{\boldsymbol{z} \to \boldsymbol{z}_0} f(\boldsymbol{z})$, there exists a $\boldsymbol{z}_1$ such that

$$\boldsymbol{z}_1 \in ((\boldsymbol{x}+V) \backslash \{\boldsymbol{x}\}) \cap (D \backslash \{\boldsymbol{z}_0\}) \subseteq (\boldsymbol{x}+V) \cap (D \backslash \{\boldsymbol{x}\})$$

and

$$f(\boldsymbol{z}_1) \leqq \hat{f}(\boldsymbol{z}_0) + \varepsilon.$$

This proves

$$\inf \{ f(\boldsymbol{z}) \mid \boldsymbol{z} \in (\boldsymbol{x}+V) \cap (D \backslash \{\boldsymbol{x}\}) \} \leqq \hat{f}(\boldsymbol{z}_0).$$

Hence

$$\inf \{ f(\boldsymbol{z}) \mid \boldsymbol{z} \in (\boldsymbol{x}+V) \cap (D \backslash \{\boldsymbol{x}\}) \}$$

$$\leqq \inf \{ \hat{f}(\boldsymbol{z}) \mid \boldsymbol{z} \in (\boldsymbol{x}+V) \cap (\hat{D} \backslash \{\boldsymbol{x}\}) \},$$

and thus

$$\liminf_{\boldsymbol{z} \to \boldsymbol{x}} f(\boldsymbol{z}) \leqq \liminf_{\boldsymbol{z} \to \boldsymbol{x}} \hat{f}(\boldsymbol{z}).$$

d) $(\hat{D}, \hat{f})$ *is a closed function.*

Proof of d). Let $\boldsymbol{x}$ be a point in $\overline{\hat{D}} = \overline{D}$ such that $\liminf_{\boldsymbol{z} \to \boldsymbol{x}} \hat{f}(\boldsymbol{z}) < \infty$. From c) and the definition of $(\hat{D}, \hat{f})$ it follows that $\boldsymbol{x} \in \hat{D}$ and $\hat{f}(\boldsymbol{x}) = \liminf_{\boldsymbol{z} \to \boldsymbol{x}} \hat{f}(\boldsymbol{z})$. Hence, $(\hat{D}, \hat{f})$ is closed.

Now, from a), b) and d) it follows that (D, f) has a closed convex minorant. Thus, (D, f) has a conjugate.

3.13. Theorem. *If* (D, f) *is a convex function, and it has a conjugate, then the second conjugate* (D'', f'') *is determined by*

$$D'' = \{ \boldsymbol{x} \in \overline{D} \mid \liminf_{\boldsymbol{z} \to \boldsymbol{x}} f(\boldsymbol{z}) < \infty \},$$

$$f''(x) = \liminf_{z \to x} f(z) \qquad \text{for } x \in D''.$$

Consequently, if f is lower semi-continuous at $x \in D$, then $f''(x) = f(x)$.

PROOF. Let (D, f) be convex. If it has a conjugate, then $\liminf_{z \to x} f(z) > -\infty$ for all $x \in \bar{D}$. Hence, we may define $(\hat{D}, \hat{f})$ as in the preceding proof and prove that $(\hat{D}, \hat{f})$ is a closed convex minorant of (D, f). In fact $(\hat{D}, \hat{f})$ is the greatest closed convex minorant of (D, f). For, let (D_1, f_1) be a closed minorant of (D, f). Then for every $x \in \hat{D}$

$$\liminf_{z \to x} f_1(z) \leq \liminf_{z \to x} f(z) = \hat{f}(x) < \infty.$$

Since (D_1, f_1) is closed, this implies $x \in D_1$ and $f_1(x) \leq \hat{f}(x)$, i.e. (D_1, f_1) is a minorant of $(\hat{D}, \hat{f})$. Thus, by 3.11, we have $(\hat{D}, \hat{f}) = (D'', f'')$, which proves the theorem.

4. The conjugates of functions derived from others

In this section we shall consider questions of the following kind. Suppose, a function (D, f) is derived in a certain way from functions (D_i, f_i), $i \in J$, where J is an index set. Is the conjugate (D', f') determined by the conjugates (D_i', f_i'), and in the affirmative case, in what manner?

4.1. THEOREM. *Let the function (D_0, f_0) have a conjugate (D_0', f_0'), and let (D, f) be defined by*

$$D = x_0 + lD_0$$
$$f(x) = kf_0(l^{-1}(x - x_0)) + \xi_0 x + h,$$

where $x_0 \in E_1$, $\xi_0 \in E_2$, and h, k and l are reals such that $k > 0$ and $l \neq 0$. Then (D, f) has a conjugate (D', f') which is determined by

$$D' = \xi_0 + kl^{-1}D_0'$$
$$f'(\xi) = kf_0'(lk^{-1}(\xi - \xi_0)) + (\xi - \xi_0)\, x_0 - h.$$

PROOF. For all $\xi \in E_2$ we have

$$\sup_{x \in D} (\xi x - f(x)) = \sup_{x \in D} (\xi x - kf_0(l^{-1}(x - x_0)) - \xi_0 x - h)$$
$$= k \cdot \sup_{y \in D_0} (lk^{-1}(\xi - \xi_0)\, y - f_0(y)) + (\xi - \xi_0)\, x_0 - h.$$

This proves the theorem.

4.2. THEOREM. *Let* (D_1, f_1) *and* (D_2, f_2) *be closed convex functions such that* $D_1 \cap D_2 \neq \emptyset$, *and let* (D, f) *be defined by*

$$D = D_1 \cap D_2, \quad f(\boldsymbol{x}) = f_1(\boldsymbol{x}) + f_2(\boldsymbol{x}).$$

Then we have:

(i) (D, f) *is a closed convex function.*

(ii) $[D', f'] = \overline{[D_1', f_1'] + [D_2', f_2']}$.

(iii) $D_1' + D_2' \subseteq D' \subseteq \overline{D_1' + D_2'}$.

(iv) *If* $[D', f']$ *has a non-empty relative interior, then*

$$f'(\xi) = \inf \{ f_1'(\xi_1) + f_2'(\xi_2) \mid \xi = \xi_1 + \xi_2, \xi_1 \in D_1', \xi_2 \in D_2' \}$$

for all ξ *in the relative interior of* D'.

PROOF. (i) The convexity is obvious. Since $\liminf_{z \to x} f_1(\boldsymbol{z}) > -\infty$ for all $\boldsymbol{x} \in \bar{D}_1$, and $\liminf_{z \to x} f_2(\boldsymbol{z}) > -\infty$ for all $\boldsymbol{x} \in \bar{D}_2$, the expression

$$\liminf_{z \to x} f_1(\boldsymbol{z}) + \liminf_{z \to x} f_2(\boldsymbol{z})$$

is well-defined for all $\boldsymbol{x} \in \bar{D} \subseteq \bar{D}_1 \cap \bar{D}_2$. Further, for all $\boldsymbol{x} \in \bar{D}$

$$\liminf_{z \to x} f_1(\boldsymbol{z}) + \liminf_{z \to x} f_2(\boldsymbol{z}) \leq \liminf_{z \to x} f(\boldsymbol{z}).$$

Let $\boldsymbol{x} \in \bar{D}$ be such that $\liminf_{z \to x} f(\boldsymbol{z}) < \infty$. Then, by the preceding inequality,

$$\liminf_{z \to x} f_1(\boldsymbol{z}) + \liminf_{z \to x} f_2(\boldsymbol{z}) < \infty.$$

As (D_1, f_1) and (D_2, f_2) are closed, this implies $\boldsymbol{x} \in D_1 \cap D_2 = D$, and

$$f(\boldsymbol{x}) = f_1(\boldsymbol{x}) + f_2(\boldsymbol{x}) \leq \liminf_{z \to x} f(\boldsymbol{z}).$$

Thus (D, f) is closed.

(ii) $D_1 \cap D_2 \neq \emptyset$ implies $[D_1, f_1] \cap [D_2, f_2] \neq \emptyset$. Hence $[D_1', f_1']$ and $[D_2', f_2']$ have a common barrier $\xi \boldsymbol{x} - \xi = x$. Then $\xi \boldsymbol{x} - \xi = 2x$ is a barrier of $[D_1', f_1'] + [D_2', f_2']$. This implies that the closed convex set $\overline{[D_1', f_1'] + [D_2', f_2']}$ is of the form $[\Gamma, \varphi]$, where (Γ, φ) is a closed convex function in E_2. Now $(\Gamma', \varphi') = (D, f)$, which may be proved in the following way. If $(\boldsymbol{x}, x) \in [\Gamma', \varphi']$, then

$$(\xi_1 + \xi_2)\, \boldsymbol{x} - (\xi_1 + \xi_2) \leq x$$

for all $(\xi_1, \xi_1) \in [D_1', f_1']$, $(\xi_2, \xi_2) \in [D_2', f_2']$, and this implies

$$\sup_{\xi \in D_1'} (\xi x - f_1'(\xi)) + \sup_{\xi \in D_2'} (\xi x - f_2'(\xi)) \leq x.$$

Hence $x \in D_1'' \cap D_2'' = D_1 \cap D_2 = D$, and

$$x \geq f_1''(x) + f_2''(x) = f_1(x) + f_2(x) = f(x),$$

that is $(x, x) \in [D, f]$. Conversely, for every $(x, x) \in [D, f]$ we have

$$(\xi_1 + \xi_2)\, x - (\xi_1 + \xi_2) \leq f_1''(x) + f_2''(x) = f_1(x) + f_2(x) = f(x) \leq x$$

for all $(\xi_1, \xi_1) \in [D_1', f_1']$, $(\xi_2, \xi_2) \in [D_2', f_2']$. Thus $\xi x - \xi \leq x$ for all $(\xi, \xi) \in [D_1', f_1'] + [D_2', f_2']$, and consequently then also for all $(\xi, \xi) \in \overline{[D_1', f_1'] + [D_2', f_2']} = [\Gamma, \varphi]$. This shows that $(x, x) \in [\Gamma', \varphi']$. Hence we have proved $(\Gamma', \varphi') = (D, f)$. As (Γ, φ) is convex and closed, this implies $(\Gamma, \varphi) = (D', f')$, which proves (ii).

(iii) This is an obvious consequence of (ii).

(iv) Since $\mathring{M} = \overline{\mathring{M}}$, M convex, $M \neq \emptyset$, it follows from (ii) that the relative interior $[D', {}^{\circ}f']$ of $[D', f']$ is equal to the relative interior of $[D_1', f_1'] + [D_2', f_2']$. (Likewise, we have by (iii) that the relative interior of D' is equal to the relative interior of $D_1' + D_2'$). Hence

$$[D', {}^{\circ}f'] \subseteq [D_1', f_1'] + [D_2', f_2'] \subseteq [D', f'].$$

Let ξ be in the relative interior of D'. Then, by 2.9, there exists a $\xi \in R$ such that $(\xi, \xi) \in [D', {}^{\circ}f']$. Since all points in $[D', f']$ can be reached from $[D', {}^{\circ}f']$, we have

$$(\xi, \zeta) \in [D', {}^{\circ}f'] \subseteq [D_1', f_1'] + [D_2', f_2']$$

for all $\zeta > f'(\xi)$. Thus

$$f'(\xi) = \inf \{\zeta \mid (\xi, \zeta) \in [D_1', f_1'] + [D_2', f_2']\},$$

which proves (iv).

In accordance with the partial order previously defined, a function (D, f) will be called a minorant of a set of functions $\{(D_i, f_i) \mid i \in J\}$ if $(D, f) \leq (D_i, f_i)$ for all $i \in J$. Analogously a majorant is defined.

If there exists a minorant of the set $\{(D_i, f_i) \mid i \in J\}$, then the function (D, f) defined by

$$D = \bigcup_{i \in J} D_i,$$

$$f(x) = \inf \{f_i(x) \mid i \in J,\ x \in D_i\}$$

is the greatest minorant. We shall denote this function by $\wedge_{i \in J} (D_i, f_i)$, or for the sake of brevity $\wedge (D_i, f_i)$, and the set $[D, f]$ by $\wedge_{i \in J} [D_i, f_i]$, or briefly $\wedge [D_i, f_i]$. (Similar abbreviations will be used below in connexion with the symbols $\hat{\wedge}$, $\vee$, $\cup$ and $\cap$). Clearly

$$\cup [D_i, f_i] \subseteq \wedge [D_i, f_i] \subseteq \overline{\cup [D_i, f_i]}.$$

If $\wedge (D_i, f_i)$ exists, then there exists a closed convex minorant of $\{(D_i, f_i)\}$ if and only if $\wedge (D_i, f_i)$ has a conjugate $(\wedge (D_i, f_i))'$. In that case there exists a greatest closed convex minorant, denoted $\hat{\wedge} (D_i, f_i)$, namely the second conjugate $(\wedge (D_i, f_i))''$ of $\wedge (D_i, f_i)$.

Of course, the greatest minorant of a set $\{(D_i, f_i)\}$ of convex functions need not be convex. However, if the set $\{(D_i, f_i)\}$ is totally ordered, $\wedge (D_i, f_i)$ is easily seen to be convex.

Suppose that there exists a majorant of $\{(D_i, f_i) \mid i \in J\}$. Then the function (D, f) defined by

$$D = \{x \in \bigcap_{i \in J} D_i \mid \sup_{i \in J} f_i(x) < \infty\},$$

$$f(x) = \sup_{i \in J} f_i(x)$$

is the smallest majorant. This function (D, f) is denoted by $\vee (D_i, f_i)$ and the set $[D, f]$ by $\vee [D_i, f_i]$.

Obviously, $\vee (D_i, f_i)$ exists if and only if $\cap [D_i, f_i]$ is non-empty, and in that case

$$\vee [D_i, f_i] = \cap [D_i, f_i].$$

Hence, the smallest majorant of a set of convex or closed functions is convex or closed, respectively.

4.3. *Given a set of functions* $\{(D_i, f_i) \mid i \in J\}$.

(i) *If* $\wedge (D_i, f_i)$ *and* $(\wedge (D_i, f_i))'$ *exist, then* $(\wedge (D_i, f_i))' = \vee (D_i', f_i')$.

(ii) *If* $\vee (D_i, f_i)$ *and at least one* (D_i', f_i') *exist, then* $(\vee (D_i, f_i))' \leq \wedge (D_i', f_i')$ (where $\wedge (D_i', f_i')$ means the greatest minorant of those (D_i', f_i') which exist).

(iii) *If all* (D_i, f_i) *are convex and closed, and* $\vee (D_i, f_i)$ *exists, then* $(\vee (D_i, f_i))' = (\wedge (D_i', f_i'))''$.

In all cases the assumptions ensure the existence of the minorants, majorants and conjugates occurring in the statements.

Proof. (i) It is easily seen that the barriers of $\wedge (D_i, f_i)$ are precisely

the common barriers of $\{(D_i, f_i)\}$. This implies that $\vee (D_i', f_i')$ exists and that (i) holds.

(ii) For all $j \in J$ we have $(D_j, f_j) \leqq \vee (D_i, f_i)$. Hence the existence of at least one (D_j', f_j') implies that of $(\vee (D_i, f_i))'$, and we have $(\vee (D_i, f_i))' \leqq (D_j', f_j')$ for every j for which (D_j', f_j') exists. This shows that $\wedge (D_i', f_i')$ exists and that (ii) holds.

(iii) Under the assumptions all (D_i', f_i') exist. From (ii) follows that $\wedge (D_i', f_i')$ and $(\vee (D_i, f_i))'$ exist and that $(\vee (D_i, f_i))' \leqq \wedge (D_i', f_i')$. This implies that $(\wedge (D_i', f_i'))'$ exists, and (i) applied to $\{(D_i', f_i')\}$ then gives

$$(\wedge (D_i', f_i'))' = \vee (D_i'', f_i'') = \vee (D_i, f_i),$$

since all (D_i, f_i) are convex and closed. Hence $(\wedge (D_i', f_i'))'' = (\vee (D_i, f_i))'$.

4.4. Theorem. *Let $\{(D_i, f_i)\}$ be a set of closed convex functions. If $\wedge (D_i, f_i)$, $(\wedge (D_i, f_i))'$ and $\vee (D_i, f_i)$ exist, then*

$$(\hat{\wedge} (D_i, f_i))' = \vee (D_i', f_i'),$$

$$(\vee (D_i, f_i))' = \hat{\wedge} (D_i', f_i').$$

Proof. This is an obvious consequence of 4.3 (i) and (iii).

4.5. Theorem. *Let $\{(D_i, f_i)\}$ be a set of closed convex functions, and suppose that $\vee (D_i, f_i)$ exists. For $(D, f) = \vee (D_i, f_i)$ we then have*

(i) $[D', f'] = \overline{\operatorname{conv} (\cup [D_i', f_i'])}$.

(ii) $\operatorname{conv} (\cup D_i') \subseteqq D' \subseteqq \overline{\operatorname{conv} (\cup D_i')}$.

(iii) *If $[D', f']$ has a non-empty relative interior, then*

$$f'(\xi) = \inf \left\{ \sum_{\nu=1}^{n} \lambda_\nu f_{i_\nu}'(\xi_\nu) \;\middle|\; \xi = \sum_{\nu=1}^{n} \lambda_\nu \xi_\nu, \xi_\nu \in D_{i_\nu}', \lambda_\nu \geqq 0, \sum_{\nu=1}^{n} \lambda_\nu = 1, n \in Z_+ \right\}$$

for all ξ in the relative interior of D'.

Proof. (i) All (D_i', f_i') and $\wedge (D_i', f_i')$ exist, and we have

$$\cup [D_i', f_i'] \subseteqq \wedge [D_i', f_i'] \subseteqq \overline{\cup [D_i', f_i']}.$$

This implies

$$\overline{\operatorname{conv} (\cup [D_i', f_i'])} = \overline{\operatorname{conv} (\wedge [D_i', f_i'])},$$

since $\overline{\operatorname{conv} M} = \overline{\operatorname{conv} \overline{M}}$ for any set M. Statement (i) then follows from 3.9 and 4.3 (iii).

(ii) This is a simple consequence of (i).

(iii) By (i) we have

$$[D', {}^{\circ}f'] \subseteq \operatorname{conv}(\cup\, [D_i', f_i']) \subseteq [D', f'],$$

$[D', {}^{\circ}f']$ denoting the relative interior of $[D', f']$. Let ξ be in the relative interior of D'. Then $(\xi, \zeta) \in [D', {}^{\circ}f']$ for all $\zeta > f'(\xi)$, that is

$$f'(\xi) = \inf \{\zeta \mid (\xi, \zeta) \in \operatorname{conv}(\cup\, [D_i', f_i'])\}.$$

5. Convex functions with domains having non-empty relative interiors

As usual, E_1 and E_2 are vector spaces in duality. We first prove a result concerning the structure of closed convex functions.

5.1. *Let (D, f) be a closed convex function in E_1. There exists one and, obviously, only one subspace F_1 of E_1, called the linearity space of (D, f), with the following properties*:

(i) *F_1 is closed.*

(ii) $D + F_1 = D$.

(iii) *For every $\boldsymbol{x} \in D$*

$$f(\boldsymbol{x} + \boldsymbol{z}) - f(\boldsymbol{x}), \quad \boldsymbol{z} \in F_1,$$

is a continuous linear function on F_1, independent of $\boldsymbol{x}$.

(iv) *Every subspace of E_1 with the properties* (ii) *and* (iii) *is a subspace of F_1.*

(v) *If (Γ, φ) denotes the conjugate of (D, f) in E_2, then*

$$m(\Gamma) = \xi + F_1^{\perp}$$

for every $\xi \in \Gamma$.

Proof. We define $F_1 = (\Gamma - \xi_0)^{\perp}$, where $\xi_0 \in \Gamma$. Thus, a point $\boldsymbol{x} \in E_1$ is in F_1 if and only if it is a constant function on Γ. Obviously F_1 is a closed subspace. For $\boldsymbol{x} \in D$ and $\boldsymbol{z} \in F_1$ we have

$$\sup_{\xi \in \Gamma} (\xi(\boldsymbol{x} + \boldsymbol{z}) - \varphi(\xi)) = \sup_{\xi \in \Gamma} (\xi \boldsymbol{x} - \varphi(\xi)) + \xi_0 \boldsymbol{z}.$$

Hence $\boldsymbol{x} + \boldsymbol{z} \in D$ and $f(\boldsymbol{x} + \boldsymbol{z}) - f(\boldsymbol{x}) = \xi_0 \boldsymbol{z}$, which proves (ii) and (iii). Let $\boldsymbol{y}_0 \neq \boldsymbol{o}$ be in a subspace with the properties (ii) and (iii). Then there exists a continuous linear function η on the subspace generated by $\boldsymbol{y}_0$ such that

$$f(\boldsymbol{x}+\alpha\boldsymbol{y}_0)-f(\boldsymbol{x})=\eta(\alpha\boldsymbol{y}_0)$$

for all $\boldsymbol{x}\in D$ and all $\alpha\in R$. Let $\boldsymbol{x}_0\in D$ and $\xi\in\Gamma$. Then we have

$$\begin{aligned}\varphi(\xi)&=\sup_{\boldsymbol{x}\in D}(\xi\boldsymbol{x}-f(\boldsymbol{x}))\\&\geqq\sup_{\alpha\in R}(\xi(\boldsymbol{x}_0+\alpha\boldsymbol{y}_0)-f(\boldsymbol{x}_0+\alpha\boldsymbol{y}_0))\\&=\sup_{\alpha\in R}(\xi-\eta)\alpha\boldsymbol{y}_0+\xi\boldsymbol{x}_0-f(\boldsymbol{x}_0),\end{aligned}$$

which implies $(\xi-\eta)\boldsymbol{y}_0=0$. Hence $\xi\boldsymbol{y}_0=\eta\boldsymbol{y}_0$ for all $\xi\in\Gamma$, that is $\boldsymbol{y}_0\in F_1$. Thus (iv) has been proved. The last statement follows from

$$F_1^{\perp}=(\Gamma-\xi)^{\perp\perp}=(m(\Gamma)-\xi)^{\perp\perp}=m(\Gamma)-\xi,\quad\xi\in\Gamma.$$

We shall now make some further assumptions on the vector spaces E_1 and E_2, namely that they are normed spaces, that the topologies induced by the norms are admissible and that

$$\|\boldsymbol{x}\|=\sup_{\substack{\|\xi\|\leqq 1\\ \xi\in E_2}}|\xi\boldsymbol{x}|,\qquad\|\xi\|=\sup_{\substack{\|\boldsymbol{x}\|\leqq 1\\ \boldsymbol{x}\in E_1}}|\xi\boldsymbol{x}|$$

for all $\boldsymbol{x}\in E_1$ and all $\xi\in E_2$. In fact, this means that E_1 and E_2 are both reflexive Banach spaces, and each space is the dual of the other one.

Let F_1 be a closed subspace of E_1. It is easily verified that the function

$$\|\boldsymbol{x}\|_{F_1}=\sup_{\substack{\|\xi\|\leqq 1\\ \xi\in F_1^{\perp}}}|\xi\boldsymbol{x}|$$

is a semi-norm in E_1, and that it has the following properties:

(i) $|\xi\boldsymbol{x}|\leqq\|\xi\|\cdot\|\boldsymbol{x}\|_{F_1}$ for $\boldsymbol{x}\in E_1$, $\xi\in F_1^{\perp}$.

(ii) $\|\boldsymbol{x}\|=\|\boldsymbol{x}\|_{F_1}$, $\boldsymbol{x}\in E_1$, if and only if $F_1=\{\boldsymbol{o}\}$.

We note that $\|\boldsymbol{x}\|_{F_1}=\inf_{\boldsymbol{z}\in F_1}\|\boldsymbol{x}-\boldsymbol{z}\|$ (cf. [7] p. 282).

5.2. Theorem. *Let (D,f) be a closed convex function in E_1, and (Γ,φ) its conjugate in E_2. Let F_1 be the linearity space of (D,f). Then a point $\xi_0\in E_2$ is a relative interior point of Γ if and only if there exist an $\boldsymbol{x}_0\in E_1$, a $\varrho\in R_+$ and a $\sigma\in R$ such that*

$$f(\boldsymbol{x})\geqq\varrho\|\boldsymbol{x}-\boldsymbol{x}_0\|_{F_1}-\sigma+\xi_0\boldsymbol{x}$$

for all $\boldsymbol{x}\in D$. In particular, ξ_0 is an interior point of Γ if and only if there exist an $\boldsymbol{x}_0\in E_1$, a $\varrho\in R_+$ and a $\sigma\in R$ such that

$$f(\boldsymbol{x}) \geqq \varrho \,||\, \boldsymbol{x} - \boldsymbol{x}_0 \,||\, - \sigma + \xi_0 \boldsymbol{x}$$

for all $\boldsymbol{x} \in D$.

PROOF. First, suppose that

$$f(\boldsymbol{x}) \geqq \varrho \,||\, \boldsymbol{x} - \boldsymbol{x}_0 \,||_{F_1} - \sigma + \xi_0 \boldsymbol{x}$$

for all $\boldsymbol{x} \in D$. Then

$$\sup_{\boldsymbol{x} \in D} (\xi_0 \boldsymbol{x} - f(\boldsymbol{x})) \leqq \sigma$$

that is $\xi_0 \in \Gamma$. For every $\xi \in m(\Gamma) = \xi_0 + F_1^{\perp}$ such that $||\, \xi - \xi_0 \,|| \leqq \varrho$ we have

$$\begin{aligned}
\sup_{\boldsymbol{x} \in D} (\xi \boldsymbol{x} - f(\boldsymbol{x})) &\leqq \sup_{\boldsymbol{x} \in D} (\xi \boldsymbol{x} - \varrho \,||\, \boldsymbol{x} - \boldsymbol{x}_0 \,||_{F_1} + \sigma - \xi_0 \boldsymbol{x}) \\
&= \sup_{\boldsymbol{x} \in D} ((\xi - \xi_0)(\boldsymbol{x} - \boldsymbol{x}_0) - \varrho \,||\, \boldsymbol{x} - \boldsymbol{x}_0 \,||_{F_1}) + (\xi - \xi_0)\, \boldsymbol{x}_0 + \sigma \\
&\leqq \sup_{\boldsymbol{x} \in D} ((||\, \xi - \xi_0 \,|| - \varrho)||\, \boldsymbol{x} - \boldsymbol{x}_0 \,||_{F_1}) + (\xi - \xi_0)\, \boldsymbol{x}_0 + \sigma \\
&\leqq (\xi - \xi_0)\, \boldsymbol{x}_0 + \sigma .
\end{aligned}$$

Hence $\xi \in \Gamma$, which proves that ξ_0 is a relative interior point of Γ.

If for all $\boldsymbol{x} \in D$

$$f(\boldsymbol{x}) \geqq \varrho ||\, \boldsymbol{x} - \boldsymbol{x}_0 \,|| - \sigma + \xi_0 \boldsymbol{x},$$

then $F_1 = \{\boldsymbol{o}\}$. For let $\boldsymbol{z}_0 \in D$ and $\boldsymbol{y}_0 \in F_1$. There exists a continuous linear function η on F_1 such that for all $\alpha \in R$

$$\begin{aligned}
f(\boldsymbol{z}_0 + \alpha \boldsymbol{y}_0) &= f(\boldsymbol{z}_0) + \eta(\alpha \boldsymbol{y}_0) \\
&\geqq \varrho ||\, \boldsymbol{z}_0 + \alpha \boldsymbol{y}_0 - \boldsymbol{x}_0 \,|| - \sigma + \xi_0 (\boldsymbol{z}_0 + \alpha \boldsymbol{y}_0) \\
&\geqq \varrho |\, \alpha \,| \cdot ||\, \boldsymbol{y}_0 \,|| - \varrho ||\, \boldsymbol{z}_0 - \boldsymbol{x}_0 \,|| - \sigma + \xi_0 \boldsymbol{z}_0 + \xi_0 (\alpha \boldsymbol{y}_0).
\end{aligned}$$

This implies $\boldsymbol{y}_0 = \boldsymbol{o}$, that is $F_1 = \{\boldsymbol{o}\}$. Hence $||\, \boldsymbol{x} \,||_{F_1} = ||\, \boldsymbol{x} \,||$ for all $\boldsymbol{x} \in D$, and the proof above yields that ξ_0 is an interior point of Γ.

Next, let ξ_0 be a relative interior point of Γ. Then φ is continuous at ξ_0 (cf. 2.10). Consequently, there exist a $\varrho \in R_+$ and a $\sigma \in R$ such that

$$K = \{\xi \mid \xi \in m(\Gamma),\ ||\, \xi - \xi_0 \,|| \leqq \varrho\} \subseteq \Gamma$$

and

$$\varphi(\xi) \leqq \sigma \quad \text{for all } \xi \in K.$$

For every $\boldsymbol{x} \in D$ we then have

$$f(\boldsymbol{x}) = \sup_{\xi \in \Gamma} (\xi \boldsymbol{x} - \varphi(\xi)) \geqq \sup_{\xi \in K} (\xi \boldsymbol{x} - \varphi(\xi))$$
$$\geqq \sup_{\xi \in K} \xi \boldsymbol{x} - \sigma = \sup_{\xi \in K} (\xi - \xi_0)\, \boldsymbol{x} - \sigma + \xi_0 \boldsymbol{x}$$
$$= \varrho \| \boldsymbol{x} \|_{F_1} - \sigma + \xi_0 \boldsymbol{x}.$$

Thus, we have an equality of the form desired, with $\boldsymbol{x}_0 = \boldsymbol{o}$.

If ξ_0 is an interior point of Γ, then $F_1 = \{\boldsymbol{o}\}$. Hence $\| \boldsymbol{x} \| = \| \boldsymbol{x} \|_{F_1}$, and we have

$$f(\boldsymbol{x}) \geqq \varrho \| \boldsymbol{x} \| - \sigma + \xi_0 \boldsymbol{x}$$

for all $\boldsymbol{x} \in D$.

Now, the main theorem of this section follows immediately from theorem 5.2 and the dual statement:

5.3. THEOREM. *Let $\mathfrak{C}_1$ denote the class of closed convex functions (D, f) in E_1 with the following two properties*:

(i) *D has a non-empty relative interior.*

(ii) *For some $\boldsymbol{x}_0 \in E_1$, $\xi_0 \in E_2$, $\varrho \in R_+$ and $\sigma \in R$ we have*

$$f(\boldsymbol{x}) \geqq \varrho \| \boldsymbol{x} - \boldsymbol{x}_0 \|_{F_1} - \sigma + \xi_0 \boldsymbol{x} \quad \text{for} \quad \boldsymbol{x} \in D,$$

F_1 denoting the linearity space of (D, f).

The class of conjugates of the functions in $\mathfrak{C}_1$ is the analogously defined class $\mathfrak{C}_2$ in E_2, and conversely. If (D, f) in E_1 and (Γ, φ) in E_2 are closed convex functions with the property (i), *such that each function is the conjugate of the other one, then (D, f) is in $\mathfrak{C}_1$ and (Γ, φ) is in $\mathfrak{C}_2$.*

The same statement holds for the subclass $\mathfrak{D}_1$ of $\mathfrak{C}_1$ consisting of those closed convex functions (D, f) for which

(i) *D has a non-empty interior.*

(ii) *For some $\boldsymbol{x}_0 \in E_1$, $\xi_0 \in E_2$, $\varrho \in R_+$ and $\sigma \in R$ we have*

$$f(\boldsymbol{x}) \geqq \varrho \| \boldsymbol{x} - \boldsymbol{x}_0 \| - \sigma + \xi_0 \boldsymbol{x} \quad \text{for} \quad \boldsymbol{x} \in D.$$

In that case $F_1 = \{\boldsymbol{o}\}$ for the functions involved.

References

(1) Z. Birnbaum und W. Orlicz, *Über die Verallgemeinerung des Begriffes der zueinander konjugierten Potenzen.* Studia Math. 3 (1931), 1 – 67.

(2) N. Bourbaki, *Éléments de Mathématique*, Livre V, *Espaces vectoriels topologiques*, Chap. 1–2. Act. Sci. Ind. 1189, Paris, 1953.

(3) W. Fenchel, *On conjugate convex functions.* Canadian J. Math. 1 (1949), 73–77.

(4) W. Fenchel, *Convex cones, sets, and functions.* Lecture notes, Princeton University, 1953.

(5) W. L. Jones, *On conjugate functionals.* Doctoral Dissertation, Columbia University, 1960.

(6) S. Karlin, *Mathematical methods and theory in games, programming, and economics*, I. Reading, Mass.-London, 1959.

(7) G. Köthe, *Topologische lineare Räume*, I. Berlin-Göttingen-Heidelberg, 1960.

(8) S. Mandelbrojt, *Sur les fonctions convexes.* C.R. Acad. Sci. Paris 209 (1939), 977–978.

(9) J. J. Moreau, *Fonctions convexes duales et points proximaux dans un espace hilbertien.* C. R. Acad. Sci. Paris 255 (1962), 2897–2899.

(10) J. J. Moreau, *Fonctions convexes en dualité.* Faculté des Sciences de Montpellier, Séminaires de Mathématiques, 1962.

(11) J. J. Moreau, *Inf-convolution.* Faculté des Sciences de Montpellier, Séminaires de Mathématiques, 1963.

Indleveret til Selskabet den 3. juli 1963.
Færdig fra trykkeriet den 10. februar 1964.

Matematisk-fysiske Meddelelser
udgivet af
Det Kongelige Danske Videnskabernes Selskab
Bind **34,** nr. 3

Mat. Fys. Medd. Dan. Vid. Selsk. **34,** no. 3 (1964)

MOMENTUM AND ENERGY IN GENERAL RELATIVITY AND GRAVITATIONAL RADIATION

BY

C. MØLLER

København 1964
Kommissionær: Ejnar Munksgaard

CONTENTS

Synopsis

The energy-momentum complex, which was formulated in terms of tetrad variables in an earlier paper in Mat. Fys. Skr., is applied to the exact asymptotic solution of Einstein's field equations for an axi-symmetric system given by BONDI and his collaborators. The formulae derived for the gravitational energy radiated per unit time and for the total energy of the system at any time confirm a conjecture by BONDI. The transformation properties of the total momentum and energy for a non-closed system under asymptotic Lorentz transformations are derived and the approximate plane gravitational waves at large distances from a radiating system are investigated. As regards energy and momentum, such waves are closely analogous to electromagnetic waves emitted by a system of accelerated electrically charged particles.

PRINTED IN DENMARK
BIANCO LUNOS BOGTRYKKERI A/S

1. Introduction and Summary

Since the first years of Einstein's theory of gravitation the question whether or not a system of accelerated massive bodies loses energy by emission of gravitational radiation has given rise to many controversial discussions. The main reasons for this somewhat unusual situation in physics are the following. On account of the non-linear character of Einstein's field equations it is difficult to find sufficiently general exact solutions of these equations and most of the discussions on gravitational radiation have therefore been based on solutions of the "linearized" field equations. However, in many cases, such solutions have been shown to be good approximations to the solutions of the exact field equations only over limited parts of space and it has been doubted whether the results obtained by means of these solutions can be fully trusted. Moreover, until recently one did not have a consistent expression for the gravitational energy current which, in analogy with Poynting's theorem, could be used for calculating the amount of energy carried away by the gravitational waves.

It is well known that the energy-momentum complex Θ_i^k given by EINSTEIN many years ago does not allow to calculate the distribution of the energy and the energy flux in a physically satisfactory way, since the result depends on the spatial coordinates used. But even if one is interested only in the total energy and its possible variation in time, such as in calculations of the energy emission from an insular system, the complex Θ_i^k is applicable only in special systems of coordinates. In the trivial case of a completely empty space, for instance, Einstein's expression gives an infinite value for the total energy when calculated in polar coordinates, in contrast to the correct value zero obtained if one uses Cartesian coordinates. This means, strictly speaking, that this expression is *not* in accordance with the general principle of relativity according to which all relations between measurable physical quantities, such as the total energy and the components of the metric tensor, must have the same form in all systems of space-time coordinates.

The difficulties mentioned above have now been overcome. In a recent, most interesting paper, BONDI et al.[1] have been able to give the exact form of the metric at large spatial distances from an axi-symmetric, but otherwise arbitrary, insular system of matter that emits gravitational waves into the surrounding empty space, and, in a paper from 1961[2], we arrived at an expression T_i^k for the energy-momentum complex which is in accordance with the principle of relativity and which therefore meets the objections raised against Einstein's expression Θ_i^k. In the present paper, the complex T_i^k is applied to the solutions of BONDI et al. Thereby we obtain consistent expressions for the total momentum and energy as well as for the time variations of these quantities in the case of an arbitrary axi-symmetric system emitting gravitational waves. Some of the results of these calculations have been published previously in a note in Physics Letters[3].

In section 2, we give an outline of the basic theory and a survey of earlier results as well as some new results regarding the energy-momentum complex. In contrast to the complex Θ_i^k which can be expressed directly in terms of the metric components and its derivatives, the complex T_i^k is given directly in terms of tetrad fields which are determined by the metric only up to arbitrary Lorentz rotations of the tetrads. T_i^k is not invariant under such rotations. However, as will be shown in detail in section 6, the values of the total energy and momentum obtained by means of T_i^k are invariant under all Lorentz rotations of the tetrads which are in accordance with the boundary conditions formulated in section 2.

Section 3 contains a survey of the main results obtained by BONDI et al. in[1] and it is shown that Einstein's expression Θ_i^k gives unreasonable results for the energy radiation and the total energy in the system of coordinates adopted in[1]. In contrast to this result it is shown, in section 4, that the complex T_i^k gives a consistent value for the energy radiation, which confirms a conjecture by BONDI regarding the total energy radiated by an axi-symmetric system. In addition to that, the intensity of the energy radiation in different directions is determined.

The total energy and momentum at any time are defined and calculated in section 5 and, as regards the energy, the result confirms a conjecture by BONDI in part D of [1]. The change in the total momentum per unit time is shown to correspond to a recoil effect of the emitted gravitational radiation of the same kind as for emission of photons.

In section 7, we investigate the transformation properties of the total momentum and energy of the matter system as well as of the emitted radia-

tion under asymptotically Lorentzian transformations. Finally, it is shown in section 8 that the gravitational radiation at large distances from the system has the form of approximate plane waves with an everywhere positive energy density and a momentum density equal to the energy current density divided by c^2 like in the case of a plane electromagnetic wave. Details of the calculations are collected in the Appendix.

2. The Energy-Momentum Complex

In general relativity the energy and momentum of the complete system of matter plus gravitational field is described by an energy-momentum complex of the form

$$\mathsf{T}_i^{\,k} = \mathfrak{T}_i^{\,k} + \mathfrak{t}_i^{\,k}. \tag{2.1}$$

Here, $\mathfrak{T}_i^{\,k}$ is the energy-momentum tensor density of the matter, which is a function of the matter field variables *and* the gravitational variables, while the complex $\mathfrak{t}_i^{\,k}$ of the gravitational field is an algebraic function of the gravitational field variables only. $\mathfrak{T}_i^{\,k}$ also appears as the source of the gravitational field in Einstein's field equations

$$\mathfrak{G}_i^{\,k} \equiv \mathfrak{R}_i^{\,k} - \frac{1}{2}\,\delta_i^{\,k}\,\mathfrak{R} = -\varkappa\,\mathfrak{T}_i^{\,k} \tag{2.2}$$

which determine the metric for a given matter distribution. If we eliminate $\mathsf{T}_i^{\,k}$ in (2.1) by means of the field equations, the complex $\mathsf{T}_i^{\,k}$ appears as a function of the gravitational field variables only.

A satisfactory solution of the energy problem in general relativity requires that the energy-momentum complex satisfies the following conditions:

1. $\mathsf{T}_i^{\,k}(x)$ is an afine tensor density depending algebraically on the gravitational field variables and their derivatives of the first and second orders and it satisfies the divergence relation

$$\mathsf{T}_i^{\,k}{}_{,\,k} \equiv \frac{\partial\,\mathsf{T}_i^{\,k}}{\partial x^k} = 0\,. \tag{2.3}$$

2. A matter system for which the metric asymptotically at large spatial distances from the system is of the Schwarzschild type is called a *closed*

system. In this case we can use coordinates which are asymptotically rectilinear and then we must require that the quantities*

$$P_i = \int\limits_{x^4 = \text{const.}} \int\int\int \mathsf{T}_i^{\,4}\, dx^1\, dx^2\, dx^3 \tag{2.4}$$

are constant in time and that they transform as the covariant components of a free vector under linear space-time transformations. This property is essential for the interpretation of $P_i = \{P_l - H\}$ as the total momentum and energy vector.

3. $\mathsf{T}^k \equiv \mathsf{T}_4^{\,k}$ is transformed like a 4-vector density under the group of purely spatial transformations

$$\bar{x}^l = f^l(x^\varkappa), \quad \bar{x}^4 = x^4 \tag{2.5}$$

which leave the time scale and the system of reference unchanged. This property makes the "energy content of any volume of space V", i.e.

$$H_V = -\int\limits_V \int\int\int \mathsf{T}_4^{\,4}\, dx^1\, dx^2\, dx^3 = -\int\limits_V \int\int\int \overline{\mathsf{T}}_4^{\,4}\, d\bar{x}^1\, d\bar{x}^2\, d\bar{x}^3 \tag{2.6}$$

independent of the spatial coordinates used in the evaluation of the integral. Thus, *3.* is the condition of localizability of the energy in a gravitational field.

The classical expression for the energy-momentum complex given by EINSTEIN many years ago [4] is of the form

$$\Theta_i^{\,k} = \mathfrak{T}_i^{\,k} + \vartheta_i^{\,k}. \tag{2.7}$$

Here, $\vartheta_i^{\,k}$ is a homogeneous quadratic function of the first-order derivatives of the metric tensor which is obtained from the Lagrangian

$$\mathfrak{L}_E = \sqrt{-g}\, g^{ik} (\Gamma^l_{ik}\, \Gamma^m_{lm} - \Gamma^l_{im}\, \Gamma^m_{kl}) \tag{2.8}$$

by the equation

$$\vartheta_i^{\,k} = \frac{1}{2\varkappa} \left\{ \frac{\partial \mathfrak{L}_E}{\partial g^{lm}{}_{,k}}\, g^{lm}{}_{,i} - \delta_i^{\,k}\, \mathfrak{L}_E \right\}. \tag{2.9}$$

* In the following, we shall use natural units in which the velocity of light c and Newton's gravitational constant k are equal to one. Consequently, Einstein's constant $\varkappa$ has the value 8π. Further, Latin indices run from 1 to 4, Greek indices from 1 to 3, and the signature is $\varepsilon_i = \{1, 1, 1, -1\}$.

The explicit expression for $\vartheta_i^{\ k}$ is

$$\vartheta_i^{\ k} = \frac{1}{2\varkappa}\left\{\Gamma_{lm}^{k}\left(\sqrt{-g}\, g^{lm}\right)_{,\,i} - \Gamma_{ml}^{l}\left(\sqrt{-g}\, g^{km}\right)_{,\,i} - \delta_i^{\ k}\, \mathfrak{L}_E\right\}. \tag{2.10}$$

If we eliminate $\mathfrak{T}_i^{\ k}$ in (2.7) by means of the field equations (2.2), the complex $\Theta_i^{\ k}$ can be written, as was first shown by v. FREUD[5], in the form

$$\Theta_i^{\ k} = h_i^{\ kl}{}_{,\,l} \tag{2.11}$$

with the superpotential

$$h_i^{\ kl} = -\, h_i^{\ lk} = \frac{g_{in}}{2\varkappa\sqrt{-g}}\left[(-g)\left(g^{kn}\, g^{lm} - g^{ln}\, g^{km}\right)\right]_{,\,m}. \tag{2.12}$$

As is well known, Einstein's expression $\Theta_i^{\ k}$ satisfies the conditions *1.* and *2.*, but *not* the localizability condition *3.* Therefore, EINSTEIN came to the conclusion that, in general relativity, the energy content H_V of a finite part of space has no exact physical meaning.
Only the total energy

$$H_E = -\iiint \Theta_4^{\ 4}\, dx^1\, dx^2\, dx^3, \tag{2.13}$$

obtained by integrating over the whole 3-dimensional space with $t = x^4 =$ const., should have a well-defined physical meaning. It has been argued that this is quite natural, since it is difficult to imagine how one could measure the energy contained in a small part of the system. On the other hand, the total energy is certainly a measurable quantity, since the total mass can be measured, for instance, by weighing the system on a balance or by measuring its reaction under the influence of external forces. Therefore, it would seem that Einstein's point of view is in accordance with the nature of the problem.

Nevertheless, one may have some doubts as to the validity of the expression (2.13) for the total energy, since it is *not* in accordance with the general principle of relativity. According to this principle, *any relation between measurable physical quantities*, such as the total energy or mass and the components of the metric tensor, *must have the same form in any system of coordinates*. In other words, we can only trust an expression like (2.13) if it represents the energy in any system of coordinates, and this is obviously not the case. Take, for instance, two systems of coordinates connected by a purely spatial transformation (2.5); then, the total energy must

certainly have the same value in these two systems, for the result of an experiment, which allows to determine the total mass, is of course completely independent of the way we choose to name the different points in space. However, since the complex Θ_i^k does not satisfy the condition *3.*, the equation (2.13) gives in general quite different values for the total energy in the two systems of coordinates of the type considered.

As was pointed out long ago by BAUER[6], this holds even for the trivial case of a completely empty space where space-time is flat. In Cartesian coordinates, H_E is here zero as it should be, but if we use the metric corresponding to polar coordinates in the evaluation of H_E, we get an entirely different result. In fact, the integral in (2.13) is divergent in this case, and it should be noted that the divergence arises from the large distances r and not from the singular point $r = 0$. A similar situation we meet in the case of an arbitrary physical system, and this cannot be considered satisfactory in a general theory of relativity.

The importance of the restricted group of transformations (2.5) lies only in the fact that we can be sure that the total energy must be unchanged under these transformations. For a more general transformation where the time scale and the motion of the frame of reference are changed, as for instance for a simple Lorentz transformation, we must in general expect a change in the total energy of the physical system. The invariance of the total energy under the transformations (2.5) requires that the energy-momentum complex satisfies also the condition *3.* At first sight, one might think that the condition *3.* is too stringent if we give up the idea of localizability and only regard the *total* energy as a measurable quantity, for with *3.* the equation (2.6) is valid for any finite volume V and not only for V equal to the whole 3-dimensional space. However, it should be remembered that the system of coordinates in a given system of reference often consists of an "atlas" of different overlapping local maps, inside which the components of the metric tensor are regular [7], and it is then essential that the equation (2.6) holds for any volume V which lies inside a region of overlapping of two coordinate patches.

It seems therefore that a satisfactory solution of the energy problem in accordance with the general principle of relativity requires the existence of an energy-momentum complex with all the properties *1.–3.* Now, it can be shown [8] that, if the gravitational variables are taken to be the components of the metric tensor, the only complex which satisfies the conditions *1.* and *2.* is Einstein's expression Θ_i^k, and it is thus impossible also to have *3.* satisfied. Therefore, it seems that we are in a hopeless situation. However,

gravitational fields may also be described by so-called tetrad fields instead of by the metric tensor. There are even certain matter systems where one has to use a tetrad description of the gravitational field. This holds, for instance, in the case of a fermion field under the influence of a gravitational field, where the latter has to be described by a tetrad field. In fact, in the usual generally covariant form of the Dirac equation [9], the gravitational field is represented by a tetrad field and not directly by the metric. It is therefore natural to assume that the tetrad field variables are the fundamental gravitational variables and, as was shown in reference 2, with this assumption it is possible to define an energy-momentum complex which satisfies all the conditions *1.–3.*

Let $h^{(a)}{}_i$ be the covariant components of the a'th tetrad vector which is space-like for $a = 1, 2, 3$ and time-like for $a = 4$. Further, let us put

$$h_{(a)\,i} = \eta_{(ab)}\, h^{(b)}{}_i, \tag{2.14}$$

where $\eta_{(ab)}$ is the constant diagonal matrix with the diagonal elements $\{1, 1, 1, -1\}$. Then, the connection between the tetrad field and the metric field at every point is given by

$$h^{(a)}{}_i\, h_{(a)\,k} = g_{ik} \tag{2.15}$$

$$h^{(a)}{}_i\, h_{(b)}{}^i = \delta^a_b. \tag{2.16}$$

Further, we have

$$\sqrt{-g} = |h|, \tag{2.17}$$

where $h = \det\{h_{(a)\,i}\}$ is the determinant with $h_{(a)\,i}$ in the a'th row and i'th column.

The starting point of the developments in [2] was the remark that the curvature scalar density $\mathfrak{R}$, when expressed in terms of the tetrad field by means of (2.15), takes the form

$$\mathfrak{R} = \mathfrak{L} + \mathfrak{h}, \tag{2.18}$$

where $\mathfrak{h}$ has the form of a usual divergence, which is of no importance in the variational principle, and

$$\mathfrak{L} = |h|\,[h_{(a)}{}^r{}_{;s}\, h^{(a)\,s}{}_{;r} - h_{(a)}{}^r{}_{;r}\, h^{(a)\,s}{}_{;s}]. \tag{2.19}$$

Here, the semicolon means covariant differentiation so that the Langrangian $\mathfrak{L}$ is a scalar density under arbitrary space-time transformations (a true scalar density) in contrast to the Lagrangian $\mathfrak{L}_E$ in (2.8) which has this

property under linear transformations only. Further, since the Christoffel symbols by (2.15) are seen to be linear functions of the first-order derivatives of the tetrad variables, the same holds for $h_{(a)}{}^{r}{}_{;s}$. Hence, $\mathfrak{L}$ (just as $\mathfrak{L}_E$) has the important property of being a homogeneous quadratic function of the first-order derivatives of the gravitational field variables.

The energy-momentum complex $\mathfrak{T}_i^k$ which, in [2], was shown to satisfy the conditions *1.–3.*, is

$$\mathfrak{T}_i^k = \mathfrak{T}_i^k + \mathfrak{t}_i^k$$

with

$$\left.\begin{aligned} \mathfrak{t}_i^k \equiv \sqrt{-g}\, t_i^k &= \frac{1}{2\varkappa}\left[\frac{\partial \mathfrak{L}}{\partial h^{(a)\,l}{}_{,k}}\, h^{(a)\,l}{}_{,i} - \delta_i^k\, \mathfrak{L}\right] \\ &= \frac{1}{2\varkappa}\left[\frac{\partial \mathfrak{L}}{\partial h^{(a)}{}_{l,\,k}}\, h^{(a)}{}_{l,\,i} - \delta_i^k\, \mathfrak{L}\right]. \end{aligned}\right\} \tag{2.20}$$

In terms of the tetrad fields, Einstein's field equations take the form

$$-\frac{1}{\varkappa}\,\mathfrak{G}_i^k \equiv \frac{1}{2\varkappa}\, h^{(a)}{}_i \frac{\delta \mathfrak{L}}{\delta h_k^{(a)}} \equiv \frac{1}{2\varkappa}\, h^{(a)\,k} \frac{\delta \mathfrak{L}}{\delta h^{(a)\,i}} = \mathfrak{T}_i^k, \tag{2.21}$$

where $\dfrac{\delta \mathfrak{L}}{\delta h_k^{(a)}}$ is the variational derivative of $\mathfrak{L}$ with respect to $h_k^{(a)}$. The complex $\mathfrak{T}_i^k$ is derivable from a superpotential $\mathfrak{U}_i^{kl}$, i.e.

$$\mathfrak{T}_i^k = \mathfrak{U}_i^{kl}{}_{,\,l} \tag{2.22}$$

with

$$\mathfrak{U}_i^{kl} = -\,\mathfrak{U}_i^{lk} = \frac{1}{2\varkappa} \frac{\partial \mathfrak{L}}{h^{(a)\,i}{}_{,\,l}}\, h^{(a)\,k} = \frac{1}{2\varkappa}\, h_i^{(a)} \frac{\partial \mathfrak{L}}{\partial h_{l,\,k}^{(a)}} \tag{2.23}$$

(see Eqs. (2.31)–(2.38) in [2], and also [10]).

The explicit expressions for the complex $\mathfrak{t}_i^k$ and the superpotential are (Eqs. (2.39), (2.40) in [2])

$$\mathfrak{t}_i^k = \frac{|h|}{\varkappa}\left[h^{(a)\,k}{}_{;\,l}\, h^{\;l}_{(a),\,i} - h^{(a)\,r}{}_{;\,r}\, h^{\;k}_{(a),\,i} + h_r^{(a)}\, h^{r}_{(a),\,i}\, h^{(b)\,k}\, h^{s}_{(b);\,s}\right] - \frac{1}{2\varkappa}\,\delta_i^k\,\mathfrak{L} \tag{2.24}$$

$$\mathfrak{U}_i^{kl} = \frac{|h|}{\varkappa}\left[h^{k}_{(a)}\, h^{(a)\,l}{}_{;\,i} + (\delta_k^i\, h^{(a)\,l} - \delta_i^l\, h^{(a)\,k})\, h^{s}_{(a);\,s}\right]. \tag{2.25}$$

In contrast to the superpotential h_i^{kl} in Einstein's theory, the superpotential $\mathfrak{U}_i^{kl}$ is seen to be a true tensor density of rank 3.

It is convenient to introduce the tensors

$$\left.\begin{aligned} \gamma_{ikl} &= h^{(a)}{}_i\, h_{(a)\,k;\,l} = -\gamma_{kil} \\ \Lambda_{ikl} &= \gamma_{ikl} - \gamma_{ilk} = h^{(a)}{}_i\,(h_{(a)\,k,\,l} - h_{(a)\,k,\,l}) = -\Lambda_{ilk} \\ \Phi_k &= \gamma^i{}_{ki} = \Lambda^i{}_{ki} = h^{(a)\,i}\, h_{(a)\,k;\,i} \end{aligned}\right\} \tag{2.26}$$

and the symbol

$$\Delta^i{}_{kl} = h^{(a)\,i}\, h_{(a)\,k,\,l} \tag{2.27}$$

which is connected with the Christoffel symbol by the relation

$$\Delta^i{}_{kl} = \Gamma^i_{kl} + \gamma^i{}_{kl}\,. \tag{2.28}$$

In terms of these quantities the expressions (2.19)–(2.25) take the form (Eqs. (3.12), (3.14), (D 34) in [2])

$$\mathfrak{L} = |\,h\,|\,[\gamma_{rst}\,\gamma^{tsr} - \Phi_r\,\Phi^r] \tag{2.29}$$

$$\mathfrak{U}_i^{kl} = \frac{|\,h\,|}{\varkappa}\,[\gamma^{kl}{}_i - \delta^k_i\,\Phi^l + \delta^l_i\,\Phi^k] \tag{2.30}$$

$$\mathfrak{t}_i^k = \frac{|\,h\,|}{\varkappa}\,[\gamma^{km}{}_l\,\Delta^l{}_{mi} - \Phi^l\,\gamma^k{}_{li} + \Delta^l{}_{li}\,\Phi^k] - \frac{1}{2\,\varkappa}\,\delta^k_i\,\mathfrak{L} \tag{2.31}$$

or

$$\mathfrak{t}_i^k = \mathfrak{U}_i^k + \mathfrak{U}_m{}^{kl}\,\Delta^m{}_{il}, \tag{2.32}$$

where $\mathfrak{U}_i^k$ is the tensor density

$$\mathfrak{U}_i^k = \frac{|\,h\,|}{\varkappa}\,\Lambda_{mli}\,\gamma^{klm} - \Phi_i\,\Phi^k + \Lambda^k{}_{il}\,\Phi^l] - \frac{1}{2\,\varkappa}\,\delta^k_i\,\mathfrak{L}\,. \tag{2.33}$$

All the quantities introduced here are true tensors or tensor densities, except $\mathfrak{t}_i^k$ and $\mathfrak{T}_i^k$ which deviate from a true tensor density by the term $\mathfrak{U}_m{}^{kl}\,\Delta^m_{il}$. Thus, we get the following transformation law for $\mathfrak{T}_i^k$ and $\mathfrak{t}_i^k$ under an arbitrary space-time transformation $(x^i) \to (x'^i)$ (Eq. (D. 37) in [2]):

$$\mathfrak{T}'^{\,k}_i = J\,\frac{\partial x'^{\,k}}{\partial x^m}\left[\frac{\partial x^l}{\partial x'^{\,i}}\,\mathfrak{T}_l^m + \frac{\partial}{\partial x^n}\left(\frac{\partial x^r}{\partial x'^{\,i}}\right)\mathfrak{U}_r{}^{mn}\right], \tag{2.34}$$

where J is the Jacobian of the transformation

$$J = \frac{\partial\,(x^1 \cdot\cdot\, x^4)}{\partial\,(x'^{\,1} \cdot\cdot\, x'^{\,4})} = \det\left\{\frac{\partial x^i}{\partial x'^{\,k}}\right\}. \tag{2.35}$$

From (2.34) we see that the most general group of transformations under which the quantities $\mathsf{T}^k \equiv \mathsf{T}_4{}^k$ transform as a 4-vector density are those for which

$$\frac{\partial x^r}{\partial x'^4} = \delta_4^r . \tag{2.36}$$

This also follows from (2.22) because $\mathfrak{U}_i^{kl}$ is a true tensor density, i.e.

$$\mathfrak{U}_4'^{kl} = J \frac{\partial x^r}{\partial x'^4} \frac{\partial x'^k}{\partial x^s} \frac{\partial x'^l}{\partial x^t} \mathfrak{U}_r{}^{st} = J \frac{\partial x'^k}{\partial x^s} \frac{\partial x'^l}{\partial x^t} \mathfrak{U}_4{}^{st} \tag{2.37}$$

on account of (2.36). Thus, $\mathfrak{U}_4{}^{kl}$ is an antisymmetric tensor density of rank 2 under all transformations of the type (2.36), which means that

$$\mathsf{T}^k = \mathfrak{U}_4{}^{kl}{}_{,l} \tag{2.38}$$

is a vector density.

The most general transformation of the type (2.36) has the form

$$\left.\begin{aligned} x'^\iota &= f^\iota(x^\varkappa) \\ x'^4 &= x^4 + f(x^\varkappa), \end{aligned}\right\} \tag{2.39}$$

where f^ι and f are arbitrary functions of the spatial coordinates. It contains the group of purely spatial transformations (2.5) as a subgroup. Under the latter group the fourth component of T^k, i.e. $\mathsf{T}_4{}^4$, is a scalar density, which means that

$$H_V = -\iiint_V \mathsf{T}_4{}^4 \, dx^1 \, dx^2 \, dx^3 \tag{2.40}$$

is invariant.

If we now introduce the expression $\mathsf{T}_4{}^4 = \mathfrak{U}_4{}^{4\lambda}{}_{,\lambda}$ into (2.40) we get, by means of Gauss' theorem,

$$H_V = -\iint_F \mathfrak{U}_4{}^{4\lambda} \, dS_\lambda , \tag{2.41}$$

where the integration is extended over the boundary surface F of the volume V. Here,

$$dS_\lambda = \delta_{\lambda\varkappa\mu} \, dx^\varkappa \, \delta x^\mu , \tag{2.42}$$

where $\delta_{\lambda\varkappa\mu}$ is the 3-dimensional Levi-Civita symbol and $dx^\varkappa$, δx^μ are infinitesimal 3-vectors spanning the surface element on F. Since $\mathfrak{U}_4{}^{4\lambda}$ trans-

forms as a 3-vector density under the group of purely spatial transformations (2.5), $\mathfrak{U}_4{}^{4\lambda}\, dS_\lambda$ is invariant, which again shows that H_V in (2.41) is invariant under these transformations. The expression (2.41) is valid also if the spatial system of coordinates is composed of different coordinate patches.

Let us now consider the integrals

$$(P_V)_\iota = \iiint\limits_V \mathsf{T}_\iota{}^4\, dx^1\, dx^2\, dx^3 = \iiint\limits_V \mathfrak{U}_\iota{}^{4\lambda}{}_{,\lambda}\, dx^1\, dx^2\, dx^3 \tag{2.43}$$

obtained from (2.4) with $i = \iota$ by integrating over a finite part V of 3-space. Then, if $\mathfrak{U}_\iota{}^{4\lambda}$ is continuous inside V, we get again by means of Gauss' theorem

$$(P_V)_\iota = \iint\limits_F \mathfrak{U}_\iota{}^{4\lambda}\, dS_\lambda = \iint\limits_F A_\iota(x). \tag{2.44}$$

Since $\mathfrak{U}_i^{kl}$ is a true tensor density, it follows that

$$A_\iota(x) \equiv \mathfrak{U}_\iota{}^{4\lambda}\, dS_\lambda \tag{2.45}$$

at each point on F transforms as a 3-vector under the group of spatial transformations (2.5). Nevertheless, the sum (or integral) of the components of the vectors A_ι in different points of F, of course, has in general no simple physical meaning. However, this should not be regarded as a defect of the theory, since we have a similar situation already in special relativity if we use curvilinear coordinates in space.

In the limit of special relativity where space-time can be regarded as flat, we have, in a system of inertia a momentum density given by the components $\mathfrak{T}_\iota{}^4$ of the matter tensor density, which transform as a 3-vector density under arbitrary spatial transformations, so that

$$B_\iota = \mathfrak{T}_\iota{}^4\, dx^1\, dx^2\, dx^3 \tag{2.46}$$

are the covariant components of a 3-vector. Nevertheless, the three integrals

$$(P_V^{(m)})_\iota = \iiint\limits_V \mathfrak{T}_\iota{}^4(x)\, dx^1\, dx^2\, dx^3 = \iiint\limits_V B_\iota(x) \tag{2.47}$$

have in general no physical meaning at all.

This will be the case only in a system of rectilinear coordinates where

the integrals (2.47) are the components of the total linear momentum inside V, which is a free vector $\vec{P}_V^{(m)}$. Now, a free vector can by parallel displacement be attached to any point p in space, and in a system of rectilinear coordinates its components are the same in every point. However, by a transformation to curvilinear coordinates, the components of the free vector $\vec{P}_V^{(m)}$ will be different in different points p.

Of course, this does not prevent us from using curvilinear coordinates, but then we have in (2.47) to substitute the arithmetical sum of the vector components B_ι of the vector $\vec{B}$ by the geometrical sum of the vectors $\vec{B}(x)$. Thus, the components of the free vector $\vec{P}_V^{(m)}$ in a point p are obtained by parallel displacement of the vectors $\vec{B}(x)$ to the point p, i.e.

$$(P_V^{(m)})_\iota = \iiint_V B_\iota^*(p), \tag{2.48}$$

where the $B_\iota^*(p)$ are the components of the vectors obtained by parallel displacement of the vectors $B_\iota(x)$ from the various points (x) to the point p.

In special relativity, this procedure leads to a unique result in any system of coordinates, since the space is flat and the result of a parallel displacement therefore is independent of the curve along which the displacement has been made. However, in general relativity where the space may be curved, it would seem impossible in this way to get an unambiguous expression for the linear momentum of a physical system in a given system of reference. This is certainly also true if we consider the matter alone. It is different, however, if we consider the momentum of the complete system of matter plus gravitational field, in which case it turns out to be possible to get a unique expression for the total linear momentum at least for any *insular* system where the matter is confined to a finite part of space.

The reason for this is the following. For an insular system, space-time can be regarded as flat at sufficiently large spatial distances from the system and, consequently, we may introduce coordinates which are at least asymptotically rectilinear. Further, in contrast to the integrals (2.47), the quantities $(P_V)_\iota$ in (2.44) have the form of a sum of vector components A_ι situated on the boundary surface F. Therefore, if we make the volume V so large that F lies entirely in the region where the space may be regarded as flat, the situation is exactly as in special relativity. In a system of coordinates which is rectilinear in this region, the components of the total momentum of the physical system inside the surface F are consistently given by (2.44), i.e.

by the arithmetical sum of the components of the vectors A_ι on F. The total momentum $\vec{P}_V$ is a free vector and, since the quantities A_ι in (2.44) are 3-vectors under spatial transformations (2.5), we get the components $(P_V)_\iota(p)$ in a point p in arbitrary spatial curvilinear coordinates by parallel displacement of the vectors $\vec{A}(x)$ to the point p, i.e.

$$(P_V)_\iota(p) = \iint_F A_\iota^*(p) \tag{2.49}$$

on the analogy of (2.48). This gives a unique result provided that the curves along which the displacements are made are chosen to lie entirely inside the region where the space may be considered as flat.[1]

If we had used Einstein's expression Θ_i^k for the energy-momentum complex instead of $\mathfrak{T}_i^k$, the just mentioned procedure would not have given consistent results for, in this case, the equations (2.43), (2.44) would be replaced by

$$(P_V^E)_\iota = \iiint_V \Theta_\iota^4 \, dx^1 \, dx^2 \, dx^3 = \iint_F h_\iota^{4\lambda} \, dS_\lambda \tag{2.50}$$

and, in contrast to A_ι in (2.44), (2.45), the quantity $h_\iota^{4\lambda} \, dS_\lambda$ does not transform as a 3-vector under the transformations (2.5) except if the functions $f^\iota(x^\varkappa)$ are linear. In curvilinear coordinates we would therefore not know how to perform the above mentioned parallel displacement, and we can only hope that the equations (2.50) give correct results for systems of coordinates which are asymptotically rectilinear. The results obtained in sections 4 and 5 of the present paper seem to justify this hope.

Finally, it should also be remarked that the preceding considerations are somewhat loose, since we have assumed that the space is flat for a sufficiently large surface F. Actually, the flatness of the space at large spatial distances from an insular system is only an asymptotic property and we have in each case to state more precisely how large the surface F has to be chosen.

There is another important question which we have disregarded so far. For a given tetrad field, the metric is determined by the equations (2.15), but for a given metric tensor $g_{ik}(x)$ the tetrad field is not uniquely deter-

[1] In a forthcoming paper it will be shown that the preceding considerations regarding the 3-momentum vector in curvilinear coordinates inside a given system of reference can easily be carried through also for the 4-momentum P_i in the 4-dimensional space, which enables us to give a meaning to P_i for arbitrary curvilinear space-time coordinates.

mined by these equations. If $h_i^{(a)}(x)$ represents a solution, then the tetrads

$$\check{h}_i^{(a)} = \Omega^{(a)}{}_{(b)}(x)\, h_i^{(b)} \tag{2.51}$$

also satisfy the equations (2.15), providedth at the scalar functions $\Omega^{(a)}{}_{(b)}(x)$ at each point (x) satisfy the orthogonality relations of a Lorentz rotation, i.e.

$$\Omega^{(a)}{}_{(c)}\, \Omega_{(b)}{}^{(c)} = \Omega_{(c)}{}^{(a)}\, \Omega^{(c)}{}_{(b)} = \delta_b^a \tag{2.52}$$

(the indices in parenthesis are lowered and raised by the same rule as in (2.14)).

It is usually assumed that all measurable physical quantities and all relations between such quantities must be invariant under arbitrary Lorentz rotations (2.51) of the tetrads. In the case of the covariant Dirac equation for fermion fields, for instance, measurable quantities such as the charge and current densities are unchanged under the transformations (2.51), in contrast to the field function $\psi(x)$ which transforms as an 'undor'. Now, the components of the complex T_i^k are invariant under (2.51) only if the rotation coefficients are constants $\overset{(o)}{\Omega}{}^{(a)}{}_{(b)}$, i.e. independent of (x). In fact, from the definition (2.26) of γ_{ikl} one finds at once the transformation law

$$\check{\gamma}^{ikl} \equiv \check{h}_i^{(a)}\, \check{h}_{(a)\,k;\,l} = \gamma_{ikl} + X_{ikl}, \tag{2.53}$$

where the tensor $X_{ikl} = -X_{kil}$ is given by

$$X_{ikl} = \Omega^{(c)}{}_{(a)}\, \Omega_{(cb),\,l}\, h_i^{(a)}\, h_k^{(b)}. \tag{2.54}$$

Further, since $h = \sqrt{-g}$ is invariant under (2.51), the transformation of the superpotential (2.30) is given by

$$\check{\mathfrak{U}}_i^{kl} = \mathfrak{U}_i^{kl} + Y_i^{kl} \tag{2.55}$$

with

$$Y_i^{kl} = -Y_i^{lk} = \frac{|h|}{\varkappa}\left[X^{kl}{}_i - \delta_i^k X^l + \delta_i^l X^k\right] \tag{2.56}$$

$$X^k = X^{ik}{}_i = \Omega^{(c)}{}_{(a)}\, \Omega_{(cb),\,i}\, h^{(a)\,i}\, h^{(b)\,k}. \tag{2.57}$$

Finally, we get from (2.22) the following transformation equation for the complex T_i^k under tetrad rotations (2.51):

$$\check{\mathsf{T}}_i^k = \check{\mathfrak{U}}_i^{kl}{}_{,\,l} = \mathsf{T}_i^k + Y_i^{kl}{}_{,\,l} \tag{2.58}$$

and the last term is in general not zero, unless the rotation coefficients $\Omega^{(a)}{}_{(b)}$ are constant.

Thus, Einstein's field equations which determine the metric only do not allow to calculate the complex T_i^k uniquely. Therefore, if one regards the energy density or more generally T_i^k as a measurable quantity, one will try to set up further equations which, together with Einstein's field equations, allow to determine the tetrad field so accurately that T_i^k can be calculated uniquely. Geometrically speaking, besides the curvature of 4-space which is determined by Einstein's equations, we need a set of supplementary equations which allow to calculate the torsion of the space (or the tetrad lattice), i.e. the tensor γ_{ikl}.

In the trivial case of a completely empty space where $\mathfrak{T}_i^k$ is everywhere zero, one usually assumes that space-time is flat, i.e.

$$R_{iklm} = 0\,. \tag{2.59}$$

In that case we must assume that also the torsion is zero, i.e.

$$\gamma_{ikl} = 0 \quad \text{or} \quad h^{(a)}_{i;\,k} = 0\,, \tag{2.60}$$

for only with this assumption will T_i^k be equal to zero, as we should have for a completely empty space. Since R_{iklm} is a linear function of the covariant derivatives of the $h_{(a)\,i}$ of the second order, the equations (2.60) are compatible with (2.59). In contrast to Θ_i^k which is different from zero in curvilinear coordinates, the covariant equations (2.60) ensure that $\mathsf{T}_i^k = 0$ in all systems of coordinates.

The equations (2.60) can also be written

$$\gamma_{(abc)} = 0\,, \tag{2.61}$$

where

$$\gamma_{(abc)} = \gamma_{ikl}\, h^i_{(a)}\, h^k_{(b)}\, h^l_{(c)} = h_{(a)\,k;\,l}\, h^k_{(b)}\, h^l_{(c)} \tag{2.62}$$

are the Ricci rotation coefficients. This means that the tetrad field in a completely empty space has to be chosen so that 'absolute' parallelism with respect to these tetrads (see reference 2, section 5) coincides with the Levi-Civita parallelism which is also global in the case of a flat space, where we can use pseudo-Cartesian or Lorentzian coordinates. In such coordinates

$$g_{ik} = \eta_{ik} \tag{2.63}$$

and (2.60), (2.61) mean that we may choose

$$h_i^{(a)} = \delta_i^a \tag{2.64}$$

or, more generally,

$$h_i^{(a)} = \overset{(o)}{\Omega}{}^{(a)}{}_{(i)}, \tag{2.65}$$

where $\overset{(o)}{\Omega}{}^{(a)}{}_{(b)}$ is any set of constant rotation coefficients satisfying the relations (2.52).

For a system with matter it is clear that (2.60) or (2.61) cannot be valid, for this would entail (2.59) which would be in contradiction with Einstein's field equations. However, for an insular system where space-time is asymptotically flat at large spatial distances r, (2.61) must hold asymptotically, i.e.

$$\gamma_{(abc)} \to 0 \quad \text{for} \quad r \to \infty. \tag{2.66}$$

Thus, in an asymptotically Lorentzian system of coordinates the tetrads must satisfy the boundary conditions.

A. $$h_i^{(a)} - \overset{(o)}{\Omega}{}^{(a)}{}_{(i)} \to \infty \quad \text{for} \quad r \to \infty. \tag{2.67}$$

Further, as regards the manner in which this quantity tends to zero, we shall make the following natural assumption:

B. $h_i^{(a)} - \overset{(o)}{\Omega}{}^{(a)}{}_{(i)}$ *shows the same asymptotic behaviour as the metric quantities* $g_{ik} - \eta_{ik}$.

This behaviour depends of course on the type of physical system we are dealing with. For a system with outgoing radiation, only, the boundary condition will have the character of Sommerfeld's radiation condition. The form of the boundary conditions will of course also depend on the system of coordinates. Although it may be convenient to use asymptotically rectilinear coordinates, the boundary conditions can of course be formulated in any system of coordinates.

As regards the supplementary equations which, together with Einstein's field equations and the boundary conditions, should determine the complex T_i^k uniquely, it was shown in reference 2 that the following six covariant equations would serve this purpose:

$$\gamma_{ik}{}^{l}{}_{;l} + \gamma_{ikl} \Phi^l = 0. \tag{2.68}$$

However, these equations are not the only possible ones and the arbitrariness in the choice of the supplementary equations is even somewhat larger than was assumed in reference 2. In an interesting paper by PELLEGRINI and PLEBANSKY[11], this arbitrariness is diminished by the requirement that all the equations for the tetrad field should be derived from a variational principle. In this way, they arrive at a theory which, in the weak-field approximation and in the case of a spherically symmetric system, is prac-

tically identical with the theory in reference 2. But in addition to that, their formulation opens up the possibility of an interesting generalization of the usual theory of gravitation, in particular as regards systems containing fermion fields. However, also this theory contains some arbitrariness and the equations determining the metric tensor are not exactly identical with Einstein's field equations. For this reason, it may be for the time preferable to work with the formulation developed in reference 2.

When we have made a certain choice as regards the supplementary equations, for instance the equations (2.68), the energy-momentum complex for a given physical system is a definite function of the space-time coordinates, which means that we may calculate the energy distribution throughout space. However, if it is true that the energy content in a small part of space is unmeasurable, then we have obviously obtained too much. Now, it is an interesting fact that, if we only regard the *total* energy and momentum as measurable quantities, the question of the exact form of the supplementary conditions does not arise. In fact, as we shall see in section 6, the energy and momentum contained in a sufficiently large volume V are invariant under all tetrad rotations (2.51) which respect the boundary conditions A and B for the tetrads formulated on p. 18. On the other hand, the distribution of the energy throughout space will in general be different after a tetrad rotation. This is quite satisfactory if the energy *distribution* is unmeasurable. The situation is then here somewhat similar to the case of the covariant Dirac equation where the measurable quantities, like the charge and current densities, are invariant under tetrad rotations, while the wave functions themselves are not invariant. From this point of view the tetrad field variables have to be regarded as subsidiary quantities like the potentials in electrodynamics, and the tetrad rotations are a kind of gauge transformations under which the measurable quantities, such as total energy and moment, are invariant. Supplementary equations of the type (2.68) are then not necessary, but sometimes it may be convenient to 'fix the gauge' by applying such covariant equations.*

3. The Gravitational Field at Large Spatial Distances from an Insular System with Axial Symmetry

In order to calculate the gravitational energy emitted from a physical system as well as the total energy and momentum of the system by means

* In some cases it may even be advantageous, just as in electrodynamics, to fix the gauge in a non-covariant way; this is not in contradiction with the principle of relativity, since the gauge of the tetrads in this point of view is considered unobservable. In this connection, cf. also reference 14.

of the theory outlined in the preceding section, we have to know the field at large spatial distances only. In reference 1, BONDI, VAN DER BURG and METZNER have given the exact form of the metric at large spatial distances from any axi-symmetric system with no ingoing radiation. These investigations were extended to an arbitrary system in a subsequent paper by SACHS[12]. In the present paper we shall, for simplicity, confine ourselves to the consideration of axi-symmetric systems and start by quoting some of the relevant results obtained by BONDI et al.

Although it is in principle allowed to use any system of coordinates in general relativity, there are certain classes of coordinate systems in which the boundary conditions have a particularly simple form.

In the system of coordinates S' with coordinates

$$(x'^i) = \{r, \theta, \varphi, u\} \tag{3.1}$$

introduced by BONDI et al., θ and φ are a kind of polar angles with the symmetry axis as polar axis, and r is a 'radial' coordinate chosen in such a way that the 2-surface $du = dr = 0$ has the area $4\pi r^2$. Further, the time variable u is defined so that the curve $du = d\theta = d\varphi = 0$ represents an *outgoing* light ray.

In S' the metric tensor g'_{ik} has the form

$$g'_{ik} = \left.\begin{pmatrix} 0 & 0 & 0 & -e^{2\beta} \\ 0 & r^2 e^{2\gamma} & 0 & -r^2 U e^{2\gamma} \\ 0 & 0 & r^2 \sin^2\Theta e^{-2\gamma} & 0 \\ -e^{2\beta} & -r^2 U e^{2\gamma} & 0 & -(r^{-1} V e^{2\beta} - r^2 U^2 e^{2\gamma}) \end{pmatrix}\right\} \tag{3.2}$$

where U, V, β, γ are functions of r, θ and u. The corresponding determinant $g' = \det\{g'_{ik}\}$ is given by

$$\sqrt{-g'} = r^2 \sin\theta\, e^{2\beta}. \tag{3.3}$$

The contravariant components of the metric tensor are

$$g'^{ik} = \left.\begin{pmatrix} r^{-1} V e^{-2\beta} & -U e^{-2\beta} & 0 & -e^{-2\beta} \\ -U e^{-2\beta} & r^{-2} e^{-2\gamma} & 0 & 0 \\ 0 & 0 & (r\sin\theta)^{-2} e^{2\gamma} & 0 \\ -e^{-2\beta} & 0 & 0 & 0 \end{pmatrix}\right\}. \tag{3.4}$$

To ensure regularity in the neighbourhood of the polar axis the functions V, β, $U/\sin\theta$, $\gamma/\sin^2\theta$ have to be regular as $\sin\theta$ goes to zero. Although dif-

ferent coordinate patches in general may be necessary throughout space-time, it is believed that the space sufficiently far from the system is covered by one patch of coordinates of the type (3.1)–(3.4). In these coordinates the absence of inward flowing radiation may be expressed by the assumption that the functions U, V, β, γ for sufficiently large distances r can be written as a power series in $1/r$ with coefficients depending on θ and u only. By introduction of the corresponding series expansion for g'_{ik} into Einstein's field equations for the empty space outside the matter one obtains

$$\left.\begin{aligned}
\gamma &= c\,(u,\theta)\,r^{-1} + O_3 \\
\beta &= -\frac{1}{4}\,c\,(u,\theta)^2\,r^{-2} + O_3 \\
U &= -(c + 2\,c\cot\theta)\,r^{-2} \\
&\quad + [2\,N\,(u,\theta) + 3\,cc_2 + 4\,c^2\cot\theta]\,r^{-3} + O_4 \\
V &= r - 2\,M\,(u,\theta) \\
&\quad - \left[N_2 + N\cot\theta - {c_2}^2 - 4\,cc_2\cot\theta - \frac{1}{2}\,c^2\,(1 + 8\cot^2\theta)\right] r^{-1} + O_2 .
\end{aligned}\right\} \tag{3.5}$$

Here, O_n means a term which vanishes as r^{-n} for $r \to \infty$. $c(u, \Theta)$, $M(u, \Theta)$, $N(u, \Theta)$ are functions of integrations which depend on the type of matter system we are dealing with and the suffix 2 means partial differentiation with respect to Θ for constant r, φ, u. In general we shall use the notation

$$(\ )_1 = \frac{\partial}{\partial r},\ (\ )_2 = \frac{\partial}{\partial \theta},\ (\ )_3 = \frac{\partial}{\partial \varphi},\ (\ )_0 = \frac{\partial}{\partial u}. \tag{3.6}$$

The functions c, M, N are not independent, they are connected by the relations

$$\left.\begin{aligned}
M_0 &= -{c_0}^2 + \frac{1}{2}\,A_0 \\
-3\,N_0 &= M_2 + 3\,cc_{02} + 4\,cc_0\cot\theta + c_0\,c_2
\end{aligned}\right\} \tag{3.7}$$

with

$$\left.\begin{aligned}
A &= c_{22} + 3\,c_2\cot\theta - 2\,c \\
&= (c_2\sin\theta + 2\,c\cos\theta)_2/\sin\theta \\
&= \left[\frac{(c\sin^2\theta)_2}{\sin\theta}\right]_2 /\sin\theta .
\end{aligned}\right\} \tag{3.8}$$

Thus, if $c(u, \theta)$ is given, the functions M and N may be obtained by integration of (3.7) and the flow of information in the system is entirely controlled by the function c which, in reference 1, is called the *news function*. Further, since

$$g'_{44} = -\left(1 - \frac{2M(u, \theta)}{r} + O_2\right) \tag{3.9}$$

on account of (3.2) and (3.5), the function $M(u, \theta)$ is called the *mass aspect*. In the case of a static system, M is simply equal to the total mass m of the system, i.e.

$$M = m. \tag{3.10}$$

In part D of reference 1, BONDI proves the interesting theorem that the mean value $m(u)$ of $M(u, \Theta)$ over all directions is a never increasing function of time. In fact, with

$$m(u) = \frac{1}{2}\int_0^\pi M(u, \theta) \sin\theta \, d\theta \tag{3.11}$$

we get, by means of (3.7), (3.8),

$$-m(u)_0 = -\frac{1}{2}\int_0^\pi M_0 \sin\theta \, d\theta = \frac{1}{2}\int_0^\pi {c_0}^2 \sin\theta \, d\theta. \tag{3.12}$$

Here we have used that

$$\int_0^\pi A \sin\theta \, d\theta = \frac{(c \sin^2\theta)_2}{\sin\theta}\Bigg|_0^\pi = 0 \tag{3.13}$$

on account of the regularity condition for $\gamma/\sin^2\theta$ for $\sin\theta \to 0$ which, by the first equation (3.5), leads to the following limiting behaviour for the news function c:

$$c \simeq k(u) \sin^2\theta \quad \text{for} \quad \sin\theta \to 0. \tag{3.14}$$

For a static system the quantity (3.11) is equal to the total mass or energy of the system and, since the right-hand side in (3.12) is always positive unless $c_0 = 0$, we see that a system which is initially and finally static must lose energy if the news function c_0 is different from zero in the intermediate stage.

This important result of BONDI was limited to the case where the system initially and finally is in a static state. By means of the theory of the preceding section we are now able to prove this theorem for any (axi-symmetric) system and we shall also verify Bondi's conjecture that the quantity $m(u)$ in (3.11) is equal to the total energy for all times, so that the formula (3.12) gives the energy radiated per unit time at any stage of the development of the system.

Let us first calculate the energy flux through a large sphere of 'radius' r using Einstein's energy-momentum complex Θ_i^k. According to (2.10) and (3.3), the energy current density should be

$$-\vartheta_4'^{\varkappa} = -\frac{r^2 \sin\Theta}{2\varkappa}\left[\Gamma'^{\varkappa}_{lm}\,(e^{2\beta}\,g'^{lm})_0 - \Gamma'^{s}_{ms}\,(e^{2\beta}\,g^{\varkappa m})_0\right]. \tag{3.15}$$

Further, if

$$dx'^{\varkappa} = \{0,\, d\theta,\, 0\},\quad \delta x'^{\varkappa} = \{0,\, 0,\, d\varphi\} \tag{3.16}$$

are two infinitesimal 3-vectors lying on the sphere of radius r in the directions of increasing θ and φ, respectively, the quantity (2.42), representing the surface element spanned by these vectors, becomes

$$dS'_{\varkappa} = \delta_{\varkappa\lambda\mu}\,dx'^{\lambda}\,\delta x'^{\mu} = \{d\theta\,d\varphi,\, 0,\, 0\}. \tag{3.17}$$

The energy flux in the outward direction through this surface element should then be

$$S'_E\,d\theta\,d\varphi = -\vartheta_4'^{\mu}\,dS'_{\varkappa} = -\vartheta_4'^{1}\,d\theta\,d\varphi. \tag{3.18}$$

By introducing the series expansion of the metric tensor (3.2)–(3.3) following from (3.5) into the right-hand side of (3.15) we get, as shown in the Appendix,

$$-\vartheta_4'^{\varkappa} = \frac{2\sin\theta}{\varkappa}\left[c_0^{\,2} - M_0 + \frac{1}{4}\cot\theta\,(c_{20} + 2\,c_0\cot\theta)\right]\delta_1^{\varkappa} + O_1. \tag{3.19}$$

For sufficiently large values of r we can neglect the term O_1 and we get for the differential energy flux (3.18) by means of the first equation (3.7)

$$S'_E\,d\theta\,d\varphi = \frac{2}{\varkappa}\left[2\,c_0^{\,2} - \frac{1}{2}A_0 + \frac{1}{4}\cot\theta\,(c_{20} + 2\,c_0\cot\theta)\right]\sin\theta\,d\theta\,d\varphi. \tag{3.20}$$

Thus, according to Einstein's expression for the energy flux, the total energy which per unit time is leaving a sphere with a sufficiently large radius should be

$$\iint S'_E \, d\theta \, d\varphi = \int_0^{\pi} {c_0}^2 \sin\theta \, d\theta + \frac{1}{8} \int_0^{\pi} c_0 \frac{1 + \cos^2\theta}{1 - \cos^2\theta} \sin\theta \, d\theta . \tag{3.21}$$

Here, we have introduced the value $\varkappa = 8\pi$ and used the equation (3.13) as well as the condition (3.14), which gives

$$\left.\begin{aligned} \int_0^{\pi} \left(c_{02} \cos\theta + 2 \, c_0 \frac{\cos^2\theta}{\sin\theta} \right) d\theta &= c_0 \cos\theta \Big|_0^{\pi} \\ + \int_0^{\pi} \left(2 \, c_0 \frac{\cos^2\theta}{\sin\theta} + c_0 \sin\theta \right) d\theta &= \int_0^{\pi} c_0 \frac{1 + \cos^2\theta}{1 - \cos^2\theta} \sin\theta \, d\theta . \end{aligned}\right\} \tag{3.22}$$

The expression (3.21) is not in accordance with Bondi's equation (3.12), in particular it does not have the essential property of being always positive since the integrant in the last term is linear in c_0.

The inadequacy of Einstein's expression $\Theta_i^{\,k}$ in the system of coordinates used by Bondi et al. is even more apparent if we calculate the total energy in a large sphere of radius r. By means of (2.13), (2.11) and (3.17) we get for this quantity

$$\left.\begin{aligned} H'_E(r) &= -\iiint \theta'^{\,4}_4 \, dx'^{\,1} \, dx'^{\,2} \, dx'^{\,3} \\ &= -\iiint \frac{\partial h'^{\,4\lambda}_4}{\partial x'^{\,\lambda}} \, dx'^{\,1} \, dx'^{\,2} \, dx'^{\,3} = -\iint h'^{\,4\lambda}_4 \, dS'_\lambda \\ &= -\iint h'^{\,41}_4 \, d\theta \, d\varphi , \end{aligned}\right\} \tag{3.23}$$

provided that the system of coordinates can be continued into the interior of the matter system in such a way that $h'^{\,4\lambda}_4$ is everywhere continuous. In the Appendix it is shown that $h'^{\,41}_4$ for large values of r is of the form

$$h'^{\,41}_4 = -\frac{2 \, r \sin\theta}{\varkappa} + O_0 , \tag{3.24}$$

which shows that

$$H'_E(r) \to \infty \quad \text{for} \quad r \to \infty . \tag{3.25}$$

It should be noted that the first term in (3.24), which causes the divergence, is completely independent of the functions c and M which characterize the system, i.e. the divergence is of the type mentioned earlier which was noticed

already by BAUER[6] for a completely empty world. If we, quite arbitrarily, subtract this infinity, the term O_0 in (3.24), when introduced into (3.23), does not give the correct value of the total energy even for a static system. According to the considerations in the preceding section, this could also be expected.

4. Gravitational Energy Radiation from an Axi-Symmetric System

In this section we shall show that the complex T_i^k (in contrast to Θ_i^k) gives a value for the energy radiation which is in agreement with Bondi's equation (3.12). In performing the calculations it is convenient to introduce a new system of coordinates S with coordinates

$$(x^i) = \{x, y, z, t\} \tag{4.1}$$

connected with the coordinates (3.1) of the system S' by the transformation

$$\left.\begin{aligned} &x = r\sin\theta\cos\varphi, \quad y = r\sin\theta\sin\varphi, \quad z = r\cos\theta \\ &x^4 = t = r + u. \end{aligned}\right\} \tag{4.2}$$

The advantage of the system S is that it is asymptotically Lorentzian and that the components of the metric tensor have a series expansion in $1/r$ starting with the power zero. Since T_i^k and $\mathfrak{U}_i^{kl}$ transform in a simple way, it is easy afterwards to find the components of these quantities in the system S'.

The transformation coefficients corresponding to (4.2) are

$$\left.\begin{aligned} \frac{\partial x^i}{\partial x'^k} = \begin{pmatrix} \sin\theta\cos\varphi & r\cos\theta\cos\varphi & -r\sin\theta\sin\varphi & 0 \\ \sin\theta\sin\varphi & r\cos\theta\sin\varphi & r\sin\theta\cos\varphi & 0 \\ \cos\theta & -r\sin\theta & 0 & 0 \\ 1 & 0 & 0 & 1 \end{pmatrix} \end{aligned}\right\} \tag{4.3}$$

with

$$r = \sqrt{x^2 + y^2 + z^2}. \tag{4.4}$$

The corresponding Jacobian is

$$J = \det\left\{\frac{\partial x^i}{\partial x'^k}\right\} = r^2\sin\theta. \tag{4.5}$$

Therefore, by (3.3),

$$\sqrt{-g} = \frac{1}{J}\sqrt{-g'} = e^{2\beta}. \tag{4.6}$$

For the calculations it is convenient to introduce the following four-component quantities:

$$\left.\begin{aligned} n_i &= \frac{\partial r}{\partial x^i} = \{\sin\theta\cos\varphi,\ \sin\theta\sin\varphi,\ \cos\theta,\ 0\} \\ m_i &= \{\cos\theta\cos\varphi,\ \cos\theta\sin\varphi,\ -\sin\theta,\ 0\} \\ l &= \{-\sin\varphi,\ \cos\varphi,\ 0,\ 0\} \\ \mu_i &= \frac{\partial u}{\partial x^i} = -(\eta_{i4} + n_i) = \{-\sin\theta\cos\varphi,\ -\sin\theta\sin\varphi,\ -\cos\theta,\ 1\} \end{aligned}\right\} \tag{4.7}$$

and the corresponding quantities n^i, m^i, l^i, μ^i with indices raised by means of the constant matrix $\eta^{ik} = \eta_{ik}$, i.e.

$$n^i = n_i,\ m^i = m_i,\ l^i = l_i,\ \mu^i = \eta^{ik}\mu_k = \{\mu_\iota,\ -1\}. \tag{4.8}$$

Then, obviously,

$$\left.\begin{aligned} n_i n^i &= m_i m^i = l_i l^i = 1, \qquad \mu_i \mu^i = 0 \\ n_i m^i &= n_i l^i = m_i l^i = m_i \mu^i = l_i \mu^i = 0,\ n_i \mu^i = -1. \end{aligned}\right\} \tag{4.9}$$

The derivatives of the quantities (4.7) with respect to u and r are zero, i.e.

$$(n_i)_0 = (n_i)_1 = (m_i)_0 = \cdots\cdots = (\mu_i)_0 = (\mu_i)_1 = 0 \tag{4.10}$$

and the derivatives with respect to θ and φ are at once seen to be

$$\left.\begin{aligned} &(n_i)_2 = m_i,\ (m_i)_2 = -n_i,\ (l_i)_2 = 0,\ (\mu_i)_2 = -m_i \\ &(n_i)_3 = \sin\theta\, l_i,\ (m_i)_3 = \cos\theta\, l_i, \\ &(l_i)_3 = -(\cos\theta\, m_i + \sin\theta\, n_i) \\ &(\mu_i)_3 = -\sin\theta\, l_i. \end{aligned}\right\} \tag{4.11}$$

Further, it follows from (4.7) that

$$\left.\begin{aligned} &m_i m_k + l_i l_k + \mu_i \mu_k + \eta_{i4}\mu_k + \mu_i \eta_{k4} \\ &= m_i m_k + l_i l_k - (\mu_i n_k + n_i \mu_k) - \mu_i \mu_k = \eta_{ik}. \end{aligned}\right\} \tag{4.12}$$

The transformation coefficients (4.3) may now be written as a row matrix

$$\left.\begin{aligned} \frac{\partial x^i}{\partial x'^k} &= (-\mu^i,\ r m^i,\ r\sin\theta\, l^i,\ \delta_4^i) \\ k &= \quad 1 \qquad 2 \qquad 3 \qquad 4\,. \end{aligned}\right\} \tag{4.13}$$

The inverse coefficients are then the column matrix

$$\left.\frac{\partial x'^i}{\partial x^k} = \begin{pmatrix} n_k \\ r^{-1} m_k \\ (r\sin\theta)^{-1} l_k \\ \mu_k \end{pmatrix}\right\} \tag{4.14}$$

since

$$\left.\begin{aligned} \frac{\partial x^i}{\partial x'^l}\frac{\partial x'^l}{\partial x^k} &= -\mu^i n_k + m^i m_k + l^i l_k + \delta_4^i \mu_k \\ &= m^i m_k + l^i l_k + \mu^i \mu_k + \mu^i \eta_{k4} + \eta_4^i \mu_k = \delta_k^i \end{aligned}\right\} \tag{4.15}$$

on account of (4.12).

For the covariant components of the metric tensor in S we get, by (3.2) and (4.14),

$$\left.\begin{aligned} g_{ik} = \frac{\partial x'^l}{\partial x^i}\frac{\partial x'^m}{\partial x^k} g'_{lm} &= e^{2\gamma} m_i m_k + e^{-2\gamma} l_i l_k \\ -(r^{-1} V e^{2\beta} - r^2 U^2 e^{2\gamma})\,\mu_i \mu_k &- e^{2\beta}(\mu_i n_k + n_i \mu_k) \\ - r U e^{2\gamma}(m_i \mu_k + \mu_i m_k)&. \end{aligned}\right\} \tag{4.16}$$

Similarly, by (3.4) and (4.13),

$$\left.\begin{aligned} g^{ik} = \frac{\partial x^i}{\partial x'^l}\frac{\partial x^k}{\partial x'^m} g'^{lm} &= e^{-2\gamma} m^i m^k + e^{2\gamma} l^i l^k + r^{-1} V e^{-2\beta} \mu^i \mu^k \\ + e^{-2\beta}(\mu^i \eta_4^k + \eta_4^i \mu^k) &+ r U e^{-2\beta}(\mu^i m^k + m^i \mu^k)\,. \end{aligned}\right\} \tag{4.17}$$

At large distances r, the components of the metric tensor appear as a power series in $1/r$ with coefficients depending on u, θ, φ. In the following we shall only need explicit expressions for the terms up to the second power. By introduction of the expansions (3.5) into (4.16), and using (4.12), one easily finds

$$g_{ik} = \eta_{ik} + y_{ik} + z_{ik} + O_3 \tag{4.18}$$

with

$$y_{ik} = \alpha_{ik}\, r^{-1}, \qquad z_{ik} = \beta_{ik}\, r^{-2} \tag{4.19}$$

and

$$\left.\begin{aligned} \alpha_{ik} = \alpha_{ki} &= 2c\,(m_i m_k - l_i l_k) + 2M\,\mu_i \mu_k \\ &\quad + (c_2 + 2c\cot\theta)\,(m_i \mu_k + \mu_i m_k), \\ \beta_{ik} = \beta_{ki} &= 2c^2\,(m_i m_k + l_i l_k) + \frac{1}{2}\,c^2\,(\mu_i n_k + n_i \mu_k) \\ &\quad + (N_2 + N\cot\theta)\,\mu_i \mu_k - (2N + cc_2)\,(m_i \mu_k + \mu_i m_k). \end{aligned}\right\} \tag{4.20}$$

If we define the quantities y^{ik}, z^{ik}, α^{ik}, β^{ik} with indices raised by means of the constant matrix η^{ik} as in (4.8), then α^{ik} and β^{ik} are obtained from (4.20) by substituting m_i, l_i, μ_i and n_i by the quantities (4.8).

Now, it is easily seen that the contravariant components of the metric tensor have the following series expansion:

$$g^{ik} = \eta^{ik} - y^{ik} - z^{ik} + y^{ir}\, y_r{}^k + O_3, \tag{4.21}$$

for this expression satisfies the relation

$$g^{il}\, g_{kl} = \delta^i_k \tag{4.22}$$

up to the terms of second power in $1/r$. The expression (4.21) can also be obtained by introduction of the expansions (3.5) into (4.17).

Let $\psi\,(u, r, \theta, \varphi)$ be any function of the variables (x'^i) and let us denote the derivatives with respect to x^l by

$$\psi_{,l} \equiv \frac{\partial \psi}{\partial x^l} \tag{4.23}$$

with a comma in front of the index l, in contrast to the derivatives (3.6) with respect to x'^l which are written without a comma.

Then, by means of (4.14),

$$\left.\begin{aligned} \psi_{,l} &= \frac{\partial x'^m}{\partial x^l}\,\frac{\partial \psi}{\partial x'^m} \\ &= \psi_0\, \mu_l + \psi_1\, n_l + \frac{\psi_2\, m_l}{r} + \frac{\psi_3\, l_l}{r\sin\theta}. \end{aligned}\right\} \tag{4.24}$$

If ψ is equal to the function y_{ik} defined by (4.19), we have

$$y_{ik,\,l} = \frac{(\alpha_{ik})_0}{r}\,\mu_l + \frac{-\alpha_{ik}\,n_l + (\alpha_{ik})_2\,m_l + (\alpha_{ik})_3\,l_l/\sin\theta}{r^2}. \tag{4.25}$$

On the other hand, if ψ is a quantity of the type O_2, like z_{ik} or $y_{ir}\,y^r_k$, we have simply

$$z_{ik,\,l} = (z_{ik})_0\,\mu_l + O_3 = \frac{(\beta_{ik})_0}{r^2}\,\mu_l + O_3. \tag{4.26}$$

From (4.6), (3.5) and (4.21) we get the following expansion for $\mathfrak{g}^{ik} = \sqrt{-g}\,g^{ik}$

$$\mathfrak{g}^{ik} = \eta^{ik} - \frac{\alpha^{ik}}{r} - \frac{\beta^{ik} - \alpha^{ir}\,\alpha^k_r + \eta^{ik}\,c^2/2}{r^2} + O_3 \tag{4.27}$$

and, by means of (4.25), (4.26) and (4.9)–(4.11), one finds, as seen in the Appendix (A.1–A.8),

$$\mathfrak{g}^{ik}{}_{,\,k} = \frac{2\,M - A}{r^2}\,\mu^i + O_3. \tag{4.28}$$

This shows that our system of coordinates is harmonic only apart from terms of the type O_2.

In order to calculate the total energy and momentum as well as the energy emitted by means of the complex $\mathfrak{T}_i{}^k$ we need an expression for the tetrad field $h^{(a)}{}_i$ corresponding to the metric (4.18)–(4.21). As explained in section 2, the tetrad field is not uniquely determined by the equation (2.15), since any tetrad rotation (2.51) will leave the metric unchanged. However, as was mentioned already in section 2 and as will be shown in detail in section 6, the values of the total energy and momentum given by (2.41) and (2.44) with a sufficiently large surface F are the same for any tetrad field satisfying (2.15) and the boundary conditions A and B on p. 18. Therefore we can choose any tetrad field satisfying these conditions, for instance

$$h_{(a)\,i} = \eta_{ai} + \frac{1}{2}\,y_{ai} + \frac{1}{2}\left(z_{ai} - \frac{1}{4}\,y_{ar}\,y^r_i\right) + O_3, \tag{4.29}$$

which is symmetrical in a and i. This expression is in accordance with the equation (2.15), for we have

$$h_i^{(a)}\, h_{(a)\,k} = \eta_{ik} + \frac{1}{2}(y_{ik} + y_{ki}) + \frac{1}{2}\left(z_{ik} - \frac{1}{4}\, y_{ir}\, y_k^r\right)$$
$$+ \frac{1}{2}\left(z_{ki} - \frac{1}{4}\, y_{kr}\, y_i^r\right) + \frac{1}{4}\, y_i^a\, y_{ak} + O_3$$
$$= \eta_{ik} + y_{ik} + z_{ik} + O_3 = g_{ik}$$

on account of (4.18). Further, since $h_{(a)\,i}$ in (4.29) is an algebraic function of the quantities y_{ik} and z_{ik} entering in the expression (4.18) for $g_{ik} - \eta_{ik}$, it is clear that this tetrad field satisfies the conditions A and B.

We shall now calculate the complex $\mathfrak{t}_i^k$, defined by (2.31), up to terms of power 2 in $1/r$. To this end, we only need to calculate the quantities (2.26), (2.27), which occur quadratically in $\mathfrak{t}_i^k$ up to the first power in $1/r$. According to (4.18), the Christoffel symbols are simply

$$\Gamma_{i,\,kl} = \frac{1}{2}(y_{ik,\,l} + y_{il,\,k} - y_{kl,\,i}) + O_2\,. \tag{4.30}$$

Further, since

$$\left.\begin{aligned} \gamma_{ikl} &= h_i^{(a)}\, h_{(a)\,k;\,l} = h_i^{(a)}\,(h_{(a)\,k,\,l} - \Gamma_{kl}^r\, h_{(a)\,r}) \\ &= h_i^{(a)}\, h_{(a)\,k,\,l} - \Gamma_{i,\,kl}\,, \end{aligned}\right\} \tag{4.31}$$

we get, by (4.29), (4.30) and (4.25),

$$\left.\begin{aligned} \gamma_{ikl} &= \delta_i^a\, \frac{1}{2}\, y_{ak,\,l} - \frac{1}{2}(y_{ik,\,l} + y_{il,\,k} - y_{kl,\,i}) + O_2 \\ &= \frac{1}{2}(y_{kl,\,i} - y_{il,\,k}) + O_2 \\ &= \frac{1}{2\,r}\,[(\alpha_{kl})_0\, \mu_i - (\alpha_{il})_0\, \mu_k] + O_2\,. \end{aligned}\right\} \tag{4.32}$$

Thus,

$$\Phi^k = \gamma^i_{ki} = \frac{1}{2\,r}\,[(\alpha_{ki})_0\, \mu^i - (\alpha_i^i)_0\, \mu_k] + O_2 = O_2 \tag{4.33}$$

on account of the relations

$$\alpha_i^i = 0\,, \quad \alpha_{ki}\, \mu^i = 0 \tag{4.34}$$

following from (4.20) and (4.9).

From (4.32)–(4.34) and (4.9) one easily finds that the Lagrangian (2.29) is zero up to terms of the second power in $1/r$. In fact, we have

$$\mathfrak{L} = \frac{1}{4\,r^2}\left[(\alpha_{kl})_0\,\mu_i - (\alpha_{il})_0\,\mu_k\right]\left[(\alpha^{ki})_0\,\mu^l - (\alpha^{li})_0\,\mu^k\right] + O_3 = O_3. \tag{4.35}$$

Finally, since

$$\left.\begin{aligned} \Delta^l{}_{mi} &= h^{(a)\,l}\,h_{(a)\,m,\,i} = \eta^{al}\,\frac{1}{2}\,y_{am,\,i} + O_2 \\ &= \frac{1}{2\,r}\,(\alpha^l_m)_0\,\mu_i + O_2 \end{aligned}\right\} \tag{4.36}$$

we get for the complex $\mathfrak{t}_i^{\,k}$ in (2.31)

$$\begin{aligned} \mathfrak{t}_i^{\,k} &= \frac{1}{\varkappa}\,\gamma^{km}{}_l\,\Delta^l{}_{mi} + O_3 \\ &= \frac{1}{4\,\varkappa r^2}\left[(\alpha^m_l)_0\,\mu^k - (\alpha^k_l)_0\,\mu^m\right](\alpha^l_m)_0\,\mu_i + O_3. \end{aligned}$$

Hence, outside the matter where $\mathfrak{T}_i^{\,k} = 0$,

$$\left.\begin{aligned} \mathsf{T}_i^{\,k} = \mathfrak{t}_i^{\,k} &= \frac{1}{4\,\varkappa r^2}\,(\alpha_{lm})_0\,(\alpha^{lm})_0\,\mu_i\,\mu^k + O_3 \\ &= \frac{2\,{c_0}^2}{\varkappa r^2}\,\mu_i\,\mu^k + O_3. \end{aligned}\right\} \tag{4.37}$$

Here, we have again used (4.34) and the relation

$$(\alpha_{ik})_0\,(\alpha^{ik})_0 = 8\,{c_0}^2 \tag{4.38}$$

following from (4.20) and (4.9).

For sufficiently large values of r where we can neglect the term O_3, the 3-vector density

$$\mathfrak{S}^\varkappa = -\mathfrak{t}_4^{\,\varkappa} = \frac{2\,{c_0}^2}{\varkappa r^2}\,n^\varkappa, \tag{4.39}$$

which represents the energy current, lies in the direction of increasing r. Now, let dx^λ and δx^μ denote two infinitesimal 3-vectors which are tangents to the sphere of radius r in the directions of increasing θ and φ, respectively. Then,

$$dx^{\lambda} = \{r\cos\theta\cos\varphi\, d\theta,\ r\cos\theta\sin\varphi\, d\theta,\ -r\sin\theta\, d\theta\} = r m^{\lambda}\, d\theta$$
$$\delta x^{\mu} = \{-r\sin\theta\sin\varphi\, d\varphi,\ r\sin\theta\cos\varphi\, d\varphi,\quad 0\quad\} = r\sin\theta\, l^{\mu}\, d\varphi$$

and the quantity $dS_{\varkappa} = \delta_{\varkappa\lambda\mu}\, dx^{\lambda}\, \delta x^{\mu}$, representing the surface element spanned by these vectors, is

$$dS_{\varkappa} = n_{\varkappa}\, r^2 \sin\theta\, d\theta\, d\varphi . \tag{4.40}$$

Therefore, the energy flux through this surface element is, for sufficiently large values of r,

$$S d\theta\, d\varphi = \mathfrak{S}^{\varkappa}\, dS_{\varkappa} = \frac{2\, c_0^{\,2}}{\varkappa} \sin\theta\, d\theta\, d\varphi . \tag{4.41}$$

The total energy which per unit time leaves the sphere of radius r is obtained by integrating over all directions, i.e.,

$$-\frac{dH}{dt} = \int\!\!\int S d\theta\, d\varphi = \frac{1}{2}\int_0^{\pi} c_0^{\,2} \sin\theta\, d\theta . \tag{4.42}$$

This expression is in accordance with Bondi's equation (3.12), but the calculation has here been performed in the system S instead of in S', and we have to show that the same result holds in the system of coordinates used by Bondi et al. By means of the transformation law (2.34) for the energy-momentum complex it is now easy to calculate the quantity $\mathfrak{t}_4'^{k}$ in the system S'. Since the coordinate transformation (4.2) is of the type (2.36), $\mathfrak{t}_4^{\,k}$ transforms as a vector density.

Hence, by (4.5) and (4.37),

$$\mathfrak{t}_4'^{k} = r^2 \sin\theta\, \frac{\partial x'^{k}}{\partial x^{m}}\, \mathfrak{t}_4^{\,m} = \frac{2\, c_0^{\,2}}{\varkappa}\, \mu'^{k} \sin\theta + O_1 \tag{4.43}$$

with

$$\mu'^{k} = \frac{\partial x'^{k}}{\partial x^{m}}\, \mu^{m} = \{-1, 0, 0, 0\}. \tag{4.44}$$

Here we have used (4.14) and (4.9). Thus, we get for the 3-vector density

$$\mathfrak{S}'^{\varkappa} = -\mathfrak{t}_4'^{\varkappa} = \frac{2\, c_0^{\,2} \sin\theta}{\varkappa}\, \delta_1^{\varkappa} + O_1 \tag{4.45}$$

and, for sufficiently large values of r, the energy flux through the surface element defined by (3.17) becomes

$$S' d\theta d\varphi = \mathfrak{S}'^{\varkappa} dS'_{\varkappa} = \frac{2 c_0^2}{\varkappa} \sin\theta d\theta d\varphi . \tag{4.46}$$

As one should expect, a comparison with (4.41) shows that the energy flux is the same in the system S' as in S, since the transformation (4.2) does neither change the system of reference nor the time scale.

On the other hand, Einstein's expression (2.10) does not have this important property. In the system S we get, by means of (4.30) and (4.25), for the Lagrangian $\mathfrak{L}_E$ defined by (2.8)

$$\left.\begin{aligned} \mathfrak{L}_E = -\frac{1}{4 r^2} [(\alpha^{lk})_0 \mu_m + (\alpha^l_m)_0 \mu^k - (\alpha^k_m)_0 \mu^l] \\ \times [(\alpha^m_k)_0 \mu_l + (\alpha^m_l)_0 \mu_k - (\alpha_{kl})_0 \mu^m] + O_3 = O_3 \end{aligned}\right\} \tag{4.47}$$

on account of (4.34) and (4.9). Further, since

$$\Gamma^s_{ms} = \frac{(\sqrt{-g})_{,m}}{\sqrt{-g}} = O_2$$

and

$$(\sqrt{-g}\, g^{lm})_{,i} = -\gamma^{lm}{}_{,i} + O_2 = -\frac{(\alpha^{lm})_0}{r} \mu_i + O_2 ,$$

we get from (2.10)

$$\begin{aligned} \vartheta_i{}^k &= \frac{1}{2\varkappa} \Gamma^k_{lm} (\sqrt{-g}\, g^{lm})_{,i} + O_3 \\ &= -\frac{1}{4\varkappa r^2} [(\alpha^k_l)_0 \mu_m + (\alpha^k_m)_0 \mu_l - (\alpha_{lm})_0 \mu^k] (\alpha^{lm})_0 \mu_i + O_3 \\ &= \frac{1}{4\varkappa r^2} (\alpha_{lm})_0 (\alpha^{lm})_0 \mu_i \mu^k + O_3 \end{aligned}$$

or, by (4.38),

$$\vartheta_i{}^k = \frac{2 c_0^2}{\varkappa r^2} \mu_i \mu^k + O_3 . \tag{4.48}$$

A comparison of (4.48) with (4.37) shows that Einstein's expression for the energy-momentum complex gives the correct value (4.41) for the energy flux when calculated in the system S. However, since $\vartheta_4{}^k$ transforms in an unphysical way under the transformation (4.2), it leads to the wrong result (3.20) for the radiated energy in the system S' adopted by Bondi et al.

The calculations of the present section have corroborated the conjec-

ture of BONDI regarding the total energy flux from an axi-symmetric system expressed by the equation (3.12). In addition to that, our equation (4.41) gives the angular distribution of the energy flux which must be regarded as a measurable quantity, provided we can construct a receiver of gravitational energy which can be placed at large distances from the emitter in different directions. According to (4.41), the energy flux per unit solid angle is given by the square of the news function $c_0(t-r, \theta)$ and, by (3.14), we see that the energy flux must be zero in the direction of the symmetry axis.

For a detailed account of the angular distribution of the radiation from a given physical system we have to know the angular dependence of c_0. This requires a continuation of the solutions (3.2), (3.5) of the field equations at large distances into the interior of the system. So far this has been achieved exactly for a static system only. However, for a quasi-static system and sufficiently weak radiation, BONDI[1] found the following approximate expression for the news function $c(u, \theta)$:

$$c = \frac{1}{2} Q_{00} \sin^2 \theta, \tag{4.49}$$

where $Q(u)$ is the quadrupole moment of the system. According to this expression we should expect a steep maximum for the energy radiation in directions perpendicular to the axis of symmetry.

5. The Total Energy and Momentum

We begin this section by performing a calculation of the total energy which, as we shall see, leads to a verification of Bondi's conjecture that the quantity $m(u)$ in (3.11) represents the total mass or energy of the system. Also here it is most convenient to work in the system S instead of in S', but first we must show that the total energy is the same in both systems. According to (2.41), the energy contained in a large sphere of radius r at the time t is in the system S

$$H(u, r) = -\iint \mathfrak{U}_4^{\,4\lambda}\, dS_\lambda. \tag{5.1}$$

Similarly in S'

$$H'(u, r) = -\iint \mathfrak{U}_4'^{\,4\lambda}\, dS'_\lambda. \tag{5.2}$$

In this integral (5.1), r and t are constant, while in (5.2) r and u have to be kept constant.

Since $u = t - r$, the 2-surfaces over which the integrations in (5.1) and (5.2) are to be performed are identical. On account of (3.17), the integrant in the last integral is

$$\mathfrak{U}_4'^{4\lambda}\, dS_\lambda' = \mathfrak{U}_4'^{41}\, d\theta\, d\varphi. \tag{5.3}$$

Further, since $\mathfrak{U}_i^{kl}$ is a tensor density, we get, by means of (4.5), (4.13) and (4.14),

$$\left.\begin{aligned} \mathfrak{U}_4'^{41} &= J \frac{\partial x^r}{\partial x'^4} \frac{\partial x'^4}{\partial x^s} \frac{\partial x'^1}{\partial x^t}\, \mathfrak{U}_r^{st} \\ &= r^2 \sin\theta\, \delta_4^r\, \mu_s\, n_t\, \mathfrak{U}_r^{st}. \end{aligned}\right\} \tag{5.4}$$

Now, $\mathfrak{U}_r^{st}$ is antisymmetric in s and t and, according to (4.7), $\mu_s = \delta_s^4 - n_s$. Therefore, by (5.3), (5.4) and (4.40),

$$\mathfrak{U}_4'^{4\lambda}\, dS_\lambda' = \mathfrak{U}_4^{4\tau}\, n_\tau\, r^2 \sin\theta\, d\theta\, d\varphi = \mathfrak{U}_4^{4\tau}\, dS_\tau, \tag{5.5}$$

which shows that the integrals in (5.1) and (5.2) are equal:

$$H'(u, r) = H(u, r). \tag{5.6}$$

The integrant in (5.1) can, by (4.40) and (4.7), be written

$$-\mathfrak{U}_4^{4\lambda}\, dS_\lambda = \mathfrak{U}_4^{4l}\, \mu_l\, r^2 \sin\theta\, d\theta\, d\varphi, \tag{5.7}$$

which shows that we have to calculate $\mathfrak{U}_4^{4l}\, \mu_l$ up to terms of the second power in $1/r$. More generally we have, by (2.30) and (4.6),

$$\mathfrak{U}_i^{kl}\, \mu_l = \frac{e^2 \beta}{\varkappa} \left[\gamma^{kl}{}_i - \delta_i^k\, \Phi^l\, \mu_l + \mu_i\, \Phi^k\right]. \tag{5.8}$$

The calculation of $\gamma^{kl}{}_i$ and Φ^l for the tetrad field (4.29) is carried out in the Appendix (A.9–A.15) and gives the result

$$\mathfrak{U}_i^{kl}\, \mu_l = \frac{1}{2\varkappa r^2} \left\{(-4M + A)\, \mu_i\, \mu^k - (c_2 + 2c\cot\theta)\, m_i\, \mu^k\right\} + O_3. \tag{5.9}$$

By introduction of this expression with $i = k = 4$ into (5.7) and (5.1) we get

$$\left.\begin{aligned} H(u, r) &= \iint \mathfrak{U}_4{}^{4l}\, \mu_l\, r^2 \sin\theta\, d\theta\, d\varphi \\ &= \frac{1}{2\varkappa}\iint (4M - A)\sin\theta\, d\theta\, d\varphi + O_1 \end{aligned}\right\} \tag{5.10}$$

or, by means of (3.13) and (3.11) and putting $\varkappa = 8\pi$,

$$H(u, r) = m(u) + O_1 . \tag{5.11}$$

For sufficiently large values of r we can neglect the last term in (5.11) and the remaining term, which is a function of u only, we shall *define* as the total energy H of a non-closed system. Thus, the total energy

$$H = m(u) = \frac{1}{2}\int_0^{\pi} M(u, \theta)\sin\theta\, d\theta \tag{5.12}$$

is just given by Bondi's expression (3.11).

We shall now perform a similar calculation of the total momentum of the system. As explained in section 2, this quantity is given by the simple expression (2.44) if, and only if, the system of coordinates is asymptotically rectilinear. This is obviously the case with S but not with S'. Thus, in S we get for the linear momentum contained in a large sphere of radius r, by (2.44), (4.40) and (5.9),

$$\left.\begin{aligned} P_l(u, r) &= \iint \mathfrak{U}_l{}^{4\lambda}\, dS_\lambda = -\iint \mathfrak{U}_l{}^{4l}\, \mu_l\, r^2 \sin\theta\, d\theta\, d\varphi \\ &= \frac{1}{2\varkappa}\iint (4M - A)\, n_l \sin\theta\, d\theta\, d\varphi \\ &\quad - \frac{1}{2\varkappa}\iint (c_2 + 2c\cot\theta)\, m_l \sin\theta\, d\theta\, d\varphi + O_1 . \end{aligned}\right\} \tag{5.13}$$

Thus,

$$P_l(u, r) = P_l(u) + O_1 \tag{5.14}$$

with

$$\left.\begin{aligned} P_l &= \frac{1}{2\varkappa}\iint (4M - A)\, n_l \sin\theta\, d\theta\, d\varphi \\ &\quad - \frac{1}{2\varkappa}\iint (c_2 + 2c\cot\theta)\, m_l \sin\theta\, d\theta\, d\varphi . \end{aligned}\right\} \tag{5.15}$$

Again we can neglect the last term O_1 in (5.14) for sufficiently large values of r and *define* the 'total momentum P_l' of a non-closed system by the remaining term (5.15) which is a function of u only. Since M, A and c are independent of φ for an axi-symmetric system, while n_1, n_2, m_1, m_2 are proportional to $\cos\varphi$ or $\sin\varphi$, the integration over φ in (5.15) gives at once the value zero for the components of the total momentum in a direction perpendicular to the symmetry axis, as one should expect:

$$P_1 = P_2 = 0\,. \tag{5.16}$$

For the component along the symmetry axis we get, by (5.15), (3.8) and (4.7),

$$P_3 = \frac{4\pi}{\varkappa}\int_0^{\pi} M\cos\theta\sin\theta\,d\theta$$
$$-\frac{\pi}{\varkappa}\int_0^{\pi}[(c_2\sin\theta + 2\,c\cos\theta)_2\cos\theta - (c_2\sin\theta + 2\,c\cos\theta)\sin\theta]\,d\theta\,. \tag{5.17}$$

The last integral is easily seen to be zero, for it is obviously equal to

$$\int_0^{\pi}[(c_2\sin\theta + 2\,c\cos\theta)\cos\theta]_2\,d\theta = (c_2\sin\theta + 2\,c\cos\theta)\cos\theta\,|_0^{\pi} = 0$$

on account of (3.14). Hence,

$$P_3 = \frac{1}{2}\int_0^{\pi} M(u,\theta)\cos\theta\sin\theta\,d\theta\,. \tag{5.18}$$

The equations (5.12), (5.16) and (5.18) show that the components of the 'total four-momentum'

$$P_i = \{P_l, -H\} \tag{5.19}$$

are

$$P_i = \left\{0\,,\ 0\,,\ \frac{1}{2}\int_0^{\pi} M\cos\theta\sin\theta\,d\theta\,,\ -\frac{1}{2}\int_0^{\pi} M\sin\theta\,d\theta\right\}. \tag{5.20}$$

For the time derivatives of these quantities we get, by means of (3.7) and (3.13),

$$\frac{dP_1}{dt} = \frac{dP_2}{dt} = 0 \tag{5.21}$$

$$\left.\begin{aligned} \frac{dP_4}{dt} = -\frac{dH}{dt} &= -\frac{1}{2}\int_0^{\pi} M_0 \sin\theta \, d\theta \\ &= \frac{1}{4\pi}\iint c_0{}^2 \, d\Omega = \frac{1}{4\pi}\iint (\vec{\mathfrak{S}}\vec{n}) \, r^2 \, d\Omega , \end{aligned}\right\} \tag{5.22}$$

where $\vec{\mathfrak{S}}$ is the energy current density (4.39) and

$$d\Omega = \sin\theta \, d\theta \, d\varphi .$$

(5.22) shows that the energy is conserved.

Further,

$$\frac{dP_3}{dt} = \frac{1}{2}\int_0^{\pi} M_0 \cos\theta \sin d\theta = -\frac{1}{4\pi}\iint c_0{}^2 \cos\theta \, d\Omega = -\iint \mathfrak{S}^3 \, r^2 \, d\Omega , \tag{5.23}$$

where $\mathfrak{S}^3$ is the component of the vector density (4.39) in the direction of the symmetry axis. Here we have used that the integral

$$\begin{aligned} \int_0^{\pi} A_0 \cos\theta \sin\theta \, d\theta &= \int_0^{\pi} [c_{22} \sin\theta \cos\theta + 3 \, c_2 \cos^2\theta - 2 \, c \sin\theta \cos\theta]_0 \, d\theta \\ &= \int_0^{\pi} [c_{20} \sin\theta \cos\theta + c_0 \, (1 + \cos^2\theta)]_2 \, d\theta \\ &= [c_{20} \sin\theta \cos\theta + c_0 \, (1 + \cos^2\theta)] \, |_0^{\pi} = 0 \end{aligned}$$

on account of (3.14). The equations (5.21), (5.23) show that *the gravitational energy radiated administers a recoil to the system of the same amount as in the case of electromagnetic radiation.*

The relations (5.21)–(5.23) could also be obtained directly from (2.3). If we integrate this equation over the interior of a large sphere of radius r, we get

$$\frac{d}{dt}\iiint \mathsf{T}_i^4 \, dx^1 \, dx^2 \, dx^3 = -\iiint \mathsf{T}_i^{\varkappa}{}_{,\varkappa} \, dx^1 \, dx^2 \, dx^3 = -\iint \mathsf{T}_i^{\varkappa} \, dS_{\varkappa} . \tag{5.24}$$

In virtue of (4.37) and (4.40) this gives, for sufficiently large values of r,

$$\left.\begin{aligned}\frac{dP_i}{dt} &= -\int\!\!\int \frac{2\,c_0^2}{\varkappa r^2}\,\mu_i\,\mu^{\varkappa}\,n_{\varkappa}\,r^2\sin\theta\,d\theta\,d\varphi = \frac{1}{4\pi}\int\!\!\int c_0^2\,\mu_i\,d\Omega \\ &= \left\{0\,,\,0\,,\,-\frac{1}{2}\int_0^{\pi} c_0^2\cos\theta\sin\theta\,d\theta\,,\,\frac{1}{2}\int_0^{\pi} c_0^2\sin\theta\,d\theta\right\}\end{aligned}\right\} \tag{5.25}$$

in accordance with (5.20)–(5.23).

In this section we have *defined* the 'total momentum and energy' as the quantities obtained from (5.11) and (5.14) by neglecting terms of the type O_1. This amounts to neglecting all terms of the type O_3 in $\mathfrak{U}_i^{4l}\mu_l$ in the surface integrals (5.10) and (5.13). Therefore, P_i will be equal to the momentum and energy contained in a sphere of radius r only if the terms O_3 occurring in the series expansion of $\mathfrak{U}_i^{4l}\mu_l$ are really negligible. For this to be true it is necessary that r is so large that the different terms of ascending powers in our series expansion of the metric correspond to decreasing orders of magnitude, i.e. we must have

$$1 \gg |\,y_{ik}\,| \gg |\,z_{ik}\,| \gg \cdots\cdots. \tag{5.26}$$

Further, we must require that r is so large that the last terms in (4.25), (4.26) are small compared with the first terms, i.e.

$$|\,(y_{ik})_0\,| \gg |\,y_{ik}\,|\cdot r^{-1} \tag{5.27}$$

and a similar relation for z_{ik}.

In view of the expressions (4.18)–(4.20) for y_{ik} and z_{ik} the condition (5.26) demands

$$\frac{|\,c\,|}{r} \ll 1, \quad \frac{|\,M\,|}{r} \ll 1, \quad \frac{|\,N\,|}{r} \ll |\,M\,|, \cdots\cdots. \tag{5.28}$$

Further, if λ is the order of magnitude of the wavelengths of the radiation emitted, we have

$$c_0 \sim \frac{c}{\lambda}, \quad M_0 \sim \frac{M}{\lambda}, \quad N_0 \sim \frac{N}{\lambda} \cdots\cdots \tag{5.29}$$

and (5.27) then means

$$r \gg \lambda. \tag{5.30}$$

Thus, the radius r has to be large compared with the wavelengths of the radiated waves, i.e. only if the surface of the sphere is lying in the 'wave

zone' of the radiation will the momentum and energy contained in the sphere be equal to the 'total momentum and energy' P_i of the system. In all practical cases, c_0 and M_0 are very small quantities and it is easily seen that the conditions (5.28)–(5.30) are compatible with the relations (3.7), (3.8).

6. Invariance of P_i and of the Asymptotic Form of T_i^k under Tetrad Rotations

In section 2 it was shown that the complex T_i^k transforms according to Eq. (2.58) under tetrad rotations (2.51) and it is unchanged only if the rotation coefficients are constants. However, as also mentioned in section 2 and as we shall show now, the total four-momentum P_i as well as the asymptotic form of T_i^k are invariant under any rotation (2.51) for which also the new tetrads $\check{h}_i^{(a)}$ satisfy the boundary conditions A and B on p. 18. In our proof of this statement we shall again work in the system of coordinates S, where the boundary conditions have a particularly simple form, but since it is a statement regarding covariant quantities the proof is of course valid in any system of coordinates.

From (2.51) and (2.16) it follows that

$$\Omega^{(a)}{}_{(b)}(x) = \check{h}_i^{(a)} h^i_{(b)}. \tag{6.1}$$

Therefore, since the tetrads (4.29) have the limit

$$h^i_{(b)} \to \delta^i_b \quad \text{for} \quad r \to \infty, \tag{6.2}$$

the boundary condition A for $\check{h}_i^{(a)}$ yields

$$\Omega^{(a)}{}_{(b)}(x) \to \overset{(o)}{\Omega}{}^{(a)}{}_{(i)}\, \delta^i_b = \overset{(o)}{\Omega}{}^{(a)}{}_{(b)}, \tag{6.3}$$

where the coefficients $\overset{(o)}{\Omega}{}^{(a)}{}_{(b)}$ are constants.

However, T_i^k is unchanged under constant tetrad rotations so that we may choose $\overset{(o)}{\Omega}{}^{(a)}{}_{(b)} = \delta^a_b$ without any loss in generality. This means that $\overset{(o)}{\Omega}{}^{(a)}{}_{(b)}(x)$ must be of the form

$$\Omega^{(a)}{}_{(b)}(x) = \delta^a_b + \omega^a{}_b(x), \tag{6.4}$$

where

$$\omega^a{}_b(x) \to 0 \quad \text{for} \quad r \to \infty. \tag{6.5}$$

The indices a and b in $\omega^a{}_b$ are, of course, raised and lowered according to the same rule as in $\Omega^{(a)}{}_{(b)}$.

We shall now apply the boundary condition B to the new tetrad vector $\check{h}_i^{(a)}$, which requires that $\check{h}_i^{(a)} - \delta_i^a$ must have the same asymptotic behaviour as the metric quantities $\psi = g_{ik} - \eta_{ik}$. In the system S the boundary condition for ψ has the form of a Sommerfeld radiation condition, i.e. $\psi(u, r, \theta, \varphi)$ as a function of $u = t - r$, r, θ, and φ satisfies the condition

$C.$ $$(r\psi)_1 = O_1' \to 0$$

for $r \to \infty$ *under constant* u, θ, φ.
Moreover, ψ *and its first-order derivatives go to zero at least as* $\frac{1}{r}$ *for* $r \to \infty$.

Now, condition B requires that C must hold also for $\psi = \check{h}_i^{(a)} - \delta_i^a$ which, on account of (6.1) and (6.4), implies that also the function $\psi = \omega_{ab}$ satisfies the condition C.

This means that $\omega_{ab}(u, r, \theta, \varphi)$ and its derivatives have the following asymptotic behaviour for $r \to \infty$: ω_{ab}, $(\omega_{ab})_0$, $(\omega_{ab})_2$ and $(\omega_{ab})_3$ go to zero at least as $1/r$, and $(\omega_{ab})_1$ goes to zero at least as $1/r^2$.

Symbolically this is expressed by

$$\left.\begin{aligned} \{\omega_{ab}, (\omega_{ab})_0, (\omega_{ab})_2, (\omega_{ab})_3\} &= O_1' \\ (\omega_{ab})_1 &= O_2', \end{aligned}\right\} \quad (6.6)$$

where O_n' means a term which goes to zero at least as $\frac{1}{r^n}$.

Otherwise the scalar functions ω_{ab} can be chosen completely arbitrarily apart, of course, from the orthogonality relations (2.52) which imply the following conditions:

$$\left.\begin{aligned} \omega_{ab} + \omega_{ab} + \omega^c{}_a\, \omega_{cb} &= 0 \\ \omega_a{}^c\, \omega_{bc} &= \omega^c{}_a\, \omega_{cb}. \end{aligned}\right\} \quad (6.7)$$

From the first of these equations and (6.6) we get for the symmetrical combination

$$\omega_{\{ab\}} \equiv \omega_{ab} + \omega_{ba} \quad (6.8)$$

$$\left.\begin{aligned} \{\omega_{\{ab\}}, (\omega_{\{ab\}})_0, (\omega_{\{ab\}})_2, (\omega_{\{ab\}})_3\} &= O_2' \\ (\omega_{\{ab\}})_1 &= O_3'. \end{aligned}\right\} \quad (6.9)$$

Further, from (4.24) with $\psi = \omega$

$$\omega_{ab,\,l} = (\omega_{ab})_0\, \mu_l + \left[(\omega_{ab})_1\, n_l + \frac{1}{r}\,(\omega_{ab})_2\, m_l + \frac{1}{r\sin\theta}\,(\omega_{ab})_3\, l_l\right], \tag{6.10}$$

where the bracket term is of the type O_2' on account of (6.6). Hence,

$$\omega_{\{ab\},\,l} = (\omega_{\{ab\}})_0\, \mu_l + O_3' = -(\omega^c{}_a\, \omega_{cb})_0\, \mu_l + O_3' \tag{6.11}$$

and, since

$$\mu_{l,\,i} = \frac{\partial \mu_l}{\partial x_i} = \frac{\partial^2 u}{\partial x^l\, \partial x^i} = O_1, \tag{6.12}$$

$$\omega_{\{ab\},\,l,\,i} = -(\omega^c{}_a\, \omega_{cb})_{00}\, \mu_l\, \mu_i + O_3'. \tag{6.13}$$

We shall now calculate the asymptotic form of the complex $\check{\mathsf{T}}_i{}^k$ corresponding to the tetrads $\check{h}_i^{(a)}$. By the asymptotic form we mean the expression for $\mathsf{T}_i{}^k$ obtained by neglecting all terms of type O_3, i.e. the expression which determines the energy radiated from the system.

According to (2.58) we have

$$\check{\mathsf{T}}_i{}^k - \mathsf{T}_i{}^k = Y_i{}^{kl}{}_{,\,l} \tag{6.14}$$

and we shall see that this quantity is really zero for large r if we neglect all terms O_3. To this power in $1/r$ we get, by (2.54), (4.29), (4.21) and (6.4)–(6.10),

$$\left.\begin{aligned} X^{kl}{}_i &= h^{(a)\,k}\, h^{(b)\,l}\, \Omega^{(c)}{}_{(a)}\, \Omega_{(cb),\,i} \\ &= \left(\eta^{ak} - \frac{1}{2}\, y^{ak}\right)\left(\eta^{bl} - \frac{1}{2}\, y^{bl}\right)(\delta^c_a + \omega^c{}_a)\, \omega_{cb,\,i} \\ &= \omega^{kl}{}_{,\,i} + \left[\omega^{rk}\,(\omega_r{}^l)_0 - \frac{1}{2}\, y^{rk}\,(\omega_r{}^l)_0 - \frac{1}{2}\, y^{rl}\,(\omega^k{}_r)_0\right]\mu_i + O_3'. \end{aligned}\right\} \tag{6.15}$$

Further, since $h = 1 + O_2$, we get from (2.56)

$$\left.\begin{aligned} \varkappa\, Y_i{}^{kl}{}_{,\,l} &= X^{kl}{}_{i,\,l} + X^k{}_{,\,i} - \delta^k_i\, X^l{}_{,\,l} + O_3' \\ &= Z_i^k - \frac{1}{2}\,\delta^k_i\, Z_l{}^l + O_3'. \end{aligned}\right\} \tag{6.16}$$

Here we have put

$$Z_i^k \equiv X^{kl}{}_{i,\,l} + X^k{}_{,\,i} = X^{kl}{}_{i,\,l} + X^{lk}{}_{l,\,i} \tag{6.17}$$

which gives

$$Z_i^i = X^{il}{}_{i,\,l} + X^{li}{}_{l,\,i} = 2\, X^l{}_{,\,l}. \tag{6.18}$$

Now, we get from (6.17), (6.15) and (6.6)–(6.12)

$$\left.\begin{aligned} Z_i^k &= \omega^{kl}{}_{,i,l} + \omega^{lk}{}_{,l,i} \\ &+ \left[\omega^{rk}(\omega_r{}^l)_0 - \frac{1}{2}\,y^{rk}(\omega_r{}^l)_0 - \frac{1}{2}\,y^{rl}(\omega^k{}_r)_0\right]_0 \mu_i\mu_l \\ &+ \left[\omega^{rl}(\omega_r{}^k)_0 - \frac{1}{2}\,y^{rl}(\omega_r{}^k)_0 - \frac{1}{2}\,y^{rk}(\omega^l{}_r)_0\right]_0 \mu_l\mu_i + O_3' \\ &= \omega^{\{kl\}}{}_{,l,i} + \left[(\omega^{rk}\omega_r{}^l)_0 - \frac{1}{2}\,y_r{}^k(\omega^{\{rl\}})_0\right]_0 \mu_i\mu_l + O_3'. \end{aligned}\right\} \tag{6.19}$$

Here we have used the relations

$$y^{rl}\mu_l = (y^{rl})_0\,\mu_l = 0 \tag{6.20}$$

following from the second equation (4.34).

By means of (6.9) and (6.13) the equations (6.19) and (6.16) give

$$Z_i^k = O_3', \quad Z_l^l = O_3' \tag{6.21}$$

and

$$Y_i^{kl}{}_{,l} = O_3'. \tag{6.22}$$

Thus, the asymptotic form of T_i^k, obtained by neglecting all terms of the type O_3, is unchanged under all tetrad rotations which respect the boundary conditions A, B, and it is therefore uniquely given by the equation (4.37). In particular this holds for the gravitational energy emitted, which is uniquely given by the expressions (4.39)–(4.42).

We shall now show that also the total four-momentum P_i is invariant under these rotations. According to our definition of P_i and in view of (5.10), (5.13) and (2.55), the change in P_i under a tetrad rotation is given by

$$\left.\begin{aligned} \check{P} - P_i &= -\int\!\!\int (\check{\mathfrak{U}}_i^{4l} - \mathfrak{U}_i^{4l})\,\mu_l r^2 \sin\theta\, d\theta\, d\varphi \\ &= -\int\!\!\int Y_i^{4l}\mu_l r^2 \sin\theta\, d\theta\, d\varphi, \end{aligned}\right\} \tag{6.23}$$

where the integration is extended over the surface of a large sphere of radius r and *all terms of the type* O_1 *have to be discarded*. The calculation of $Y_i^{4l}\mu_l$, which runs along similar lines as the calculation of $Y_i^{kl}{}_{,l}$ in (6.15)–(6.22), is performed in the Appendix (A.16–A.22). The result is, neglecting terms of the type O_3,

$$\left.\begin{aligned} \varkappa Y_i^{4\,l}\mu_l = {} & \frac{(\omega^{4\lambda})_2}{r}(m_\lambda n_i - m_i n_\lambda) + \frac{(\omega^{4\lambda})_3}{r\sin\theta}(l_\lambda n_i - l_i n_\lambda) \\ & + \delta_i^4\left[\frac{(\omega^{\varkappa\lambda})_2}{2r}(m_\varkappa n_\lambda - m_\lambda n_\varkappa) + \frac{(\omega^{\varkappa\lambda})_3}{2r\sin\theta}(l_\varkappa n_\lambda - l_\lambda n_\varkappa)\right]. \end{aligned}\right\} \tag{6.24}$$

From the definitions (4.7) of n_i, m_i and l_i it follows that

$$\left.\begin{aligned} m_\varkappa n_\lambda - m_\lambda n_\varkappa &= -\delta_{\varkappa\lambda\nu} l^\nu \\ l_\varkappa n_\lambda - l_\lambda n_\varkappa &= \delta_{\varkappa\lambda\nu} m^\nu. \end{aligned}\right\} \tag{6.25}$$

Therefore, we get from (6.23)–(6.25) with $i = 4$

$$\check{P}_4 - P_4 = H - \check{H} = \frac{r\,\delta_{\varkappa\lambda\nu}}{2\varkappa}\int_0^\pi d\theta \int_0^{2\pi} d\varphi\,[(\omega^{\varkappa\lambda})_2\, l^\nu \sin\theta - (\omega^{\varkappa\lambda})_3\, m^\nu]. \tag{6.26}$$

By partial integrations of the first and second member with respect to θ and φ, respectively, we get, since the contributions from the boundaries cancel,

$$\check{P}_4 - P_4 = \frac{r\,\delta_{\varkappa\lambda\nu}}{2\varkappa}\int_0^\pi d\theta \int_0^{2\pi} d\varphi\,\omega^{\varkappa\lambda}\,[-l^\nu\cos\theta + (m^\nu)_3] = 0 \tag{6.27}$$

on account of (4.11). Similarly we get from (6.23)–(6.25) with $i = \iota$

$$\check{P}_\iota - \check{P}_\iota = 0\,. \tag{6.28}$$

Thus, also the total four-momentum P_i is invariant under all tetrad rotations which respect the boundary conditions A and B, and P_i is therefore uniquely given by the equation (5.20).

7. Transformation of P_i under Asymptotic Lorentz Transformations

We have seen that the total energy is invariant under the transformations (4.2) and (2.5) which leave the system of reference and the time scale unchanged. For more general coordinate transformations this will of course not be the case. We shall in particular investigate the transformation properties of P_i under transformations which, at large spatial distances from the

system, have the form of a Lorentz transformation. For simplicity, we shall only consider such transformations of this type which lead from the system S with coordinates (4.1) to a system $\bar{S}$ with coordinates

$$\left.\begin{aligned}(\bar{x}^i) &= \{\bar{x}, \bar{y}, \bar{z}, \bar{t}\} \\ &= \{\bar{r}\sin\bar{\theta}\cos\bar{\varphi}, \bar{r}\sin\bar{\theta}\sin\bar{\varphi}, \bar{r}\cos\bar{\theta}, \bar{u}+\bar{r}\}\end{aligned}\right\} \tag{7.1}$$

for which the metric tensor $\bar{g}_{ik}$ asymptotically is of the same form as in (4.18)–(4.21). In part C and in the Appendix 3 of reference 2, A. W. K. METZNER has given the most general asymptotic form of a transformation of this kind. A special class of these transformations (a pure K-transformation) is given by

$$\left.\begin{aligned} r &= K\bar{r} + \bar{u}\left(\cosh\nu - \frac{1}{K}\right) + O_1 \\ \theta &= \sin^{-1}\left(\frac{\sin\bar{\theta}}{K}\right) + \frac{\bar{u}}{\bar{r}}\frac{K'}{K^2} + O_2 \\ \varphi &= \bar{\varphi} \\ u &= \frac{\bar{u}}{K} - \frac{\bar{u}^2}{2\bar{r}}\frac{(K')^2}{K^3} + O_2 .\end{aligned}\right\} \tag{7.2}$$

Here,

$$K = K(\bar{\theta}) = \cosh\nu + \sinh\nu\cdot\cos\bar{\theta} > 0, \tag{7.3}$$

where ν is an arbitrary constant and

$$K' = \frac{dK}{d\bar{\theta}} = -\sinh\nu\sin\bar{\theta}. \tag{7.4}$$

From the second equation (7.2) it follows that

$$\sin\theta = \frac{\sin\bar{\theta}}{K}\left[1 - \frac{\bar{u}\,(K\cosh\nu - 1)}{\bar{r}K^2} + O_2\right] \tag{7.5}$$

$$\cos\theta = \frac{\sinh\nu + \cosh\nu\cos\bar{\theta}}{K} + O_1 . \tag{7.6}$$

It is easily verified that the transformations (7.2), when written in terms of the variables (4.2), (7.1), asymptotically are of the form

$$\left.\begin{aligned} x &= \bar{x} + O_1, \qquad y = \bar{y} + O_1, \\ z &= \bar{z}\cosh\nu + \bar{t}\sinh\nu + O_1 \\ t &= \bar{t}\cosh\nu + \bar{z}\sinh\nu + O_1 \end{aligned}\right\} \tag{7.7}$$

which is a special Lorentz transformation with a relative velocity

$$v = \tan\nu \tag{7.8}$$

in the direction of the symmetry axis. Thus, far away from the matter system, the reference points of the system $\bar{S}$ are moving with the constant velocity v in the direction of the z-axis with respect to the system S.

The news function $\bar{c}(\bar{u}, \bar{\theta})$ and the mass aspect $\bar{M}(\bar{u}, \bar{\theta})$ in the system $\bar{S}$ are connected with the corresponding quantities in the system S by the following relations:

$$\left.\begin{aligned} c &= K\bar{c},\ c_0 = K^2\bar{c}_0,\ c_{00} = K^3\bar{c}_{00}, \\ M &= K^3\left[\bar{M} + f(\bar{u}, \bar{\theta})\right], \end{aligned}\right\} \tag{7.9}$$

where

$$f(\bar{u}, \bar{\theta}) = \frac{2\,\bar{u}\,\bar{c}_0}{K^2}\left[1 - K\cosh\nu + KK'\right] + \bar{u}\,\bar{c}_{02}K' + \frac{K'^2\,\bar{u}^2\bar{c}_{00}}{K^3}\left[K^2 - \frac{K}{2}\right] \tag{7.9a}$$

is a function of $\bar{u}$ and $\bar{\theta}$ which depends linearly on the derivatives $\bar{c}_0$, $\bar{c}_{00}$, $\bar{c}_{02}$ of the news function $\bar{c}(\bar{u}, \bar{\theta})$ with respect to $\bar{u}$ and $\bar{\theta}$. Therefore, for a system which does not radiate, i.e. for $\bar{c}_0 = 0$, the function $f(\bar{u}, \bar{\theta})$ vanishes. (Note that, if $\bar{c}_0 = 0$, then also $\bar{c}_0 = 0$ on account of (7.9)). Further, since we also in $\bar{S}$ have relations of the type (3.7), (3.8) we see that in this case also $\bar{M}_0 = 0$, i.e. $\bar{M} = \bar{M}(\bar{\theta})$ is a function of $\bar{\theta}$ only.

For the total momentum and energy in the system $\bar{S}$ we get, on the analogy of (5.20),

$$\bar{P}_i(\bar{u}) = \left\{0,\ 0,\ \frac{1}{2}\int_0^{\pi}\bar{M}(\bar{u}, \bar{\theta})\cos\bar{\theta}\sin\bar{\theta}\,d\bar{\theta},\ -\frac{1}{2}\int_0^{\pi}\bar{M}(\bar{u}, \bar{\theta})\sin\bar{\theta}\,d\bar{\theta}\right\}. \tag{7.10}$$

Thus,

$$P_1 = \bar{P}_1, \qquad P_2 = \bar{P}_2 \tag{7.11}$$

i.e. the components in a spatial direction perpendicular to the relative motion are transformed as if P_i were a vector. However, the transformation of the components P_3 and P_4 is in general much more complicated. For instance, take the expression (5.20) for P_4,

$$P_4(u) = -\frac{1}{2}\int_0^{\pi} M(u, \theta) \sin\theta \, d\theta, \tag{7.12}$$

and introduce the variable $\bar{\theta}$ defined by the asymptotic form of (7.5), (7.6) as new variable of integration. Then we have

$$\sin\theta \, d\theta = \frac{\sin\bar{\theta} \, d\bar{\theta}}{K^2} \tag{7.13}$$

and, on account of (7.9) and (7.2),

$$P_4(u) = -\frac{1}{2}\int_0^{\pi} [\overline{M}(Ku, \bar{\theta}) + f(Ku, \bar{\theta})] \, K(\bar{\theta}) \sin\bar{\theta} \, d\bar{\theta}, \tag{7.14}$$

where u during the integration has to be kept constant in the argument $\bar{u} = K \cdot u$ in the functions $M(\bar{u}, \bar{\Theta})$, $f(\bar{u}, \bar{\Theta})$.

Similarly, using also (7.6),

$$\left.\begin{aligned} P_3(u) &= \frac{1}{2}\int_0^{\pi} M(u, \theta) \cos\theta \sin\theta \, d\theta \\ &= \frac{1}{2}\int_0^{\pi} [\overline{M}(Ku, \bar{\theta}) + f(Ku, \bar{\theta})] \, [\sinh\nu + \cosh\nu \cos\bar{\theta}] \sin\bar{\theta} \, d\bar{\theta}. \end{aligned}\right\} \tag{7.15}$$

Since the variable $\bar{u} = K(\bar{\theta})u$ in $M(u, \bar{\theta})$ is varying over the range of integration in (7.14), (7.15), it is seen that there is in general no simple connection between (P_3, P_4) and $(\overline{P}_3, \overline{P}_4)$.

However, if the system for a certain period does not radiate, i.e. for $c_0 = \bar{c}_0 = 0$, then both P_i and $\overline{P}_i$ are constant in time. Further, we have then $f(\bar{u}, \bar{\theta}) = 0$ and $\overline{M}_0 = 0$, i.e. $\overline{M} = \overline{M}(\bar{\theta})$ is independent of $\bar{u}$, and in this case we get from (7.14), (7.15) and (7.10)

$$\left.\begin{aligned} P_3 &= \frac{1}{2}\int_0^{\pi} \overline{M}(\bar{\theta}) \, [\sinh\nu + \cosh\nu \cos\bar{\theta}] \sin\bar{\theta} \, d\bar{\theta} = \overline{P}_3 \cosh\nu - \overline{P}_4 \sinh\nu \\ P_4 &= -\frac{1}{2}\int_0^{\pi} \overline{M}(\bar{\theta}) \, [\cosh\nu + \sinh\nu \cos\bar{\theta}] \sin\bar{\theta} \, d\bar{\theta} = \overline{P}_4 \cosh\nu - \overline{P}_3 \sinh\nu. \end{aligned}\right\} \tag{7.16}$$

Thus, for a non-radiative system, the quantities P_i transform as the covariant components of a free 4-vector under the asymptotic Lorentz transformations considered, i.e. under the K-transformations (7.2), (7.3).

This result is easily seen to hold for arbitrary asymptotic Lorentz transformations. To prove this statement we only need to show that $c_0 = 0$ implies

$$\mathsf{T}_i^k = O_4 \quad \text{for} \quad r \to \infty, \tag{7.17}$$

for, according to a well-known argument (see f. inst. reference 8), the 4-vector character of P_i is an immediate consequence of (2.3) and (7.17). Now, with $c_0 = 0$, (3.7) and (4.19) give

$$(\alpha_i^k)_0 = 0 \tag{7.18}$$

and (4.24), (4.29)

$$h_{(a)\,k,\,l} = \frac{1}{2}(\gamma_{ak})_0 \mu_l + O_2 = O_2. \tag{7.19}$$

Further, by (4.32), (4.33), (4.36),

$$\{\Delta^i_{kl}, \gamma_{ikl}, \Phi_k, \Lambda_{ikl}\} = O_2 \tag{7.20}$$

and, since $\mathfrak{L}$ and $\mathfrak{t}_i^k$ are homogeneous quadratic expressions in these quantities,

$$\left.\begin{aligned} \mathfrak{L} &= O_4 \\ \mathsf{T}_i^k = \mathfrak{t}_i^k &= O_4, \end{aligned}\right\} \tag{7.21}$$

i.e. (7.17).

From (7.11) and (7.16) it follows that

$$\eta^{ik} P_i P_k = \eta^{ik} \bar{P}_i \bar{P}_k = -m_0^2 \tag{7.22}$$

is an invariant, and we may assume that this quantity is negative so that we can define a real total rest mass m_0 of the system by (7.22). Then it is always possible by a suitable K-transformation to make $\bar{P}_\iota = 0$, and in this 'rest system' we have

$$\bar{H} = m_0. \tag{7.23}$$

For a radiative system we have seen that the total momentum and energy P_i does not transform in a simple way under the transformations (7.2), (7.7) and the same holds generally also for the gravitational energy and momentum radiated in a given time interval. However, if the radiation is going on a certain finite time only, so that $c_0(u, \theta)$ is different from zero in a time interval $u_1 < u < u_2$ but zero outside this interval, it is easily

seen that the total gravitational four-momentum p_i emitted during the radiation period must again be a 4-vector under asymptotic Lorentz transformations. This follows at once from the law of conservation of energy and momentum which yields

$$p_i = P_i^{(1)} - P_i^{(2)}, \tag{7.24}$$

where $P_i^{(1)}$ and $P_i^{(2)}$ are the total four-momentum of the system before and after the radiation period, respectively. Since $P_i^{(1)}$ and $P_i^{(2)}$ are then 4-vectors the same holds of course for p_i.

An explicit expression for the gravitational four-momentum p_i is obtained by integrating (5.25) over the radiation period, i.e.

$$p_i = \left\{ 0, 0, \frac{1}{2}\int_{u_1}^{u_2} du \int_0^{\pi} c_0(u,\theta)^2 \cos\theta \sin\theta \, d\theta, -\frac{1}{2}\int_{u_1}^{u_2} du \int_0^{\pi} c_0(u,\theta)^2 \sin\theta \, d\theta \right\} \tag{7.25}$$

with an analogous expression for $\bar{p}_i$ in the system $\bar{S}$.

The 4-vector character of p_i is easily demonstrated directly by introducing the new variables of integration $\bar{u}$, $\bar{X}\bar{\theta}$ obtained from (7.2), (7.4) by neglecting terms of the type O_1, i.e.

$$u = \frac{\bar{u}}{K}, \quad \sin\theta = \frac{\sin\bar{\theta}}{K}. \tag{7.26}$$

The corresponding Jacobian is, on account of (7.26) and (7.13),

$$\left| \begin{matrix} \frac{\partial u}{\partial \bar{u}} & \frac{\partial u}{\partial \bar{\theta}} \\ \frac{\partial \theta}{\partial \bar{u}} & \frac{\partial \theta}{\partial \bar{\theta}} \end{matrix} \right| = \left| \begin{matrix} \frac{1}{K} - \frac{\bar{u}K'}{K^2} \\ 0 \quad \frac{1}{K} \end{matrix} \right| = \frac{1}{K^2}. \tag{7.27}$$

Thus, using (7.9) and (7.25),

$$\begin{aligned} p_4 &= -\frac{1}{2}\int\int c_0^2 \sin\theta \, du \, d\theta = -\frac{1}{2}\int\int K\bar{c}_0^2 \sin\bar{\theta} \, d\bar{u} \, d\bar{\theta} \\ &= \bar{p}_4 \cosh\nu - \bar{p}_3 \sinh\nu. \end{aligned} \tag{7.28}$$

Similarly,

$$\begin{aligned} p_3 &= \bar{p}_3 \cosh\nu - \bar{p}_4 \sinh\nu \\ p_1 &= \bar{p}_1 = 0, \quad p_2 = \bar{p} = 0. \end{aligned} \tag{7.29}$$

The emitted gravitational energy

$$h = -p_4 = \frac{1}{2}\int\int c_0\,(u,\,\theta)^2 \sin\theta\, du\, d\theta \tag{7.30}$$

is always positive, and from (7.25) we see that

$$p_4{}^2 > p_3{}^2. \tag{7.31}$$

Hence,

$$\eta^{ik} p_i p_k = p_3{}^2 - p_4{}^2 = -\mu^2 \tag{7.32}$$

with a real value for the 'rest mass' μ of the gravitational radiation. As far as energy and momentum are concerned, the loss in these quantities during the radiation period is exactly as if the system had emitted a particle of rest mass μ with the velocity

$$w = \left|\frac{p_3}{p_4}\right| < 1 \tag{7.33}$$

in the direction of the symmetry axis.

Although P_i in general is not exactly a 4-vector, this will be true with very good approximation in all practical cases. From the approximate expression (4.49) for c one can see that c_0 for all systems in nature is an extremely small quantity, so that we have

$$\bar{u}\,\bar{c}_0 \ll \overline{M} \tag{7.34}$$

for a large interval of $\bar{u}$. According to (5.25) and (7.9a) this means that P_i is only a slowly varying function of time and that the function f in (7.14), (7.15) can be neglected. Further we get by a Taylor expansion in $\bar{u} - u = u(K-1)$, and by means of the first equation (3.7) and (3.8) written in the system $\overline{S}$,

$$\left.\begin{aligned} \overline{M}\,(\bar{u},\,\bar{\theta}) &= \overline{M}\,(u,\,\bar{\theta}) + \overline{M}_0\,(u,\,\bar{\theta})\,(\bar{u}-u) \\ &= \overline{M}\,(u,\,\bar{\theta}) + O\,(\bar{u}\,\bar{c}_0) \end{aligned}\right\} \tag{7.35}$$

so that we can neglect the last term on account of (7.34). Then, the equations (7.14) and (7.15) are reduced to (7.16) with $\bar{u} = u$ in $\overline{P}_i\,(\bar{u})$ on the right-hand side of (7.16). This means that $P_i(u)$ transforms approximately as a 4-vector under asymptotic Lorentz transformations.

8. Approximate Plane Waves Emitted by a Distant Matter System

In this section we consider the gravitational radiation in a spatial region V of linear dimensions l at a large distance R from the matter system so that

$$l \ll R \tag{8.1}$$

and that V lies entirely in the wave zone defined by the relations (5.26)–(5.30). Then, it is easily seen that the solution (4.18)–(4.20) of Einstein's field equations inside V has the form of a weak field expansion

$$g_{ik} = \eta_{ik} + \overset{(1)}{y}_{ik} + \overset{(2)}{y}_{ik} + \cdots, \tag{8.2}$$

where the first approximation $\overset{(1)}{y}_{ik}$ represents a plane wave. Let us in particular consider the case where the region V is lying around the point $x = R$, $y = z = 0$ on the positive x-axis. Then it is convenient to introduce new coordinates

$$\left.\begin{aligned} (\bar{x}^i) &= \{\bar{x}, \bar{y}, \bar{z}, \bar{t}\}, \\ x &= \bar{x} + R,\ y = \bar{y},\ z = \bar{z},\ t = \bar{t} \end{aligned}\right\} \tag{8.3}$$

so that inside V

$$\left\{\frac{\bar{x}}{R}, \frac{\bar{y}}{R}, \frac{\bar{z}}{R}\right\} \ll 1 \tag{8.4}$$

$$r = \sqrt{(R+\bar{x})^2 + \bar{y}^2 + \bar{z}^2} = R + \bar{x} + O_1, \tag{8.5}$$

where O_n throughout this section means a term which is small of the n'th order. Further, if we put

$$\bar{u} = \bar{t} - \bar{x}, \tag{8.6}$$

we have

$$\left.\begin{aligned} u &= t - r = \bar{u} - R + O_1 \\ \cos\theta &= \frac{z}{r} = \frac{\bar{z}}{R} + O_2 = O_1, \quad \sin\theta = 1 + O_2 \\ \theta &= \frac{\pi}{2} + O_1 \\ \sin\varphi &= \frac{y}{r\sin\theta} = O_1, \quad \cos\varphi = 1 + O_2. \end{aligned}\right\} \tag{8.7}$$

Therefore, the quantities defined by (4.7) are of the form

$$\{n_i, m_i, l_i, \mu_i\} = \{\bar{n}_i, \bar{m}_i, \bar{l}_i, \bar{\mu}_i\} + O_1 \tag{8.8}$$

with

$$\left.\begin{aligned} \bar{n}_i &= \{1, 0, 0, 0\} \\ \bar{m}_i &= \{0, 0, -1, 0\} \\ \bar{l}_i &= \{0, 1, 0, 0\} \\ \bar{\mu}_i &= \{-1, 0, 0, 1\} = \delta_i^4 - \bar{n}_i. \end{aligned}\right\} \tag{8.9}$$

The quantities (8.9) are constants which obviously satisfy the same relations (4.9), (4.12) as the quantities (4.7).

On account of (8.7) the functions $c(u, \theta)$, $M(u, \theta)$, $c_2(u, \theta)$ occurring in the expression (4.20) for α_{ik} have the following form inside V:

$$\left.\begin{aligned} &\{c(u, \theta), M(u, \theta), c_2(u, \theta)\} = \\ &\left\{c\left(\bar{u} - R, \frac{\pi}{2}\right), M\left(\bar{u} - R, \frac{\pi}{2}\right), c_2\left(\bar{u} - R, \frac{\pi}{2}\right)\right\} + O_1. \end{aligned}\right\} \tag{8.10}$$

The quantities inside the curly brackets on the right-hand side of (8.10) are functions of $\bar{u}$, which we denote by $R\bar{c}(\bar{u})$, $R\bar{M}(\bar{u})$, $R\bar{c}_2(\bar{u})$, respectively. Then, inside V the quantity y_{ik} in (4.18) takes the form

$$y_{ik} = \overset{(1)}{y}_{ik} + O_2, \tag{8.11}$$

where

$$\overset{(1)}{y}_{ik} = 2\,\bar{c}\,(\bar{u})\,(\bar{m}_i\bar{m}_k - \bar{l}_i\bar{l}_k) + 2\,\bar{M}\,(\bar{u})\,\bar{\mu}_i\bar{\mu}_k + \bar{c}_2\,(\bar{u})\,(\bar{m}_i\bar{\mu}_k + \bar{\mu}_i\bar{m}_k) \tag{8.12}$$

is a function of $\bar{u} = t - \bar{x}$ only and therefore represents a plane wave travelling in the direction of the positive $\bar{x}$-axis. On the other hand, the term O_2 in (8.11) depends on $\bar{x}$, $\bar{y}$, $\bar{z}$ besides on $\bar{u}$ and, since this term is of the same order as z_{ik} in (4.18), we see that already the term of the second order $\overset{(2)}{y}_{ik}$ in (8.2) is *not* a pure plane wave.

Inside V the tetrad field (4.29) is of the form

$$h_{(a)\,i} = \eta_{ai} + \frac{1}{2}\overset{(1)}{y}_{ai} + O_2. \tag{8.13}$$

Further, in the same region we get from (4.37) and (4.48)

$$\mathsf{T}_i^k = \mathrm{t}_i^k = \frac{2\,\bar{c}'\,(\bar{u})^2}{\varkappa}\,\bar{\mu}_i\bar{\mu}_k + O_3 \tag{8.14}$$

$$\theta_i^k = \vartheta_i^k = \frac{2\,\bar{c}'(\bar{u})^2}{\varkappa}\,\bar{\mu}_i\bar{\mu}^k + O_3, \tag{8.15}$$

where the prime means derivation with respect to $\bar{u}$, i.e.

$$\bar{c}'(\bar{u}) = \frac{d\bar{c}\,(\bar{u})}{d\bar{u}}. \tag{8.16}$$

Thus, in the system of coordinates $(\bar{x}_i)$, Einstein's expression Θ_i^k and the complex T_i^k give identical results if we neglect all terms of order O_3. The first order metric tensor

$$\bar{g}_{ik} = \eta_{ik} + \overset{(1)}{y}_{ik} \tag{8.17}$$

is a solution of the *linearized* field equations and it has the form

$$\left.\begin{aligned} \bar{g}_{ik} = \begin{pmatrix} 1+2\,\overline{M} & 0 & \bar{c}_2 & -2\,\overline{M} \\ 0 & 1-2\,\bar{c} & 0 & 0 \\ \bar{c}_2 & 0 & 1+2\,\bar{c} & -\bar{c}_2 \\ -2\,\overline{M} & 0 & -\bar{c}_2 & -1+2\,\overline{M} \end{pmatrix}. \end{aligned}\right\} \tag{8.18}$$

To the same order of magnitude we have

$$\bar{\mathfrak{g}}^{ik} = \eta^{ik} - \overset{(1)}{y}ik \tag{8.19}$$

which satisfies the de Donder condition

$$\bar{\mathfrak{g}}^{ik}{}_{,\,k} = 0 \tag{8.20}$$

in accordance with the equation (4.28). This latter equation also shows that the de Donder condition is *not* satisfied in higher approximation. Introduction of the approximate metric tensor (8.17) into the expression (2.10) for ϑ_i^k gives of course just the formula (8.15). This is the usual procedure by which the energy flux in a weak plane gravitational wave has been calculated on the basis of Einstein's theory [13] and, on account of the accordance between Θ_i^k and T_i^k expressed in (8.14) and (8.15), this procedure seems to be justified.

However, it should be noted that the accordance between Θ_i^k and T_i^k holds in special coordinates only, and if we base our calculations on the complex Θ_i^k it is in general not easy to decide in which systems of coordi-

nates this expression is valid. To illustrate this point let us again for a moment consider the case of a completely empty space, where we can use Lorentzian coordinates (X^i) with the metric tensor η_{ik}. In these coordinates the quantity $\vartheta_i^{\,k}$ in (2.10) is zero. By an infinitesimal coordinate transformation

$$X^i = x^i + \xi^i(x), \tag{8.21}$$

where the $\xi^i(x)$ are arbitrary functions of (x^i) which are small of the first order, we obtain for the metric tensor g_{ik} in the new system of coordinates an expression of the type (8.2) with the first order term

$$\overset{(1)}{\gamma}_{ik} = \xi_{i,\,k} + \xi_{k,\,i} \tag{8.22}$$

$$\xi_i = \eta_{ik}\,\xi^k. \tag{8.23}$$

Then, a simple calculation shows that the quantity $\vartheta_i^{\,k}$ in (2.10) corresponding to the metric tensor g_{ik} in general is different from zero, i.e.

$$\vartheta_i^{\,k} \neq 0. \tag{8.24}$$

As shown in the Appendix (A.23)–(A.36), this arbitrariness in the value of Einstein's energy-momentum complex cannot be removed simply by requiring that we should use only harmonic systems of coordinates where the de Donder condition is satisfied. It is true that $\vartheta_i^{\,k}$ is equal to zero in all such systems (x^i) for which the quantities ξ^i in (8.21) are functions of $x^4 - x^1$ only, and this might indicate that Einstein's expression can be applied safely to those solutions of the field equations in empty space which are first order plane waves. On the other hand, the fact that a simple transformation of coordinates in a flat space may create a $\vartheta_i^{\,k}$ of the same order of magnitude as a 'real' gravitational field makes one feel uneasy in applying Einstein's expression in general.

The just mentioned difficulty does not arise with the complex $\mathfrak{T}_i^{\,k}$, for in a completely empty space we have in all systems of coordinates exactly

$$\mathfrak{T}_i^{\,k} = \mathfrak{t}_i^{\,k} = 0 \tag{8.25}$$

on account of the condition (2.60) imposed in this case. For a weak gravitational field of the type (8.18) we have then also to require that $h_i^{(a)}$ deviates from the values (2.64) or (2.65), valid in a completely empty space, by a quantity which is small of the first order. This requirement is of course satisfied by the expression (8.13) which is symmetrical in a and i. If we

introduce this tetrad field into the expression (2.31) for t_i^k we get of course just the formula (8.14). Now, the proof in section 6 for the invariance of T_i^k under tetrad rotations of the type (6.4)–(6.7) leads to the result that $T_i^k = t_i^k$ inside V is unchanged under all rotations of the tetrads (8.13) with coefficients $\Omega_{(ab)}$ of the form

$$\Omega_{(ab)} = \eta_{ab} + \overline{\omega}_{ab}(\bar{u}), \tag{8.26}$$

where the quantity $\overline{\omega}_{ab}(\bar{u})$ is any function of $\bar{u} = t - \bar{x}$ which is small of the first order and antisymmetric in the indices a and b. The invariance of the second order expression for t_i^k under such rotations is shown explicitly in the Appendix (A.37)–(A.45). A finite rotation with constant coefficients $\overset{(0)}{\Omega}_{(ab)}$ will of course also leave T_i^k unchanged.

An infinitesimal coordinate transformation $(\bar{x}^i) \to (x'^i)$ of the type

$$x'^i = \bar{x}^i + \xi^i(\bar{x}) \tag{8.27}$$

changes the complex T_i^k given by (8.14) into

$$T'^k_i = T_i^k - \xi^r{}_{,i,n}\, \overset{(1)}{\mathfrak{U}}_r^{kn}. \tag{8.28}$$

Here, in using (2.34), we have neglected all terms of order O_3 and

$$\overset{(1)}{\mathfrak{U}}_r^{kn} = \frac{1}{2\varkappa}\left[\left(\overset{(1)}{y}_r^n\right)' \overline{\mu}^k - \left(\overset{(1)}{y}_r^k\right)' \overline{\mu}^n\right] \tag{8.29}$$

is the first order expression of the superpotential (2.30) corresponding to the tetrads (8.13). If $\xi^i = \xi^i(\bar{u})$ is a function of $\bar{u} = t - \bar{x}$ only, we have

$$\xi^r{}_{,i,n} = (\xi^r)''\, \overline{\mu}_i\, \overline{\mu}_n \tag{8.30}$$

and, since

$$\overline{\mu}_n\, \overset{(1)}{\mathfrak{U}}_r^{kn} = 0, \tag{8.31}$$

we have in this case

$$T'^k_i = T_i^k. \tag{8.32}$$

Thus, to the second order the energy-momentum complex is unchanged under infinitesimal coordinate transformations where ξ^i is a function of $\bar{u}$ only. By a transformation of this type the metric (8.18) can be brought into one of its two standard forms [13]. If we choose ξ_i of the form

$$\xi_i = \chi(\bar{u})\, \overline{\mu}_i + \Phi(\bar{u})\, \overline{m}_i, \tag{8.33}$$

where χ and Φ are functions of $\bar{u}$ only, we have

$$\xi_{i,k} = \chi'(\bar{u})\,\bar{\mu}_i\,\bar{\mu}_k + \Phi'(\bar{u})\,\bar{m}_i\,\bar{\mu}_k. \tag{8.34}$$

Then, we get for the metric tensor in the new system

$$\left.\begin{aligned} g'_{ik} &= \eta_{ik} + \overset{(1)}{y'_{ik}}, \\ \overset{(1)}{y'_{ik}} &= \overset{(1)}{y_{ik}} - \xi_{i,k} - \xi_{k,i} = 2\,\bar{c}\,(\bar{m}_i\,\bar{m}_k - \bar{l}_i\,\bar{l}_k) \\ &+ 2\,(\overline{M} - \chi')\,\bar{\mu}_i\,\bar{\mu}_k + (\bar{c}_2 - \Phi')\,(\bar{m}_i\,\bar{\mu}_k + \bar{m}_k\,\bar{\mu}_i). \end{aligned}\right\} \tag{8.35}$$

With

$$\chi(\bar{u}) = \int \overline{M}(\bar{u})\,d\bar{u}, \qquad \Phi(\bar{u}) = \int \bar{c}_2(\bar{u})\,d\bar{u} \tag{8.36}$$

this gives

$$\overset{(1)}{y'_{ik}} = 2\,\bar{c}\,(\bar{m}_i\,\bar{m}_k - \bar{l}_i\,\bar{l}_k) \tag{8.37}$$

or

$$\left.\begin{aligned} g'_{ik} = \begin{pmatrix} 1 & 0 & 0 & 0 \\ 0 & 1-2\,\bar{c} & 0 & 0 \\ 0 & 0 & 1+2\,\bar{c} & 0 \\ 0 & 0 & 0 & -1 \end{pmatrix}. \end{aligned}\right\} \tag{8.38}$$

Thus, the new system of coordinates is a 'rectangular' system and since

$$u' \equiv t' - x' = \bar{t} - \chi - (\bar{x} - \chi) = \bar{t} - \bar{x} = \bar{u} \tag{8.39}$$

we have

$$\bar{c} = \bar{c}(\bar{u}) = \bar{c}(u'). \tag{8.40}$$

On account of (8.32), the energy-momentum complex $\mathsf{T}'^{\,k}_{i}$ in this system is also given by (8.14).

The components of the tetrads (8.13) in the system $(x'^{\,i})$ are

$$\left.\begin{aligned} h'_{(a)\,i} &= \frac{\partial x^k}{\partial x'^{\,i}}\,h_{(a)\,k} = (\delta^k_i - \xi^k{}_{,i})\left(\eta_{ak} + \frac{1}{2}\overset{(1)}{y}_{ak}\right) \\ &= \eta_{ai} + \bar{c}\,(\bar{m}_a\,\bar{m}_i - \bar{l}_a\,\bar{l}_i) + \frac{1}{2}\,\bar{c}_2\,(\bar{\mu}_a\,\bar{m}_i - \bar{m}_a\,\bar{\mu}), \end{aligned}\right\} \tag{8.41}$$

an expression which is not symmetrical in a and i. By a rotation of the tetrads of the form (8.26), which leaves $\mathsf{T}^{\,k}_{i}$ unchanged, we get

$$\check{h}'_{(a)\,i} = (\delta^b_a + \bar{\omega}_a{}^b(\bar{u}))\,h'_{(b)\,i} = h'_{(a)\,i} + \bar{\omega}_{ai}(\bar{u}). \tag{8.42}$$

Thus, if we choose

$$\bar{\omega}_{ab}(\bar{u}) = -\frac{1}{2}\bar{c}_2(\bar{u})(\bar{\mu}_a \bar{m}_b - \bar{m}_a \bar{\mu}_b) = -\bar{\omega}_{ba}, \tag{8.43}$$

$\check{h}'_{(a)i}$ takes the form

$$\check{h}'_{(a)i} = \eta_{ai} + \bar{c}(\bar{m}_a \bar{m}_i - \bar{l}_a \bar{l}_i) = \eta_{ai} + \frac{1}{2}\overset{(1)}{y}_{ai}, \tag{8.44}$$

i.e. also in the rectangular system the tetrads can be chosen symmetrical in the tetrad- and vector indices.

Finally, a spatial rotation about the x'^1-axis through the angle $\pi/4$ leads to a system of coordinates (x''^i) in which the metric has the other standard form [13]:

$$g''_{ik} = \eta_{ik} + \overset{(1)}{y}''_{ik}, \tag{8.45}$$

where

$$\overset{(1)}{y}''_{23} = \overset{(1)}{y}''_{32} = 2\bar{c} \tag{8.46}$$

and all the other components are zero. If we perform the same constant rotation of the tetrads $\check{h}'_{(a)i}$, which leaves T_i^k unchanged, we see that also in this system the tetrads can be chosen symmetrical in a and i, i.e. for the rotated tetrads we have

$$\check{h}''_{(a)i} = \eta_{ai} + \frac{1}{2}\overset{(1)}{y}''_{ai}. \tag{8.47}$$

Let us now consider a sandwich wave, where $\bar{c}'(\bar{u}) = 0$ outside an interval $\bar{u}_1 < \bar{u} < \bar{u}_2$. The momentum and energy per unit area in the $(\bar{y}, \bar{z})$-plane of the system $(\bar{x}^i)$ is then, in virtue of (8.14) and (8.9),

$$\bar{p}_i = \int \mathfrak{t}_i^4 \, d\bar{x} = -\frac{2}{\varkappa}\bar{\mu}_i \int_{\bar{u}_1}^{\bar{u}_2} (\bar{c}')^2 \, d\bar{u}, \tag{8.48}$$

i.e.

$$\bar{p}_i = \left\{ \frac{2}{\varkappa}\int_{\bar{u}_1}^{\bar{u}_2} \bar{c}'(\bar{u})^2 \, d\bar{u},\ 0,\ 0,\ -\frac{2}{\varkappa}\int_{u_1}^{\bar{u}_2} \bar{c}'(\bar{u})^2 \, d\bar{u} \right\}. \tag{8.49}$$

It is also clear that $\bar{p}_i$ transforms as a 4-vector under Lorentz transformations

$$x'^i = a^i{}_k \bar{x}^k \tag{8.50}$$

for, according to (2.34), T_i^k transforms as a tensor under such transformations. Let us briefly consider a special Lorentz transformation in the direction of the $\bar{x}$-axis, i.e.

$$\left.\begin{aligned} \bar{x} &= x' \cosh \nu + t' \sinh \nu \\ \bar{t} &= t' \cosh \nu + x' \sinh \nu \\ \bar{y} &= y', \ \bar{z} = z'. \end{aligned}\right\} \tag{8.51}$$

Then,

$$\left.\begin{aligned} \bar{u} = \bar{t} - \bar{x} &= (\cosh \nu - \sinh \nu)\, u' \\ u' &\equiv t' - x', \end{aligned}\right\} \tag{8.52}$$

and

$$\mathsf{T}'^{k}_{i} = \frac{2}{\varkappa} \bar{c}' (u')^2 \mu'_i \mu'^k \tag{8.53}$$

with

$$\mu'_i = \frac{\partial \bar{x}^k}{\partial x'^i} \bar{\mu}_k = -\frac{\partial \bar{x}^1}{\partial x'^i} + \frac{\partial \bar{x}^4}{\partial \bar{x}'^i} = (\cosh \nu - \sinh \nu)\, \bar{\mu}_i . \tag{8.54}$$

Thus,

$$\left.\begin{aligned} p'_i &= \int \mathsf{T}'^4_i \, dx' = \int \mathsf{T}'^4_i \, du' = -\frac{2}{\varkappa} (\cosh \nu - \sinh \nu)^2 \, \bar{\mu}_i \int \bar{c}\, (\bar{u})^2 \, du' \\ &= -(\cosh \nu - \sinh \nu) \frac{2}{\varkappa} \bar{\mu}_i \int_{\bar{u}_1}^{\bar{u}_2} \bar{c}' \, (\bar{u})^2 \, d\bar{u}, \end{aligned}\right\} \tag{8.55}$$

or

$$\left.\begin{aligned} p'_1 &= \bar{p}_1 \cosh \nu + \bar{p}_4 \sinh \nu, \quad p'_2 = p_2, \\ p'_3 &= \bar{p}_3, \quad p'_4 = \bar{p}_1 \sinh \nu + \bar{p}_4 \cosh \nu \end{aligned}\right\} \tag{8.56}$$

in accordance with the transformation law for a four-momentum vector.

We can now always combine the Lorentz transformations (8.50) of the coordinates with the corresponding rotation of the tetrads, i.e.

$$\check{h}_{(a)\,i} = \Omega_{(a)}{}^{(b)} h_{(b)\,i} = a_a{}^b h_{(b)\,i} \tag{8.57}$$

which leaves the T_i^k unchanged. Then it is clear that the components of the rotated tetrads in the transformed system of coordinates are again given by

$$\check{h}'_{(a)\,i} = \eta_{ai} + \frac{1}{2} \overset{(1)}{g'_{ik}}, \tag{8.58}$$

where $\overset{(1)}{g'_{ik}}$ is the first order term of the transformed metric tensor g'_{ik}.

As regards energy and momentum, the wave packet of gravitational radiation with the four-momentum $\bar{p}_i$ is quite analogous to a corresponding electromagnetic wave. From (8.49) we see that the invariant norm of the four-momentum is zero, i.e.

$$\bar{p}_i \bar{p} = p_i' p'^i = 0, \tag{8.59}$$

which corresponds to a vanishing "rest mass" of the packet.

Appendix

We start by establishing a few relations needed in the following calculations. They are all consequences of the expressions (4.20) for α_{ik} and β_{ik} and of the equations (4.9)–(4.11). First, we quote again the relations (4.34), (4.38), and some immediate consequences of these equations:

$$\left.\begin{aligned} \alpha_i^i = 0, \quad \alpha^{ik}\mu_k = 0, \quad \alpha^{ik} n_k = \alpha^{i4} \\ (\alpha^{ik})_0 \mu_k = 0, \quad (\alpha^{ik})_2 \mu_k = -\alpha^{ik}(\mu_k)_2 = \alpha^{ik} m_k, \\ (\alpha^{ik})_3 \mu_k = -\alpha^{ik}(\mu_k)_3 = \sin\theta\, \alpha^{ik} l_k, \; (\alpha_{ik})_0 (\alpha^{ik})_0 = 8 c_0{}^2. \end{aligned}\right\} \tag{A.1}$$

Similarly, we have

$$\left.\begin{aligned} \alpha_{ik}\alpha^{ik} = 8c^2, \quad (\alpha_{ik})_0 \alpha^{ik} = 8 c c_0 \\ \beta_i^i = 3c^2, \quad (\beta_i^i)_0 = 6 c c_0 \\ \beta^{ik}\mu_k = -\frac{c^2}{2}\mu^i, \quad (\beta^{ik})_0 \mu_k = -c c_0 \mu^i. \end{aligned}\right\} \tag{A.2}$$

Further,

$$\left.\begin{aligned} \alpha^{ik} m_k = 2 c m^i + (c_2 + 2 c \cot\theta)\mu^i \\ \alpha^{ik} l_k = -2 c l^i. \end{aligned}\right\} \tag{A.3}$$

By differentation of these equations with respect to θ and φ, respectively, and by using (4.11) and (A.1), we obtain

$$\left.\begin{aligned} (\alpha^{ik})_2 m_k = \alpha^{i4} + (c_2 - 2 c \cot\theta) m^i + \left(c_{22} + 2 c_2 \cot\theta - \frac{2c}{\sin^2\theta}\right)\mu^i - 2 c n^i \\ \frac{1}{\sin\theta}(\alpha^{ik})_3 l_k = \alpha^{i4} + \cot\theta\,[4 c m^i + (c_2 + 2 c \cot\theta)\mu^i] + 2 c n_i. \end{aligned}\right\} \tag{A.4}$$

Hence,

$$(\alpha^{ik})_2 m_k + \frac{1}{\sin\theta}(\alpha^{ik})_3 l_k = 2\alpha^{i4} + (c_2 + 2 c \cot\theta) m^i + A\mu^i$$

with A given by (3.8). Further, since

$$\alpha^{i\,4} = -2\,M\mu^i - (c_2 + 2\,c\cot\theta)\,m^i, \tag{A.5}$$

this may be written

$$(\alpha^{ik})_2\,m_k + \frac{1}{\sin\theta}\,(\alpha^{ik})_3\,l_k = \alpha^{i\,4} + (A - 2\,M)\,\mu^i. \tag{A.6}$$

Now, we get from (4.25), (A.1), and (A.6)

$$\left.\begin{aligned} y^{ik}{}_{,\,k} &= \left(\frac{\alpha^{ik}}{r}\right)_{,\,k} = \frac{(\alpha^{ik})_0}{r}\,\mu_k + \frac{-\alpha^{i\,4} + \alpha^{i\,4} + (A - 2\,M)\,\mu^i}{r^2} \\ &= \frac{(A - 2\,M)\,\mu^i}{r^2} \end{aligned}\right\} \tag{A.7}$$

and, therefore, by (4.27), (A.1), (A.2),

$$\left.\begin{aligned} g^{ik}{}_{,\,k} &= -(y^{ik})_{,\,k} - \frac{(\beta^{ik})_0 - (\alpha^{ir}\,\alpha^k_r)_0 + cc_0\,\eta^{ik}}{r^2}\,\mu_k + O_3 \\ &= \frac{2\,M - A}{r^2}\,\mu^i + O_3, \end{aligned}\right\} \tag{A.8}$$

i.e. the equation (4.28) in the text.

We shall now calculate the tensor $\gamma^{kl}{}_i$ and the vector Φ^l for the tetrad field (4.29) up to terms of the second power in $1/r$. From (4.31) and (4.29) we get

$$\begin{aligned} \gamma_{rsi} &= h^{(a)}_r\,h_{(a)\,s,\,i} - \Gamma_{r,\,si} \\ &= \left(\delta^a_r + \frac{1}{2}\,y^a_r\right)\frac{1}{2}\left[y_{as,\,i} + z_{as,\,i} - \frac{1}{4}\,(y_{at}\,y^t_s)_{,\,i}\right] - \frac{1}{2}\,(g_{rs,\,i} + g_{ri,\,s} - g_{si,\,r}) + O_3 \\ &= \frac{1}{2}\left[g_{is,\,r} - g_{ir,\,s} + \frac{1}{4}\,(y_{rt}\,y^t_{s,\,i} - y^t_{r,\,i}\,y_{st})\right] + O_3. \end{aligned}$$

On account of (4.25), (4.26), this gives

$$\left.\begin{aligned} \gamma_{rsi} &= A_{rsi} - A_{sri} + O_3 \\ A_{rsi} &= \frac{(\alpha_{is})_0}{2\,r}\,\mu_r + \frac{1}{2\,r^2}\left[-\alpha_{is}\,n_r + (\alpha_{is})_2\,m_r + (\alpha_{is})_3\,l_r/\sin\theta + (\beta_{is})_0\,\mu_r + \frac{1}{4}\,\alpha_{rt}\,(\alpha^t_s)_0\,\mu^i\right] \end{aligned}\right\} \tag{A.9}$$

Finally, by raising the two first indices by means of (4.21),

$$\begin{aligned}\gamma^{kl}{}_i &= g^{kr}\, g^{ls}\, \gamma_{rsi} \\ &= \eta^{kr}\, \eta^{ls}\, \gamma^{rsi} - \frac{1}{2\,r^2}\,(\eta^{kr}\,\alpha^{ls} + \eta^{ls}\,\alpha^{kr})\,[(\alpha_{is})_0\,\mu_r - (\alpha_{ir})_0\,\mu_s] + O_3.\end{aligned}$$

Thus,

$$\left.\begin{aligned}\gamma^{kl}{}_i &= \frac{1}{2\,r}\,[(\alpha_i^l)_0\,\mu^k - (\alpha_i^k)_0\,\mu^l] \\ &+ \frac{1}{2\,r^2}\Big\{-\alpha_i^l\,n^k + \alpha_i{}^k\,n^l + (\alpha_i{}^l)_2\,m^k - (\alpha_i{}^k)_2\,m^l \\ &+ \frac{1}{\sin\theta}\,[(\alpha_i{}^l)_3\,l^k - (\alpha_i{}^k)_3\,l^l] + \mu^k\,[(\beta_i^l)_0 - (\alpha_{ir})_0\,\alpha^{lr}] \\ &- \mu^l\,[(\beta_i^k)_0 - (\alpha_{ir})_0\,\alpha^{kr}] + \frac{1}{4}\,[\alpha_r^k\,(\alpha^{rl})_0 - \alpha^l{}_r\,(\alpha^{rk})_0]\,\mu_i\Big\} + O_3.\end{aligned}\right\} \tag{A.10}$$

By contraction of this expression with respect to i and k, we get by means of (A.1), (A.2), and (A.6) for the vector Φ^l

$$\left.\begin{aligned}\Phi^l = \gamma^{il}{}_i &= \frac{1}{2r^2}\Big\{-\alpha^{l\,4} + (\alpha_i{}^l)_2\,m^i + \frac{1}{\sin\theta}\,(\alpha^l{}_i)_3\,l^i \\ &- cc_0\,\mu^l - 6\,cc_0\,\mu^l + \mu^l\,(\alpha_{rs})_0\,\alpha^{rs}\Big\} + O_3 \\ &= \frac{1}{2\,r^2}\,[A - 2\,M + cc_0]\,\mu^l + O_3.\end{aligned}\right\} \tag{A.11}$$

From this we see that

$$\Phi^l\,\mu_l = O_3 \tag{A.12}$$

and

$$\Phi^k\,\mu_i = \frac{1}{2\,r^2}\,[A - 2\,M + cc_0]\,\mu^k\,\mu_i + O_3. \tag{A.13}$$

Further, from (A.10), by applying (A.1), (A.2), and (4.9),

$$\gamma^{kl}{}_i\,\mu_l = \frac{1}{2\,r^2}\,\{-\alpha_l^k + \alpha_i^l\,m_l\,m^k + \alpha_i^l\,l_l\,l^k - \mu^k\,cc_0\,\mu_i\} + O_3$$

or, using (A.3),

$$\gamma^{kl}{}_i\,\mu_l = -\frac{1}{2\,r^2}\,\{(2\,M + cc_0)\,\mu_i\,\mu^k + (c_2 + 2\,c\cot\theta)\,m_i\,\mu^k\} + O_3. \tag{A.14}$$

Therefore, since $h = e^{2\beta} = 1 + O^2$, we get from (5.8), (A.12)–(A.14),

$$\mathfrak{U}_i^{kl}\mu_l = \frac{1}{2\varkappa r^2}\{(-4M + A)\mu_i\mu^k - (c_2 + 2c\cot\theta)\, m_i\mu^k\} + O_3, \qquad \text{(A.15)}$$

which is the formula (5.9) in the text.

Our next task is to prove the formula (6.24) for the quantity $\varkappa Y_i^{4l}\mu_l$. To the order required we have, just as in (6.16),

$$\varkappa Y_i^{kl}\mu_l = Z_i^k - \frac{1}{2} Z_l^l \delta_i^k + O_3', \qquad \text{(A.16)}$$

where now

$$Z_i^k = X^{kl}{}_{il}\mu_l + X^{lk}{}_{il}\mu_i. \qquad \text{(A.17)}$$

From (6.15) and (6.20) we get for this quantity

$$\left.\begin{aligned} Z_i^k = {} & \omega^{kl}{}_{,i}\mu_l + \omega^{lk}{}_{,l}\mu_i + [\omega^{rk}(\omega_r^l)_0 + \omega^{rl}(\omega_r{}^k)_0]\mu_i\mu_l \\ & - \frac{1}{2} y_r^k (\omega^{rl} + \omega^{lr})_0 \mu_i\mu_l + O_3'. \end{aligned}\right\} \qquad \text{(A.18)}$$

Here, the last term but one is also of the order of O_3' on account of (6.9) and, by means of (6.10), we get

$$\left.\begin{aligned} Z_i^k = {} & (\omega^{kl} + \omega^{lk} + \omega^{rk}\omega_r{}^l)_0 \mu_i\mu_l \\ & + (\omega^{kl})_1 n_i\mu_l + (\omega^{lk})_1 n_l\mu_i \\ & + \frac{1}{r}[(\omega^{kl})_2 m_i\mu_l + (\omega^{lk})_2 m_l\mu_i] \\ & + \frac{1}{r\sin\theta}[(\omega^{kl})_3 l_i\mu_l + (\omega^{lk})_3 l_l\mu_i] + O_3'. \end{aligned}\right\} \qquad \text{(A.19)}$$

The first term in this expression is zero on account of (6.7), and in the remaining terms ω^{kl} can be treated as antisymmetric in k and l in virtue of (6. 9). Finally, since $\mu_i = \delta_i^4 - n_i$, we get

$$\left.\begin{aligned} Z_i^k = {} & (\omega^{k4})_1 n_i + \frac{1}{r}(\omega^{k4})_2 m_i + \frac{1}{r\sin\theta}(\omega^{k4})_3 l_i \\ & + \delta_i^4\left[(\omega^{lk})_1 n_l + \frac{1}{r}(\omega^{lk})_2 m_l + \frac{1}{r\sin\theta}(\omega^{lk})_3 l_l\right] \\ & + \frac{1}{r}(\omega^{kl})_2 (n_i m_l - m_i n_l) + \frac{1}{r\sin\theta}(\omega^{kl})_3 (n_i l_l - l_i n_l) + O_3' \end{aligned}\right\} \qquad \text{(A.20)}$$

and

$$\left.\begin{aligned}\frac{1}{2}Z_k{}^k &= (\omega^{l4})_1\, n_l + \frac{1}{r}(\omega^{l4})_2\, m_l + \frac{1}{r\sin\theta}(\omega^{l4})_3\, l_l \\ &+ \frac{1}{2r}(\omega^{\varkappa\lambda})_2\,(n_\varkappa m_\lambda - m_\varkappa n_\lambda) \\ &+ \frac{1}{2r\sin\theta}(\omega^{\varkappa\lambda})_3\,(n_\varkappa l_\lambda - l_\varkappa n_\lambda) + O_3'.\end{aligned}\right\} \quad (A.21)$$

Hence,

$$\left.\begin{aligned}\varkappa Y_i{}^{4l}\mu_l &= Z_i{}^4 - \frac{1}{2}Z_k{}^k\,\delta_i^4 \\ &= \frac{1}{r}(\omega^{4\lambda})_2\,(n_i m_\lambda - m_i n_\lambda) + \frac{1}{r\sin\theta}(\omega^{4\lambda})_3\,(n_i l_\lambda - l_i n_\lambda) \\ &- \delta_i^4\left[\frac{(\omega^{\varkappa\lambda})_2}{2r}(n_\varkappa m_\lambda - m_\varkappa n_\lambda) + \frac{(\omega^{\varkappa\lambda})_3}{2r\sin\theta}(n_\varkappa l_\lambda - l_\varkappa n_\lambda)\right] + O_3',\end{aligned}\right\} \quad (A.22)$$

which is the formula (6.24) in the text.

Next, we shall calculate the complex $\vartheta_i{}^k$ created in a completely empty space by the infinitesimal transformation (8.21). Since

$$\frac{\partial X^i}{\partial x^k} = \delta_k^i + \xi^i{}_{,k}, \quad (A.23)$$

we get for the matrix tensor g_{ik} to the first order

$$\left.\begin{aligned}g^{ik} &= \frac{\partial X^l}{\partial x^i}\frac{\partial X^m}{\partial x^k}\,\eta^{lm} = \eta_{ik} + \xi_{i,k} + \xi_{k,i} \\ g^{lk} &= \eta^{ik} - \xi^{i,k} - \xi^{k,i}\end{aligned}\right\} \quad (A.24)$$

with

$$\xi_i = \eta_{ik}\xi^k, \quad \xi^{i,k} = \eta^{kl}\xi^i{}_{,l}. \quad (A.25)$$

To the same order we have

$$\left.\begin{aligned}\Gamma_{kl}^i &= \frac{\eta^{ir}}{2}(g_{rk,l} + g_{rl,k} - g_{kl,r}) = \xi^i{}_{,k,l} \\ \Gamma_{lm}^m &= \xi^r{}_{,r,l}.\end{aligned}\right\} \quad (A.26)$$

Further, since

$$\sqrt{-g} = 1 + \xi^r{}_{,r}, \quad (A.27)$$

we get

$$\left(\sqrt{-g}\,g^{lm}\right)_{,i} = \eta^{lm}\xi^r{}_{,r,i} - \xi^{l,m}{}_{,i} - \xi^{m,l}{}_{,i}. \quad (A.28)$$

Thus, the Einstein Lagrangian (2.8) is to the second order

$$\mathfrak{L}_E = \xi^r{}_{,r,s} \Box \xi^s - \xi_{r,s,t} \xi^{t,s,r} \tag{A.29}$$

with

$$\Box \xi^i = \xi^i{}_{,k}{}^{,k}, \tag{A.30}$$

and for Einstein's energy-momentum complex (2.10) we get to the same order

$$\left.\begin{aligned} \vartheta_i^k = \frac{1}{2\varkappa} \{ & \xi^r{}_{,r,i} \Box \xi^k - 2\, \xi^k{}_{,l,m} \xi^{l,m}{}_{,i} - \xi^r{}_{,r}{}^{,k} \xi^s{}_{,s,i} \\ & + (\xi^{k,m}{}_{,i} + \xi^{m,k}{}_{,i})\, \xi^r{}_{,r,m} - \delta_i^k \mathfrak{L}_E \} \end{aligned}\right\} \tag{A.31}$$

which in general does not vanish. Even if we require that the new system should be harmonic, we have in general $\vartheta_i^k \neq 0$. From (A.28) we see that the new system is harmonic if

$$(\sqrt{-g}\, g^{ik})_{,k} = -\Box \xi^i = 0, \tag{A.32}$$

which only will make the first terms in (A.29) and (A.31) disappear.

On the other hand, if $\xi^i = \xi^i(u)$ is a function of $u = x^4 - x^1$ only, so that the metric tensor (A.24) has the form of a plane wave, we have

$$\xi^i{}_{,k,l} = (\xi^i)'' \bar{\mu}_k \bar{\mu}_l, \tag{A.33}$$

where $\bar{\mu}_k$ are the quantities defined by (8.9) for which

$$\bar{\mu}_k \bar{\mu}^k = 0. \tag{A.34}$$

In this case, we get at once from (A.29)–(A.34)

$$(\sqrt{-g}\, g^{ik})_{,k} = -\Box \xi^i = 0, \qquad \mathfrak{L}_E = 0 \tag{A.35}$$

and

$$\vartheta_i^k = \frac{1}{2\varkappa} \{ -(\xi^r)'' \bar{\mu}_r \bar{\mu}^k (\xi^s)'' \bar{\mu}_s \bar{\mu}_i + (\xi^m)'' \bar{\mu}^k \bar{\mu}_i (\xi^r)'' \bar{\mu}_r \bar{\mu}_m \} = 0. \tag{A.36}$$

Finally, we shall show that a rotation of the tetrads (8.13) with coefficients $\Omega_{(ab)}$ of the type (8.26) does not change the value (8.14) of the complex $\mathfrak{t}_i^k$ defined by (2.31). To the first order, the rotated tetrads are

$$\check{h}_{(a)\,i} = \Omega_{(a)}{}^{(b)}\, h_{(b)\,i} = \eta_{ai} + \frac{1}{2}\, \overset{(1)}{y}_{ai} + \bar{\omega}_{ai}. \tag{A.37}$$

Since both $\overset{(1)}{y}_{ai}$ and $\bar{\omega}_{ai}$ are functions of $\bar{u} = \bar{l} - \bar{x}$ only, we get to the same order

$$\check{\gamma}_{ikl} = \check{h}_i^{(a)}\, \check{h}_{(a)\, k;\, l} = \left[\frac{1}{2}\, \overset{(1)}{y}_{kl}\, \bar{\mu}_i - \frac{1}{2}\, \overset{(1)}{y}_{il}\, \bar{\mu}_k + \bar{\omega}_{ik}\, \bar{\mu}_l\right]'. \tag{A.38}$$

Here, $\bar{\mu}_i$ are the constant numbers defined by (8.9), and the prime means differentiation with respect to $\bar{u}$. Similarly, we get

$$\left.\begin{aligned} \check{\Delta}^i{}_{kl} &= \check{h}^{(a)\, i}\, \check{h}_{(a)\, k,\, l} = \left[\frac{1}{2}\, \overset{(1)}{y}{}^i_k + \bar{\omega}^i{}_k\right]' \bar{\mu}_l \\ \check{\Phi}_k &= \check{\gamma}^i{}_{ki} = [\bar{\omega}^i{}_k\, \bar{\mu}_i]', \end{aligned}\right\} \tag{A.39}$$

where we have used the relations

$$\overset{(1)}{y}_{ik}\, \bar{\mu}^k = 0\,, \qquad \overset{(1)}{y}{}^i_i = 0 \tag{A.40}$$

following from (8.12).

By means of these expressions we can now calculate the Lagrangian (2.29) corresponding to the rotated tetrads to the second order, which gives

$$\left.\begin{aligned} \check{\mathfrak{L}} &= \check{\gamma}_{ikl}\, \check{\gamma}^{lki} - \check{\Phi}_k\, \check{\Phi}^k \\ &= \left[\frac{1}{2}\, \overset{(1)}{y}_{kl}\, \bar{\mu}_i - \frac{1}{2}\, \overset{(1)}{y}_{il}\, \bar{\mu}_k + \bar{\omega}_{ik}\, \bar{\mu}_l\right]' \left[\frac{1}{2}\, \overset{(1)}{y}{}^{ki}\, \bar{\mu}^l - \frac{1}{2}\, \overset{(1)}{y}{}^{li}\, \bar{\mu}^k + \bar{\omega}^{lk}\, \bar{\mu}^i\right]' \\ &\quad - [\bar{\omega}^i{}_k\, \bar{\mu}_i]'\, [\bar{\omega}^{lk}\, \bar{\mu}_l]' \\ &= (\bar{\omega}_{ik})'\, (\bar{\omega}^{lk})\; \bar{\mu}^i\, \bar{\mu}_l - (\bar{\omega}^i{}_k)'\, (\bar{\omega}^{lk})'\, \bar{\mu}_i\, \bar{\mu}_l = 0\,. \end{aligned}\right\} \tag{A.41}$$

Similarly, by means of (2.31),

$$\left.\begin{aligned} \varkappa \check{\mathfrak{t}}_i^{\,k} &= \check{\gamma}^{km}{}_l\, \check{\Delta}^l{}_{mi} - \check{\Phi}^l\, \check{\Delta}^k{}_{li} + \check{\Delta}^l{}_{li}\, \check{\Phi}^k \\ &= \left[\frac{1}{2}\, \overset{(1)}{y}{}^m_l\, \bar{\mu}^k - \frac{1}{2}\, \overset{(1)}{y}{}^k_l\, \bar{\mu}^m + \bar{\omega}^{km}\, \bar{\mu}_l\right]' \left[\frac{1}{2}\, \overset{(1)}{y}{}^l_m + \bar{\omega}^l{}_m\right]' \bar{\mu}_i \\ &\quad - [\bar{\omega}^{rl}\, \bar{\mu}_r]' \left[\frac{1}{2}\, \overset{(1)}{y}{}^k_l + \bar{\omega}^k{}_l\right]' \bar{\mu}_i + \left[\frac{1}{2}\, \overset{(1)}{y}{}^l_l + \bar{\omega}^l{}_l\right]' \bar{\mu}_i\, [\bar{\omega}^{rk}\, \bar{\mu}_r]' \\ &= \left[\frac{1}{4}\left(\overset{(1)}{y}_{lm}\right)' \left(\overset{(1)}{y}{}^{lm}\right)' + \frac{1}{2}\left(\overset{(1)}{y}{}^{lm}\right)' (\bar{\omega}_{lm})'\right] \bar{\mu}_i\, \bar{\mu}^k \\ &\quad + (\bar{\omega}^l{}_l)'\, (\bar{\omega}^{rk})'\, \bar{\mu}_i\, \bar{\mu}_r. \end{aligned}\right\} \tag{A.42}$$

Here we have again used the relations (A.40). Finally, we shall make use of the fact that $\bar{\omega}_{lm}$ is antisymmetrical in l and m, i.e.

$$\bar{\omega}_{lm} = -\bar{\omega}_{ml}, \qquad \omega^{l}{}_{l} = 0, \tag{A.43}$$

while $\overset{(1)}{y}{}^{lm}$ is symmetrical. Therefore, since

$$\left(\overset{(1)}{y}_{lm}\right)' \left(\overset{(1)}{y}{}^{lm}\right)' = 8\,\bar{c}'\,(\bar{u})^2, \tag{A.44}$$

we get for the complex $\check{\mathfrak{t}}_i{}^k$

$$\check{\mathfrak{t}}_i{}^k = \frac{2}{\varkappa}\,\bar{c}'\,(\bar{u})^2\,\bar{\mu}_i\,\bar{\mu}^k = \mathfrak{t}_i{}^k, \tag{A.45}$$

which completes the proof of the invariance of the energy-momentum complex under the rotations of the type (8.26).

References

1. H. Bondi, M.G.I. Van der Burg and A. W. K. Metzner, Proc. Roy. Soc. A **269**, 21 (1962).
2. C. Møller, Mat. Fys. Skr. Dan. Vid. Selsk. **1**, no. 10 (1961).
3. C. Møller, Phys. Letters **3**, no. 7, 329 (1963).
4. A. Einstein, Berl. Ber. 778 (1915); 167 (1916); 154 and 448 (1918); see also H. A. Lorentz, Amsterdam Versl. **25**, 468 (1916) and F. Klein, Gött. Nachr. Math.-phys. Kl. 394 (1918).
5. Ph. von Freud, Am. Math. Journ. **40**, 417 (1939).
6. H. Bauer, Phys. Z. **19**, 163 (1918).
7. A. Lichnérowicz, Théories Relativistes de la Gravitation et de l'Electromagnetisme, Masson, Paris (1955).
8. C. Møller, Annals of Physics **12**, 118 (1961).
9. V. Fock, Z. Phys. **57**, 261 (1929);
   L. Infeld and B. L. van der Waerden, Berl. Ber. 380 (1933);
   E. Schrödinger, Berl. Ber. 105 (1932);
   H. Weyl Z. Phys. **56**, 330 (1929);
   P. A. M. Dirac, Max Planck Festschrift p. 339, Berlin (1958).
10. C. Møller, Conservation Laws in the Tetrad Theory of Gravitation. Report of the 1962 Warszawa Conference.
11. C. Pellegrini and J. Plebanski, Mat. Fys. Skr. Dan. Vid. Selsk. **2**, no. 4 (1963).
12. R. K. Sachs, Proc. Roy. Soc. A **270**, 103 (1962).
13. A. Einstein and N. Rosen, J. Franklin Inst. **223**, 43 (1937).
14. S. Deser, Phys. Letters **7**, nr. 1 (1963).

Indleveret til selskabet den 13. november 1963.
Færdig fra trykkeriet den 14. april 1964.

Matematisk-fysiske Meddelelser
udgivet af
Det Kongelige Danske Videnskabernes Selskab
Bind **34,** nr. 4

Mat. Fys. Medd. Dan. Vid. Selsk. **34,** no. 4 (1964)

STOPPING POWER OF ELECTRON GAS AND EQUIPARTITION RULE

BY

JENS LINDHARD AND AAGE WINTHER

København 1964
Kommissionær: Ejnar Munksgaard

Contents

Synopsis

In a self-consistent perturbation treatment, the stopping power of matter for swift charged particles is conveniently expressed by means of the dielectric constant. In the present paper we have studied the results for degenerate, free electron gases, using an explicit expression for the dielectric constant, as derived previously. Approximate results for the stopping at low and high velocities are obtained. At low velocities the stopping is closely proportional to particle velocity, while at high velocities the corrections to the familiar logarithmic dependence on velocity are analogous to atomic shell corrections. The analytic results are compared with direct numerical computations, the results of which are presented in the form of tables and figures.

We prove, and make extensive use of, an equipartition rule, stating exact equality of the stopping contributions from, respectively, close collisions and distant resonance collisions. Possible applications of the results to stopping in other media are discussed.

PRINTED IN DENMARK
BIANCO LUNOS BOGTRYKKERI A/S

§ 1. Introduction

The stopping power of a free electron gas for swift heavy particles of low charge is of considerable interest to actual slowing-down problems. In point of fact, the free electron gas offers an interesting illustration of properties of atomic systems, and the effect of particle interaction on oscillator strength distribution. The free electron gas also elucidates the important question of deviations from the Bethe-Bloch stopping formula at moderate and low velocities.[1]

A basic approximation in the theory of slowing-down is to consider the effect of the particle as a perturbation, so that the energy loss is proportional to the square of the particle charge. In this case, the theory of slowing-down is simplified to a treatment of properties of the medium only, and a linear description of these properties may be applied. The linear properties of an infinite gas of free electrons can be described by the longitudinal and transverse dielectric constants $\varepsilon^l(k,\omega)$ and $\varepsilon^{tr}(k,\omega)$, which are complex functions of wave number and frequency, and which contain collective as well as individual particle aspects of the gas.

In the following non-relativistic problems we need only consider the longitudinal dielectric constant ε^l, which function gives the connection between the Fourier components of the total potential,

$$\Phi(\vec{r},\, t) = \sum_{k,\omega} \Phi(\vec{k},\omega)\, e^{i\vec{k}\cdot\vec{r} - i\omega t} ,$$

and those of the source charge density ϱ_0 through the relation

$$\varepsilon^l(k,\omega)\, k^2 \Phi(\vec{k},\omega) = 4\pi \varrho_0(\vec{k},\omega). \tag{1}$$

For a heavy particle of charge $Z_1 e$ and velocity $\vec{v}$, the source density is given by $\varrho_0(\vec{r},t) = Z_1 e\, \delta(\vec{r}-\vec{v}t)$, corresponding to rectilinear motion. Introducing this charge density in (1), we immediately obtain the retarding force acting on the particle, i. e. the specific energy loss. For a gas of density n electrons per unit volume it is convenient to write the resulting stopping formula in the form

$$\frac{dE}{dx} = \frac{4\pi Z_1^2 e^4}{mv^2} \cdot n \cdot L, \tag{2}$$

where m is the electron mass, and L the dimensionless quantity

$$L = \frac{i}{\pi \omega_0{}^2} \int_0^\infty \frac{dk}{k} \int_{-kv}^{kv} \omega \, d\omega \left(\frac{1}{\varepsilon^l(k,\omega)} - 1 \right). \tag{3}$$

We have here introduced the plasma frequency ω_0, given by

$$\omega_0{}^2 = \frac{4\pi ne^2}{m}.$$

It may be noted that in the retarded ε^l, as used here, the imaginary part is an odd function of ω, whereas the real part is even in ω. The bounds $|\omega| < kv$ in the integration over ω in (3) is simply due to conservation of total energy and momentum between the heavy particle and the system of electrons.

The formula (2) may be used for any atomic system if n is interpreted as the atomic number times the number of atoms per unit volume. The Bethe-Bloch formula, without relativistic corrections, is then given by (2) with

$$L = \log \frac{2mv^2}{I}, \tag{4}$$

where the average excitation potential I is a constant characteristic of the substance in question.

The present work was commenced as an attempt to get comparatively accurate estimates of stopping by an electron gas for various gas densities, and at any velocity of a heavy penetrating particle. Previous estimates have been more or less qualitative, and we thought it worth-while to make numerical calculations, based on a simple dielectric constant of the gas. In this connection we also utilized the analytic properties of the dielectric constant. Thus, we had recourse to the Bethe sum rule, at moderate and high particle velocities, and to asymptotic expansions at low and high velocities. However, prompted by intricacies of the numerical calculations along the plasma resonance curve, we found that quite other types of summation rules could be useful. In particular, we have applied an equipartition rule, stating equality of stopping contributions from plasma resonance excitation and close collisions with gas electrons. In the equipartition rule, summation is made at constant phase velocity, ω/k, of the emitted waves, corresponding to a definite direction of emission of energy.

By the above means, a comparatively accurate description is obtained

of the energy dissipation by charged particles in a degenerate electron gas. It appears to us that the results for free electron gases, in particular as regards deviations from the Bethe-Bloch formula (4), may be carried over to atoms. Thus, in the whole region of low particle velocities, where the so-called shell corrections have been used, the present corrections to stopping power may be summed over the electron density distribution of atoms. This seems justified already from the circumstance that the first terms in series developments of the correction in both distant and close collisions are the same for the electron gas as in the Bethe-Walske procedure.[4]

In § 2 we discuss main features of slowing-down, based on the simple dielectric constant. We make asymptotic expansions at low and high particle velocities, and utilize summation rules. We briefly mention the connection to slowing-down by atoms. The numerical computations are presented in § 3. In § 4 the equipartition rule is derived.

§ 2. Dielectric Constant and Basic Theoretical Treatment

The stopping of a particle as a function of its velocity may be computed from (3) by analytical or numerical means, if the dielectric constant is known. For a free electron gas, a quantum mechanical perturbation treatment leads to the following general formula for the dielectric constant to first order [2]

$$\varepsilon^l(k,\omega) = 1 + \frac{2m^2\omega_0^2}{\hbar^2 k^2} \sum_n \frac{f(E_n)}{N} \left\{ \frac{1}{k^2 + 2\vec{k}\cdot\vec{k}_n - \frac{2m}{\hbar}(\omega + i\delta)} + \right.$$
$$\left. + \frac{1}{k^2 - 2\vec{k}\cdot\vec{k}_n + \frac{2m}{\hbar}(\omega + i\delta)} \right\}. \qquad (5)$$

Here, E_n is the energy and $\vec{k}_n$ the wave vector of the electron in the n'th state. The distribution function $f(E_n)$ is an even function of $\vec{k}_n$, and normalized so that $N = \sum_n f(E_n)$ is the total number of electrons. In equation (5) we shall consider only the retarded dielectric constant of a system in its ground state, corresponding to a small positive value of δ.

In the case of a degenerate free electron gas with Fermi energy E_F the distribution function is $f(E_n) = 1$ for $E_n < E_F$, and $f(E_n) = 0$ for $E_n > E_F$. The Fermi energy is related to the density n of the gas by the familiar relation

$$E_F = \frac{1}{2} m v_F^2 = \frac{\hbar^2 k_F^2}{2m} = \frac{\hbar^2}{2m} (3\pi^2 n)^{2/3}.$$

The summation in (5) may now be performed and the result is conveniently written in the form

$$\varepsilon^l(u,z) = 1 + \frac{\chi^2}{z^2}\{f_1(u,z) + i f_2(u,z)\}, \tag{6}$$

where

$$\left.\begin{aligned} f_1(u,z) = \frac{1}{2} + \frac{1}{8z}\{1-(z-u)^2\}\log\left|\frac{z-u+1}{z-u-1}\right| + \\ + \frac{1}{8z}\{1-(z+u)^2\}\log\left|\frac{z+u+1}{z+u-1}\right|, \end{aligned}\right\}$$

and

$$f_2(u,z) = \begin{cases} \dfrac{\pi}{2} u, & \text{for } z+u<1, \\ \dfrac{\pi}{8z}\{1-(z-u)^2\}, & \text{for } |z-u|<1<z+u, \\ 0, & \text{for } |z-u|>1. \end{cases} \tag{6'}$$

The variables k and ω are here replaced by dimensionless variables z and u, where

$$z = \frac{k}{2k_F} \quad \text{and} \quad u = \frac{\omega}{k v_F}.$$

Moreover, the parameter χ^2 in (6), defined by

$$\chi^2 = \frac{e^2}{\pi \hbar v_F}, \tag{7}$$

is proportional to $n^{-1/3}$. At the same time, χ^2 is a measure of the ratio between the potential energy of two neighbouring particles and their kinetic energy. This indicates that only for small values of χ^2 can the present free particle picture be used.

It should be noted that our present approximate dielectric constant is based on a first order perturbation procedure starting from free electrons, and with self-consistent fields. In higher order, account can be taken of the circumstance that the electrons are not free; corrections of this type are important mainly when $\chi^2 \gtrsim 1$, i.e. at low gas densities.

When one introduces the dielectric constant (6) of the free gas in (3), the factor L in the specific energy loss takes the form [2]

$$L = \frac{-6}{\pi\chi^2}\int_0^{v/v_F} u\,du \int_0^{\infty} z\,dz\ \mathrm{Im}\ \left(\frac{1}{\varepsilon^l} - 1\right)$$
$$= \frac{6}{\pi}\int_0^{v/v_F} u\,du \int_0^{\infty} dz\ \frac{z^3 f_2(u,z)}{\{z^2 + \chi^2 f_1(u,z)\}^2 + \{\chi^2 f_2(u,z)\}^2}. \tag{8}$$

It is seen from (6) that the integral (8) receives contributions from the domain $|u-z|<1$ where $f_2(u,z) \neq 0$, and also from a curve in the region $u>z+1$, for which $\varepsilon^l = 0$, i.e. $z^2+\chi^2 f_1(u,z) = 0$. In the latter case the double integral degenerates to a line integral. The former contribution

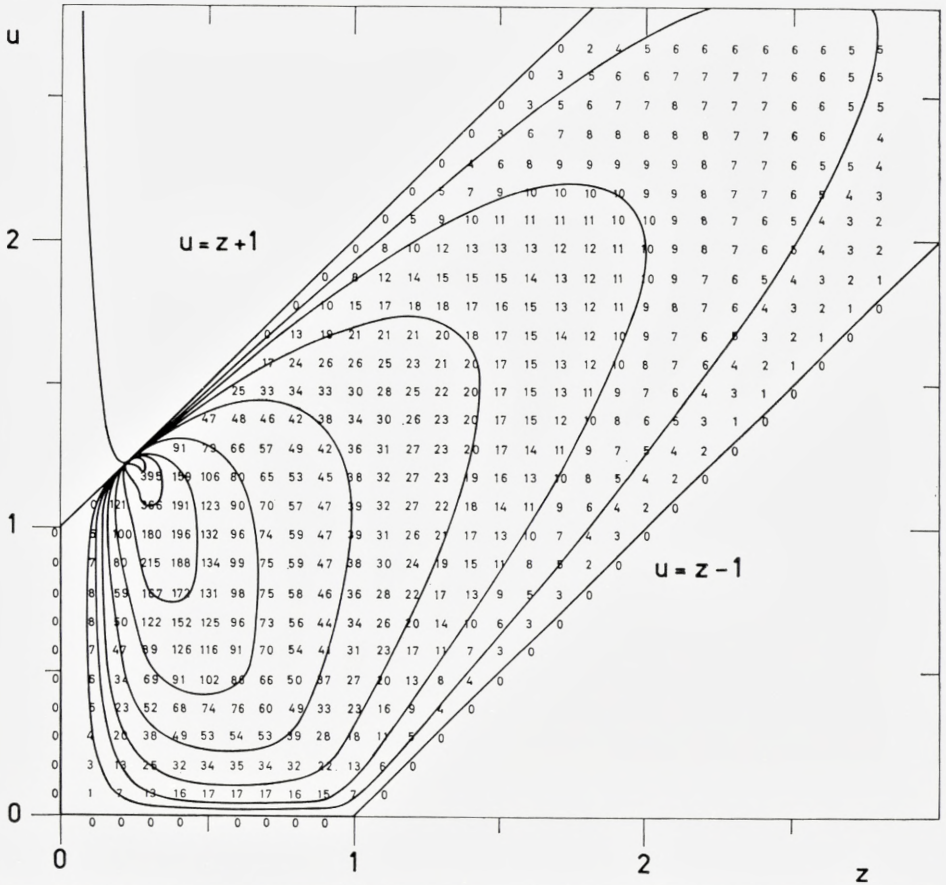

Fig. 1. The quantity $A = -z\ \mathrm{Im}\,(1/\varepsilon^l - 1)$ as a function of the parameters u and z for $\chi^2 = 0.1$. Numbers indicated on the figure give values of A times 10^4, at the points $u = 0,\ 0.1,\ 0.2,\ \ldots$ etc., and $z = 0,\ 0.1,\ 0.2,\ \ldots$ etc. Contour lines are drawn through points where $10^4 \cdot A$ equals respectively 5, 10, 20, 40, 80, 160 and 320. The position of the resonance curve is also indicated. At the point where it joins the domain $|u-z|<1$, it has the line $u = z+1$ as a tangent.

mainly corresponds to close collisions, while the latter arises from plasma resonance at distant collisions.

The behaviour of the integrand in (8) is illustrated in Fig. 1, for the case $\chi^2 = 0.1$. In particular, the figure indicates the magnitude of the absorption in the area between the two parallel lines $u = z+1$ and $u = z-1$. These lines correspond to absorption by electrons at the Fermi surface having, respectively, momentum parallel and antiparallel to the momentum transfer $\vec{k}$. Roughly, there is a maximum of absorption at $u = z$, but for low values of z the behaviour is more complicated. In the neighbourhood of $(z,u) = (0,1)$ the absorption tends quickly to zero, whereas a strong absorption is found as a continuation of the resonance curve. This curve has the line $u = z+1$ as a tangent, in the point $(u_0 - 1, u_0)$ where it joins the domain $|u-z| \leq 1$. For the purpose of an investigation of the behaviour of the resonance curve further apart from this domain, we perform a series expansion of $f_1(u,z)$ in (6′), assuming $|u-z|$ to be large compared to unity:

$$f_1(u,z) = \frac{1}{3(z^2-u^2)} + \frac{z^2+3u^2}{15(z^2-u^2)^3} + \cdots\cdots . \tag{9}$$

The position of the resonance curve is determined by the dispersion relation $\varepsilon^l = 0$, i.e. according to (9)

$$u^2 = \frac{\chi^2}{3z^2} + \frac{3}{5} + \cdots\cdots , \text{ or } \omega = \omega_0 + \frac{3}{10}\frac{{v_F}^2}{\omega_0}k^2 + \cdots\cdots . \tag{10}$$

In the limit of large u, the dispersion relation (10) approaches the hyperbola $u \cdot z = \chi/\sqrt{3}$, or $\omega = \omega_0$.

In § 3 we give the results of numerical evaluation of the double integral (8). Before that we shall discuss on an analytic basis the behaviour of L in the extremes of low and high velocities. In equation (8) the velocity v is measured in units of the Fermi velocity v_F. In the following, however, it turns out that, instead of v/v_F, the parameter

$$y = \frac{2mv^2}{\hbar\omega_0} = \frac{3^{1/2}}{\chi}\left(\frac{v}{v_F}\right)^2 \tag{11}$$

will be useful. The variable y measures the velocity in a unit $(\hbar\omega_0/2m)^{1/2}$, defined by the plasma frequency.

Low velocities.

For extremely low particle velocities we find directly from (8) and (6′) that L is approximately proportional to v^3, i.e.[2]

TABLE 1

The coefficients C_1 and $C_1 \cdot (\chi^2/3)^{3/4}$ as functions of the density parameter χ^2 in (7). These coefficients determine the asymptotic behaviour of L for low particle velocities.

χ^2	0.01	0.02154	0.04642	0.1	0.3163	1.0
C_1	1.823	1.463	1.108	0.787	0.387	0.134
$C_1 \cdot (\chi^2/3)^{3/4}$	0.0253	0.0361	0.0486	0.0614	0.0716	0.0587

$$L = C_1(\chi) \cdot \left(\frac{v}{v_F}\right)^3 = \left(\frac{\chi^2}{3}\right)^{3/4} C_1(\chi) y^{3/2}, \tag{12}$$

where

$$C_1(\chi) = \int_0^1 \frac{z^3 dz}{(z^2 + \chi^2 f_1(0,z))^2}. \tag{13}$$

The function $C_1(\chi)$ has been evaluated numerically for six values of χ^2, and the results are given in Table 1, together with $C_1 \cdot (\chi^2/3)^{3/4}$, which is the coefficient of $y^{3/2}$ in (12). It is seen from Table 1 that this coefficient is nearly independent of the density of the gas, varying by less than a factor of 3, when the density changes by a factor of 10^6. For comparison, it may be mentioned that $\chi^2 = 1$ corresponds to $n = 0.84 \cdot 10^{22}$ cm^{-3}.

We note that the function $C_1(\chi)$ can be approximated quite well by substituting for $f_1(0,z)$ the first two terms in a series expansion in powers of z^2, i.e.

$$f_1(0,z) \simeq 1 - \frac{1}{3} z^2. \tag{14}$$

It then follows from (13) that

$$C_1(\chi) \simeq \frac{1}{2\left(1 + \frac{\chi^2}{3}\right)^2} \left[\log \frac{1 + \frac{2}{3}\chi^2}{\chi^2} - \frac{1 - \frac{1}{3}\chi^2}{1 + \frac{2}{3}\chi^2} \right]. \tag{15}$$

The accuracy of this approximation is illustrated in Fig. 2. The coefficient of $y^{3/2}$ in (12) with $C_1(\chi)$ determined by (15) is here compared with the result of the numerical integration of (13).

The approximation used in (12)–(15) implies that L behaves as v^3, i.e. stopping is proportional to velocity. The velocity region in which this proportionality holds may be inferred from the numerical results in §3. It is seen from Fig. 5 that the approximation remains quite accurate even when v/v_F becomes as large as ~ 1.

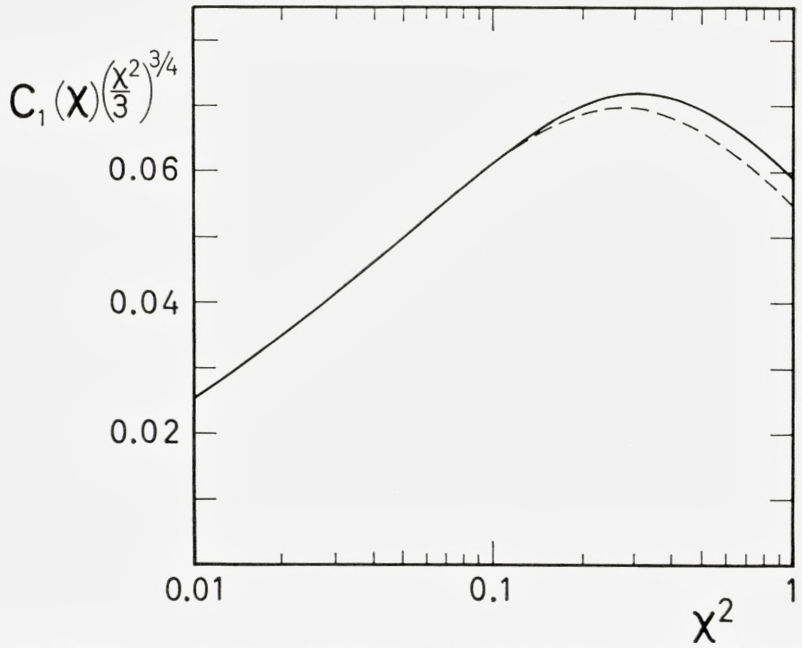

Fig. 2. The coefficient $C_1 \cdot (\chi^2/3)^{3/4}$ as a function of χ^2. The full-drawn curve was obtained from numerical integration of (13). For comparison the approximate formula (15) is also shown (dashed curve). The two curves join when $\chi^2 \sim 0.1$.

High velocities.

Consider next the case of large, but not relativistic, particle velocities. As mentioned in the introduction, in this limit the general formula (2) is reduced to the simple Bethe-Bloch formula (4) for any atomic system. In order to compute the average excitation potential I and stopping at large velocities, one usually has recourse to the Bethe sum rule for generalized oscillator strengths. For a free electron gas, the Bethe sum rule is[3]

$$\int_{-\infty}^{\infty} d\omega \frac{\omega}{i\pi\omega_0^2}\left(\frac{1}{\varepsilon^l(k,\omega)} - 1\right) = 1 . \tag{16}$$

A brief discussion of (16) is given in §4.

The sum rule (16) contains an unbounded integration over ω for fixed k. Now, for some values of k the integration over ω in (3) can in fact be extended to infinity if only ε has no imaginary part and no zeros outside the ω-interval $|\omega| < kv$. If this condition is fulfilled in the k-interval $k_{\min} < k < k_{\max}$, we find immediately from (16) that this k-interval gives the contribution $\log(k_{\max}/k_{\min})$ to L. It is qualitatively clear that for a heavy particle

of high velocity an upper limit, $\hbar k_{\max}$, is given by $2mv$, the maximum momentum transfer to a free electron at rest, while the lower limit, $k_{\min}$, is the adiabatic one, of order of ω_0/v. This simple consideration therefore leads to an estimate of L approximately given by (4) with $I \approx \hbar\omega_0$.

In order to obtain an accurate estimate of I, as well as correction terms to (4) at finite velocities, we may formulate the above consideration in the more convenient u, z-variables. The double integral has the bounds $0 < z < \infty$, $0 < u < v/v_F$. It is seen directly from Fig. 3 that, except for the three shaded

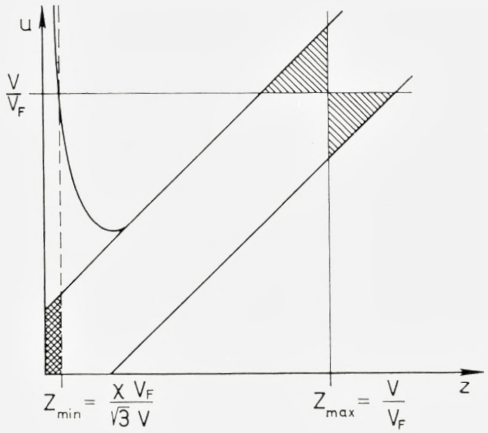

Fig. 3. Illustration of those regions in the u, z-plane, where $\mathrm{Im}\,(1/\varepsilon^l - 1)$ is non-vanishing. In the text is explained the meaning of the shaded areas, and of $z_{\max}$ and $z_{\min}$.

areas, the integral may instead be given the bounds $0 < u < \infty$ and $z_{\min} < z < z_{\max}$. Here, the upper limit is given by $z_{\max} = v/v_F$, while $z_{\min}$ is the value of z at the resonance curve (10) for $u = v/v_F$. For large velocities this leads to $z_{\min} \approx \chi v_F/(v\sqrt{3})$. It is easily shown that the corrections to L from the three shaded areas tend to zero in the limit of high velocities. Firstly, in the two hatched domains the contributions to the integrand (8) tend to zero, while the areas remain constant. Secondly, in the cross-hatched domain ($z < z_{\min} << 1$, $0 < u < z+1$), the integrand as well as the area tend to zero; in fact, the integral vanishes as constant $\cdot\, z^4{}_{\min}$. Applying the sum rule (16) we therefore obtain in the limit of large velocities the formula (4) with

$$I = \hbar\omega_0. \tag{17}$$

Having determined the asymptotic stopping formula, i.e. the constant I in (4), we may next consider deviations from it at lower velocities. The

deviations are analogous to the so-called shell corrections in the atomic case, as treated by BETHE, WALSKE[4], and others. The shell corrections to be added to (4) are normally denoted as $-C/Z$, Z being the atomic number of the medium. In the atomic case, as well as in the present case, several types of estimates of the corrections may be used. Thus, numerical evaluations may be attempted; this has proved rather difficult to carry through completely in the atomic case, whereas the results for an electron gas are easily obtained, cf. §3. Also, at high velocities a series expansion in powers of $1/v^2$ may be attempted. The series expansion is again comparatively simple for the electron gas.

We consider at first accurate formulae for the corrections to (4). As before, for large values of u we are concerned with stopping contributions from the two branches illustrated in Fig. 3, i.e. resonance absorption and close collisions. It would be comparatively easy to make separate computations for each of the two branches. It is simpler, however, to apply the equipartition rule, the use of which renders superfluous one of the two branch computations.

The equipartition rule (cf. §4) states that at particle velocities where resonance occurs, the change in L with velocity receives exactly equal contributions from the resonance curve and from the close collisions. The increase in L between two velocities v_1 and v_2 is thus twice the contribution from the resonance curve, i.e.

$$L(v_1) - L(v_2) = 2\int_{z_r(v_2/v_F)}^{z_r(v_1/v_F)} \frac{dz}{z} F_r(z), \tag{18}$$

where $F_r(z)$ is the oscillator strength of the resonance curve, as a function of z, and $z_r(u)$ denotes the value of z on the resonance curve as a function of the variable u, i.e. $z_r^2(u) = -\chi^2 f_1(u, z_r(u))$. By direct integration over the resonance curve, $F_r(z)$ is easily obtained,

$$F_r(z) = \frac{-6}{\pi\chi^2}\int u du\, z^2 \operatorname{Im}\left(\frac{1}{\varepsilon^l(u,z)} - 1\right) = \frac{6z^4}{\chi^4\left(\dfrac{\partial f_1(u,z)}{u\partial u}\right)_r}, \tag{18'}$$

where the integral over u is from below to above the resonance curve. The quantity $(\partial f_1(u,z)/u\partial u)_r$ is the partial derivative for constant z, taken at the resonance curve. The oscillator strength F_r remains close to unity in the upper part of the resonance curve. In fact, from (18′) we find by series expansion in powers of u^{-2},

$$F_r = 1 - \frac{12}{175u^4} + o\left(\frac{1}{u^6}, \frac{\chi^2}{u^4}\right),$$

where we note the absence of a term proportional to u^{-2}.

In order to obtain a series expansion of L we write (18) as

$$L(v_1) - L(v_2) = \frac{6}{\chi^2} \int_{v_2/v_F}^{v_1/v_F} \frac{z_r^2(u)\, u\, du}{1 + \frac{\chi^2}{2 z_r} \left(\frac{\partial f_1(u,z)}{\partial z} \right)_r}, \tag{19}$$

and neglecting terms of higher order in χ^2 we obtain

$$L(v_1) - L(v_2) = \left\{ u^3 \log \frac{u+1}{u-1} + \log (u^2 - 1) - 2u^2 + o\left(\frac{\chi^2}{u^4} \right) \right\} \Bigg|_{v_2/v_F}^{v_1/v_F}. \tag{19'}$$

Combining (19′) with (17), and taking only the first terms in a series expansion in v_F^2/v^2, the result is

$$\begin{aligned} L &= \log \frac{2mv^2}{\hbar\omega_0} - \frac{3 v_F^2}{5 v^2} - \frac{3 v_F^4}{14 v^4} - \cdots + o\left(\frac{\chi^2 v_F^4}{v^4} \right) = \\ &= \log y - \frac{3^{3/2}}{5\chi} \frac{1}{y} - \frac{9}{14 \chi^2 y^2} - \cdots . \end{aligned} \tag{20}$$

The formula (20) is applicable when v/v_F is above the minimum of the resonance curve. According to the equipartition rule, every term in (20) is contributed equally from the resonance curve and from close collisions, except for the additive constant obtained by integration over the region where u is below the minimum of the resonance curve.

It may be noted that the first correction term in (20) is the average kinetic energy, $\langle mv_i^2/2 \rangle = (3/10)\, m v_F^2$, of an electron in the gas, divided by $mv^2/2$*. This appearance of the average kinetic energy seems to be quite general for an atomic system. At least, FANO and TURNER [5] obtained this result for any atom in the case of resonance collisions, while WALSKE [4] obtained it for both resonance and close collisions in the hydrogen atom. Moreover, the equipartition rule is found to hold for the v^{-2} and v^{-4}-terms in expansions of shell corrections for atomic systems (cf. refs. 5 and 4).

The comparisons made here indicate a wide applicability of the notion of a free gas, in the case of atomic electrons. As we have seen, an average over free electron gases gives asymptotically the same v^{-2}-correction as a direct computation. The picture of the close collisions involving free electrons, with momentum distribution given by their local kinetic energies in the atom, seems appropriate and useful. Having such results in mind, it would seem profitable to estimate stopping in atomic systems on the basis of approximate results for electron gases. If a suitable approximation

* In a more comprehensive manner, and apart from a constant, we may write (20) as the average $\langle \log (v^2 - v_i^2) \rangle$.

is introduced for the electron gas, it may be averaged over the atom in order to obtain, e.g., the shell correction $-C/Z$, which quantity has been notoriously difficult to estimate in other ways. This approach is quite similar to that used previously [1] in a more crude approximation.

§ 3. Numerical Results

In the preceding chapter, the behaviour of the factor L in the specific energy loss was discussed on the basis of sum rules and series developments. In the present chapter we present the results of a direct numerical evaluation of L.

The double integral (8), which constitutes the basis for the numerical computation of L, cannot be evaluated by simple quadrature. When the functions f_1 and f_2 given by (6′) are introduced in the integrand, it is found that in the domain $u > z+1$ the integral degenerates into a line integral.

The integral is thus composed of two different parts. One is the line integral along the curve given implicitly by $\varepsilon^l(u,z) = 0$ in the region $u > z+1$. The other is the double integral over the region of close collisions, $|u-z|<1$, in which region $f_2(u,z)>0$. A direct numerical integration in the latter region is quite straightforward, except for a singularity appearing at the point $(u,z) = (u_0, u_0-1)$, where the resonance curve joins the region of close collisions. Similarly, it is particularly difficult to identify the resonance curve in the neighbourhood of this point.

For numerical evaluations it is important that the line integral along the resonance curve need not at all be performed, since, according to the equipartition rule, it is equal to the corresponding integral over close collisions. Moreover, computations of the double integral in the difficult region around $u = u_0$ may be avoided too. This is because the integral $L(v_1)$ at very high velocities is given accurately by the two first terms in formula (20). Therefore, a numerical calculation of the difference $L(v_1) - L(v_2)$, which is twice the contribution from the region $|z-u|<1$, can give us $L(v_2)$ for all $v_2 > v_F \cdot u_0$.

Numerical computations along these lines were performed by Dr. Peter Naur on the electronic computer DASK. The main results are shown in Table 2. The quantity L is here given as a function of the variable y defined in (11), and for six values of χ^2, as in Table 1.

In the numerical treatment we actually did make computations which are unnecessary according to the above. We evaluated the line integral along the resonance curve, and because of the above-mentioned difficult-

ies near the point $(u_0, u_0 - 1)$, we were led to a closer scrutiny of the integral, which suggested the validity of an equipartition rule. The equipartition rule is thus confirmed by the numerical calculations, as far as they go.

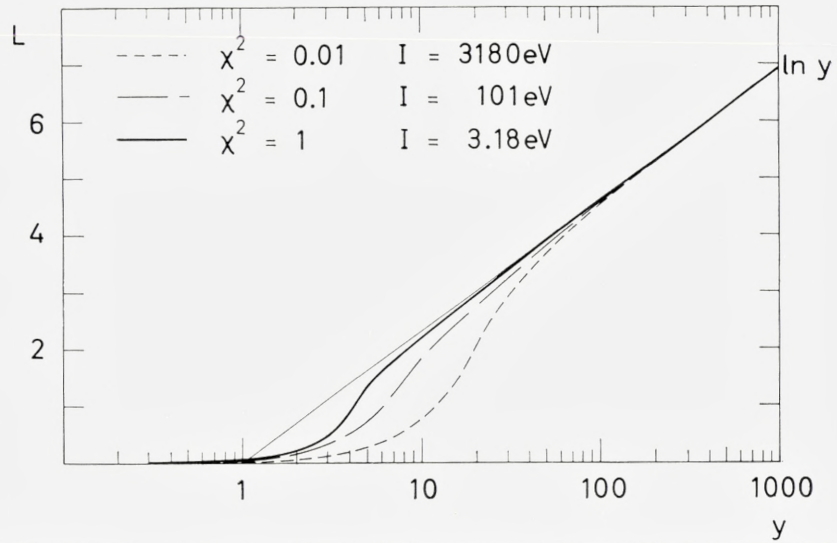

Fig. 4. The factor L as a function of the velocity parameter y from (11), for three gas densities, $\chi^2 = 1$, 0.1 and 0.01, i. e., $I = \hbar\omega_0 = 3.18$, 101 and 3180 eV, respectively. Straight line indicates asymptotic behaviour, $L = \log y$.

The numerical results for $L(y)$ contained in Table 2 are illustrated on the Figs. 4 and 5. In Fig. 4 the results are shown for $\chi^2 = 1$, 0.1 and 0.01, the abscissa y being given in a logarithmic scale. These three values of χ^2 correspond to gas densities $n = 0.84 \cdot 10^{22}$, $0.84 \cdot 10^{25}$ and $0.84 \cdot 10^{28}$ cm^{-3}, or to average excitation potentials $I = \hbar\omega_0 = 3.18$, 101 and 3180 eV, respectively. It is seen that the curves approach the straight line $\log y$, which is the asymptotic limit for large values of y.

A more detailed comparison with asymptotic formulas is shown in Fig. 5, where the full-drawn curves show $L(y)$ as a function of y for $\chi^2 = 0.1$ and 0.01. The dashed curves which join the $L(y)$ curves for small values of y represent formula (12), with the coefficient C_1 taken from Table 1. For large values of y the $L(y)$ curves approach another set of dashed curves. These curves represent the two first terms in the expansion (20), i.e. correction terms of order v^{-2} to the limiting expression, $\log y$, also indicated on the figure. It is noted that the v^{-2} term gives a substantial improvement over the simple expression (4) for low gas densities, and that the two for-

TABLE 2

The factor L in the specific energy loss computed numerically as a function of the particle velocity for six values of the density parameter in (7), $\chi^2 = 1$, $10^{-1/2}$, 10^{-1}, $10^{-4/3}$, $10^{-5/3}$ and 10^{-2}. L is given as a function of the parameter y, defined in (11).

y	log y	$\chi^2 = 0.01$		$\chi^2 = 0.02154$		$\chi^2 = 0.046416$	
		v/v_F	$L\,(y)$	v/v_F	$L\,(y)$	v/v_F	$L\,(y)$
0.10000	–	0.07598	0.0007995	0.09206	0.001145	0.1115	0.001540
0.31623	–	0.13512	0.004491	0.1637	0.006398	0.1983	0.008642
1.0000	0	0.2403	0.02522	0.2909	0.03575	0.3527	0.04839
1.7783	0.5757	0.3204	0.05963	0.3882	0.08459	0.4703	0.1141
3.1623	1.1513	0.4273	0.1407	0.5177	0.1990	0.6272	0.2675
5.6235	1.7269	0.5698	0.3306	0.6903	0.4647	0.8363	0.6220
10.000	2.3026	0.7598	0.7772	0.9206	1.067	1.115	1.420
14.678	2.6864	0.9205	1.341	1.115	1.833	1.351	2.247
21.544	3.0701	1.115	2.280	1.351	2.641	1.637	2.804
31.623	3.4539	1.351	3.029	1.637	3.191	1.983	3.285
56.235	4.0295	1.802	3.820	2.183	3.893	2.645	3.939
100.00	4.6052	2.403	4.496	2.909	4.530	3.527	4.555
316.23	5.7565	4.273	5.724	5.177	5.734	6.272	5.741
1000.0	6.9078	7.598	6.898	9.206	6.901	11.15	6.903

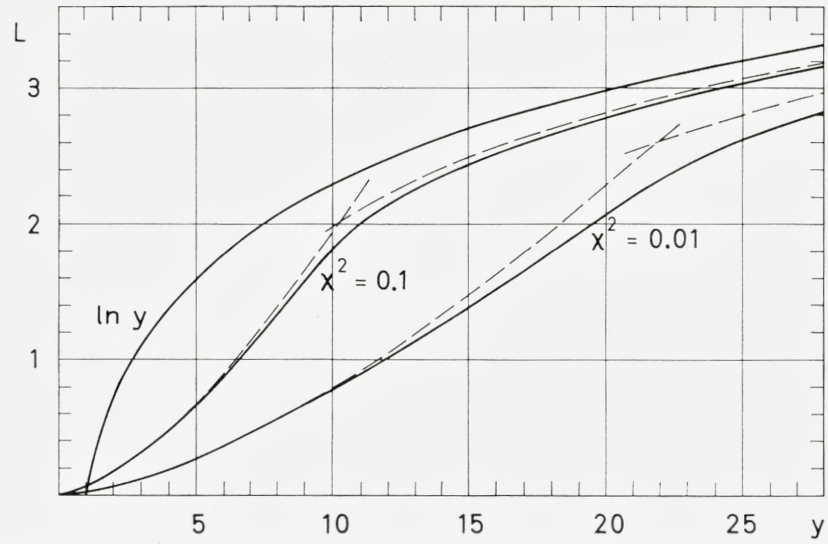

Fig. 5. The factor L as a function of the velocity parameter y from (11), for $y < 25$ and for two gas densities, $\chi^2 = 0.1$ and 0.01. Dashed curves indicate asymptotic formulas (12) and $L = \log y - 3^{3/2}\,(5\,\chi\,y)^{-1}$, valid for small and large y, respectively. The function $\log y$ is also indicated.

TABLE 2 (cont'd)

For large y, L approaches the asymptotic formula $L = \log y$, shown in the second column. For each value of χ^2 the velocity is also given in units of the Fermi velocity v_F.

y	$\log y$	$\chi^2 = 0.1$		$\chi^2 = 0.31623$		$\chi^2 = 1$	
		v/v_F	$L(y)$	v/v_F	$L(y)$	v/v_F	$L(y)$
0.10000	–	0.1351	0.001941	0.1802	0.002282	0.2403	0.001971
0.31623	–	0.2403	0.01091	0.3204	0.01299	0.4273	0.01182
1.0000	0	0.4273	0.06119	0.5698	0.07451	0.7598	0.0743
1.7783	0.5757	0.5698	0.1443	0.7598	0.1791	1.013	0.191
3.1623	1.1513	0.7598	0.3386	1.013	0.4323	1.351	0.502
5.6235	1.7269	1.013	0.7879	1.351	1.078	1.802	1.448
10.000	2.3026	1.351	1.838	1.802	2.074	2.403	2.177
14.678	2.6864	1.637	2.414	2.183	2.542	2.911	2.604
21.544	3.0701	1.983	2.898	2.645	2.976	3.527	3.016
31.623	3.4539	2.403	3.342	3.204	3.392	4.273	3.418
56.235	4.0295	3.204	3.968	4.273	3.996	5.698	4.009
100.00	4.6052	4.273	4.572	5.698	4.586	7.598	4.595
316.23	5.7565	7.598	5.746	10.13	5.751	13.51	5.753
1000.0	6.9078	13.51	6.904	18.02	6.906	24.03	6.907

mulas (12) and (20) taken together essentially reproduce $L(y)$ for $\chi^2 \gtrsim 0.1$. For large densities, higher order terms in (20) are important. They can be of the same order of magnitude as the v^{-2} terms, and they have the same sign.

§ 4. Summation Rules

In this section are treated various properties of integrals over generalized oscillator strengths. These integral properties we call summation rules. In the preceding sections two such rules were used repeatedly, viz. the familiar Bethe sum rule and the equipartition rule. The Bethe sum rule has been previously discussed by several authors.[3] Still, we shall give a derivation of it in the present case, in order to check the properties of the dielectric constant given by (5), and also as an introductory to the equipartition rule, where we utilize the analytic properties of the dielectric constant as a function of momentum, k, and phase velocity, ω/k.

The Bethe sum rule.

In the dielectric formulation, the field equations and the absorption are contained in the dielectric constant. The Bethe sum rule concerns an inte-

gration over ω of $1/\varepsilon^l$, for fixed k. In the integration we have to do with retarded solutions of the equations of motion. This is equivalent to the requirement that an external disturbance of the system, represented by e.g. $\varrho_0(\vec{r},t) = f(\vec{r})\delta(t-t_0)$, never gives rise to a field different from zero prior to the disturbance, i.e. for $t < t_0$. When integrating $1/\varepsilon^l$ over the frequency ω in order to find physical effects, this requirement fixes the path of integration in the complex ω-plane to be above all poles of $1/\varepsilon^l$.

Returning to the Bethe sum rule (16), and using the just mentioned path of integration, we are entitled to change the contour to a large semi-circle, $|\omega| = \text{const.}$, in the upper half of the complex ω-plane, since there are no poles above the original path of integration. However, in the region of large ω and for fixed k, ε^l must always behave as

$$\varepsilon^l(k,\omega) \to 1 - \frac{{\omega_0}^2}{\omega^2}, \quad \text{for } |\omega| \to \infty. \tag{21}$$

We apply (21) to the integration over the semi-circle and obtain (16).

The sum rule is thus directly a consequence of the demand of retardation. In the present description of an electron gas in the ground state, the requirement of retardation is expressed in (5) by the replacement of ω by $\omega + i\delta$, leading to a retarded dielectric constant $\varepsilon^l(k,\omega)$, which is a complex function of k and ω. In this description the path of integration is on the real ω-axis. The path is in fact above all poles of $1/\varepsilon^l$, as can be shown explicitly from (5). In order to prove it, we may note that ε^l in (5) is a real and even function of ω', where $\omega' = \omega + i\delta$. This function has $2N$ zeros, which all lie on the real ω'-axis. For $k > 2k_F$ (or $z > 1$) this is easily seen from the fact that ε^l has $2N$ poles on the real ω'-axis. In between these poles are trapped $2N-2$ zeros of ε^l, and outside the poles are two more zeros, since ε^l has to increase from a negative value to $+1$. The two latter zeros ultimately become the plasma resonance, at low values of k. In order to show that all $2N$ zeros lie on the real ω'-axis also for $k < 2k_F$, one must further take into account that the gas is in its ground state, $f(E_n)$ being the distribution function of a degenerate Fermi gas.

The equipartition rule.

While the Bethe sum rule concerns the integral of $1/\varepsilon^l$ over ω or u for fixed k or z, the equipartition rule has to do with the integral of $1/\varepsilon^l$ over z for fixed u. The rule states that an integral – proportional to that in (8) –

$$\mathfrak{J} = \operatorname{Im} \int_0^\infty 2z\,dz \left(\frac{1}{\varepsilon^l(u,z)} - 1 \right) = \mathfrak{J}_r + \mathfrak{J}_c \tag{22}$$

receives equal contributions, $\mathfrak{J}_r$ and $\mathfrak{J}_c$, respectively, from the plasma resonance and from the region of close collisions, $u-1<z<u+1$ (cf. Fig. 3). In order to prove this, it is important to find the poles of $1/\varepsilon^l$, i.e. the zeros of ε^l, as a function of z for fixed u. It is seen from (5) that whereas ε^l has N zeros as a function of ω'^2 (or $u'^2=\omega'^2/k^2v_F^2$) for fixed z, there must be $N+1$ zeros of ε^l as a function of $x=z^2$ for fixed u'. For a large real value of u', above the value which corresponds to the minimum in the plasma resonance in Fig. 3, all $N+1$ zeros lie on the real x-axis. One zero occurs at a low x-value, and is determined by the intersection with the plasma resonance curve. The remaining N zeros are grouped together in the interval $(u'-1)^2 \lessapprox x<(u'+1)^2$, and may be identified with the N zeros of ε^l as a function of u'^2 for fixed z and $u'>1-z$.

We note that in the retarded dielectric constant used in (22), u' has a small positive imaginary part. Suppose now that ω is positive. It is seen directly from (5) that a small positive imaginary part $i\delta$ added to ω, or to u, is equivalent to a displacement of the zeros of $\varepsilon^l(u,x^{1/2})$ in the complex x-plane in such a way that the zero at plasma resonance lies below the real x-axis, while the zeros in the region $(u-1)^2<x<(u+1)^2$ lie above this axis. The opposite sense of displacement in these two cases appears because the slope du/dz is negative at the plasma curve, but positive at the other zero curves in the u,z-plane, cf. Fig. 3. The integral (22) may thus alternatively be written

$$\mathfrak{J}=-\frac{i}{2}\int_C dx\left(\frac{1}{\varepsilon^l(u',x^{1/2})}-1\right). \tag{23}$$

Here, ε^l is a real function of u' and x, and the path of integration C is indicated on Fig. 6.

In order to complete the proof of the equipartition rule, we merely note that, if we revert the sign of the plasma resonance contribution, $\mathfrak{J}_r$, in (22), we obtain the path of integration C' (cf. Fig. 6), which may be deformed into a large circle, $|x|=$ const., in the complex x-plane. However, for large values of $|x|$ (or $|k|$), the dielectric constant must behave as

$$\varepsilon^l\to 1+\frac{\chi^2}{3x^2},\quad \text{for } |x|\to\infty, \tag{24}$$

according to (5). Since the integral of $1/(1+\chi^2/3x^2)-1$ along a large circle tends to zero, we observe that a change of sign of $\mathfrak{J}_r$ in (23) makes the integral vanish, i.e. $\mathfrak{J}_r=\mathfrak{J}_c$. This is the equipartition rule. It is based on the circumstances that the integral around the plasma resonance in the x-plane is in the opposite sense of the integration around the remaining

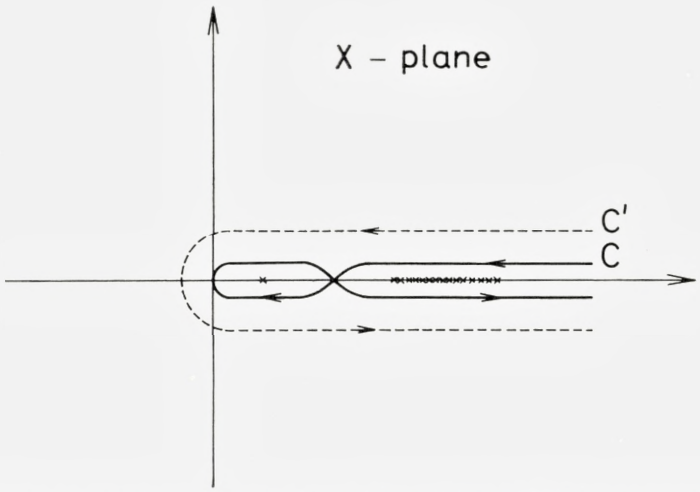

Fig. 6. Illustration of contours C and C', in complex x-plane. Isolated cross on real x-axis indicates plasma pole; group of crosses indicates poles in close collisions. For further explanation cf. text.

resonances, and that the integral of $(1/\varepsilon^l - 1)$ vanishes at large x. Moreover, it can only be used for u-values ($u \gtrsim u_0$, cf. Fig. 3) where plasma resonance occurs. For lower values of u, the plasma resonance splits up in two poles in the complex x-plane.

The contents of the equipartition rule may be stated in a more pictorial way. Thus, a constant value of u implies a constant phase velocity, $v_{ph} = \omega/k = u \cdot v_F$, of the emitted waves. When the creation of waves is due to a heavy particle travelling with constant velocity v, all waves emitted with the phase velocity v_{ph} will have an angle ϑ with the particle motion where $\cos \vartheta = v_{ph}/v$. In this direction two kinds of waves travel, i.e. plasma resonance waves and essentially single electron waves, and according to the equipartition rule the two waves moving in the direction ϑ carry an equal amount of energy. It may be interesting to compare the group velocities of the two wave types. The electron waves have approximately the connection $\omega = \hbar k^2/2m$ between k and ω, if v_{ph} is large compared to v_F. Accordingly, they have a group velocity $v_{gr}^{el} \simeq 2 v_{ph}$, i.e. larger than the phase velocity. The plasma waves, on the other hand, have a rather well-defined group velocity, v_{gr}^{pl}, which according to the dispersion relation (10) is given by

$$v_{gr}^{pl} \simeq \frac{3}{5} v_F^2 / v_{ph} = \langle v_i^2 \rangle / v_{ph} ,$$

and thus much less than v_{ph}, since $v_{ph} > v_F$.

We shall not treat the equipartition rule for an atomic system in general. However, it may be noted that the asymptotic relation (24) always holds in the non-relativistic case, which implies that the sum of residues in the complex k^2-plane is zero. Therefore, if residues are vanishing except on the real, positive k^2-axis, the contributions to energy loss at constant phase velocity, ω/k, may be divided in two parts with equal contribution to energy loss, so that an equipartition rule holds. The two parts are analogous to, respectively, the plasma resonance and the close collisions in Fig. 6; they have the same sequence on the k^2-axis, and the path of integration should be as in Fig. 6.

Acknowledgments

MORTEN SCHARFF took an active part in the present investigation at its early stages, and we discussed with him most of its aspects.

We are much indebted to Dr. PETER NAUR, who performed the numerical computations on the electronic computer DASK. In this connection Dr. NAUR also made many valuable suggestions.

The assistance by Miss S. TOLDI and Mrs. A. GRANDJEAN in the preparation of the manuscript is gratefully acknowledged.

Institute of Physics,
University of Aarhus.

Institute for Theoretical Physics,
University of Copenhagen.

References

(1) J. LINDHARD and M. SCHARFF, Mat. Fys. Medd. Dan. Vid. Selsk. **27**, no. 15 (1953).
(2) J. LINDHARD, Mat. Fys. Medd. Dan. Vid. Selsk. **28**, no. 8 (1954).
(3) H. A. BETHE, Ann. d. Phys. **5**, 325 (1930); P. NOZIÈRES and D. PINES, Il Nuovo Cimento **9**, 470 (1958).
(4) M. C. WALSKE, Phys. Rev. **88**, 1283 (1952); ibid. **101**, 940 (1956).
(5) U. FANO, Ann. Rev. Nucl. Science, **13**,1 (1963); U. FANO and J. E. TURNER, NAS-NRC Publication 1133 (1964).

Indleveret til Selskabet den 10. december 1963.
Færdig fra trykkeriet den 22. maj 1964.

Matematisk-fysiske Meddelelser
udgivet af
Det Kongelige Danske Videnskabernes Selskab
Bind **34,** nr. 5

Mat. Fys. Medd. Dan. Vid. Selsk. **34,** no. 5 (1964)

STOPPING OF 50 keV IONS IN GASES

BY

N. O. LASSEN, N. O. ROY POULSEN, G. SIDENIUS
AND LISE VISTISEN

København 1964
Kommissionær: Ejnar Munksgaard

Synopsis

Ions of radioactive isotopes were from an isotope separator passed through a small hole into a chamber filled with a stopping gas at low pressure. The thermalized ions were collected by a transverse electric field; from studies of the activity distribution on the collector plates information was obtained about the charge state of the particles, and about the most probable and the mean range, the straggling, and the scattering. The results are compared to the theory by Lindhard, Scharff and Schiøtt.

Printed in Denmark
Bianco Lunos Bogtrykkeri A/S

1. Introduction

Measurements of the ranges of gallium ions of energies about one MeV were reported in a previous paper[1]. The results are in general agreement with a range formula given by LINDHARD and SCHARFF[2]. It was an interesting observation that the range R_D in deuterium is longer than the range R_H in hydrogen, a difference which must be ascribed to the influence of nuclear encounters. However, the relative difference $(R_D - R_H)/R_H$ seemed to decrease with decreasing ion energy; at first sight this is strange, since the nuclear stopping plays a larger role at smaller energies, but it is in accord with the result of HARVEY et. al.[3], who found a shorter range in deuterium than in hydrogen for Th-ions of a somewhat smaller velocity. In our previous investigations the lower limit for the accessible energy interval was about 0.5 MeV. It was desirable to study the ranges of Ga-ions at much smaller energy; the ratio R_D/R_H depends not only on the relative influence of nuclear and electronic stopping, but also on the more detailed behaviour of the former. When two ions meet in a close collision, the potential describing the force between them is not the simple r^{-1}-potential, because the nuclei are screened by the accompanying electrons. For low energy, where the energy loss due to electronic encounters may be neglected, the range in deuterium, according to LINDHARD and SCHARFF[4], will be longer or shorter than the range in hydrogen, depending on whether the screened potential varies slower or faster than r^{-2}. Recently, a more detailed theory for low-energy-ion stopping phenomena has been worked out[5], and it became even more interesting to extend the measurements not only to small energies but also to other ions and other gases.

2. Experimental techniques

The principle of the method was the same as in our previous experiment[1]. The ions were stopped in a gas; the gas volume was located between two parallel plates and the stopped ions were collected on one of the plates by a transverse electric field. Radioactive ions were used, and the activity

distribution on the plate gave directly the range distribution. In fact, in favourable experiments, a two-dimensional activity distribution, giving information also on the scattering, was obtained.

The measuring chamber is shown in fig. 1. 50 keV ions were produced by means of the Copenhagen isotope separator. Some of the ions entered the chamber through a narrow slit between two steel plates pressed against a teflon disk; a hole in the teflon determined the length of the slit (1 mm),

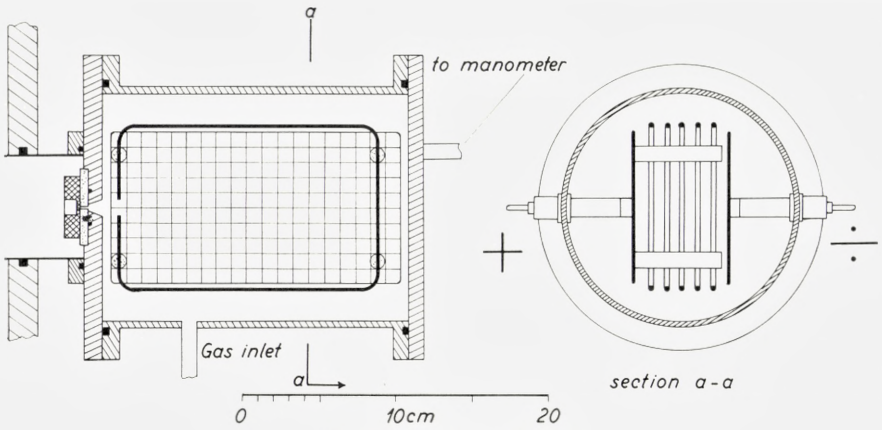

Fig. 1. Stopping chamber.

whereas the width was determined by the distance between the steel plates, which was 0.01–0.05 mm, different for different gases and ions. At the place of the slit the steel plates were 2 mm thick; in order to enable the ion beam to penetrate through the slit, the latter had to be oriented in the proper direction; this could be done by tilting the whole chamber. The chamber was filled with a pure gas to a suitable pressure, 0.5–6 mm Hg, which was measured by means of a calibrated manometer filled with Apiezon B oil. The gas continuously leaked out into the separator vacuum through the slit; new gas was admitted from a storage tank through a needle valve, and the pressure in the measuring chamber was kept constant within $\pm 2\,\%$, or better in favourable cases.

The electric field was applied between two brass plates, $10 \times 19\ \mathrm{cm}^2$, held parallel to each other at a distance of 4–9 cm, varying for different experiments. Each of the plates was supported by two teflon insulators, and one was held at a positive, the other at a negative potential with respect to the chamber wall. The voltages were ± 220 V or less, and it is easily seen

that the path of the ions is hardly influenced by the electric field as long as they are not stopped down to thermal velocities. Rings of 1.5 mm copper wire, spaced one centimeter and held at the appropriate potentials, were used to improve the homogeneity of the field. In contrast to our earlier measurements[1]), the present investigations were probably not disturbed by space charges in the gas volume. In this connection, it may be noted that the role of the isotope separator is not only that it produces and accelerates the ions, but the actual mass separation is also highly important. When measuring the range of Na^{24} ions, for example, the strong beam of the carrier Na^{23} does not enter the measuring chamber; if it did, one might fear that space charges would distort the field and that, therefore, the activity distribution on the plate would not correspond to the actual distribution of the end-points of the ion paths.

The ions coming from the separator are positively charged. Experience shows that, in some gases and for some ion types, most of them also have a positive charge when they are stopped down to thermal velocities. This is the basis for the method. It may be important that the electrons produced by ionization are quickly removed from the gas volume; for this reason, attempts were made to use pure gases in which no electron attachment would take place. For all gases except helium the storage tank was provided with a purifier with hot calcium, through which the gas was continuously circulated; when helium was used, it was passed through charcoal in liquid air.

Of course, the purity of the gas is also important because the range varies from gas to gas. It is especially important for the light gases, because here the ranges are much longer than in the heavier gases (as measured in cm NTP). Assuming the components of a gas mixture to act independent of each other in the stopping process, and assuming a velocity independent stopping power, one finds that an impurity of n percent of nitrogen in hydrogen will cause an error (decrease) in the range of about $6\,n$ percent. The purifier removes electronegative gases such as oxygen and water vapor, but not nitrogen; therefore, the tightness of the apparatus was thoroughly investigated before each run. In a few cases a leak developed in the gas inlet tubing, and a much too small value for the hydrogen range was obtained; at the same time, the form of the activity distribution showed that something was wrong. The measurements in hydrogen were repeated, often with long time intervals, and it is believed to be extremely improbable that impurities should have caused significant errors. For Na^{24} and Ga^{66} more than $99\,\%$ of the ions are collected on the negative plate, when hydrogen

or deuterium is the filling gas. The ranges in these two gases were measured in experiments made immediately after each other; in between, the apparatus was not touched except for the inversion of the field and the necessary operation of some stopcocks and the needle valve to change from hydrogen to deuterium, so that one plate gave the hydrogen distribution, the other the deuterium distribution.

The collector plates were covered with 3 mg/cm^2 aluminium foils, which were cut into pieces 1×1 cm^2; each piece could be placed in its own little specimen tube, and the γ-activity was measured by means of a 3×3 inch NaJ-crystal in a well screened set-up with a low background. In some experiments smaller units 0.5×0.5 cm^2 were used; instead of the foil method another technique was employed, the activity being collected on the end faces of many small aluminium blocks, $0.5 \times 0.5 \times 1.0$ cm^3, screwed together in such a way as to give a smooth collector surface.

Measurements were made on Na^{24}, Ga^{66} and Au^{198} ions. Activities of the order of 100 mC were needed; in these experiments the ion separator beam normally had a cross section of about 0.2 cm^2, the transmission through the entrance slit of the measuring chamber thus being about 10^{-3}; the separator efficiency was about 0.01–0.05. Ga^{66} was produced by bombarding copper with 20 MeV α-particles from the Copenhagen cyclotron. The activity was scraped off the copper target, carriers were added, and copper and zink were chemically removed. Galliumoxid was produced, and in the ion source of the separator it was transformed into galliumchlorid by addition of CCl_4 [6]. Gold and the chloride of sodium were bombarded with neutrons in the Danish reactor DR2 at Risø and subsequently, without further treatment, placed into the ion source oven.

3. Results. Discussion of particle charge and collection

3.1. Ga^{66} ions

Figs. 2 and 3 show the activity distributions on the negative plate when the stopping gas was hydrogen and nitrogen, respectively. In the light gases the range is sharply defined, and the scattering is small; in the heavier gases the straggling and scattering give considerably broader distributions, both lengthwise and sidewise.

In fig. 4 the range distributions in hydrogen and deuterium are shown. A whole row of the aluminium blocks were counted simultaneously; i. e. the ordinates give the activities on 0.5 cm wide strips of the plate perpendicular to the original beam direction (when this is taken as X-axis: $\Delta x = 0.5$

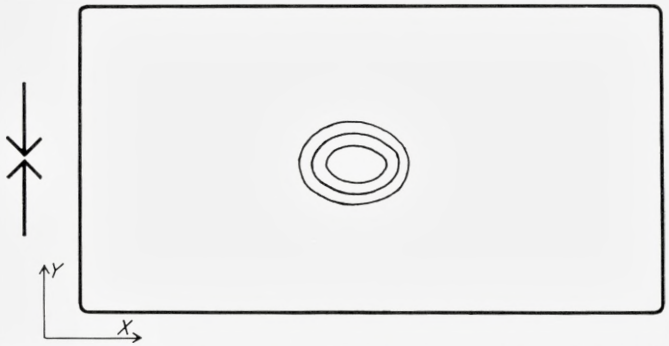

Fig. 2. Distribution of Ga^{66} activity on the negative collector plate, when hydrogen at a pressure of 3.1 mm Hg is used as stopping gas. The lines are drawn through points corresponding to 75 %, 50 % and 25 % of the maximum density of activity.

cm, $\Delta y = 4$ cm). Except for a very small tail on the left side of the hydrogen peak, the distributions are Gaussian.

Fig. 5 gives the range distribution in nitrogen. 96 % of the activity were found on the negative plate, and the activity distribution on this plate may safely be taken as a good picture of the range distribution. It is not Gaussian; since it is unsymmetric, we may distinguish between the most probable range R_p and the mean range R_m.

The activity distribution on the positive plate is not so well determined, because the activity was too small. It seems to be more symmetric; the mean range S_m for these ions is almost equal to R_m, maybe slightly longer. Probably a small part of the particles are neutralized near the end of their paths, and after being stopped down to thermal velocities by nuclear collisions they diffuse around, some of them ultimately reaching the positive, some the negative plate. Since in this diffusion process they move more or less

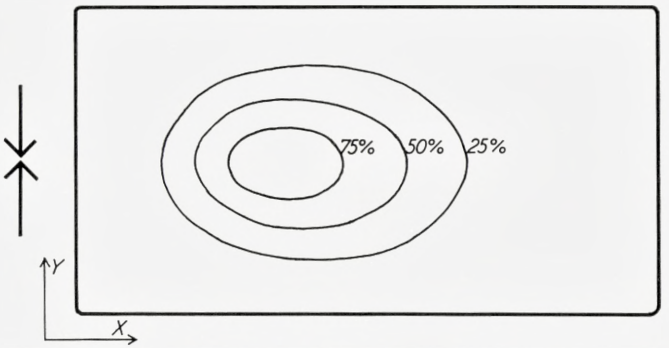

Fig. 3. The same as fig. 2 with nitrogen at a pressure of 0.56 mm Hg.

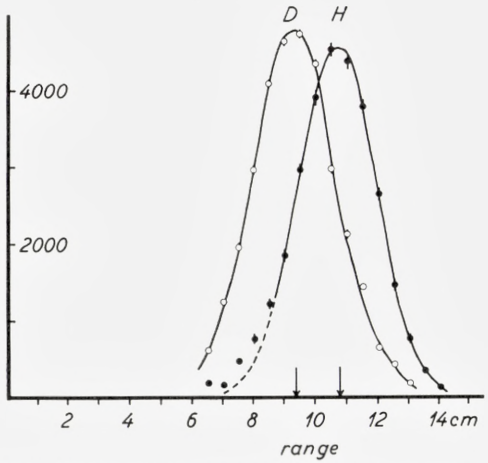

Fig. 4. Range distribution of Ga^{66} ions in hydrogen and deuterium for a pressure of 3.1 mm Hg. The curves are Gaussian, fitted to the points.

isotropically in all directions, the distribution on the positive plate should be smeared out as compared to the actual range distribution, but the mean range should not be much affected. If the neutralization takes place at some distance from the end of their paths, they might have a longer range than the not neutralized ions. However, it should be considered that the travelling particles probably undergo many charge exchange processes and, consequently, it does not seem reasonable to talk about two types of ions— neutrale and positive—as long as they move with velocities at which reversible charge exchanges may occur. Apparently most of the particles are or become positive at the very end of the track, but a few fail to do so.

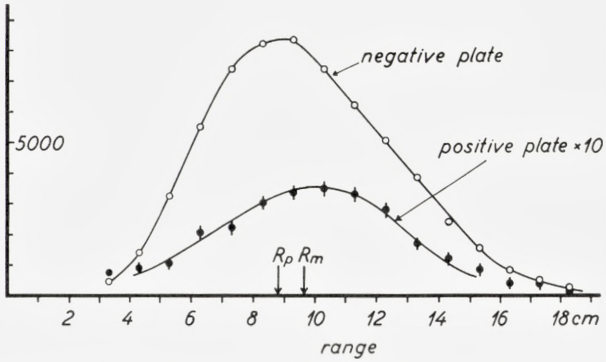

Fig. 5. Range distribution of Ga^{66} ions in nitrogen. Pressure 0.56 mm Hg.

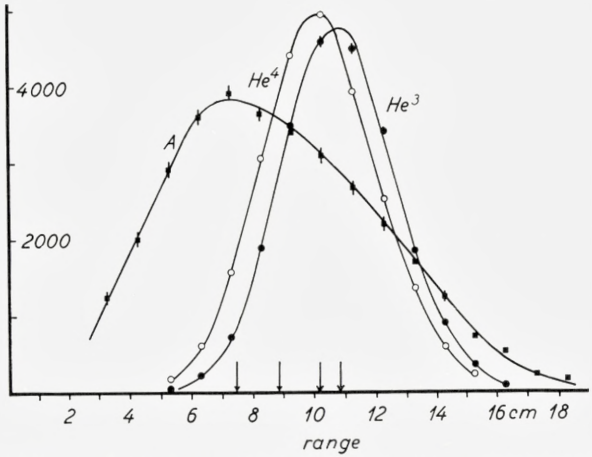

Fig. 6. Range distributions of Ga^{66} ions in He^3, He^4 and A. The curves for He^3 and He^4 refer to the same pressure, 2.95 mm Hg, whereas the argon pressure was 0.60 mm Hg. The two helium curves are Gaussian. For A the figures on the activity axis should be reduced by a factor of two. Arrows indicate: R_p for A, R_m for A, R_p for He^4 and R_p for He^3.

If this explanation is true, the same amount of neutral particles must reach the negative plate. A correction to the range distribution curve would therefore be appropriate; because of the smallness it has been neglected. The distribution on the positive plate should be expected to be broader than that on the negative plate, but this is hardly confirmed by the experiments. The half-widths of the lengthwise distributions are nearly equal, and the same is valid for the transversal distributions (see table 1) when the latter are determined by measuring the activity across a 6 cm wide strip ($\Delta x = 6$, $\Delta y = 1$).

Fig. 6 shows the range distributions in He^3, He^4 and A. In the helium gases the distributions are Gaussian; all activity was found on the negative plate. In argon the distribution is more unsymmetric than in nitrogen; about 10 % of the activity was collected on the positive plate, but the distribution was not measured.

3.2. Au^{198} ions

In hydrogen about 25 % of the Au^{198} activity was found on the positive plate. In this case a difference between the distributions on the two plates was found (see fig. 7), which clearly points at the above proposed explanation for the activity on the positive plate: Some particles are neutral when stopped, and they produce by diffusion a broad range distribution on both

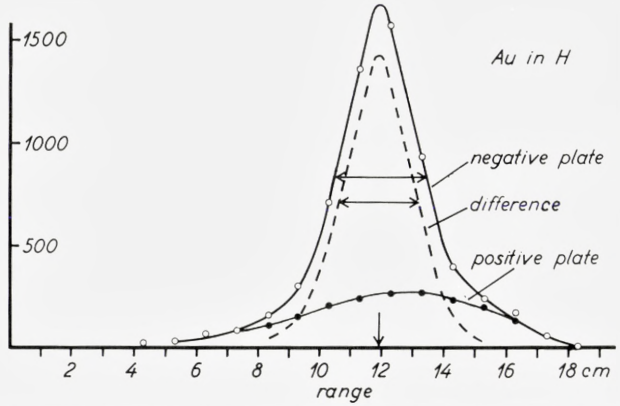

Fig. 7. Distribution of Au^{198} activity on the negative and positive collector plates with hydrogen at 2.9 mm Hg. The difference is assumed to give the range distribution, see text.

plates. This distribution is directly observed on the positive plate; on the negative plate it appears as the "wings" on the much sharper distribution produced by the positive ions. The same difference was found in the transversal distributions, and very similar results were obtained in deuterium (see fig. 8). Consequently, the difference between the activity distributions on the negative and positive plate may be assumed to give the best picture of the true distribution of the particle end-points.

In neon the range distribution is broader and slightly unsymmetric; about 20 % of the activity was found on the positive plate, but it was too small to permit a measurement of the distribution.

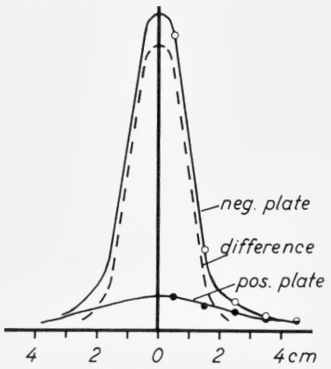

Fig. 8. Distribution of Au^{198} activity across the negative and positive collector plates with deuterium at 2.4 mm Hg. The distributions were assumed to be symmetric. For symmetrically placed aluminium foils only the activity sum was measured.

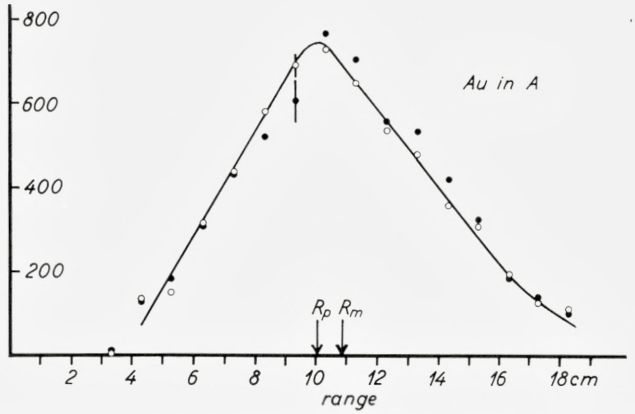

Fig. 9. Distribution of Au^{198} activity along the negative and positive collector plates with argon at 0.38 mm Hg. Open circles correspond to the negative plate; full circles to the activity on the positive plate multiplied by 1.6.

Fig. 9 shows the distributions in range obtained in argon. The activity was divided between the two plates in the ratio 62:38; the range distributions as well as the transversal distributions were almost equally shaped on the two plates. This may indicate that the particles at the end-points of their paths appear in positive, negative and neutral states.

3.3. Na^{24} ions

In hydrogen and deuterium all activity was found on the negative plate; the range distributions were Gaussian. In neon a slight asymmetry was observed, and about 20 % of the particles went to the positive plate.

The range distributions on the two plates obtained in argon are shown in fig. 10. In this case the distribution on the positive plate is the narrower, and we cannot explain things as simple as for Au^{198} ions in the light gases. It has to be taken into account that the experimental conditions are not the very best in this case, since, due to the large straggling and scattering, the activity is distributed over the entire area of the collector plates (see figs. 10 and 11). A small part of the particles may reach the collector plates before being thermalized; the narrower distribution on the positive plate may in part be caused by such particles. In fact, if we consider particles with end-points at a certain distance T from the median plane, their range distribution is the narrower, the larger T is. In fig. 10 the open squares give the range distribution as measured for the middle four centimeters ($\Delta x = 1$, $\Delta y = 4$); by including also the outermost three centimeters on both sides

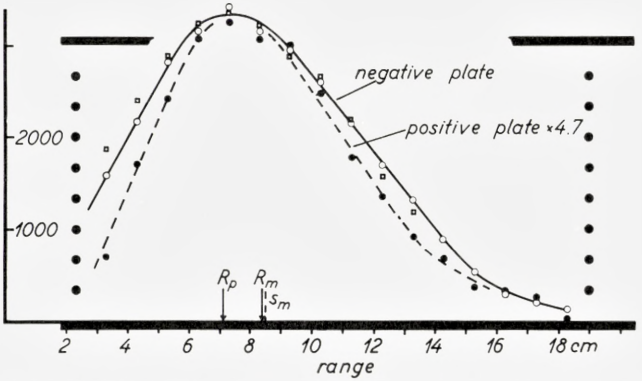

Fig. 10. Distribution of Na^{24} activity along the collector plates with argon at 1.7 mm Hg. Full circles correspond to the positive plate (the activity being multiplied by 4.7); open circles and squares to the negative plate. Squares are measured with $\Delta y = 4$ cm, circles with $\Delta y = 10$ cm. The figure also shows the geometry of the collector plates and the grid wires.

one obtains the narrower distribution given by the open circles ($\Delta x = 1$, $\Delta y = 10$). However, if the activity on the positive plate were caused only by particles striking it before being thermalized, the negative plate would receive the same number of particles in flight. That would correspond to 32 % of the particles striking the plates and, judging from figs. 10 and 11, this number seems completely unreasonable. Probably some particles are neutral at the end of their paths; now those particles lying close to one of the plates (with large T values) will have a higher chance of reaching this plate by diffusion than particles lying farther away (f. ex. with $T = 0$). This is another effect tending to give a narrower distribution on the positive than on the negative plate.

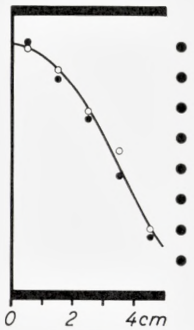

Fig. 11. Transversal distribution of Na^{24} activity with argon in the chamber. Measured with $\Delta x = 4$ cm and with x-values corresponding to the position of the peak in the lengthwise distribution in fig. 10. Again the geometry is shown. The experimental points represent the activity sum of symmetrically placed aluminium foils like in fig. 8.

3.4. Summary of results

The experimental results are summarized in table 1. Here R_p is the most probable range as determined from the activity distribution on the negative plate. R_m is the mean range from the same distribution, ΔR and ΔT are the half-widths of the lengthwise and crosswise distributions on the same plate. ΔR refers to measurements in which $\Delta x = 1$ cm, $\Delta y = 8$ cm (except for Ga ions in hydrogen and deuterium, where $\Delta x = \frac{1}{2}$ cm, $\Delta y = \frac{8}{2}$ cm). ΔT refers to measurements with $\Delta y = 1$ cm, $\Delta x \sim 6$ cm, taken for x-values around the peak in the R-distribution. "Int." is the activity found on the positive plate, in percent of the total activity found on both plates; if it is ascribed to neutral particles, the same number will have diffused to the negative plate and some will have escaped through the grid to the chamber walls. S_m, ΔR^+ and ΔT^+ have similar meanings as R_m, ΔR and ΔT, but they refer to the activity distribution on the positive plate.

TABLE 1. Experimental results

		Negative Collector Plate				Positive Collector Plate			
		R_p $\mu g/cm^2$	R_m/R_p %	$\Delta R/R_p$ %	$\Delta T/R_p$ %	Int. %	S_m/R_p %	$\Delta R^+/R_p$ %	$\Delta T^+/R_p$ %
Na^{24}	H_2	7.51	100	39	25	< 1	..	..	..
	D_2	17.9	100	47	28	< 1	..	..	..
	Ne	21.2	103	93	60	~ 20	..	..	..
	A	26.9	117	122	100	16[1]	118	100	95
Ga^{66}	H_2	3.64	100	27	17	< 3	..	..	..
	D_2	6.45	100	33	20	..	..	..	..
	He^3	5.25	100	40	26	..	..	..	..
	He^4	6.70	100	44	28	< 2	..	..	..
	N_2	7.5	110	82	55	4	112	88	56
	A	9.8	117	115	75	~ 10	..	..	..
Au^{198}	H_2	3.74	100	18[2, 3]	15[2, 3]	25	104	60	40
	D_2	6.25	100	18[2, 3]	15[2, 3]	20	104	75	45
	Ne	7.20	103	48	..	15–20	..	..	..
	A	8.20	109	75	55	38	110	75	55

[1] A small part of this activity may be due to particles reaching the positive collector plate before being thermalized.

[2] Figures obtained from the difference between the activity distributions on the negative and positive plate.

[3] Corrected for influence of finite width of aluminium pieces.

In some cases, indicated in the table, where the measured half-widths are small, the finite widths of the aluminium pieces justified a correction. For example, one finds that a Gaussian with a true half-width $\Delta R/R = 15\,\%$ will give a measured half-width of $18\,\%$ when $\Delta x/R = 0.1$, Δx being the length of the aluminium pieces.

4. Discussion

4.1. Shapes of the range distributions

The difference in shape of the range distributions in the light and heavy gases is a most conspicuous result. In hydrogen and helium the distributions are Gaussian, but in the heavier gases they exhibit an increasing skewness. For these rather low velocity ions the stopping is mainly caused by nuclear collisions and the difference in straggling is related to the magnitude of the energy loss in single encounters. The maximum energy transfer is

$$T_m = \frac{4\,M_1 M_2}{(M_1+M_2)^2} \cdot E = \gamma E, \tag{1}$$

where E is the energy, M_1 and M_2 are the mass numbers of the incoming and the struck nucleus, respectively. Although the average energy loss per collision is much smaller, we may expect some correlation between γ and the skewness. In table 2 the values of γ are shown; comparing these values with the values for R_m/R_p from table 1 we note the similarity between gold ions in argon and gallium ions in nitrogen, as well as between sodium and gallium ions in argon. Actually, the latter result, the same values for R_m/R_p for sodium and gallium ions in argon, is rather surprising,

TABLE 2. Maximum fractional energy transfer, γ

	Na^{24}	Ga^{66}	Au^{198}
H^1	0.154	0.059	0.020
D^2	0.28	0.114	0.040
He^3	..	0.17	..
He^4	..	0.22	..
N^{14}	..	0.58	..
Ne^{20}	0.99	..	0.33
A^{40}	0.94	0.94	0.56

since we may expect some difference between cases with $M_2 > M_1$ and those with $M_2 < M_1$ [7]. In fact, for sodium ions the skewness is small both in neon and in argon; this may indicate the influence of electronic stopping.

4.2. Range straggling.

For pure nuclear stopping LINDHARD and SCHARFF give the formula

$$\left(\frac{\sigma'}{R'_m}\right)^2 = \frac{1}{6}\,\gamma, \tag{2}$$

where σ' is the fluctuation in path length and R'_m is the mean length measured along the actual path. This expression results, when a potential proportional to r^{-2} is assumed between the colliding particles, but it should give a good approximation also for somewhat different exponents in the potential. LINDHARD, SCHARFF and SCHIØTT[5] (in the following cited as LSS) have assumed, as a better approximation, a potential of the form $r^{-1}\cdot\varphi_0(r/a)$, where φ_0 is the Fermi function, and the screening parameter is given by

$$a = \frac{\hbar^2}{me^2}\cdot 0.8853\,(Z_1^{2/3}+Z_2^{2/3})^{-1/2}, \tag{3}$$

m being the electronic mass, Z_1 and Z_2 the nuclear charge numbers of the incoming and the struck particle, respectively. They also take into account the influence of electronic stopping, assuming the contribution to the straggling from electronic collisions to be negligible. Their results are given in graphs (LSS fig. 6) showing $\frac{1}{\gamma}\left(\frac{\sigma'}{R'_m}\right)^2$ plotted against a dimensionless energy parameter ε defined by

$$\varepsilon = E\,a\,\frac{M_2}{Z_1 Z_2\,e^2(M_1+M_2)}. \tag{4}$$

Furthermore, they use a dimensionless range parameter

$$\varrho = R'N M_2\,4\pi\,a^2\,\frac{M_1}{(M_1+M_2)^2}, \tag{5}$$

where N is the number of stopping atoms per cm^3. In these units the electronic stopping is supposed to be given by

$$\frac{d\varepsilon}{d\varrho} = k\cdot\varepsilon^{1/2} \tag{6}$$

with

$$k = Z_1^{1/6} \frac{0.0793\, Z_1^{1/2} Z_2^{1/2} (M_1 + M_2)^{3/2}}{(Z_1^{2/3} + Z_2^{2/3})^{3/4} M_1^{3/2} M_2^{1/2}} . \tag{7}$$

The values of ε and k calculated according to (4) and (7) are given in table 3, which also gives the ratio R'/R between the path length and the (projected) range. This ratio is found from the graphs in LSS, figs. 8 and 9, and the values are slightly different from those which would be obtained from the approximate formula[4)]

$$R' = R\left(1 + \frac{1}{3}\frac{M_2}{M_1}\right). \tag{8}$$

By means of the ratio R'/R and the values given in table 1 we obtain the figures which in table 3 are denoted "experimental" for the quantity σ/R'_m, where $\sigma = \Delta R/2.34$. For comparison, the theoretical values for σ'/R'_m denoted "LSS_{n+e}" and obtained from LSS fig. 6, are given. In the last column, values corresponding to pure nuclear stopping and obtained from the same graphs, LSS fig. 6, are tabulated.

We do not know the exact relation between σ and σ'. This is unimportant for the light gases, where R and R' are nearly the same and where one may

TABLE 3.

		ε	k	R'/R	σ/R'_m "exp."	σ'/R'_m LSS_{n+e}	σ'/R'_m LSS_n
Na^{24} $V = 0.29\ V_0$	H	2.42	0.11	1.01	0.17	0.12	0.15
	D	4.66	0.08	1.03	0.19	0.15	0.20
	Ne	2.18	0.13	1.25	0.31	0.30	0.39
	A	1.49	0.18	1.51	0.29	0.29	0.38
Ga^{66} $V = 0.18\ V_0$	H	0.237	0.13	1.00	0.12	0.08	0.09
	D	0.467	0.10	1.01	0.14	0.12	0.13
	He^3	0.337	0.11	1.02	0.17	0.14	0.16
	He^4	0.443	0.10	1.02	0.18	0.16	0.18
	N	0.356	0.11	1.08	0.29	0.27	0.29
	A	0.269	0.13	1.25	0.33	0.34	0.36
Au^{198} $V = 0.10\ V_0$	H	0.0234	0.16	1.00	0.08	0.05	0.05
	D	0.0468	0.11	1.00	0.08	0.07	0.07
	Ne	0.0396	0.11	1.04	0.19	0.20	0.21
	A	0.0383	0.11	1.08	0.27	0.26	0.27

also put $\sigma = \sigma'$. LSS have calculated the ratio σ'/σ for $M_1 = M_2$ and for pure nuclear scattering corresponding to a potential r^{-s} with $\frac{3}{2} < s < 3$. This ratio is smaller than the ratio R'/R, and possibly the influence of electronic stopping will make it still smaller. We may, as a first approximation, assume $\sigma' \approx \sigma$ and therefore we should expect our "experimental" values for σ/R'_m and the theoretical values $\mathrm{LSS_{n+e}}$ for σ'/R'_m to be nearly the same. In fact, the agreement is very close for the heavy gases. It may be noted that the experimental values for Na^{24} ions in neon and argon are consistent with the theory, according to which the electronic stopping is appreciable even for such small velocities.

For the light gases the experimental values for the straggling are larger than the theoretical ones. Of course we cannot feel quite sure that the thermalized ions follow exactly the electric field lines, or that the experimental distributions are not broadened for some other unknown reasons. However, the theoretical estimates are only approximate, and since they are based on the Thomas-Fermi model of the atom, the approximation may be better for the heavy than for the light gases.

4.3. Transversal Distributions

The scattering is small in the light gases, and it increases with increasing Z_2 roughly proportional to the range straggling. The maximum fractional transverse momentum transfer is $M_2/(M_1+M_2)$, and we might look for a possible correlation between this quantity and the width of the transverse distribution. For this purpose values of $\sigma_T \sqrt{(M_1+M_2)/M_2}/R_m$ are given in table 4, σ_T being the measured half-width divided by 2.34.

TABLE 4. $\sigma_T \sqrt{(M_1+M_2)/M_2}/R_m$

	Na^{24}	Ga^{66}	Au^{198}
H	0.54	0.59	0.90
D	0.43	0.50	0.64
He^3	..	0.53	..
He^4	..	0.50	..
N	..	0.51	..
Ne	0.37	..	..
A	0.46	0.45	0.52

It may be seen from table 4, that the values are of the order of 0.5, except for gold ions in the light gases. In just these cases the values are somewhat uncertain, since there are considerable corrections from neutral particles. Other errors, such as angular width of the incoming beam from the separator and the scattering in the entrance slit, may possibly also play a role for these narrow distributions. However, it may be expected that σ_T also depends on the charge numbers Z_1 and Z_2.

4.4. Comparison of the range values with theory

From the experimental mean ranges R_m given in table 1 we find the mean path lengths R'_m by means of the values for R'/R in table 3. Next, from R'_m the corresponding values of ϱ_m are calculated according to formula (5). Furthermore, using the ε- and k-values from table 3 and the graphs LSS figs. 3, 4, 12 and 13, we obtain theoretical values for ϱ_m. The results are given in table 5.

TABLE 5. The reduced mean range ϱ_m

	Na^{24}			Ga^{66}			Au^{198}		
	"exp."	theor.	$\frac{\text{theor.}}{\text{exp.}}$	"exp."	theor.	$\frac{\text{theor.}}{\text{exp.}}$	"exp."	theor.	$\frac{\text{theor.}}{\text{exp.}}$
H	8.1	5.5	0.68	0.82	0.66	0.80	0.160	0.128	0.80
D	18.3	11.7	0.64	1.42	1.17	0.83	0.264	0.204	0.77
He^3	..	..	..	1.07	0.88	0.82	..	..	..
He^4	..	..	..	1.34	1.14	0.86	..	..	..
N	..	..	..	1.13	0.89	0.79	..	..	..
Ne	5.8	4.7	0.81	..	..	..	0.231	0.182	0.79
A	3.9	3.1	0.80	0.83	0.62	0.75	0.222	0.180	0.81

It will be seen that the variation of the ϱ-values with ε predicted by the theory is well reproduced by the experiments. The theoretical values are all lower than the experimental ones, on an average about 20 %. We estimate the uncertainty in the experimental values to be 3 %, not including the uncertainty in R'/R. One can imagine several systematic errors, all giving too *small* experimental ranges, but we hope to have avoided them.

4.5. Ranges in isotopic stopping media

As already mentioned in the Introduction, measurements in isotopic stopping media may be of special interest, since range differences in such materials must be due entirely to nuclear stopping. Table 6 gives the ratio

R_D/R_H of the range in deuterium and hydrogen for three kinds of incoming particles and the ratio R_{He^4}/R_{He^3} for Ga^{66} ions (range in cm). It may be seen that, for the rather slow 50 keV gallium ions, the range is shorter in deuterium than in hydrogen, opposite to what was found for somewhat faster gallium ions[1]. For the still slower 50 keV gold ions the deuterium range is still shorter as compared to the hydrogen range, whereas for the slightly faster 50 keV sodium ions the range in deuterium is the longer. This peculiar behaviour shows that the nuclear stopping is sometimes larger, sometimes smaller in deuterium than in hydrogen. That the theory is able to account for this phenomenon may be seen already from table 5, but in order to facilitate a comparison, we have in table 6 given also the theoretical values. The experimental and theoretical values agree within the limits of error.

TABLE 6. Range ratios for 50 keV ions

	R_D/R_H		R_{He^4}/R_{He^3}	
	exp.	theor.	exp.	theor.
Na^{24}	1.19	1.15	..	..
Ga^{66}	0.89	0.92	0.96	1.00
Au^{198}	0.84	0.80	..	..

According to LSS, the nuclear stopping cross section for $M_1 \gg M_2$ is proportional to $M_2^{1-2/s}$, when the effective potential in the collisions is proportional to r^{-s}. Fast ions are able to approach each other closely; then, the potential resembles the pure Coulomb potential r^{-1}, and for such ions deuterium has the smaller nuclear stopping cross section and hence the longer range. For slow ions the distance of closest approach is larger, and s is increased. For $s > 2$, deuterium will have the higher stopping power. According to LSS, the shift should take place for ε-values slightly smaller than 0.5; this is confirmed by the experimental results.

4.6. Other experimental range measurements

To our knowledge, there are no other measurements with the same projectiles, the same energy and the same stopping gases. There are many measurements with somewhat similar projectiles etc. (see for instance [8] [9] for summaries). However, a direct comparison is difficult; instead, one can compare the various experimental results with the theory of LSS, see ref. [5].

We wish to thank PH. DAM, techn. eng., for help in the production of Ga^{66} in the cyclotron and MOGENS JØRGENSEN, M. Sc. Chem. Eng., for the chemical treatment of the bombarded target. Furthermore, we gratefully acknowledge the assistance of Mr. H. CHRISTENSEN in cutting the foils, and counting.

References

1. LISE BRYDE, N. O. LASSEN and N. O. ROY POULSEN: Mat. Fys. Medd. Dan. Vid. Selsk. **33**, no. 8, 1962.
2. J. LINDHARD and M. SCHARFF: Private communication.
3. B. G. HARVEY, P. F. DONOVAN, J. R. MORTON and E. W. VALYOCSIK: U.C.R.L. 8618, p. 17, 1959.
4. J. LINDHARD and M. SCHARFF: Phys. Rev. **124**, 128, 1961.
5. J. LINDHARD, M. SCHARFF and H. E. SCHIØTT. Mat. Fys. Medd. Dan. Vid. Selsk. **33**, no. 14, 1963. In the present paper cited as LSS.
6. G. SIDENIUS and O. SKILBREID: E. M. Separations with High Efficiency of Microgramme Quantities. In: E. M. Separation of Radioactive Isotopes. Springer Verlag, Wien 1961.
7. K. O. NIELSEN: Electromagnetically Enriched Isotopes and Mass Spectroscopy. Butterworth Scientific Publications, London 1956, p. 68.
8. S. K. ALLISON and M. GARCIA MUNOZ: Reports National Academy of Sciences, National Research Council, Washington D. C., April 1962.
9. B. G. HARVEY: Ann. Rev. Nucl. Sci. **10**, 235, 1960.

Indleveret til Selskabet den 7. februar 1964.
Færdig fra trykkeriet den 11. juni 1964.

Matematisk-fysiske Meddelelser
udgivet af
Det Kongelige Danske Videnskabernes Selskab
Bind **34,** nr. 6

Mat. Fys. Medd. Dan. Vid. Selsk. **34,** no. 6 (1964)

ÜBER DIE FOURIERSCHEN KOEFFIZIENTEN DER EISENSTEINSCHEN REIHEN

VON

CARL LUDWIG SIEGEL

København 1964
Kommissionær: Ejnar Munksgaard

Synopsis

Es sei $\mathfrak{Z}$ ein Punkt der verallgemeinerten oberen Halbebene n-ten Grades, g eine gerade Zahl und

$$s_g(\mathfrak{Z}) = \sum_{\mathfrak{C},\mathfrak{D}}{}' |\mathfrak{C}\mathfrak{Z} + \mathfrak{D}|^{-g} \qquad (g > n+1)$$

die Eisensteinsche Reihe des Gewichtes g. Sie hat eine absolut konvergente Fouriersche Entwicklung

$$s_g(\mathfrak{Z}) = \sum_{\mathfrak{T} \geq 0} a_g(\mathfrak{T}) e^{\pi i \sigma(\mathfrak{T}\mathfrak{Z})},$$

worin $\mathfrak{T}$ alle nicht-negativen geraden symmetrischen Matrizen von n Reihen durchläuft. In einer Arbeit des Verfassers vom Jahre 1939 wurde bewiesen, dass alle Koeffizienten $a_g(\mathfrak{T})$ rationale Zahlen sind. E. Witt hat dann 1941 zeigen können, dass die Nenner dieser Koeffizienten sogar beschränkt sind, falls g durch 4 teilbar ist, indem er nachwies, dass die Funktion $s_g(\mathfrak{Z})$ in diesem Fall mit der analytischen Invariante des Geschlechtes der positiven geraden quadratischen Formen von $2g$ Variablen und der Determinante 1 übereinstimmt. Mit Benutzung dieses Zusammenhanges wird hier für $4 \mid g$ bewiesen, dass die Koeffizienten einen gemeinsamen Nenner haben, der sich in einfacher Weise durch g und die Bernoullischen Zahlen ausdrücken lässt. Im restlichen Fall, wo g nicht durch 4 teilbar ist, wird ein entsprechendes Resultat auf mühsamere Weise mit Hilfe der analytischen Theorie der indefiniten quadratischen Formen und der verallgemeinerten Gauss-Bonnetschen Formel erhalten.

PRINTED IN DENMARK
BIANCO LUNOS BOGTRYKKERI A-S

Im Folgenden wird die Kenntnis meiner Veröffentlichungen [1] bis [7] vorausgesetzt.

Es sei $\mathfrak{Z}$ ein Punkt der verallgemeinerten oberen Halbebene n-ten Grades, g eine gerade Zahl und

$$s_g(\mathfrak{Z}) = \sum_{\mathfrak{C},\mathfrak{D}}{}' |\mathfrak{C}\mathfrak{Z} + \mathfrak{D}|^{-g} \qquad (g > n+1) \tag{1}$$

die Eisensteinsche Reihe des Gewichtes g. Sie hat eine absolut konvergente Fouriersche Entwicklung

$$s_g(\mathfrak{Z}) = \sum_{\mathfrak{T} \geq 0} a_g(\mathfrak{T})\, e^{\pi i \sigma(\mathfrak{T}\mathfrak{Z})}, \tag{2}$$

worin $\mathfrak{T}$ alle nicht-negativen geraden symmetrischen Matrizen von n Reihen durchläuft. Ich habe bewiesen, dass alle Koeffizienten $a_g(\mathfrak{T})$ rationale Zahlen sind. In einer sehr bemerkenswerten Untersuchung hat dann Witt [8] sogar die Beschränktheit der Nenner dieser Koeffizienten gezeigt, falls die feste Zahl g durch 4 teilbar ist. Witt weist nämlich dort nach, dass in jenem Falle die Funktion $s_g(\mathfrak{Z})$ gleich der analytischen Invariante des Geschlechtes der positiven geraden quadratischen Formen von $2g$ Variabeln und der Determinante 1 ist. Aus diesen Zusammenhang ergibt sich nun, wie in den beiden ersten Paragraphen ausgeführt wird, als gemeinsamer Nenner der $a_g(\mathfrak{T})$ im Falle $4 \mid g$ ein einfacher Wert, in welchem nur die Bernoullischen Zahlen $B_2 = \frac{1}{6}$, $B_4 = -\frac{1}{30}, \ldots$ noch auftreten.

Im weiteren Verlauf der Arbeit wird auf mühsamere Weise der restliche Fall behandelt, wobei also g nicht durch 4 teilbar ist. Hierfür ist die analytische Theorie der indefiniten quadratischen Formen heranzuziehen, und die arithmetische Untersuchung der auftretenden Masszahlen erfolgt mittels der verallgemeinerten Gauss-Bonnetschen Formel. Man erhält das folgende Ergebnis.

Satz: *Es sei d_g das Produkt der Zähler der g Zahlen B_{2k}/k ($k = 1,2,\ldots,g-1$ und $g/2$) und $2z_g$ die höchste Potenz von 2 unterhalb g. Im Falle $4 \mid g$ ist dann d_g gemeinsamer Nenner aller Fourierschen Koeffizienten $a_g(\mathfrak{T})$, und im Falle $4 \nmid g$ ist $z_g d_g$ gemeinsamer Nenner.*

Es bleibt unentschieden, ob der Faktor z_g wirklich in der Aussage des Satzes nötig ist, und es wird auch nicht behauptet, dass d_g im ersten Falle der genaue Hauptnenner ist. Bekanntlich [9] gehen in d_g nur irreguläre Primzahlen p auf, für welche also nach Kummer die Klassenzahl des Körpers der p-ten Einheitswurzeln durch p teilbar ist.

§ 1. Fouriersche Entwicklung

Für $\mathfrak{T} = 0$ ist trivialerweise $a_g(\mathfrak{T}) = 1$. Es sei $\mathfrak{T} \neq 0$, also vom Range r mit $0 < r \leq n$, und es werde $m - r = f$, $m = 2g$ gesetzt. Es gibt dann eine primitive Matrix $\mathfrak{L}^{(r,n)}$ und eine positive gerade symmetrische Matrix $\mathfrak{T}_1^{(r)}$, so dass $\mathfrak{T} = \mathfrak{T}_1[\mathfrak{L}]$ wird. Durchläuft $\mathfrak{R}^{(r)}$ ein volles System rationaler symmetrischer Matrizen modulo 1, so gilt nach § 7 von [3] die Formel

$$a_g(\mathfrak{T}) = (-1)^{\frac{gr}{2}} \frac{\varrho_m}{\varrho_f} 2^r |\mathfrak{T}_1|^{\frac{f-1}{2}} \sum_{\mathfrak{R}} e^{\pi i \sigma(\mathfrak{T}_1 \mathfrak{R})} (\nu(\mathfrak{R}))^{-g}; \tag{3}$$

dabei ist zur Abkürzung

$$\varrho_k = \prod_{l=1}^{k} \frac{\pi^{\frac{l}{2}}}{\Gamma\left(\frac{l}{2}\right)} \qquad (k = 1,2,\ldots) \tag{4}$$

gesetzt, und $\nu(\mathfrak{R})$ bedeutet das Produkt der Nenner der Elementarteiler von $\mathfrak{R}$. Wegen der absoluten Konvergenz der Eisensteinschen Reihe in (1) ist auch die rechte Seite von (3) absolut konvergent. Für die weitere Umformung kommt es darauf an, die Zahl $(\nu(\mathfrak{R}))^{-g}$ durch einen rechnerisch brauchbaren Ausdruck mit Hilfe verallgemeinerter Gaussischer Summen darzustellen.

Es seien r rationale Zahlen

$$c_k = \frac{u_k}{t_k} \qquad (k = 1,\ldots,r)$$

mit den gekürzten positiven Nennern t_k gegeben, und es sei q irgend ein

positiver gemeinschaftlicher Nenner. Durchlaufen die beiden ganzzahligen Variabeln x_k, y_k je ein volles Restsystem modulo q, so wird

$$\sum_{x_k,\, y_k} e^{2\pi i c_k x_k y_k} = q^2 t_k^{-1} \qquad (k = 1, \ldots, r).$$

Es seien $\mathfrak{x}$ und $\mathfrak{y}$ die aus den Elementen x_k und y_k $(k = 1, \ldots, r)$ gebildeten Spalten. Da für jede unimodulare Matrix $\mathfrak{U}^{(r)}$ mit $\mathfrak{x}$ auch $\mathfrak{U}\mathfrak{x}$ ein volles Restsystem modulo q durchläuft, so folgt

$$\sum_{\mathfrak{x},\, \mathfrak{y} \pmod q} e^{2\pi i \mathfrak{x}' \mathfrak{R} \mathfrak{y}} = q^{2r} (\nu(\mathfrak{R}))^{-1},$$

falls $q\mathfrak{R}$ ganz ist. Setzt man noch

$$\mathfrak{S}^{(m)} = \begin{pmatrix} 0 & \mathfrak{E}^{(g)} \\ \mathfrak{E}^{(g)} & 0 \end{pmatrix}$$

und versteht unter $\mathfrak{R}$ eine variable ganze Matrix mit m Zeilen und r Spalten, so wird also

$$\sum_{\mathfrak{R} \pmod q} e^{\pi i \sigma(\mathfrak{S}[\mathfrak{R}]\mathfrak{R})} = q^{mr} (\nu(\mathfrak{R}))^{-g} \qquad (q\mathfrak{R} \text{ ganz}). \tag{5}$$

Diese Vereinfachung einer von mir benutzten Formel wurde von Witt a. a. O. gegeben.

Bei geradem q setze man $\mathfrak{R} = q^{-1}\mathfrak{P}$ und lasse die r Diagonalelemente von $\mathfrak{P}$ unabhängig voneinander die $\frac{1}{2}q$ Restklassen gerader Zahlen modulo q durchlaufen, die übrigen Elemente von $\mathfrak{P}$ jedoch volle Restsysteme modulo q. Dann wird

$$\sum_{\mathfrak{P}} \sum_{\mathfrak{R} \pmod q} e^{\pi i \sigma(\mathfrak{R}(\mathfrak{S}[\mathfrak{R}] - \mathfrak{T}_1))} = 2^{-r} q^{\frac{r(r+1)}{2}} A_q(\mathfrak{S}, \mathfrak{T}_1), \tag{6}$$

wenn $A_q(\mathfrak{S}, \mathfrak{T}_1)$ die Lösungsanzahl von

$$\mathfrak{S}[\mathfrak{R}] \equiv \mathfrak{T}_1 \pmod q$$

in modulo q inkongruenten $\mathfrak{R}$ bezeichnet. Schliesslich möge q eine Folge $q_1, q_2, \ldots$ durchlaufen, in welcher fast alle Elemente durch jede vorgegebene natürliche Zahl teilbar sind. Ersetzt man in (3) die Matrix $\mathfrak{R}$ durch $-\mathfrak{R}$, so ergibt sich nach (5) und (6) die Beziehung

$$a_g(\mathfrak{T}) = (-1)^{\frac{gr}{2}} \frac{\varrho_m}{\varrho_f} |\mathfrak{T}_1|^{\frac{f-1}{2}} \lim_{q \to \infty} \left(q^{\frac{r(r+1)}{2} - mr} A_q(\mathfrak{S}, \mathfrak{T}_1) \right). \tag{7}$$

Nun sei q ein Vielfaches von 4, also m durch 8 teilbar. Dann existiert ein Geschlecht positiver gerader quadratischer Formen von m Variabeln mit der Determinante 1, und zwar genau ein solches. Ist $\mathfrak{S}_0^{(m)}$ die Matrix einer Form dieses Geschlechtes, so sind $\mathfrak{S}_0$ und $\mathfrak{S}$ nach jedem Modul q äquivalent, und daher gilt auch

$$A_q(\mathfrak{S}_0, \mathfrak{T}_1) = A_q(\mathfrak{S}, \mathfrak{T}_1). \tag{8}$$

Nach der Massformel [1] ist andererseits

$$\frac{\sum_{k=1}^{h} \frac{A(\mathfrak{S}_k, \mathfrak{T}_1)}{E(\mathfrak{S}_k)}}{\sum_{k=1}^{h} \frac{1}{E(\mathfrak{S}_k)}} = \frac{\varrho_m}{\varrho_f} |\mathfrak{T}_1|^{\frac{f-1}{2}} \lim_{q \to \infty} \left(q^{\frac{r(r+1)}{2} - mr} A_q(\mathfrak{S}_0, \mathfrak{T}_1) \right); \tag{9}$$

dabei bedeuten $\mathfrak{S}_1, \ldots, \mathfrak{S}_h$ Repräsentanten der sämtlichen verschiedenen Klassen des Geschlechtes von $\mathfrak{S}_0$, ferner ist $A(\mathfrak{S}_k, \mathfrak{T}_1)$ die Anzahl der Darstellungen von $\mathfrak{T}_1$ durch $\mathfrak{S}_k$ und $E(\mathfrak{S}_k)$ die Anzahl der Einheiten von $\mathfrak{S}_k$. Aus (2), (7), (8), (9) folgt das von Witt gefundene Resultat

$$s_g(\mathfrak{Z}) = F(\mathfrak{S}_0, \mathfrak{Z}) \qquad (4|g) \tag{10}$$

mit

$$F(\mathfrak{S}_0, \mathfrak{Z}) = \frac{\sum_{k=1}^{h} \frac{f(\mathfrak{S}_k, \mathfrak{Z})}{E(\mathfrak{S}_k)}}{\sum_{k=1}^{h} \frac{1}{E(\mathfrak{S}_k)}}, \tag{11}$$

$$f(\mathfrak{S}_k, \mathfrak{Z}) = \sum_{\mathfrak{G}} e^{\pi i \sigma(\mathfrak{S}_k[\mathfrak{G}]\mathfrak{Z})} \tag{12}$$

bei Summation über alle ganzen $\mathfrak{G}^{(m,n)}$.

§ 2. Beweis des ersten Teiles des Satzes

Es laufe $\mathfrak{B}^{(r)}$ über ein volles System linksseitig nicht-assoziierter ganzer Matrizen mit positiven Determinanten, für welche $\mathfrak{T}_1[\mathfrak{B}^{-1}]$ ganz ist, und es

bedeute $B(\mathfrak{S}_k, \mathfrak{T}_1[\mathfrak{B}^{-1}])$ die Anzahl der primitiven Darstellungen von $\mathfrak{T}_1[\mathfrak{B}^{-1}]$ durch $\mathfrak{S}_k$. Dann ist

$$A(\mathfrak{S}_k, \mathfrak{T}_1) = \sum_{\mathfrak{B}} B(\mathfrak{S}_k, \mathfrak{T}_1[\mathfrak{B}^{-1}]). \tag{13}$$

Durchläuft nun $\mathfrak{U}$ alle Einheiten von $\mathfrak{S}_k$, so erhält man aus irgend einer primitiven Lösung $\mathfrak{C}^{(m,r)}$ von $\mathfrak{S}_k[\mathfrak{C}] = \mathfrak{T}_1[\mathfrak{B}^{-1}]$ durch die Matrizen $\mathfrak{U}\mathfrak{C}$ insgesamt j verschiedene Darstellungen, wenn j den Index der durch die Bedingung $\mathfrak{U}\mathfrak{C} = \mathfrak{C}$ erklärten Untergruppe in der vollen Einheitengruppe bedeutet. Man verwende jetzt den Satz von der quadratischen Ergänzung, wie er in Hilfssatz 11 von [1] ausgesprochen ist, wobei dort $\mathfrak{S}$ und $\mathfrak{T}$ durch $\mathfrak{S}_k$ und $\mathfrak{T}_1[\mathfrak{B}^{-1}]$ ersetzt werden. Dann wird jene Untergruppe isomorph einer gewissen Untergruppe der Einheitengruppe von $\mathfrak{H}^{(f)}$ und folglich j ein Vielfaches der Zahl $E(\mathfrak{S}_k)/E(\mathfrak{H})$.

Es sei b_k der Nenner der rationalen Zahl B_{2k}/k $(k = 1,2,\ldots)$ und

$$\overline{l} = 2^l b_1 b_2 \ldots b_{\left[\frac{l}{2}\right]} \qquad (l = 1,2,\ldots). \tag{14}$$

Nach einem Minkowskischen Satze [10] ist dann die Gruppenordnung $E(\mathfrak{H})$ ein Teiler der Zahl $\overline{f}$. Mit Rücksicht auf (13) erweist sich also $\overline{f}$ als gemeinschaftlicher Nenner der h Brüche $A(\mathfrak{S}_k, \mathfrak{T}_1)/E(\mathfrak{S}_k)$. Bezeichnet

$$M(\mathfrak{S}_0) = \sum_{k=1}^{h} \frac{1}{E(\mathfrak{S}_k)}$$

das Mass des Geschlechtes von $\mathfrak{S}_0$, so ist daher zufolge (2), (10), (11), (12) die Zahl $\overline{f}\, M(\mathfrak{S}_0) a_q(\mathfrak{T})$ ganz.

Zur Berechnung von $M(\mathfrak{S}_0)$ benutzen wir die Minkowskische Massformel

$$\frac{1}{M(\mathfrak{S}_0)} = \frac{\varrho_m}{2} \lim_{q \to \infty} \left(2^{-\omega(q)} q^{-\frac{m(m-1)}{2}} E_q(\mathfrak{S})\right),$$

wobei $\omega(q)$ die Anzahl der verschiedenen Primteiler von q bedeutet. Ist q Potenz einer Primzahl p und $a_p = 2^m$ für $p = 2$, $a_p = 1$ für $p \neq 2$, so gilt

$$\tfrac{1}{2} q^{-\frac{m(m-1)}{2}} E_q(\mathfrak{S}) = a_p (1 - p^{-g}) \prod_{l=1}^{g-1} (1 - p^{-2l}) \qquad (m = 2g),$$

also

$$M(\mathfrak{S}_0) = 2^{1-m} \varrho_m^{-1} \zeta(g) \prod_{l=1}^{g-1} \zeta(2l).$$

Nun ist

$$\zeta(2l) = (-1)^{l-1}\frac{(2\pi)^{2l}}{2(2l)!}B_{2l} \qquad (l = 1,2,\ldots)$$

und nach (4) die Zahl

$$\varrho_m = \frac{\pi^g}{\Gamma(g)}\prod_{l=1}^{g-1}\frac{(2\pi)^{2l}}{2\Gamma(2l)},$$

so dass sich die Formel

$$M(\Xi_0) = \frac{B_g}{2g}\prod_{l=1}^{g-1}\frac{B_{2l}}{4l} \tag{15}$$

ergibt.

Es werde

$$\left[\frac{f}{2}\right] = c$$

gesetzt. Da dann $c \leq g-1$ ist, so ist zufolge (14) und (15) die Zahl

$$f\,M(\Xi_0) = 2^{-r}\frac{2B_g}{g}\prod_{l=1}^{c}\frac{b_l B_{2l}}{l}\prod_{l=c+1}^{g-1}\frac{B_{2l}}{l} = d_{g,r} \tag{16}$$

ein Teiler der im Wortlaut des Satzes erklärten natürlichen Zahl d_g. Damit ist die erste Aussage des Satzes bewiesen.

§ 3. Anwendung der Massformel für indefinite Formen

Wenn m nicht durch 8 teilbar ist, so existiert nach einem Satze von WITT [8] keine definite gerade quadratische Form mit m Variabeln und der Determinante 1. Aus diesem Grunde werden nun indefinite Formen herangezogen.

Wir betrachten eine Zerlegung $g = 4w + 2t$ mit ganzen nicht-negativen w und t. Im Falle $g \equiv 2 \pmod 4$, der uns weiterhin vorwiegend interessiert, sind dann die Werte $t = 1,3,\ldots,\frac{1}{2}g$ zulässig, und im Falle $g \equiv 0 \pmod 4$ die Werte $t = 0,2,\ldots,\frac{1}{2}g$. Mit der früheren Bedeutung von $\Xi_0^{(8w)}$ und $\Xi^{(4t)}$ wird anstelle von $\Xi_0^{(m)}$ allgemeiner die m-reihige Matrix

$$\Xi^* = \begin{pmatrix} \varepsilon\Xi_0^{(8w)} & 0 \\ 0 & \Xi^{(4t)} \end{pmatrix} \qquad (\varepsilon = \pm 1)$$

gebildet. Sie ist ebenfalls symmetrisch, gerade und von der Determinante 1; ihre Signatur ist $8w + 2t$, $2t$ für $\varepsilon = 1$ und $2t$, $8w + 2t$ für $\varepsilon = -1$. Die Formel (8) gilt dann auch für $\mathfrak{S}^*$ anstelle von $\mathfrak{S}_0$.

Nach dem Ergebnis meiner Arbeit [2] ist

$$\frac{\mu(\mathfrak{S}^*, \mathfrak{T}_1)}{\mu(\mathfrak{S}^*)} = \lim_{q \to \infty} \left(q^{\frac{r(r+1)}{2} - mr} A_q(\mathfrak{S}, \mathfrak{T}_1)\right) \tag{17}$$

sowie

$$\mu(\mathfrak{S}^*) = \varrho_m M(\mathfrak{S}_0), \tag{18}$$

wenn die Masse $\mu(\mathfrak{S}^*, \mathfrak{T}_1)$ und $\mu(\mathfrak{S}^*)$ in den dort auf S. 231 und S. 232 erklärten Bedeutungen verstanden werden. Da $\mathfrak{T}_1$ die Signatur $r, 0$ hat, so muss im Falle $\varepsilon = -1$ noch $2t \geq r$ vorausgesetzt werden. Dagegen ist im Falle $\varepsilon = 1$ die entsprechende Voraussetzung $8w + 2t \geq r$ wegen

$$r \leq n < g - 1 = m - g - 1 < m - 2t = 8w + 2t$$

von selbst erfüllt. Sind jetzt $\mathfrak{S}_1, \ldots, \mathfrak{S}_h$ Repräsentanten der sämtlichen verschiedenen Klassen des Geschlechtes von $\mathfrak{S}^*$, so ist

$$\mu(\mathfrak{S}^*, \mathfrak{T}_1) = \sum_{k=1}^{h} \sum_{\mathfrak{C}_k} \varrho(\mathfrak{S}_k, \mathfrak{C}_k) \tag{19}$$

definiert, wobei $\varrho(\mathfrak{S}_k, \mathfrak{C}_k)$ das Mass einer Darstellung $\mathfrak{S}_k[\mathfrak{C}_k] = \mathfrak{T}_1$ bedeutet und über ein volles System solcher $\mathfrak{C}_k$ summiert wird, die bezüglich der Einheitengruppe von $\mathfrak{S}_k$ nicht-assoziiert sind.

Es sei $\mathfrak{C}_k$ fest gewählt und $\mathfrak{C}_k \mathfrak{B}^{-1} = \mathfrak{C}$ primitiv. Mit analoger Bedeutung von $\mathfrak{H}^{(f)}$ wie in § 2 erhalten wir dann nach den Hilfssätzen 18, 17 von [2] und der Formel (110) von [5] die Beziehungen

$$\varrho(\mathfrak{S}_k, \mathfrak{C}_k) = (\mathrm{abs}\,\mathfrak{B})^{1-f} \varrho(\mathfrak{S}_k, \mathfrak{C}), \tag{20}$$

$$\varrho(\mathfrak{S}_k, \mathfrak{C}) = j |\mathfrak{T}_1[\mathfrak{B}^{-1}]|^{-f} \varrho(\mathfrak{H}), \tag{21}$$

$$\varrho(\mathfrak{H}) = \tfrac{1}{2} \varrho_a \varrho_b |\mathfrak{T}_1[\mathfrak{B}^{-1}]|^{\frac{f+1}{2}} v(\mathfrak{H}); \tag{22}$$

darin ist $j = j(\mathfrak{S}_k, \mathfrak{C})$ ein gewisser endlicher Gruppenindex, also eine natürliche Zahl, und $v(\mathfrak{H})$ das Volumen eines Fundamentalbereiches F der Einheitengruppe Γ von $\mathfrak{H}$, ferner $a = m - 2t - r$, $b = 2t$ für $\varepsilon = 1$ und $a = 2t - r$, $b = m - 2t$ für $\varepsilon = -1$ die Signatur von $\mathfrak{H}$. Im Falle $ab = 0$ ist $\varrho_0 = 1$ und

$v(\mathfrak{H}) = 2/E(\mathfrak{H})$ zu setzen. Weiterhin sei $ab > 0$ bis zum Ende des fünften Paragraphen.

Das Volumen von F ist gemäss den Formeln (103), (104) von [5] und (1), (2), (5) von [6] auf folgende Weise zu berechnen. Wir betrachten den Raum Q aller positiven reellen symmetrischen $\mathfrak{Q}^{(f)}$ mit $\mathfrak{H}^{-1}[\mathfrak{Q}] = \mathfrak{H}^{-1}$, der ab Dimensionen besitzt, wählen darauf einen Fundamentalbereich F bezüglich Γ und führen durch die Gleichung

$$s^2 = \tfrac{1}{8}\sigma(\dot{\mathfrak{Q}}\mathfrak{Q}^{-1}\dot{\mathfrak{Q}}\mathfrak{Q}^{-1}) \tag{23}$$

eine Riemannsche Metrik ein. Eine Parameterdarstellung von Q erhält man nach Formel (34) von [4] in der Gestalt

$$\mathfrak{Q} = 2\mathfrak{W}^{-1}[\mathfrak{y}'\mathfrak{H}] + \mathfrak{H}, \qquad -\mathfrak{H}[\mathfrak{y}] = \mathfrak{W} > 0 \tag{24}$$

mit variablem reellen $\mathfrak{y}^{(f,b)}$. Dabei ist zu beachten, dass für beliebiges umkehrbares reelles $\mathfrak{K}^{(b)}$ die Matrizen $\mathfrak{y}$ und $\mathfrak{y}\mathfrak{K}$ denselben Punkt $\mathfrak{Q}$ von Q liefern. Indem man noch $\mathfrak{H}$ durch eine reelle Transformation in

$$\mathfrak{H}[\mathfrak{L}] = \begin{pmatrix} \mathfrak{E}^{(a)} & 0 \\ 0 & -\mathfrak{E}^{(b)} \end{pmatrix}$$

überführt und für $\mathfrak{L}^{-1}\mathfrak{y}$ wieder $\mathfrak{y}$ schreibt, kann man die Normierung

$$\mathfrak{y} = \begin{pmatrix} \mathfrak{X}^{(a,b)} \\ \mathfrak{E}^{(b)} \end{pmatrix}, \qquad \mathfrak{E}^{(b)} - \mathfrak{X}'\mathfrak{X} > 0$$

treffen, wobei jetzt die Elemente von $\mathfrak{X}$ unabhängige reelle Variable werden. Damit erhalten wir

$$s^2 = \sigma\big(\dot{\mathfrak{X}}(\mathfrak{E}^{(b)} - \mathfrak{X}'\mathfrak{X})^{-1}\dot{\mathfrak{X}}'(\mathfrak{E}^{(a)} - \mathfrak{X}\mathfrak{X}')^{-1}\big) \tag{25}$$

und das entsprechende Volumenelement

$$dv = |\mathfrak{E} - \mathfrak{X}'\mathfrak{X}|^{-\frac{f}{2}}\{d\mathfrak{X}\}.$$

Der Inhalt $v(\mathfrak{H})$ ändert sich seiner Definition nach nicht, wenn die Matrix $\mathfrak{H}$ mit einem von 0 verschiedenen skalaren Faktor multipliziert wird. In der bisherigen Bedeutung waren die Elemente von $\mathfrak{H}$ rationale Zahlen. Zur Untersuchung von $v(\mathfrak{H})$ kann also weiterhin $\mathfrak{H}$ als ganz vorausgesetzt werden.

Es sei Γ_0 die orthogonale Gruppe bezüglich $\mathfrak{H}$, die durch die reellen Lösungen $\mathfrak{F}$ von $\mathfrak{H}[\mathfrak{F}] = \mathfrak{H}$ erklärt ist. Vermöge (23) und (24) sind die Abbildungen $\mathfrak{Y} \to \mathfrak{F}\mathfrak{Y}$ mit $\mathfrak{Q} \to \mathfrak{Q}[\mathfrak{F}^{-1}]$ gleichbedeutend und auf Q isometrisch. Da sie ausserdem auf Q transitiv wirken, so ist die zur Metrik (23) gehörige Killing-Lipschitzsche skalare Krümmung $\varkappa$ auf Q konstant.

Ist G eine geschlossene Mannigfaltigkeit mit der durch (23) gegebenen Riemannschen Metrik, so sind bekanntlich [11] [12] [13] ihr Volumen $v(G)$ und ihre Eulersche Charakteristik $\chi(G)$ durch die verallgemeinerte Gauss-Bonnetsche Formel

$$\chi(G) = \pi^{-\frac{ab+1}{2}} \Gamma\left(\frac{ab+1}{2}\right) \varkappa v(G) \tag{26}$$

miteinander verknüpft. Man beachte dabei, dass die Dimensionenzahl ab gerade ist, weil nämlich b es ist. Der Anwendung von (26) auf den Fundamentalbereich F der Einheitengruppe Γ stellen sich nun aber drei Schwierigkeiten entgegen: 1) Es können Fixpunkte für gewisse von $\pm \mathfrak{E}$ verschiedene Elemente von Γ auftreten. 2) Der Bereich F ist in Q nicht kompakt. 3) Die Krümmung $\varkappa$ ist bisher nicht für den vorliegenden Fall bestimmt worden. Wir wollen nun zunächst die dritte Schwierigkeit behandeln.

§ 4. Berechnung der Krümmung

Die direkte Berechnung von $\varkappa$ mittels Verjüngung des Riemannschen Krümmungstensors führt auf kombinatorische Schwierigkeiten. Deswegen wird folgender Kunstgriff verwendet. Es wird die durch (25) gegebene Riemannsche Metrik dadurch abgeändert, dass dort auf der rechten Seite das negative Vorzeichen an beiden Stellen durch das positive ersetzt wird, also nunmehr

$$s^2 = \sigma\left(\dot{\mathfrak{X}}(\mathfrak{E}^{(b)} + \mathfrak{X}'\mathfrak{X})^{-1}\dot{\mathfrak{X}}'(\mathfrak{E}^{(a)} + \mathfrak{X}\mathfrak{X}')^{-1}\right) \tag{27}$$

erklärt. Entsprechend wird dann $\mathfrak{H}$ durch $-\mathfrak{E}^{(f)}$ ersetzt und Γ_0 durch die gewöhnliche reelle orthogonale Gruppe. Sie wirkt transitiv auf die Grassmannsche Mannigfaltigkeit Q^*, welche von den reellen Matrizen $\mathfrak{Y}^{(f,b)}$ des Ranges b gebildet wird, und diese ist nun aber kompakt. Es ist durch die Untersuchungen von E. Cartan bekannt und auch nach (25) und (27) durch Angabe des Riemannschen Tensors leicht zu verifizieren, dass die skalare Krümmung bezüglich (27) gleich dem absoluten Betrage von $\varkappa$ ist, wobei sich

als Vorzeichen von $\varkappa$ der Wert $(-1)^{\frac{ab}{2}}$ ergibt. Bedeutet dann $\chi(Q^*)$ die Eulersche Charakteristik von Q^* und $v(Q^*)$ den mit dem Volumenelement

$$dv = |\mathfrak{E} + \mathfrak{X}'\mathfrak{X}|^{-\frac{f}{2}}\{d\mathfrak{X}\}$$

berechneten Inhalt von Q^*, so gilt analog zu (26) die Formel

$$\chi(Q^*) = (-1)^{\frac{ab}{2}} \pi^{-\frac{ab+1}{2}} \Gamma\left(\frac{ab+1}{2}\right) \varkappa v(Q^*). \tag{28}$$

Die Bestimmung von $\varkappa$ ist damit auf die von $v(Q^*)$ und $\chi(Q^*)$ zurückgeführt.

Bedeutet P den Raum aller positiven reellen symmetrischen $\mathfrak{P}^{(h)}$, so wird

$$\int_P |\mathfrak{P}|^{\varrho - \frac{h+1}{2}} e^{-\sigma(\mathfrak{P}\mathfrak{R})}\{d\mathfrak{P}\} = \pi^{\frac{h(h-1)}{4}} |\mathfrak{R}|^{-\varrho} \prod_{l=0}^{h-1} \Gamma\left(\varrho - \frac{l}{2}\right) \quad \left(\varrho > \frac{h-1}{2};\ \mathfrak{R}^{(h)} > 0\right).$$

Wählt man hierin speziell

$$h = b, \qquad \varrho = \frac{f}{2}, \qquad \mathfrak{R} = \mathfrak{E}^{(b)} + \mathfrak{X}'\mathfrak{X},$$

so folgt

$$\pi^{\frac{b(b-1)}{4}} v(Q^*) \prod_{l=0}^{b-1} \Gamma\left(\frac{f-l}{2}\right) = \int_{Q^*} \left(\int_P |\mathfrak{P}|^{\frac{a-1}{2}} e^{-\sigma(\mathfrak{P}(\mathfrak{E} + \mathfrak{X}'\mathfrak{X}))}\{d\mathfrak{P}\} \right) \{d\mathfrak{X}\}$$

$$= \pi^{\frac{ab}{2}} \int_P |\mathfrak{P}|^{-\frac{1}{2}} e^{-\sigma(\mathfrak{P})}\{d\mathfrak{P}\} = \pi^{\frac{ab}{2} + \frac{b(b-1)}{4}} \prod_{l=0}^{b-1} \Gamma\left(\frac{b-l}{2}\right),$$

also

$$v(Q^*) = \frac{\varrho_f}{\varrho_a \varrho_b}, \tag{29}$$

womit das Volumen von Q^* bekannt ist.

Die Charakteristik $\chi(Q^*)$ bestimmt sich nach dem von Hopf und Samelson [14] bewiesenen Satz durch die Anzahl der Fixpunkte, welche eine eigentlich orthogonale Abbildung $\mathfrak{y} \to \mathfrak{F}\mathfrak{y}$ auf Q^* besitzt; dabei ist vorauszusetzen, dass diese Anzahl endlich ist. Wir setzen weiterhin

$$\left[\frac{f}{2}\right] = \left[\frac{a+b}{2}\right] = c, \qquad \frac{b}{2} = d$$

und wählen $\mathfrak{F}$ speziell auf die folgende Art. Wenn r gerade ist, also $c = \frac{f}{2}$, so sei $\mathfrak{F}$ aus c zweireihigen eigentlich orthogonalen Kästchen $\mathfrak{F}_1, \ldots, \mathfrak{F}_c$ aufgebaut; wenn r ungerade ist, also $c = \frac{f-1}{2}$, so nehme man zu diesen c Kästchen noch das weitere Diagonalelement 1. Zur Bestimmung der Fixpunkte hat man

$$\mathfrak{F}\mathfrak{Y} = \mathfrak{Y}\mathfrak{K}$$

zu setzen, wobei $\mathfrak{Y}$ reell und vom Range b sein soll. Sind die Eigenwerte von $\mathfrak{F}$ alle voneinander verschieden, so muss $\mathfrak{K}$ reell äquivalent einer Matrix sein, die aus d von jenen Kästchen $\mathfrak{F}_1, \ldots, \mathfrak{F}_c$ zusammengesetzt ist, und $\mathfrak{Y}$ ergibt sich dann eindeutig aus $\mathfrak{K}$. Für die Wahl von d Kästchen hat man nun insgesamt $\binom{c}{d}$ Möglichkeiten, und es folgt also

$$\chi(Q^*) = \binom{c}{d}.$$

Aus (28) und (29) ergibt sich damit die gewünschte Beziehung

$$\pi^{-\frac{ab+1}{2}} \Gamma\left(\frac{ab+1}{2}\right) \varkappa = (-1)^{\frac{ab}{2}} \binom{c}{d} \frac{\varrho_a \varrho_b}{\varrho_f}. \tag{30}$$

Bei dieser Gelegenheit sei darauf hingewiesen, dass die zur Bestimmung von $\varkappa$ benutzte Methode auch bei den Wirkungsräumen anderer Lieschen Gruppen verwendet werden kann. Von Interesse ist dabei der Fall der verallgemeinerten oberen Halbebene mit der symplektischen Metrik, die durch

$$\dot{s}^2 = \sigma(\mathfrak{Y}^{-1}\dot{\mathfrak{Z}}\mathfrak{Y}^{-1}\dot{\bar{\mathfrak{Z}}}) \qquad (\mathfrak{Z}^{(n)} = \mathfrak{X} + i\mathfrak{Y};\ \mathfrak{Y} > 0)$$

definiert wird. Legt man vermöge der Abbildung

$$\mathfrak{Z} = i(\mathfrak{E} + \mathfrak{W})(\mathfrak{E} - \mathfrak{W})^{-1}$$

den verallgemeinerten Einheitskreis

$$\mathfrak{E} - \mathfrak{W}\overline{\mathfrak{W}} > 0 \qquad (\mathfrak{W} = \mathfrak{W}')$$

zugrunde, so wird

$$\dot{s}^2 = 4\sigma\left(\overline{\dot{\mathfrak{W}}}(\mathfrak{E} - \mathfrak{W}\overline{\mathfrak{W}})^{-1}\dot{\mathfrak{W}}(\mathfrak{E} - \overline{\mathfrak{W}}\mathfrak{W})^{-1}\right). \tag{31}$$

Erklärt man statt dessen die Metrik durch

$$\dot{s}^2 = 4\sigma\left(\overline{\dot{\mathfrak{W}}}(\mathfrak{E} + \mathfrak{W}\overline{\mathfrak{W}})^{-1}\dot{\mathfrak{W}}(\mathfrak{E} + \overline{\mathfrak{W}}\mathfrak{W})^{-1}\right) \tag{32}$$

mit beliebigem komplexen symmetrischen $\mathfrak{W}^{(n)}$, so stehen die zu (31) und (32) gehörigen skalaren Krümmungen K und K^* in der Beziehung

$$(-1)^{\nu}K = K^* > 0, \tag{33}$$

wobei $\nu = \frac{1}{2}n(n+1)$ gesetzt ist. Mit

$$\mathfrak{W} = \mathfrak{W}\mathfrak{N}^{-1}, \qquad \begin{pmatrix}\mathfrak{N}\\ \mathfrak{W}\end{pmatrix} = \mathfrak{Q}, \qquad \begin{pmatrix}0 & \mathfrak{E}^{(n)}\\ -\mathfrak{E}^{(n)} & 0\end{pmatrix} = \mathfrak{J}$$

wird $\mathfrak{Q}'\mathfrak{J}\mathfrak{Q} = 0$, und die komplexe Matrix $\mathfrak{Q}^{(2n,\,n)}$ besitzt den Rang n. Durch diese homogene Schreibweise wird der Raum W der $\mathfrak{W}$ kompakt und vermöge der Abbildungen $\mathfrak{Q} \to \mathfrak{U}\mathfrak{Q}$ ein Wirkungsraum der Gruppe aller symplektischen unitären $\mathfrak{U}^{(2n)}$. Das gemäss (32) bestimmte Volumenelement ist dann

$$d\omega = 2^{3\nu-n}|\mathfrak{E} + \mathfrak{W}\overline{\mathfrak{W}}|^{-n-1}\{d\mathfrak{W}\},$$

und die Berechnung des Inhaltes von W liefert ein hübsches Beispiel zur Integralrechnung, mit dem Resultat

$$v(W) = \int_W d\omega = 2^{3\nu}\pi^{\nu}\prod_{l=1}^{n}\frac{l!}{(2l)!}.$$

Der Satz von Hopf und Samelson ergibt andererseits leicht die Eulersche Charakteristik

$$\chi(W) = 2^n,$$

sodass nach der verallgemeinerten Gauss-Bonnetschen Formel

$$\pi^{-\nu-\frac{1}{2}}\Gamma(\nu+\tfrac{1}{2})K^* = 2^{n-3\nu}\pi^{-\nu}\prod_{l=1}^{n}\frac{(2l)!}{l!} \tag{34}$$

wird. Dadurch lässt sich auch der Wert

$$a_n = (-1)^{\nu}2^{\nu-2n}(2\nu)!\,K$$

ermitteln, dessen allgemeine Bestimmung als expliziter Funktion von n mir bei einer früheren Untersuchung [15] nicht gelungen war. Vermöge (33) und (34) erhalten wir

$$\frac{a_n}{\nu!} = \prod_{k=1}^{n}\frac{(2k-1)!}{(k-1)!}$$

in Übereinstimmung mit einer Formel, die F. Hirzebruch vor einigen Jahren bei einer mathematischen Konferenz in Princeton, N. J. angegeben und auf komplizierterem Wege bewiesen hat. In [15] ist übrigens, wie schon Hirzebruch bemerkte, der für a_3 ausgerechnete Wert falsch und durch das Vierfache zu ersetzen.

§ 5. Anwendung der Gauss-Bonnetschen Formel auf den Fundamentalbereich der Einheitengruppe

Nachdem die Krümmung $\varkappa$ bestimmt ist, müssen noch die beiden anderen früher erwähnten Schwierigkeiten eliminiert werden.

Es sei q eine natürliche Zahl > 2 und Γ_q die Gruppe aller Elemente $\mathfrak{M}$ von Γ mit $\mathfrak{M} \equiv \mathfrak{E} \pmod q$. Da $\mathfrak{M}$ ganz ist, so ist dann nach einem Minkowskischen Satze [10] keine Potenz $\mathfrak{M}^k$ $(k = 1,2,\ldots)$ gleich $\mathfrak{E}$, ausser wenn bereits $\mathfrak{M} = \mathfrak{E}$ ist. Nun ist Γ diskontinuierlich auf Q, und folglich ist Γ_q fixpunktfrei. Bedeutet j_q den Index von Γ_q bezüglich Γ, so zerfallen die Elemente von Γ in genau j_q verschiedene Restklassen modulo q.

Es sei insbesondere q teilerfremd zu $|\mathfrak{H}|$. Wir betrachten die Gruppe der Einheiten modulo q, die von den inkongruenten ganzen Lösungen $\mathfrak{X}$ der Kongruenz $\mathfrak{H}[\mathfrak{X}] \equiv \mathfrak{H} \pmod q$ gebildet wird und die Ordnung $E_q(\mathfrak{H})$ habe. Es ist klar, dass die obigen j_q Restklassen eine Untergruppe der Einheitengruppe modulo q ergeben, und folglich ist $E_q(\mathfrak{H})$ durch j_q teilbar. Wenn wir für q alle zu $|\mathfrak{H}|$ teilerfremden Zahlen > 2 zulassen, so ergibt ein weiterer Satz von Minkowski [10], dass der grösste gemeinsame Teiler der entsprechenden Ordnungen $E_q(\mathfrak{H})$ ein Faktor der Zahl $\overline{f}|$ ist. Also gilt dies auch für den grössten gemeinsamen Teiler der j_q.

Wir müssen nun auf die Konstruktion des Fundamentalbereiches F näher eingehen, wie sie zuerst in [4] ausgeführt wurde. Es sei R der Bereich aller im Minkowskischen Sinne reduzierten reellen positiven $\mathfrak{P}^{(f)}$ mit der festen Determinante $|\mathfrak{P}| = |\mathfrak{H}|$. Bei unimodularem $\mathfrak{U}^{(f)}$ bedeute $R(\mathfrak{U})$ das durch die Zuordnung $\mathfrak{P} \to \mathfrak{P}[\mathfrak{U}]$ entstehende Bild von R. Wenn der Durchschnitt von $R(\mathfrak{U})$ und Q nicht leer ist, so heisst $\mathfrak{H}[\mathfrak{U}^{-1}]$ reduziert. Es gibt dann nur endlich viele verschiedene zu $\mathfrak{H}$ äquivalente reduzierte Matrizen, die mit $\mathfrak{H}_1,\ldots,\mathfrak{H}_v$ bezeichnet seien. Zu $\mathfrak{H}_k$ $(k = 1,\ldots,v)$ wähle man eine feste unimodulare Matrix $\mathfrak{U}_k$ mit $\mathfrak{H}_k[\mathfrak{U}_k] = \mathfrak{H}$ und setze

$$R_k = R(\mathfrak{U}_k) \qquad (k = 1,\ldots,n), \qquad F = \bigcup_k (Q \cap R_k),$$

wodurch F ein Fundamentalbereich auf Q bezüglich der Gruppe Γ wird.

Da $f = m - r \geq g + g - n \geq g + 2 \geq 6$ und $ab \neq 0$ ist, so ist $\mathfrak{H}[\mathfrak{x}]$ eine Nullform und folglich F nicht kompakt. Es sei δ eine positive Zahl, die nachher gegen 0 streben soll, und p das erste Diagonalelement von $\mathfrak{P}$. Auf R werde der durch die Ungleichung $p \geq \delta$ erklärte Teilbereich $R(\delta)$ betrachtet, der kompakt ist. Geht dann $R(\delta)$ durch die Abbildung $\mathfrak{P} \to \mathfrak{P}[\mathfrak{U}_k]$ in $R_k(\delta)$ über, so ist auch der Bereich

$$F(\delta) = \bigcup_k \left(Q \cap R_k(\delta)\right)$$

kompakt und

$$\lim_{\delta \to 0} F(\delta) = F.$$

Nun seien $\mathfrak{Q}$ und $\mathfrak{Q}^*$ zwei Punkte von Q, die bezüglich Γ äquivalent sind, und $\mathfrak{Q}[\mathfrak{U}] = \mathfrak{P}$, $\mathfrak{Q}^*[\mathfrak{U}^*] = \mathfrak{P}^*$ mit unimodularen $\mathfrak{U},\mathfrak{U}^*$ in R gelegen. Aus der Minkowskischen Definition des Bereiches R folgt dann, dass $\mathfrak{P}$ und $\mathfrak{P}^*$ das gleiche erste Diagonalelement $p = p^*$ haben. Es liegt also $\mathfrak{P}$ genau dann auf dem Randteil $p = \delta$ von $R(\delta)$, wenn $\mathfrak{P}^*$ dies tut, und beide liegen zugleich innerhalb oder ausserhalb von $R(\delta)$. Bedeutet nun $Q(\delta)$ denjenigen Teil von Q, zu dessen Punkten $\mathfrak{Q}$ es äquivalente Punkte $\mathfrak{Q}[\mathfrak{U}] = \mathfrak{P}$ in $R(\delta)$ gibt, so ist wegen der Endlichkeit von j_q und v der Raum

$$Q_q(\delta)/\Gamma_q = G_q(\delta)$$

kompakt, und seine Randpunkte bestehen genau aus den $\mathfrak{Q}$ mit $p = \delta$. Dieser Raum entsteht aus $\frac{1}{2}j_q$ Bildern von $F(\delta)$, wenn sie an gewissen Rändern geeignet verheftet werden.

Da Γ_q fixpunktfrei ist, so lässt sich auf die berandete Mannigfaltigkeit $G_q(\delta)$ die verallgemeinerte Gauss-Bonnetsche Formel [16] [17] anwenden. So erhalten wir anstelle von (26) die Beziehung

$$\chi(G_q(\delta)) = \pi^{-\frac{ab+1}{2}} \Gamma\left(\frac{ab+1}{2}\right) \varkappa v(G_q(\delta)) + \eta(\delta);$$

dabei ist $\eta(\delta)$ ein Randintegral, dessen Integrand bei isometrischen Abbildungen von Q auf sich invariant bleibt, und $\chi(G_q(\delta))$ bedeutet die innere Eulersche Charakteristik von $G_q(\delta)$, also eine ganze Zahl. Nun ist

$$\lim_{\delta \to 0} v(G_q(\delta)) = \tfrac{1}{2} j_q \lim_{\delta \to 0} v(F(\delta)) = \tfrac{1}{2} j_q v(\mathfrak{H}).$$

Wenn wir noch die Aussage

$$\lim_{\delta \to 0} \eta(\delta) = 0 \tag{35}$$

beweisen können, so folgt, dass die Zahl

$$\tfrac{1}{2}\pi^{-\frac{ab+1}{2}} \Gamma\left(\frac{ab+1}{2}\right) \varkappa j_q v(\mathfrak{H}) = v_q \tag{36}$$

ganz ist. Zum Nachweise von (32) genügt es aber, ein analoges Randintegral zu betrachten, das bei festem unimodularen $\mathfrak{U}$ über alle reduzierten $\mathfrak{Q}[\mathfrak{U}] = \mathfrak{P}$ mit $p = \delta$ zu erstrecken ist.

Weiterhin sei $\delta < 1$. Zufolge [4] S. 234–235 und [7] § 13 kann man bei der Integration als Variable die Elemente der dort auf S. 51–53 mit $\mathfrak{H}_1, \mathfrak{H}_2, \mathfrak{F}, \mathfrak{G}$ bezeichneten Matrizen einführen. Dabei ist

$$\mathfrak{H}_1 = \mathfrak{H}_1^{(s)} > 0, \qquad \mathfrak{H}_2 = \mathfrak{H}_2^{(f-2s)} > 0, \qquad \mathfrak{F} = \mathfrak{F}^{(f-2s,s)}, \qquad \mathfrak{G} = -\mathfrak{G}' = \mathfrak{G}^{(s)},$$

ferner $0 < s \leq \frac{f}{2}$ und p das erste Diagonalelement von $\mathfrak{H}_1$. Wie aus [7] § 13 ersichtlich wird, lassen sich zwei Punkte von Q stets durch ein derartiges Element von Γ_0 ineinander transformieren, dass dabei die Koordinate p nur mit einem von den sämtlichen anderen Koordinaten unabhängigen Faktor multipliziert wird, es erfährt nämlich insbesondere $\mathfrak{H}_1$ eine Jacobische Transformation. Wegen dieser besonderen Art der Transitivität ergibt sich nun aber, dass der dabei invariante Integrand des noch abzuschätzenden Randintegrales folgendermassen gebildet werden kann. Man nehme das durch [7] (79) erklärte Volumenelement, ersetze darin dp durch p und multipliziere noch mit einem gewissen nur von a, b und s abhängigen positiven Faktor, auf den es jedoch für den Zweck der Restabschätzung (35) nicht ankommt.

Bei der Integration sind $\mathfrak{H}_2, \mathfrak{F}, \mathfrak{G}$ gleichmässig in δ beschränkt. Nach der in [7] § 18 verwendeten Überlegung haben wir schliesslich das Integral I von

$$(h_1 \ldots h_s)^{\frac{f}{2}-s-1} (h_1^{s-1} h_2^{s-2} \ldots h_{s-1}) h_1 dh_2 \ldots dh_s$$

mit $h_1 = p = \delta$ abzuschätzen, wobei über das Gebiet $\delta < h_2 < h_3 < \ldots < h_s < 1$ integriert wird. Nun ist $f \geq 6$, also

$$h_1^{\frac{f}{2}-1} \leq \delta^2.$$

Substituiert man

$$\frac{h_k}{h_{k+1}} = y_{k-1} \qquad (k = 2, \ldots, s-1), \qquad h_s = y_{s-1},$$

so folgt

$$I \leq \delta^2 \prod_{l=1}^{s-1} \left(\int_0^1 y_l^{\frac{l}{2}(f-l-3)-1} dy_l \right).$$

Wegen

$$f - l - 3 \geq f - s - 2 \geq \begin{cases} s-2 > 0 & (s > 2) \\ 2 & (s = 2) \end{cases}$$

konvergieren die einzelnen einfachen Integrale. Also erhalten wir die Restabschätzungen

$$I = O(\delta^2), \qquad \eta_l(\delta) = O(\delta^2)$$

und damit das Gewünschte.

Eine ähnliche Abschätzung findet sich für den Fall der Modulgruppe n-ten Grades bei SATAKE [18], wo aber die Überlegungen nicht einwandfrei durchgeführt worden sind.

§ 6. Schluss des Beweises

Zu Beginn des vorigen Paragraphen wurde gezeigt, dass der grösste gemeinsame Teiler aller Zahlen j_q mit $q > 2$ und $(q, |\mathfrak{H}|) = 1$ in $\bar{f}$ aufgeht. Ferner ist die in (36) erklärte Zahl v_q ganz. Zufolge (19), (20), (21), (22), (30) ist dann

$$\binom{c}{d} \bar{f} \varrho_f^{-1} |\mathfrak{T}_1|^{\frac{f-1}{2}} \mu(\mathfrak{S}^*, \mathfrak{T}_1)$$

ganz, also schliesslich nach (7), (14), (15), (16), (17), (18) auch

$$a_g(\mathfrak{T}) \binom{c}{d} 2^{-r} \frac{2B_g}{g} \prod_{k=1}^{c} \frac{b_k B_{2k}}{k} \prod_{l=c+1}^{g-1} \frac{B_{2l}}{l} = a_g(\mathfrak{T}) \binom{c}{d} d_{g,r} \tag{37}$$

eine ganze Zahl. Dabei wurde $ab > 0$ vorausgesetzt. Im Falle $ab = 0$ ist in (22) für $v(\mathfrak{H})$ der Wert $2/E(\mathfrak{H})$ zu setzen, und dann kann man mit der in § 2 benutzten direkten Schlussweise feststellen, dass $a_g(\mathfrak{T}) d_{g,r}$ ganz ist; ferner ist dafür $\binom{c}{d} = 1$.

Zum Beweise des Satzes kann weiterhin $g \equiv 2 \pmod 4$ angenommen werden. Es ist $c = \left[\frac{f}{2}\right]$ und $d = \frac{b}{2}$; dabei sind für $\varepsilon = 1$ die Werte $d = t = 1, 3, \ldots, \frac{g}{2}$ zulässig und für $\varepsilon = -1$ die Werte $d = g - t \leq g - \frac{r}{2}$. Ist nun $r \equiv 2 \pmod 4$, so kann man speziell $\varepsilon = -1$, $t = \frac{r}{2}$, $a = ab = 0$ wählen. Ist $r \equiv 1 \pmod 4$, so nehme man entsprechend $\varepsilon = -1$, $t = \frac{r+1}{2}$, $d = g - \frac{r+1}{2} = c$, also $\binom{c}{d} = 1$. Ist $r \equiv 0$ oder $3 \pmod 4$, so ist c gerade, und dann nehme man für d sämtliche mit $\varepsilon = 1$ oder $\varepsilon = -1$ zulässigen Werte, also $d = 1, 3, \ldots, c-3, c-1$. Enthält nun die gerade Zahl c eine ungerade Primzahl p zur genauen Potenz p^k $(k > 0)$, so ist der binomische Koeffizient $\binom{c}{d}$ für $d = p^k$ zu p teilerfremd. Bei $p = 2$ folgt leicht, dass die Zahlen $\binom{c}{1}, \binom{c}{3}, \ldots, \binom{c}{c-1}$ alle durch 2^k teilbar sind, während aber c nicht durch 2^{k+1} teilbar ist. Also ist dann 2^k der grösste gemeinsame Teiler jener binomischen Koeffizienten, und in der Aussage bei (37) kann daher $\binom{c}{d}$ durch 2^k ersetzt werden. Da $r \geq 1$ ist, so folgt jetzt die restliche Behauptung des Satzes.

Es wäre wünschenswert, für den Satz auch im Falle $g \equiv 2 \pmod 4$ einen einfacheren Beweis zu geben, doch ist mir dies nicht gelungen. Von gewissem Interesse dürfte noch folgende Bemerkung sein. Indem man die algebraischen Beziehungen zwischen den Modulformen $s_g(\mathfrak{Z})$ benutzt, kann man den Eisensteinschen Satz über die Potenzreihen algebraischer Funktionen sinngemäss übertragen und insbesondere zeigen, dass auf grund des ersten Teiles unseres Satzes auch im Falle $g \equiv 2 \pmod 4$ nur endlich viele verschiedene Primzahlen in den Nennern aller $a_g(\mathfrak{T})$ bei festem g auftreten können. Die Beschränktheit der Nenner ergibt sich aber auf diesem Wege nicht.

Literatur

[1] Siegel, C. L.: Über die analytische Theorie der quadratischen Formen. Ann. of Math. 36, 527–606 (1935).

[2] Siegel, C. L.: Über die analytische Theorie der quadratischen Formen II. Ann. of Math. 37, 230–263 (1936).

[3] Siegel, C. L.: Einführung in die Theorie der Modulfunktionen n-ten Grades. Math. Ann. 116, 617–657 (1939).

[4] Siegel, C. L.: Einheiten quadratischer Formen. Abh. Math. Sem. Hansischen Univ. 13, 209–239 (1940).

[5] Siegel, C. L.: On the theory of indefinite quadratic forms. Ann. of Math. 45, 577–622 (1944).

[6] Siegel, C. L.: Some remarks on discontinuous groups. Ann. of Math. 46, 708–718 (1945).

[7] Siegel, C. L.: Zur Reduktionstheorie quadratischer Formen. Publ. Math. Soc. Japan 5, VII + 69 S. (1959).

[8] Witt, E.: Eine Identität zwischen Modulformen zweiten Grades. Abh. Math. Sem. Hansischen Univ. 14, 323–337 (1941).

[9] Jensen, K. L.: Om talteoretiske Egenskaber ved de Bernoulliske Tal. Nyt Tidskr. for Mat. B 26, 73–83 (1915).

[10] Minkowski, H.: Zur Theorie der positiven quadratischen Formen. Journ. reine angew. Math. 101, 196–202 (1887).

[11] Allendoerfer, C. B.: The Euler number of a Riemannian manifold. Amer. J. Math. 62, 243–248 (1940).

[12] Fenchel, W.: On total curvatures of Riemannian manifolds I. Journ. London Math. Soc. 15, 15–22 (1940).

[13] Chern, S.-S.: A simple intrinsic proof of the Gauss-Bonnet formula for closed Riemannian manifolds. Ann. of Math. 45, 747–752 (1944).

[14] Hopf, H. und Samelson, H.: Ein Satz über die Wirkungsräume geschlossener Liescher Gruppen. Comm. Math. Helv. 13, 240–251 (1941).

[15] Siegel, C. L.: Symplectic geometry. Amer. J. Math. 65, 1–86 (1943).

[16] Allendoerfer, C. B. and Weil, A.: The Gauss-Bonnet theorem for Riemannian polyhedra. Trans. Amer. Math. Soc. 53, 101–129 (1943).

[17] Chern, S.-S.: On the curvatura integra in a Riemannian manifold. Ann. of Math. 46, 674–684 (1945).

[18] Satake, J.: The Gauss-Bonnet theorem for V-manifolds. J. Math. Soc. Japan 9, 464–492 (1957).

Indleveret til Selskabet den 6. marts 1964.
Færdig fra trykkeriet den 24. november 1964.

Matematisk-fysiske Meddelelser
udgivet af
Det Kongelige Danske Videnskabernes Selskab
Bind **34,** nr. 7

Mat. Fys. Medd. Dan. Vid. Selsk. **34,** no. 7 (1964)

DIE FOURIERKOEFFIZIENTEN DER EISENSTEINREIHEN ZWEITEN GRADES

VON

HANS MAASS

København 1964
Kommissionær: Ejnar Munksgaard

Synopsis

Die Fourierkoeffizienten $a_k(T)$ der Eisensteinreihen zur Modulgruppe n-ten Grades und zur Dimension $-k$ lassen sich, wenn man von einem elementaren Faktor absieht, nach C. L. SIEGEL als Produkt gewisser p-adischer Darstellungsdichten schreiben. Durch Berechnung dieser Dichten gelangt man im Falle $n = 2$ zu einer expliziten Formel für die $a_k(T)$ zu primitiven Matrizen T. Auf diesen speziellen Fall kann die Berechnung beliebiger Fourierkoeffizienten mit Hilfe einer Rekursionsformel zurückgeführt werden, die man aus der verallgemeinerten Heckeschen Operatorentheorie bezieht. Eine eingehende Analyse ergibt nun für die rationalen Zahlen $a_k(T)$ im Falle $n = 2$ bei festem k einen gemeinsamen Nenner, der sich nur aus irregulären Primzahlen (im Sinne Kummers) zusammensetzt. Für $k = 4, 6, 8, 10, 12$ wird insbesondere der größte gemeinsame Teiler aller $a_k(T)$ mitgeteilt.

PRINTED IN DENMARK
BIANCO LUNOS BOGTRYKKERI A/S

Die Fourierkoeffizienten $a_k(T)$ der von C. L. SIEGEL eingeführten Eisensteinreihen n-ten Grades zur Dimension $-k$ $\left(k \equiv 0 \pmod 2,\ k > n+1\right)$:

$$G_{-k}(Z) = \sum_{\{C,D\}} |CZ + D|^{-k}, \tag{1}$$

wobei über ein volles System von n-reihigen nicht-assoziierten teilerfremden symmetrischen Matrizenpaaren C,D summiert wird und Z eine symmetrische komplexe Matrix mit positivem Imaginärteil bezeichnet, sind bisher wenig untersucht worden. Es ist seit langem bekannt [4], daß diese Koeffizienten rational sind und von Fall zu Fall numerisch berechnet werden können. Solche Berechnungen werden aber selbst im Falle $n = 2$ als sehr mühselig angesehen [1]. Eine interessante Entdeckung Siegels, die wesentlich über [4] hinausführt, ist neueren Datums [6]. Sie besagt, daß das Produkt der gekürzten Zähler der k mit Bernoullischen Zahlen gebildeten Quotienten $\frac{B_{2\nu}}{2\nu}$ $(\nu = 1,2,\ldots,k-1)$ und $\frac{B_k}{k}$, von einer Potenz von 2 abgesehen, einen gemeinsamen Nenner aller $a_k(T)$ bei gegebenen k und n bildet. Einem Satz von K. L. JENSEN [2] zufolge setzen sich die gekürzten Nenner der $a_k(T)$ demnach nur aus der Primzahl 2 und gewissen irregulären Primzahlen p zusammen. p heißt irregulär, wenn die Klassenzahl des Körpers der p-ten Einheitzwurseln durch p teilbar ist. Die Bernoullischen Zahlen B_ν werden hier in ihrer Gesamtheit symbolisch $(B^\nu \to B_\nu)$ durch $(B+1)^h - B^h = 0$ für $h \geqq 2$ definiert.

Bei dieser Sachlage hielt ich eine Beschränkung auf den Fall $n = 2$ für gerechtfertigt, um die Analyse der $a_k(T)$ möglichst weit treiben zu können. Wir setzen nun

$$2T = \begin{pmatrix} 2t_0 & t_1 \\ t_1 & 2t_2 \end{pmatrix} \quad \text{und} \quad e(T) = \text{g.g.T.}(t_0,t_1,t_2) \tag{2}$$

mit ganz rationalen t_0,t_1,t_2. Es darf und soll angenommen werden, daß T positiv ist, da $a_k(T)$ im Falle $|T| = 0$ als Fourierkoeffizient einer Eisen-

steinreihe ersten Grades hinreichend bekannt ist. Es gelingt die explizite Berechnung von $a_k(T)$ für primitive, durch $e(T) = 1$ gekennzeichnete T. Der Fall eines beliebigen $T > 0$ wird auf den soeben bezeichneten Spezialfall mit Hilfe einer allgemeinen Koeffizientenrelation aus der Theorie der verallgemeinerten Heckeschen Operatoren [3] rekursiv zurückgeführt. Auf Grund der angegebenen Formeln ist festzustellen, daß $a_k(T)$ bei gegebenem k im Falle $n = 2$ durch $e(T)$ und $|2T|$ eindeutig bestimmt ist. Dieser Satz steht in bemerkenswerter Analogie zu der Aussage, daß die Klassenzahl des Geschlechts von $2T$ nur von den Ordnungsinvarianten, nämlich $e(T)$ und $|2T|$ abhängt, stellt aber wohl eine Besonderheit des Falles $n = 2$ dar. Ferner ergibt sich, daß ein gemeinsamer Nenner der Koeffizienten $a_k(T)$ zu primitiven T bei gegebenem k auch ein Nenner aller $a_k(T)$ ist. Schließlich zeigt sich, daß

$$m_k = \frac{k(2k-2)}{qB_kB_{2k-2}} \tag{3}$$

im Falle $n = 2$ ein gemeinsamer Teiler aller $a_k(T)$ mit $T > 0$ ist. Hierin ist q der größte Teiler von $(k-1)N_{2k-2}$, der sich nur aus Primteilern $p \equiv -1 \pmod 4$ des gekürzten Nenners N_{2k-2} von B_{2k-2} zusammensetzt. Diese Teilbarkeitsaussage stellt eine Verschärfung des Siegelschen Resultats für den Spezialfall $n = 2$ dar. Tatsächlich ist m_k für $k = 4,6,8,10,12$ sogar der größe gemeinsame Teiler der Fourierkoeffizienten $a_k(T)$ mit $T > 0$.

§ 1. Die allgemeine Koeffizientenformel

Für beliebiges n, halbganze symmetrische Matrizen $T > 0$ und gerades $k > n+1$ entnimmt man aus [4] die Darstellung

$$a_k(T) = (-1)^{\frac{nk}{2}} 2^{n\left(k-\frac{n-1}{2}\right)} \prod_{\nu=0}^{n-1} \frac{\pi^{k-\frac{\nu}{2}}}{\Gamma\left(k-\frac{\nu}{2}\right)} |T|^{k-\frac{n+1}{2}} \prod_p S_p, \tag{4}$$

wobei p alle Primzahlen durchläuft und S_p den p-Beitrag zur sogenannten singulären Reihe bezeichnet. Er ist gegeben durch

$$S_p = \sum_{R_p \bmod 1} e^{-2\pi i \sigma(TR_p)} (\nu(R_p))^{-k}. \tag{5}$$

Summiert wird hier über ein vollständiges System mod 1 verschiedener n-reihiger symmetrischer rationaler Matrizen R_p mit einer Potenz von p als

Nenner. $\nu(R_p)$ bezeichnet das Produkt der gekürzten Nenner der Elementarteiler von R_p und allgemein $\sigma(A)$ die Spur von A. Um S_p in gewisser Weise als p-adische Darstellungsdichte zu deuten, empfiehlt sich in der weiteren Behandlung von S_p gegenüber [4] eine geringfügige Modifikation, die auf einem Gedanken von E. WITT [7] beruht. Sie gestattet eine einheitliche Behandlung aller Primzahlen sowie eine Vereinfachung in der Berechnung der benötigten Gaußschen Summen und führt schließlich zu dem Ergebnis in der gewünschten Form. Um $(\nu(R_p))^{-k}$ in geeigneter Weise durch Gaußsche Summen auszudrücken, führen wir

$$G = \sum_{K \bmod q} e^{2\pi i \sigma(FR_p[K])} \qquad (q = p^a) \tag{6}$$

mit

$$F = \begin{pmatrix} 0 & \frac{1}{2} \\ \frac{1}{2} & 0 \end{pmatrix}$$

ein. a sei so groß gewählt, daß qR_p ganz ist. Summiert wird über ein volles System $\bmod q$ verschiedener ganzer Matrizen $K = K^{(n,2)}$.

Da G nur von $R_p \bmod 1$ abhängt und gegenüber den Transformationen $R_p \to R_p[U]$ mit unimodularen Matrizen U invariant ist, so kann R_p in G durch eine Normalform der folgenden Art ersetzt werden:

$$R_p[U] \equiv \left(\begin{array}{cccc|ccc} a_1 q^{-\mu_1} & & & & & & \\ & a_2 p^{-\mu_2} & & 0 & & & \\ & & \ddots & & & 0 & \\ & 0 & & a_r p^{-\mu_r} & & & \\ \hline & & & & F_1 p^{-\nu_1} & & 0 \\ & & & & & F_2 p^{-\nu_2} & \\ & 0 & & & 0 & & \ddots \\ & & & & & & F_s p^{-\nu_s} \end{array}\right) \pmod 1.$$

Hierin ist

$$F_h = \begin{pmatrix} \alpha_h & \beta_h \\ \beta_h & \gamma_h \end{pmatrix} \quad (h = 1,2,\ldots,s),$$

also $r + 2s = n$, und

$$(a_h, p) = (\beta_h, p) = 1, \quad \alpha_h \equiv \gamma_h \equiv 0 \pmod p.$$

Im Falle $p > 2$ kann überdies $s = 0$ angenommen werden, wovon hier jedoch kein Gebrauch gemacht wird. Offenbar ist

$$\nu(R_p) = \nu(R_p[U]) = p^{\mu_1 + \ldots + \mu_r + 2\nu_1 + \ldots + 2\nu_s}.$$

Mit der angegebenen Normalform an Stelle von R_p in G und der Zerlegung

$$K' = (\mathfrak{l}_1, \ldots, \mathfrak{l}_r, L_1 \ldots, L_s), \quad \mathfrak{l}_h = \mathfrak{l}_h^{(2,1)}, \quad L_h = L_h^{(2)}$$

ergibt sich unmittelbar, wenn unnötige Indices nachträglich gestrichen werden,

$$\begin{aligned} G &= \prod_{h=1}^{r} \sum_{\mathfrak{l} \bmod q} e^{2\pi i a_h p^{-\mu_h} F[\mathfrak{l}]} \prod_{h=1}^{s} \sum_{L \bmod q} e^{2\pi i p^{-\nu_h} \sigma(F[L] F_h)} \\ &= q^{2(r+2s)} p^{-\mu_1 - \ldots - \mu_r - 2\nu_1 - \ldots - 2\nu_s} \end{aligned}$$

oder auch

$$G^k = q^{2nk} (\nu(R_p))^{-k}.$$

Andererseits folgt mit

$$H = H^{(2k)} = \begin{pmatrix} F & & & 0 \\ & F & & \\ & & \ddots & \\ 0 & & & F \end{pmatrix},$$

da diese Matrix mit Hilfe einer unimodularen Matrix in

$$S = \begin{pmatrix} 0 & \frac{1}{2}E \\ \frac{1}{2}E & 0 \end{pmatrix} \quad (E = E^{(k)} = \text{Einheitsmatrix})$$

übergeführt werden kann,

$$\begin{aligned} G^k &= \prod_{h=1}^{k} \sum_{K_h \bmod q} e^{2\pi i \sigma(F R_p[K_h])} \\ &= \sum_{K \bmod q} e^{2\pi i \sigma(H R_p[K])} = \sum_{K \bmod q} e^{2\pi i \sigma(S R_p[K])}, \end{aligned}$$

wobei $K = K^{(n,2k)} = (K_1, K_2, \ldots, K_k)$ gesetzt ist. Nunmehr schließt man wie in [4] und erhält

$$S_p = \lim_{a \to \infty} q^{\frac{n(n+1)}{2} - 2nk} A_q(T), \tag{7}$$

wenn $A_q(T)$ die Anzahl der mod q verschiedenen ganzen Matrizen $C = C^{(2k,n)}$ bezeichnet, für welche $\frac{2}{q}(S[C] - T)$ eine gerade ganze Matrix wird. Die Rationalität von S_p ist eine Folge von

Lemma 1: *Es seien $S = S^{(m)}$ und $T = T^{(n)}$ mit $m \geqq n$ halbganze symmetrische Matrizen, p eine Primzahl und p^b die höchste Potenz von p, welche $|2T|$ teilt. Wir setzen $q = p^a$ und bezeichnen mit $A_q(S,T)$ die Anzahl der* mod q *verschiedenen ganzen Matrizen $C = C^{(m,n)}$, für welche $\frac{2}{q}(S[C] - T)$ eine gerade ganze Matrix wird. Ist $a > 2b$, so ist $q^{\frac{n(n+1)}{2} - mn} A_q(S,T)$ von a unabhängig.*

Für $p > 2$ deckt sich die Aussage dieses Lemmas mit einer Teilaussage von Hilfssatz 13 in [5]. Der Fall $p = 2$ erfordert keine wesentlich neuen Überlegungen und läßt sich in den Beweis entsprechend mit einbeziehen.

Um $A_q(T)$ als Lösungszahl eines Systems von Kongruenzen zu interpretieren, zerlegen wir C in

$$C = \begin{pmatrix} G \\ H \end{pmatrix} \quad \text{mit} \quad G = G^{(k,n)}, \quad H = H^{(k,n)}.$$

$A_q(T)$ ist dann die Anzahl der mod q verschiedenen ganzen Matrizenpaare G,H, für welche

$$\frac{1}{q}(G'H + H'G - 2T) \quad \text{ganz und gerade} \tag{8}$$

ist. Bezeichnen $\mathfrak{g}_1, \mathfrak{g}_2, \ldots \mathfrak{g}_n$ bzw. $\mathfrak{h}_1, \mathfrak{h}_2, \ldots, \mathfrak{h}_n$ die Spalten von G bzw. H und wird $2T = ((1 + \delta_{\mu\nu})t_{\mu\nu})$ mit dem Kroneckersymbol $\delta_{\mu\nu}$ gesetzt, so tritt an Stelle von (8) das gleichwertige Kongruenzensystem

$$\left.\begin{aligned} \mathfrak{g}'_\alpha \mathfrak{h}_\alpha &\equiv t_{\alpha\alpha}, \quad \mathfrak{g}'_\alpha \mathfrak{h}_\beta + \mathfrak{g}'_\beta \mathfrak{h}_\alpha \equiv t_{\alpha\beta} \pmod{q} \\ &(1 \leq \alpha, \beta \leq n, \ \alpha \neq \beta) \end{aligned}\right\} \tag{9}$$

Es ist zu beachten, daß sich die Lösungszahl $A_q(T)$ nicht ändert, wenn man T mit einer unimodularen Matrix V transformiert und mit einer zu q primen ganzen Zahl g multipliziert; denn die Forderung (8) bleibt bei einer simultanen Transformation

$$T \to gT[V], \quad H \to UHV, \quad G \to gU^*GV$$

erhalten, wenn neben V auch U eine unimodulare Matrix $\bmod q$ ist, so daß eine ganze Matrix U^* mit $U'U^* \equiv E(q)$ existiert. Wir benutzen diesen Sachverhalt im Falle $n = 2$, um zunächst T geeignet zu normieren. Sodann bestimmen wir die $H \bmod q$, für welche das System (9) Lösungen besitzt. Wegen der angegebenen Invarianz genügt es, wenn aus der Klasse der mit H äquivalenten Matrizen $\{UH \mid U \text{ unimodular } \bmod q\}$ jeweils ein eindeutig bestimmter Repräsentant H ausgewählt wird. Die Anzahl der Lösungen $G \bmod q$ hängt offenbar nur von der Äquivalenzklasse von $H \bmod q$ ab.

§ 2. Die Berechnung von $a_k(T)$ im Falle $e(T) = 1$

Wir befassen uns fortan nur noch mit dem Fall $n = 2$. $d = d(T)$ bezeichne durchweg die Diskriminante des imaginär-quadratischen Zahlkörpers, der von $\sqrt{-|2T|}$ erzeugt wird; sie ist gegenüber den invertierbaren Transformationen $T \to gT[V]$ mit rationalen g und $V = V^{(2)}$ invariant. Es sei p eine vorgegebene Primzahl, p^b die höchste Potenz von p, welche $|2T|$ teilt, und $q = p^a$ mit beliebigem $a > b$. Unter der Voraussetzung $e(T) = 1$ darf angenommen werden, daß T unter die drei Typen fällt, die durch die Kongruenzen

$$t_0 \equiv 1(q) \begin{cases} t_1 \equiv 0 \ (q) & \begin{cases} t_2 \equiv up^b \ (q), & p > 2 \\ t_2 \equiv u2^{b-2} \ (q) \end{cases} \\ t_1 \equiv 1 \ (2), \quad t_2 \equiv u2^c \ (q) & p = 2 \end{cases} u \not\equiv 0 \ (p) \qquad (10)$$

definiert werden; denn für $gT[V]$ trifft dies zu, wenn die unimodulare Matrix V und die zu q prime ganze Zahl g geeignet gewählt werden. Wegen $a > b$ erscheint b in (10) in richtiger Bedeutung. Im dritten Fall ist c irgend eine nicht negative ganze Zahl. Entsprechend den drei Fällen (10) gilt

$$-|2T| \equiv \begin{cases} -4up^b \\ -u2^b \\ t_1^2 - u2^{c+2} \end{cases} (\bmod q) \quad \text{für} \begin{cases} p > 2 \\ p = 2 \begin{cases} b \geqq 2 \\ b = 0 \end{cases} \end{cases} \qquad (11)$$

und daher

$$\left(\frac{d}{p}\right) = \begin{cases} \left(\dfrac{-u}{p}\right) & \text{für } b \equiv 0 \ (2) \\ 0 & \text{für } b \equiv 1 \ (2) \end{cases} p > 2 \qquad (12)$$

sowie

$$\left(\frac{d}{2}\right) = \left\{\begin{array}{lll} 1 & \text{für} \begin{cases} b = 0, & c > 0 \\ b \equiv 0 \ (2), & b > 0, \quad u \equiv 7 \ (8) \end{cases} & \\ -1 & \text{für} \begin{cases} b = 0, & c = 0 \\ b \equiv 0 \ (2), & b > 0, \quad u \equiv 3 \ (8) \end{cases} & p = 2 \\ 0 & \text{für} \begin{cases} b \equiv 1 \ (2) & \\ b \equiv 0 \ (2), & b > 0, \quad u \equiv 1 \ (4) \end{cases} & \end{array}\right\} \quad (13)$$

In jeder Äquivalenzklasse $H \bmod q$ gibt es, wie leicht einzusehen ist, einen Repräsentanten $H = H^{(k,2)} = (h_{\alpha\beta})$ der folgenden Art:

$$\left.\begin{array}{c} h_{11} \equiv p^{\mu}, \quad h_{22} \equiv p^{\nu}, \quad h_{\alpha\beta} \equiv 0 \pmod q \\ (0 \leqq \mu,\nu \leqq a; \quad \alpha > \beta) \end{array}\right\} \quad (14)$$

während $h = h_{12}$ aus einem festen Vertretersystem der Restklassen $\bmod p^{\nu}$ ausgewählt werden kann. Mit diesem speziellen H und $G = (g_{\alpha\beta})$ nimmt das System (9) wegen $t_0 \equiv 1 \pmod q$ die folgende Gestalt an:

$$\left.\begin{array}{c} g_{11}p^{\mu} \equiv 1, \quad g_{12}h + g_{22}p^{\nu} \equiv t_2 \\ g_{12}p^{\mu} + g_{11}h + g_{21}p^{\nu} \equiv t_1 \end{array} \pmod q\right\} \quad (15)$$

Wir bestimmen sämtliche μ,ν,h, für welche das System (15) Lösungen $g_{\alpha\beta}$ besitzt. Offenbar ist stets $\mu = 0$ und $g_{11} \equiv 1 \pmod q$. Es verbleibt

$$g_{12}h + g_{22}p^{\nu} \equiv t_2, \quad g_{12} \equiv t_1 - h - g_{21}p^{\nu} \pmod q. \quad (16)$$

Elimination von g_{12} ergibt

$$h(t_1 - h) + (g_{22} - hg_{21})p^{\nu} \equiv t_2 \pmod q,$$

und diese Kongruenz ist genau dann lösbar, wenn

$$h(t_1 - h) \equiv t_2 \pmod{p^{\nu}} \quad (17)$$

ist. Eine einfache Abzählung ergibt nun für die Anzahl $A(h,p^{\nu})$ der $\bmod q$ verschiedenen ganzen Lösungen $(g_{11},g_{12},g_{21},g_{22})$ von (15) den Wert $p^{\nu}q$ oder 0, je nachdem (17) befriedigt ist oder nicht. Eine vollständige Übersicht über die Lösungen von (17) gibt das folgende Schema. Hierin bezeichnet $A(p^{\nu})$ die Anzahl der $\bmod p^{\nu}$ verschiedenen Lösungen h von (17).

Haupttypus von T:	ν:	$A(p^\nu)$:	Nr.:
$p \neq 2$ oder $b = 0$	$0 \leqq \nu \leqq b$	$p^{\nu - \left[\frac{\nu+1}{2}\right]}$	1
	$b < \nu \leqq a$	$p^{\frac{1}{2}b}\left(1 + \left(\frac{d}{p}\right)\right)\left(\frac{d}{p}\right)$	2
$p = 2$ und $b \geqq 2$	$0 \leqq \nu < b - 1$	$2^{\nu - \left[\frac{\nu+1}{2}\right]}$	3
	$\nu = b - 1$	$2^{\frac{1}{2}b-1}\delta\left(\frac{b}{2}\right)$	4
	$\nu = b$	$2^{\frac{1}{2}b}\left(\frac{d}{2}\right)^2$	5
	$b < \nu \leqq a$	$2^{\frac{1}{2}b}\left(1 + \left(\frac{d}{2}\right)\right)\left(\frac{d}{2}\right)$	6

Hierin ist $\delta(x) = 1$ oder 0, je nachdem x ganz rational ist oder nicht. Um die Vollständigkeit der Tabelle zu belegen, hat man die Kongruenz (17) für die drei Haupttypen von T zu diskutieren.

1. $p > 2$: Nach (10) hat man

$$h^2 \equiv -up^b \pmod{p^\nu}$$

zu lösen. Hier mag der Hinweis genügen, daß Lösungen für $\nu > b$ nur dann existieren, wenn $b \equiv 0 \pmod 2$ und $\left(\frac{-u}{p}\right) = 1$ ist, was so viel wie $\left(\frac{d}{p}\right) = 1$ bedeutet. Man findet nun leicht die unter Nr. 1 und 2 angegebenen Werte von $A(p^\nu)$ für $p > 2$.

2. $p = 2$, $b \geqq 2$: Nun ist

$$h^2 \equiv -u2^{b-2} \pmod{2^\nu}$$

zu lösen. Hier ist zu beachten, daß $\nu > b - 2$ nur dann Lösungen gestattet, wenn $b \equiv 0 \pmod 2$ ist. $\nu = b - 1$ ergibt keine weitere Bedingung. Für $\nu = b$ hat man zusätzlich $-u \equiv 1 \pmod 4$, also $\left(\frac{d}{2}\right) \neq 0$ zu fordern

und im Falle $v > b$ darüber hinaus $-u \equiv 1 \pmod 8$ oder $\left(\frac{d}{2}\right) = 1$. Einfache Abzählungen ergeben die unter Nr. 3 bis 6 angegebenen Werte für $A(2^v)$.

3. $p = 2$, $b = 0$: Wir multiplizieren (17) mit -4 und erhalten die gleichwertige Kongruenz

$$(2h - t_1)^2 \equiv t_1^2 - u2^{c+2} \pmod{2^{v+2}}.$$

Wir konstatieren, daß $v = 0$ genau eine Lösung gestattet und daß im Falle $v > 0$ notwendig $c > 0$, d. h. $\left(\frac{d}{2}\right) = 1$ ist. Ist diese Bedingung erfüllt, so gibt es genau zwei Lösungen, womit $A(p^v)$ unter Nr. 1 und 2 für $p = 2$ verifiziert ist.

Da die Elemente $g_{\alpha\beta}$ für $\alpha > 2$ willkürlich gewählt werden können, so ist die Anzahl $B(h,p^v)$ der $\bmod q$ verschiedenen Lösungen G von (9), sofern H den durch h und p^v gekennzeichneten speziellen Repräsentanten in der Äquivalenzklasse $\bmod q$ von H bezeichnet und (17) erfüllt ist, gleich $q^{2(k-2)}A(h,p^v) = q^{2k-3}p^v$. Wir brauchen jetzt nur noch die Anzahl $C(h,p^v)$ der $\bmod q$ verschiedenen Matrizen UH in der Äquivalenzklasse $\bmod q$ von H zu bestimmen. Dabei ist U eine beliebige unimodulare Matrix $\bmod q$. Sind $\mathfrak{u}_1,\mathfrak{u}_2$ die beiden ersten Spalten von U, so ist

$$UH \equiv (\mathfrak{u}_1, \mathfrak{u}_1 h + \mathfrak{u}_2 p^v) \pmod q,$$

woraus hervorgeht, daß $C(h,p^v)$ von h unabhängig ist, so daß zur Bestimmung von $C(h,p^v)$ das Element h durch 0 ersetzt werden kann. Die $\bmod q$ primitiven Spalten $\mathfrak{u}_1$, die zu einer unimodularen Matrix $\bmod q$ ergänzt werden können, sind dadurch bestimmt, daß nicht alle ihre Elemente durch p teilbar sind. Für die Anzahl der $\bmod q$ verschiedenen $\mathfrak{u}_1$ findet man somit den Ausdruck

$$q^k - p^{(a-1)k} = q^k(1 - p^{-k}).$$

Gefragt wird nun nach der Anzahl der $\bmod p^{a-v}$ verschiedenen primitiven Spalten $\mathfrak{u}_2 \bmod q$ derart, daß $(\mathfrak{u}_1,\mathfrak{u}_2)$ zu einer primitiven Matrix $\bmod q$ ergänzbar wird. Diese Anzahl hängt offenbar von der speziellen Wahl von $\mathfrak{u}_1$ nicht ab, so daß für $\mathfrak{u}_1$ auch die erste Spalte der Einheitsmatrix gewählt werden kann. Bezüglich $\mathfrak{u}_2$ ist dann zu fordern, daß die aus den $k-1$ letzten Elementen von $\mathfrak{u}_2$ bestehende Spalte eine primitive Spalte $\bmod q$ ist,

während das erste Element von u_2 willkürlich wählbar ist. Die Anzahl der primitiven $u_2 \bmod p^{a-\nu}$ zu gegebenem u_1 ist also

$$p^{a-\nu}(p^{(k-1)(a-\nu)} - p^{(k-1)(a-\nu-1)}) = p^{(a-\nu)k}(1-p^{1-k}) \quad \text{oder } 1,$$

je nachdem $a < \nu$ oder $a = \nu$ ist. Damit ergibt sich

$$C(h,p^\nu) = \begin{cases} q^{2k}p^{-\nu k}(1-p^{-k})(1-p^{1-k}) & \text{für } \nu < a, \\ q^{2k}p^{-ak}(1-p^{-k}) & \text{für } \nu = a \end{cases}$$

und für die Anzahl $A_q(T)$ der $\bmod q$ verschiedenen Lösungen G,H von (9) schließlich

$$\begin{aligned} A_q(T) &= \sum_{\substack{0 \leqq \nu \leqq a \\ h \bmod p^\nu}} B(h,p^\nu)C(h,p^\nu) \\ &= q^{4k-3}(1-p^{-k}) \sum_{\substack{0 \leqq \nu \leqq a \\ h \bmod p^\nu}} p^{\nu(1-k)}(1-p^{1-k})^* \\ &= q^{4k-3}(1-p^{-k}) \sum_{0 \leqq \nu \leqq a} A(p^\nu)p^{\nu(1-k)}(1-p^{1-k})^*. \end{aligned}$$

Die Summation erfolgt hier über alle Lösungen $h \bmod p^\nu$ von (17). Die mit einem Stern* bezeichnete Klammer ist im Falle $\nu = a$ durch 1 zu ersetzen. Nach kurzer Rechnung erhält man mit Hilfe von

$$\sum_{\nu=0}^{b} p^{\nu - \left[\frac{\nu+1}{2}\right]} p^{\nu(1-k)} = (1+p^{1-k}) \sum_{\mu=0}^{\left[\frac{b-1}{2}\right]} p^{\mu(3-2k)} + \delta\left(\frac{b}{2}\right) p^{\frac{b}{2}(3-2k)}$$

für $a > b$ die Kongruenzlösungsanzahlen

$$A_q(T) = q^{4k-3} \frac{(1-p^{-k})(1-p^{2-2k})}{1-\left(\frac{d}{p}\right)p^{1-k}} \left\{ \left(1 - \left(\frac{d}{p}\right)p^{1-k}\right) \sum_{\mu=0}^{j} p^{\mu(3-2k)} + \left(\frac{d}{p}\right)^2 p^{(j+1)(3-2k)} \right\} \tag{18}$$

mit

$$j = \begin{cases} \left[\frac{b-1}{2}\right] & \text{für } p > 2, \\ \left[\frac{b-2}{2}\right] & \text{für } p = 2, \end{cases}$$

folglich

$$S_p = q^{3-4k} A_q(T) \quad \text{für } a > b. \tag{19}$$

Es sei $\chi(h)$ der Charakter mod d, der für $h > 0$ mit $\left(\frac{d}{h}\right)$ übereinstimmt. Wir setzen

$$\zeta(s) = \sum_{h=1}^{\infty} h^{-s}, \quad L(s,\chi) = \sum_{h=1}^{\infty} \chi(h) h^{-s}. \tag{20}$$

Aus (4) ergibt sich dann mit Hilfe von (18) und (19) für $n = 2$ und $e(T) = 1$ die Koeffizientenformel

$$\left.\begin{aligned} a_k(T) = {} & \frac{2(2\pi)^{2k-1} L(k-1,\chi)}{(2k-2)!\,\zeta(k)\zeta(2k-2)} \cdot \\ & \cdot |2T|^{k-\frac{3}{2}} \prod_{p \mid 2\,|2T|} \left\{ \left(1 - \left(\frac{d}{p}\right) p^{1-k}\right) \sum_{\mu=0}^{j} p^{\mu(3-2k)} + \left(\frac{d}{p}\right)^2 p^{(j+1)(3-2k)} \right\}. \end{aligned}\right\} \tag{21}$$

Bekanntlich ist

$$\zeta(k) = \frac{(-1)^{\frac{k}{2}-1} (2\pi)^k}{2 \cdot k!} B_k, \quad \zeta(2k-2) = \frac{(2\pi)^{2k-2}}{2 \cdot (2k-2)!} B_{2k-2} \tag{22}$$

und

$$L(k-1,\chi) = \frac{1}{\sqrt{|d|}} \sum_{q=1}^{|d|-1} \left(\frac{d}{q}\right) \sum_{m=1}^{\infty} \frac{\sin\left(2\pi \frac{d}{|q|} m\right)}{m^{k-1}} \qquad (d < 0).$$

Die unendliche Reihe über m kann, wenn man von einem elementaren Faktor absieht, als Funktionswert des Bernoullischen Polynoms $(x+B)^{k-1}$ in symbolischer Schreibweise $(B^\nu \to B_\nu)$ einfach dargestellt werden. Man erhält so

$$L(k-1,\chi) = \frac{(-1)^{\frac{k}{2}} (2\pi)^{k-1}}{2(k-1)!\sqrt{|d|}} \sum_{q=1}^{|d|-1} \left(\frac{d}{q}\right) \left(\frac{q}{|d|} + B\right)^{k-1} \tag{23}$$

und schließlich das folgende Resultat:

Satz 1: *Für $n = 2$, $k \equiv 0 \pmod 2$, $k \geq 4$ und $T > 0$, $e(T) = 1$ ist*

$$a_k(T) = -\frac{4k}{B_k B_{2k-2}} \frac{1}{|d|} \sum_{q=1}^{|d|-1} \left(\frac{d}{q}\right) (q + |d|B)^{k-1} b_k(T)$$

mit

$$b_k(T) = \left(\frac{|2T|}{|d|}\right)^{k-\frac{3}{2}} \prod_{p|2|2T|} \left\{\left(1 - \left(\frac{d}{p}\right)p^{1-k}\right) \sum_{\mu=0}^{j} p^{\mu(3-2k)} + \left(\frac{d}{p}\right)^2 p^{(j+1)(3-2k)}\right\}.$$

Hierin ist p^b *die höchste Potenz von* p, *welche* $|2T|$ *teilt, und* $j = \left[\frac{b-1}{2}\right]$ *oder* $\left[\frac{b-2}{2}\right]$, *je nachdem* $p > 2$ *oder* $p = 2$ *ist.* $b_k(T)$ *ist stets ganz rational.*

Um auch noch die Ganzzahligkeit von $b_k(T)$ zu beweisen, setzen wir $b = b_p$, $j = j_p$ sowie

$$d = -\prod_{p \geq 2} p^{\alpha_p}.$$

Aus den Diskriminanteneigenschaften folgt

$$b_p = \alpha_p + 2(j_p + \varepsilon_p) \quad \text{mit } \varepsilon_p = \left(\frac{d}{p}\right)^2 \quad \text{für } p \geq 2,$$

mithin

$$\left(\frac{|2T|}{|d|}\right)^{k-\frac{3}{2}} = \left(\prod_{p \geq 2} p^{b_p - \alpha_p}\right)^{k-\frac{3}{2}} = \prod_{p \geq 2} p^{(j_p + \varepsilon_p)(2k-3)},$$

woraus die behauptete Ganzzahligkeit von $b_k(T)$ erhellt.

§ 3. Die Reduktion auf den Fall $e(T) = 1$

Ist der Rang der halbganzen Matrix $T = T^{(n)} \geq 0$ kleiner als zwei, so tritt $a_k(T)$ auch als Fourierkoeffizient der Eisensteinreihe ersten Grades auf. Insbesondere ist $a_k(T) = a_k(t)$, wenn alle Elemente von $T = (t_{\mu\nu})$ mit eventueller Ausnahme von $t = t_{11}$ verschwinden. p bezeichne eine beliebige Primzahl. Auf Grund von [3], S. 117 (126) kann festgestellt werden, daß die Fourierkoeffizienten $a_k(T)$ der Eisensteinreihe n-ten Grades der folgenden Beziehung genügen:

$$\left.\begin{aligned} &\prod_{\nu=2}^{n} (1 + p^{\nu-k}) a_k(p) a_k(T) = \\ &p^{k-1} a_k(1) \sum_{\nu=0}^{n} \sum_{U} a_k\left(\frac{1}{p} T[US_{p,\nu}]\right) p^{\frac{1}{2}(n-\nu)(n+1-\nu-2k)}. \end{aligned}\right\} \quad (24)$$

Hierin ist

$$S_{p,\nu} = \begin{pmatrix} E^{(\nu)} & 0 \\ 0 & pE^{(n-\nu)} \end{pmatrix} \quad (25)$$

und bei gegebenem ν durchläuft $U = (Q^{(n,\nu)}, *)$ ein volles System von unimodularen Matrizen, so daß die aus den ν ersten Spalten von U bestehenden Teilmatrizen $Q \bmod p$ paarweise nicht assoziiert und

$$\frac{1}{p} T[US_{p,\nu}] \quad \text{halbganze Matrizen} \tag{26}$$

sind. Zwei Matrizen Q_1, Q_2 heißen $\bmod p$ assoziiert, wenn $Q_2 = Q_1 V$ mit einer unimodularen Matrix $\bmod p$ $V = V^{(\nu)}$ gilt. Auf die Forderung (26) werden wir verzichten und statt dessen $a_k(T) = 0$ für nicht-halbganze T setzen. Da die Eisensteinreihe nicht im Sinne von [3] normiert ist, so erscheint auf der rechten Seite von (24) abweichend von der zitierten Formel der Faktor $a_k(1)$; er fällt wieder heraus, wenn man

$$a_k(t) = a_k(1) \sum_{\substack{g/t \\ g > 0}} g^{k-1} \tag{27}$$

berücksichtigt.

Im Falle $n = 2$ nimmt (24) mit

$$U = \begin{cases} \begin{pmatrix} 1 & 0 \\ 0 & 1 \end{pmatrix}, \quad \begin{pmatrix} u & 1 \\ 1 & 0 \end{pmatrix} \ (u = 0,1,2,\ldots,p-1) & \text{für } \nu = 1 \\ \begin{pmatrix} 1 & 0 \\ 0 & 1 \end{pmatrix} & \text{für } \nu = 0,2 \end{cases}$$

nach einfacher Umformung folgende Gestalt an:

$$\left.\begin{aligned} a_k(pT) = (1 + p^{k-1})(1 + p^{k-2}) a_k(T) - p^{2k-3} a_k\left(\frac{1}{p} T\right) - \\ - p^{k-2} a_k\left(\frac{1}{p} T \begin{bmatrix} 1 & 0 \\ 0 & p \end{bmatrix}\right) - \sum_{u=0}^{p-1} p^{k-2} a_k\left(\frac{1}{p} T \begin{bmatrix} u & p \\ 1 & 0 \end{bmatrix}\right). \end{aligned}\right\} \tag{28}$$

Diese Formel gestattet, wie sogleich ausgeführt wird, die Berechnung von $a_k(T)$ auf den schon behandelten Fall $e(T) = 1$ zurückzuführen.

Satz 2: *Im Falle $n = 2$ ist $a_k(T)$ für $T > 0$ durch*

$$e = e(T) \quad \text{und} \quad D = D(T) = |2T| e^{-2} \tag{29}$$

eindeutig bestimmt, so daß

$$a_k(T) = \alpha_k(e, D) \tag{30}$$

gesetzt werden kann. Es gilt

$$\alpha_k(pe,D) = \left\{(1+p^{k-1})(1+p^{k-2}) - \left(1+\left(\frac{-D}{p}\right)\right)p^{k-2}\right\}\alpha_k(e,D) -$$

$$-\left(p-\left(\frac{-D}{p}\right)\right)p^{k-2}\alpha_k(p^{-1}e,p^2D) - p^{2k-3}\alpha_k(p^{-1}e,D)$$

für eine beliebige Primzahl $p \geqq 2$ *mit der Maßgabe, daß* $\alpha_k(e,D) = 0$ *zu setzen ist, wenn* e *keine natürliche Zahl ist.*

Wir rechtfertigen den Ansatz (30) auf Grund von (28) mit vollständiger Induktion nach der Anzahl $h(T)$ der Primzahlen, aus denen sich $e(T)$ zusammensetzt:

$$e(T) = \prod_{p \geq 2} p^{\nu_p}, \quad h(T) = \sum_{p \geq 2} \nu_p.$$

Im Falle $h(T) = 0$ ist (30) eine Folge von Satz 1. Wir nehmen an, daß (30) für alle Matrizen S an Stelle von T mit $h(S) \leqq h(T)$ schon gilt, und beweisen dann (30) für pe an Stelle von e, d. h. für $h(T)+1$ an Stelle von $h(T)$. Da $a_k(T)$ gegenüber den unimodularen Transformationen $T \to T[U]$ invariant ist, können wir uns T bezüglich p immer so normiert denken, daß t_0 durch keine höhere Potenz von p teilbar ist wie $e(T)$, so daß $t_0 e^{-1}$ eine zu p prime ganze Zahl ist. $e_p = e_p(T)$ bezeichne die größte Potenz von p, welche $e(T)$ teilt. Neben (2) verwenden wir die Bezeichnung $2S = \begin{pmatrix} 2s_0 & s_1 \\ s_1 & 2s_2 \end{pmatrix}$. Wir diskutieren die in (28) bezeichneten Fälle von S:

1. Für $S = \frac{1}{p}T$ ist ersichtlich $e(S) = p^{-1}e(T)$ und

$$D(S) = |2S|e^{-2}(S) = |2T|e^{-2}(T) = D(T),$$

also

$$a_k\left(\frac{1}{p}T\right) = \alpha_k(p^{-1}e,D).$$

2. Für $S = \frac{1}{p}T\begin{bmatrix} 1 & 0 \\ 0 & p \end{bmatrix}$ ist $s_0 = p^{-1}t_0$, $s_1 = t_1$, $s_2 = pt_2$. Gemäß unserer Normierung ist also

$$e(S) = \text{g.g.T.}(p^{-1}t_0, t_1, pt_2) = p^{-1}e(T)$$

sowie

$$D(S) = |2S|e^{-2}(S) = |2T|e^{-2}(T)p^2 = p^2D(T),$$

folglich

$$a_k\left(\frac{1}{p}T\begin{bmatrix}1 & 0\\ 0 & p\end{bmatrix}\right) = \alpha_k(p^{-1}e, p^2D).$$

3. Für $S = \frac{1}{p}T\begin{bmatrix}u & p\\ 1 & 0\end{bmatrix}$ hat man

$$s_0 = p^{-1}(t_0u^2 + t_1u + t_2), \quad s_1 = 2t_0u + t_1, \quad s_2 = pt_0,$$

so daß offenbar $|2S| = |2T|$ und

$$e(S) = e(T) \quad \text{oder} \quad p^{-1}e(T)$$

gilt. Der erste Fall ist gleichwertig mit $s_0 \equiv 0 \pmod{e_p}$. Wir haben demnach die Anzahl der $\bmod p$ verschiedenen Lösungen von

$$t_0u^2 + t_1u + t_2 \equiv 0 \pmod{pe_p} \tag{31}$$

zu bestimmen. Gemäß der Bedeutung von e_p sind die durch $t_\nu = r_\nu e_p$ bestimmten Zahlen r_ν ganz; gemäß unserer Normierung ist p kein Teiler von r_0. Außerdem unterscheidet sich

$$D_p = 4r_0r_2 - r_1^2 = |2T|e_p^{-2}(T)$$

von $D = |2T|e^{-2}(T)$ nur um das Quadrat einer ganzen durch p nicht teilbaren Zahl, so daß $\left(\frac{-D_p}{p}\right) = \left(\frac{-D}{p}\right)$ ist. An Stelle von (31) erhalten wir nun

$$r_0u^2 + r_1u + r_2 \equiv 0 \pmod{p}. \tag{32}$$

Eine gleichwertige Kongruenz ergibt sich nach Multiplikation mit $4r_0$ in der Gestalt

$$(2r_0u + r_1)^2 \equiv -D_p \pmod{p^\alpha} \quad \text{mit } \alpha = \begin{cases}1 \text{ für } p > 2,\\ 3 \text{ für } p = 2,\end{cases} \tag{33}$$

woraus erhellt, daß die Anzahl der $\bmod p$ verschiedenen Lösungen u in jedem Fall gleich $1 + \left(\frac{-D}{p}\right)$ ist. Es ist demnach

$$a_k\left(\frac{1}{p}T\begin{bmatrix}u & p\\ 1 & 0\end{bmatrix}\right) = \begin{cases}\alpha_k(e,D) & \text{in } 1 + \left(\frac{-D}{p}\right) \text{ Fällen,}\\ \alpha_k(p^{-1}e, p^2D) & \text{in } p - 1 - \left(\frac{-D}{p}\right) \text{ Fällen.}\end{cases}$$

Insgesamt kann (28) damit in

$$a_k(pT) = \left\{(1+p^{k-1})(1+p^{k-2}) - \left(1+\left(\frac{-D}{p}\right)\right)p^{k-2}\right\}\alpha_k(e,D) -$$

$$- p^{2k-3}\alpha_k(p^{-1}e,D) - \left(p - \left(\frac{-D}{p}\right)\right)p^{k-2}\alpha_k(p^{-1}e,p^2D)$$

übergeführt werden. $\alpha_k(pT)$ ist also auch durch

$$e(pT) = pe, \quad D(pT) = |2pT|e^{-2}(pT) = D$$

eindeutig bestimmt. Damit ist (30), zugleich auch die Rekursionsformel von Satz 2 bewiesen.

Mit vollständiger Induktion nach $h(T)$ beweist man schließlich noch die Gültigkeit einer Darstellung

$$\alpha_k(e,D) = \sum_{\substack{t^2|e \\ t>0}} c_k(e,D,t)\alpha_k(1,t^2D) \tag{34}$$

mit gewissen ganz rationalen Koeffizienten $c_k(e,D,t)$, die allerdings von recht komplizierter Struktur sind.

§ 4. Teilerprobleme

Es ist im Fall $n = 2$ leicht einzusehen, daß die Diskriminanten aller imaginär-quadratischen Körper in der Gestalt $d = -|2T|$ durch halbganze $T > 0$ mit $e(T) = 1$ realisiert werden können. Der in Satz 1 definierte ganz rationale Faktor $b_k(T)$ ist dann gleich 1. Im Hinblick auf (34) ist nun festzustellen, daß eine Bestimmung des größten gemeinsamen Teilers aller $a_k(T)$ mit $T > 0$ zu gegebenem k darauf hinausläuft, den größten gemeinsamen Teiler der Summen

$$W_{k-1}(d) = \frac{1}{|d|}\sum_{q=1}^{|d|-1}\left(\frac{d}{q}\right)(q+|d|B)^{k-1} \tag{35}$$

zu berechnen. Wir werden das Problem nicht in dieser Allgemeinheit lösen, sondern nur einen gemeinsamen, im allgemeinen gebrochenen Teiler aller $a_k(T)$ mit $T > 0$ zu gegebenem k bestimmen, der sich vom größten gemeinsamen Teiler vermutlich „nicht wesentlich" unterscheidet. Jedenfalls stimmt er mit diesem für $k = 4, 6, 8, 10, 12$ überein.

Im folgenden sei $N_{2\nu}$ der gekürzte positive Nenner der Bernoullischen Zahl $B_{2\nu}$, mithin $Z_{2\nu} = B_{2\nu}N_{2\nu}$ ihr Zähler. $N_{2\nu}$ setzt sich aus den verschiedenen Primzahlen p zusammen, für die $p-1$ ein Teiler von 2ν ist:

$$N_{2\nu} = \prod_{p-1/2\nu} p. \tag{36}$$

Bestimmt man sämtliche Primteiler der gekürzten Zähler sämtlicher Quotienten $\frac{B_{2\nu}}{2\nu}$ ($\nu = 1,2,3,\ldots$), so erhält man nach einem Satz von K. L. Jensen [2] genau alle irregulären Primzahlen, d. h. diejenigen Primzahlen p, für welche die Klassenzahl des Körpers der p-ten Einheitswurzeln durch p teilbar ist. Schließlich machen wir noch Gebrauch von der folgenden Identität (in symbolischer Schreibweise):

$$\sum_{a=1}^{m-1} a^h = \frac{1}{h+1}\{(m+B)^{h+1} - B^{h+1}\},$$

wobei h,m beliebige natürliche Zahlen sind. Speziell für $k = h+2$ folgt

$$(m+B)^{k-1} \equiv 0 \pmod{k-1}. \tag{37}$$

Mit dieser Kongruenz beweisen wir

Lemma 2: *Es sei t der größte Teiler von $k-1$, der mit der Diskriminante d keinen echten Teiler gemeinsam hat. Dann ist*

$$W_{k-1}(d) \equiv 0 \left(\mathrm{mod}\,\frac{t}{d}\right). \tag{38}$$

Ist w das Produkt aller Primzahlen $p < k$, die nicht in d aufgehen, so ist wd eine gemeinsamer Nenner aller Bernoullischen Zahlen auf der linken Seite der Kongruenz (37). Wir multiplizieren diese mit $|d|$ und erhalten

$$(|d|m + |d|B)^{k-1} \equiv 0 \pmod{t}.$$

Wegen $(d,wt) = 1$ kann m so bestimmt werden, daß

$$|d|m \equiv q \pmod{wt},$$

also $|d|m = q + gwt$ mit ganzem g wird. Es folgt

$$
\begin{aligned}
0 &\equiv (q + gwt + |d|B)^{k-1} \\
&\equiv (q + gwt)^{k-1} - \frac{k-1}{2}(q + gwt)^{k-2}|d| + \\
&\quad + \sum_{\nu=0}^{\frac{k}{2}-1} \binom{k-1}{2\nu} (q + gwt)^{k-1-2\nu}|d|^{2\nu} B_{2\nu} \\
&\equiv q^{k-1} - \frac{k-1}{2} q^{k-2} + \sum_{\nu=0}^{\frac{k}{2}-1} \binom{k-1}{2\nu} q^{k-1-2\nu}|d|^{2\nu} B_{2\nu} \\
&\equiv (q + |d|B)^{k-1} \pmod{t},
\end{aligned}
$$

damit auch die Behauptung von Lemma 2.

Wir bestimmen analoge Teilbarkeitseigenschaften von $W_{k-1}(d)$ bezüglich der Primteiler von d. Die folgenden Aussagen über die Summen

$$S_h(d) = \sum_{q=1}^{|d|-1} \left(\frac{d}{q}\right) q^h \tag{39}$$

dienen zur Vorbereitung.

Lemma 3: *Es sei s der größte Teiler von $k-1$, der sich nur aus Primteilern der Diskriminante d zusammensetzt. Dann ist*

$$S_{k-1}(d) \equiv 0 \pmod{sd} \tag{40}$$

mit Ausnahme der folgenden Fälle:

1. $d = -4$:

$$S_{k-1}(d) \equiv 2 \pmod 4. \tag{41}$$

2. $d = -p$ (*Primzahl*), p/N_{2k-2}:

$$S_{k-1}(d) \equiv p - 1 \pmod p. \tag{42}$$

Zum Beweis führen wir den Charakter $\chi(h) \bmod d$ ein, der für $h > 0$ mit $\left(\frac{d}{h}\right)$ übereinstimmt. Es sei p^ϱ bzw. p^α die höchste Potenz eines gegebenen Primteilers p von d, welche $k-1$ bzw. d teilt, insbesondere also $\alpha = 2$ oder 3 für $p = 2$ und $\alpha = 1$ für $p > 2$. Es ist dann

$$S_{k-1}(d) \equiv \sum_{q \bmod d} \chi(q) q^{k-1} \pmod{p^{\varrho+\alpha}}; \tag{43}$$

denn $q^{k-1} \bmod p^{\varrho+\alpha}$ hängt nur von $q \bmod d$ ab, wie aus

$$(q+gd)^{k-1} = \sum_{\nu=0}^{k-1} \binom{k-1}{\nu} q^{k-1-\nu}(gd)^{\nu} \quad (g \text{ ganz})$$

unmittelbar hervorgeht, da $\binom{k-1}{\nu} d^{\nu}$ für $\nu > 0$ durch $p^{\varrho+\alpha}$ teilbar ist. Die Fälle $p > 2$ und $p = 2$ werden nun getrennt behandelt.

1. $p > 2$: Sind a und d teilerfremd, so durchläuft aq mit q auch alle Restklassen $\bmod d$. Aus (43) folgt dann

$$S_{k-1}(d) \equiv \chi(a) a^{k-1} S_{k-1}(d) \pmod{p^{\varrho+\alpha}}. \tag{44}$$

Gibt es ein a mit

$$\chi(a) a^{k-1} \not\equiv 1 \pmod{p},$$

so folgt aus (44) sofort $S_{k-1}(d) \equiv 0 \pmod{p^{\varrho+\alpha}}$. Diese Teilbarkeit wird in (40) bezüglich p behauptet. Wir brauchen also nur noch den Fall zu diskutieren, daß $\chi(a) \equiv a^{k-1} \pmod{p}$ für alle zu d primen a gilt. Hieraus folgt $d = -p$; denn wenn p ein echter Teiler von d ist, dann läßt sich, weil χ ein eigentlicher Charakter $\bmod d$ ist, ein zu d primes $a \equiv 1 \pmod{p}$ mit $\chi(a) = -1$ bestimmen. Das würde einen Widerspruch ergeben. Da χ die Ordnung zwei hat, so folgt $p-1/2k-2$, was so viel wie p/N_{2k-2} bedeutet, wegen $\alpha = 1$ schließlich auch $S_{k-1}(-p) \equiv p-1 \pmod{p}$. Es liegt also der zweite Ausnahmefall vor.

2. $p = 2$: Wegen $\varrho = 0$, $\alpha \leqq 3$, $k \equiv 0 \pmod{2}$ ist nach (43)

$$S_{k-1}(d) \equiv \sum_{q=1}^{|d|-1} \chi(q) q \pmod{2^{\varrho+\alpha}}.$$

Bekanntlich ist diese Summe durch d teilbar, wenn wir den Fall $d = -4$ ausnehmen. Unter dieser Voraussetzung folgt dann wieder $S_{k-1}(d) \equiv 0 \pmod{2^{\varrho+\alpha}}$, d. h. die Teilbarkeitsaussage (40) bezüglich $p = 2$. Der Fall $d = -4$ ist der erste Ausnahmefall. Hier ist $S_{k-1}(-4) \equiv 2 \pmod{4}$ evident. Die Kongruenz (40) ist also immer gültig, wenn für d nicht die Ausnahmefälle gelten. Lemma 3 ist damit bewiesen.

Wir merken noch an

$$S_{2h}(d) \equiv 0 \pmod{8} \quad \text{für } d \equiv 0 \pmod{2}, \tag{45}$$

was evident ist, da $q^2 \equiv 1 \pmod{8}$ für ungerade q gilt.

Mit dem oben eingeführten w erhalten wir ausführlich

$$\left.\begin{aligned} wW_{k-1}(d) &= \frac{w}{|d|}S_{k-1}(d) - \frac{k-1}{2}wS_{k-2}(d) + \\ &+ \frac{w|d|}{2\cdot 3}(k-1)\left(\frac{k}{2}-1\right)S_{k-3}(d) + \sum_{\nu=0}^{\frac{k}{2}-1}\binom{k-1}{2\nu}|d|^{2\nu-2}S_{k-1-2\nu}(d)(w|d|B_{\nu 2}). \end{aligned}\right\} \quad (46)$$

Für einen Primteiler p von d sei

$$k-1 = p^{\varrho}u, \quad 2\nu = p^{\beta}v, \quad uw \not\equiv 0 \pmod{p}.$$

In geläufiger Weise zeigt man, daß $\binom{k-1}{2\nu}|d|^{2\nu-2}$ für $\nu \geqq 2$ durch p^{σ} teilbar ist, wenn $\sigma = \varrho - \beta + 2\nu - 2$ gesetzt wird. Aus der Abschätzung $2\nu \geqq 2^{\beta}$ und $\nu \geqq 2$ folgt $2\nu \geqq \beta + 2$, also $\sigma \geqq \varrho$. Beachtet man ferner, daß $wS_{k-2}(d)$ nach (45) gerade und $w|d|$ durch 6 teilbar ist, so ergibt sich schließlich

$$W_{k-1}(d) \equiv \frac{1}{|d|}S_{k-1}(d) \left(\bmod \frac{s}{w}\right); \quad (47)$$

denn jeder Term auf der rechten Seite von (46) mit Ausnahme des ersten ist durch $s = \prod_{p|d} p^{\varrho}$ teilbar.

Aus Lemma 3 folgt in Verbindung mit (47) sofort

Lemma 4: *Es sei w das Produkt aller Primzahlen $p < k$, welche die Diskriminante d nicht teilen, und s der größte Teiler von $k-1$, der sich nur aus Primteilern von d zusammensetzt. Dann ist*

$$W_{k-1}(d) \equiv 0 \left(\bmod \frac{s}{w}\right)$$

mit Ausnahme der folgenden Fälle:

1. $d = -4$:

$$W_{k-1}(d) \equiv -\frac{1}{2} \left(\bmod \frac{1}{w}\right) \quad \textit{mit } s = 1.$$

2. $d = -p$ *(Primzahl)*, p/N_{2k-2}:

$$W_{k-1}(d) \equiv -\frac{1}{p} \left(\bmod \frac{1}{w}\right) \quad \textit{mit } s = p^{\varrho}.$$

Dieses Ergebnis liefert mit Lemma 2 das folgende Resultat

Lemma 5: *Es ist*

$$W_{k-1}(d) \equiv 0 \pmod{k-1}$$

mit Ausnahme der folgenden Fälle:

1. $d = -4$:

$$2W_{k-1}(d) \equiv 0 \pmod{k-1}, \quad 2W_{k-1}(d) \equiv -1 \pmod{2}$$

2. $d = -p$ *(Primzahl)*, p/N_{2k-2}:

$$pW_{k-1}(d) \equiv 0 \left(\mathrm{mod}\frac{k-1}{p^{\varrho}}\right), \quad pW_{k-1}(d) \equiv -1 \pmod{p}$$

Dabei ist p^{ϱ} die größte Potenz von p, welche $k-1$ teilt.

Da die Fourierkoeffizienten $\alpha_k(1,t^2D)$ in (34) bei gegebenem D alle zur selben Diskriminante d gehören, so können wir auf Grund von Satz 1

$$a_k(T) \equiv 0 \left(\mathrm{mod}\frac{4k}{B_kB_{2k-2}}W_{k-1}(d)\right) \quad \text{für } T > 0$$

schließen. Unter Berücksichtigung von Lemma 5 folgt hieraus

Satz 3: *Für $n = 2$, $k \equiv 0 \pmod{2}$, $k > 3$ und $T > 0$ ist*

$$a_k(T) \equiv 0 \left(\mathrm{mod}\frac{4k(k-1)}{B_kB_{2k-2}}\right)$$

mit Ausnahme der Fälle:

1. $d = -4$:

$$a_k(T) \equiv 0 \left(\mathrm{mod}\frac{2k(k-1)}{B_kB_{2k-2}}\right)$$

2. $d = -p$ *(Primzahl)*, p/N_{2k-2}:

$$a_k(T) \equiv 0 \left(\mathrm{mod}\frac{4k(k-1)}{B_kB_{2k-2}p^{\varrho+1}}\right)$$

Dabei ist p^{ϱ} die höchste Potenz von p, welche $k-1$ teilt. In den Ausnahmefällen ist der Primteiler p von d in optimaler Potenz in dem jeweiligen Modul enthalten, sofern $d = -|2T|$ ist.

Da jeder Primteiler $p \equiv -1 \pmod{4}$ von N_{2k-2} eine Ausnahmediskriminante $d = -p$ ergibt, so gelangen wir zu einem von T unabhängigen Modul, indem wir gewisse Kürzungen gemäß den Angaben von Satz 3 vornehmen. Wir erreichen damit das Ziel unserer Betrachtungen:

Satz 4: *Es sei $n = 2$, $k \equiv 0 \pmod{2}$, $k > 3$, $T > 0$ und q der größte Teiler von $(k-1)N_{2k-2}$, der sich nur aus Primteilern $p \equiv -1 \pmod{4}$ von N_{2k-2} zusammensetzt. Dann ist*

$$a_k(T) \equiv 0 \left(\mathrm{mod}\frac{k(2k-2)}{qB_kB_{2k-2}}\right).$$

Der gekürzte Nenner des Moduls setzt sich nur aus irregulären Primteilern der Zähler von B_k und B_{2k-2} zusammen.

Die letzte Aussage bezüglich des Modulnenners folgt aus dem zitierten Satz von K. L. Jensen, wenn man beachtet, daß q mit dem Zähler Z_{2k-2} von B_{2k-2} keinen echten Teiler gemeinsam hat.

Wir teilen noch einige schon von Igusa [1] berechnete Koeffizienten mit. Auf Grund dieser Zahlenangaben sowie der Feststellungen in Satz 3 ist der größte gemeinsame Teiler t_k aller $a_k(T)$ mit $T > 0$ für die fünf ersten Werte von k zu berechnen. Man entnimmt die Werte der folgenden Aufstellung.

k	$a_k\begin{pmatrix}1 & 0\\ 0 & 1\end{pmatrix}$
4	$2^5 3^3 5 \cdot 7$
6	$2^4 3^3 5 \cdot 7 \cdot 11$
8	$2^6 3^2 5 \cdot 61$
10	$2^4 3^4 5 \cdot 7 \cdot 11 \cdot 19 \cdot 277 \cdot 43867^{-1}$
12	$2^5 3^3 5 \cdot 7 \cdot 13 \cdot 19 \cdot 23 \cdot 2659 \cdot 131^{-1} \cdot 593^{-1} \cdot 691^{-1}$
k	$a_k\begin{pmatrix}1 & \frac{1}{2}\\ \frac{1}{2} & 1\end{pmatrix}$
4	$2^7 3 \cdot 5 \cdot 7$
6	$2^6 3^2 7 \cdot 11$
8	$2^8 3 \cdot 5 \cdot 7$
10	$2^6 3 \cdot 7 \cdot 11 \cdot 19 \cdot 809 \cdot 43867^{-1}$
12	$2^7 3^2 5 \cdot 7 \cdot 13 \cdot 23 \cdot 1847 \cdot 131^{-1} \cdot 593^{-1} \cdot 691^{-1}$
k	t_k
4	$2^5 3 \cdot 5$
6	$2^4 3^2 7$
8	$2^6 3 \cdot 5$
10	$2^4 3 \cdot 11 \cdot 43867^{-1}$
12	$2^5 3^2 5 \cdot 7 \cdot 13 \cdot 131^{-1} \cdot 593^{-1} \cdot 691^{-1}$

Weitere Fourierkoeffizienten können mit den von H. Zassenhaus [8] angegebenen L-Reihenwerten berechnet werden.

Literatur

[1] J.-I. IGUSA: On Siegel modular forms of genus two. Amer. J. Math. **84** (1962), 175–200.

[2] K. L. JENSEN: Om talteoretiske Egenskaber ved de Bernoulliske Tal. Nyt Tidsskr. for Mat. B **26** (1915), 73–83.

[3] H. MAASS: Die Primzahlen in der Theorie der Siegelschen Modulfunktionen. Math. Ann. **124** (1951), 87–122.

[4] C. L. SIEGEL: Einführung in die Theorie der Modulfunktionen n-ten Grades. Math. Ann. **116** (1939), 617–657.

[5] C. L. SIEGEL: Über die analytische Theorie der quadratischen Formen. Ann. of Math. **36** (1935), 527–606.

[6] C. L. SIEGEL: Über die Fourierschen Koeffizienten der Eisensteinschen Reihen. Mat. Fys. Medd. Dan. Vid. Selsk. **34**, Nr. 6, (1964).

[7] E. WITT: Eine Identität zwischen Modulformen zweiten Grades. Abh. Math. Sem. Hansische Univ. **14** (1941), 323–337.

[8] H. ZASSENHAUS: Tabelle der Absolutglieder der Eisensteinreihen $E_2(\tau)$ für die ersten Primzahlen und Dimensionen. Abh. Math. Sem. Hansische Univ. 14 (1941), 285–288.

Indleveret til Selskabet den 15. april 1964.
Færdig fra trykkeriet den 24. november 1964.

Matematisk-fysiske Meddelelser
udgivet af
Det Kongelige Danske Videnskabernes Selskab
Bind **34,** nr. 8

Mat. Fys. Medd. Dan. Vid. Selsk. **34,** no. 8 (1964)

COULOMB EXCITATION OF LEVELS IN Cu^{63} AND Cu^{65}

BY

B. ELBEK, H. E. GOVE AND B. HERSKIND

København 1964
Kommissionær: Ejnar Munksgaard

CONTENTS

Synopsis

Levels in Cu^{63} at 0.668, 0.961 and 1.327 MeV and in Cu^{65} at 0.770, 1.114 and 1.482 MeV have been studied by the technique of Coulomb excitation, using 36 MeV O^{16} ions. Spin assignments of 1/2, 5/2 and 7/2, respectively, for the two sets of levels were made, based on angular correlations of the cross-over gamma rays to the ground state measured in coincidence with O^{16} ions scattered into a counter near 180°. Relative $B(E2)$ for the levels in Cu^{63} as given above were found to be 1.00, 1.01 ± 0.03 and 1.10 ± 0.03, while that for the 1.862 MeV level was less than 0.2 (assuming $J = 3/2$). In Cu^{65} the values were 1.00, 1.11 ± 0.04 and 0.97 ± 0.03, while that for the 1.623 MeV level was less than 0.2 (again assuming $J = 3/2$). The absolute values of $B(E2)$ for decay of the 0.845 Mev level in Fe^{56}, the 0.668 Mev level in Cu^{63} and the 0.770 Mev level in Cu^{65} were measured to be 0.019, 0.021 and 0.016 (in units of $e^2 \times 10^{-48}$ cm^4), respectively. The 1.327 Mev level in Cu^{63} branches to the 0.668 Mev level with a 9 % probability and the 1.482 Mev level in Cu^{65} branches to that at 0.770 Mev 24 % of the time. $E2$–$M1$ amplitude ratios for the transition between the 5/2-level and the ground state in both nuclei were measured to be −0.2. Estimates were made of various second-order Coulomb excitation effects which can change the relative $B(E2)$. The experimental results are considered in relation to various current core excitation models.

PRINTED IN DENMARK
BIANCO LUNOS BOGTRYKKERI A/S

1. Introduction

In regions of the periodic table where the low energy spectra of even-even nuclei can be approximately described as quadrupole vibrations one may attempt to analyze the spectra of odd-mass nuclei in terms of such vibrations coupled to the motion of the last odd particle. The understanding of such a system is, of course, a central problem in nuclear physics but, in spite of this, relatively little progress has been made in the experimental and theoretical investigation of the coupled system.

This paper describes some measurements on the low lying levels in the two isotopes of copper, Cu^{63} and Cu^{65}. In these nuclei there are several indications that the low levels are due to the coupling of the odd proton ($p_{3/2}$) in the ground state to the $2+$ excited state of the even-even core. The phenomena associated with this coupling might here be especially well displayed as the odd proton is the only particle outside the closed $f_{7/2}$ shell.

If a coupling of the type discussed here is very weak it would give rise to a degenerate multiplet in the energy spectrum of the nucleus. The spins of the states in this multiplet would be those possible from the vector coupling of the particle angular momentum j to the angular momentum 2 of the quadrupole vibration (Fig. 1). The downwards reduced transition probabilities would all be equal as they correspond to a one-phonon transition which leaves the odd particle unaffected. The states will therefore have the large reduced transition probabilities characteristic of the vibrational excitation in the even-even nucleus. Other excited states correspond to a shift of the odd particle from one orbit to another, but these transitions proceed by approximately single-particle strength.

However, this simple picture can hardly be expected to reproduce the properties of real nuclei. A significant coupling is expected due to the fact that, when the nucleus vibrates, there are corresponding fluctuations in the shape of the field in which the particle moves. To leading order, the coupling is proportional to the amplitude of the nuclear vibration. An estimate of the strength of the coupling together with the empirically determined vibra-

tional parameters show that the conditions for the validity of the weak coupling picture are far from being fulfilled.

It is then necessary to carry the calculations to higher orders, thereby including higher phonons. Such calculations are in general very complicated but, for the special case $j = 3/2$, BAYMAN and SILVERBERG[1] have been able to solve the problem exactly. Their calculation shows that the 1/2, 5/2 and

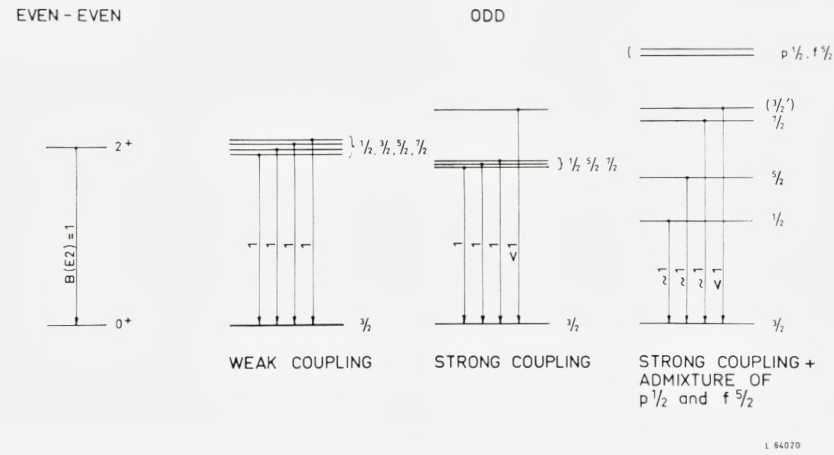

Fig. 1. Schematic representation of the low-lying energy levels in the copper isotopes for different types of particle-vibration coupling.

7/2 states stay degenerate independent of the coupling strength, whereas the 3/2 state increases in energy as the coupling strength increases (Fig. 1). The $B(E2)$ value of the degenerate states are only slightly affected by the coupling in contrast to the $B(E2)$ value of the 3/2 state which is markedly reduced.

Calculations such as those mentioned above still represent a simplification in two respects: a) They assume that the nuclear vibration resembles that of a harmonic oscillator. From the experimental information available[2, 3] it is clear that, although higher phonon states indeed may be found, major deviations from the simple harmonic picture exist. It is at present impossible to take these deviations into account. b) It must be expected that the presence of other single-particle states also gives rise to changes in the orbit of the last odd particle.

In the case of the copper isotopes the most important single-particle states are the $p_{1/2}$ and $f_{5/2}$. This type of coupling has been studied by BOUTEN

and VAN LEUVEN[4]. Their calculation shows that the 1/2 and 5/2 excited states of the multiplet get a considerable contribution from the corresponding single-particle states if the experimentally observed level positions are to be reproduced. The 7/2 level, however, is an almost pure configuration of excited core and $p_{3/2}$ particle.

Another indication of strong admixtures from other single-particle states comes from the recent experiments on the $Ni^{62}(He^3,d)Cu^{63}$ reaction by BLAIR and ARMSTRONG[5]. From these measurements it appears that the 1/2 state in Cu^{63} carries most of the single-particle $p_{1/2}$-strength. Similarly, the 5/2 state gets a significant contribution from the $f_{5/2}$ single-particle level.

These results are qualitatively but not quantitatively in agreement with the wave functions calculated by BOUTEN and VAN LEUVEN. It is of some interest to understand how these data can be brought into agreement with the other features of the Cu-spectra which so strongly support the interpretation in terms of a particle coupled to a vibration.

In the discussions of spectra of the type considered here reference is often made to a "center-of-gravity" theorem[6, 7]. This theorem can be derived in two simple limiting cases: a) If the ground state and the excited state of the core can both be described in terms of the same $(j)^n$ configuration, and if this core interacts with the particle in a definite orbit $j' \neq j$ which is not identical to those of the core particles. b) If the coupling between the core and the odd particle is linear in the vibration amplitude (for harmonic vibrations), and if the single particle is confined to a definite orbit the energy shifts are of second order in the coupling and leave the center-of-mass unchanged.

One hardly expects any of these conditions to be very well realized especially since one must in general expect significant couplings to other single-particle states. Also the experimental evidence, which is most complete for nuclei with spin 1/2, shows that usually the center-of-mass shift is comparable with the splitting between the two first excited states.

Coulomb excitation immediately suggests itself as a method of testing the ideas outlined in the introduction, and in the present paper an account is given of some measurements of the Coulomb excitation of Cu^{63} and Cu^{65}, using a beam of O^{16} ions from the tandem accelerator at the Institute for Theoretical Physics, Copenhagen. The energy levels of both nuclei have been previously measured in some detail[8] and the first two excited states had been studied by Coulomb excitation[9]. Information about the spins of the first two levels had been inferred from β-ray measurements[10], but without great certainty. It was therefore decided to carry out Coulomb

excitation angular correlation measurements as well in order to make unambiguous spin assignments. The use of O^{16} ions as the bombarding particle permits higher excited states to be measured with greater ease than when lighter bombarding particles are employed. In the case of 35 Mev O^{16} ions incident on Cu^{65}, the parameter $\xi^{(11)}$ on which the cross section is sensitively dependent has a value of 0.69 for a level at an excitation energy of 1.623 Mev and, of course, smaller values for lower excited states. This means that the cross section for Coulomb excitation of a level at this energy is sufficiently great to be detected rather readily, provided, of course, that the reduced quadrupole matrix element is of the same order of magnitude as that for the lower levels[9].

2. Experimental Method

A schematic diagram of the apparatus used in these experiments is shown in Fig. 2. The beam of O^{16} ions from the tandem accelerator, focussed by two quadrupole lenses, 2 meters and 14 meters, respectively, from the exit of the 90° analyzing magnet is incident on the target chamber shown in Fig. 2, located 19 meters from the analyzing magnet. Two tantalum apertures are employed, the second of which insures that no beam strikes the particle counters. Thick targets were used and all the beam collected by the insulated target was measured. For most of the experiments 36 Mev O^{16} ions in the charge five state were used and the beam currents were approximately 0.1 μa or less.

The geometry employed for the particle detectors is shown in the inset of Fig. 2. Two gold-surface barrier devices[12], 12 mm × 6 mm in area, separated by 6 mm were connected in parallel to the input of a charge sensitive pre-amplifier[13]. From the output of this pre-amplifier the signal went to a slow amplifier and to fast amplifiers[14]. The latter fed one input of a time-to-pulse height converter which provided a coincidence resolving time of about 20 nano-seconds, while the former after further amplification and clipping passed through a single-channel analyzer, a slow coincidence circuit and gate to a 512 channel analyzer. A combined fast-slow pre-amplifier on the gamma spectrometer provided signals to the other input of the time-to-pulse height converter after amplification in a fast amplifier[14] and to a slow amplifier and single-channel analyzer which, in turn, was connected to the slow coincidence and gate. After amplification, the coincidence pulse from the time-to-pulse height converter passed a single-channel analyzer and then the slow coincidence and gate. This latter unit

was arranged so that the multi-channel analyzer could examine the direct particle, gamma or time spectrum as well as anyone of the three coincident spectra with discriminator gates set on particular portions of the direct spectra from the other two.

The gamma-ray detector, as shown in Fig. 2, was a 7.6 cm diameter by 7.6 cm long NaI crystal optically coupled to an EMI 9531A photomulti-

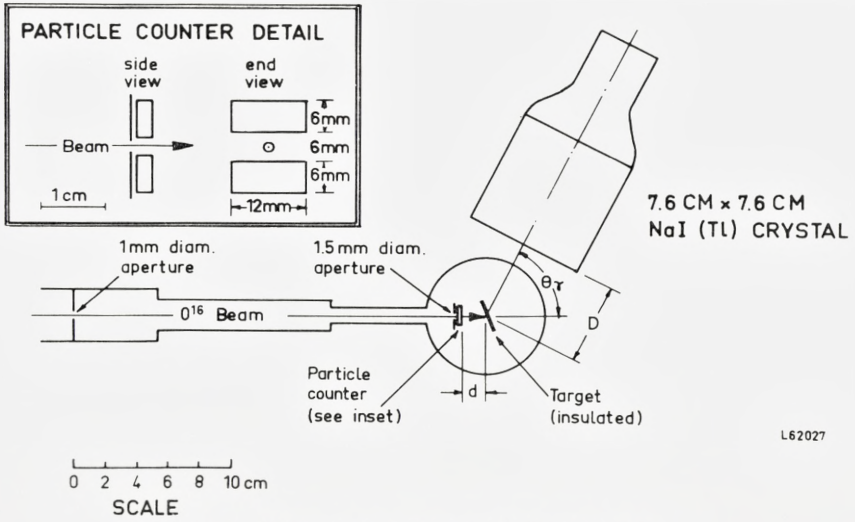

Fig. 2. Scheme of angular correlation apparatus.

plier. This counter could be rotated in angle about the target center and at each angle the gamma ray spectrum was recorded, in coincidence with a gate set on the particle spectrum and on the time spectrum. Since thick targets were employed, the particle spectrum was relatively flat up to pulse heights corresponding to the O^{16} ions back scattered from the target surface, and then fell off rapidly. The gate on this spectrum was usually adjusted to include the upper third of the pulses.

Measurements were made with two different combinations of particle-counter and gamma-counter distances to the target. In the first series of runs these distances were 9 mm and 46 mm, respectively, and in the second 15 mm and 58 mm, respectively. The second set was chosen because the first gave too large an attenuation of the coefficient of the fourth-order Legendre polynomial in the angular distributions. The coincident angular correlations were measured with the gamma counter set at every 10° from

0° to 90°. It was found that, in the first series of runs, because of gain drifts in the particle counter, it was not possible to measure angular correlations reliably without normalizing to the intensity of the gamma-ray line resulting from de-excitation of the first excited states of Cu^{63} or Cu^{65} which have $J = 1/2$ and, hence, give rise to spherically symmetric angular correlations. In the second series of experiments this problem was overcome by using

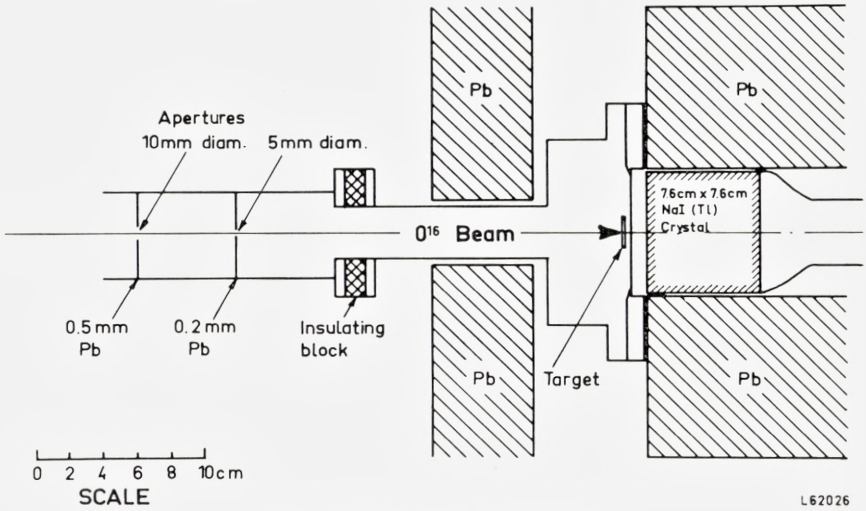

Fig. 3. Scheme of yield apparatus.

a second 7.6 × 7.6 cm NaI(Tl) crystal at a fixed angle, parallelling its output to that of the moving crystal into the fast coincidence part of the circuit and recording its gamma spectrum in a 256 channel analyzer in coincidence with the same gate on the particle spectrum. Any shift in the gain of the particle counters caused equal fractional changes in both coincident gamma spectra.

In addition to the coincident angular correlation measurements described above two other types of measurements were made. The direct yield curves of the gamma rays from the thick target Coulomb excitation of levels in Cu^{63} and Cu^{65} were measured with O^{16} ions from 24 to 40 Mev by means of the experimental arrangement shown in Fig. 3. In this experiment, the 7.6 × 7.6 cm crystal was placed at 0° to the beam and about 13 mm from the target. The Faraday-cup nature of the target chamber ensured that an accurate measurement of the beam current could be made.

Finally, some gamma-gamma coincidence measurements were made, as will be described subsequently. For these measurements a 7.6×7.6 cm NaI crystal and pre-amplifier were substituted for the particle counter in the circuit.

The targets employed were thick targets of both natural copper and the separated isotope of Cu^{65}[15]. The latter was prepared[16] by an electroplating technique. The Cu^{65} oxide powder was converted into another form of the oxide which dissolved readily in H_2SO_4. The electroplating solution comprised $Cu^{65}SO_4$, sodium oxalate, triethanolamine, and water. The copper was electroplated on gold, using a platinum anode. Five hours of electroplating produced a target about 0.5 cm^2 with an areal density of 13.5 mg/cm^2. About 35 % of the isotope was recovered.

In some of the preliminary experiments, thin (about 1 mg/cm^2) self-supporting foils of the separated isotopes of both Cu^{63} and Cu^{65} were used.

3. Coulomb Excitation Theory

a) Angular Distribution

Because of the particle-counter geometry employed in this experiment (see Fig. 2), particularly its large solid angle and lack of cylindrical symmetry about the beam axis, it is not possible to use the simplified expressions of Litherland and Ferguson[17] for a particle counter at 0° or 180°. It is, however, of some interest to compare their expression with that for pure Coulomb excitation obtained by Alder et al.[11], and such a comparison is made in Appendix I. Expressions for the actual theoretical angular distributions for the particle-detector geometries employed in the present experiment are also derived in Appendix I. To compare these expressions with experiment, however, it is necessary to know the values for Q_2 and Q_4, the attenuation constants which take account of the finite geometry of the gamma detector. If the complete area under the measured spectrum of a monoenergetic gamma ray is calculated at each angle, then the attenuation coefficients of Rutledge[18] can be used directly, but in the case of a complex spectrum comprising several gamma rays it is much more convenient and accurate to measure the area under the total absorption peak alone. Since total absorption of the gamma rays is more likely to occur near the center of the crystal rather than near the edges, one would expect the actual attenuation factor to be larger (ɔ: less attenuation) than the computed ones and, further, one would expect the percentage difference to be greater for

Q_4 than for Q_2. It is therefore useful to measure these coefficients, and this was accomplished in the case of the second geometry employed (particle counter 15 mm from the target and gamma counter 58 mm away) by measuring the coincidence angular correlation of 845 kev gamma rays resulting from the Coulomb excitation of the first excited state in Fe^{56} by 33 Mev O^{16} ions. Since the ground and first excited state of Fe^{56} have $J = 0+$ and $2+$, respectively, both the excitation and decay are pure $E2$. Further-

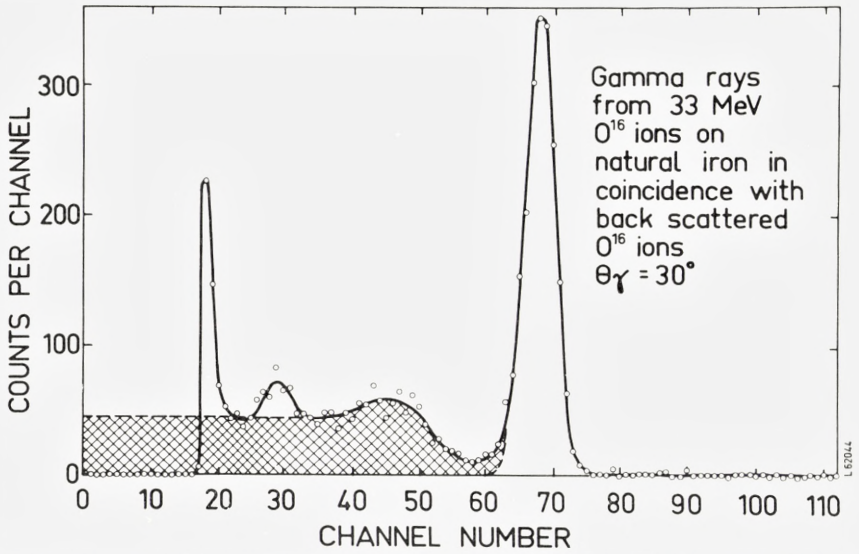

Fig. 4. Spectrum of 845 kev gamma rays from 33 Mev O^{16} ions on a thick natural iron target measured at 90° in coincidence with back scattered O^{16} ions. The counter distances were $d = 15$ mm and $D = 58$ mm, respectively (see Fig. 2). The two ways of measuring the area are indicated.

more, theory predicts both a large coefficient of P_2 and of P_4 in the coincidence correlation. The coincident gamma-ray spectrum is shown in Fig. 4; indicated on this figure are the two methods of measuring the area, in the first case all the pulses in the spectrum were counted and in the second only those in the total absorption peak. In this measurement a monitor counter measured the coincident counting rate at a fixed angle; the resulting angular correlations normalized by the monitor counter are shown in Fig. 5. The solid curves are least square fits of the data to a Legendre polynomial expansion of the form given by equation (20) in Appendix I. For a 7.6 cm × 7.6 cm NaI(Tl) counter at 58 mm from the target the tables of RUTLEDGE[18] give values of the attenuation coefficients Q_2 and Q_4 of 0.84 and 0.53, re-

spectively. The table of ALDER et al.[11] gives $A_2^{(2)} = 0.3571$ and $A_4^{(2)} = 1.143$ for a $0-2-0$ gamma-gamma correlation. Substituting these values, equation (20) of Appendix I results in the coefficients listed in the column

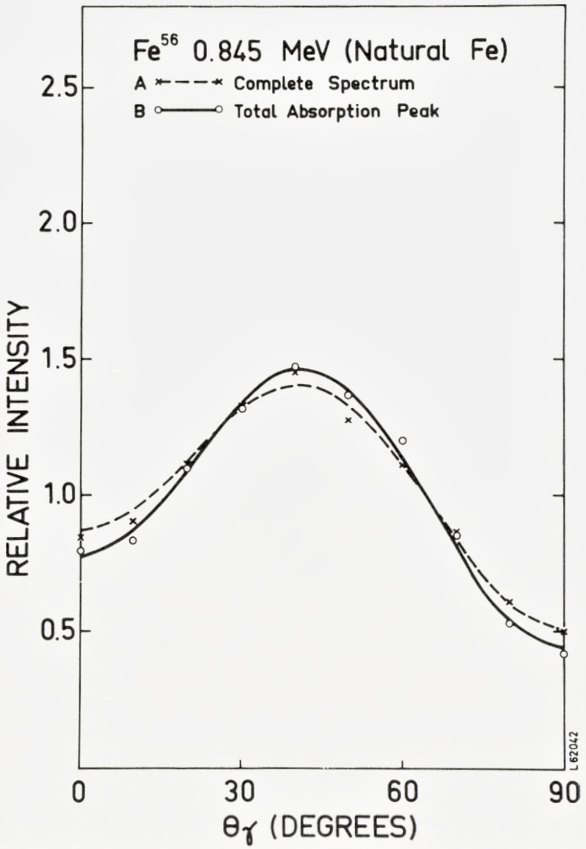

Fig. 5. Angular correlations of 845 kev gamma rays from 33 Mev O^{16} ions on a thick natural iron target measured in coincidence with back scattered O^{16} ions. The counter distances were $d = 15$ mm and $D = 58$ mm, respectively (see Fig. 2). Correlation A involved measuring all the pulses in the spectrum, while for B only the area under the total absorption peak was taken.

headed "theoretical values" in Table I. Agreement with the experimental coefficients derived from the total spectrum is quite good in consideration of the uncertainty of the total number of counts in the gamma spectrum. This comparison confirms that the method of averaging over the particle-counter area is valid.

TABLE I.

Coincidence correlations for $Fe^{56}(O^{16}, O^{16}, \gamma)' E_\gamma = 0.845$ Mev, using 33 Mev O^{16} ions and counter spacings $d = 15$ mm $D = 58$ mm.

	Theoretical values	Experimental values using complete spectrum	Experimental values using total absorption peak only
a_2/a_0	0.490	$0.506 \pm .039$	$0.524 \pm .020$
a_4/a_0	-0.638	$-0.638 \pm .047$	$-0.768 \pm .024$

$$W(\theta) = 1 + a_2/a_0 P_2(\cos\theta_\gamma) + a_4/a_0 P_4(\cos\theta_\gamma)$$

In this comparison between experiment and theory, of course, it has been assumed that first-order Coulomb excitation was dominant. Second-order effects due to re-orientation of the nucleus in its excited 2+ state before emission of the gamma ray can be appreciable under certain conditions. Such effects are discussed in Appendix II, but their chief influence is on the cross section measured at 180° and is negligible as far as the coincident angular correlations are concerned.

One can now compare the theoretical expression of equation (20), Appendix I, with the experimental coefficients listed in the fourth column of Table I, obtained when only the area under the total absorption peak is measured allowing Q_2 and Q_4 to be unknown parameters. This results in values of Q_2 and Q_4 equal to 0.91 ± 0.05 and 0.64 ± 0.02, respectively. Comparing these with the Rutledge values one notes that, although Q_2 is only increased by about 9 %, Q_4 is increased by 20 %. This effect has also been considered recently by ECCLESHALL et al.[19]. Our results for the attenuation factors are collected in Table II. The values of Q_2 and Q_4, actually employed to fit the angular distributions in copper measured in the same geometry, were 0.91 and 0.66, respectively.

TABLE II.

Attenuation factors for the 0.845 Mev γ-ray in Fe^{56}.

	Theoretical values	Experimental values for complete spectrum	Experimental values for total absorption peak only
Q_2	0.836	0.860	0.908
Q_4	0.530	0.532	0.640

Prior to this, however, preliminary measurements of the copper angular distributions were made with the particle- and gamma-counter distances 9 mm and 46 mm, respectively. These measurements, as will be discussed later, allowed spin assignments but not multipole mixing ratios to be measured.

b) Thick Target Yields

The use of thick targets for an absolute determination of $B(E2)$ necessitates an integration of the theoretical cross section for $E2$-Coulomb excitation over the range of the projectile. This means that the following integration has to be performed:

$$Y(E) = B(E2) \times c_{E2} \int_0^{R(E)} E(x) f_{E2}(\xi(E(x)))dx. \tag{2}$$

Here, $Y(E)$ is the thick target yield per incident particle at the energy E, $R(E)$ is the range of the projectile, and c_{E2} a numerical constant. The function $f(\xi)$ is tabulated in ALDER et al.[11].

If one introduces the differential energy loss $-dE/dx$, one can in the usual way change (2) into an integral, $F_{E2}(E)$, over energy

$$F_{E2}(E) = \int_0^E \frac{E f_{E2}(\xi(E))}{dE/dx} dE. \tag{3}$$

In principle, this integral must be evaluated for each combination of projectile, target and excitation energy. However, for practical purposes, certain simplifications are possible[20].

It is first noted that ξ can be split into two factors, one containing the bombarding energy only, whereas the other depends on the particular experimental situation. If the energies are in Mev,

$$\xi = \Lambda \frac{1}{E^{3/2}}; \quad \Lambda = \frac{Z_1 Z_2 A_1^{1/2} \Delta E'}{12.65}, \tag{4}$$

where indices 1 and 2 refer to projectile and target, respectively. The expression $\Delta E' = E(1 + A_1/A_2)$ is a reduced excitation energy.

Secondly, the differential energy loss for any element to a good approximation can be related to the energy loss in a standard material. If

gold ($Z = 79$) is chosen as standard material, the differential energy loss in an element with atomic number Z is[20]

$$\left(\frac{dE}{dx}\right)_Z = \left(\frac{dE}{dx}\right)_{Au} \frac{116}{Z+37}. \tag{5}$$

The values of $-dE/dx$ for gold used in the evaluation of (3) are given in Table III.

By use of the simplifications outlined above one can evaluate the integral (3) for a few values of A covering the range of practical interest ($0 < A < 300$) and then interpolate for other values of A. In this way,

TABLE III.

dE/dx in units of Mev/cm^2/mg for O^{16} ions in gold

E(Mev)	$-dE/dx$
0	2.08
10	2.20
20	2.38
30	2.44
40	2.30
50	2.15

universal integrals are obtained, which for a given projectile easily permits determination of the thick target yield for any excitation energy, and by means of (4) and (5) for any target material.

The $F_{E2}(E)$ for oxygen ions is given in Fig. 6. Expressed by means of the $F_{E2}(E)$ the thick target yield per incident ion is

$$Y(E) = 2.88\times10^{-3}(1 + A_1/A_2)^{-2} \frac{A_1}{A_2 Z_2^2} \frac{Z_2 + 37}{116} F_{E2} \times B(E2). \tag{6}$$

The measured thick target yields of gamma rays per incident O^{16} ion can then be compared to the values obtained from (6) and the values of $B(E2)$ deduced. In practice, as will be described below, the relative $B(E2)$'s for the various levels excited in Cu^{63} and Cu^{65} were calculated from the angular correlations measured in coincidence with back scattered O^{16} ions in the first geometry. Absolute cross sections and from these absolute $B(E2)$'s for excitation of the 0.668 Mev level in Cu^{63} and the 0.845 Mev level in Fe^{56} were measured in the apparatus shown in Fig. 3.

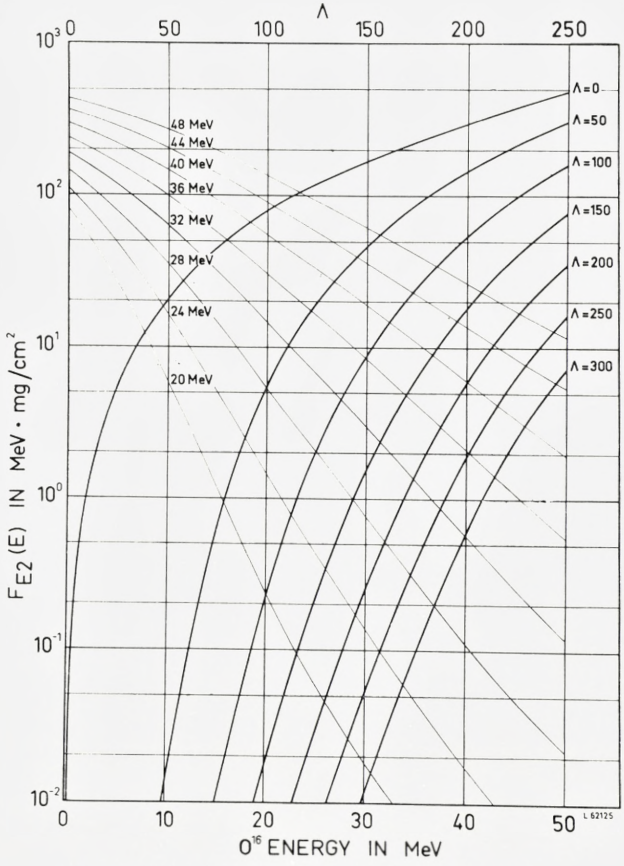

Fig. 6. Thick target yields for O^{16} ions on gold.

4. Experimental Results

a) Relative and Absolute Yields

As mentioned previously, two geometrical arrangements were used in measuring gamma-ray correlations from copper in coincidence with back scattered O^{16} ions. In the preliminary experiments the distance between particle counter and target and gamma-ray counter and target were 9 mm and 46 mm, respectively (distances d and D on Fig. 2). No coincidence monitor counter was available for these preliminary experiments.

Despite the rather poor geometry and the lack of a monitor it was decided to measure the coincidence angular distributions principally to obtain re-

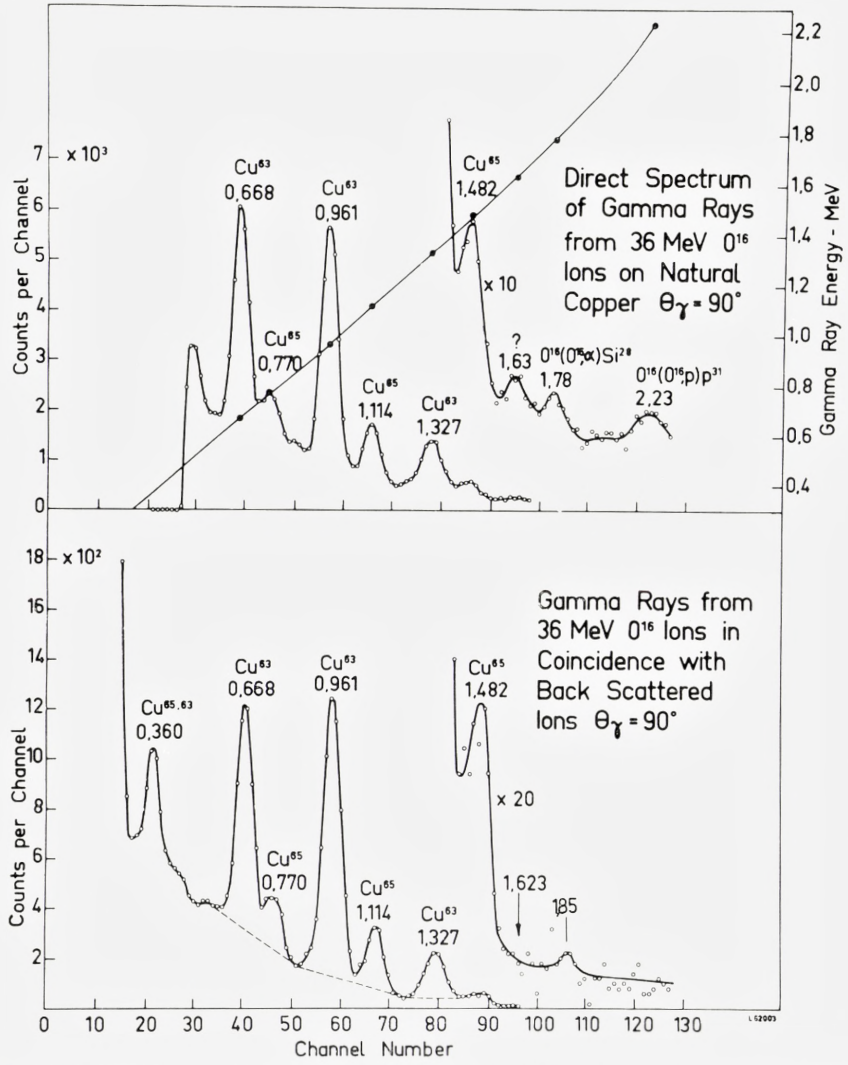

Fig. 7. Direct gamma-ray spectrum (top half of figure) and the gamma ray spectrum in coincidence with back scattered ions (bottom half of figure) are shown for 36 Mev O^{16} ions incident on a thick natural copper target.

lative intensities of the various gamma rays and, in analyzing these distributions, to normalize to the intensity of the gamma ray arising from the de-excitation of the first excited state (at 668 kev in Cu^{63} when a natural copper target was used and at 770 kev in Cu^{65} when a separated Cu^{65} target was

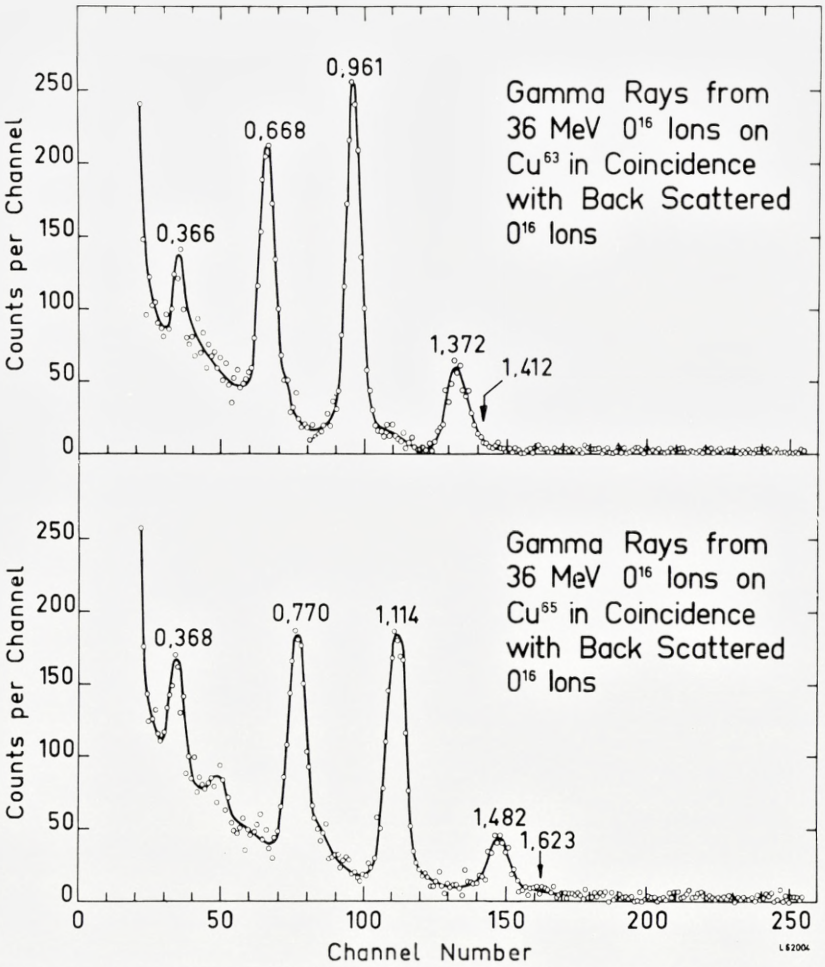

Fig. 8. Gamma ray spectra measured in coincidence with back scattered ions from 36 Mev O^{16} ions incident on thick separated targets of Cu^{63} and Cu^{65}.

employed). Since these levels are almost certainly 1/2− the gamma ray coincidence correlations will be spherically symmetric. Before these measurements, however, the gamma-ray spectra both direct and coincident with back scattered O^{16} ions were measured, using even larger solid angles than obtained from the 9 mm and 46 mm distances. (A solid angle of 5 % of a sphere for the particle counter and a distance of 30 mm for the gamma detector). The results for 36 Mev O^{16} ions on a thick natural copper target

are shown in Fig. 7 where both the direct and coincidence spectrum are displayed. The lack of linearity between energy and pulse height is attributed to the particular slow gate that was used. Coincidence spectra, using 36 Mev O^{16} ions and thick separated targets of Cu^{63} and Cu^{65}, are shown in Fig. 8.

Similar spectra to these, although with appreciably poorer statistics, were taken at 10° intervals from 0° to 90° in coincidence with back scattered ions, using both a thick unseparated target and a thick separated Cu^{65} target, at a bombarding energy of 36 Mev. The areas under the total absorption peaks of the 0.668, 0.961 and 1.327 Mev gamma rays in Cu^{63} and the 0.770, 1.114 and 1.482 Mev gamma rays in Cu^{65} were measured for the natural copper target, and for the latter three in the case of the separated Cu^{65} target. In the case of the separated Cu^{65} target the areas under the total absorption peaks could be readily estimated. Allowance was made for the pulses from 1.482 Mev gamma rays under both the 1.114 and 0.770 Mev peaks (see lower half of Fig. 8) and, since the intensity of 1.482 Mev gamma rays was low compared to the two lower energy gamma rays, uncertainties in this estimate are a small effect. A Zn^{65} source was used to get the line shape for 1.114 Mev gamma rays and, thus, to correct for pulses from these under the 0.770 Mev peak. In the case of the unseparated copper target a somewhat more arbitrary although reasonably reproducible scheme was used to get the peak areas. The dotted lines shown on the spectrum in the lower half of Fig. 7 were drawn and the peak areas above these lines were measured. This is, in fact, a reasonably good approximation to the true photopeak areas. Ratios to the area under the 0.668 Mev peak of the five other gamma peaks were then calculated for the natural target and to the 0.770 Mev peak for the 1.114 and 1.482 Mev peaks in the case of the Cu^{65} target. These were then fitted[21] by a least square procedure to a Legendre polynomial expansion given by equation (19), Appendix I, and the resulting coefficients for a_0 (from which the relative intensities can be calculated) are given in Table IV. As can be seen from the lower half of Fig. 7, it is difficult to estimate the area under the 1.482 Mev total absorption peak, even in the good statistics run on natural copper, so the intensity ratio of 1.482 Mev to 0.668 Mev gamma rays is not included in Table IV. The same comment applies to the ratio of 1.114 to 0.668 Mev gamma rays.

The values of the intensity ratios in Table IV obtained from the coefficient of P_0 in the least square fitting program plus the isotope ratio of Cu^{63} (69.1 %) and Cu^{65} (30.9 %) in natural copper permit relative yields of gamma rays per incident ion to be calculated for each of the three excited states of Cu^{63} and Cu^{65}, provided the relative total absorption peak efficiency

TABLE IV.

Relative peak intensities of gamma rays observed from 36 Mev O^{16} ions on thick targets of both natural copper and separated Cu^{65} in coincidence with back scattered ions. The results are averaged over angle.

Target	Gamma energy Mev	Isotope	Peak intensity
Copper	0.668	Cu^{63}	1.000
Copper	0.770	Cu^{65}	0.237 ± 0.008
Copper	0.961	Cu^{63}	1.190 ± 0.032
Copper	1.327	Cu^{63}	0.431 ± 0.011
Cu^{65}	0.770	Cu^{65}	1.000
Cu^{65}	1.114	Cu^{65}	1.170 ± 0.037
Cu^{65}	1.482	Cu^{65}	0.282 ± 0.007

of a 7.6 cm × 7.6 cm NaI(Tl) crystal at 46 mm distance is known as a function of the gamma-ray energy, and the branching ratios of the various levels are known. The total absorption peak efficiency was taken from curves of the total efficiency and of peak to total ratios[22]. As for the branching ratios, the only evidence for other than direct ground-state transitions is the presence of approximately 370 kev radiation observed in Figs. 7 and 8. Gamma-gamma coincidence experiments described below established that this radiation was in coincidence with 0.961 and 1.114 Mev gamma rays in Cu^{63} and Cu^{65}, respectively; no gamma-gamma coincidences between gamma rays of other energies were detected. The branching ratios of the 1.327 and 1.482 Mev levels were taken directly from the data of Fig. 8 where the solid angles of both particle and gamma counter were sufficiently large[1] so that no averaging over angle is necessary. The branching ratio for the 1.327 Mev level in Cu^{63} is 91 % by 1.327 Mev gamma rays and 9 % by 0.366 Mev gamma rays, and for the 1.482 Mev level in Cu^{65} it is 76 % by 1.482 Mev gamma rays and 24 % by 0.368 Mev gamma rays. These branching ratios, of course, must be used to correct both the observed intensities of 1.327 and 1.482 Mev gamma rays and also those of the 0.961 and 1.114 Mev gamma rays—part of whose yield results from the branching of the upper level. The experimentally determined relative gamma-ray intensities corrected for the various factors discussed above are listed in the last column of Table V. The third column in this table lists the thick target yields taken for 36 Mev O^{16} ions from Fig. 6, multiplied by $(2J + 1)$,

[1] The particle counter had a solid angle of about 5 % of a sphere and the gamma counter was 3 cm from the target center.

TABLE V.

Relative yields for various levels in Cu^{63} and Cu^{65}.

Level	J	$Y(2J+1)$ theory	Relative intensities (experimental)
0.668	1/2	1 (assumed)	1 (assumed)
0.961	5/2	1.58	1.60
1.327	7/2	0.835	0.918
1.862	(3/2)	0.106	≤ 0.021
0.770	1/2	1 (assumed)	1 (assumed)
1.114	5/2	1.34	1.49
1.482	7/2	0.723	0.699
1.623	(3/2)	0.253	< 0.050
0.668	1/2	1 (assumed)	1 (assumed)
0.770	1/2	0.801	0.766

where J is the spin of the excited state determined in the angular-correlation experiments described later and normalized to the value for the 0.668 and 0.770 Mev levels, respectively. To obtain relative values of $B(E2)$ it is merely necessary to divide the numbers in the last column by the corresponding numbers in the previous column and the results are tabulated in Table VI. The errors for the 0.961, 1.327 and 1.482 levels come from those calculated in the least square fitting procedure and listed in Table IV.

TABLE VI.

Relative values of $B(E2)$ for various levels in Cu^{63} and Cu^{65}.

Level (Mev)	Isotope	Spin	Relative $B(E2)\downarrow$
0.668	Cu^{63}	1/2	1.00
0.961		5/2	1.01 ± 0.03
1.327		7/2	1.10 ± 0.03
1.862		(3/2)	< 0.20
0.770	Cu^{65}	1/2	1.00
1.114		5/2	1.11 ± 0.04
1.482		7/2	0.97 ± 0.03
1.623		(3/2)	< 0.20
0.668	Cu^{63}	1/2	1.00
0.770	Cu^{65}	1/2	0.77 ± 0.03

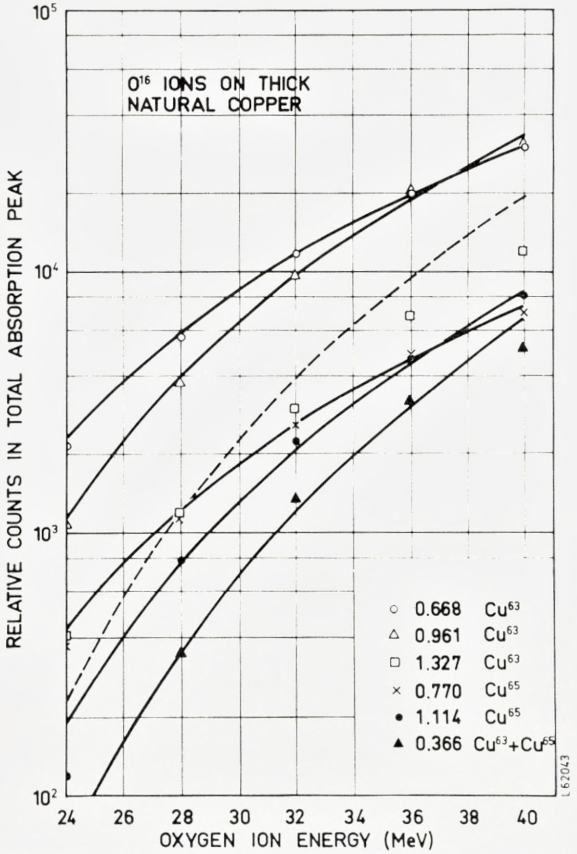

Fig. 9. Relative counts in the total absorption peak as a function of O^{16} ion energy of the six gamma-ray lines observed when a thick natural copper target is bombarded by O^{16} ions. Solid lines through the points are the best fits taken from the theoretical curves on Fig. 6.

The limits on the relative $B(E2)$ values listed in Tables V and VI for the 1.862 Mev level in Cu^{65} and the 1.623 Mev level in Cu^{65} were obtained from an analysis of the run shown in the lower half of Fig. 7 and another good statistics run taken later, also using a natural copper target. The upper limit on the intensities was obtained assuming the peaks to be less than half the intensity of the background at the place in the spectrum where the peaks would be expected to occur.

Absolute cross sections were measured with the apparatus shown in Fig. 3. In these experiments the direct gamma-ray spectrum from a thick natural copper target was measured at a number of O^{16} ion energies be-

TABLE VII.

Counts in photopeak for O^{16} ions on a thick natural copper target.

EO^{16}	E_γ	0.668	0.770	0.961	1.114	1.327	0.360
24		2.13 (3)	3.75 (2)	1.09 (3)	1.18 (2)	4.03 (2)	
28		5.60 (3)	1.14 (3)	3.78 (3)	7.82 (2)	1.19 (3)	3.51 (2)
32		1.16 (4)	2.61 (3)	9.71 (3)	2.23 (3)	2.98 (3)	1.35 (3)
36		1.99 (4)	4.86 (3)	2.03 (4)	4.74 (3)	6.78 (3)	3.24 (3)
40		2.98 (4)	6.97 (3)	3.07 (4)	8.05 (3)	1.20 (4)	5.18 (3)

tween 24 and 40 Mev. At each energy the counts in the photopeak of each gamma ray in the spectrum were measured by the technique previously described. These numbers are listed in Table VII and plotted in Fig. 9. The experimental points were then fitted by the theoretical yields from Fig. 6. The dotted curve in Fig. 9 is the theoretical yield from Coulomb excitation of the 1.327 Mev level in Cu^{63} and is seen to give rather bad agreement with the experimental points. The explanation is that a substantial fraction of the gamma rays of this energy actually arises from the reaction $C^{12}(O^{16},\alpha)Mg^{24}$ where the first excited state of Mg^{24} is strongly fed. The consequent 1.37 Mev gamma rays cannot be resolved from those due to copper. This emphasizes the importance of making measurements in coincidence with back scattered O^{16}, ions since these light element contamination reactions are peaked in both energy and intensity in the forward direction. The resulting improvement in the spectrum can be clearly seen in Fig. 7. The theoretical curve in Fig. 9 through the 0.366 Mev gamma-ray yield is that for the yield of a combination of 1.327 and 1.482 Mev gamma rays and is consistent with the fact that the 0.366 Mev gamma rays arise from cascades between the third and second excited states in the two isotopes.

The absolute yield for the 0.668 Mev level in Cu^{63} and the 0.770 Mev level in Cu^{65} were calculated from this data. The total charge collected during each run was measured by a calibrated beam integrator. The total absorption peak efficiency for a 7.6×7.6 cm NaI(Tl) counter at the distance of 5 mm (13 mm to the actual face of the NaI(Tl) crystal) used in these experiments was taken from the tables of HEATH[22]. An attenuation of 6 % for the material between the front face of the target and the surface of sodium iodide was estimated. The O^{16} beam employed was assumed to be in its charge V state as selected by the analyzing magnet. The results yielded absolute values of $B(E2)$ and these are listed in Table VIII. To check these results the same measurements were made on a thick natural iron target and the resulting values of $B(E2)$ are also given in Table VIII.

TABLE VIII.

Absolute values of $B(E2)\uparrow$ and $B(E2)\downarrow$ for the first excited state of Cu^{63}, Cu^{65} and Fe^{56}.

Target	E_γ(Mev)	Level $J\pi$		$B(E2)\uparrow$	$B(E2)\downarrow$
		Gnd	Exc		
Fe^{56}	0.845	0+	2+	0.097	0.019
Cu^{63}	0.668	3/2−	1/2−	0.0104	0.021
Cu^{65}	0.770	3/2−	1/2−	0.0078	0.015

b) Gamma-Gamma Coincidence Measurements

In this experiment the particle detector was replaced by a second 7.6 cm × 7.6 cm NaI(Tl) counter and coincidence spectra were measured in one gamma-ray detector with gates on the other set on various portions of the direct spectrum. The results are summarized in Fig. 10. The only coincidence observed both in the low energy portion of the spectrum (shown in Fig. 10) and the high energy part were those between 0.36 Mev gamma rays and 1.114 and 0.961 Mev gamma rays, respectively. A search was made to see whether any of the levels above 1.48 Mev decayed predominantly by cascade and hence explain the absence of direct transitions in the spectrum, but no evidence for such cascading was found. Having established, in this experiment, the origin of the 360 kev gamma rays the branching ratios of the third excited states in the two copper isotopes could be calculated from the data of Fig. 8, as described previously. It should be noted, in Fig. 10, that the peak at about 190 kev is due to Compton scattering from one crystal to the other and is highest when the voltage gate is set on the Compton edge of the 0.961 Mev gamma ray, that is on 770 kev pulses.

c) Particle-Gamma Angular Correlations

The results of the particle-gamma coincident angular correlation measurements, using the apparatus of Fig. 2 with $d = 15$ and $D = 58$ mm, normalized by the coincidence counts in a second fixed sodium iodide crystal are presented in Figs. 11, 12 and 13. Again, both thick natural copper targets and thick separated Cu^{65} targets were employed. To minimize contributions to the 1.327 Mev gamma peak from natural copper from the reaction $C^{12}(O^{16},\alpha)Mg^{24}$, $E_\gamma = 1.37$ Mev, the vertical position of the target was changed after each run. This was not possible in the case of the separated

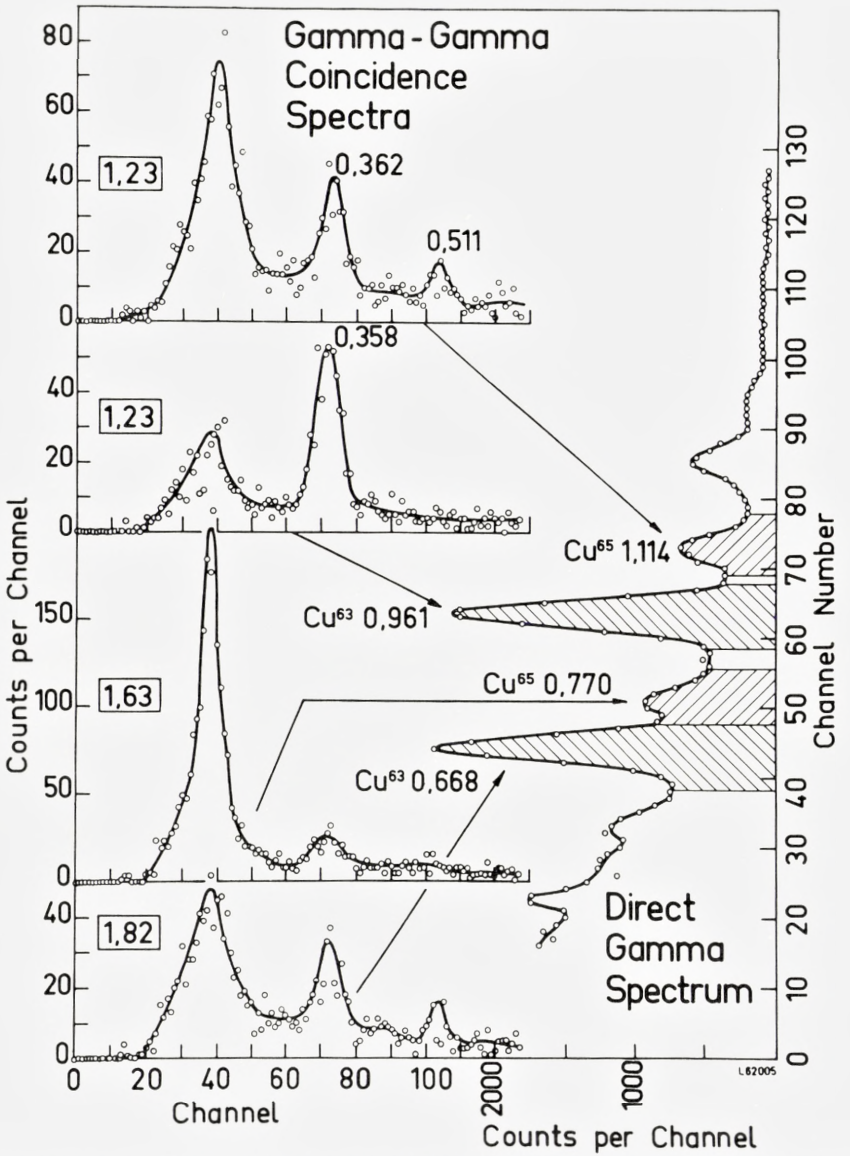

Fig. 10. Gamma-gamma coincidence measurements. The direct spectrum of gamma rays from 36 Mev O^{16} ions on a thick natural copper target is shown along the right side of the figure. Spectra in the second gamma-ray detector measured in coincidence with the respective gates (shown shaded on the direct spectrum) are shown on the left. The numbers in square boxes are proportional to the total gate counts in each case.

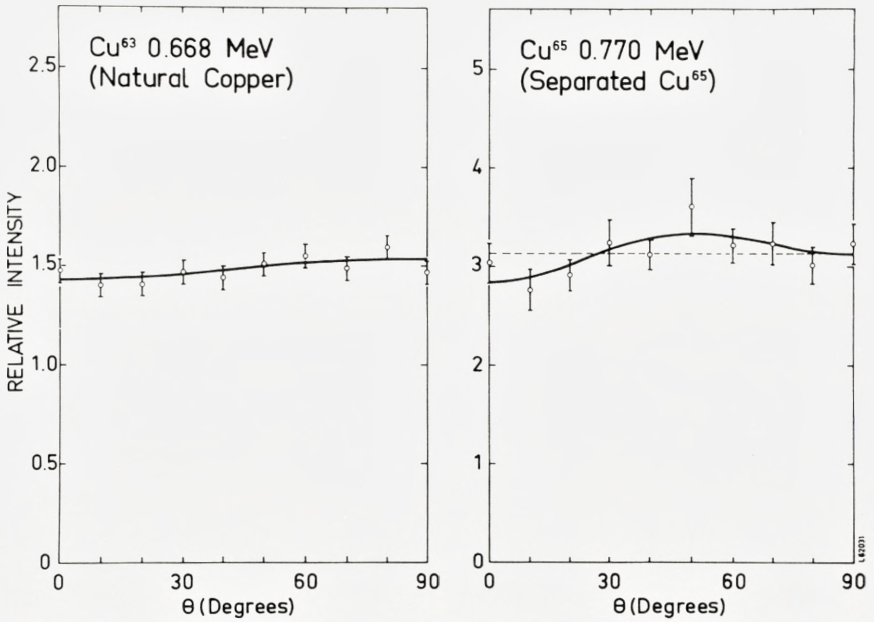

Fig. 11. Coincident angular correlations of 0.668 Mev gamma rays from a natural copper target and 0.770 Mev gamma rays from a separated Cu^{65} target normalized by coincident counts in the monitor gamma detector as described in the text. The solid curves are least square fits to a Legendre polynomial expansion. The dotted line is the average value of the intensity of 0.770 Mev gamma rays.

Cu^{65} target because of its small area. A pronounced 1.37 peak was observed in these spectra, which increased as a function of time as the carbon contamination built up on the target. Natural copper was used for measuring angular distributions of the 0.668, 0.961, 1.327 and 1.482 Mev gamma rays, while the separated Cu^{65} target gave the results for the 0.770 and 1.114 Mev gamma rays.

In both cases, background under each total absorption peak was estimated by drawing straight sloping lines as indicated on Fig. 7. In the case of the natural copper target, all pulses above about 550 kev in the coincident monitor spectrum were used to normalize the counts in each peak in the coincidence spectrum from the moving crystal at each angle. For the separated targets, however, the contamination gamma rays in the coincidence spectra prevented such an analysis; therefore, the counts in the total absorption peaks of 0.770 and 1.114 Mev gamma rays were used.

The six correlations were fitted by the method of least squares to the

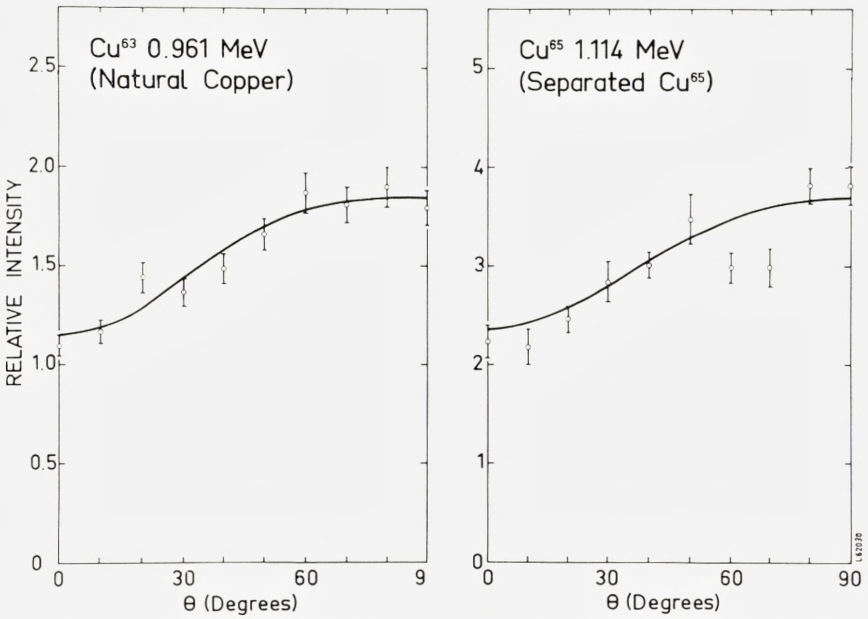

Fig. 12. Coincident angular correlations of 0.961 Mev gamma rays from a natural copper target and 1.114 Mev gamma rays from a separated Cu^{65} target. The solid curves are least square fits to a Legendre polynomial expansion.

TABLE IX.

Legendre polynomial coefficients obtained from a least square analysis of coincident angular correlation data on natural copper and separated Cu^{65} targets.

Level energy Mev	Isotope	Target	a_2/a	a_4/a_0
0.668	Cu^{63}	Copper	-0.045 ± 0.026	-0.004 ± 0.032
0.770	Cu^{65}	Cu^{65}	-0.015 ± 0.046	-0.100 ± 0.055
0.961	Cu^{63}	Copper	-0.242 ± 0.026	-0.080 ± 0.031
1.114	Cu^{65}	Cu^{65}	-0.252 ± 0.040	-0.040 ± 0.047
1.327	Cu^{63}	Copper	$+0.240 \pm 0.330$	-0.072 ± 0.039
1.482	Cu^{65}	Copper	$+0.250 \pm 0.079$	$+0.016 \pm 0.094$

$$W(\theta) = 1 + (a_2/a_0)P_2(\cos\theta) + (a_4/a_0)P_4(\cos\theta)$$

Theory 3/2−7/2−3/2 +0.36 −0.09

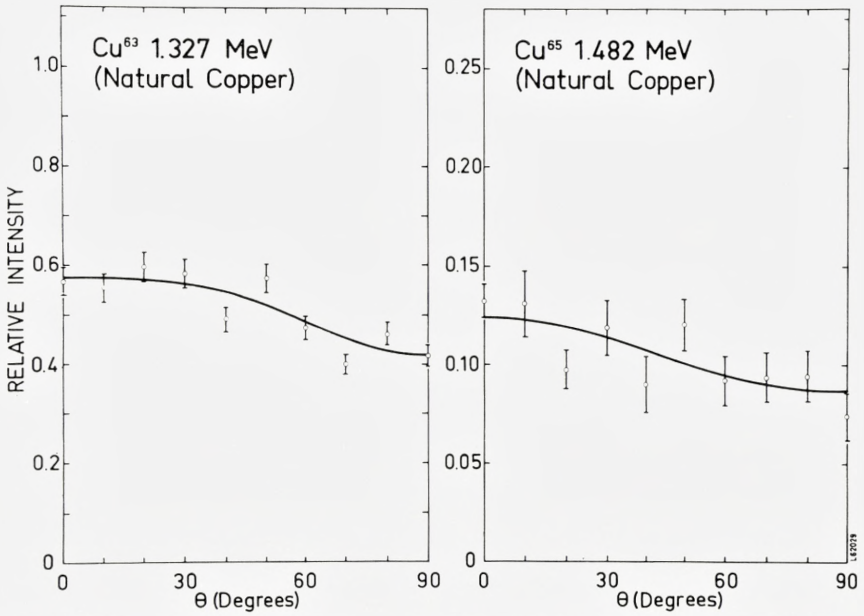

Fig. 13. Coincident angular correlations of 1.327 and 1.482 Mev gamma rays from a natural copper target. The solid curves are least square fits to a Legendre polynomial expansion.

Legendre polynomial expansion given by equation (19) in Appendix I, and the values are listed in Table IX. The errors on each coefficient were calculated from the average statistical error on the points in each distribution. The resulting Legendre polynomial expansions are plotted as solid lines in Figs. 11 to 13.

5. Discussion of Experimental Results

In this experiment it has been possible to excite with certainty, by the Coulomb excitation process, three levels in both Cu^{63} and Cu^{65}. There is no evidence that the level at 1.86 Mev is excited in Cu^{63}, and a lower limit has been placed on its $B(E2)$. There is no evidence either for Coulomb excitation of the known fourth excited state in either nucleus, and in the case of Cu^{65} a lower limit has been placed on its $B(E2)$. In each nucleus the three levels excited have equal values of $B(E2)\downarrow$ within a few percent.

The absolute value of $B(E2) = 0.097 \times e^2 \times 10^{-48}$ cm^4 measured for the 0.845 Mev level in Fe^{56} is in good agreement with previous values of 0.10 by Temmer and Heydenburg[9], 0.10 by Broude and Gove[23], and

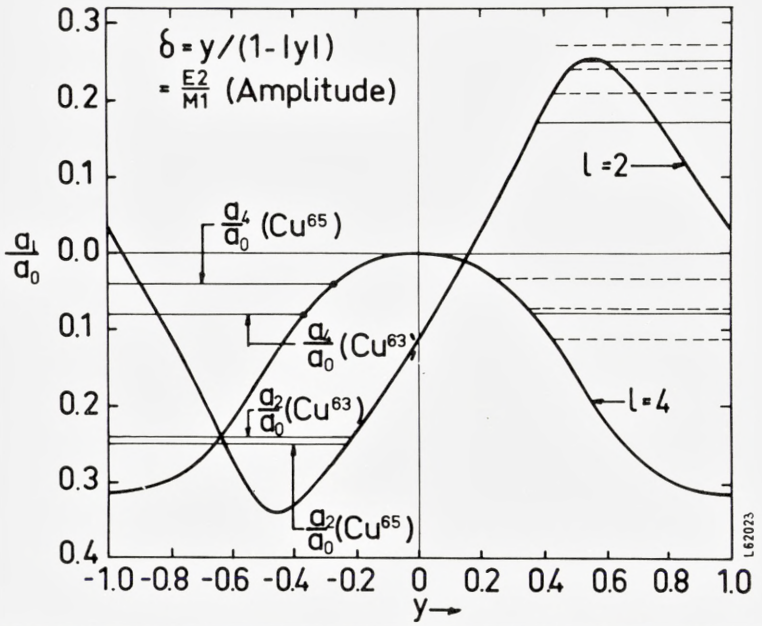

Fig. 14. a_2/a_0 and a_4/a_0 vs. y for the case of $E2$ Coulomb excitation of a state of spin 3/2 to a state of spin 5/2 with subsequent decay by an $E2$–$M1$ mixture. These angular correlation coefficients are calculated for the particular geometry employed in the present experiments. The experimentally determined values for the 0.961 Mev level in Cu^{63} and the 1.114 Mev levels in Cu^{65} are shown.

$0.100 \pm .025$ by Eccleshall, Adams and Yates[24]. It is about 40 % higher than the value of 0.07 obtained by Alkazov et al.[25]. The present results for the copper isotopes are not in good agreement with recent measurements by Yerohkina and Lemberg[26], using 36 Mev N^{14} ions, who obtain values which are between 30 and 50 % higher than those reported here. In the present measurements the ratio of $B(E2)$ for the 0.668 Mev level in C^{63} to $B(E2)$ for the 0.845 Mev level in Fe^{56} is a particularly accurate experimental number, since it is independent of a knowledge of the absolute beam current or absolute gamma counter efficiency. The measured ratio is 1.075 ± 0.010.

The yield curves as a function of O^{16} ion energy shown in Fig. 9 agree reasonably well with $E2$ Coulomb excitation theory up to 40 Mev, despite the fact that this must be very close to the barrier. This implies, in particular, that the theoretical expressions for the angular correlations given by Alder et al.[11] can be used with confidence in analyzing the angular distribution

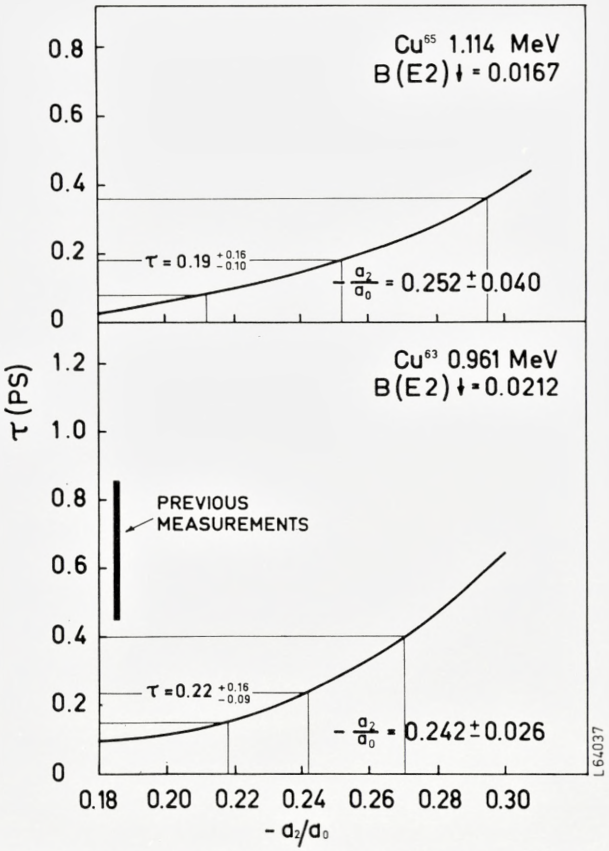

Fig. 15. The mean lifetime τ in picoseconds for the 0.961 Mev level in Cu^{63} (lower half) and the 1.114 Mev level in Cu^{65} (upper half) plotted as a function of a_2/a_0, where a_2/a_0 is the coefficient of $P_2(\cos\theta)$ in the theoretical expression for the coincidence angular correlation measured in the geometry used in the present experiments. In deriving these relationships the measured values of $B(E2)$ given on the figure were used. Experimentally measured values of a_2/a_0 and hence of τ are shown. The vertical black bar shows the range of values determined by others.

results, at least as far as first-order effects are concerned. Second-order effects are discussed in Appendix II, where they are shown to be negligible.

It can be concluded with considerable certainty that the three ground-state gamma-ray transitions observed in both Cu^{63} and Cu^{65}, when these isotopes are bombarded with O^{16} ions, can arise as a result of electric quadrupole Coulomb excitation. Hence, their spins and parities must be 1/2-, 3/2-, 5/2- or 7/2-. For both the case of spin 1/2 and spin 3/2 the gamma-gamma angular correlation coefficients $A_2^{(2)}$ and $A_4^{(2)}$ vanish, in the first

case for obvious reasons and in the second because of an accidental vanishing of the Racah coefficient $W(2,3/2,\ 2,3/2;\ 3/2,\ 2)$. For spin 7/2 the angular correlation is unique, because the de-excitation gamma rays must be pure $E2$. For spin 5/2 the angular correlations depend on δ, the $E2$ to $M1$ amplitude mixture of the de-excitation gamma rays.

The coincidence angular correlations of 845 kev gamma rays from $Fe^{56}(O^{16}, O^{16\prime}\gamma)$ following Coulomb excitation by 33 Mev O^{16} ions agree with the theoretical prediction for a 0–2–0 situation and, in particular, demonstrate that coefficients of $P_4(\cos\theta)$ in the angular correlations are only attenuated by about a factor of 3 over what they would be for a point-particle counter at 180° and a point-gamma counter. Severe though this factor may appear it still permits a_4 coefficients to be measured with sufficient precision to make spin assignments and to measure $E2$–$M1$ mixtures.

The angular correlations for the three levels in Cu^{63} and Cu^{65} are shown in Figs. 11, 12 and 13, and results of the least square fits are listed in Table VIII. For both the 0.668 Mev level in Cu^{63} and the 0.770 Mev level in Cu^{65} the correlations are spherically symmetric within the counting statistics. This is consistent with spin assignments of 1/2- or 3/2- for the levels and, in fact, can even be fitted by a spin of 5/2-, provided an appropriate value of the $E2$–$M1$ mixing is chosen. This can be seen by referring to Fig. 14, where the theoretical predictions for a_2/a_0 and a_4/a_0 obtained from equations (19) and (20) in Appendix I are plotted as a function of y, where y is related to the $E2$–$M1$ amplitude ratio δ as follows

$$\delta = \frac{y}{1 - |y|}. \tag{7}$$

For a value of $y = 0.15$, both a_2/a_0 and a_4/a_0 are essentially zero. However, on the basis of other evidence, a spin assignment of 1/2- is almost certain for both levels. A discussion of this assignment has been given by Cumming et al.[27]).

Of the four possible spin assignments, the only one which can result in a negative a_2/a_0 term in the distribution is 5/2-, since the predicted distribution for the geometry used in this experiment for a spin of 7/2- is

$$W(\theta) = 1 + 0.36P_2(\cos\theta) - 0.09P_4(\cos\theta). \tag{8}$$

Hence, the 0.961 Mev level in Cu^{63} and the 1.114 Mev level in Cu^{65} have both spin and parity 5/2-. The small a_4/a_0 term observed, in both cases,

removes the ambiguity of the double value of a_2/a_0 and allows a unique assignment of the $E2$–$M1$ amplitude ratio δ (see Fig. 14). The values of δ are, respectively, -0.21 ± 0.08 for the .961 Mev level in Cu^{63} and -0.24 ± 0.13 for the 1.114 Mev level in Cu^{65}. The former value is somewhat smaller than the value of $\delta^2 = 0.16$ measured by CUMMING et al.[27].

The angular correlations of both the 1.327 Mev gamma rays from Cu^{63} and 1.482 Mev gamma rays from Cu^{65} have large positive a_2/a_0 coefficients. Reference to Fig. 14 shows that this is not consistent with a 5/2 spin assignment since, for the observed values of a_2/a_0, one would expect values of a_4/a_0 in the vicinity of -0.2. The only other possible assignment then is 7/2-, and the theoretical expression for this is given above. Both the experimental distributions have smaller values of a_2/a_0 than predicted theoretically although, in the case of the 1.482 Mev gamma rays, the experimental uncertainty virtually includes the theoretical value. A number of possible explanations for this discrepancy have been considered and found to be unsatisfactory. It cannot be due to a ξ dependence of the coefficients since this has been shown to be negligibly small. It cannot be due, in the case of the 1.327 Mev gamma ray in Cu^{63}, to the presence of 1.37 Mev gamma rays from $C^{12}(O^{16},\alpha)Mg^{24}$ since the 0-2-0 nature of the latter's angular distribution would have the effect of making a_2/a_0 larger and also of introducing a large negative P_4 term. It is unlikely that any higher levels in either isotope are excited and subsequently decay through the 1.327 or 1.482 Mev levels. Finally, it cannot be due to second-order effects as discussed in Appendix II. Despite the discrepancy, it is concluded that both the 1.327 and 1.482 Mev levels have spin and parity 7/2-.

The combined measurements of $B(E2)$ and δ for the 0.961 and 1.114 Mev levels in Cu^{63} and Cu^{65}, respectively, allow the lifetimes of these two levels to be estimated. Using the measured values of $B(E2)$, a plot of lifetime vs a_2/a_0, the coefficient of $P_2(\cos\theta)$ in the angular distribution can be made and such plots are shown in Fig. 15. The resulting values of the mean lifetime from the measured values of $B(E2)$ and a_2/a_0 obtained in this experiment are $0.19\ ^{+0.16}_{-0.10}$ ps for the 1.114 Mev level in Cu^{65} and $0.22\ ^{+0.16}_{-0.09}$ ps for the 0.961 Mev level in Cu^{63}. Several previous measurements have been made for the latter level[27, 28, 29, 30] from which an average value of 0.645 ± 0.2 ps has been estimated. The present measurement is in reasonable agreement considering the indirect method involved.

6. Conclusions and Comparison with Theory

The results of the present experiment as shown in Fig. 16 establish that the spins of the second and third excited states in Cu^{63} and Cu^{65} are 5/2 and 7/2, respectively. In both cases, the measurements are consistent with a spin of 1/2 for the first excited state, and this assignment is also consistent with other measurements. Since the Coulomb excitation is almost certainly electric quadrupole, the parities of all three excited states in both nuclei are the same as the ground state. In both cases, the third excited state branches to the second as well as decaying directly to ground and the second excited state has an $E2$ to $M1$ amplitude mixture in its ground state transition of $\delta = -0.2$. This amplitude ratio with its associated uncertainty obtained from Fig. 14, when combined with the measured values of the absolute $B(E2)$, yield retardation factors over the Weisskopf unit[31] in the range from 7 to 20 for the $M1$ part of the 0.961 Mev radiation in Cu^{63} and in the range from 6–29 for the $M1$ part of the 1.114 Mev radiation in Cu^{65}.

The values of $B(E2)$ for each of the three levels in Cu^{63} are the same within the experimental uncertainty and this is true too for Cu^{65}. The absolute values of $B(E2)$ are also quite similar to those for the adjacent even-even nuclei Ni^{62} and Ni^{64} [32] as well as for Ni^{58} and Ni^{60} [32, 23].

As discussed in the introduction, there are several reasons why the weak-coupling picture is not appropriate. The observation of an $M1$ component in the decay between the 5/2-- state and the ground state is also in disagreement with this model. A detailed comparison of the present and other data with the predictions of various models proposed to explain the properties of odd-A nuclei has been given elsewhere[33].

There is no evidence in the present experiments for the missing 3/2- excited state in either Cu^{63} or Cu^{65}. This is in contrast with recent work on the elastic scattering of 43 Mev alpha particles from Cu^{63} and Cu^{65} [35]. In Cu^{63}, for example, the 1.862 Mev level is excited and possibly the level at 1.547 Mev. In the case of the 1.862 Mev level the intensity is such as to indicate a $B(E2)$, which is 0.3 ± 0.07 times the average of the $B(E2)$ for the first three excited states. The measurements reported here indicate that the factor is less than 0.2. Similar results from the alpha-scattering experiments are found for Cu^{65}.

The splitting in energy between members of the quartet of levels formed by coupling a $p_{3/2}$ proton to the 2+ core state arises from the interaction between this odd particle and the core. This interaction can be written as a multipole expansion of the product of two tensors of degree r, one of

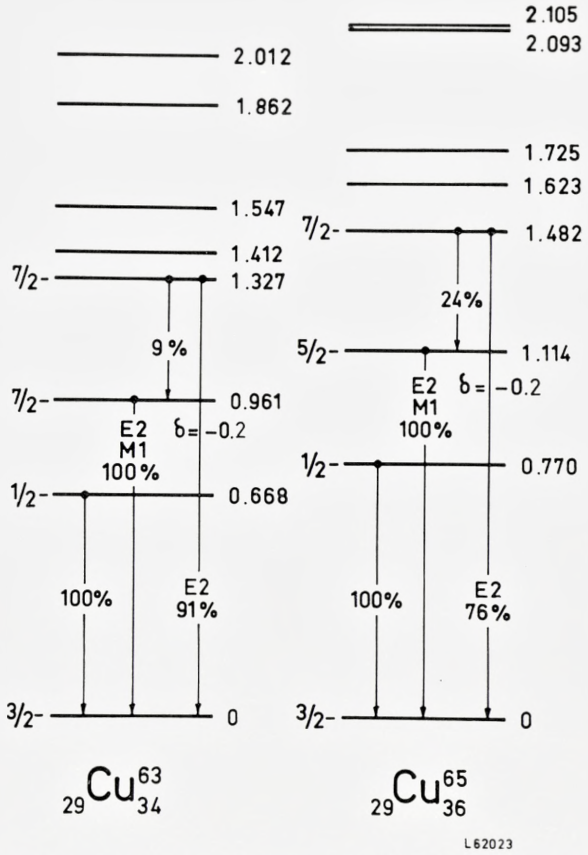

Fig. 16. Level diagrams for low lying states in Cu^{63} and Cu^{65}.

which operates on the core degrees of freedom and the other on the degrees of freedom of the particle. The tensorial degree r, in this case, can have values from 0 to 3, being limited by twice the spin of the odd particle. Such expansions yield a set of four spectra associated with monopole, dipole, quadrupole and octupole interactions between the particle and core, the sum of which gives the observed spectra. This expansion has been carried out[36] for Cu^{63} and Cu^{65}, assuming that the 3/2- state is at 1.412 and 1.623 Mev, respectively, in the two nuclei; the results are shown in Fig. 17. In both cases, a large positive octupole interaction is indicated with a smaller positive dipole and an almost negligible positive quadrupole. The monopole—or center-of-gravity position for Cu^{63} deviates from that of the 2 +

state in Ni^{62} by only 4 kev in 1.172 Mev and for Cu^{65} by 11 kev in 1.34 Mev. If, on the other hand, one assumes that the 3/2- level in Cu^{63} is at 1.86 Mev, an even larger positive octupole, the same very small positive quadrupole, and a negligible dipole term are obtained. In fact, to an excellent approximation, a positive octupole term alone reproduces the spectrum rather exactly. The center of gravity now, however, deviates from that in Ni^{62} by 87 kev. Similar results would be obtained for Cu^{65} if the 3/2- level were assumed to be near 2 Mev excitation.

The dominance of an octupole term in both copper isotopes for the particle-core interaction is rather surprising. It is not compatible, for example, with a naive model of the copper nuclides in which one assumes the $p_{3/2}$ neutron shell and the $f_{7/2}$ proton shell is really closed and describes Cu^{63} as a $p_{3/2}$ proton coupled to two neutrons in the $f_{5/2}$ shell and Cu^{65} as a $p_{3/2}$ proton coupled to two holes in the $f_{5/2}$ neutron shell. In this case, the two are identical except that the quadrupole level sequence will be inverted. In fact, if the interaction is exclusively between the $p_{3/2}$ shell (for protons) and the $f_{5/2}$ shell (for neutrons), then Nordheim's number is even and the interaction is expected to have a large quadrupole term, a smaller dipole term, and a negligible octupole term[37]. If, however, the odd particle, no matter what its configuration may be, is coupled to vibrational levels in the core, then the quadrupole part of the multipole expansion will vanish simply because it is proportional to the quadrupole moment of the vibrational state, and this is zero. One can therefore conclude that the negligible quadrupole contribution in both the copper isotopes is evidence for the fact that the 2+ excited state of the appropriate nickel isotope is a vibrational state. A multipole expansion of the levels in Au^{197} was also carried out and a rather small quadrupole contribution was found, which again supports the assumption that one is dealing with a vibrational core.

In conclusion, one might say that the low lying levels of the copper isotopes show many of the features expected from the coupling of a single particle to a vibrating core. It is remarkable that the equality of the reduced transition probability for decay of the three lowest levels is preserved in spite of heavy mixing with other single-particle levels. This mixing is evidenced by the level splittings but maybe is most clearly seen from the recent stripping experiments[5].

Whereas the Coulomb excitation mainly measures the collective part of the wave function, the stripping experiments measure the single-particle contribution to the nuclear states. It seems possible in this way to obtain an experimental set of expansion coefficients which ought to give a consistent picture of the properties of these nuclei.

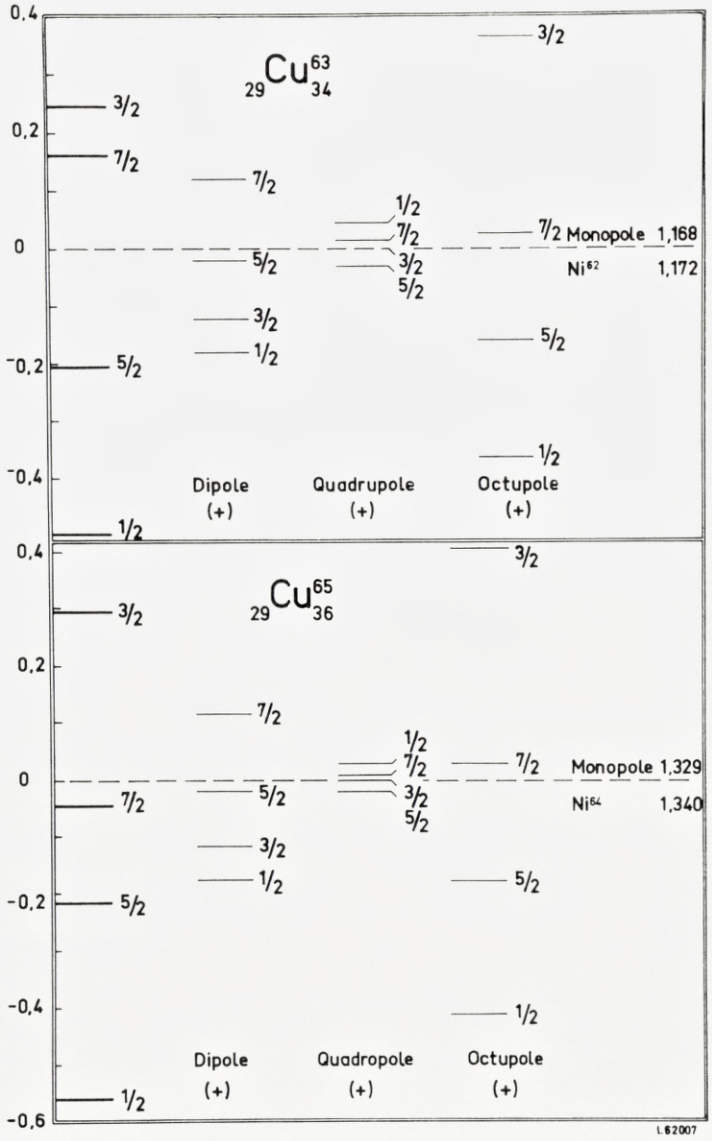

Fig. 17. Multipole expansion of the particle-core interaction in Cu^{63} and Cu^{65} if the missing 3/2-level is at 1.412 and 1.623 Mev, respectively.

7. Acknowledgement

It is a pleasure to acknowledge the many informative discussions on aspects of the experimental work with O. Nathan and Y. Yoshizawa and on the theoretical interpretation with A. Bohr, J. B. French, M. Harvey, E. Vogt and D. Beder. One of us (HEG) expresses his sincere appreciation to the Institute for Theoretical Physics, University of Copenhagen, for the hospitality extended to him during his one year's stay there.

Appendix I

a) Theoretical Angular Distributions

In a pure $E2$ Coulomb excitation process the coincidence angular correlation between a gamma counter moving in a plane and making angles θ with respect to the incident beam and a particle counter fixed at 180° to the beam (assuming point counters in both cases) is given by[11]

$$W(\theta) = 1 + 2A_2^{(2)}P_2(\cos\theta) - 1.5A_4^{(2)}P_4(\cos\theta), \tag{9}$$

where $A_2^{(2)}$ and $A_4^{(2)}$ are tabulated[11] gamma-gamma angular correlation functions. On the other hand, if only the direct angular distribution of the gamma rays is measured following $E2$ Coulomb excitation, the angular correlation in the classical limit is given by

$$W(\theta) = 1 + 0.5A_2^{(2)}P_2(\cos\theta) + 0.01A_4^{(2)}P_4(\cos\theta). \tag{10}$$

In this latter case, the coefficients actually depend on the parameter ξ[11] and equation (10) applies when $\xi = 0.3$. In the former case, not only is there no ξ dependence, but the correlations are much more asymmetric, in particular the coefficient of P_4 is very much larger, making it easier to measure multipole mixing in the de-excitation gamma radiation. It should be emphasized that, in the derivation of the above expressions, it has been assumed that the reaction mechanism is pure first order $E2$ Coulomb excitation in the classical limit, and this assumption is justified in the case of the present experiment, as shown in Appendix II.

Litherland and Ferguson[17] have derived a more general expression for the angular correlation of gamma rays arising from a particle-in particle-out reaction in the case when the gamma rays are detected in coincidence with the outgoing particle measured at either 0° or 180° to the incoming particle beam. Their expression is parameterized in terms of the relative

populations of magnetic substates of the level emitting the gamma ray. The gamma ray angular distribution is given by the following expression:

$$W(\theta) = \sum_{P_1 m_{f_1} k} (-1)^r P(m_f) \delta^p (I_f I_f m_f - m_f \mid k0) Z_1(LI_f L' I_f, I_i k) P_k(\cos\theta), \quad (11)$$

where I_f and m_f are the total angular momentum and its projection along some axis (in this case the beam direction) of the state emitting the gamma radiation, I_i is the total angular momentum of the nucleus after the gamma ray is emitted, $P(m_f)$ is the population of the magnetic substate m_f, δ is the amplitude mixing ratio of quadrupole to dipole radiation ($p = 0$ for $LL' = 11$, $p = 1$ for $LL' = 12$ and $p = 2$ for $LL' = 22$; the term with $LL' = 12$ has an additional factor of 2); Z_1 is a coefficient tabulated by SHARP et al.[38] $P_k(\cos\theta)$ is the Legendre polynomial and $r = J_i + m_f + L + L' + k/2$.

In equation (11), one normally regards the magnetic substate populations as parameters to be determined experimentally since they depend on the mechanism of the reaction used to populate them. In the case of Coulomb excitation, of course, the reaction mechanism is known and the magnetic substate populations can be calculated. The incoming and outgoing particles are directed along the z-axis and no change in the quantum number of the magnetic substate can occur. If the Coulomb excitation is by an electric quadrupole transition, then $E2$ transitions can only connect initial and final states having the same magnetic quantum number, and the population $P_f(m_i)$ of a final state with magnetic quantum number m_i is related to the population $P_i(m_i)$ of the initial state with magnetic quantum number m_i by the relation

$$P_f(m_i) = P_i(m_i)(I_i 2 m_i 0 \mid I_f m_i)^2. \quad (12)$$

It can readily be shown that inserting equation (12) into (11) results in the same expression as given in equation (9), since, in the ground state, all the magnetic substates are equally populated.

Again, because the reaction mechanism is known in the case of Coulomb excitation, it becomes possible readily to calculate the angular correlation to be expected when particle counters of finite solid angle are used, and this is discussed in the following section.

b) Corrections for Finite Solid Angle of Particle Detectors

A general expression for the coincidence angular correlations between inelastically scattered particles and gamma rays following Coulomb excitation has been given by ALDER et al.[11]. It can be written as follows:

$$W(\theta,\varphi,\theta_\gamma,\varphi_\gamma) = \sum_{k,\varkappa} b^{\lambda}_{k\varkappa}(\theta,\varphi,\xi) A_k^{(\lambda)} Y_{k\varkappa}(\theta_\gamma,\varphi_\gamma), \tag{13}$$

where the parameter ξ on which the cross section depends rather sensitively is given explicitly by ALDER et al.[11], $A_k^{(\lambda)}$ is the tabulated gamma-gamma correlation function[11], $Y_{k\varkappa}(\theta,\varphi)$ are the normalized spherical harmonics[39, 17], and the formula for the $b^{\lambda}_{k\varkappa}(\theta,\varphi,\xi)$ is given[11] for electric Coulomb excitation in a frame of reference in which the incident beam direction is taken as the z-axis; θ, φ, θ_γ, φ_γ, are the polar and azimuthal angles, respectively, of the particle and gamma counter. Since the plane in which the gamma counter moves can be defined as the zero for azimuthal angles, one can let $\varphi_\gamma = 0$. Furthermore, because the gamma counters have azimuthal symmetry, finite solid angle corrections may be introduced by inserting a factor Q_k in equation (13). If all pulses in the gamma-ray spectrum are counted at each angle these attenuation factors Q_k for a 7.6×7.6 cm NaI(Tl) counter may be obtained from the tables of RUTLEDGE[18].

Equation (13) is rather complicated in the general case, but considerable simplifications occur if the particle-counter geometry is chosen correctly. For example, all terms with $\varkappa$ = odd can be eliminated in a number of different geometries, viz:

1. An annular counter through which the beam passes
2. Two-particle counters $\theta_1 = \theta_2$, $\varphi_1 = \varphi$, $\varphi_2 = \varphi + 180^\circ$
3. Three-particle counters $\theta_1 = \theta_2 = \theta_3$, $\varphi_1 = 0$, $\varphi_2 = 120^\circ$, $\varphi_3 = 240^\circ$
4. Four-particle counters $\theta_1 = \theta_2 = \theta_3 = \theta_4$, $\varphi_1 = 0^\circ$, $\varphi_2 = 90^\circ$, $\varphi_3 = 180^\circ$, $\varphi_4 = 270^\circ$
5. Five-particle counters all at the same θ and equally spaced in φ with $\varphi_1 = 0$.

The elimination of odd $\varkappa$ has the advantage that the resulting expression for the angular correlation can be expanded in ordinary Legendre polynomials.

In these cases, the angular correlation expression (equation 13) is the following[40]:

$$\left.\begin{aligned} W(\theta,\varphi,\theta_\gamma) &= A + A_2^{(2)} Q_2 (C + 6D\cos(\pi+\theta) P_2^0(\cos\theta_\gamma) \\ &+ 1/2\cos 2\varphi(2D\cos(\pi+\theta) - C) P_2^2(\cos\theta_\gamma) - A_4^{(2)} Q_4 \\ &3/32\{(3B + 20D\cos(\pi+\theta) + 70E\cos 2(\pi+\theta)) P_4(\cos\theta_\gamma) \\ &- 1/3\cos 2\varphi(B + 4D\cos(\pi+\theta) - 14E\cos 2(\pi+\theta) P_4^2(\cos\theta_\gamma) \\ &+ 1/24\cos 4\varphi(B - 4D\cos(\pi+\theta) + 2E\cos 2(\pi+\theta) P_4^4(\cos\theta_\gamma)\}, \end{aligned}\right\} \tag{14}$$

where the quantities A, B, C, D and E are functions of $I_{2\mu}(\theta,\xi)$, the classical orbital integrals for $E2$ Coulomb excitation[11] as follows:

$$\left.\begin{aligned} A &= 2I_{20}I_{20} + 3(I_{22}I_{22} + I_{2-2}I_{2-2}) \\ B &= 4I_{20}I_{20} + I_{22}I_{22} + I_{2-2}I_{2-2} \\ C &= -2I_{20}I_{20} + 3(I_{22}I_{22} + I_{2-2}I_{2-2}) \\ D &= I_{20}I_{22} + I_{20}I_{2-2} \\ E &= I_{22}I_{2-2}. \end{aligned}\right\} \quad (15)$$

It can readily be shown that, when $\theta = 180°$, equation (14) reduces to equation (9). In the case of an annular counter the above expression becomes independent of φ and has the following relatively simple form:

$$\left.\begin{aligned} W(\theta,\theta_\gamma) &= 1 + A_2^{(2)}Q_2\left\{\frac{6D\cos(\pi+\theta)+C}{A}\right\}P_2(\cos\theta_\gamma) - 3/32 \\ & A_4^{(2)}Q_4\left\{\frac{3B+20D\cos(\pi+\theta)+70E\cos 2(\pi+\theta)}{A}\right\}P_4(\cos\theta_\gamma), \end{aligned}\right\} \quad (16)$$

where the quantities in curly brackets are functions of both θ and ξ and can be readily evaluated by graphical or numerical integration for any dimensions of an annular counter. The dependence of these quantities on θ for an annular counter with a mean angle equal to that of the counter used in the present experiment is discussed below.

The counter geometry used in the present experiments does not resemble any of the geometries listed above, except in that terms in equation (13) with $\varkappa$ odd are eliminated and hence equation (14) applies. This is always true if the counter is symmetric about the plane in which the gamma counter is moved. It is therefore necessary to perform some sort of numerical integration over the counter area. In the present work, this was done by dividing the area of each counter into six equal areas, calculating the angular distribution for each according to equation (14), weighting each by the relative solid angles and then adding the six distributions together. For a counter of the dimensions shown in Fig. 2, when the distance d between counter and target is 9 mm, the angular correlation is given by

$$\left.\begin{aligned} W(\theta_\gamma) = 1 &+ A_2^{(2)}Q_2(1.70P_2^0 + 0.0269P_2^2) - A_4^{(2)}(0.843P_4^0 \\ &+ 0.0171P_4^2 - 0.428\times 10^{-5}P_4^4). \end{aligned}\right\} \quad (17)$$

The P_l^ms, of course, are all functions of $\cos\theta_\gamma$.

The term in P_4^4 is negligible here and also for the case when d is 15 mm where the correlation becomes

$$\left.\begin{aligned} W(\theta_\gamma) = 1 + A_2^{(2)}Q_2(1.86P_2^0 + 0.0133P_2^2) - A_4^{(2)}Q_4 \\ (1.16P_4^0 + 0.00915P_4^2). \end{aligned}\right\} \quad (18)$$

Since both equations (17) and (18) have been calculated for $\xi = 0.3$, it is necessary to inquire whether the calculated coefficients are seriously dependent on ξ. It is known, for example, that for the direct gamma correlations the coefficients in equation (10) are very strongly dependent[11]. In order to answer this question readily, calculations were made for an annular counter with the same mean angle θ as for the counters employed in this experiment. This mean angle for the second geometry is 155°. Using this angle the coefficients in curly brackets in equation (16) which will be designated as a_2 and a_4, respectively, were evaluated for ξ in the range 0 to 1. Over this extensive range a_2 varied from 1.87 to 1.82 and a_4 from 1.18 to 1.08. It should be noted, incidentally, that the values at $\xi = 0.3$ are identical to the coefficients of P_2^0 and P_4^0, respectively, in equation (18), which indicates that the geometry employed is a rather good approximation to an annulus. Of course, for a counter exactly at 180°, there is no ξ-dependence and the above calculation demonstrates that even for angles up to 155° the ξ-dependence is negligible. This is a very considerable advantage of the correlation technique in which coincidences are taken with back scattered ions as opposed to measurements of the direct gamma-ray angular distributions.

These expressions have the unfortunate feature that it is difficult directly to compare them with experiment since the experimental data is fitted to a Legendre polynomial expansion of the form

$$W(\theta_\gamma) = a_0 + a_2P_2(\cos\theta_\gamma) + a_4P_4(\cos\theta_\gamma), \quad (19)$$

particularly when the radiation is mixed dipole-quadrupole. They can, however, be reduced to this form where, of course, both the coefficients a_0 and a_2 will be functions of $A_2^{(2)}Q_2$ and $A_4^{(2)}Q_4$. For a particle counter distance of 15 mm the expression becomes

$$\left.\begin{aligned} 1 + 0.03A_4^{(2)}Q_2 - 0.019A_4^{(2)}Q_4 + (1.83A_2^{(2)}Q_2 - 0.093A_4^{(2)}Q_4)P_2^0 \\ - 1.05A_4^{(2)}Q_4P_4^0. \end{aligned}\right\} \quad (20)$$

Appendix II

Second-Order Coulomb Excitation Effects

Because the relative $B(E2)$ for the three levels in Cu^{63} and Cu^{65} were obtained from gamma-ray spectra measured in coincidence with back scattered O^{16} ions detected in a counter near 180°, it is necessary to estimate how the results might be changed by second-order Coulomb excitation effects. Such effects are known to have their maximum values in this geometry and with heavy bombarding ions. Recently, BEDER[41] has written a computer program for calculating second-order Coulomb excitation cross sections and has shown that, in certain circumstances, the interference term between first and second order can be quite large.

The situation in odd-A nuclei with ground-state spins greater than 1/2, such as one is dealing with here, is complicated by the fact that the second-order effects can involve re-orientation of both the ground and excited states as well as double excitation. In order to calculate all the contributions it is necessary to know both the sign and magnitude of the $B(E2)$ for each level as well as those connecting various levels. The Coulomb excitation cross section between the ground state x of a nucleus and some excited state y can be written

$$d\sigma_{xy} = d\sigma_{xy}^{(1)} + \sum_{z} d\sigma_{xzy}^{(1,2)}, \tag{21}$$

where it can be shown that the higher order terms are negligible. The direct term $d\sigma_{xy}^{(1)}$ is proportional to $B_{xy}(E2)$ while the interference terms $d\sigma_{xzy}{}^{(1,2)}$ are proportional to $(B_{xz}(E2)\ B_{zy}(E2))^{1/2}$. For convenience, the levels in Cu^{63} at 0, 0.668, 0.961, 1.327 and a fictitious level at 2.00 Mev with spins and parities of 3/2-, 1/2-, 5/2-, 7/2- and 3/2- (assumed) will be labelled 0, 1, 2, 3, 4, respectively. Using these labels, the only $B(E2)$'s which are known experimentally are $B_{00}(E2)$, $B_{01}(E2)$, $B_{02}(E2)$ and $B_{03}(E2)$. It is therefore necessary to estimate the other $B(E2)$'s which are required. These estimates have been made and the second-order calculations have been carried out for Cu^{63} by HARVEY and VOGT[42]. The ratio of $B_{33}(E2)$ to $B_{03}(E2)$ can be obtained from the BAYMAN-SILVERBERG model[1]. It depends on the coupling strength y (see ref. 1) but deviates appreciably from the strong coupling value only for $y < 0.1$ where the ratio approaches zero. It has therefore been assumed that $B_{33}(E2)/B_{03}(E2)$ has the strong coupling limit value of 0.11[42]. The other $B(E2)$'s involve transitions within or between the levels 1, 2 and 3 and are equal to $B_{33}(E2)$ multiplied by the ratio of two vector coupling coefficients of the symplectic group[1]. These coefficients are not

TABLE X

Second-order coulomb excitation cross sections for Cu^{63}.

First-order process	Second-order process	$d\sigma^{(1,2)}/d\sigma^{(1)}$
0–1	0–0–1	+0.045
	0–2–1	0.045
	0–4–1	0.045
0–2	0–0–2	+0.045
	0–2–2	0.018
	0–1–2	0.003
	0–3–2	0.041
	0–4–2	0.024
0–3	0–0–3	−0.022
	0–3–3	+0.039
	0–2–3	0.012
	0–4–3	0.010

For notation see appendix II. In column 3 unless the sign is given it is not known.

available and will be assumed to be of the order of unity, giving $B_{12}(E2) = B_{21}(E2) = B_{22}(E2) = B_{23}(E2) = B_{32}(E2) = B_{33}(E2) = 0.11 \times B_{03}(E2)$. The $B(E2)$'s connecting level 4 to levels 0, 1, 2, and 3 have neither been calculated nor measured. They depend on the coupling parameter y in a different way than does $B_{33}(E2)$, and it has arbitrarily been assumed that $B_{04}(E2) = \frac{1}{2}(B_{01}(E2) + B_{02}(E2))$ and $B_{41}(E2) = B_{42}(E2) = B_{43}(E2) = B_{33}(E2)$. With this somewhat arbitrary selection of $B(E2)$'s the ratios $d\sigma^{(1,2)}/d\sigma^{(1)}$ were calculated and are listed in Table XI. The individual contributions range in value from 0.003 to 0.045 but, in general, the relative phases are unknown. The maximum effect for the 0.668 Mev level can be 13.5 %, for the 0.961 Mev level 13.1 % and for the 1.327 Mev level 4.9 %. These are important contributions to the observed values and could be determined with more certainty if the vector coupling coefficients of the symplectic group were known. They are unlikely, however, to have the maximum values.

To investigate the effect of second-order Coulomb excitation on the angular correlations measured in coincidence with back scattered ions detected in a counter near 180°, the following calculation was made, using Beder's computer program[41]. The reaction assumed was that for 34 Mev O^{16} ions incident on Fe^{56} exciting the level at 0.845 Mev. The particle counter was assumed to be a thin ring with the beam as axis making an angle θ_p

TABLE XI

Second-order Coulomb excitation effects on angular correlations of gamma rays measured in coincidence with particles scattered into a ring counter at θ_p with the beam as axis. The calculations are for 34 Mev O^{16} ions on Fe^{56} (thin target) exciting the 0.845 Mev level. The angular correlation is given by $W(\theta_\gamma) = a_0 + a_2 P_2(\cos\theta\gamma) + a_4 P_4(\cos\theta\gamma)$ and a_l^1 includes only first-order effects and a_l^{1+2} includes first plus second.

θ_p	a_0^{1+2}/a_0^1	$\left(\frac{a_2^{1+2}}{a_0^{1+2}}\right)\Big/\left(\frac{a_2^1}{a_0^1}\right)$	$\left(\frac{a_4^{1+2}}{a_0^{1+2}}\right)\Big/\left(\frac{a_4^1}{a_0^1}\right)$
140	1.162	0.994	0.952
150	1.176	0.996	0.979
160	1.186	0.998	0.992
170	1.192	0.999	0.998

with respect to the target center. The computer calculated the coefficients in the Legendre polynomial expansion of the angular distribution given by equation (19) both in first order (a_0^1, a_2^1 and a_4^1) and in first plus second order (a_0^{1+2}, a_4^{1+2} and a_4^{1+2}); the results for various values of θ_p are given in Table XI. It can be seen that for values of $\theta_p > 150°$ the effect on the angular correlations is negligible, although the cross section (proportional to a_0) is strongly affected. The calculations were also made for 32 and 30 Mev O^{16} ions and the effect on the correlations was even smaller. It is clear that no correction from such effects has to be applied to the angular correlations.

Institute for Theoretical Physics
University of Copenhagen.

References

1. B. F. Bayman and L. Silverberg: Nuclear Physics **16**, 625 (1960).
2. Y. Yoshizawa: Physics Letters **2**, 261 (1962).
3. O. Nathan and S. G. Nilsson: Review article to be published in Alpha-, Beta- and Gamma-Ray Spectroscopy, ed. Kai Siegbahn.
4. M. Bouten and P. van Leuven: Nuclear Physics **32**, 499 (1962).
5. A. Blair and D. Armstrong, private communication.
6. R. D. Lawson and J. L. Uretsky: Phys. Rev. **108**, 1300 (1957).
7. A. de Shalit: Phys. Rev. **122**, 1530 (1961).
8. M. Mazari, W. W. Buechner and R. P. de Figueiredo: Phys. Rev. **108**, 373 (1957).
9. G. M. Temmer and N. P. Heydenburg: Phys. Rev. **104**, 967 (1956).
10. For references to properties of levels in Cu^{63} and Cu^{65} from γ-ray measurements, see Nuclear Data Sheets – National Academy of Sciences – National Research Council, Washington, D.C.
11. K. Alder, A. Bohr, T. Huus, B. Mottelson and A. Winther: Revs. Mod. Phys. **28**, 432 (1956).
12. Obtained from R. M. Latimer, Lawrence Radiation Laboratory, University of California, Berkeley, California.
13. Obtained from Oak Ridge Technical Entreprises Corporation, Oak Ridge, Tennessee.
14. Obtained from Hewlett-Packard, Palo Alto, California.
15. Obtained from Oak Ridge National Laboratories, Oak Ridge, Tennessee.
16. We are indebted to Mr. Jørn Borggreen for preparing these targets.
17. A. E. Litherland and A. J. Ferguson: Can. Journal of Phys. **39**, 788 (1961).
18. A. R. Ruthledge CRP-851: Atomic Energy of Canada Limited, Chalk River, Ontario, Canada, July, 1959.
19. D. Eccleshall, B. M. Hinds and M. J. L. Yates: Nuclear Physics **32**, 190 (1962).
20. R. M. Diamond, B. Elbek and F. S. Stephens: Nuclear Physics **43**, 560 (1963).
21. These fits were carried out on the Datatron Computor, Atomic Energy of Canada Limited, Chalk River, Ontario, Canada.
22. R. L. Heath IDO-16408 Phillips Petroleum Co., Atomic Energy Division, Idaho Falls, Idaho, U.S.A.
23. C. Broude and H. E. Gove: Proceedings of the Second Conference on Reactions Between Complex Nuclei, ed. A. Zucker, F. T. Howard and E. C. Halbert. John Wiley and Sons Inc., New York, 1960.

24. B. M. Adams, D. Eccleshall and M. J. L. Yates: Proceedings of the Second Conference on Reactions Between Complex Nuclei, ed. A. Zucker, F. T. Howard and E. C. Halbert. John Wiley and Sons Inc., New York, 1960.
25. D. G. Alkazov, A. P. Grenberg, K. I. Yerokhina and I. Kh. Lemberg: Izvest. Akad. Nauk SSSR Ser. Fiz. **23**, 233 (1959).
26. K. I. Yerokhina and I. Kh. Lemberg: Izvest. Akad. Nauk SSSR Ser. Fiz. **26**, 205 (1962).
27. J. B. Cumming, A. Schwarzochild, A. W. Sunyar and N. T. Porile: Phys. Rev. **120**, 2128 (1960).
28. T. Rothem, E. R. Metzger and C. P. Swann: Bull. Am. Phys. Soc. Ser. 2, **5**, 266 (1960).
29. E. C. Booth: Nuclear Physics **19**, 426 (1960) and E. C. Booth and K. A. Wright, Nuclear Physics **35**, 472 (1962).
30. K. Ilakovac: Proc. Phys. Soc. (London) **67** A, 601 (1954).
31. D. H. Wilkinson: Nuclear Spectroscopy Part B, ed. F. Ajzenberg–Selove, Academic Press, New York, 1960.
32. D. S. Andreyev, A. P. Grenberg, K. I. Yerokhina and I. Kh. Lemberg: Nuclear Physics **19**, 400 (1960).
33. H. E. Gove Physics Letters **4**, 249 (1963).
34. M. Harvey: Nuclear Physics **48**, 578 (1963).
35. Barloutaud, Chaminade, Faraggi, Garetts and Harvey (private communication).
36. The authors are indebted to J. B. French for suggesting this procedure.
37. J. B. French (private communication).
38. W. T. Sharp, J. M. Kennedy, B. J. Sears, and M. G. Hoyle: "Tables of Coefficients for Angular Distribution Analysis" AECL no. 97, Chalk River, Ontario, Canada, August 1954.
39. E. U. Condon and G. H. Shortley: Theory of Atomic Spectra, Cambridge University Press, New York, 1935.
40. We are indebted to Y. Yoshizawa for providing us with this equation.
41. D. Beder: Physics Letters **3**, 206 (1963).
42. M. Harvey and E. Vogt (private communication).

Indleveret til Selskabet den 16. april 1964.
Færdig fra trykkeriet den 17. november 1964.

Matematisk-fysiske Meddelelser
udgivet af
Det Kongelige Danske Videnskabernes Selskab
Bind **34,** nr. 9

Mat. Fys. Medd. Dan. Vid. Selsk. **34,** no. 9 (1964)

$C^{12}(C^{12},\alpha)Ne^{20}$ CROSS SECTION MEASUREMENTS

BY

J. BORGGREEN, B. ELBEK,
AND R. B. LEACHMAN

København 1964
Kommissionær Ejnar Munksgaard

Contents

Synopsis

The reaction $C^{12}(C^{12},\alpha)Ne^{20}$ has been investigated from 9 to 16 MeV center-of-mass energies. The alpha particles were detected with semiconductor detectors in a geometry which resolved the individual alpha-particle groups feeding the five lowest states in Ne^{20}. Excitation functions of the differential cross sections at center-of-mass angles of 0°, 37.3°, and 90° showed strong fluctuations in the yields with no definite cross correlation between the positions of the maxima for different alpha-particle groups.

In most cases, the angular distributions of the alpha-particles to the ground state contained a dominant contribution from a squared Legendre polynomial of one definite order, usually 8 or 10. Angular distributions for each of the alpha-particle groups populating the excited states were more complex.

The general structure of the yield curves and angular distributions is in agreement with the statistical theory of overlapping resonances of the compound nucleus.

PRINTED IN DENMARK
BIANCO LUNOS BOGTRYKKERI A/S

1. Introduction

The fluctuations in the cross sections of the reactions from C^{12} bombardment of C^{12} have generally been interpreted[1) 2)] in terms of "quasi-molecular" resonances and clustering in the compound Mg^{24}. At energies up to about 8 MeV center-of-mass, ALMQVIST et al.[1)] indeed observed cross correlations of the cross sections (cross sections for different emitted particles having maxima at the same energy), and thus isolated levels of some type apparently were observed. However, at higher energies extending to about 13 MeV, cross correlations in these cross sections were not apparent, nor were they observed by KUEHNER et al.[2)] for the reaction $C^{12}(C^{12},\alpha)Ne^{20}$ to the ground and first excited state of Ne^{20}. This lack of cross correlation argues against the "quasi-molecular" resonance and Mg^{24} clustering interpretations of the fluctuations in these measured excitation functions at the higher energies.

LASSEN and OLSEN[3)] observed the inverse reaction $Ne^{20}(\alpha,C^{12})C^{12}$ for a wider span of Mg^{24} excitation energy, but only to the ground state of C^{12}. As in the measurements of KUEHNER et al.[2)], both fluctuations in the excitation functions and unusually well defined angular distributions were observed. A particularly interesting angular distribution for the ground-state reaction observed in both experiments was at 25.3 MeV excitation energy of the compound nucleus, at which energy a maximum in the cross section occurs. This angular distribution was reasonably well fitted[3)] by the square of a Legendre polynomial of a single order, in this case 8. These observations led to the present investigation of more extensive excitation functions and angular distribution of the $C^{12}(C^{12},\alpha)Ne^{20}$ reaction to the ground state and to the lowest excited states of Ne^{20}.

In the present experiment, excitation functions and angular distribution of alpha-particle groups have been measured with instrumental resolutions less than the average width Γ of the compound nucleus levels and at energies such that Γ was greater than the average level spacing D, i. e. $\Gamma > D$. These are the conditions for observing statistical fluctuations in nuclear cross sections[4) 5)].

The statistical theory for the present reaction between identical bosons is particularly simple since only even values of the compound nucleus angular momentum J are possible. Cross sections at selected angles and for final nucleus states of selected spins and parities have further simplicity. These are discussed by BONDORF and LEACHMAN[6] in the following paper. In the present measurements, advantage is taken of these simplicities to increase the sensitivity of testing the statistical theory of nuclear reactions. These tests, to establish that a statistical combination of incoherent and coherent reaction amplitudes from overlapping resonances lead to the observed cross sections, are

1) No cross correlations between excitation functions for the alpha-particle groups to the ground state and the various excited states in Ne^{20} should exist. This test is most meaningful for the cross section integrated over all angles, rather than for the differential cross section.

2) Even for the 0+ ground-state reaction (for which the orbital angular momentum l equals J) the angular distribution is not expected to be a pure Legendre polynomial of one single order, but the polynomial of the usually dominant spin is expected to be statistically combined with admixtures of polynomials of different orders.

3) Angular distributions with orders of the dominant Legendre polynomials that are exceptions to the usually dominant order are expected.

4) Probability distributions of the cross sections are expected to follow χ^2 distributions with the number of degrees of freedom in the distributions predicted by theory.

BONDORF and LEACHMAN[6] have analysed some of the present data in terms of the last two tests.

2. Experiment

The C^{12} beam for the reaction $C^{12}(C^{12},\alpha)Ne^{20}$ was obtained from the tandem Van de Graaff accelerator at the Institute for Theoretical Physics. After separation in the analysing magnet, the ions had a charge of 4+. After passing through the target, the C^{12} ions have a larger effective charge according to the semi-empirical equation of NORTHCLIFFE[7]. Over the energy range of this experiment the effective ionic charge is calculated to vary less than 2 % from an average value of 96 % of the nuclear charge 6. Therefore, the beam current could be read directly from the Faraday cup stopping the beam. The beam intensities obtained were between 0.3×10^{-7} and 1.5×10^{-7} A.

The targets were evaporated, self-supporting carbon films with thicknesses from 20 to 70 $\mu g/cm^2$; for some targets, thicknesses were determined either by Mott scattering or by weighing, or both. For other targets, the thicknesses were determined by reaction yield intercomparisons. The beam had an energy spread of about ± 50 keV and the target thicknesses correspond to energy losses[8] of approximately 80 to 240 keV for C^{12} ions at 25 MeV in the laboratory system. This resulted in an instrumental resolution within the limits 65 keV $< \Delta E <$ 130 keV in the center-of-mass system for the compound nucleus formation.

The alpha particles from the disintegration of the Mg^{24} compound nuclei were observed by one or two 10^4 Ω-cm p-type semiconductor detectors which could be rotated around the target from the outside. The beam was defined by 3-mm-diameter collimators, but burn spots on the target indicated that the beam size at the target was in general smaller than this. The counter apertures were 3 mm in diameter. The distances between target and counter were 65 mm for some measurements and 70 mm for others, and so the angular resolutions were approximately $\pm 1.3°$ (Lab.) from a point beam spot on the target. Uncertainties in the angular alignment were about $\pm 0.3°$.

For 0° measurements, a 24.2 mg/cm^2 gold absorber was mounted 10 mm in front of the counter to absorb the beam of C^{12} particles but transmit the reaction alpha particles. A measurement of the beam current was provided by C^{12} particles elastically scattered from the C^{12} target and detected by another counter at 20° (Lab.). The special simplicity of the distribution in the cross section expected for 0° has been calculated by Gibbs[9] to become rapidly more complicated with angle; already at 4° considerable change in the cross section distribution is expected. Thus, the reaction alpha particles leaving the target at 4° or more, and undergoing Rutherford scattering from the absorber into the counter centered at 0°, is of concern*. Approximate calculations indicate that the number of such scattered alpha particles detected is approximately a few percent of the reaction alpha particles leaving the target at angles in the admittance cone of the 0° detector. However, this scattering, the possibility of a full 3-mm-diameter beam on the target increasing the resolution to about $\pm 3°$, and alignment errors can all combine to cause an appreciable yield of approximately 4° reaction products to be observed by the 0° centered counter.

A run at each energy amounted to an irradiation corresponding to about 2×10^{-5} coulomb which required typically 3 min. at the beam currents used. For the targets and solid angles used, the conversion between the differential

* We are grateful to E. Almqvist for suggesting this effect.

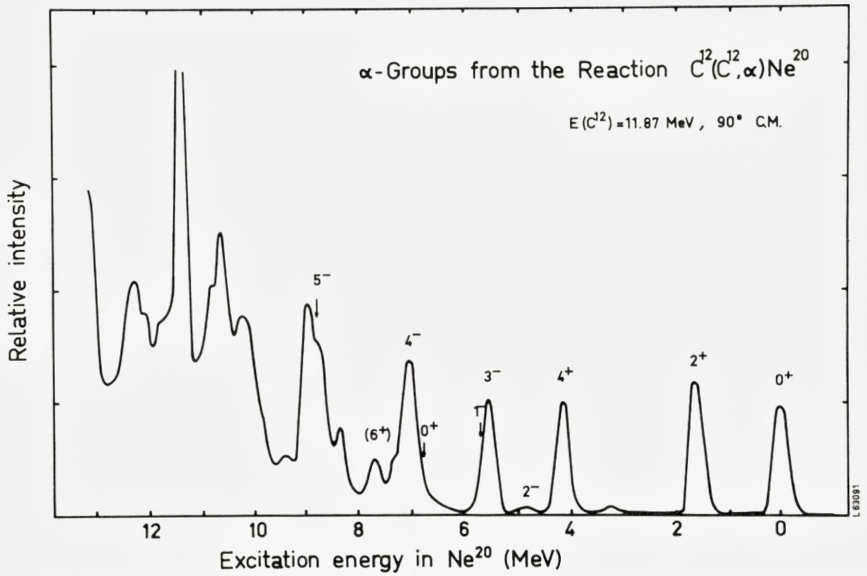

Fig. 1. Partial spectrum of alpha particles populating the states indicated in Ne^{20}. The absolute energy of the ground-state alpha-particle group is 15.3 MeV.

cross section and the number of alpha particles in the group being measured was typically 1 mb/ster for about 50 alpha particles detected. Effects of the statistical uncertainties in these small numbers have not been included in the analyses.

A typical spectrum of observed alpha particles is shown in fig. 1. As seen from the figure, only the alpha-particle groups to the five lowest states in Ne^{20} were resolved. The observed resolution resulted from the combination of the angular resolution and the reaction kinematics; the inherent resolutions of the counters were considerably better than the observed resolution. The small peak at 3.3 MeV on the energy scale is due to alpha particles from the reaction $O^{16}(C^{12},\alpha)Mg^{24}$, where the oxygen presumably is a contamination from pump oil buildup on the target. Under the worst conditions, the buildup on the target also increased the C^{12} thickness by 1 $\mu g/cm^2/h$. Corrections to the cross-section measurements were made for this buildup.

To anticipate such unresolved alpha-particle groups, we have calculated the relative energies of the groups from the oxygen and carbon reactions as functions of bombarding energy at the three different laboratory angles. These curves are shown on figs. 2–4 with the experimental energy resolution indicated so that the identity of possible unresolved alpha-particle groups

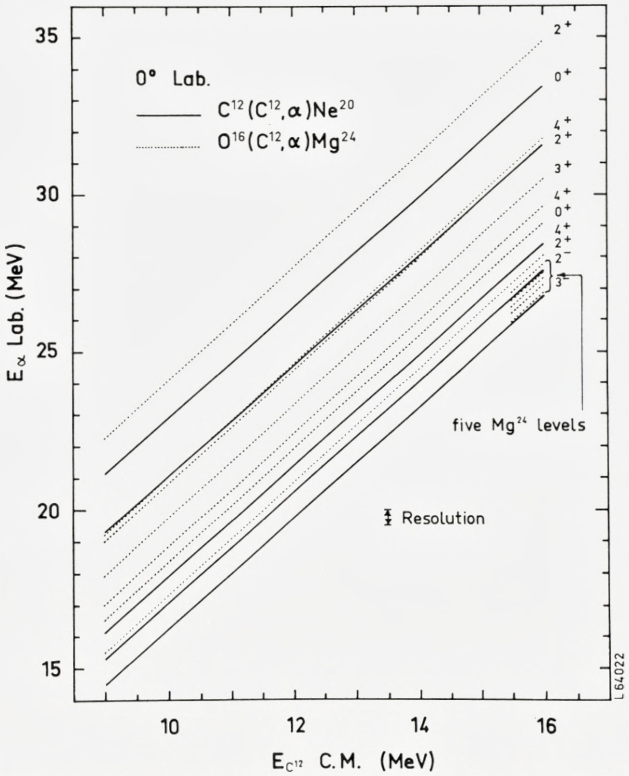

Fig. 2. Calculated energies of the alpha-particle groups from the reactions $C^{12}(C^{12},\alpha)Ne^{20}$ and $O^{16}(C^{12},\alpha)Mg^{24}$ as a function of the bombarding energy measured in the center-of-mass system of the carbon-carbon reaction. The observed energy resolution of the alpha-particle counter is indicated.

can be established. Unresolved alpha particles from the different reactions from oxygen contribute an incoherent amplitude to the cross section and thus increase the apparent number of degrees of freedom in the distribution of the observed cross section. The number of these other alpha particles is determined by the amount of O^{16} on the target and the cross section, which increases with increasing spin of the final state in Mg^{24}.

3. Angular Distributions

The angular distributions of the ground-state alpha particles from the $C^{12}(C^{12},\alpha)Ne^{20}$ reaction are expected to be relatively simple for the following reasons.

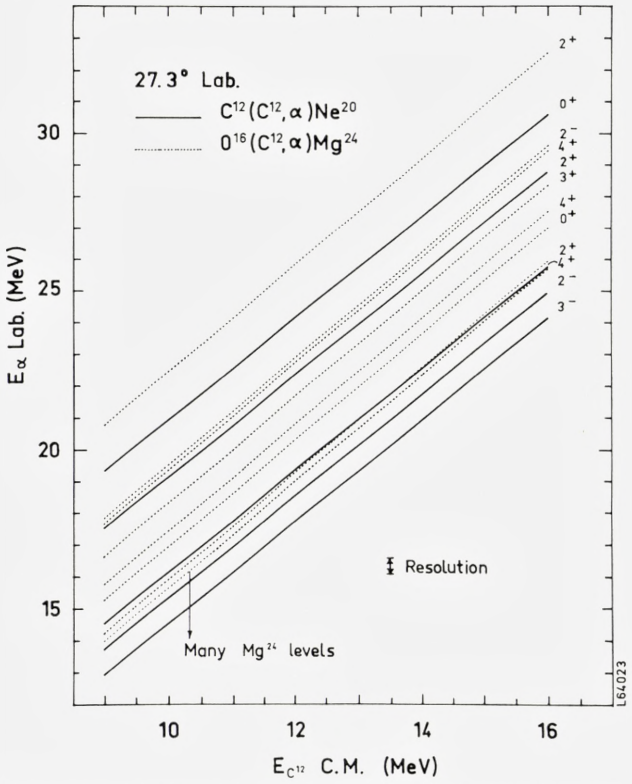

Fig. 3. Calculated energies for 27.3° lab., which corresponds to 37.3° C.M. in the $C^{12} + C^{12}$ system. See caption to Fig. 2.

1) The identity of the projectile and target nuclei makes the angular dependence of the alpha particle symmetric about 90° in the center-of-mass system independent of the type of reaction.

2) Since both of the colliding particles are bosons, the reaction is described by a symmetric wave function. Thus, the parity is even, and only states with even J in the compound nucleus are formed.

3) If the compound states are isolated resonances with angular momentum J or are overlapping resonance of essentially only one angular momentum J, then the alpha particles to the ground state in the Ne^{20} nuclei must have an angular momentum l equal to J, and the distribution of the alphas is the square of a Legendre polynomial of order l, i. e. $[P_l(\cos\theta)]^2$.

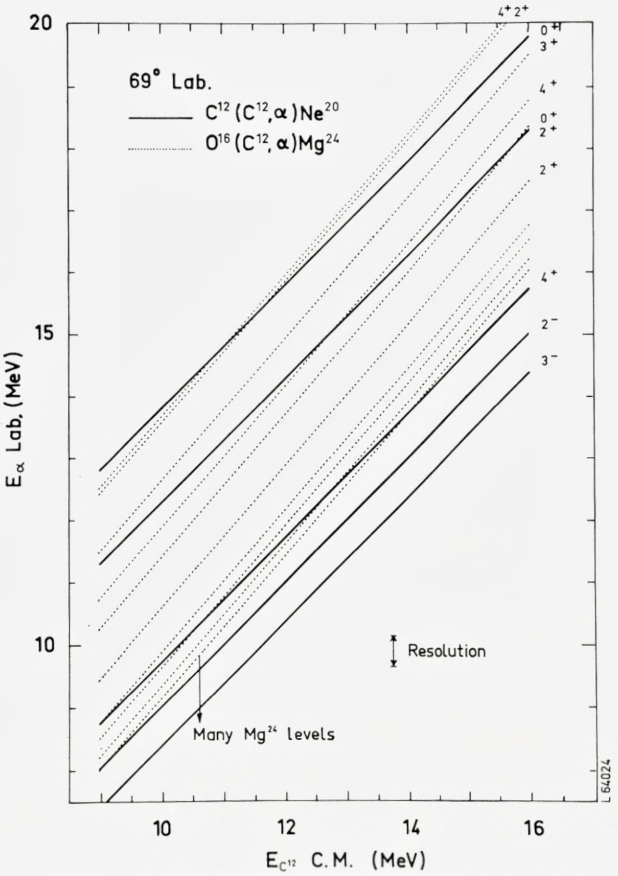

Fig. 4. Calculated energies for 69° lab., which corresponds to 90° C.M. in the $C^{12} + C^{12}$ system. See caption to Fig. 2.

The distribution of ground-state alpha particles at a bombarding energy of 11.5 MeV is shown in fig. 5 in the center-of-mass system; parts of this distribution have been reported earlier[2) 3)]. The positions of the peaks and valleys are rather well reproduced by the square of the eighth order Legendre polynomial $[P_8(\cos\theta)]^2$, but the curve itself is only moderately well fitted by this function. This confirms the expectation from the statistical theory for overlapping resonances that reaction amplitudes of more than one angular momentum J in general contribute to the observed cross section.

A survey of most of the ground-state distributions measured in this experiment is shown in fig. 6. It is evident that the angular distributions at

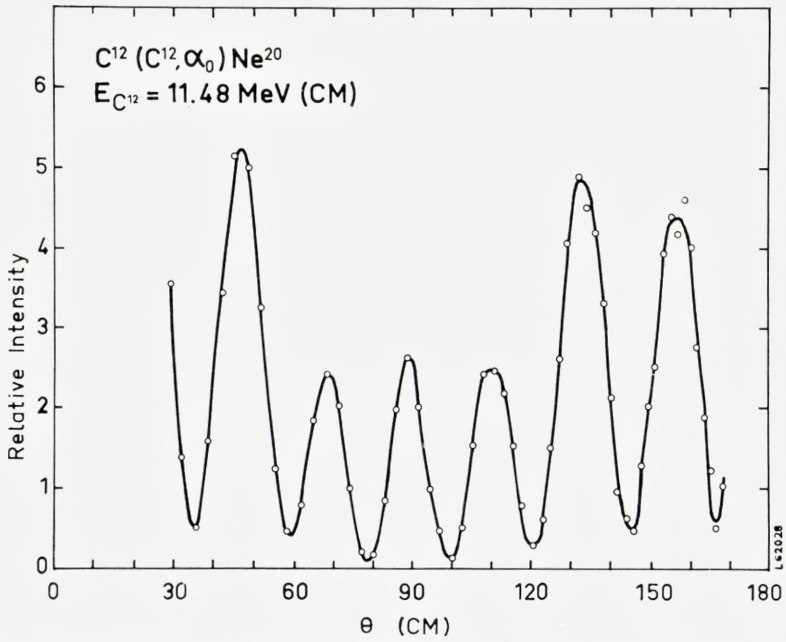

Fig. 5. Angular distribution of alpha particles to the ground state in Ne^{20} for 11.5 MeV C.M. C^{12} + C^{12}.

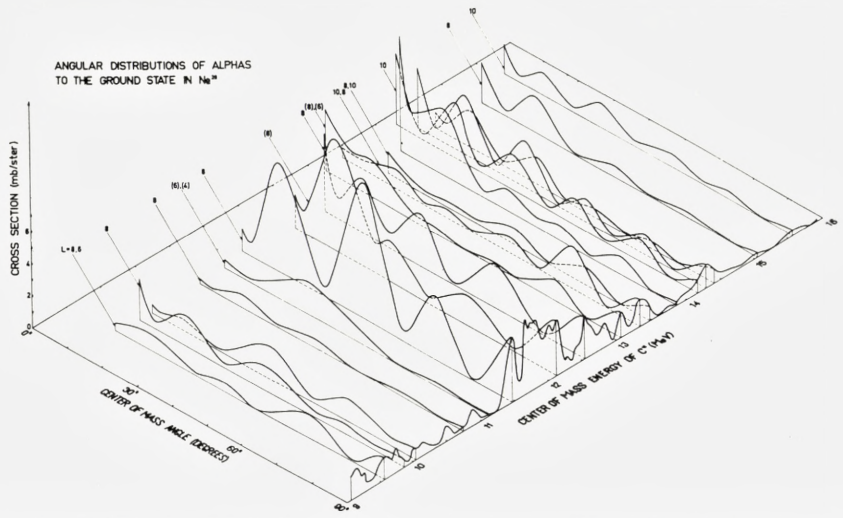

Fig. 6. Survey of angular distribution of alpha particles to the ground state in Ne^{20}. The l values are assigned according to the simple rules discussed in the text; where two values are given, the first refers to the main contribution. Parenthesis indicates a less certain determination of l.

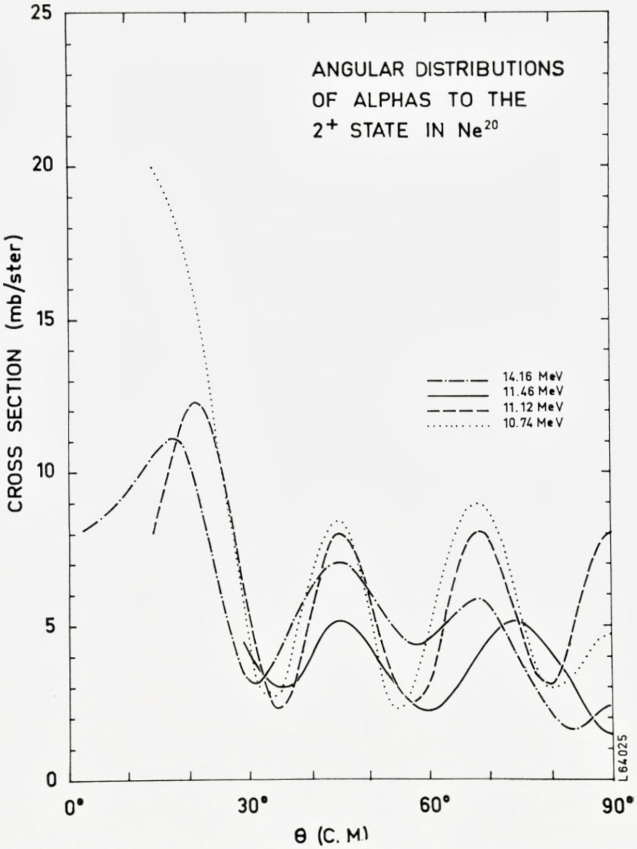

Fig. 7. Typical angular distributions of alpha particles to the 2+ state in Ne^{20} for different carbon bombarding energies (C.M.).

11.5 MeV and at 14.2 MeV each have an exceptionally dominant J value resulting in nearly pure $[P_8(\cos\theta)]^2$ and $[P_{10}(\cos\theta)]^2$ angular distributions, respectively. All the other angular distributions are more complex.

The angular distributions are expected[6] to be of the form

$$|P_l + (\alpha + i\beta)P_{l'}]^2 = (P_l)^2 + (\alpha^2 + \beta^2)(P_{l'})^2 + 2\alpha P_l P_{l'}.$$

In cases where the admixture of the angular momentum $l' = l \pm 2$ is relatively small, it is in general possible to determine the l value of the main contribution just from the number of maxima or minima in the experimental distribution between 0° and 90°. The sign of α has a marked effect on the envelope of the angular distribution. One notes that, if $P_l(\cos 90°)$ is po-

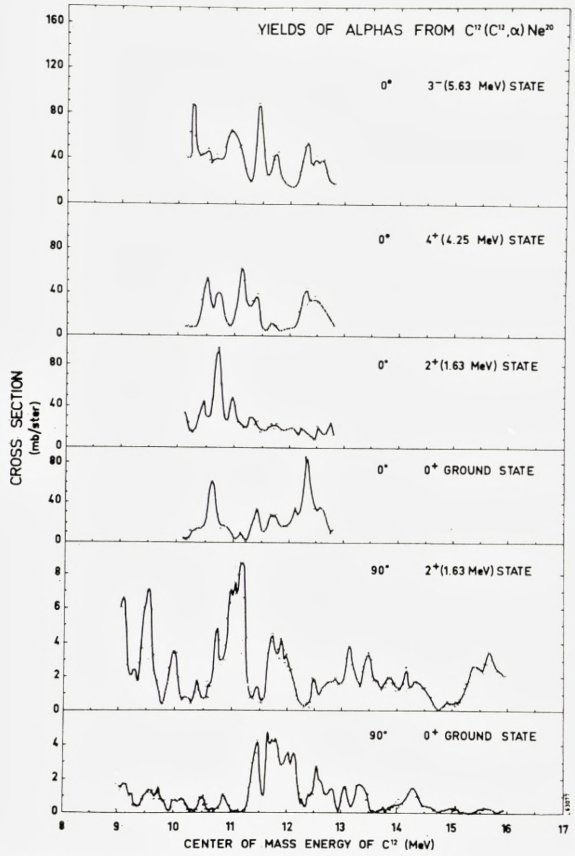

Fig. 8. Excitation functions for different alpha-particle groups at 0° and 90° C.M. The energy axis corresponds to zero target thickness. At 0° there is no yield of alphas to the 2— state in Ne^{20}. The 3— state at 0° was only poorly resolved from the neighbouring 1— state of Ne^{20}.

sitive, then $P_{l\pm 2}(\cos 90°)$ is negative, and vice versa, and that $P_l(\cos 0°)$ is always positive. A positive α will therefore decrease the yield at 90°; a negative α will decrease the yield at 0° and increase the yield at 90°. In the latter case, the envelope of the angular distribution can be almost constant with angle. (See the distribution at 13.48 MeV in fig. 6).

One can determine the value of l' by observing the direction of the shift of the positions of the minima from those of the distribution of the main component. With a positive α, $l' = l+2$ and $l-2$ will cause a shift towards 0° and 90°, respectively; the opposite is true for a negative α.

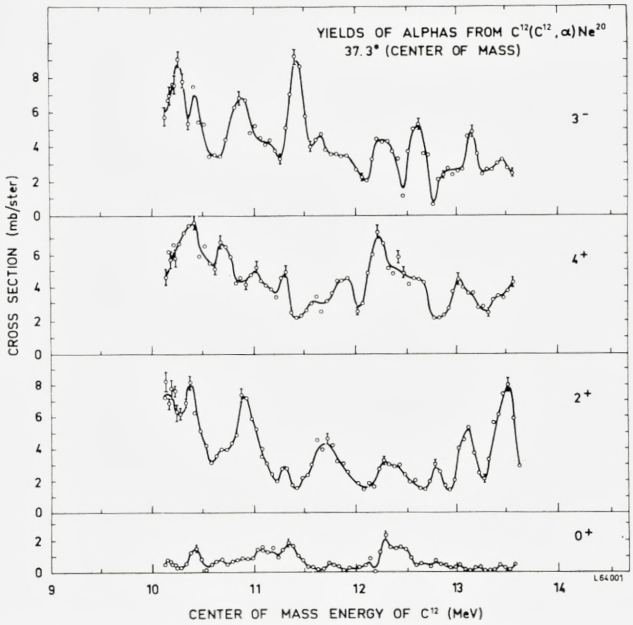

Fig. 9. Excitation functions at 37.3° C.M. The energy axis corresponds to zero target thickness. The 3— state was only poorly resolved from the two neighbouring 2— and 1— states of Ne^{20}.

Values of l and l' determined by the simple method discussed above are indicated in fig. 6.

In fig. 7 are shown some angular distributions of alpha particles populating the 2+ first excited state of Ne^{20}. The more complex structures of these angular distributions follow from the number of associated Legendre polynomials $P_l^M(\cos\theta)$ that combine for the various orbital angular momenta l and substates M allowed for each J. The allowed values are $J+2 \geq l \geq J-2$ and $2 \geq |M| \geq 0$.

4. Excitation Functions

The measured excitation functions of the differential cross sections at 0° and 90° (C.M.) for the clearly resolved groups are shown in fig. 8. The yield curves in fig. 9 were obtained at 37.3° (C.M.), this angle being a null angle for the Legendre polynomial of order eight. Both results are for a larger span of Mg^{24} compound nucleus energy than that observed by Kuehner et al.[2] or by Lassen and Olsen[3], and are with considerably better energy resolution than the latter.

The following points regarding the present excitation functions are of significance.

1) The use of thinner carbon targets did not change the excitation functions appreciably. This indicates that the instrumental resolution is smaller than the level width in the compound nucleus in this region of excitation.

2) The yield of the ground-state alpha particles at 37.3° in fig. 9 is unusually low. The expectation from BONDORF and LEACHMAN[6] and from fig. 6 that the dominant J value over most of this energy region is $J = 8$ is thus confirmed by the low cross section resulting from this suppressed major component. The cross section to the excited states is of approximately normal amplitude because the reaction amplitudes from all but ($l = 8$, $M = 0$) contribute to the observed cross section.

3) There is a complete lack of cross correlation between peaks in the yield curves for the various alpha-particle groups. This cross correlation behaviour is difficult to understand if the peaks are interpreted as originating in single, isolated resonances in the compound nucleus. The differences between the yield curves for the various alpha-particle groups exceed what can be expected from differences in barrier penetrabilities[6] for different angular momenta resulting from different spins of the final nuclei and cannot be related in a systematical way to such differences.

The theoretical cross sections are shown in fig. 4 of BONDORF and LEACHMAN[6] for the partial cross sections $\langle \sigma_J \rangle$ (averaged over overlapping levels of the compound nucleus) integrated over angle for reactions going through compound states of spin $J = l$, and also for the average cross section $\langle \sigma \rangle$ over all spins.

The theory indicates that one should be able to observe energy regions with usually a single dominant J value. This is indeed confirmed by the experimental results in fig. 6. We emphasize that the cross sections are expected[6] to fluctuate around the calculated averages. Thus, we should expect occasionally to observe for the 0+ ground state case an angular distribution characterized by an l value other than the calculated usually dominant J for that region. Such exceptions are an $l = 6$ distribution at 11.12 MeV in the usually $J = 8$ region and an $l = 8$ distribution at 15.05 MeV in the usually $J = 10$ region. This probability of exceptions is expected by theory[6].

5. Discussion

The regions of excitation in the compound system covered by the yield curves in figs. 8 and 9 range from 23 MeV to 30 MeV. In this region of

excitation, the level density in the compound nucleus is of course very high. However, one must remember that the $C^{12}(C^{12},\alpha)Ne^{20}$ reaction is only one of many open channels because the compound state can decay by many channels of protons, neutrons, and low energy alpha particles in competition with alpha particles going directly to the ground state or the other low-lying states of interest. For states of large angular momentum, the emission of alpha particles populating the low-lying levels of Ne^{20} will be enhanced compared with the other decay modes because of the larger transmission coefficients T_l for large orbital momentum l of alpha particles than of neutrons and protons[10].

In an excited nucleus with high angular momentum, part of the excitation energy is taken by the nuclear rotation. This effectively reduces the energy entering in the exponential of the statistical expression for the level density so that the density of nuclear states ϱ_J with angular momentum J is given by

$$\varrho_J = (2J+1)\exp\left[-\frac{J(J+1)}{2S^2}\right]\varrho_0$$

relative to the density ϱ_0 of states with angular momentum zero. The quantity S^2 is related to the nuclear moment of inertia $\Im$ and the nuclear temperature t through

$$S^2 = t\Im/\hbar^2.$$

From an analysis of experimental data, the nuclear temperature is expected to be around 2.1 MeV (see BONDORF and LEACHMAN[6]). The value of $\hbar^2/(2\Im)$ for the highly excited system must be close to the rigid value. The latter is 150 keV for a nuclear radius of $1.25\,A^{1/3}$ fermi and a deformation parameter $\beta = 0.35$. With these values the average level spacing $1/\varrho_8$ of spin 8 states at an excitation energy of 25 MeV is calculated to be about 100 keV. The level spacings calculated in this manner are of course extremely dependent on the values of $\Im$ and t entering in the exponent. Reasonable changes in these two parameters cause variations in $1/\varrho_8$ from $\sim$20 to $\sim$500 keV.

Although it is thus possible by a suitable choice of parameters to calculate a level density of the compound nucleus resonances that would result in resonances spaced at the observed energy spacings of enhanced cross sections, there are two important arguments against an interpretation in terms of individual resonances. One is the lack of cross correlation between

the maxima in the yields of the different alpha groups discussed above. The other argument is based on the relation

$$\frac{\Gamma}{D} = \frac{\Sigma T}{2\pi}$$

between the average width Γ and spacing D of compound resonances. The sums ΣT over the transmission coefficients for all open channels are $\gg 2\pi$ (cf. table V of BONDORF and LEACHMAN[6]) in the cases considered here, with the result that the average width is considerably larger than the average spacing of levels. Under such circumstances, the observation of individual resonances is highly unlikely, and the fluctuations in the yield functions must be ascribed to the random, but coherent, combination of the reaction amplitudes from overlapping resonances of various J values. The data also confirm[6] that fluctuations are reduced by the incoherent combination of reaction amplitudes characterized by different values of the magnetic quantum numbers M.

The analysis in the following paper shows that such a picture explains the fluctuations in our observed yield curves not only in a qualitative way, but also in a quite detailed manner accounts for the statistical behaviour of the distribution in the differential cross sections measured at different angles and in the measured cross section integrated over angle[2].

Some qualitative features of the cross-section probability distributions bear on questions of angular resolution and on O^{16} contamination of the target. The effects of these experimental difficulties are particularly easy to observe for the excitation functions for which ν, the number of degrees of freedom in the probability distribution, is expected to be equal to two from the "simple theory" of BONDORF and LEACHMAN[6]. For two degrees of freedom, the cross-section probability follows

$$P(\sigma) = \frac{\exp\left(-\frac{\sigma}{2}\right)}{2},$$

and so the cross-section probability decreases from a maximum at zero cross section. All observations of alpha particles to the ground state and all observations at 0° are expected to exhibit this property. These are shown in fig. 10 in comparison with the theoretical χ^2 distribution of two degrees of freedom.

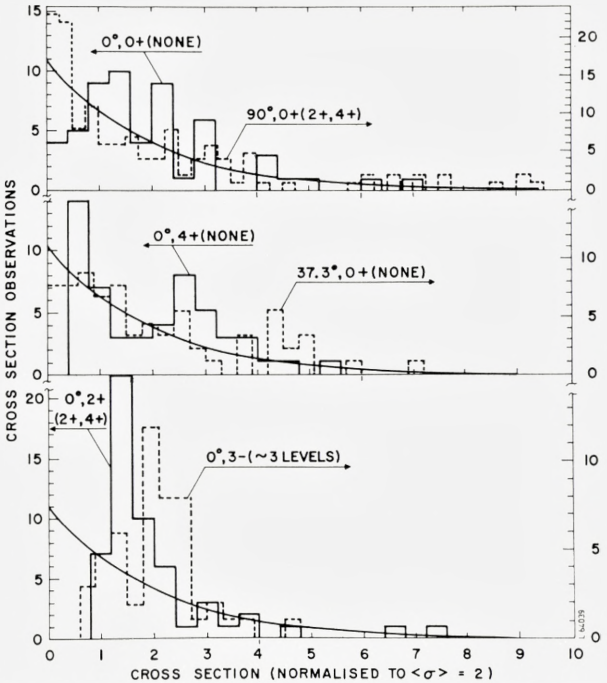

Fig. 10. Histograms of differential cross section data from Figs. 8 and 9 compared to normalized χ^2 curves with two degrees of freedom. Numbers in parentheses indicate possible alpha groups to states in Mg^{24} which could not be resolved from the alpha-particle group to the Ne^{20} state considered. At 0° the poor resolution of the 3— state from the neighbouring 1— state of Ne^{20} contributed additional incoherent amplitudes.

This expectation for the 0+ ground state cases is qualitatively confirmed by the excitation functions at 0°, 37.3° and 90° in figs. 8 and 9 and their histograms in fig. 10, which have the nearly zero cross sections being the most probable. No unresolved alpha particles from $O^{16}(C^{12},\alpha)Mg^{24}$ levels are expected with the ground-state alpha particles at 0° and 37.3°, as is seen from figs. 2 and 3, respectively. For the 90° case, fig. 4 shows that alpha groups to two $O^{16}(C^{12},\alpha)Mg^{24}$ levels are unresolved from the ground-state alpha particles. The observed large probability for nearly zero cross sections implies that the O^{16} contamination in this run was negligible in terms of the cross-section probability distribution. The small buildup of C^{12} on the target during the 90° runs agrees with this.

On the other hand, the histograms in fig. 10 show that only the alpha particles for the 0+ ground state cases (for any angle) qualitatively have

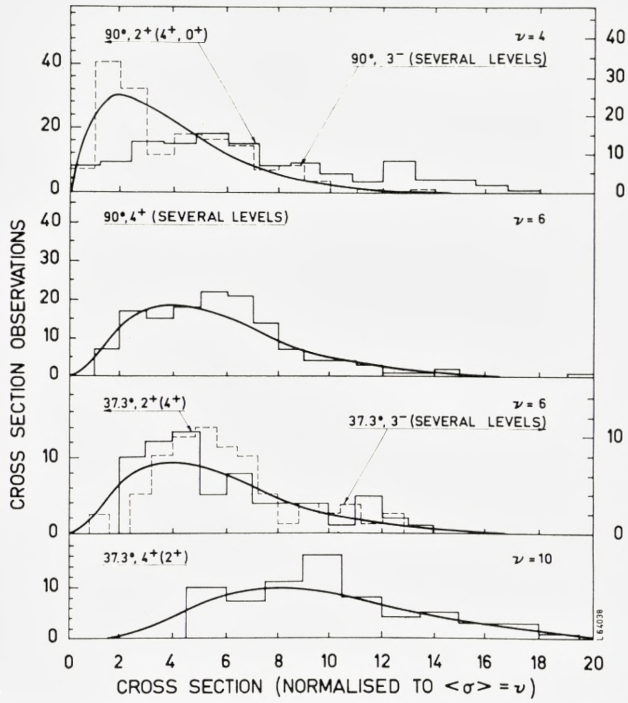

Fig. 11. Histograms of differential cross section data from Figs. 8 and 9 and ref.[10] compared to χ^2 curves with various numbers of degrees of freedom. ν predicted by the "simple theory" of BONDORF and LEACHMAN[6]. For numbers in parentheses, see caption to Fig. 10. The poor resolution of the 3— state from the neighbouring 2— and 1—states of Ne^{20} contributed additional incoherent amplitudes. All the 90° curves contain data between 9 and 16 MeV although not the full energy span is published in ref.[10].

the most probable cross section being nearly zero. The combination of ground state and 0° is surely expected to result in two degrees of freedom, because fig. 2 shows no interfering levels and the angular resolution is of less consequence for this ground state case, which results in two degrees of freedom for any angle (provided the angular resolution is smaller than the coherence angle). We emphasize that the excitation function for alpha particles to the 4+ state at 0° is not affected by unresolved groups from the O^{16} reaction (see fig. 2), but yet the histogram in fig. 10 (from the excitation function in fig. 8) shows that the nearly zero cross sections are clearly not the most probable. This gives a strong indication that the angular resolution effects discussed in section 2 are playing a role. Even greater deviations from the expectation of the nearly zero cross sections being the most pro-

bable are observed from the histograms in fig. 10 (again obtained from the excitation functions of fig. 8) for the observation at 0° to the 2+ and 3− states. However, unresolved levels seen in fig. 2 are an additional factor in these cases, and the target in this case was known experimentally to have a large buildup, as indicated by the growth of C^{12} on the target during the runs.

Thus, in a qualitative manner, we can account for the agreement and disagreement with the two degrees of freedom expectation for the excitation functions in figs. 8 and 9. Another possible cause for disagreement is the finite size of the sample of cross sections analysed[11], particularly for 0° and 37.3° data.

Shown in fig. 11 are histograms of data from figs. 8 and 9 and ref.[10] for which larger numbers of degrees of freedom are expected. It is seen that generally good agreement with the χ^2 distributions is obtained with the number of degrees of freedom from the "simple theory" of BONDORF and LEACHMAN[6]. However, these comparisons with the larger number of degrees of freedom ν in fig. 11 do not provide as sensitive a test of the agreement between theory and data as do the comparisons for two degrees of freedom in fig. 10.

Acknowledgements

The authors appreciate the participation of M. C. OLESEN and N. O. R. POULSEN in the early phases of these measurements. One of us (RBL) thanks the Institute for hospitality and appreciates financial support from a Fulbright Fellowship and from the Los Alamos Scientific Laboratory.

Institute for Theoretical Physics
University of Copenhagen, May, 1964.

Fulbright Fellow on Leave from the
Los Alamos Scientific Laboratory.

References

1) E. Almqvist, D. A. Bromley and J. A. Kuehner, Phys. Rev. Letters **4**, 515 (1960).
2) J. A. Kuehner, J. D. Prentice and E. Almqvist, Physics Letters **4**, 332 (1963).
3) N. O. Lassen and J. S. Olsen, Mat. Fys. Medd. Dan. Vid. Selsk. **33**, no. 13 (1963).
4) T. Ericson, Physics Letters **4**, 258 (1963).
5) D. M. Brink and R. O. Stephen, Physics Letters **5**, 77 (1963).
6) J. Bondorf and R. B. Leachman, Mat. Fys. Medd. Dan. Vid. Selsk. **34**, no. 10 (1964).
7) L. C. Northcliffe, Phys. Rev. **120**, 1744 (1960).
8) E. L. Hubbard, University of California Report UCRL-9053; unpublished (1960).
9) W. Gibbs, private communication (1964).
10) J. Borggreen, B. Elbek, R. B. Leachman, M. C. Olesen, and N. O. R. Poulsen, *Proceedings of the Third Conference on Reactions Between Complex Nuclei*, Adilomar. University of California Press, Berkeley, 1963, p. 201.
11) E. Almqvist, J. A. Kuehner, D. McPherson, and E. Vogt, Phys. Rev. (to be published).

Indleveret til Selskabet den 23. juni 1964.
Færdig fra trykkeriet den 5. oktober 1964.

Matematisk-fysiske Meddelelser
udgivet af
Det Kongelige Danske Videnskabernes Selskab
Bind **34,** nr. 10

Mat. Fys. Medd. Dan. Vid. Selsk. **34,** no. 10 (1965)

STATISTICAL FLUCTUATIONS IN THE EXCITATION FUNCTIONS FROM $C^{12}(C^{12},\alpha)Ne^{20}$

BY

J. P. BONDORF AND R. B. LEACHMAN

København 1965
Kommissionær: Ejnar Munksgaard

CONTENTS

Synopsis

The theory of statistical fluctuations in the cross sections for the energy region of completely overlapping levels is developed for the case of incident particles being zero spin and identical. To facilitate analysis of data, the development is in terms of the correlation coefficient, which is proportional to the difference between the mean square cross section and the square of the mean cross section. Simple expressions are derived relating the correlation coefficient with the number of degrees of freedom in the probability distribution of the cross section. For the differential cross sections, the number of degrees of freedom is twice the effective number of magnetic quantum substates; for the cross section integrated over angle, the number of degrees of freedom depends upon the number of compound spins, the size of the compound spin, and the spin of the final nucleus. Special cases are cited for which selection rules and spherical harmonics reduce the number of degrees of freedom.

Cross section data from the reaction $C^{12}(C^{12}, \alpha)Ne^{20}$ are analysed. Level densities and widths calculated from statistical theories of levels for all energies but the lowest confirm that the populated levels are completely overlapping. Satisfactory agreement is found between the number of degrees of freedom in the cross section distribution as determined from the data and from theory.

PRINTED IN DENMARK
BIANCO LUNOS BOGTRYKKERI A/S

1. Introduction

The theory of fluctuations in the excitation functions (cross section versus energy) in compound nuclear reactions has recently been developed by ERICSON [1] [2] [3] [4] and by BRINK et al. [4] [5] in the region of overlapping compound resonances. Correlation functions and distributions play important roles in fluctuation theory. On the basis of assumptions for the correlation between reduced widths for different channels, ERICSON [2] gives a theory which predicts the self- and cross-correlation functions for excitation functions in reaction channels. In [5] ERICSON calculates the distribution of the cross section in the spin zero case. Comparison with data has been made by ALMQVIST et al. [6].

In this paper, the fluctuation theory has been formulated with special reference to analysis in terms of distributions. The angular momentum effects on the cross section distributions are discussed (see also ref. [4]). It is described how one can make quantitative predictions of the cross section distributions from the calculation of absolute cross sections in the theory of statistical reactions. The fluctuation theory has been applied to analyse the strongly fluctuating cross sections in the reaction $C^{12}(C^{12},\alpha)Ne^{20}$, which has been studied experimentally by ALMQVIST et al. [6] [7] [8] and by BORGGREEN et al. [9] [10]. The reaction $C^{12}(C^{12},\alpha)Ne^{20}$ is of particular interest in another context since the resonance behaviour of the cross section has been used in the argumentation for the existence of "quasimolecular" states in nuclei [7].

2. Theory

2.1 Reaction formalism

Consider a reaction which is caused by the collision of two identical particles of spin 0 and *CM* kinetic energy ε_i (entrance channel i) where the projectile moves along the z-axis (fig. 1). The angular momentum of the total system is J, which for incident identical bosons is even. After the collision the emitted particle with spin s and spin projection μ moves in the

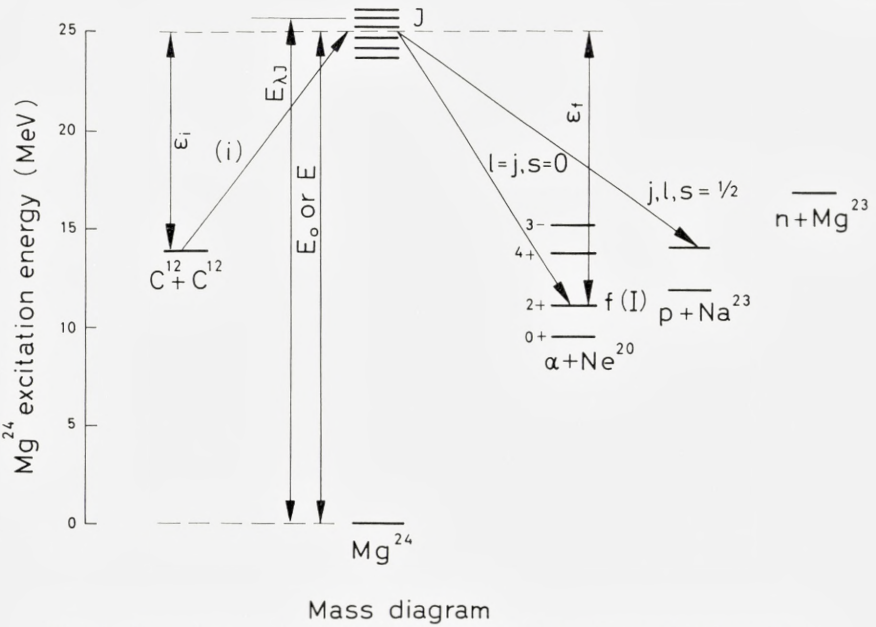

Fig. 1. Mass diagram for the reaction through the compound system Mg^{24}.

direction (θ, φ). The index f is used to identify the set $f = \{I, s\}$ of the final nucleus and particle spins. Their projections are $\{M, \mu\}$. The relative orbital angular momentum in the exit channel is l, and $\mathbf{l} + \mathbf{s} = \mathbf{j}$.

With this notation one can write the differential cross section for a reaction $i \to \{f, M, \mu\}$:

$$\left.\begin{aligned}\left(\frac{d\sigma}{d\Omega}\right)_{if M\mu} &= \Bigg| \sum_{\substack{\text{even } J=0 \\ |J-I| \le j \le J+I \\ l = j \pm s}}^{\infty} a(i,J,j,l,f) \times \\ (i)^l (l, s, -M-\mu, \mu \mid j-M)(jI, -MM \mid J0)\, Y_{l,-M-\mu}(\theta,\varphi)\Bigg|^2,\end{aligned}\right\} \quad (1)$$

where one has to remember conservation of parity in the sum. The vector coupling coefficients are as defined in PRESTON [11].

In an arbitrary channel c we define $\lambda\!\!\!^{-}_c = 1/k_c = \hbar/\sqrt{2m_c\varepsilon_c}$, where m_c is the reduced mass and ε_c the kinetic energy.

In the theory of resonance reactions [12] the reaction amplitude for $f \neq i$ can be written

$$a(i,J,j,l,f) = -i \cdot 2^{\frac{1}{2}} \pi^{\frac{1}{2}} \lambda\!\!\!^{-}_i (2J+1)^{\frac{1}{2}} \sum_{\lambda} \frac{g_{\lambda J i} g_{\lambda J j l f}}{E_{\lambda J} - E - \frac{i}{2}\Gamma_{\lambda J}}. \quad (2)$$

The resonance at energy $E_{\lambda J}$ has a total width $\Gamma_{\lambda J} = \sum_c \Gamma_{\lambda Jc}$, which is a sum over all open channels c of partial widths $\Gamma_{\lambda Jc} = |g_{\lambda Jc}|^2$. The channel amplitude $g_{\lambda Jc}$ is the product $2^{\frac{1}{2}} P_c \alpha_{\lambda Jc}$, where P_c is the penetration factor [11] evaluated at the channel radius R_c and is a function of l and $k_c R_c$. The reduced width $\alpha_{\lambda Jc}$ is generally a complex number which is proportional to the radial wave function evaluated at the channel radius R_c for the resonance λJ. For the present case of identical projectiles, all resonances have even parity, and the amplitude (2) has an extra factor of $\sqrt{2}$ compared to the general case.

When M and μ are not determined, the differential cross section resulting from the sum of the quantities in (1) is

$$\left(\frac{d\sigma}{d\Omega}\right)_{if} = \sum_{M,\mu} \left(\frac{d\sigma}{d\Omega}\right)_{ifM\mu}, \tag{3}$$

and the cross section integrated over all angles is, with use the of (1) and (3),

$$\sigma_{if} = \sum_{M,\mu} \int \left(\frac{d\sigma}{d\Omega}\right)_{ifM\mu} d\Omega = \sum_{\substack{\text{even } J=0 \\ |J-I| \le j \le J+I \\ l = j \pm s}}^{\infty} |a(i,J,j,l,f)|^2. \tag{4}$$

In equations (3) and (4) the cross sections are sums of incoherent quantities, and it is just this summation that reduces the fluctuations in the cross sections as discussed in the next section.

To condense the notation, the sums of incoherent quantities in (3) and (4) are rewritten simply as

$$\frac{d\sigma}{d\Omega} = \sum_{M,\mu} \left(\frac{d\sigma}{d\Omega}\right)_{\alpha}, \qquad \text{where} \qquad \alpha = \{i,f,M,\mu\}, \tag{5a}$$

$$\sigma = \sum_{J,j,l} \sigma_{\beta}, \qquad \text{where} \qquad \beta = \{i,J,j,l,f\}. \tag{5b}$$

2.2 The statistical properties of cross sections

In the theory of reactions through resonances, the conditions for purely statistical reactions are that the channel amplitudes obey the randomness assumption [2]

and
$$\left.\begin{aligned} &<g_{\lambda Jc}g_{\lambda Jc'}> = 0 \quad \text{for} \quad c \neq c' \\ &<g_{\lambda Jc}g_{\lambda' J'c'}> = 0 \quad \text{for} \quad J \neq J' \quad \text{and} \quad c \neq c', \end{aligned}\right\} \tag{6}$$

where the averages are taken over the resonances λ or $\{\lambda, \lambda'\}$ in an interval ΔE containing many resonances. In the case $\Gamma_{\lambda J} >> \langle D_J \rangle$, where $\langle D_J \rangle$ is the average energy difference between resonances with a given compound spin J and a given parity, it follows from (6) that the real and the imaginary part of the reaction amplitude $a(i, J, j, l, f)$ are statistically independent and gaussian distributed around zero with the same dispersion. Then the probability distributions of the cross sections $\left(\frac{d\sigma}{d\Omega}\right)_\alpha$ and σ_β, taken over an energy range $\Delta E >> \Gamma_{\lambda J}$, are χ^2 distributions of 2 degrees of freedom, i.e., decreasing exponentials [1] [3] [5] (see Appendix).

To facilitate the analysis of data in terms of the number of degrees of freedom in the statistical fluctuations, it is convenient to consider correlation functions [1], which involve the first and second moments of the cross section distributions. A χ^2 distribution of 2 degrees of freedom has the property that the correlation coefficient of the variable σ_β is

$$R = \frac{<(\sigma_\beta - <\sigma_\beta>)^2>}{<\sigma_\beta>^2} = \frac{<\sigma_\beta{}^2>}{<\sigma_\beta>^2} - 1 = 1. \tag{7}$$

Since a cross section which is fluctuating with a χ^2 distribution of 2 degrees of freedom plays a fundamental role for compound reactions in the region of overlapping levels, we shall call it a *basic cross section*.

The integrated cross section $\sigma = \sum_\beta \sigma_\beta$ fluctuates as a result of the fluctuations in the various contributing σ_β, but the amount of the fluctuation of course depends on the relations between the various σ_β. These cross section relations will now be considered in terms of the relations between the reaction amplitudes $a(i, J, j, l, f)$. The randomness assumptions (6) essentially state that the average of the product of two different amplitudes over an interval $\Delta E >> \Gamma_{\lambda J}$ is zero:

$$<a(i, J, j, l, f)\, a(i, J', j', l', f')> = 0 \tag{8}$$

[1] The *cross correlation function* of two functions $\sigma_1(E)$ and $\sigma_2(E)$ as a function of the incremental energy δ is

$$R_{1,2}(\delta) = \frac{<[\sigma_1(E) - <\sigma_1(E)>][\sigma_2(E+\delta) - <\sigma_2(E)>]>}{<\sigma_1(E)><\sigma_2(E)>}.$$

The *self-correlation function* for a function $\sigma_1(E)$ is $R_{1,1}(\delta)$. The *correlation coefficient* R is defined as the self-correlation function for $\delta = 0$.

for $\{J,j,l,f\} \neq \{J',j',l',f'\}$. The equation (7), which characterizes the probability distribution in the basic cross section, states that

$$\frac{<|a(i,J,j,l,f)|^4>}{<|a(i,J,j,l,f)|^2>^2} = 2. \tag{9}$$

We wish to analyse actual cross sections σ in terms of the correlation coefficient

$$R = \frac{<\sigma^2>}{<\sigma>^2} - 1. \tag{10}$$

The relation (9) can be used to reduce (10) when it is expanded in the basic cross sections of σ. Also in the expansion are the averages $<|a(i,J,j,l,f)|^2|a(i,J',j',l',f')|^2>$, which to simplify involve more than the randomness assumptions. If one assumes, however, the *reaction amplitudes* $a(i,J',j,l,f)$ and $a(i,J',j',l',f')$ to be completely *independent* for $\{i,J,j,l,f\} \neq \{i,J',j',l',f'\}$ in the interval ΔE, the simplification of the independence approximation

$$<|a(i,J,j,l,f)|^2|a(i,J',j',l',f')|^2> = <|a(i,J,j,l,f)|^2><|a(i,J',j',l',f')|^2> \tag{11}$$

follows. In condensed notation for $\beta = \{i,J,j,l,f\}$ and $\beta' = \{i,J',j',l',f'\}$ where $\beta \neq \beta'$,

$$<\sigma_\beta \sigma_{\beta'}> = <\sigma_\beta><\sigma_{\beta'}>. \tag{12}$$

Similar expressions follow for all higher powers of the amplitudes $a(i,J,j,l,f)$ as consequence a of the independence assumption. It is, however, apparent that the use of R in the analysis tests the independence of the basic cross sections only to the order involved in (12), but not the full independence of reaction amplitudes a.

In the differential cross section (3), the cross sections $\left(\frac{d\sigma}{d\Omega}\right)_{ifM\mu}$ characterized by the individual magnetic quantum numbers are all functions of the same set of energy-dependent amplitudes $a(i,J,j,l,f)$ with coefficients which are products of the $\{M,\mu\}$-dependent, but energy-independent, vector coupling coefficients and spherical harmonics. Since these energy-independent coefficients vary in sign from one set α to another, one obtains to the extent of

$$<\left(\frac{d\sigma}{d\Omega}\right)_\alpha \left(\frac{d\sigma}{d\Omega}\right)_{\alpha'}> \approx <\left(\frac{d\sigma}{d\Omega}\right)_\alpha><\left(\frac{d\sigma}{d\Omega}\right)_{\alpha'}>, \tag{13}$$

where $\alpha = \{i,f,M,\mu\}$ and $\alpha' = \{i,f',M',\mu'\}$, an approximate independence between the various basic cross sections $\left(\frac{d\sigma}{d\Omega}\right)_{ifM\mu}$ contributing to the differential cross section. However, the number N_1 of such approximately independent basic cross sections cannot exceed the number N_2 of different contributing amplitudes $a(i,J,j,l,f)$ to the cross section. When N_1 is small compared to N_2, which is the case in all cross sections examined in the reaction considered, one expects (13) to be valid with sufficient accuracy. We shall therefore in all cases examined consider the basic cross sections in (5a) and (5b) to be independent to the extent of (12) or (13).

With the use of (12) and (5b), the correlation coefficient (10) of integrated cross sections can be reduced to

$$R = \frac{\sum\limits_{J,j,l} <\sigma_\beta>^2}{<\sum\limits_{J,j,l} \sigma_\beta>^2} \equiv \frac{2}{\nu_{\text{eff}}}. \tag{14}$$

For the differential cross sections (5a), one can similarly define a correlation coefficient which with the use of (13) becomes

$$R = \frac{<\left(\frac{d\sigma}{d\Omega}\right)^2>}{<\frac{d\sigma}{d\Omega}>^2} - 1 \simeq \frac{\sum\limits_{M,\mu} <\left(\frac{d\sigma}{d\Omega}\right)_\alpha>^2}{<\sum\limits_{M,\mu}\left(\frac{d\sigma}{d\Omega}\right)_\alpha>^2} \equiv \frac{2}{\nu_{\text{eff}}}. \tag{15}$$

In analogy with the formal ν of (A3) in the Appendix, (14) and (15) define ν_{eff}, which characterizes the fluctuation and which is generally not an integer.

If all the averages of n independent basic cross sections are equal in (14) or (15), the correlation coefficient is simply

$$R = \frac{n}{n^2} = \frac{1}{n}. \tag{16}$$

Thus, the correlation coefficient of the cross section directly reflects the number of independent basic cross sections in (5a) and (5b). The result of the simple theory is then $\nu_{\text{eff}} = 2n$, where ν_{eff} becomes an integer, and the distribution function of the cross section is a χ^2 distribution of $2n$ degrees of freedom.

When ν_{eff} is a non-integer, we expect that the cross section distribution is similar to a χ^2 distribution which, however, is only defined for integer values of ν. As seen in the Appendix, it is possible to use ν as a continuous variable, and therefore one expects the cross section distribution in this case to be approximately (A1) with $\nu = \nu_{\text{eff}}$ (a gamma distribution).

2.3 Special cases for the differential cross section

Selection rules and the spherical harmonic properties can result in some basic cross sections in (5a) being zero. This fact strongly affects the fluctuation, and therefore we analyse these cases in some detail.

For alpha-particle channels, $s = 0$, $j = l$, and $\mu = 0$. The following selection rules affect the number of $\alpha = M$ values.

a) Because $(lI - MM|J0)Y_{l-M} = (-)^{I+l-J}(lIM - M|J0)Y^*_{lM}(-)^M$, we see that $\dfrac{d\sigma}{d\Omega} = \sum_M \left(\dfrac{d\sigma}{d\Omega}\right)_M = \sum_{M \geq 0} \left(\dfrac{d\sigma}{d\Omega}\right)_M (2 - \delta_{M0})$. This decreases the number of M values to the value of $I+1$ or $l+1$, whichever is smaller.

b) The vector coupling coefficient is $(lI00|J0) = 0$ for odd values of $l+I+J$; this eliminates the $M = 0$ values for the unnatural parity exit channels. (This rule is also valid for incident spin-zero nonidentical particles).

c) For $\theta = 0$ or π, $Y_{lM}(\theta, \varphi) = 0$ for $M \neq 0$. In these cases only the one $M = 0$ value contributes to the cross section.

d) For $\theta = \dfrac{\pi}{2}$, the property $P_{lM}(\cos\theta) = (-)^{l+M}P_{lM}(-\cos\theta)$ of the associated Legendre polynomials gives even M for even parity exit channels and odd M for odd parity exit channels.

Some results of a) through d) are presented in table I. The neutron and proton exit channels can be analysed in a similar way, but these are not required in the present analysis. If the magnitude of $<\left(\dfrac{d\sigma}{d\Omega}\right)_\alpha>$ over the energy interval considered is the same for all α values, the simple theory (16) gives ν_{eff} equal to twice the number of M values allowed by a) through d) above.

TABLE I. Number of nonvanishing independent basic cross sections (effective number of α values) in the differential cross section for the reaction $C^{12}(C^{12},\alpha)Ne^{20}$. (See sections 2.2 and 2.3.)

Spin I and parity of the final state in Ne^{20}	Effective number of α values		
	At an arbitrary angle θ	$\theta = 0°$	$\theta = 90°$
0+	1	1	1
0−	0	0	0
1+	2	0	1
1−	1	1	1
2+	3	1	2
2−	2	0	1
3+	4	0	2
3−	3	1	2
4+	5	1	3
4−	4	0	2
5+	6	0	3
5−	5	1	3
6+	7	1	4
6−	6	0	3
7+	8	0	4
7−	7	1	4

2.4 Average cross sections

To predict ν_{eff} from (14) or (15), it is necessary to know the average cross sections $<\sigma_{if}>$ or $<\left(\frac{d\sigma}{d\Omega}\right)_{if}>$, respectively. With the randomness assumptions (6) for reaction amplitudes, the average of the differential cross section is

$$\left.\begin{aligned} <\left(\frac{d\sigma}{d\Omega}\right)_{if}> &= \sum_{M,\mu} <\left(\frac{d\sigma}{d\Omega}\right)_{\alpha}> \\ &= \sum_{M,\mu} <\Big| \sum_{J,l,j} a(i,J,j,l,f)(l,s,-M-\mu,\mu|j,-M) \\ &\qquad \times (jI,-MM|J0)\,Y_{l,-M-\mu}(\theta,\varphi)|^2> \\ &= \sum_{\substack{J,l,j \\ M,\mu}} <|a(i,J,j,l,f)|^2>(l,s,-M-\mu,\mu|j,-M)^2 \\ &\qquad \times (jI,-MM|J0)^2 Y_{l,-M-\mu}(\theta,\varphi)|^2. \end{aligned}\right\} \quad (17)$$

Similarly, the average of the integrated cross section is

$$<\sigma_{if}> = \sum_{J,j,l} <\sigma_\beta> = \sum_{J,j,l} <|a(i,J,j,l,f)|^2>. \tag{18}$$

Both (17) and (18) contain the average $<|a(i,J,j,l,f)|^2>$ which, with the use of (2), can be written

$$<|a(i,J,j,l,f)|^2> = 2\pi\lambda_i^2(2J+1)<\left|\sum_\lambda \frac{g_{\lambda Ji}g_{\lambda Jjlf}}{E_{\lambda J} - E - \frac{i}{2}\Gamma_{\lambda J}}\right|^2>. \tag{19}$$

With the use of (5), (19) is reduced to

$$<|a(i,J,j,l,f)|^2> = 2\pi\lambda_i^2(2J+1)\frac{2\pi}{<D_J>}<\frac{\Gamma_{\lambda Ji}\Gamma_{\lambda Jjlf}}{\Gamma_{\lambda J}}>, \tag{20}$$

where $<D_J>$ is the average spacing between resonances with a definite spin J and parity. The cross section average is taken over an energy interval $\Delta E >> \Gamma_{\lambda J}$ around E_0, and the relative error (a finite sample effect [2]) is of the order of $(\Gamma_{\lambda J}/\Delta E)^{\frac{1}{2}}$. The total width $\Gamma_{\lambda J}$ is nearly constant between nearby states λ of given J.

We assume $\Gamma_{\lambda Ji}$ and $\Gamma_{\lambda Jjlf}$ to be statistically independent and identify $2\pi\frac{<\Gamma_{\lambda Jc}>}{<D_J>}$ with the transmission coefficient T_c^J calculated from the optical model for a particle with *CM* energy ε_c in channel $\{c,J\}$. Then (20) can be transformed to the usual Hauser-Feshbach expression [13]

$$<|a(i,J,j,l,f)|^2> = 2\pi\lambda_i^2(2J+1)T_i^J(\varepsilon_i)\frac{T_f^J(\varepsilon_f)}{\sum T_c^J(\varepsilon_c)}, \tag{21}$$

and the total width is

$$<\Gamma_{\lambda J}> \equiv \Gamma_J = \frac{<D_J>}{2\pi}\sum_c T_c^J(\varepsilon_c). \tag{22}$$

The relations (21) and (22) are justified only for $T_c^J << 1$, but here $T_c^J \sim 1$ for most of the channels. MOLDAUER [14] [15] and KRIEGER and PORTER [16] have considered this problem in some detail and have developed expressions for the average cross section when $T_c^J \sim 1$. These expressions require a detailed knowledge about the statistical properties of the compound system, and so we shall simply use (21) for the average cross section. The transmission coefficients in (21) depend on the kinetic energy ε_c in channel c. They are determined as

$$T_c = 1 - \exp(-4Im\delta_c), \tag{23}$$

where δ_c is the phase shift in channel c determined from optical model calculations. We assume that all the parameters of the optical potentials are the same for the elastic scattering on a nucleus in an excited state as for the elastic scattering on a nucleus in the ground state. We therefore omit the labels J and f on the transmission coefficient which is then labelled by the quantum number l for alpha particles, and by j, l for neutrons and protons.

3. Comparison with experiment

3.1 General assumptions

One of the striking features of the $C^{12}(C^{12}, \alpha)Ne^{20}$ reaction is the strongly fluctuating excitation functions [6] [7] [8] [9] [10].

In fig. 2 is shown the cross correlation function $R_{1,2}$ between the integrated cross sections [6] [8] of the ground and first excited state in the residual nucleus Ne^{20}. This lack of correlation between the observed peaks in the cross section for different exit channels indicates that the reaction proceeds via a compound mechanism in the region of overlapping resonances. Whether there is also a direct amplitude cannot be seen in a forward-backward asymmetry. This is because the colliding particles are identical, and thus the angular distribution is automatically symmetric around $\theta = 90°$. The statistical model has earlier been applied to analyse three cross section peaks observed in the integrated cross section to the ground state channel under the assumption that they are isolated resonances [8]. We shall not use this last assumption, but instead analyse the reaction as a pure compound reaction with overlapping resonances and then look for possible discrepancies between the theoretical calculations and the experiments.

3.2 Average cross sections and fluctuation widths

In the optical model calculations the following potential was used [17]:

$$(\mathrm{ReV} + i\,\mathrm{ImV})\varrho(r) + V_{so}\left(\frac{\hbar}{m_\mu c}\right)^2 \frac{1}{r}\frac{d\varrho(r)}{dr}\,\sigma\cdot\mathbf{l} + V_{coul},$$

where

$$\varrho(r) = 1/\left(\exp\frac{r-R}{a} + 1\right)$$

and

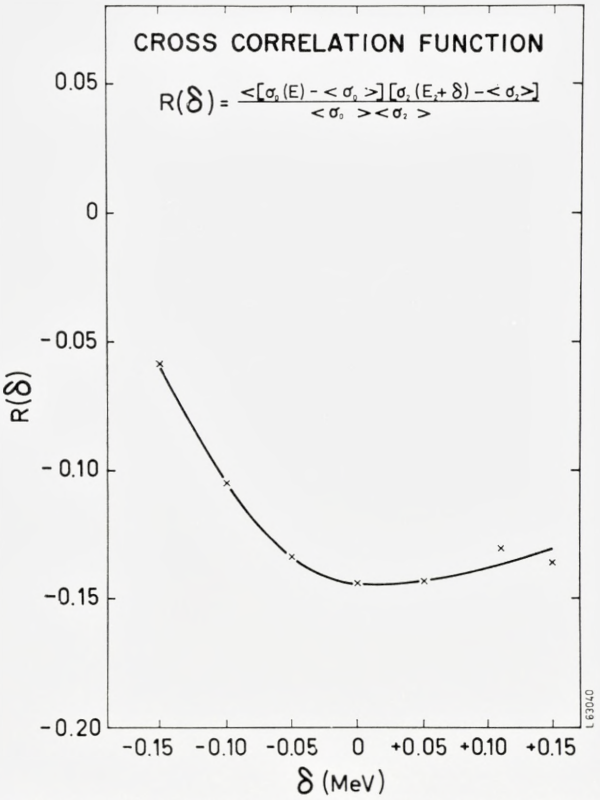

Fig. 2. Cross correlation function for the observed integrated cross sections in the $\alpha + Ne^{20}_{+0}$ and $\alpha + Ne^{20}_{2+}$ channels. Data are from ALMQVIST et al.[6] [8].

$$V_{\text{coul}} = \begin{cases} \dfrac{Z_1 Z_2 e^2}{r} & \text{for} \quad r \geqslant R \\ \dfrac{Z_1 Z_2 e^2}{2R}\left(3 - \dfrac{r^2}{R^2}\right) & \text{for} \quad r < R \end{cases}$$

with the parameters given in table II. This calculation gives transmission coefficients $T_{lj}(\varepsilon_f)$, which are then used in the Hauser-Feshbach expression (21). The calculation T_l for the important channels of alpha particles and C^{12} are shown in fig. 3. (For the T_{lj} of the neutron and proton channels, see BORGGREEN et al.[9], where the j dependence was neglected).

To calculate $\sum_c T_c$, it is in principle necessary to know all the spins,

TABLE II. Optical model parameters used for $C^{12}+C^{12}$, $\alpha+Ne^{20}$, $p+Na^{23}$, and $n+Mg^{23}$ in section 3.2.

Channel	ReV (MeV)	ImV (MeV)	a (fm)	R (fm)	Reference
$C^{12}+C^{12}$	48	5.75	0.575	5.838	18)
$\alpha+Ne^{20}$	50	5.3	0,576	4.95	19)
$p+Na^{23}$	40	9	0.73	3.695	20)
$n+Mg^{23}$	45.5	9.5	0.65	3.553	21)

energies, and parities of the states in the residual nuclei. For the lower energies of the compound system there are so few exit channels that one has this knowledge, but at higher excitation energies one has to take advantage of both the experimental and theoretical knowledge of the density of states and spin distributions. This results in an integral over unidentified states in addition to the sum over identified states. For the higher excitation energy region of unidentified states a theoretical expression [22] with adjustable parameters for the level density including states with both parities and all spins

$$\omega(E^*) = C_\omega \frac{\exp\left[2\sqrt{a_\omega U}\right]}{(U+t)^2} \tag{24}$$

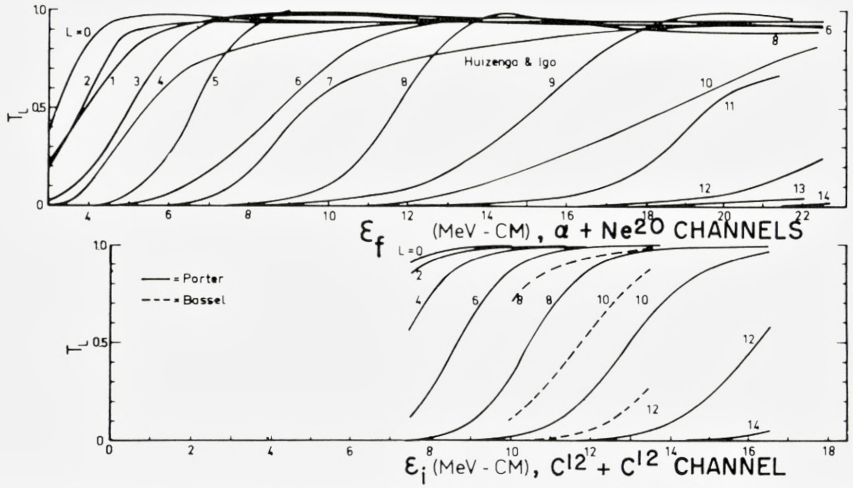

Fig. 3. Transmission coefficients from optical model calculations of $C^{12}+C^{12}$ and $\alpha+Ne^{20}$ channels. The optical model results from the parameters of BASSEL and DRISKO [R. H. Bassel and R.M. Drisko, *Proceedings of the International Conference on Nuclear Structure*, Kingston (University of Toronto Press, Toronto, 1960), p. 212] were not used in the present calculations.

TABLE III. Parameters used in the level distributions (24) for Ne^{20}, Mg^{23}, Na^{23}, and Mg^{24}.

Nucleus	C_ω(MeV)	a_ω(MeV^{-1})	Δ(MeV)	t(MeV)
Ne^{20}	0.539	2.240	4.95	2.75
Mg^{23}, Na^{23}	1.94	2.035	2.48	2.22
Mg^{24}	0.217	2.99	4.58	2.11

TABLE IV. "Spin cutoff factors" for Ne^{20}, Mg^{23}, Na^{23}, and Mg^{24} in (25).

Nucleus	S^2
Ne^{20}	5.55
Na^{23}, Mg^{23}	6.53
Mg^{24}	6.84

was used, where $U = E^* - \Delta$, E^* is the excitation energy, and Δ is the pairing energy. Pairing energy values of CAMERON [23] were used. The nuclear temperature t and the constants C_ω and a_ω were determined from best fits to known level schemes [24] [25]. The constants used in the calculation are shown in table III.

The spin distribution was chosen to be the usual expression

$$G(I) = C_G(2I+1)\exp\left[-\frac{I(I+1)}{2S^2}\right], \tag{25}$$

where C_G is the normalization constant. The "spin cutoff factor" S was considered to be independent of the excitation energy E^*. Values were obtained from best fits of the functional relation $S^2 \propto A^{7/6}$ to the values [26] given for the three nuclei Al^{26}, S^{33}, and A^{37}. The "spin cutoff factors" S used are given in table IV.

The part of $\sum_c T_c$ that was an integration over unidentified levels was calculated with the parameters in tables III and IV for alpha-particle, carbon, proton, and neutron exit channels[1]. In this region of high excitation energy, the average distance between levels of a definite spin and parity for the residual nucleus is

$$<D_I> = \frac{2}{\omega(E^*)G(I)}. \tag{26}$$

[1] Optical model calculations were kindly made by L. Stewart at Los Alamos Scientific Laboratory and E. Auerbach at Brookhaven National Laboratory.

TABLE V. Calculated values of $<D_J>$, $\sum_c T_c$, and $\Gamma_J = \frac{<D_J>}{2\pi}\sum_c T_c$ for Mg^{24} as a function of the excitation energy E_0 in Mg^{24}. The contribution to $\sum_c T_c$ from the neutron and C^{12} channels is small. The contribution from the proton channels is largest for $J = 0, 2, 4$, the alpha-particle and proton channels contribute nearly equally for $J = 6$, and the alpha-particle channel contributions are largest for $J = 8, 10$.

J	ε_i (MeV)	E_0 (MeV)	$<D_J>$ (keV)	$\sum_c T_c$	Γ_J (keV)
0	8	21.9	28.7	37	171
	12	25.9	8.5	152	206
	16	29.9	2.8	560	249
2	8	21.9	8.9	101	143
	12	25.9	2.6	487	202
	16	29.9	0.9	1953	280
4	8	21.9	13.7	44	157
	12	25.9	4.1	381	249
	16	29.9	1.3	1571	325
6	8	21.9	47.4	30	227
	12	25.9	14.1	169	379
	16	29.9	4.6	705	516
8	8	21.9	318	8.0	403
	12	25.9	94.7	47.5	717
	16	29.9	30.9	204.0	1003
10	8	21.9	4160	1.2	830
	12	25.9	1220	11.1	2150
	16	29.9	396	47.4	2910

(A corresponding equation gives the spacing $\langle D_J \rangle$ for the compound nucleus). The factor 2 in the numerator comes from the choice of a definite parity. In the region of low excitation energy, compilations of identified levels [24] [25] were used.

Table V shows the calculated $<D_J>$, $\sum_c T_c$, and Γ_J for the compound nucleus Mg^{24} as a function of ε_i. The calculated Γ_J can now be compared with the measured fluctuation width. (See section 4).

In figure 4 the integrated cross section calculated from (18) and (21) is shown for the ground-state channel. This cross section is a sum of contributions from only even values of the compound spins $J = l = 0, 2, 4, 6, 8, 10$ etc. Consequently, in the excitation functions rather broad intervals of the

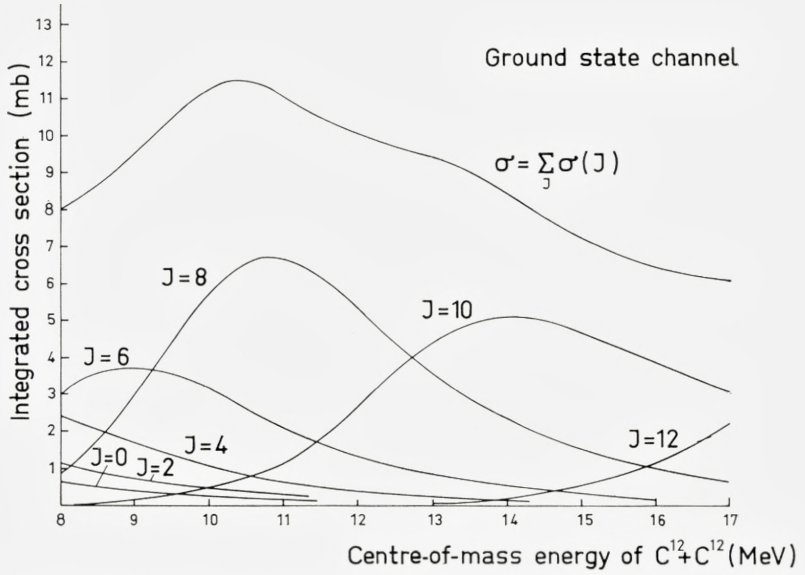

Fig. 4. Calculated integrated average cross section in the $\alpha + Ne^{20}_{0+}$ channel as a function of incident $C^{12} + C^{12}$ energy ε_i.

energy ε_i occur in which usually a single compound spin dominates in the angular distributions of this differential cross section

$$\frac{d\sigma}{d\Omega} = \left| \sum_J a(i,J,j = J,l = J,f) Y_{J,0}(\theta,\omega) \right|^2 \tag{27}$$

simplified from (1) for the $I = 0$ ground-state channel. Such angular distributions at different bombarding energies have been measured by LASSEN and OLSEN [28] in the compound spin $J = 4$ to $J = 8$ region, by BORGGREEN et al. [10] in the $J = 6$ to $J = 10$ region, and by ALMQVIST et al. [6] [8] in the $J = 8$ region. The compound spins that usually dominate are given in table VI together with their calculated and observed energy intervals.

The average cross sections calculated from (17) and (18) with the use of (21) vary slowly with energy E_0. To compare these calculated cross sections with the experimental cross sections, (17) and (18) have been averaged over energy intervals corresponding to the experimental intervals to give $\bar{\sigma}$ and $\overline{\left(\frac{d\sigma}{d\Omega}\right)}$. (See eq. (30) of the next section). The results of this calculation are shown for some examples in table VII.

TABLE VI. Intervals of the usually dominant spin J in the $C^{12}(C^{12},\alpha)Ne^{20}$ ground-state reaction.

Usually dominant spin J	Experimental ε_i energy interval (MeV)	Theoretical ε_i energy interval (MeV)
4	—10.6	— 7.9
6	—11.1	7.9— 9.4
8	9.5—15.0	9.4—12.7
10	13.0—	12.7—17.4
12		17.4—

TABLE VII. Theoretical and observed average cross sections and fluctuation parameters. "Simple theory" results are twice the values in table I. "Refined theory" refers to (29a) and (29b) of section 3.3.

E^* Ne^{20} (MeV)	Ne^{20} final state spin I and parity	Cross section	θ	Energy interval $\Delta\varepsilon_i$(MeV)	Experimental average cross section	Calculated average cross section	ν_{exp}	ν_{theor}	
								Simple theory	Refined theory
0	0+	Differential	0°	10.1—12.8	24.4 mb/sr	13.2 mb/sr	3.9	2	2.0
		Differential	90°	9.0—15.9	0.90 mb/sr	0.94 mb/sr	1.7	2	1.9
		Integrated		10.1—12.8	20 mb	10.5 mb	3.9		5.2
1.63	2+	Differential	0°	10.1—12.8	26.4 mb/sr	11.1 mb/sr	5.6	2	2.0
		Differential	90°	9.0—15.9	2.13 mb/sr	1.74 mb/sr	2.6	4	3.6
		Integrated		10.1—12.8	64 mb	28.0 mb	10.6		14.6
4.25	4+	Differential	0°	10.1—12.8	24.8 mb/sr	7.2 mb/sr	4.2	2	1.9
		Differential	90°	9.0—15.9	2.42 mb/sr	2.24 mb/sr	6.6	6	5.3
5.63	3−	Differential	0°	10.1—12.8	40.9 mb/sr	6.5 mb/sr	8.5	2	2.0
		Differential	90°	9.0—15.9	2.21 mb/sr	1.02 mb/sr	4.2	4	3.5

3.3 Fluctuation of cross sections

There are various ways of analysing the fluctuation of a function. However, in general, the information one can extract depends on prior knowledge or an assumption of the variation of the average function about which the fluctuation occurs. Therefore, the theoretical considerations can influence a fluctuation analysis of the experimental data in a somewhat arbitrary manner, although the better a possible average variation is known,

the more one can rely on the fluctuation analysis. A specific example of this is the general requirement for normalizing (to a constant cross section) the smoothed cross section, thus giving a normalized cross section including fluctuations over the energy region of the excitation function considered either experimentally or theoretically. This is to avoid giving the larger of the smoothed cross sections in the energy interval undue weight in the fluctuation analysis. However, the averaged (smoothed) cross sections calculated in section 3.2 and given in fig. 4 are already nearly constant in the energy intervals analysed, and so these normalizations are neglected in the following fluctuation analyses of the experimental data.

We now make fluctuation analyses of probability distributions shown in figs. 5–7 for the measured [6] [8] [9] [10] cross sections. Histograms of the cross section probabilities are constructed directly from the experimental points in the excitation functions, which were measured with equal intervals of energy. For these analyses, use is made of the correlation coefficients of the experimental data

$$R_{\mathrm{exp}} = \frac{\left[\left(\frac{d\sigma}{d\Omega}\right)^2_{\mathrm{exp}}\right]_{av}}{\left[\left(\frac{d\sigma}{d\Omega}\right)_{\mathrm{exp}}\right]^2_{av}} - 1 \equiv \frac{2}{\nu_{\mathrm{exp}}} \tag{28a}$$

$$R_{\mathrm{exp}} = \frac{(\sigma^2_{\mathrm{exp}})_{av}}{(\sigma_{\mathrm{exp}})^2_{av}} - 1 \equiv \frac{2}{\nu_{\mathrm{exp}}}, \tag{28b}$$

which define the experimental fluctuation parameter ν_{exp} analogous to ν_{eff} of (15) and (14), respectively. The averages are over the experimental cross sections occurring through the energy interval ΔE_0 considered. The resulting ν_{exp} values are given in figs. 5–7 and in table VII.

To provide a comparison of ν_{exp} with theory, we define the equivalent quantity ν_{theor} by the correlation coefficients

$$R_{\mathrm{theor}} = \frac{\overline{\left(\frac{d\sigma}{d\Omega}\right)^2}}{\overline{\left(\frac{d\sigma}{d\Omega}\right)}^2} - 1 \equiv \frac{2}{\nu_{\mathrm{theor}}} \tag{29a}$$

$$R_{\mathrm{theor}} = \frac{\overline{\sigma^2}}{\bar{\sigma}^2} - 1 \equiv \frac{2}{\nu_{\mathrm{theor}}}. \tag{29b}$$

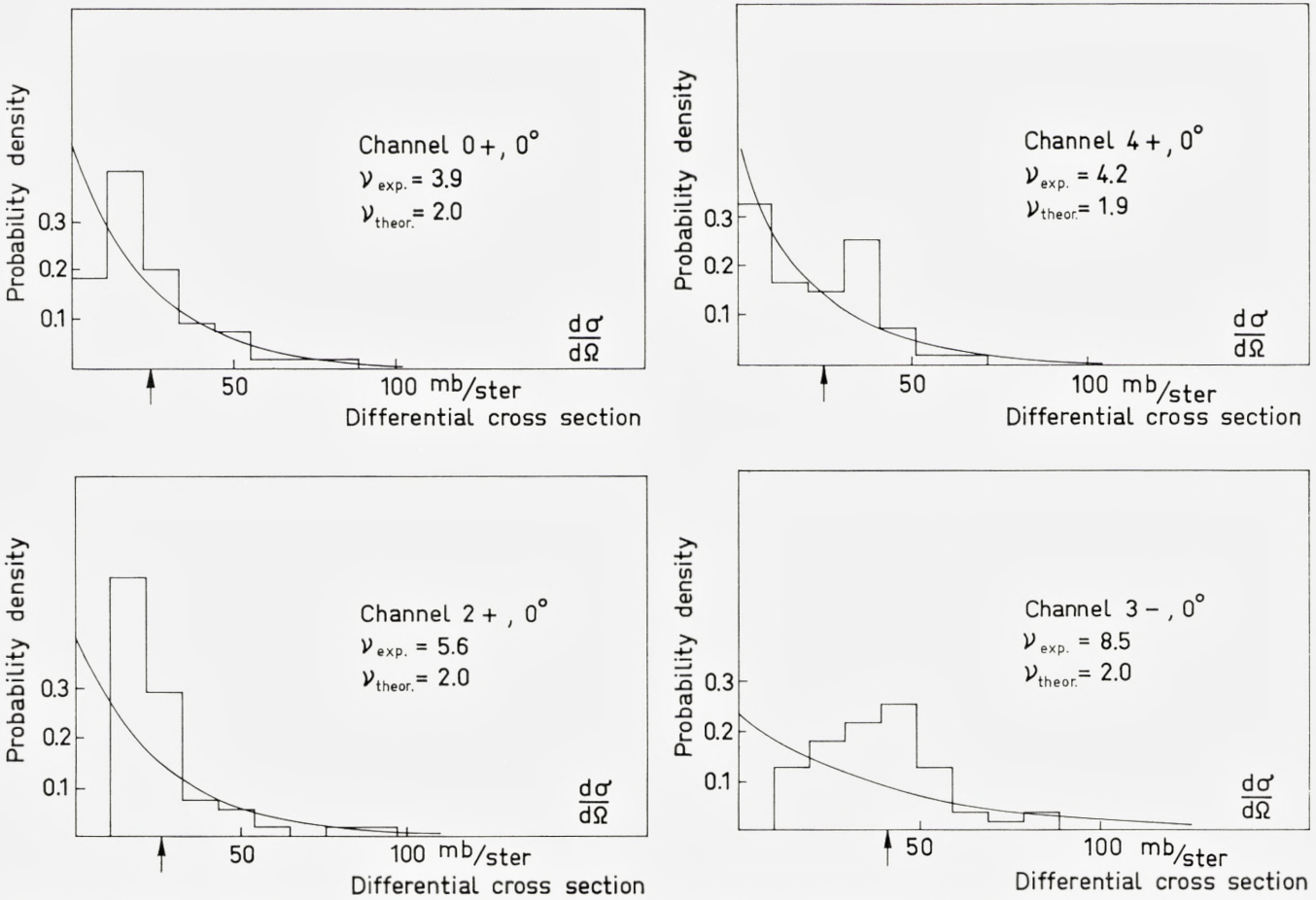

Fig. 5. Probability distributions of differential cross sections for 0° channels. Experimental data are from BORGGREEN et al.[10]. The theoretical distribution functions are normalized to the same average, which is indicated by the arrows, and area as the experimental histograms. The energy intervals are given in table VII.

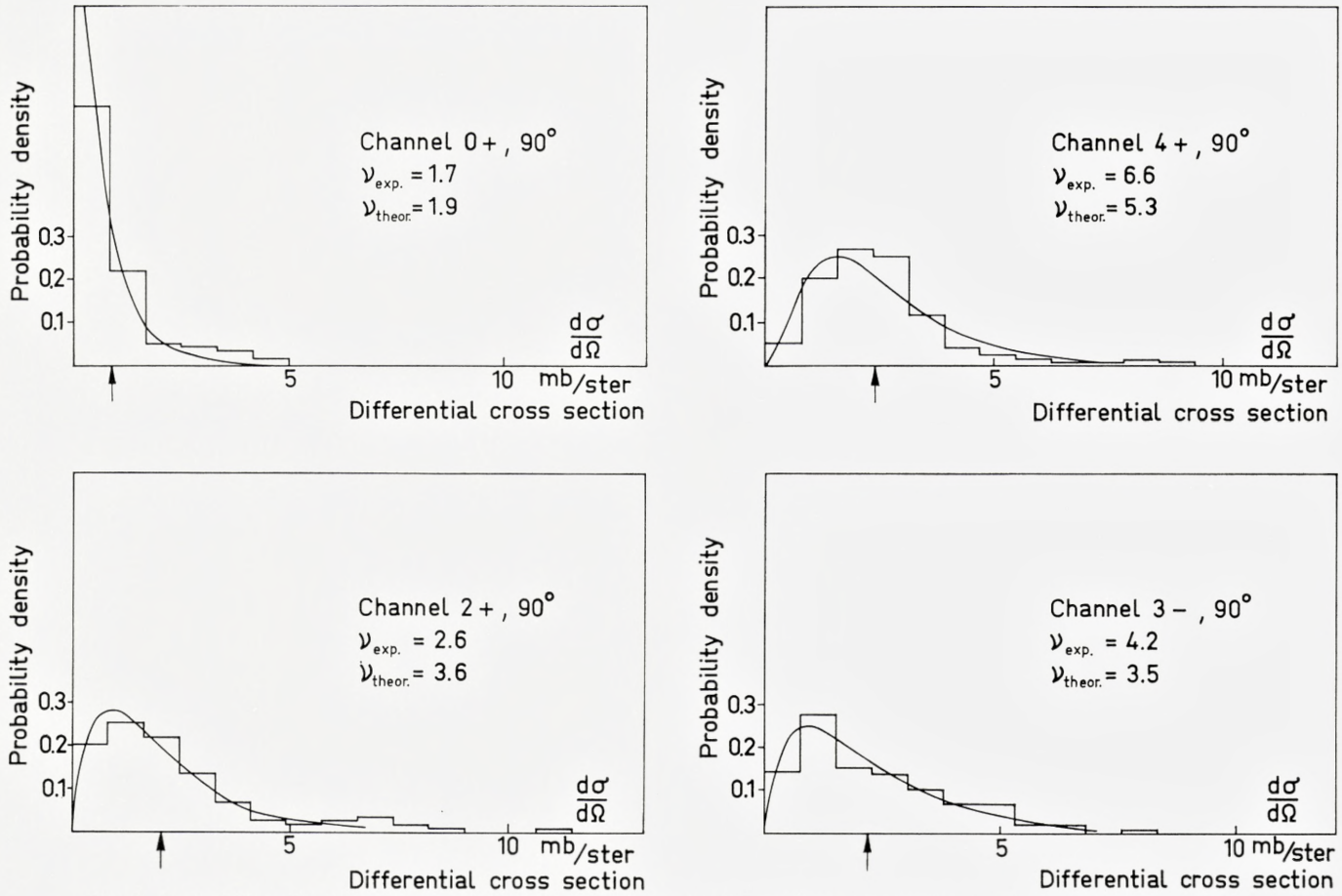

Fig. 6. Probability distributions of differential cross sections for 90° channels. See caption to fig. 5 for further details.

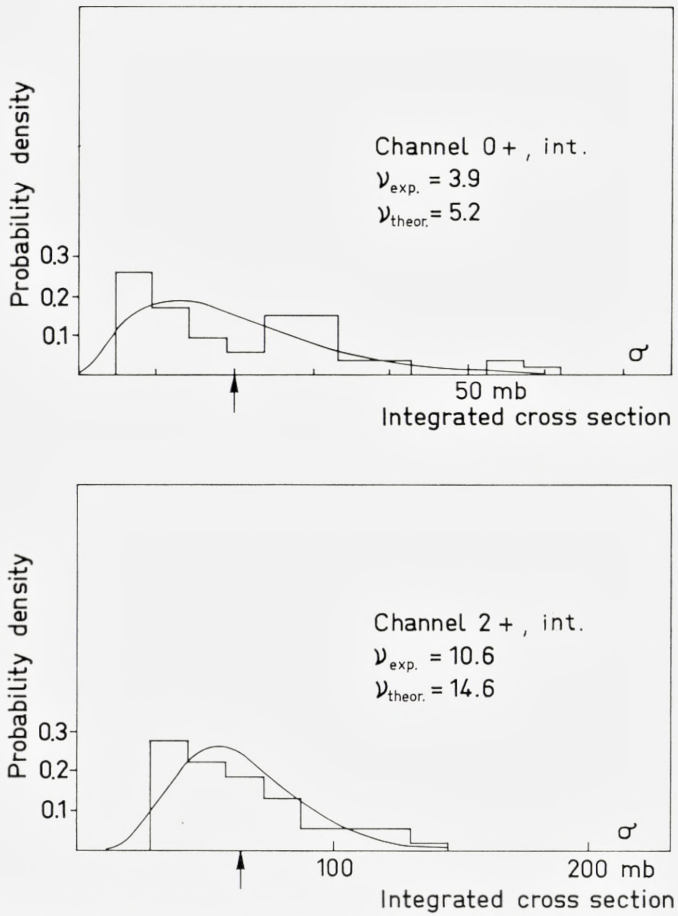

Fig. 7. Probability distributions of integrated cross sections. Experimental data are from ALMQVIST et al. [6] [8]. See caption to fig. 5 for further details.

Again, ν_{theor} is analogous to ν_{eff} of (15) and (14), respectively, in the sense that constant $<\frac{d\sigma}{d\Omega}>$ and $<\left(\frac{d\sigma}{d\Omega}\right)^2>$, or $<\sigma>$ and $<\sigma^2>$, over the energy interval ΔE_0 result in $\nu_{\text{theor}} = \nu_{\text{eff}}$.

To be comparable to the averages av in (28a) and (28b), the averages designated by bars in (29a) and (29b) must be over the same energy intervals ΔE_0. Knowing from section 2.4 that $<>$ signifies an average in the sense of the Hauser-Feshbach combination (21) of overlapping compound resonances λ, we have defined the wider interval average designated by a bar as

$$\overline{F} = \frac{1}{\Delta E_0} \int_{\Delta E_0} <F> dE_0 \qquad (30)$$

of such a <> average of a general function F over the energy interval ΔE_0. The denominator in (29a) is obtained from (17) by the square of the bar-averaged (30) sum $\sum_{M,\mu}$ of the basic cross sections $<\left(\frac{d\sigma}{d\Omega}\right)_\alpha>$, for which the reaction amplitudes a are calculated from the Hauser-Feshbach expression (21). Since $<\left(\frac{d\sigma}{d\Omega}\right)_\alpha^2> = 2<\left(\frac{d\sigma}{d\Omega}\right)_\alpha>^2$ for basic cross sections, $\overline{\left(\frac{d\sigma}{d\Omega}\right)^2}$ is similarly obtained, but from the bar-averaged sum of the squares in contrast to the square of the bar-averaged sum needed for $\left(\overline{\frac{d\sigma}{d\Omega}}\right)^2$. Similar remarks apply for the integrated cross sections, except that (18) is used with the sum $\sum_{J,j,l}$.

Calculations from (29a) and (29b) gave the ν_{theor} results shown in table VII as "refined theory" and in figs. 5–7. The numbers in the column "simple theory" in table VII are simply twice the effective number of M values from table I.

Shown together with the experimental histograms in figs. 5–7 are the χ^2 (actually gamma) distribution functions corresponding to ν_{theor} determined from (29a) and (29b). These theoretical distributions were normalized to the same average value and area as the histograms. Even if comparisons were to be made between these full distribution functions of experiment and theory, it should be emphasized that such comparisons based on the present use of the correlation coefficient would be limited in validity to the first and second moments of the cross section distributions.

3.4 Probability of dominant spin

In the ground-state channel there is a possibility of a simple, but unfortunately limited, further test of the independence approximation (13). This is the probability of an exception to the usually dominant compound spin in the energy interval of calculated dominance. We consider a mixture of two different spin values, say $J = x$ and $J = y$, having the partial average cross sections $<\sigma_x>$ and $<\sigma_y>$ with the two cross sections being independent

and having probability distributions that are decreasing exponentials. It is then easy to show that the probability of σ_x being greater than σ_y is

$$P(\sigma_x > \sigma_y) = \frac{<\sigma_x>}{<\sigma_x> + <\sigma_y>}. \tag{31}$$

In the energy interval of dominant compound spin 8, the number of angular distributions (taken with only roughly equidistant energy intervals) which show a $J \neq 8$ exception to the dominant spin was found [10] to be 1 out of 6 angular distributions, or 17%. The calculations show $<\sigma_{J=6,10}>$ to be about $<\sigma_{J=8}>/3$, which gives $P(\sigma_{J\neq 8}>\sigma_8)_{\text{theor}} = \frac{1/3}{(1/3)+1} = 25\%$, which within the poor statistics agrees with the experimental value of 17%. Approximately the same result is found [10] for the compound spin $J = 10$ region.

The very small number of observations at this time available puts severe limitations on the conclusions of this section.

4. Discussion and conclusion

The calculations result in three types of quantities which can be compared with experiment: resonance widths, absolute cross sections, and fluctuation parameters.

The calculated resonance widths shown in table V are typically 150 to 500 keV for compound spin $J = 0$ to $J = 6$ and 400 to 3000 keV for $J = 8$ and $J = 10$. These widths vary relatively little with the excitation energy of the compound system and are to be compared with the observed widths of 150 to 200 keV. Since $\sum_c T_c >> 2\pi$, one sees that the reaction is clearly in a region of overlapping levels, which is a main condition for the whole theory to be valid.

The calculated widths have uncertainties due to two effects that we now discuss. As seen from (25), the density of states of spin considerably larger than $\sqrt{2S^2}$ is very sensitive to the value of S^2. There is evidence that S^2 is not energy-independent, but rather $S^2 \propto t\Im$, where t is the nuclear temperature and $\Im$ the moment of inertia. Both t and $\Im$ increase with the excitation energy. This causes $<D_J>$ for the high spins to decrease at the higher excitation energies in the compound nucleus and, thus, a decrease in the calculated Γ_J. This is because $\sum_c T_c$ is largely originating from low lying and

low spin states in the residual nuclei for which a corresponding variation in S^2 is unimportant. On the other hand, corrections for $T_c \sim 1$ (see section 2.4) generally increase the calculated $\sum_c T_c$ and thus increase the calculated Γ_J.

The S effect tends to narrow the calculated width Γ_J for high J, but probably not as much as the discrepancy, while the correction for $T_c \sim 1$ tends to widen the calculated width. We conclude that some additional effects, such as the use of too many exit channels, account for the discrepancy between measured and calculated widths.

The calculated average cross sections are in general somewhat uncertain as a result of the rather big uncertainty in the density of final states extrapolated into the region of unidentified levels. The calculated average differential cross sections (table VII) are somewhat smaller than the observed ones for $\theta = 90°$. For $\theta = 0°$ the calculated differential cross sections are about two to six times smaller than the observed ones. This large observed 0° yield might correspond to some deviation from the randomness assumptions (6) for reaction amplitudes. In the two cases examined, the calculated integrated cross sections are about half the observed value.

The calculated fluctuation parameters ν_{theor} are generally in agreement with the experimental ones. It is seen in table VII that the "refined theory" (29a) and (29b) does not give results which differ much from the "simple theory" for the degrees of freedom in the distribution of the differential cross section. (No "simple theory" is possible to develop for the fluctuation in the integrated cross section analogous to the "simple theory" for fluctuation of the differential cross section). The largest discrepancy between ν_{exp} and ν_{theor} is seen at $\theta = 0°$, where the deviations generally are in the direction of large ν_{exp}. Possible contamination of unresolved alpha-particle energies from the reaction $O^{16}(C^{12},\alpha)Mg^{24}$ could increase ν_{exp}; the big discrepancy in the 2+, $\theta = 0°$ channel might result from such contamination. The aforementioned possible deviation from the randomness assumptions (6) (resulting from the possible existence of a direct amplitude) would also increase the fluctuation parameter ν_{exp}.

It has been postulated [8] that three "resonances" in the ground-state reaction are isolated resonances resulting from deformation of the compound system and clustering of the nucleons, which cause $\Gamma_i\Gamma_f$ to be very large. If such large resonances were isolated one would expect the same resonance to occur in the 2+ and 4+ excitation functions. No cross-correlated resonances between the 0+, 2+, and 4+ excitation functions are

seen at these "resonances", as is apparent from the example of fig. 2. This fact, in addition to the evidence from the present analysis that the reaction proceeds largely via a compound mechanism in the region of overlapping resonances, supports the idea that the three isolated "resonances" and the other peaks in the cross section can be interpreted as statistical fluctuations of the cross section.

Acknowledgements

The authors are particularly grateful to Professor B. R. Mottelson, NORDITA, for starting this investigation with his development of fluctuation theory and for his continuing, active interest in this work. Another important factor in this work was the stimulating atmosphere provided by Professor Aage Bohr at the Institute for Theoretical Physics. We also wish to thank Dr. W. Gibbs and Dr. T. Ericson for informative discussions and Mr. J. Onsgaard for some of the numerical calculations. One of us (RBL) is grateful for the hospitality of the Institute and for financial support from a Fulbright Fellowship and from the Los Alamos Scientific Laboratory.

Appendix

A χ^2 distribution of ν degrees of freedom has the analytical form [27]

$$N_\nu(\chi^2) = \frac{1}{2\Gamma(\nu/2)}\left(\frac{\chi^2}{2}\right)^{\frac{\nu}{2}-1} \exp\left(-\frac{\chi^2}{2}\right), \tag{A 1}$$

which is normalized to unity by $\int_0^\infty N_\nu(\chi^2)d\chi^2 = 1$.

We take a set of n independent quantities, say σ_β, each with a decreasing exponential of probability distribution $P(\sigma_\beta) = \frac{1}{2}\exp\left(\frac{-\sigma_\beta}{2}\right)$ with mean value 2. Then a property of $\sigma = \sum_{\beta=1}^{n} \sigma_\beta$ relevant to our application is that it is distributed with a χ^2 distribution of $\nu = 2n$ degrees of freedom,

$$N_{2n}(\sigma) = \frac{1}{2\Gamma(n)}\left(\frac{\sigma}{2}\right)^{n-1}\exp\left(-\frac{\sigma}{2}\right). \qquad \text{(A 2)}$$

If $<>$ represents the average with respect to (A 2), then

$$\frac{<\sigma^2>}{<\sigma>^2} - 1 = \frac{\nu+2}{\nu} - 1 = \frac{2}{\nu} = \frac{1}{n}. \qquad \text{(A 3)}$$

NORDITA, Copenhagen.

Institute for Theoretical Physics
University of Copenhagen.

R. B. L.
Fulbright Fellow on Leave from the
Los Alamos Scientific Laboratory.

Referencens

1) T. Ericson, *Proceedings of the International School of Physics* "Enrico Fermi" (Academic Press, New York, 1963), p. 142 and Phys. Rev. Letters **5**, 430 (1960).
2) T. Ericson, Ann. Phys. **23**, 390 (1963).
3) T. Ericson, Physics Letters **4**, 258 (1963).
4) D. M. Brink, R. O. Stephen, and N. W. Tanner. Nucl. Phys. **54**, 577 (1964).
5) D. M. Brink and R. O. Stephen, Physics Letters **5**, 77 (1963).
6) E. Almqvist, J. Kuehner, D. McPherson, and E. Vogt, Phys. Rev. **136**, B 86 (1964).
7) D. A. Bromley, J. A. Kuehner, and E. Almqvist, Phys. Rev. **123**, 878 (1961).
8) J. A. Kuehner, J. D. Prentice, and E. Almqvist, Physics Letters **4**, 332 (1963).
9) J. Borggreen, B. Elbek, R. B. Leachman, M. C. Olesen, and N. O. R. Poulsen, *Proceedings of the Third Conference on Reactions Between Complex Nuclei*, Asilomar (University of California Press, Berkeley, 1963, p. 201).
10) J. Borggreen, B. Elbek, and R. B. Leachman, Mat. Fys. Medd. Dan. Vid. Selsk. **34**, No. 9 (1964).
11) M. A. Preston, *Physics of the Nucleus*, (Addison-Wesley, Reading, 1962).
12) A. M. Lane and R. G. Thomas, Revs. Mod. Phys. **30**, 257 (1958).
13) W. Hauser and H. Feshbach, Phys. Rev. **87**, 366 (1952).

14) P. A. Moldauer, Symposium on the Statistical Properties of Atomic and Nuclear Spectra, State University of New York (1963), unpublished.
15) P. A. Moldauer, Phys. Rev. **129**, 754 (1963).
16) T. J. Krieger and C. E. Porter, J. Math. Phys. **4**, 1272 (1963).
17) P. E. Hodgson, The Optical Model of Elastic Scattering (Oxford University Press, Oxford, 1963).
18) C. E. Porter, Phys. Rev. **112**, 1722 (1958).
19) J. R. Huizenga and G. Igo, Nucl. Phys. **29**, 462 (1962).
20) M. A. Melkanoff, J. S. Nodvik, D. S. Saxon, and R. D. Woods, Phys. Rev. **106**, 793 (1957).
21) F. Bjorklund and S. Fernbach, Phys. Rev. **109**, 1295 (1958).
22) E. Erba, U. Facchini, E. Saetta Menichella, Nuovo Cimento **22**, 1237 (1961).
23) A. G. W. Cameron, Can. J. of Phys. **36**, 1040 (1958).
24) P. M. Endt and C. van der Leun, Nucl. Phys. **34**, 1 (1962).
25) *Landolt — Börnstein*, New Series, Vol. 1, edited by K. H. Hellwege (Springer-Verlag, Berlin, 1961) and T. Lauritsen and F. Ajzenberg-Selove, Energy Levels of Light Nuclei (1962).
26) M. L. Halbert and F. E. Durham, *Proceedings of the Third Conference on Reactions Between Complex Nuclei*, Asilomar (University of California Press, Berkeley, 1963, p. 223).
27) P. G. Hoel, *Introduction to Mathematical Statistics* (John Wiley and Sons Inc., New York, 1962), p. 153.
28) N. O. Lassen and Janus Staun Olsen, Mat. Fys. Medd. Dan. Vid. Selsk. **33**, No. 13 (1963).

Indleveret til Selskabet den 23. juni 1964.
Færdig fra trykkeriet den 13. maj 1965.

Matematisk-fysiske Meddelelser
udgivet af
Det Kongelige Danske Videnskabernes Selskab
Bind **34,** nr. 11

Mat. Fys. Medd. Dan. Vid. Selsk. **34,** no. 11 (1965)

EFFECT OF THE DIPOLE-QUADRUPOLE INTERACTION ON THE WIDTH AND THE STRUCTURE OF THE GIANT DIPOLE LINE IN SPHERICAL NUCLEI

PAR

JEAN LE TOURNEUX

København 1965
Kommissionær: Ejnar Munksgaard

Synopsis

A phenomenological study is made of the effect of a dipole-quadrupole interaction on the width and the structure of the giant dipole line in spherical nuclei. The broadening of the line is evaluated through the method of moments. The effect of the interaction on the structure of the line is also studied by constructing the interaction matrix and diagonalizing it. A classical limit is derived for the case of strong coupling. An attempt to correlate the calculated widths with those observed experimentally is presented.

PRINTED IN DENMARK
BIANCO LUNOS BOGTRYKKERI A/S

1. Introduction

Since the dipole state does not correspond to an eigenstate of the nuclear Hamiltonian, it is distributed over a large number of levels and the giant dipole line acquires thereby a structure of considerable complexity. This situation can be pictured as arising from a coupling of the dipole vibration to other modes of motion. The difficulty of studying theoretically the structure of the dipole line stems from the fact that, in the present state of nuclear physics, we do not possess a detailed knowledge of these other modes of motion and, a fortiori, of the form of the interaction between them and the dipole vibration. This makes it necessary to study first the interaction which seems likely to be responsible for most of the broadening of the line and then to improve this first picture by considering further types of coupling. In the case of O^{16}, for instance, one may start with a description of the dipole state in terms of single-particle excitations. The particle-hole interaction splits the five $I = 1^-$ states in such a way that most of the dipole strength is concentrated in two of the states. One can then study the broadening of each of these sharp lines which results from other types of coupling (as, for instance, the coupling to states in the continuum).

It is the purpose of the present paper to examine a mechanism which may be expected to give rise to much of the broadening of the dipole line in spherical nuclei, namely the interaction between the dipole and quadrupole vibrations. Both theoretically and experimentally it is a well-known fact that an axially symmetric static deformation of the nuclear surface splits the dipole line into two peaks. Similarly, the dynamic deformation resulting from the quadrupole vibrations of a spherical nucleus determines to a large extent the shape and the width of the line by spreading the dipole state over many levels. We will tackle this problem in a purely phenomenological way, limiting our description of the nuclear motion to that provided by the variables representing the collective degrees of freedom of the nucleus. While this approach makes the problem easily manageable, it obviously prevents us from making any estimate of the broadening of the individual levels through the admixture of configurations from the continuum.

2. The Hamiltonian

The dipole vibrations may be described in terms of the three collective coordinates $\alpha_{1\mu}$ specifying the relative distance between the centers of mass of the neutrons and the protons, and the quadrupole vibrations in terms of the five coefficients $\alpha_{2\mu}$ introduced in the familiar expansion of the nuclear surface [1]

$$R(\theta, \varphi) = R_0\Big(1 + \sum_{\mu} \alpha_{2\mu} Y^*_{2\mu}(\theta, \varphi)\Big). \tag{1}$$

In the harmonic approximation, the Hamiltonian corresponding to these two collective modes is given by

$$H_0 = \sum_{\lambda=1}^{2} \left[\frac{1}{2B_\lambda} \sum_{\mu} \pi^*_{\lambda\mu} \pi_{\lambda\mu} + \frac{1}{2} C_\lambda \sum_{\mu} \alpha^*_{\lambda\mu} \alpha_{\lambda\mu} \right], \tag{2a}$$

where the $\pi_{\lambda\mu}$ are the momenta canonically conjugate to the $\alpha_{\lambda\mu}$. The inertia and restoring force parameters B_λ and C_λ are quantities determined empirically. The form of the dipole-quadrupole interaction is established in a unique way from invariance considerations, if one limits oneself to the cubic terms containing no time-derivatives:

$$H_I = \frac{K}{\sqrt{5}} \sum_{\mu\nu} (-)^\mu \langle 11\nu\mu - \nu | 2\mu \rangle \alpha_{1\nu} \alpha_{1\mu-\nu} \alpha_{2-\mu}. \tag{3}$$

This is precisely the interaction which is responsible for the splitting of the dipole line in deformed nuclei. For the coupling constant K we use an estimate [4] based on the assumption that the dipole frequency is inversely proportional to the nuclear radius:

$$K = -\frac{5}{2} \sqrt{\frac{3}{2\pi}}\, C_1. \tag{4}$$

It is convenient to make a transformation from the $\alpha_{\lambda\mu}$ and $\pi_{\lambda\mu}$ to the creation and annihilation operators $b^+_{\lambda\mu}$ and $b_{\lambda\mu}$:

$$\left.\begin{aligned} \alpha_{\lambda\mu} &= \sqrt{\frac{\hbar}{2B_\lambda \omega_\lambda}} (b^+_{\lambda\mu} + (-)^\mu b_{\lambda-\mu}) \\ \pi_{\lambda\mu} &= i \sqrt{\frac{\hbar B_\lambda \omega_\lambda}{2}} (-)^\mu b^+_{\lambda-\mu} - b_{\lambda\mu}), \end{aligned}\right\} \tag{5}$$

where

$$\omega_\lambda = \sqrt{C_\lambda / B_\lambda}. \tag{6}$$

In terms of the new operators the uncoupled Hamiltonian takes the very simple form

$$H_0 = \sum_{\lambda=1}^{2} \sum_{\mu} (b^+_{\lambda\mu} b_{\lambda\mu} + 1/2)\hbar\omega_\lambda, \tag{6b}$$

with the eigenvalues

$$E_0(N_1, N_2) = (N_1 + 3/2)\hbar\omega_1 + (N_2 + 5/2)\hbar\omega_2, \tag{7}$$

N_1 and N_2 being the number of dipole and quadrupole phonons, respectively.

A simple glance at the coupling term H_I reveals that neither N_1 nor N_2 is a good quantum number. However, for the sake of simplicity, we shall always work in subspaces where the number of dipole phonons N_1 is constant. In view of the very large value of $\hbar\omega_1$, this is an excellent approximation since the conservation of parity would allow only the admixing of uncoupled states differing by at least two dipole phonons. This approximation is equivalent to retaining only that part of H_I which commutes with $\sum_\mu b^+_{1\mu} b_{1\mu}$:

$$H' = \frac{K\hbar}{B_1\omega_1} \sqrt{\frac{\hbar}{10 B_2 \omega_2}} \sum_{\mu\nu} (-)^\nu \langle 11\nu\mu - \nu | 2\mu \rangle b^+_{1\nu} b_{1\nu-\mu} \left(b^+_{2-\mu} + (-)^\mu b_{2\mu} \right). \tag{8}$$

We then have for the total Hamiltonian

$$H = H_0 + H'. \tag{9}$$

As a consequence of this approximation the $N_1 = 0$ states are unaffected by the presence of H'. In particular, the vacuum $|0\rangle$, defined as the state for which $N_1 = N_2 = 0$, is an eigenstate of both H_0 and $H_0 + H'$.

A complete solution of the problem involves a determination of the eigenvalues and eigenvectors of H. This is a clearly impossible task from the analytic point of view, since it is tantamount to the solution of a system of coupled differential equations in eight variables. One may have the temptation to apply an adiabatic approximation of the Born-Oppenheimer type, but such a procedure is unfortunately not justifiable here. In molecular spectroscopy, the projection of the electronic angular momentum along the symmetry axis of the molecule is considered as a good quantum number. No approximation of this kind can be made here: for each instantaneous

quadrupole deformation of the nuclear surface there will be three eigenfrequencies of the dipole vibration corresponding to the three principal axes

$$E_j(\beta,\gamma) = \hbar\omega_1\left[1 + \frac{2K}{\sqrt{30}\,C_1}\beta\cos(\gamma - j2\pi/3)\right], \tag{10}$$

where

$$\beta^2 = a_0^2 + 2a_2^2, \qquad \operatorname{tg}\gamma = \sqrt{2}\,a_2/a_0. \tag{11}$$

The variables a_0 and a_2 specify the shape of the ellipsoid in the frame of reference coinciding with its principal axes [1]. Since the three eigenfrequencies $E_j(\beta,\gamma)$ are quasi-degenerate, the corresponding eigenfunctions will surely have to be thoroughly mixed in any reasonable approximation to the actual $N_1 = 1$ wave functions. This automatically implies the obligation to solve a system of coupled differential equations in order to determine those parts of the wave functions which describe the quadrupole vibrations. Such a situation presents a great analogy with that encountered in the study of the vibronic spectrum [2]. We will try to obtain the eigenvectors of the coupled system $H_0 + H'$ as a superposition of those of the uncoupled Hamiltonian H_0. This will be achieved by calculating the energy matrix with respect to the uncoupled basis and then diagonalizing it. But before we carry out this program in detail, it is interesting to see how much information can be gathered on the broadening of the dipole line through a simple calculation using the method of moments.

3. Calculation of the width by the method of moments

Let us introduce the n^{th} moment

$$S_n = \sum_i (E_i - E_0)^n |\langle i|b_{1\mu}^+|0\rangle|^2. \tag{12}$$

The kets $|i\rangle$ are eigenvectors of the total Hamiltonian H with energies E_i. Using the closure property we can write

$$S_n = \langle 0|b_{1\mu}(H - E_0)^n b_{1\mu}^+|0\rangle. \tag{13}$$

The cross section for the excitation of a state i through dipole absorption is proportional to $(E_i - E_0)|\langle i|b_{1\mu}^+|0\rangle|^2$ and we may define the mean energy $\bar{E}$ of the dipole line as the position of the centre of gravity of the absorption cross section:

$$\bar{E} = S_2/S_1. \tag{14}$$

A possible measure of the width of the line is the root mean square deviation Δ:

$$\Delta^2 = \frac{\sum_i (E_i - E_0 - \bar{E})^2 (E_i - E_0) |\langle i | b_{1\mu}^+ | 0 \rangle|^2}{\sum_i (E_i - E_0) |\langle i | b_{1\mu}^+ | 0 \rangle|^2} = \frac{S_3}{S_1} - \left(\frac{S_2}{S_1}\right)^2. \tag{15}$$

The first three moments are readily evaluated and we obtain

$$\Delta^2 = \frac{K^2 \hbar^3 \omega_1^2 \omega_2}{6 C_1^2 C_2} \left(1 + \frac{\omega_2}{\omega_1}\right) - \frac{1}{\hbar^2 \omega_1^2} \left(\frac{K^2 \hbar^3 \omega_1^2 \omega_2}{6 C_1^2 C_2}\right)^2. \tag{16}$$

In general, the second term will be much smaller than the first one, so that in first approximation the width of the line will increase linearly with the coupling parameter K. This would have been strictly true if we had chosen to define $\bar{E}$ as the mean energy S_1 of the dipole state; in that case Δ would have been given by the first term of (16) only. In tables 2 and 3 of section 6 we give the value of 2Δ for various nuclei. For most of the cases considered this quantity turns out to be many times as large as $\hbar\omega_2$. This is the reason why we cannot study the problem by perturbation theory.

4. Construction and diagonalization of the energy matrix

The precedent calculation enabled us to evaluate the effect of the dipole-quadrupole interaction on the width of the dipole line. If, however, we want to study how it modifies its structure, we must attempt to determine explicitly the eigenvalues and eigenvectors of H. To this end we now proceed to the construction of the energy matrix and to its diagonalization.

The states over which H' spreads the dipole line have $N_1 = 1$, $I = 1$ and negative parity. They can be expressed as a linear combination of eigenvectors of the uncoupled Hamiltonian:

$$|N_1 = 1; i; I = 1, M\rangle = \sum_{N_2 v l_2} a^i_{N_2 v l_2} |N_1 = 1, l_1; N_2 v l_2; I = 1, M\rangle. \tag{17}$$

The angular momenta l_1 and l_2 of the dipole and quadrupole phonons are vector coupled to a total angular momentum $I = 1$ with projection M on the z-axis. This restricts l_2 to the values 0 and 2, since it has been shown that no $l_2 = 1$ state can arise from the quadrupole vibrations of the nuclear surface [1]. For $N_2 \geqslant 4$, it is possible to form states with the same l_2 and z-component of l_2 in more than one way. The need to remove at least part

of this degeneracy led RAKAVY [3] to introduce a new quantum number, the seniority v, which indicates how many of the N_2 phonons are not coupled pairwise to an angular momentum equal to 0. A state of N_2 phonons may have seniorities $v = N_2,\ N_2-2,\ \ldots\ldots 1$ or 0. In the conventional way of labelling the irreducible representations of R_5, those would be the $(N_2,0)$, $(N_2-2,0)\ \ldots\ldots\ (1,0)$ or $(0,0)$ representations. The decomposition of those into irreducible representations of R_3 may be effected through elementary methods (see the Appendix), and table 1 gives the multiplicities of the various values of the angular momentum found in a representation of seniority v, for values of v going up to 18. Now, we observe an interesting regularity: the states with $l_2 = 0$ or 2 never occur more than once, or both at the same time, for a given seniority. Moreover, the lowest value of l_2 is equal to 0 if $v = 3n$ and 2 if $v = 3n \pm 1$, n being an integer. We checked these rules up to $v = 18$, but could not derive them through elementary methods. Of course, these regularities simplify our calculations immensely by enabling us to characterize uniquely the unperturbed states in which we are interested by the two quantum numbers N_2 and v only. We can therefore drop the label l_2 attached to the coefficients a in (17).

It is a straightforward matter to show that the matrix elements of H' are given by

$$\langle 11; N_2' v' l_2'; 1M | H' | 11; N_2 v l_2; 1M\rangle = -\frac{K\hbar}{B_1\omega_1} W(1 l_2 1 l_2' : 12)\langle N_2' v' l_2' \| \alpha_2 \| N_2 v l_2\rangle, \quad (18)$$

where the reduced matrix element $\langle N_2' v' l_2' \| \alpha_2 \| N_2 v l_2\rangle$ is defined by

$$\langle N_2', v', l_2', m_2' | \alpha_{2\mu} | N_2, v, l_2, m_2\rangle = \frac{1}{\sqrt{2l_2'+1}}\langle l_2 2 m_2 \mu | l_2' m_2'\rangle\langle N_2' v' l_2' \| \alpha_2 \| N_2 v l_2\rangle. \quad (19)$$

The very definition of the operators $\alpha_{2\mu}$ yields the selection rules

$$\left.\begin{aligned} N_2' &= N_2 \pm 1 \\ v' &= v \pm 1. \end{aligned}\right\} \quad (20)$$

We proceed to the evaluation of the reduced matrix elements in two steps: first, by showing that all of them can be expressed in terms of those which are taken between states for which $v = N_2$ and, second, by evaluating them for that special case. Moreover, because of the trivial relation between the matrix elements of b and b^+, we have to consider only the former.

We begin by noticing that a state with $N_2 = 2\nu + v$, ν being a positive integer, can be written as

$$|2v+v,v,l_2,m_2\rangle = \frac{1}{\sqrt{C(2v+v,v)}}\{b_2^+b_2^+\}_0^v|v,v,l_2,m_2\rangle, \tag{21}$$

where

$$\{b_2^+b_2^+\}_0 = \frac{1}{\sqrt{5}}\sum_\mu(-)^\mu b_{2\mu}^+b_{2-\mu}^+. \tag{22}$$

We stick to the convention that all the kets are normalized to unity. The normalization coefficients

$$C(2v+v,v) = \left(\frac{2}{5}\right)^v v!\prod_{\alpha=1}^{v}(2\alpha+2v+3) \tag{23}$$

are immediately deduced from the recursion formula

$$\left.\begin{aligned} C(2v+v,v) &= \langle v,v,l_2,m_2|\{b_2b_2\}_0^v\{b_2^+b_2^+\}_0^v|v,v,l_2,m_2\rangle \\ &= \frac{4}{5}\sum_{\alpha=1}^{v}[2(v-\alpha)+v+5/2]\langle v,v,l_2,m_2|\{b_2b_2\}_0^{v-1}\{b_2^+b_2^+\}_0^{v-1}|v,v,l_2,m_2\rangle \\ &= \frac{2v}{5}(2v+2v+3)C(2v+v-2,v). \end{aligned}\right\} \tag{24}$$

In deriving this formula we have used the commutation relation

$$\left[\{b_2b_2\}_0,\ \{b_2^+b_2^+\}_0\right] = \frac{4}{5}N_2+2 = \frac{4}{5}\sum_\mu b_{2\mu}^+b_{2\mu}+2 \tag{25}$$

and the fact that $\{b_2b_2\}_0$ acting on a state $|v,v,l_2,m_2\rangle$ gives zero. With the help of eqs. (21), (23) and (25) we readily obtain

$$\left.\begin{aligned} &\langle N_2-1,v-1,l_2',m_2'|b_{2\mu}|N_2,v,l_2,m_2\rangle \\ &= \sqrt{\frac{N_2+v+3}{N_2+v+1}}\langle N_2-3,v-1,l_2',m_2'|b_{2\mu}|N_2-2,v,l_2,m_2\rangle \\ &= \sqrt{\frac{N_2+v+3}{2v+3}}\langle v-1,v-1,l_2',m_2'|b_{2\mu}|v,v,l_2,m_2\rangle. \end{aligned}\right\} \tag{26}$$

Similarly,

$$\left.\begin{aligned} &\langle N_2-1,v+1,l_2',m_2'|b_{2\mu}|N_2,v,l_2,m_2\rangle \\ &= \sqrt{\frac{N_2-v}{2}}\langle v+1,v+1,l_2',m_2'|b_{2\mu}|v+2,v,l_2,m_2\rangle. \end{aligned}\right\} \tag{27}$$

Then, eqs. (21), (23), the commutator

$$\left[b_{2\mu}, \{b_2^+ b_2^+\}_0\right] = \frac{2}{\sqrt{5}}(-)^\mu b_{2-\mu}^+ \tag{28}$$

and the relation between the matrix elements of b and b^+ yield

$$\left.\begin{aligned} &\langle N_2 - 1, v+1, l_2', m_2' | b_{2\mu} | N_2, v, l_2, m_2\rangle \\ &= \sqrt{\frac{N_2 - v}{2v+5}} \langle v, v, l_2, m_2 | (-)^\mu b_{2-\mu} | v+1, v+1, l_2', m_2'\rangle . \end{aligned}\right\} \tag{29}$$

In order to evaluate the matrix elements

$$\langle v-1, v-1, l_2', m_2' | b_{2\mu} | v, v, l_2, m_2\rangle$$

we must consider separately the three cases $v = 3n$, $3n+1$ and $3n-1$.

$\boxed{v = 3n}$

Since $l_2 = 0$ when $v = 3n$, we have

$$(-)^\mu b_{2\mu} | v, v, 0, 0\rangle = d(-\mu) | v-1, v-1, 2, -\mu\rangle . \tag{30}$$

The coefficients $d(-\mu)$ are easily seen to be independent of μ, so that

$$\langle v, v, 0, 0 | \sum_\mu b_{2\mu}^+ b_{2\mu} | v, v, 0, 0\rangle = 5d^2 = v \tag{31}$$

and

$$d = \sqrt{v/5} . \tag{32}$$

$\boxed{v = 3n-1}$

An annihilation operator acting on $|v = 3n-1, v, 2, M\rangle$ produces a $v = 3n-2$ state with $l_2' = 2$ or 4; moreover we see from table 1 that the $l_2' = 4$ state never occurs more than once, so that we can write

$$\left.\begin{aligned} &\sum_\mu \langle 22\mu M | LM+\mu\rangle (-)^\mu b_{2-\mu} | v, v, 2, M\rangle = e(L, M+\mu) | v-1, v-1, L, M+\mu\rangle , \\ &\qquad (L = 2 \text{ or } 4). \end{aligned}\right\} \tag{33}$$

The coefficients e are independent of $M+\mu$ and, therefore, dropping that index, we obtain from (33)

$$(-)^\mu b_{2-\mu} | v, v, 2, M\rangle = \sum_L \langle 22\mu M | LM+\mu\rangle e(L) | v-1, v-1, L, M+\mu\rangle , \tag{34}$$

whence

$$\left.\begin{aligned}\langle v,v,2,M|\sum_{\mu} b^{+}_{2\mu}b_{2\mu}|v,v,2,M\rangle &= v = \sum_{L\mu}\langle 22\mu M|LM+\mu\rangle^2 e(L)^2 \\ &= e(2)^2+\frac{9}{5}e(4)^2\end{aligned}\right\} \quad (35)$$

and

$$\left.\begin{aligned}\langle v,v,2,M|\sum_{\mu}\mu b^{+}_{2\mu}b_{2\mu}|v,v,2,M\rangle &= M \\ = -e(2)^2\sum_{\mu}\mu\langle 22\mu M|2M+\mu\rangle^2 - e(4)^2\sum_{\mu}\mu\langle 22\mu M|4M+\mu\rangle^2.\end{aligned}\right\} \quad (36)$$

For $M = 0$ this relation yields an identity, but for $M \neq 0$ it gives a unique relation

$$e(2)^2 - \frac{12}{5}e(4)^2 = 2. \quad (37)$$

Eqs. (35) and (37) can be solved for $e(2)$

$$e(2) = \sqrt{\frac{4v+6}{7}}, \quad (38)$$

which enables us to evaluate the matrix element

$$\langle v-1,v-1,2,M+\mu|(-)^{\mu}b_{2-\mu}|v,v,2,M\rangle = \langle 22\mu M|2M+\mu\rangle e(2). \quad (39)$$

$\boxed{v = 3n+1}$

Relation (29) gives

$$\langle v-1,v-1,0,0|b_{2\mu}|v,v,2,\mu\rangle = \sqrt{\frac{2v+3}{2}}\langle v,v,2,\mu|(-)^{\mu}b_{2-\mu}|v+1,v-1,0,0\rangle. \quad (40)$$

Now, we see from table 1 that

$$(-)^{\mu}b_{2-\mu}|v+1,v-1,0,0\rangle = f|v,v,2,\mu\rangle + g|v,v-2,2,\mu\rangle, \quad (41)$$

whence we deduce

$$\langle v+1,v-1,0,0|\sum_{\mu} b^{+}_{2\mu}b_{2\mu}|v+1,v-1,0,0\rangle = v+1 = 5(f^2+g^2). \quad (42)$$

The coefficient g may be evaluated from eqs. (26), (30) and (32):

$$g = \langle v,v-2,2,\mu|(-)^{\mu}b_{2-\mu}|v+1,v-1,0,0\rangle = \sqrt{\frac{2v+3}{2v+1}\left(\frac{v-1}{5}\right)}. \quad (43)$$

TABLE 1. Multiplicity $d_v(l_2)$ of the representations l_2 of R_3 contained in a representation $(v,0)$ of R_5.

$v\backslash l^2$	0	1	2	3	4	5	6	7	8	9	10	11	12	13	14	15	16	17	18	19	20	21	22	23	24	25	26	27	28	29	30	31	32	33	34	35	36
0	1																																				
1			1																																		
2			1		1																																
3	1			1	1		1																														
4			1		1	1	1		1																												
5			1		1	1	1	1	1		1																										
6	1			1	1		2	1	1	1	1		1																								
7			1		1	1	1	1	2	1	1	1	1		1																						
8			1		1	1	1	1	2	1	2	1	1	1	1		1																				
9	1			1	1		2	1	1	2	2	1	2	1	1	1	1		1																		
10			1		1	1	1	1	2	1	2	2	2	1	2	1	1	1	1		1																
11			1		1	1	1	1	2	1	2	2	2	2	2	1	2	1	1	1	1		1														
12	1			1	1		2	1	1	2	2	1	3	2	2	2	2	1	2	1	1	1	1		1												
13			1		1	1	1	1	2	1	2	2	2	2	3	2	2	2	2	1	2	1	1	1	1		1										
14			1		1	1	1	1	2	1	2	2	2	2	3	2	3	2	2	2	2	1	2	1	1	1	1		1								
15	1			1	1		2	1	1	2	2	1	3	2	2	3	3	2	3	2	2	2	2	1	2	1	1	1	1		1						
16			1		1	1	1	1	2	1	2	2	2	2	3	2	3	3	3	2	3	2	2	2	2	1	2	1	1	1	1		1				
17			1		1	1	1	1	2	1	2	2	2	2	3	2	3	3	3	3	3	2	3	2	2	2	2	1	2	1	1	1	1		1		
18	1			1	1		2	1	1	2	2	1	3	2	2	3	3	2	4	3	3	3	3	2	3	2	2	2	2	1	2	1	1	1	1		1

From eqs. (42) and (43) we then obtain

$$f = \sqrt{\frac{2v+4}{5(2v+1)}} \tag{44}$$

and from eq. (40)

$$\langle v-1, v-1, 0, 0 | b_{2\mu} | v, v, 2, \mu \rangle = \sqrt{\frac{(2v+3)(v+2)}{5(2v+1)}}. \tag{45}$$

We remark that the signs of d, $e(L)$, f and g could not be determined from the precedent algebraic relations. However, we shall consider that our arbitrary choice determines the overall phase of the $|v, v, l_2', m_2'\rangle$ states. Such an overall phase is immaterial since we will be interested only in the squares of the coefficients.

Using eqs. (5), (18), (19), (26), (29), (30), (32), (38), (39) and (45), we can write down the matrix elements of H:

$$\langle N_1' = 1, N_2 - 1, v' | H' | N_1 = 1; N_2, v \rangle = \begin{cases} k\sqrt{\dfrac{(N_2+v+3)v}{15(2v+3)}} & \text{if } v' = v-1 \quad \text{and} \quad v = 3n, \\ k\sqrt{\dfrac{N_2+v+3}{30}} & \text{if } v' = v-1 \quad \text{and} \quad v = 3n-1, \\ k\sqrt{\dfrac{(N_2+v+3)(v+2}{15(2v+1)}} & \text{if } v' = v-1 \quad \text{and} \quad v = 3n+1, \\ k\sqrt{\dfrac{(N_2-v)(v+3)}{15(2v+5)}} & \text{if } v' = v+1 \quad \text{and} \quad v = 3n, \\ k\sqrt{\dfrac{(N_2-v)(v+1)}{15(2v+5)}} & \text{if } v' = v+1 \quad \text{and} \quad v = 3n-1, \\ k\sqrt{\dfrac{N_2-v}{30}} & \text{if } v' = v+1 \quad \text{and} \quad v = 3n+1, \end{cases} \tag{46}$$

where

$$k = -\frac{K\hbar}{B_1\omega_1}\sqrt{\frac{\hbar}{2B_2\omega_2}}. \tag{47}$$

We are now in a position to construct the complete energy matrix. The rows and the columns are arranged in order of increasing N_2 and, for each N_2, of decreasing v. It is convenient to express the whole matrix in units of $\hbar\omega_2$. If the diagonal terms corresponding to $5/2(1+\omega_1/\omega_2)$ times the unit matrix are omitted, the matrix becomes

$$\begin{bmatrix}
0 & \eta\sqrt{1/3} & & & & & & & & & & \\
\eta\sqrt{1/3} & 1 & \eta\sqrt{7/30} & \eta\sqrt{2/15} & & & & & & & & \\
 & \eta\sqrt{7/30} & 2 & 0 & \eta\sqrt{1/5} & \eta\sqrt{1/15} & & & & & & \\
 & \eta\sqrt{2/15} & 0 & 2 & 0 & \eta\sqrt{7/15} & & & & & & \\
 & & \eta\sqrt{1/5} & 0 & 3 & 0 & \eta\sqrt{\frac{22}{45}} & \eta\sqrt{\frac{2}{45}} & & & & \\
 & & \eta\sqrt{1/15} & \eta\sqrt{7/15} & 0 & 3 & 0 & \eta\sqrt{3/10} & \eta\sqrt{4/15} & & & \\
 & & & & \eta\sqrt{\frac{22}{45}} & 0 & 4 & 0 & 0 & \eta\sqrt{\frac{13}{30}} & \eta\sqrt{\frac{4}{45}} & \\
 & & & & \eta\sqrt{\frac{2}{45}} & \eta\sqrt{3/10} & 0 & 4 & 0 & 0 & \eta\sqrt{\frac{11}{45}} & \eta\sqrt{2/15} \\
 & & & & & \eta\sqrt{\frac{4}{45}} & 0 & 0 & 4 & 0 & 0 & \eta\sqrt{3/5} \\
 & & & & & & \eta\sqrt{\frac{13}{30}} & 0 & 0 & 5 & 0 & 0 \\
 & & & & & & \eta\sqrt{\frac{4}{45}} & \eta\sqrt{\frac{11}{45}} & 0 & 0 & 5 & 0 \\
 & & & & & & & \eta\sqrt{\frac{2}{45}} & \eta\sqrt{3/5} & 0 & 0 & 5 \;\ldots\ldots
\end{bmatrix}$$

where

$$\eta = k/\hbar\omega_2. \tag{48}$$

This matrix was diagonalized on the GIER computer of the Astronomical Observatory of Copenhagen. As η was increased, larger and larger matrices had to be considered in order to decrease the error due to their finite size. The eigenvalues E_i of the total Hamiltonian

$$H|N_1 = 1; i; I = 1, M\rangle = E_i|N_1 = 1; i; I = 1, M\rangle \tag{49}$$

and the corresponding coefficients $a^i_{N_2 v}$ of the eigenvectors were evaluated for some values of η ranging from $\sqrt{3}$ to $6\sqrt{3}$. Figs. 1–4 represent the distribution of the dipole state amongst the various levels. The length of the lines is proportional to the square of the quantity a^i_{00}

$$a^i_{00} = \langle i|b^+_{1\mu}|0\rangle \tag{50}$$

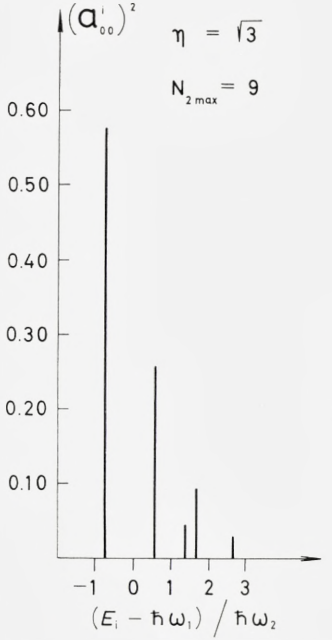

Fig. 1.

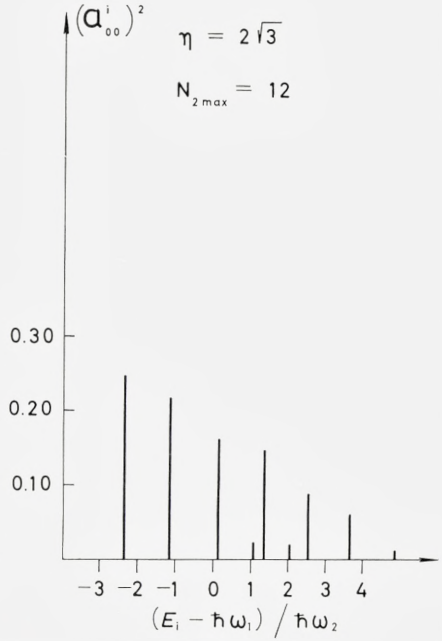

Fig. 2.

$N_{2\,max}$ is the largest number of phonons considered.

involved in the calculation of the cross sections. The coupling between the dipole and quadrupole modes appears to give rise to quite a complicated structure of the dipole line for sufficiently large values of η. It is difficult to predict how much of this structure will persist once the intrinsic widths of the levels have been added to the picture. The whole situation is made even more complicated by the fact that the dipole mode may be coupled to other modes beside the quadrupole vibrations.

5. A classical approximation

In the limit $\Delta \gg \hbar\omega_2$ it is possible to derive a classical expression for the probability $P(E)$ of exciting an eigenstate at an energy E through dipole absorption:

$$\left.\begin{aligned} P(E) &= \sum_i |\langle i|b^+_{1\mu}|0\rangle|^2 \delta(E - E_i + E_0) \\ &= \langle 0|b_{1\mu}\delta(E - H + E_0)b^+_{1\mu}|0\rangle. \end{aligned}\right\} \quad (51)$$

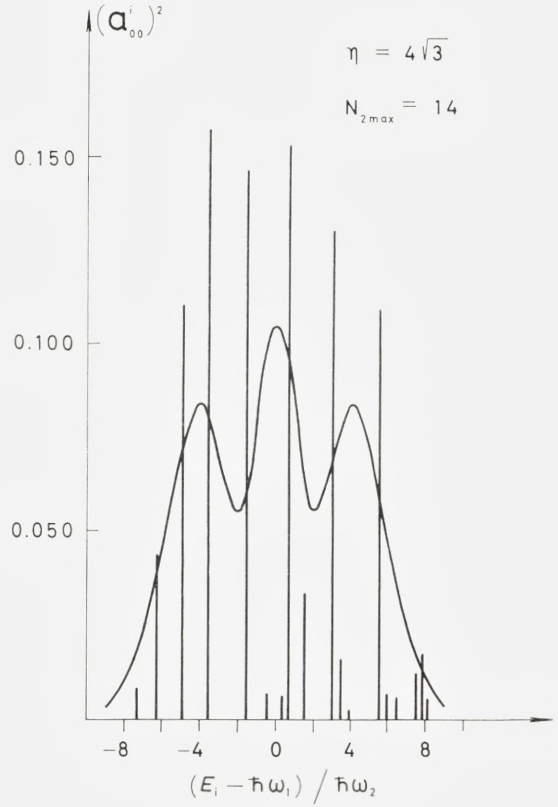

Fig. 3.

$N_{2\max}$ is the largest number of phonons considered. The curve shows the classical approximation.

We can then drop the part of the Hamiltonian which describes the quadrupole vibrations and the coupling between the normal dipole modes through the angular velocity of the intrinsic axes, keeping only the terms

$$H \simeq \sum_i (b'^+_{1j} b'_{1j} + 1/2)\left[1 + \frac{2K}{\sqrt{30}\, C_1}\beta\cos(\gamma - 2\pi j/3)\right]\hbar\omega_1, \tag{52}$$

where b'^+_{1j} and b'_{1j} are the creation and destruction operators for a dipole phonon along the axis j. Substituting (52) into (51), expressing $b^+_{1\mu}$ and $b_{1\mu}$ in terms of the primed operators and integrating over the Euler angles, we obtain

$$P(E) = \frac{1}{3}\sum_j \int |\Psi_0(\beta,\gamma)|^2 \delta\left[E - \hbar\omega_1\left(1 + \frac{2K}{\sqrt{30}\, C_1}\beta\cos(\gamma - 2\pi j/3)\right)\right]\beta^4 d\beta |\sin^3\gamma| d\gamma \tag{53}$$

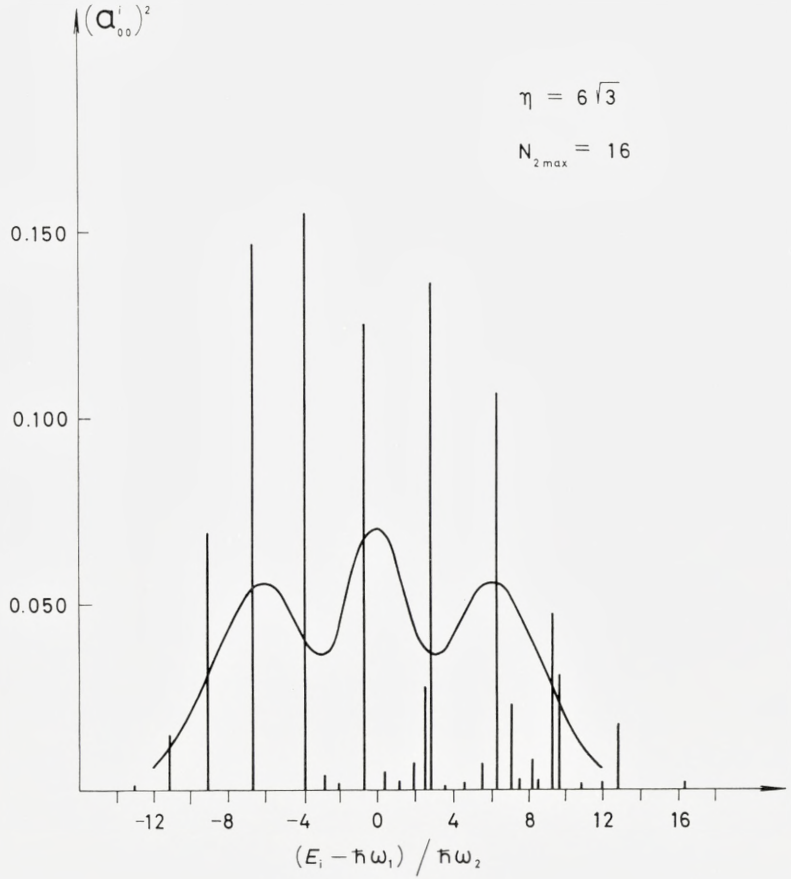

Fig. 4.

$N_{2\,max}$ is the largest number of phonons considered. The curve shows the classical approximation.

This expression has an immediate physical meaning: since the absorption of the dipole radiation takes place in a time which is very short in comparison with the period of the quadrupole vibrations[1], a nucleus possessing a deformation (β,γ) will absorb only photons with the energy required to excite one of the three normal dipole modes; the probability that this happens is proportional to $\Psi_0(\beta,\gamma)$, the ground state wave function for quadrupole oscillations. We average over the three intrinsic axes, because unpolarized nuclei are considered.

[1] It is possible to form a wave packet with an energy spread large compared with the quadrupole energy but small compared with the width of the dipole line.

The integral in (53) is evaluated without difficulty and yields

$$P(E) = \frac{2}{3}\sqrt{\frac{\alpha}{\pi}}\{e^{-\alpha(E-\hbar\omega_1)^2}[3\alpha(E-\hbar\omega_1)^2 - 1] + 2e^{-4\alpha(E-\hbar\omega_1)^2}\}, \tag{54}$$

where

$$\alpha = \frac{15B_1{}^2\omega_1{}^2B_2\omega_2}{2K^2\hbar^3}. \tag{55}$$

The classical result is shown in figs. 3 and 4. When comparing it with the exact solution, one should not forget that $P(E)$ is a probability density, so that it should be compared with $\sum(a_{00}^i)^2/\Delta E$, the summation being extended to all levels in the interval ΔE. For the values of η considered, however, the level density is still too low to make the construction of a histogram meaningful. The exact solution tends slowly towards the classical limit and it is doubtful whether the latter is of any validity for the cases of physical interest. This may seem surprising at first sight, since it is possible to study an analogous problem where the exact solution tends rather rapidly towards the classical limit, namely the motion of two coupled harmonic oscillators in one dimension with frequencies ω_1 and ω_2 such that $\omega_1 \gg \omega_2$. The situation, however, is more complex here: the classical limit has a structure and it will not be a good approximation to the exact solution until there are many lines under each of its three peaks.

6. Comparison with the experimental results

We will now attempt to compare the calculated widths with those observed experimentally. For many reasons this is not an easy task. The quantity Δ which we calculated is the root mean square deviation of the dipole absorption cross section, if one neglects the intrinsic width of each line. Of course no such quantity is known experimentally and the best we can do is to compare 2Δ with some parameter characterizing the width of the observed line. For the sake of simplicity, we choose Γ, the full width at half maximum cross section, as this parameter. Since the two compared quantities are not exactly the same, we cannot expect to do more than reproduce the general trends of the variation of the width as a function of the parameters involved. The comparison is made yet more difficult by the fact that, for many of the nuclei considered, the cross section $\sigma(\gamma, n)$ is used without any correction for the neutron multiplicity, so that we tend to have an overestimate of the actual width. Since we consider nuclei with $A \geqslant 50$,

the neglect of the (γ,p) process should not introduce a great error. Another difficulty lies in the choice of $\hbar\omega_1$. We take for this quantity the value of the energy at which the cross section $\sigma(\gamma n)$ has its maximum.

Strictly speaking, our theory is applicable to spherical even-even nuclei only. Unfortunately there is a scarcity of experimental data on the dipole line of those nuclei. For this reason, we also consider a certain number of odd-A nuclei, assuming that the odd nucleon does not have a great influence on the shape of the dipole line and, in particular, that its interaction with the nuclear surface does not perturb the interaction between the dipole and quadrupole modes. The parameters $\hbar\omega_2$ and C_2 are taken to be those of the adjacent even-even nuclei. When the experimental spectrum of the odd-A nucleus, with a certain amount of optimism, can be interpreted as resulting from the coupling of the odd nucleon to the surface vibrations of one of the adjacent nuclei, the vibrational parameters of the latter are used. In all other cases, at least in so far as the available data enable us to do so, we use an average of the parameters of both neighbours. When, however, the two sets of parameters are widely different (near a closed shell), we give separately the widths predicted for each of them.

Δ may be calculated from (16) or, alternatively, the eigenvalues and eigenvectors obtained through the diagonalization of the matrix may be used in conjunction with eqs. (15) and (50):

$$\Delta^2 = \frac{\sum_i (E_i - E_0 - \bar{E})^2 (E_i - E_0)(a_{00}^i)^2}{\sum_i (E_i - E_0)(a_{00}^i)^2}. \tag{56}$$

The first method is an exact one, whereas the second one contains a certain inaccuracy stemming from the finite size of the matrix and from its numerical diagonalization. A comparison between the results obtained in both ways is useful in that it provides an indication of the order of magnitude of this inaccuracy. The discrepancy turns out to be of a few percent only.

The experimental widths, the exact theoretical quantities 2Δ and all the relevant parameters are presented in tables 2 and 3 for even-even and odd-A nuclei, respectively. The values of the width due to the dipole-quadrupole interaction are seen to vary between one third and one half of the experimental ones. This is hardly surprising, partly because of the uncertainties in the comparison which were indicated above, partly because of the very nature of the present calculations. We have assumed that the quadrupole phonons do not interfere with each other although the inaccuracy introduced

TABLE 2.

Nucleus	$\hbar\omega_2$ (MeV)	C_2 (MeV)	Ref.	$\hbar\omega_1$ (MeV)	Γ (MeV)	Ref.	2Δ (MeV)
$_{30}\overline{Zn}$	1.03	49	5	16.3	6.3	11	3.4
$_{32}Ge^{70}$	0.88	53	5	17.5	8.0	12	3.2
$_{38}Sr^{88}$	1.85	258	6	16.3	4.0	13	2.1
$_{40}Zr^{92}$	0.92	151	7	16.9	5.5	13	1.9
$_{42}Mo^{92}$	1.52	173	8	16.0	2.7[1]	14	2.2
$_{48}Cd^{112}$	0.610	42	9	16.0	5.1[2]	11	2.8
$_{50}\overline{Sn}$	1.19	235	9	15.8	5.0[2]	15	1.7
$_{50}Sn^{112}$	1.26	280	10	16.0	5.0	16	1.6
$_{50}Sn^{124}$	1.13	240	9	15.5	5.0	16	1.6
$_{82}Pb^{208}$	–	–		13.8	3.5[2]	31	~ 0

[1] Measured by the method of residual activity.
[2] Corrected for neutron multiplicity.

when dropping the anharmonic and higher order terms of the quadrupole Hamiltonian is probably not a negligible one; moreover, we have considered only the dipole-quadrupole interaction and neglected completely the coupling to other modes of motion. The present results indicate that these other effects are of the same order of magnitude as those due to the dipole-quadrupole interaction. We therefore conclude that the latter plays an appreciable part in the broadening of the giant dipole line in spherical nuclei, although it is clearly insufficient to explain the whole width of the line.

The author wishes to express his gratitude for the hospitality extended to him at the Institute for Theoretical Physics, University of Copenhagen. He is deeply indebted to Professor BEN MOTTELSON for suggesting this problem as well as for many stimulating discussions and invaluable suggestions. Special thanks are due Professor ÅGE BOHR for his interest in this work and for many fruitful conversations, as well as Dr. J. H. GUNN for diagonalizing the matrices. It is a pleasure to acknowledge discussions with many members of the Institute, in particular with Dr. K. T. HECHT on the classification of the states of surface vibrations and with Dr. D. BRINK on the classical limit.

The award of a CIBA Fellowship is gratefully acknowledged.

TABLE 3.

Nucleus	Adjacent nuclei	$\hbar\omega_2$ (MeV)	C_2 (MeV)	Ref.	$\hbar\omega_1$ (MeV)	Γ (MeV)	Ref.	2Δ (MeV)
$_{23}V^{51}$	$_{24}Cr^{52}$	1.43	79	23	19.0[2]	7.5[1]	17	3.7
$_{25}Mn^{55}$	$_{24}Cr^{54}$, $_{26}Fe^{56}$	0.85	58	24	18.2[2]	6 [1]	18	3.2
$_{27}Co^{59}$	$_{26}Fe^{58}$, $_{28}Ni^{60}$	1.07	50	24	17.9[2]	7 [1]	17	3.8
$_{29}Cu^{63}$	$_{28}Ni^{62}$	1.17	79	25	16.3	8.5	19	2.9
$_{29}Cu^{65}$	$_{28}Ni^{64}$	1.34	122	25	17.0	8.1[3]	19	2.6
$_{33}As^{75}$	$_{32}Ge^{74}$, $_{34}Se^{76}$	0.58	15.5	5	17.3	9.0	20	4.7
$_{38}Sr^{87}$	$_{38}Sr^{88}$	1.85	258	7	15.8	5.3	13	2.0
$_{39}Y^{89}$	$_{38}Sr^{88}$	1.85	258	7	16.3	3.8	13	2.1
$_{40}Zr^{91}$	$_{40}Zr^{92}$	0.92	151	7	16.5	5.0	13	1.9
$_{41}Nb^{93}$	$_{40}Zr^{92}$	0.92	151	7	17.0	6.8	20	1.9
	$_{42}Mo^{94}$	0.874	72	9				2.7
	$_{40}Zr^{92}$, $_{42}Mo^{94}$	0.90	112	7, 9				2.2
$_{45}Rh^{103}$	$_{44}Ru^{102}$, $_{46}Pd^{104}$	0.515	24	9	16.4[2]	6 [1]	21	3.4
$_{47}Ag^{107}$	$_{46}Pd^{106}$	0.513	25	9	16.0	6 [1]	21	3.2
$_{49}In^{115}$	$_{48}Cd^{114}$	0.555	36	9	15.4[2]	5.5[1]	21	2.7
	$_{50}Sn^{116}$	1.268	260	9				1.6
	$_{48}Cd^{114}$, $_{50}Sn^{116}$	0.912	148	9				1.8
$_{53}I^{127}$	$_{52}Te^{126}$	0.673	64	9	15.5	4.9[1]	11	2.3
$_{57}La^{139}$	$_{56}Ba^{138}$, $_{58}Ce^{140}$	1.513	346	26, 27	15.5	5.2[1]	15	1.5
$_{58}Ce^{141}$	$_{58}Ce^{140}$	1.596	379	27	16.0	4.5[1]	15	1.6
	$_{58}Ce^{142}$	0.630	78	27				2.1
	$_{58}Ce^{140}$, ^{142}	1.113	229	27				1.6
$_{59}Pr^{141}$	$_{58}Ce^{140}$, $_{60}Nd^{142}$	1.583	372	27	15.0	3.0[1]	22	1.5
$_{79}Au^{197}$	$_{78}Pt^{196}$, $_{80}Hg^{198}$	0.385	69	28, 29	14.2	4.7[1]	11	1.5
$_{81}Tl$	$_{80}Hg^{202}$, ^{204}	0.433	330	29	14.6	4.6[1]	11	0.8
	$_{82}Pb^{204}$, ^{206}	0.832	1337	30				0.6
	$_{80}Hg^{202}$, ^{204} and $_{82}Pb^{204}$, ^{206}	0.633	834	29, 30				0.6
$_{82}Pb^{207}$		–	–		13.8	3.5[1]	31	~ 0
$_{83}Bi^{209}$		–	–		13.8	3.5[1]	31	~ 0

[1] Corrected for neutron multiplicity.

[2] Nucleus for which a splitting of the giant dipole line was observed. The two peaks at E_a and E_b have an integrated cross section σ_a and σ_b, respectively. We take $\hbar\omega_1 = \dfrac{\sigma_a E_a + \sigma_b E_b}{\sigma_a + \sigma_b}$.

[3] Total formation cross section, including $\sigma(\gamma, p)$.

Institute for Theoretical Physics
University of Copenhagen.

Appendix

RAKAVY [3] indicated an elementary method to determine the representations l_2 of R_3 contained in a representation $(v,0)$ of R_5. He showed that $d_v(l_2)$, the number of times l_2 that appears in $(v,0)$, is given by the simple formula

$$d_v(l_2) = b_v(l_2) - b_{v-2}(l_2) - [b_v(l_2+1) - b_{v-2}(l_2+1), \tag{A1}$$

where $b_N(M)$ is the number of ways in which N quadrupole phonons may have a projection M on the z-axis. For more than a few phonons, however, the evaluation of the quantities $b_N(M)$ becomes extremely tedious if one undertakes to determine explicitly all the possible ways of projecting N phonons on the z-axis, and we should like to indicate a graphical method which permits to obtain $b_N(M) - b_{N-2}(M)$ very rapidly.

If n_μ phonons have a projection μ on the z-axis, we have

$$N = N_2 + N_1 + N_0 \tag{A2}$$

$$M = 2\nu_2 + \nu_1, \tag{A3}$$

where

$$N_\mu = n_\mu + n_{-\mu}$$

and

$$\nu_\mu = n_\mu - n_{-\mu}.$$

From (A2) it is obvious that

$$0 \leqslant N_2 \leqslant N \tag{A4}$$

and

$$0 \leqslant N_1 \leqslant N - N_2. \tag{A5}$$

For a given value of N_μ, ν_μ can be equal to $N_\mu, N_\mu - 2, N_\mu - 4, \ldots\ldots - N_\mu$. One can then write down the array shown in table A1. It indicates all the possible ways of forming the pair (ν_1,ν_2) with N phonons and, with the help of (A3), may be used to evaluate the quantities $b_N(M)$. If one is

TABLE A1.

N_2	Possible values of ν_2	N_1	Possible values of ν_1
N	$N, N-2, N-4 \ldots\ldots\ldots\ldots -N$	0	0
$N-1$	$N-1, N-3 \ldots\ldots\ldots -N+1$	1	1 −1
		0	0
$N-2$	$N-2, N-4 \ldots\ldots\ldots -N+2$	2	2 0 −2
		1	1 −1
		0	0
.....	.....	.....	.....
0	0	N	$N, N-2, N-4 \ldots\ldots\ldots\ldots -N$
		$N-1$	$N-1, N-3, N-5 \ldots\ldots -N+1$
		$N-2$	$N-2, N-4 \ldots\ldots\ldots -N+2$
		.....	.....
		1	1 −1
		0	0

TABLE A2.

N_2	Possible values of ν_2	N_1	Possible values of ν_1
N	$N \quad , -N$	0	0
$N-1$	$N-1, -N+1$	1	1 −1
		0	0
$N-2$	$N-2, -N+2$	2	2 0 −2
		1	1 −1
		0	0
.....	.....	.....	.....
0	0	N	$N, N-2, N-4 \ldots\ldots\ldots\ldots -N$
		$N-1$	$N-1, N-3, N-5 \ldots\ldots -N+1$
		$N-2$	$N-2, N-4 \ldots\ldots\ldots -N+2$
		.....	.....
		1	1 −1
		0	0

interested in the differences $b_N(M) - b_{N-2}(M)$ only, it is possible to introduce a considerable simplification by constructing a similar array for $N-2$ phonons and "subtracting" it from that corresponding to N phonons, with the result presented in table A2. The simple symmetry properties of this array suggest to construct a tableau in the $\nu_1 - \nu_2$ plane such that at each point corresponding to the pair of integers (ν_1, ν_2) we write down the num-

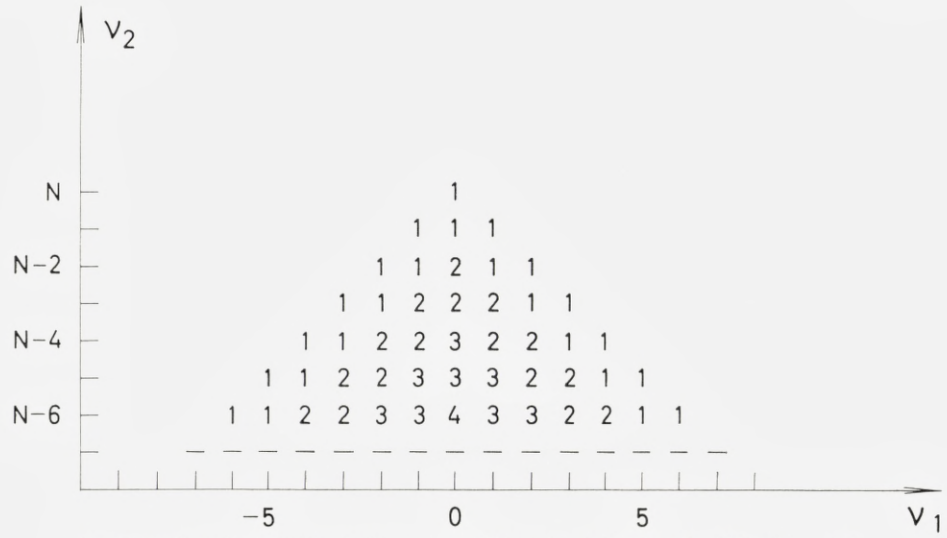

Fig. A1. Structure of the tableau permitting to determine $b_N(M) - b_{N-2}(M)$.

ber of times this pair occurs in table A2. It is immediately obvious from the latter that the tableau will have the structure shown in fig. A1 and possess reflectional symmetry with respect to the v_1 axis. If we then draw the straight line $M = 2v_2 + v_1$, and add up all the numbers of the tableau that fall on it, we obtain the quantity $b_N(M) - b_{N-2}(M)$. Once we know how to build the tableau, we can write it down immediately for any value of N. An example is given in fig. A2 for $N = 8$.

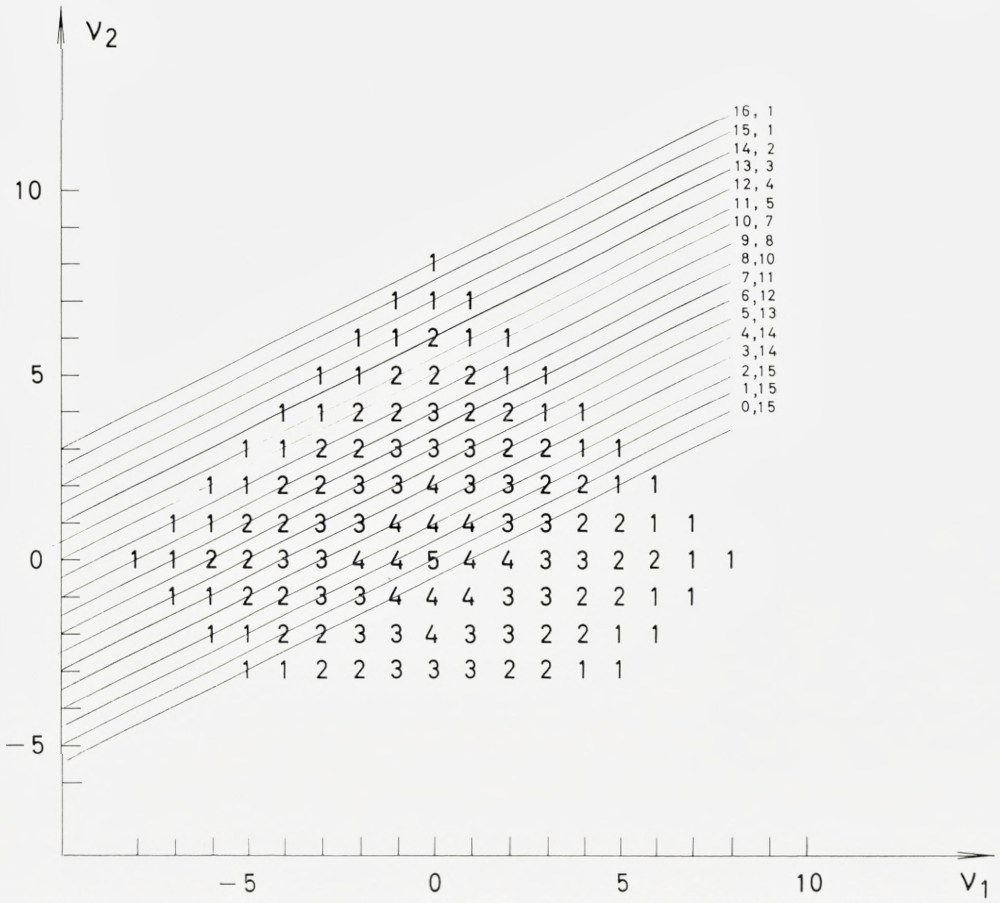

Fig. A2. The two numbers at the end of each line are M and $b_N(M) - b_{N-2}(M)$, respectively.

References

1) A. Bohr, Mat. Fys. Medd. Dan. Vid. Selsk. **26** (1952) no. 14.
2) H. C. Longuet-Higgins, U. Öpik, M. H. L. Pryce and R. A. Sack, Proc. Roy. Soc. **A 244** (1958) 1.
3) G. Rakavy, Nucl. Phys. **4** (1957) 289.
4) A. Bohr and B. Mottelson, Lectures on Nuclear Structure and Energy Spectra (Institute for Theoretical Physics and NORDITA, Copenhagen, 1962; to be published).
5) P. H. Stelson and F. K. McGowan, Nuclear Physics **32** (1962) 652.
6) S. Ofer and A. Schwarzschild, Phys. Rev. Letters **3** (1959) 384.
7) D. G. Alkhazov, A. P. Grinberg, K. I. Erokhina and I. Kh. Lemberg, Izvest. Akad. Nauk SSSR, Ser. Fiz. **23** (1959) 223.
8) O. F. Afonin, Yu. P. Gangrskiĭ, I. Kh. Lemberg, V. A. Nabichvrishvili and Yu. I. Udralov, JETP (U.S.S.R.) **43** (1962) 1995; JETP (translation) **16** (1963) 1406.
9) P. H. Stelson and F. K. McGowan, Phys. Rev. **110** (1958) 489.
10) D. G. Alkhazov, D. S. Andreev, K. I. Erokhina and I. Kh. Lemberg, JETP (U.S.S.R.) **33** (1957) 1347; JETP (translation) **6** (1958) 1036.
11) B. I. Gavrilov and L. E. Lazareva, JETP (U.S.S.R.) **30** (1956) 855; JETP (translation) **3** (1957) 871.
12) F. Ferrero, S. Ferroni, R. Malvano, S. Menardi and E. Silva, Nuclear Physics **15** (1960) 436.
13) P. F. Yergin and B. P. Fabricand, Phys. Rev. **104** (1956) 1334.
14) N. Mutsuro, Y. Ohnuki, K. Sato and M. Kimura, Jour. Phys. Soc. Jap. **14** (1959) 1649.
15) E. G. Fuller, B. Petree and M. S. Weiss, Phys. Rev. **112** (1958) 554.
16) Kuo Ch'i Ti, B. S. Ratner and B. V. Sergeev, JETP (U.S.S.R.) **40** (1961) 85; JETP (translation) **13** (1961) 60.
17) S. C. Fultz, R. L. Bramblett, J. T. Caldwell, N. E. Hansen and C. P. Jupiter, Phys. Rev. **128** (1962) 2345.
18) P. A. Flournoy, R. S. Tickle and W. D. Witehead, Phys. Rev. **120** (1960) 1424.
19) S. C. Fultz, R. L. Bramblett, J. T. Caldwell and R. R. Harvey, Phys. Rev. **133** (1964) B 1149.
20) R. Nathans and J. Halpern, Phys. Rev. **93** (1954) 437.
21) O. V. Bogdankevich, B. I. Goryachev and V. A. Zapevalov, JETP (U.S.S.R.) **42** (1962) 1502; JETP (translation) **15** (1962) 1044.

22) F. Ferrero, R. Malvano, E. Silva, J. Goldemberg and G. Moscati, Nuclear Physics **10** (1959) 423.
23) B. M. Adams, D. Eccleshall and M. J. L. Yates, Proceedings of the Second Conference on Reactions Between Complex Nuclei (John Wiley & Sons, New York, 1960) p. 95.
24) I. Kh. Lemberg, Proceedings of the Second Conference on Reactions Between Complex Nuclei (John Wiley & Sons, New York, 1960) p. 112.
25) G. Bruge, J. C. Faivre, M. Barloutaud, H. Faraggi and J. Saudinos, Physics Letters **7** (1963) 203.
26) L. A. Sliv, ГАММА ЛУЧИ, p. 180.
27) O. Nathan and V. I. Popov, Nuclear Physics **21** (1960) 631.
28) F. K. McGowan and P. H. Stelson, Phys. Rev. **122** (1961) 1274.
29) R. Barloutaud, T. Grjebine and M. Riou, Physica **22** (1956) 1129.
30) O. Nathan, Nuclear Physics **30** (1962) 332.
31) E. C. Fuller and E. Hayward, Nuclear Reactions II, edited by P. M. Endt and P. B. Smith (North-Holland Publishing Company, Amsterdam 1962) p. 113.

Indleveret til Selskabet den 21. september 1964.
Færdig fra trykkeriet den 23. februar 1965.

Matematisk-fysiske Meddelelser
udgivet af
Det Kongelige Danske Videnskabernes Selskab
Bind **34,** nr. 12

Mat. Fys. Medd. Dan. Vid. Selsk. **34,** no. 12 (1965)

HYDROTHERMAL ALTERATION ALONG THIN VEINLETS IN THE RØNNE GRANODIORITE

BY

AAGE JENSEN

København 1965
Kommissionær: Ejnar Munksgaard

Synopsis

The Rønne granodiorite constitutes the south-western part of the Precambrian of Bornholm. In places Rønne granodiorite is cut by thin and straight veinlets, which are about 1 mm wide, dark green in colour, and composed of epidote, chlorite, and sphene. The veinlets are bordered by a 1–2 cm wide zone of alteration, in which the normal dark grey colour of the Rønne granodiorite is changed to red. This change in colour is due to numerous minute grains of hematite or limonite finely dispersed through the feldspars. The iron necessary probably originated partly from alteration of some of the ilmenite content of the Rønne granodiorite to sphene, and partly from a change in the chemical composition of the primary biotite of the Rønne granodiorite. The zones of alteration also differ from unaltered Rønne granodiorite in having 2 % epidote in rather large grains, and in showing increased sericitization of feldspars, especially the potassium feldspar. The veinlets and the corresponding zones of alteration were probably formed by hydrothermal solutions.

PRINTED IN DENMARK
BIANCO LUNOS BOGTRYKKERI A/S

Introduction and field setting

The Rønne granodiorite is the darkest coloured and least silicic of the Precambrian granitic rocks of the island of Bornholm, which lies in the Baltic Sea and constitutes the south-eastern part of Denmark. Rønne granodiorite occupies the south-western part of the Precambrian of Bornholm. (Fig. 1).

The Precambrian of Bornhom has been thoroughly described by K. Callisen (1934) and more recently by H. I. Micheelsen (1961), but neither of these authors describes alterations along veinlets in Rønne granodiorite. These alterations however have been known for some time. Professor A. Rosenkrantz of the University of Copenhagen has collected some hand specimens clearly showing the alterations from quarried blocks in the quarry at Klippegård, but he has not seen these alterations in place in the granodiorite. In 1963 Professor H. Sørensen of the University of Copenhagen drew the author's attention to these alterations and suggested that a study of the alterations would imply the use of reflected-light microscopy. Therefore when the author was in Bornholm in June 1963 he visited the quarry at Klippegård. He collected a number of specimens for further investigation of the alterations, but did not succeed in finding the alterations in place in the walls of the quarry. However H. I. Micheelsen (personal communication) has seen this kind of alteration along veinlets in place in the Rønne granodiorite in a quarry situated somewhat south of Klippegård. He recorded the strike of the veinlets as N 175° E and their dip as 80° W. Although the strike of the veinlets is relatively consistent, the veinlets are somewhat wavy and often branch. The branches however soon take up the same direction as the veinlets from which they originated.

Macroscopic description of hand specimens

The Rønne granodiorite is a medium-grained rock with a dark grey colour. Except for a few centimetres nearest to the surface, where the rock is weathered and has attained a brownish-red colour, the Rønne granodiorite generally has a very fresh appearance.

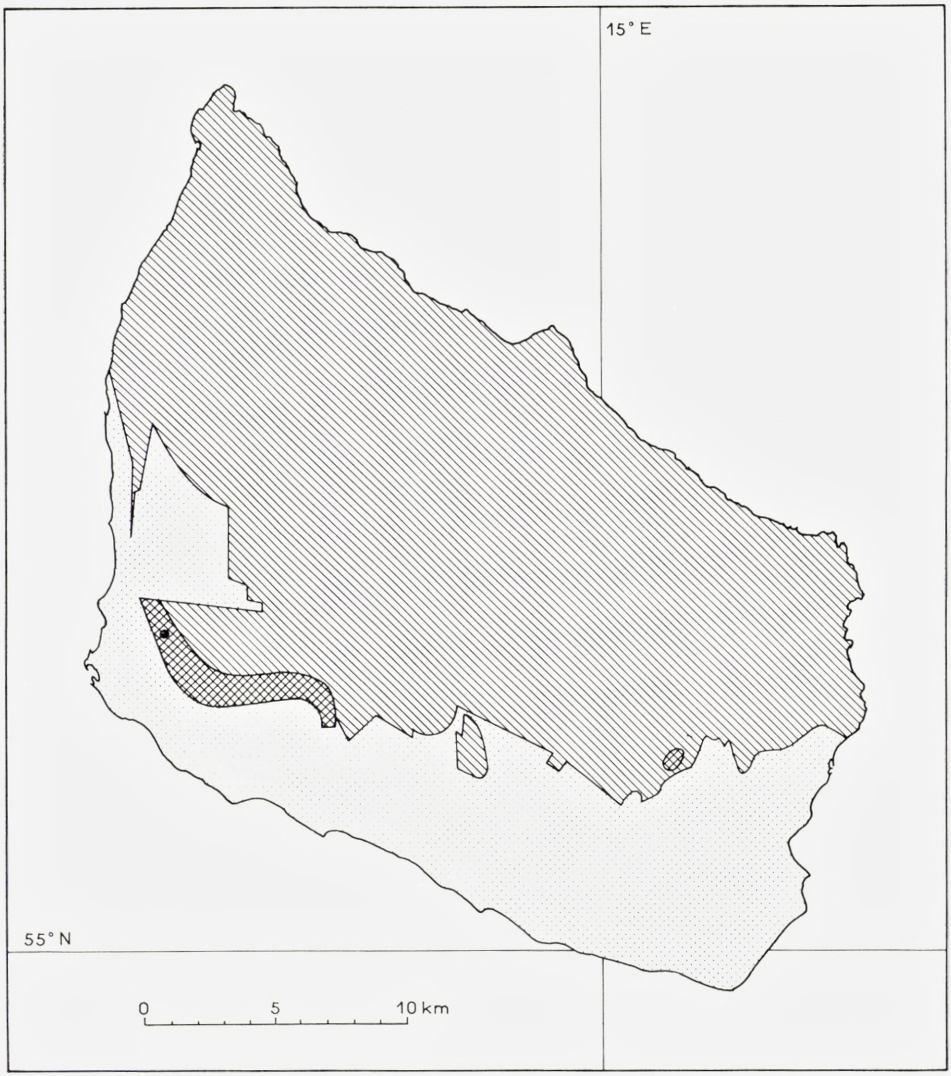

Fig. 1. Sketch map of Bornholm.

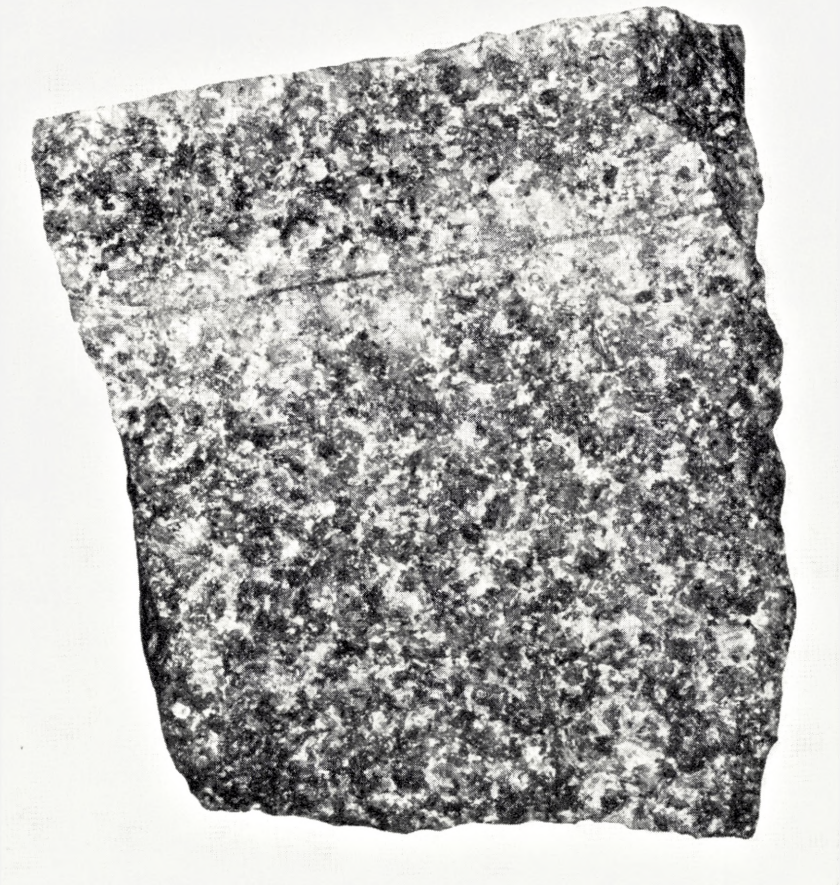

Fig. 2. Hand specimen showing the alteration. In the upper half of the figure can be seen a veinlet with adjacent zone of alteration. The upper surface of the specimen is broken along a veinlet, and part of the adjacent zone of alteration is therefore seen on top of the specimen. Natural size. C. HALKIER phot.

The veinlets along which the Rønne granodiorite is altered have a very straight course in hand specimens. The width of these veinlets is constant and very close to 1 mm. Their colour is dark green. The veinlets are bordered by a zone of alteration in which the normal dark grey colour of the Rønne granodiorite is changed to red, and these altered zones have a certain superficial resemblance to pegmatites which are also found in the granitic rocks of Bornholm. The resemblance however is only due to similarity in colour

between the zones of alteration and these pegmatites. There is no change in grain size between unaltered Rønne granodiorite and the altered zones. Closer study reveals that the change in colour has affected only the feldspar content of the rock, while quartz and the mafic minerals are unchanged in colour.

The width of the altered zones varies from about 1 cm to about 2 cm. The width is however not constant for any one veinlet, there being a considerable pinch and swell. The borders of the altered zones are not sharp but diffuse, and the zone of alteration grades imperceptibly into unaltered Rønne granodiorite. (Fig 2).

In the hand specimens the distance between two adjacent veinlets may be as little as $2^1/_2$ cm so that the corresponding zones of alteration are separated by only $^1/_2$ to 1 cm of unaltered rock.

Microscopic description of thin- and polished sections

The mineralogical composition of the Rønne granodiorite places the rock near the border between granite and granodiorite, potassium feldspar and plagioclase being present in about equal amounts, but with the plagioclase, which is an oligoclase averaging 28 % An, just slightly predominating. The mode of Rønne granodiorite is shown in the table below.

The veinlets along which the Rønne granodiorite has been altered are filled with epidote, chlorite, and sphene. Epidote is the main component and constitutes about 75 % of the vein material. The epidote grains may reach a size of 0.4×0.2 mm, but are generally considerably smaller. Chlorite and sphene amount to about 20 % and 5 % respectively. Along part of their course the veinlets are sometimes bordered by a narrow zone of fine-grained quartz, the average diameter of the quartz grains being about 0.02 mm. (Plate 1, Fig. 1). This zone of fine-grained quartz is however absent along the margin of some of the veinlets.

The composition of the red-coloured zones of alteration adjacent to the veinlets has been determined by point counting. The results found are in good agreement with the composition of unaltered Rønne granodiorite found by Micheelsen (1961). Micheelsen's values for unaltered Rønne granodiorite and the values for the zones of alteration determined by the author are given in the table below:

	Rønne granodiorite	Zones of alteration
Potassium feldspar	29 %	29½ %
Plagioclase	30 %	30 %
Quartz	21 %	21½ %
Hornblende	10 %	8½ %
Biotite	5 %	4½ %
Ore minerals	3 %	2 %
Sphene	1 %	1 %
Apatite	1 %	1 %
Epidote	0 %	2 %
	100 %	100 %

The most striking difference is the appearance of 2 % epidote in the altered zones. Epidote is a mineral which is generally lacking in unaltered Rønne granodiorite, although a few small grains may occasionally be found in the cores of sericitized plagioclase. Very minute crystals identified by the author as epidote can also be found as inclusions in quartz and more rarely in feldspars (see p. 9). Larger grains of epidote are never found in unaltered Rønne granodiorite, but in the zones of alteration may attain sizes exceeding 0.1×0.05 mm. In the zones of alteration epidote is found in both plagioclase and potassium feldspar, as well as in hornblende and along the grain boundaries of all the minerals present in the rock. However epidote is somewhat more abundant in plagioclases.

The differences in amounts of the minerals present in both unaltered and altered Rønne granodiorite are not in excess of what must be expected from two different samples of even the most homogeneous of rocks.

Although there is no significant difference in the amount of biotite between unaltered and altered rock, there is a difference in the appearance of the mineral. In unaltered Rønne granodiorite the biotite shows pleochroism from yellowish-brown to brownish-black and almost opaque. In the altered zones the biotite has changed to yellow in the lightest position and dark green and more translucent in the direction parallel to the cleavage traces. This indicates that the iron content of the biotite has decreased.

Sericitization of feldspars is generally only incipient in the altered zones, although the feldspars always have a somewhat cloudy appearance, and more pronounced sericitization may be found, especially in the cores of

plagioclases. With respect to the plagioclase there is no great difference from unaltered Rønne granodiorite, where rather strong sericitization can also be found in the cores of plagioclases. The potassium feldspar however is clearly more affected by sericitization in the altered zones than is the case in unaltered Rønne granodiorite, where the potassium feldspar is generally completely fresh.

The most abundant of the ore minerals in Rønne granodiorite is ilmenite. The appearance of the ilmenite, greyish-brown colour, strong anisotropy, reflection pleochroism, and the lack of internal reflections, indicates that the composition is rather close to pure $FeTiO_3$. In unaltered Rønne granodiorite some ilmenite grains are surrounded by a thin rim of sphene, and occasionally a somewhat more advanced alteration of ilmenite to sphene is seen. The majority of the ilmenite grains in unaltered Rønne granodiorite however do not show a relationship with sphene.

Compared with the unaltered Rønne granodiorite the altered zones have a more pronounced alteration of ilmenite to sphene. Most of the ilmenite grains have at least a partial rim of sphene, and often the ilmenite grains show more advanced alteration to sphene. Immediately adjacent to the veinlets ilmenite grains are seen to be almost completely altered to sphene, so that only small ilmenite islands are left as replacement remnants in the sphene. (Plate 1, Fig. 2).

Although the stronger alteration of ilmenite to sphene in the altered zones might at first suggest correlation with the change in ore content from 3 % in unaltered Rønne granodiorite to 2 % in the zones of alteration, the difference in ore content in the countings is believed to be casual and not to reflect the increase in alteration of ilmenite. This view is strengthened by the fact that the decrease in ore content is not balanced by a corresponding increase in the sphene content.

None of the differences between unaltered and altered Rønne granodiorite so far described could account for the macroscopic change in colour from dark grey to red. In the search for a reason for this change in colour notice was paid to some long and very thin needles rather frequently found in quartz. The needles are arranged in three directions, often making angles of about 60° with each other. The length of the needles may exceed 75 μ while their width is less than 1 μ. Partly because of the extremely small width, and partly because the needles in polished sections have always been found in positions making angles with the polished surface, it is not possible to give an adequate description of the needles. They appear dark in thin sections and are luminous white in polished sections. These needles

are believed to be rutile. Such rutile-like needles are found both in unaltered and altered Rønne granodiorite and they do not seem to influence the colour of the quartz, as the quartz in Rønne granodiorite, altered or unaltered, is completely colourless. Rutile-like needles are shown in Fig. 1 of Plate 2.

Careful inspection reveals that rutile-like needles are not only found in quartz but occasionally also in potassium feldspar. This applies to both altered and unaltered rock. In potassium feldspar however, the needles are not so numerous as they are in quartz. They are more irregularly distributed and not confined to three directions.

Rutile-like needles are not the only inclusions found in quartz. Some well-developed but very minute crystals, the size of which is about $1 \times 2^1/_2\ \mu$, are also frequently visible. These minute crystals however are generally arranged in pearl-like stringers, often with en echelon pattern. The length of the stringers is of the same order of magnitude as the needles, and like the needles the stringers are also arranged in three directions, often making angles of about 60° with each other. In transmitted light these minute crystals show a high relief and are almost colourless but with a yellowish or greenish tint. In addition to these minute grains there are also grains somewhat larger than $1 \times 2^1/_2\ \mu$ found as inclusions in the quartz. These larger grains are more heavily coloured in brownish or greenish tints and are identified as epidote. The author considers that the minute grains are also epidote, but the extremely small grain size does not permit precise identification. The very minute and the slightly larger grains are present as inclusions in the quartz of both altered and unaltered Rønne granodiorite. The much larger epidote grains with a size of 0.1×0.05 mm referred to on page 7 are present only in the altered zones.

The well-developed crystal form of the minute epidote grains is especially pronounced in polished sections, because the relations here are not blurred by the third dimension. These epidote stringers are very beautiful in polished sections because they are accompanied by strong Newtonian colour phenomena. (Plate 2, Fig. 2).

The minute crystals of epidote occur in both altered and unaltered Rønne granodiorite, and are present not only in quartz, but also in feldspars, potassium feldspar as well as plagioclase. In feldspars however the arrangement in pearl-like stringers is generally lacking and is never so pronounced as in quartz.

These inclusions have been observed already by Callisen (1934). On p. 25 under the description of quartz in Rønne granodiorite she states: "Häufig findet man kleine, feste, braunviolette oder dunkelbraune Körper

mit guter Kristallbegrenzung, welche — nach dem meistens hexagonalen Querschnitt, der hohen Lichtbrechung und dem Fehlen des Pleochroismus zu urteilen — aus Titaneisen bestehen. Im Basisschnitt erscheinen sie als zierliche Perlenreihen, die sich unter einem Winkel von 60° schneiden." And p. 26 under the description of potassium feldspar in the Rønne granodiorite Callisen says: "Kleine Blätter aus Titaneisen und dünne dunkle Nadeln, die nicht genauer bestimmt werden können, kommen ziemlich oft vor, wenn auch bei weitem nicht so zahlreich wie im Quarz."

The difference in the colour descriptions is easily explained as a result of the progress in manufacturing of polarizing microscopes since 1934. It is however difficult to understand why Callisen called these grains ilmenite when it was possible in transmitted light to observe the absence of pleochroism and the high refractive index of the grains. While the present writer's opinion that these minute grains are epidote might be open to some discussion because of the extremely small grain size, there is no doubt that the grains are translucent and not opaque.

Small opaque grains of Fe-Ti-oxides can be found in the hornblende and the biotite of both altered and unaltered Rønne granodiorite, but in unaltered Rønne granodiorite the quartz and feldspars generally are without opaque inclusions except for the rutile-like needles. Occasionally however, especially along fine cracks cutting through quartz or feldspar grains, some red internal reflections indicate the presence of minute grains of hematite or limonite.

In strong contrast to this general absence of opaque inclusions in the quartz and feldspars of unaltered Rønne granodiorite, most of the low-reflecting, translucent mineral grains in the altered zones are in reflected light seen to be peppered with small white spots. These spots are about 1 μ in diameter, and are surrounded by a halo of red internal reflections. It is considered that these small grains are composed of hematite or limonite. Because of the extremely small grain size it is impossible to distinguish between hematite and limonite. It is obvious however that the reason for the red colour of the feldspar in the altered zones lies in the presence of these small grains.

Several attempts have been made to prepare polished thin sections of the material, but all were unsuccessful as the sections became perforated by numerous holes before polishing was attained. Unfortunately therefore it is not possible to state anything about the distribution of these inclusions between plagioclase, potassium feldspar, and quartz. However as not all of the low-reflecting, translucent grains carry these inclusions surrounded

by red internal reflections, and as the quartz macroscopically is completely colourless it is believed that the inclusions do occur only in the feldspars.

Conclusions

It is considered that hydrothermal solutions advancing along steep joints in the Rønne granodiorite have transformed the joints to veinlets about 1 mm wide filled with epidote, chlorite, and sphene, and caused the formation of a 1–2 cm wide zone of alteration along these veinlets.

In the zones of alteration a relatively large amount of epidote has been introduced. This epidote occurs in rather large grains in contrast to the minute crystals of epidote already present in unaltered Rønne granodiorite. The hydrothermal solutions have also caused a certain increase in sericitization of feldspars, especially the potassium feldspar, and have changed the colour of biotite in such a manner as to indicate that iron has been released from the biotite.

The solutions have also resulted in a much stronger alteration of ilmenite to sphene than is usually found in unaltered Rønne granodiorite. The Ti and Fe released by this alteration, and the Fe released from the alteration of biotite, might to some extent have migrated towards the veinlets, but probably most of the Fe was caught on the way through the feldspars, resulting in the formation of minute inclusions of hematite or limonite, which cause the red colour of the zones of alteration.

Acknowledgements

Thanks are due to Professor A. Noe-Nygaard, Director of the Geological Institute of the University of Copenhagen, and to Professor H. Sørensen for their interest in the present work. The sketch map Fig. 1 was prepared by Mrs. R. Larsen, and the photographical work was done by Mr. C. Halkier. Mr. G. Henderson, B. Sc. kindly corrected the English manuscript.

References

Callisen, K. (1934): Das Grundgebirge von Bornholm. Danmarks Geol. Undersøgelse. II række, nr. 50. 266 pp.

Micheelsen, H. I. (1961): Bornholms grundfjæld — The Pre-Cambrian of Bornholm, Denmark. Medd. Dansk Geol. Forening. Vol. 14, Part 4. pp. 308–349.

Indleveret til Selskabet den 12. august 1964.
Færdig fra trykkeriet den 30. januar 1965.

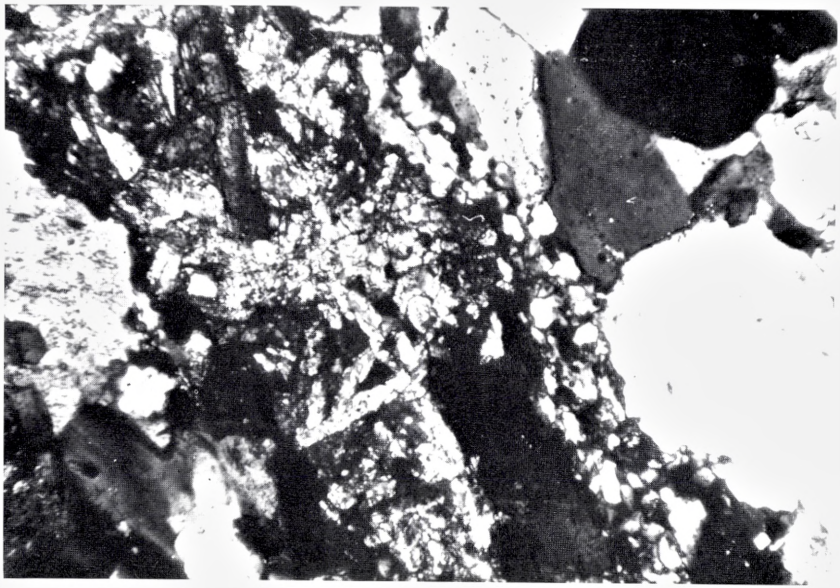

Fig. 1. Transmitted light, crossed polars. ×150.
NW–SE across the picture can be seen an epidote-, chlorite-, and sphene-filled veinlet. Towards NE the veinlet is bordered by a narrow zone of fine-grained quartz.

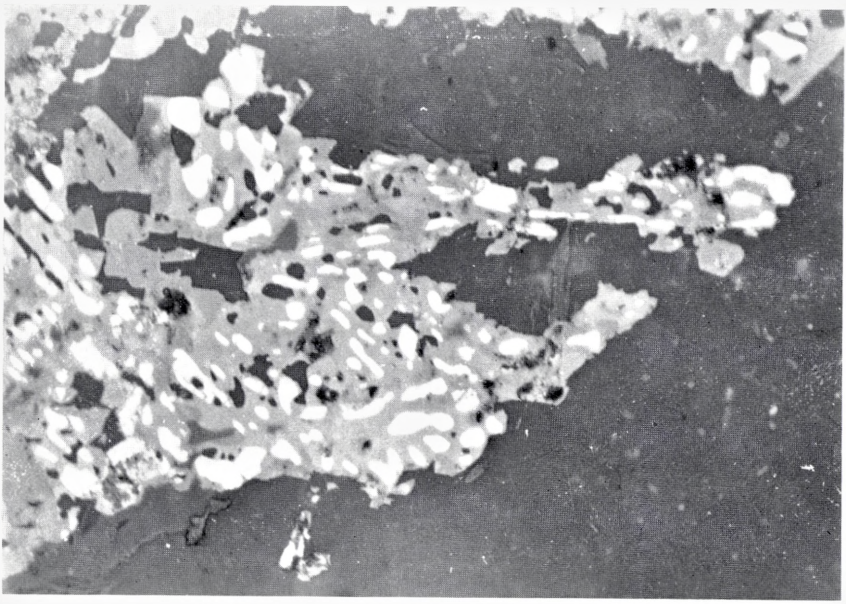

Fig. 2. Reflected light, polariser only. ×220.
Former grain of ilmenite adjacent to veinlet. The ilmenite is strongly altered to sphene, so that only small ilmenite islands are left as replacement remnants in the sphene.

Fig. 1. Reflected light, polariser only. ×800. Oil immersion.
Rutile-like needles arranged in three directions in quartz.

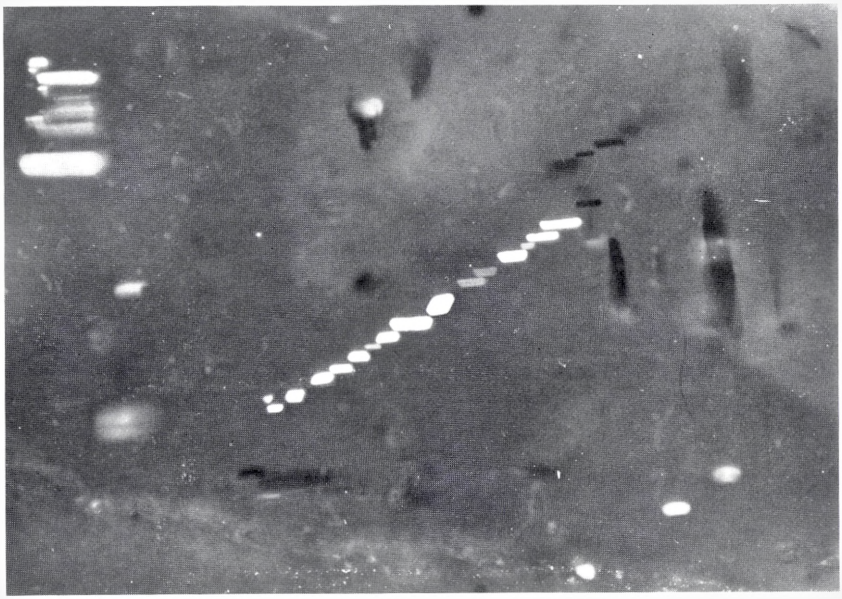

Fig. 2. Reflected light, polariser only. ×800. Oil immersion.
Pearl-like stringer of minute epidote crystals arranged en echelon in quartz.

Matematisk-fysiske Meddelelser
udgivet af
Det Kongelige Danske Videnskabernes Selskab
Bind **34,** nr. 13

Mat. Fys. Medd. Dan. Vid. Selsk. **34,** no. 13 (1965)

ENERGY LEVELS OF ORTHOAXIAL CHROMOPHORES AND THE INTERRELATION BETWEEN CUBIC PARENT CONFIGURATIONS

BY

CLAUS ERIK SCHÄFFER

AND

CHR. KLIXBÜLL JØRGENSEN

København 1965
Kommissionær: Ejnar Munksgaard

Synopsis

The Angular Overlap Model, i.e. an LCAO MO approximation equivalent to a contact term perturbation model, is applied to orthoaxial octahedral chromophores. These may contain six different ligands but always in such a way that the three Cartesian axes can be directed through the ligands. The Angular Overlap Model gives the energies of the central ion orbitals in terms of radial parameters essentially describing the σ and π anti-bonding (bonding) effects. The results are formally equivalent with those of an electrostatic model for which no restrictions have been posed on the choice of the radial parameters. For example, it is found that the contribution from two ligands which are *trans* to each other always can be expressed as a sum contribution from each of them. The concept of holohedrized symmetry is introduced.

The general expression for the orbital energy of a d-electron in these systems has been given together with its characterization as a sum of a low symmetry contribution, which has always D_{2h} symmetry or higher, and a cubic average contribution. All non-diagonal elements connecting cubic parentage orbitals, e_g and t_{2g}, vanish in orthoaxial chromophores.

The energies of the first two spin-allowed transitions in d^3 and low-spin d^6 systems have been given within the approximation of pure cubic sub-configurations. The energy levels of maximum spin-multiplicity originating in all possible cubic d^q sub-configurations have been divided into four classes within each of which the energies are interrelated in a simple way. By application of some simple operators, $\mathfrak{P}$ [Pauli] and $\mathfrak{V}$ [van Vleck], it is possible from a function, corresponding to an energy level, of each class to generate all the others of that class.

PRINTED IN DENMARK
BIANCO LUNOS BOGTRYKKERI A/S

1. Introduction

In some recent papers [1–5] a model was developed to calculate, on a semiempirical basis, the orbital energies in chromophores containing partially filled electronic shells. This model, called the *Angular Overlap Model* [5], attempts to account for the covalency between the central ion and the ligands using an approximated LCAO MO approach. We have assumed, as have MULLIKEN [6] and WOLFSBERG and HELMHOLZ [7, and ref. [8] p. 93], that the antibonding contribution to the energy of a given central ion orbital is proportional to the square of its group overlap integral with the ligands*. It has further been assumed that the central ion orbitals are separable into angular and radial parts, the latter being equal for all l-orbitals of an l^q configuration, the former, of course, being hydrogenic. The ligands are assumed not to overlap with each other.

On the basis of these assumptions it was shown [1, 5] that the Angular Overlap Model is mathematically equivalent with a contact term perturbation model if the matrix elements in the case of $\lambda > 0$ (e.g. for π and δ overlaps) are evaluated for certain functions which are simple transformations of the central ion orbitals (ref. [5]).

This mathematical equivalence leads to an extension of the model to cover also chromophores in which the ligands are not equal.

The antibonding energy of a central ion orbital is expressed as a product of an angular and a radial part. This is taken as a semiempirical parameter that is calculated from the hydrogenic angular functions. The expression of the general matrix element is

$$\sum_{\lambda\omega} \sum_{j=1}^{N} e_{\lambda j} F_{\lambda\omega}[M,A_j] F_{\lambda\omega}[M',A_j] \tag{1}$$

where $e_{\lambda j}$ is the radial contribution from the ligand j associated with its $\sigma(\lambda = 0)$, $\pi(\lambda = 1)$ or $\delta(\lambda = 2)$ overlap with the central ion l-shell containing the orbitals M and M'. A_j is the ligand orbital whose overlap is considered and could be further specified by the indices $\lambda\omega$, where ω, for

* Or rather the sum of the squares of all its possible group overlap integrals [5] corresponding to a given λ, a different constant of proportionality applying to each λ.

$\lambda > 0$, specifies the particular λ-orbital within the π sets or δ sets. In the present paper we assume that the ligands are so constituted that the components of the π and δ sets are degenerate*. This is strictly true if for each ligand the central ion and ligand atoms are placed on a straight line e.g. CN, Cl, and probably a good approximation for a number of other ligands, e.g. NH_3.

The first summation in (1) covers the $(2l+1)$ combinations of $\lambda\omega$, the second the contribution from the N ligands in the chromophore. The $F_{\lambda\omega}$ terms are the angular overlap integrals which for each ligand form a unitary matrix [5], in which each row is characterized by an M central ion orbital and each column by an $A_j\lambda\omega$ ligand orbital.

Because of the unitariness of the F-matrices, the following sum rule is valid

$$\sum_{M,j} (F_{\lambda\omega}[M,A_j])^2 = N \tag{2}$$

where there is one equation for each $\lambda\omega$ set. This rule states that for a given central ion l shell containing the orbitals M and a given $\lambda\omega$ set of ligand orbitals the sum of the squares of the angular overlap integrals with all the ligands j is equal to the number of ligands N.

In the general case, the non-diagonal elements (1) will be non-vanishing. If, however, at the same time the central ion basis functions chosen (in our case the usual real (Cartesian) sets of l-orbitals) are proper symmetry functions of the molecular point group and are distributed over the different symmetry classes in such a way that no two orbitals belong to the same row of an irreducible representation, the non-diagonal elements will be zero. This case was treated in our last paper [5].

In the present paper we are concerned with the orbital energies of octahedral, quadratic and linear chromophores in which the ligands may all be different. Furthermore, the energy levels of the octahedral chromophores are studied and a comparison is made of the low symmetry splittings of some cubic configurations corresponding to a different number of electrons in the partially filled l-shell.

It is found that, as for the electrostatic model, the Angular Overlap Model provides accidental degeneracies. These can be given the physical interpretation that a particular orbital feels the effect of two ligands aligned with the central ion just as if the sum of these effects was coming from only one side of the central ion.

* In a forthcoming paper we shall be concerned with cases in which the same classification of ligand orbitals remains useful even though the degeneracies are lifted.

We introduce here the concept of *holohedrized symmetry* where any interaction occurring at (x,y,z) is divided into two halves, one half moved to $(-x,-y,-z)$ and the other remaining at (x,y,z).

It has often been said, qualitatively, that the electrostatic model which uses arbitrarily chosen radial parameters is so successful in explaining experimental results because the model is fundamentally based on the symmetry properties of the wavefunctions. The present paper provides a somewhat more quantitative justification of this statement by showing that a model, essentially on an MO basis, leads to the same results as the electrostatic model for which no restrictions have been posed on the choice of radial parameters.

2. Orthoaxial chromophores

In regularly octahedral chromophores the Cartesian d-orbitals are separated by symmetry into the class $e_g(O_h)$, consisting of d_{z^2}, $d_{x^2-y^2}$, which is able to form σ-bonds, and the class $t_{2g}(O_h)$, consisting of d_{xy}, d_{zx}, d_{yz}, which can form π-bonds. This classification remains valid if a Cartesian coordinate system with the origin at the central ion nucleus can be placed in such a way that the axes are directed* through the ligand nuclei.

We suggest that chromophores belonging to this class be called *orthoaxial.*

By application of the angular overlap matrix [5], or directly by inspection of the angular distribution of the Cartesian d-orbitals, it is seen that the angular overlap integral is the same along the positive and the negative directions of any of the Cartesian axes. This has the same consequence as in the electrostatic model [9], and it means that for each Cartesian axis it is the sum of the radial contributions of the ligands on that axis which is important in determining its antibonding (bonding) effect on the d-orbitals.

Because of this result, it is the holohedrized symmetry of an orthoaxial chromophore, which determines the energy levels to this approximation. The holohedrized symmetry may be higher than the actual symmetry and cannot be lower than D_{2h}.

* It is also correct for linear chromophores, with, say, the z-axis as the symmetry axis, in which case the σ and π-contributions from $d_{x^2-y^2}$ and d_{xy}, respectively, vanish. These orbitals are always δ-bonding [5] in orthoaxial chromophores, and only δ-bonding in the linear case.

For polyatomic, non-linear ligands [27] the π and δ orbitals are no longer degenerate and for such systems $e_g(O_h)$ and $t_{2g}(O_h)$ may mix.

3. Orbital energies

The sum of the radial λ-antibonding contributions from the q-axis has in this paper been denoted by $e_{\lambda q}(\lambda = \sigma, \pi, \delta;\ q = z, x, y)$. In terms of these radial parameters the non-vanishing matrix elements of the contact term potential V of the Angular Overlap Model [5] are the diagonal elements,

$$\left.\begin{aligned} < d_{z^2}|V|d_{z^2} > &= e_{\sigma z} + \frac{1}{4}(e_{\sigma x} + e_{\sigma y}) + \frac{3}{4}(e_{\delta x} + e_{\delta y}) \\ < d_{x^2-y^2}|V|d_{x^2-y^2} > &= \frac{3}{4}(e_{\sigma x} + e_{\sigma y}) + e_{\delta z} + \frac{1}{4}(e_{\delta x} + e_{\delta y}) \\ < d_{zx}|V|d_{zx} > &= e_{\pi z} + e_{\pi x} + e_{\delta y} \\ < d_{yz}|V|d_{yz} > &= e_{\pi y} + e_{\pi z} + e_{\delta x} \\ < d_{xy}|V|d_{xy} > &= e_{\pi x} + e_{\pi y} + e_{\delta z} \end{aligned}\right\} \quad (3)$$

and one non-diagonal element,

$$< d_{z^2}|V|d_{x^2-y^2} > = \frac{1}{4}\sqrt{3}[(e_{\sigma y} - e_{\delta y}) - (e_{\sigma x} - e_{\delta x})] = \frac{1}{4}\sqrt{3}[e'_{\sigma y} - e'_{\sigma x}] \quad (4)$$

all the other nine non-diagonal elements vanishing. Since it is always energy differences which can be observed [27] the substitution

$$e'_{\lambda q} = e_{\lambda q} - e_{\delta q} \quad (5)$$

has been introduced into eq. (4). Because of the peculiarity of the orthoaxial chromophores that no mixing occurs between those d-orbitals which are σ-antibonding, and those which are π-antibonding (bonding), it is possible to define a cubic average contribution to the orbital energy within each of these orbital sets. These cubic average energies E have been characterized by sub-indices referring to the symmetry notations e_g and t_{2g} of the point group O_h.

$$\left.\begin{aligned} E_{e_g} &= \frac{1}{2}[e_{\sigma z} + e_{\delta z} + e_{\sigma x} + e_{\delta x} + e_{\sigma y} + e_{\delta y}] \\ E_{t_{2g}} &= \frac{2}{3}[e_{\pi z} + e_{\pi x} + e_{\pi y}] + \frac{1}{3}[e_{\delta z} + e_{\delta x} + e_{\delta y}] \end{aligned}\right\} \quad (6)$$

For six-coordinated orthoaxial chromophores, these cubic averages are convenient zero points for the orbital energies which in terms of the reduced parameters of eq. (5) are expressed as:

$$
\left.\begin{array}{ll}
e_g & \left\{\begin{array}{lcl} E_{z^2} &=& \frac{1}{2}e'_{\sigma z} - \frac{1}{4}e'_{\sigma x} - \frac{1}{4}e'_{\sigma y} \\ E_{x^2-y^2} &=& -\frac{1}{2}e'_{\sigma z} + \frac{1}{4}e'_{\sigma x} + \frac{1}{4}e'_{\sigma y} \end{array}\right. \\
t_{2g} & \left\{\begin{array}{lcl} E_{zx} &=& \frac{1}{3}e'_{\pi z} + \frac{1}{3}e'_{\pi x} - \frac{2}{3}e'_{\pi y} \\ E_{yz} &=& \frac{1}{3}e'_{\pi z} - \frac{2}{3}e'_{\pi x} + \frac{1}{3}e'_{\pi y} \\ E_{xy} &=& -\frac{2}{3}e'_{\pi z} + \frac{1}{3}e'_{\pi x} + \frac{1}{3}e'_{\pi y} \end{array}\right.
\end{array}\right\} \quad (7)
$$

where the cubic parentage symmetries are stated to the left. There are two characteristic features of these energies of deviation from cubic symmetry. Firstly, the sum of the coefficients for each orbital is zero. Secondly, the energies of the orbitals which are t_{2g} orbitals in the regular octahedron are interrelated, as they should be, by a cyclic permutation of the labels z, x, y.

4. Comparison with the electrostatic model

The expression, eq. (7), for the energies of deviation from the cubic average do not formally disagree with the corresponding expressions of the electrostatic point charge or point dipole model. For the point-dipole model, for example, the relations are

$$
\left.\begin{array}{l}
e_{\sigma q} = \mu_q\left[B_o + \frac{2}{7}B_2 + \frac{6}{21}B_4\right] \\
e_{\pi q} = \mu_q\left[B_o + \frac{1}{7}B_2 - \frac{4}{21}B_4\right] \\
e_{\delta q} = \mu_q\left[B_o - \frac{2}{7}B_2 + \frac{1}{21}B_4\right]
\end{array}\right\} \quad (8)
$$

or, in the reduced form:

$$
\left.\begin{array}{l}
e'_{\sigma q} = \mu_q\left[\frac{4}{7}B_2 + \frac{5}{21}B_4\right] \\
e'_{\pi q} = \mu_q\left[\frac{3}{7}B_2 - \frac{5}{21}B_4\right]
\end{array}\right\} \quad (9)
$$

where q represents either z, x, or y. Here μ_q is the sum of the absolute values of the dipoles of the ligands situated on the q-axis.

μ_q multiplied by the radial integrals [10], B_0, B_2, and B_4, whose subindices refer to the degree of the term in the expansion into spherical harmonics, apart from certain constants make up the radial parameters of the electrostatic model.

It is perhaps worthwhile to express $\mu_q B_2$ and $\mu_q B_4$ in terms of our e'_q parameters. From (9) we obtain:

$$\left.\begin{aligned} \mu_q B_2 &= e'_{\sigma q} + e'_{\pi q} \\ \frac{5}{3}\mu_q B_4 &= 3\,e'_{\sigma q} - 4\,e'_{\pi q} = 2 \cdot \Delta_q \end{aligned}\right\} \quad (10)$$

where* we have introduced in the last expression the term, Δ_q, which is the orbital energy difference between e_g and t_{2g} orbitals in a cubic (or when holohedrized, cubic) chromophore whose sum-contributions to e'_σ and e'_π are the same from all three axes.

One of the reasons for the criticism of the electrostatic model has been the unreasonable values which had to be chosen for the radial parameters [11]. The expressions of the angular overlap model which are formally equivalent to those of the electrostatic model, because both models are based on the symmetry [27] of the *d*-orbitals and of the chromophores, contain radial parameters, whose physical interpretation is entirely different from that of the radial parameters of the electrostatic model. However, because of the expressions (9), an electrostatic contribution might be included in our radial parameters.

According to our description the total perturbation of the central ion orbitals contains a further contribution (eq. 7) in addition to the cubic average (eq. 6). We should mention here that in some cases it may be useful to have another cubic reference state. For example, in their treatment of tetragonal complexes, $\mu_x = \mu_y$, BALLHAUSEN and MOFFITT [12] used the radial parameters Dq, Ds, and Dt which can be translated to the point dipole and angular overlap parameters as follows:

$$\left.\begin{aligned} Dq &= \frac{1}{12}\mu_x \cdot B_4 = \frac{1}{20}(3\,e'_{\sigma x} - 4\,e'_{\pi x}) = \frac{1}{10}\Delta_x \\ Ds &= \frac{1}{7}[\mu_x - \mu_z]B_2 = \frac{1}{7}[e'_{\sigma x} + e'_{\pi x} - e'_{\sigma z} - e'_{\pi z}] \\ Dt &= \frac{1}{21}[\mu_x - \mu_z]B_4 = \frac{1}{35}[3\,e'_{\sigma x} - 4\,e'_{\pi x} - 3\,e'_{\sigma z} + 4\,e'_{\pi z}] \end{aligned}\right\} \quad (11)$$

* It should here be recalled that our $e_{\lambda q}$ parameters make up the sum of the two radial contributions from each end of the q axis. This is the cause of the factor 2 in front of Δ_q in eq. (10).

The formulation in terms of Dq, Ds and Dt destroys the baricenter (center of gravity) rule for the Dt elements but has the advantage of making a comparison with the cubic complex of μ_x-type more evident.

5. Energy levels of d^3 and d^6 systems and the consequences of the holohedrized symmetry

The energy levels in tetragonal chromophores have been discussed by a number of authors [9, 12, 13, 14] using the electrostatic parameter description and by GRIFFITH and ORGEL [15], YAMATERA [16, 17] and MCCLURE [18] using an interpretation of the radial parameters similar to the present one.

These earlier results have been augmented by considering

1) a general orthoaxial chromophore of the lowest possible symmetry, i.e. C_1, although its holohedrized symmetry, as mentioned in section 2, cannot be lower than D_{2h},
2) the non-diagonal elements connecting the pure cubic configuration split components of the two spin-allowed absorption bands, and
3) the accidental degeneracies in the light of the concept of the holohedrized perturbation field.

We shall be concerned, as earlier authors have been, with the transitions which by their cubic parentage can be characterized by $t_{2g}^3 \rightarrow t_{2g}^2 e_g$ and $t_{2g}^6 \rightarrow t_{2g}^5 e_g$. However, because the cubic configurations are not pure (except for ${}^4T_{2g}\,(t_{2g}^2 e_g)$), even when taking into account our non-diagonal elements a correction must be made before a proper comparison with experimental results is possible.

The procedure of YAMATERA [16, 17] has been adopted for characterizing the one-electron transitions. The orbitals and energy levels have been labelled as symmetry functions (rep.) of the point group D_{2h}, the notation being selected so that z, x and y transform as b_{1u}, b_{2u} and b_{3u}, respectively.

The ground levels of d^3 and low-spin d^6 systems, whose cubic parentages are ${}^4A_2$ and ${}^1A_1$, have an orbital symmetry A under the point group D_2. The first two spin-allowed transitions in order of increasing energy lead to levels whose cubic parentages are ${}^4T_2$ and ${}^4T_1$ in d^3, and ${}^1T_1$ and ${}^1T_2$ in d^6 systems. The components of both T_1 and T_2 in the point group D_2 are distinguishable as B_1, B_2 and B_3. Also in the following, we often omit the parity designation.

The transitions $A \rightarrow B_1$ to the two B_1 components of the cubic spin-allowed absorption bands can in either case be characterized as combinations of the one-electron transitions $d_{xy} \rightarrow d_{x^2-y^2}$ and $d_{xy} \rightarrow d_{z^2}$. We have taken the energies of these transitions as our diagonal one-electron operator energies, which can be read directly from (3).

The corresponding non-diagonal element is given in (4) and the energy matrix can be written for $A \rightarrow B_1$:

$$\begin{bmatrix} e'_{\sigma z} + \frac{1}{4}(e'_{\sigma x} + e'_{\sigma y}) - (e'_{\pi x} + e'_{\pi y}) + a - C & \frac{1}{4}\sqrt{3}(e'_{\sigma y} - e'_{\sigma x}) \\ \frac{1}{4}\sqrt{3}(e'_{\sigma y} - e'_{\sigma x}) & \frac{3}{4}(e'_{\sigma x} + e'_{\sigma y}) - (e'_{\pi x} + e'_{\pi y}) - C \end{bmatrix} \tag{12}$$

where the eigenvalues directly correspond to the energies of the $A \rightarrow B_1$ transitions. a and C are parameters expressing the interelectronic repulsion energy* relative to that of the ground level. In terms of Racah parameters a is equal to 12 B for d^3 systems for which the Racah parameter C disappears in equ. (12) and a is 16 B for d^6 systems [19] (see also Table V).

The corresponding energy matrices for the $A \rightarrow B_2$ and $A \rightarrow B_3$ transitions can now be obtained by cyclic permutations. With our choice of labelling the D_2 symmetry functions ($x{:}b_2$, see beginning of this section) the permutation $\begin{matrix} x & y \\ y & z \\ z & x \end{matrix}$ will lead to the $A \rightarrow B_2$ matrix and $\begin{matrix} x & z \\ y & x \\ z & y \end{matrix}$ to the $A \rightarrow B_3$ matrix.

In Tables I, II and III results have been given for typical systems for which some chloro-ammines have served as examples. Troughout ammonia has been abbreviated to N and has been assumed not to have any π-anti-bonding contribution. In Tables I and II the energy levels have been characterized by their symmetry (irreducible representations, rep.) in different ways: their cubic parentage symmetry, their symmetry relative to our general reference point group D_{2h} and their symmetry relative to their proper point group. Table I contains the chromophores for which the D_{2h} functions are themselves also proper symmetry functions of the true chromophore point group. Table II contains those for which linear combinations of the D_{2h} functions are required to make up proper basis functions of the chromophore

* The description of the interelectronic repulsion [19] in terms of Racah parameters involves the additional assumption that the deformation of the central ion orbitals by the mixing with ligand orbitals can be accounted for by a nephelauxetic effect, i.e. a common reduction of the Racah parameters of all the energy levels [20]. For the third band of d^3 systems [21] this is known to be an assumption which cannot be brought into accordance with experiment.

point group. These linear combinations have been given except for their normalization constants. The accidental degeneracies B_2, B_3 in *cis* N_4Cl_2 and B_1, B_2, B_3 in *fac.* N_3Cl_3 have been pointed out previously [9, 17, 18], although it has not been mentioned that this degeneracy also remains after consideration of the non-diagonal elements. If the holohedrized symmetry (see end of introduction) is used these accidental degeneracies become a necessary consequence. If the artificial center of inversion is appreciated the holohedrized symmetry of the examples of Table I becomes D_{4h}, D_{4h} and D_{2h} and those of Table II D_{4h} and O_h, respectively.

Table III contains the diagonal splittings, derived from Tables I and II, splittings which when referred to the first and second spin-allowed absorption band have the same expression for d^3 and d^6 systems.

The well known rule that *trans* N_4Cl_2 has a diagonal splitting twice that of the mono complex N_5Cl, which itself has -1 times the splitting of the *cis* N_4Cl_2 complex is illustrated. For *mer.* N_3Cl_3 the $B_1(D_{2h})$ component, which has the same position as all the components of the pseudo cubic *fac.* N_3Cl_3 lies between the B_2 and B_3 components whose energy difference [18] is equal to the splitting of the *trans* N_4Cl_2 complex. This result has been applied to recognize a triammine as the facial isomer on the basis of a consideration of positions and widths of its absorption bands [22].

It has to our knowledge not been pointed out before that the diagonal contribution to the position of the split components of the first absorption band depends only on the relative positions of the ligands in the spectrochemical series. The expression for the orbital energy difference in a regularly octahedral chromophore is $\Delta = 3e'_\sigma - 4e'_\pi$, so that, for example, the splitting in our *trans* complex (table I) can be expressed as $\frac{1}{2}(\Delta_N - \Delta_{Cl})$. It is seen that the E component will lie below the orbitally non-degenerate component because Cl^- comes earlier (i.e. has a smaller Δ-value than ammonia) in the spectrochemical series. For the second band the σ and π contributions cannot be expressed in terms of Δ values and a two-dimensional spectrochemical series becomes necessary for describing the splittings in general terms [18, 26].

No genuine example exists in which a well defined splitting of both spin-allowed absorption bands has been observed. We shall therefore not attempt any comparison with experiments here but refer to the discussion* given by McClure [18].

* Added in proof. For a recent contribution, see Wentworth, R. A. D. and Piper, T. S., 1965, Inorg. Chem., **4** 709.

There exist many cases, e.g. tetrahedral chromophores MX_4, where the center of inversion is absent, and where the concept of holohedrized symmetry is nevertheless applicable to a surprisingly good approximation. The non-diagonal elements connecting $3d$ and $4p$ orbitals seem unimportant for the position of the energy levels in such cases, thus imitating the holohedrized situation where non-diagonal elements between orbitals of opposite parity vanish.

Two molecules can have the same symmetries but have entirely different holohedrized symmetries. This would be the case, e.g. for AsH_3 and NH_3 if the angles H-As-H were all 90°. Then the holohedrized symmetry would be O_h (like the *fac.* N_3Cl_3 isomer) and D_{3d}, respectively. Even this idealized form of AsH_3 has the actual symmetry C_{3v}, not higher than that of NH_3.

6. Interrelation between low symmetry splittings of energy levels belonging to different cubic sub-configurations

The well known Pauli hole equivalence principle relates an l^q configuration to an $l^{4\,l+2-q}$ configuration. The latter behaves in a certain sense as a full shell into which q positively charged electrons have entered. All composite wavefunctions will have the same expression and the absolute value* of all matrix elements involving only angular coordinates will be the same, the sign being occasionally reversed.

A similar relation between the energy levels of different cubic configurations has been studied by VAN VLECK [23] who found some regularities among the levels of maximum spin multiplicity. Thus the cubic ligand field perturbation energies were found, except for the sign, to be the same with the pairs d^q–d^{5-q}, and d^{5+q}–d^{10-q}.

Here the cubic sub-configurations $t_{2g}^a e_g^b$ will be divided into four classes** characterized by the irreducible representations attributed to the cubic energy levels of highest spin multiplicity to which they give rise.

In Table IV these classes of cubic configurations have been characterized by the irreducible representations of O_h which they contain. Further for each class the simplest configuration and the orbitals which specify a particular level are given together with the level's energy. This is the deviation from the cubic average energy and contains independent contributions from each of the two sub-shells (eq. 6 and 7). The level corresponds to that row

* With the exception of certain constant contributions to the interelectronic repulsion energy thoroughly discussed by GRIFFITH [25].

** The classes A. and D. of ref. [11] constitute one of our four classes. The same is true for B. and C.

of the O_h irreducible representation which transforms as the D_{2h} representation given. For the classes T and T' the energies of the B_1 component(s) of the D_{2h} reference point group have been given, as before, and for the class T' the non-diagonal element can be found in eq. (4). The energies of the B_2 and B_3 components can again be obtained by cyclic permutations of (z, x, y).

From the levels specified in Table IV all other levels belonging to the same class can be generated by the operators $\mathfrak{P}$ (Pauli) and $\mathfrak{V}$ (van Vleck). These operators, which commute and which both have squares equal to identity, have, for the present purpose, been considered as working solely on sub-shells, and, in particular, on wavefunctions having extreme M_S values. $\mathfrak{P}$ transforms a configuration into its complement relative to the full configuration, $\mathfrak{V}$ into its complement relative to that half configuration, either the first half or the second half, to which it already belongs.

The results from operations with $\mathfrak{P}$ and $\mathfrak{V}$ depend on the number of times (i.e. on their exponents) they are applied. (1) The energy contribution from a sub-shell changes sign if the sum of the exponents to all the operators ($\mathfrak{P}$ and $\mathfrak{V}$) working on that sub-shell is odd. Conversely, if the sum is even, the sign remains unchanged. (2) For $\Gamma = A$ or T, a level Γ_1 (or Γ_2) is converted into Γ_2 (or Γ_1) if the sum of the exponents to $\mathfrak{V}$, counted for both sub-configurations, is odd. If this is even, the symmetry of the level remains unaltered. The application of $\mathfrak{P}$ never alters the symmetry of the level. (3) For the class T', in which two different cubic levels occur, a specified configuration corresponding to an upper level is transformed into one of a lower level (and vice versa) if the sum of all exponents to $\mathfrak{P}$ and $\mathfrak{V}$, counted for both sub-shells, is odd. If the sum is even, a specified configuration of an upper (lower) level remains that of an upper (lower) level.

As an example of the application of these operators they have been used to generate the perturbation energies belonging to

$$\left.\begin{aligned} & t_2^2 e\ {}^4T_2\ (B_1 \colon d_{zx} d_{yz} d_{x^2-y^2}) \\ \text{and} \quad & t_2^5 e\ {}^3T_1\ (B_1 \colon d_{zx}^2 d_{yz}^2 d_{xy} d_{x^2-y^2}) \end{aligned}\right\} \qquad (13)$$

We are concerned with the class T' because two levels of maximum spin multiplicity originate from each of the configurations. $t_2 e\ {}^3T_1$ (upper level), or specified, $d_{xy} d_{x^2-y^2}$, is the simplest function of the class T' (Table IV) which therefore has been chosen to generate all the other functions of that class.

For the B_1 (D_{2h}) functions we have:

$$\left.\begin{aligned} \mathfrak{V}(t_2)(e) : {}^3T_1 \text{ (upper level)} &= t_2^2 e : {}^4T_2 \text{ (lower level) or} \\ \mathfrak{V}(d_{xy})(d_{x^2-y^2}) &= d_{zx}d_{yz}d_{x^2-y^2} \text{ (lower level)} \end{aligned}\right\} \quad (14)$$

$$\left.\begin{aligned} \mathfrak{P}(t_2)(e) : {}^3T_1 \text{ (upper level)} &= t_2^5 e : {}^3T_1 \text{ (lower level) or} \\ \mathfrak{P}(d_{xy})(d_{x^2-y^2}) &= d_{zx}^2 d_{yz}^2 d_{xy} d_{x^2-y^2} \text{ (lower level)} \end{aligned}\right\} \quad (15)$$

The energy in both cases is $-E_{xy}+E_{x^2-y^2}$, the sign being reversed on the t_2 contribution (relative to that of the starting function) because the operators working on the t_2 sub-shell ($\mathfrak{V}$ and $\mathfrak{P}$, respectively) have been applied an odd number of times (rule 1). For the d^3 case $\mathfrak{V}$ has been applied an odd number of times and therefore the T_1 level has gone into a T_2 level (rule 2). For both d^3 and d^6 cases the total number of applications of operators is odd and our original function which was an upper level function has therefore been transformed to functions which belong to lower levels (rule 3). These particular results could, of course, have been obtained directly from the specified configurations (to the right in eq. (13)) provided these had been obtained by other methods.

It should be emphasized that the half of the configurations belonging to the T' class, which has the maximum spin multiplicity 3, contributes for each spin triplet also a spin singlet level whose orbital symmetry and one electron operator energy is exactly that of the corresponding spin triplet level. This is actually the relation between the spin quartet levels of d^3 systems and the singlet levels of d^6 systems. The ground levels are related similarly, but their D_{2h} perturbation energy vanish.

The two electron operator energies which separate the T_1 and T_2 levels, which originate from each configuration of the T' class and its corresponding spin-singlet levels, are given in Table V.

7. Some reservations

We have mentioned the regularities which relate the spectra of d^3 and low-spin-d^6 systems, among others. A further similarity [24] is also expected for the systems d^3 and d^8 within our approximation of pure cubic sub-configurations. However, because of the lower energy difference between e and t_2, the cubic sub-configurations are much less pure in the typical example of Ni(II).

It should further be added that if the experimental results for d^3 and d^6 systems were to be discussed it would also be necessary for these to introduce

a correction for the impurity of the cubic sub-configurations. However, the non-cubic contributions to this mixing can be shown to be negligibly small, and the cubic contribution can, at least in principle, be calculated from the results of TANABE and SUGANO [19].

Acknowledgement. The authors are indebted to C. J. HAWKINS for suggestions which have improved the manuscript.

Department of Inorganic Chemistry
The H. C. Ørsted Institute
Universitetsparken 5, Copenhagen Ø, Denmark

Cyanamid European Research Institute
Cologny (Geneva), Switzerland

References

[1] JØRGENSEN, C. K., PAPPALARDO, R., and SCHMIDTKE, H.-H., 1963, J. Chem. Phys., **39**, 1422.
[2] JØRGENSEN, C. K., and SCHMIDTKE, H.-H., 1963, Z. physik. Chem., **38**, 118.
[3] PERKINS, W. G., and CROSBY, G. A., 1965, J. Chem. Phys., **42**, 407.
[4] SCHMIDTKE, H.-H., 1964, Z. Naturforsch., **19**a, 1502.
[5] SCHÄFFER, C. E., and JØRGENSEN, C. K., 1965, Mol. Phys.
[6] MULLIKEN, R. S., 1952, J. Phys. Chem., **56**, 295.
[7] WOLFSBERG, M., and HELMHOLZ, L., 1952, J. Chem. Phys., **20**, 837.
[8] JØRGENSEN, C. K., Orbitals in Atoms and Molecules 1962 (London: Academic Press).
[9] BALLHAUSEN, C. J., and JØRGENSEN, C. K., 1955, Mat. Fys. Medd. Dan. Vid. Selsk., **29**, nr. 14.
[10] BALLHAUSEN, C. J., 1954, Mat. Fys. Medd. Dan. Vid. Selsk., **29**, nr. 4.
[11] JØRGENSEN, C. K., 1958, Faraday Soc. Disc., **26**, 172.
[12] BALLHAUSEN, C. J., and MOFFITT, W., 1956, J. Inorg. Nucl. Chem., **3**, 178.
[13] HARTMANN, H., and KRUSE, H.-H., 1955, Z. physik. Chem. N.F., **5**, 9.
[14] BASOLO, F., BALLHAUSEN, C. J., and BJERRUM, J., 1955, Acta Chem. Scand., **9**, 810.
[15] GRIFFITH, J. S., and ORGEL, L. E., 1956, J. Chem. Soc. London, 4981.
[16] YAMATERA, H., 1957, Naturwissenschaften, **44**, 375.
[17] YAMATERA, H., 1958, Bull. Chem. Soc. Japan, **31**, 95.
[18] MCCLURE, D. S., 1961, Advances in the Chemistry of the Coordination Compounds. Ed. S. Kirschner. (Macmillan, New York) p. 498.
[19] TANABE, Y., and SUGANO, S., 1954, J. Phys. Soc. Japan, **9**, 753.
[20] JØRGENSEN, C. K., 1962, Progress Inorg. Chem., **4**, 73.
[21] SCHÄFFER, C. E., 1958, J. Inorg. Nucl. Chem., **8**, 149.
[22] SCHÄFFER, C. E., and ANDERSEN, P., 1964, Theory and Structure of Complex Compounds. Ed. B. Jezowska-Trzebiatowska. (Pergamon Press) p. 571.
[23] VAN VLECK, J. H., 1932, Phys. Rev., **41**, 208.
[24] JØRGENSEN, C. K., 1955, Acta Chem. Scand., **9**, 116.
[25] GRIFFITH, J. S., Theory of Transition-Metal Ions. Cambridge University Press 1961, p. 234.
[26] JØRGENSEN, C. K., 1963, Advances Chem. Phys., **5**, 33.
[27] SCHÄFFER, C. E., to be submitted to Mol. Phys.

Legend of Tables I and II

One electron operator contribution to the position of the two spin-allowed absorption bands of some simple orthoaxial chromophores. The ground levels serve as zero points of energy. Each level is characterized by different symmetry designations, referring to the cubic parentage, the D_{2h} common reference and the chromophore point group. The phases of the corresponding wavefunctions are interrelated in such a way that a cyclic permutation of (z,x,y) brings $B_1(D_{2h})$ functions into B_2 functions and B_2 functions into B_3 functions. The B_1 and B_2 designations in C_{2v} symmetry are those usually found in the literature, but of course can be permuted without any physical consequence. The three nitrogen atoms of *mer.* N_3Cl_3 have been placed in the zx-plane*. In table II the linear combinations of the D_{2h} functions, required for forming basis functions of the proper chromophore point group, are given. From the form of the linear combinations of the D_2 functions, which make up the levels $A_2(C_{2v})$ and $B_2(C_{2v})$ in the chromophore *cis* N_4Cl_2, it can be seen that the degeneracy of these levels remains after consideration of the non-diagonal elements.

* In the case of *cis* N_4Cl_2 we have chosen $B_1(C_{2v})$ to be symmetrical with respect to the symmetry plane containing the two Cl.

TABLE I.

	Chromophore Atoms on the z-axis of D_{2h} Point group			N_5Cl N-Cl C_{4v}			*trans* N_4Cl_2 Cl-Cl D_{4h}			*mer.* N_3Cl_3 N-Cl C_{2v}		
	O_h rep.		D_{2h} rep.	C_{4v} rep.		energies	D_{4h} rep.		energies	C_{2v} rep.		energies
	d^3	d^6		d^3	d^6		d^3	d^6		d^3	d^6	
Diagonal energies	$^4A_{2g}$	$^1A_{1g}$	A_g	B_1	A_1	0	B_{1g}	A_{1g}	0	A_1	A_1	0
	$^4T_{2g}$	$^1T_{1g}$	B_{1g}	B_2	A_2	$3e'_{\sigma N}$	B_{2g}	A_{2g}	$3e'_{\sigma N}$	A_2	A_2	$\frac{3}{2}e'_{\sigma N}+\frac{3}{2}e'_{\sigma Cl}-2e'_{\pi Cl}$
			B_{2g}	E	E	$\frac{9}{4}e'_{\sigma N}+\frac{3}{4}e'_{\sigma Cl}-e'_{\pi Cl}$	E_g	E_g	$\frac{3}{2}e'_{\sigma N}+\frac{3}{2}e'_{\sigma Cl}-2e'_{\pi Cl}$	B_2	B_2	$\frac{3}{4}e'_{\sigma N}+\frac{9}{4}e'_{\sigma Cl}-3e'_{\pi Cl}$
			B_{3g}							B_1	B_1	$\frac{9}{4}e'_{\sigma N}+\frac{3}{4}e'_{\sigma Cl}-e'_{\pi Cl}$
	$^4T_{1g}$	$^1T_{2g}$	B_{1g}	A_2	B_2	$2e'_{\sigma N}+e'_{\sigma Cl}$	A_{2g}	B_{2g}	$e'_{\sigma N}+2e'_{\sigma Cl}$	A_2	A_2	$\frac{3}{2}e'_{\sigma N}+\frac{3}{2}e'_{\sigma Cl}-2e'_{\pi Cl}$
			B_{2g}	E	E	$\frac{11}{4}e'_{\sigma N}+\frac{1}{4}e'_{\sigma Cl}-e'_{\pi Cl}$	E_g	E_g	$\frac{5}{2}e'_{\sigma N}+\frac{1}{2}e'_{\sigma Cl}-2e'_{\pi Cl}$	B_2	B_2	$\frac{9}{4}e'_{\sigma N}+\frac{3}{4}e'_{\sigma Cl}-3e'_{\pi Cl}$
			B_{3g}							B_1	B_1	$\frac{3}{4}e'_{\sigma N}+\frac{9}{4}e'_{\sigma Cl}-e'_{\sigma Cl}$
Non-diagonal energies			B_{1g}			0			0			$-\frac{1}{2}\sqrt{3}(e'_{\sigma N}-e'_{\sigma Cl})$
			B_{2g}			$-\frac{1}{4}\sqrt{3}(e'_{\sigma N}-e'_{\sigma Cl})$			$-\frac{1}{2}\sqrt{3}(e'_{\sigma N}-e'_{\sigma Cl})$			$\frac{1}{4}\sqrt{3}(e'_{\sigma N}-e'_{\sigma Cl})$
			B_{3g}			$+\frac{1}{4}\sqrt{3}(e'_{\sigma N}-e'_{\sigma Cl})$			$+\frac{1}{2}\sqrt{3}(e'_{\sigma N}-e'_{\sigma Cl})$			$\frac{1}{4}\sqrt{3}(e'_{\sigma N}-e'_{\sigma Cl})$

TABLE II.

	Cromophore Atoms on the z-axis of D_{2h} Point group		*cis* N_4Cl_2 N-N C_{2v}						*fac.* N_3Cl_3 N-Cl C_{3v}			
	O_h rep.		D_{2h} rep.	C_{2v} rep.		D_{2h} rep. combination making up C_{2v} rep.		energies	C_{3v} rep.		D_{2h} rep. combination making up C_{3v} rep.	energies
	d^3	d^6		d^3	d^6	d^3	d^6		d^3	d^6	d^3 and d^6	
Diagonal energies	$^4A_{2g}$	$^1A_{1g}$	A_g	B_1	A_1	A_g	A_g	0	A_2	A_1	A_g	0
	$^4T_{2g}$	$^1T_{1g}$	B_{1g}	A_1	B_1	B_{1g}	B_{1g}	$\frac{3}{2}e'_{\sigma N}+\frac{3}{2}e'_{\sigma Cl}-2e'_{\pi Cl}$	A_1	A_2	$B_{1g}+B_{2g}+B_{3g}$	$\frac{3}{2}e'_{\sigma N}+\frac{3}{2}e'_{\sigma Cl}-2e'_{\pi Cl}$
			B_{2g}	A_2	A_2	$B_{2g}-B_{3g}$	$B_{2g}+B_{3g}$	$\frac{9}{4}e'_{\sigma N}+\frac{3}{4}e'_{\sigma Cl}-e'_{\pi Cl}$	E	E	$B_{2g}+B_{3g}-2B_{1g}$	$\frac{3}{2}e'_{\sigma N}+\frac{3}{2}e'_{\sigma Cl}-2e'_{\pi Cl}$
			B_{3g}	B_2	B_2	$B_{2g}+B_{3g}$	$B_{2g}-B_{3g}$	$\frac{9}{4}e'_{\sigma N}+\frac{3}{4}e'_{\sigma Cl}-e'_{\pi Cl}$			$B_{2g}-B_{3g}$	$\frac{3}{2}e'_{\sigma N}+\frac{3}{2}e'_{\sigma Cl}-2e'_{\pi Cl}$
	$^4T_{1g}$	$^1T_{2g}$	B_{1g}	B_1	A_1	B_{1g}	B_{1g}	$\frac{5}{2}e'_{\sigma N}+\frac{1}{2}e'_{\sigma Cl}-2e'_{\pi Cl}$	A_2	A_1	$B_{1g}+B_{2g}+B_{3g}$	$\frac{3}{2}e'_{\sigma N}+\frac{3}{2}e'_{\sigma Cl}-2e'_{\pi Cl}$
			B_{2g}	A_2	A_2	$B_{2g}+B_{3g}$	$B_{2g}-B_{3g}$	$\frac{7}{4}e'_{\sigma N}+\frac{5}{4}e'_{\sigma Cl}-e'_{\pi Cl}$	E	E	$B_{2g}+B_{3g}-2B_{1g}$	$\frac{3}{2}e'_{\sigma N}+\frac{3}{2}e'_{\sigma Cl}-2e'_{\pi Cl}$
			B_{3g}	B_2	B_2	$B_{2g}-B_{3g}$	$B_{2g}+B_{3g}$	$\frac{7}{4}e'_{\sigma N}+\frac{5}{4}e'_{\sigma Cl}-e'_{\pi Cl}$			$B_{2g}-B_{3g}$	$\frac{3}{2}e'_{\sigma N}+\frac{3}{2}e'_{\sigma Cl}-2e'_{\sigma Cl}$
Non-diagonal energies			B_{1g}					0				0
			B_{2g}					$\frac{1}{4}\sqrt{3}(e'_{\sigma N}-e'_{\sigma Cl})$				0
			B_{3g}					$-\frac{1}{4}\sqrt{3}(e'_{\sigma N}-e'_{\sigma Cl})$				0

TABLE III.

Diagonal splittings of the spin-allowed absorption bands of d^3 and d^6 orthoaxial chromophores for which further details are given in tables I and II.

	D_{2h} designations	*cis* N_4Cl_2	N_5Cl	*trans* N_4Cl_2	*mer.* N_3Cl_3
First absorption band	$B_{1g}-B_{2g}$	$-\frac{3}{4}e'_{\sigma N}+\frac{3}{4}e'_{\sigma Cl}-e'_{\pi Cl}$	$\frac{3}{4}e'_{\sigma N}-\frac{3}{4}e'_{\sigma Cl}+e'_{\pi Cl}$	$\frac{3}{2}e'_{\sigma N}-\frac{3}{2}e'_{\sigma Cl}+2e'_{\pi Cl}$	$\frac{3}{4}e'_{\sigma N}-\frac{3}{4}e'_{\sigma Cl}+e'_{\pi Cl}$
	$B_{1g}-B_{3g}$				$-\frac{3}{4}e'_{\sigma N}+\frac{3}{4}e'_{\sigma Cl}-e'_{\pi Cl}$
Second absorption band	$B_{1g}-B_{2g}$	$\frac{3}{4}e'_{\sigma N}-\frac{3}{4}e'_{\sigma Cl}-e'_{\pi Cl}$	$-\frac{3}{4}e'_{\sigma N}+\frac{3}{4}e'_{\sigma Cl}+e'_{\pi Cl}$	$-\frac{3}{2}e'_{\sigma N}+\frac{3}{2}e'_{\sigma Cl}+2e'_{\pi Cl}$	$-\frac{3}{4}e'_{\sigma N}+\frac{3}{4}e'_{\sigma Cl}+e'_{\pi Cl}$
	$B_{1g}-B_{3g}$				$\frac{3}{4}e'_{\sigma N}-\frac{3}{4}e'_{\sigma Cl}-e'_{\pi Cl}$

TABLE IV.

Cubic sub-configurations classified according to their energy levels of maximum spin-multiplicity. Within each generating function (column 4) the m_s values of the one electron component functions should be the same $\left(\text{either } +\frac{1}{2} \text{ or } -\frac{1}{2}\right)$. The energies of these particular functions are given in column 6 with reference to eq. (7).

class	O_h-rep.	Simplest configurations	Specification of row of rep.	D_{2h} rep.	energy
A	A_{1g} or A_{2g}	$t_{2g}^o e_g^o$		A_g	0
E	E_g	$t_{2g}^o e_g$	$d_{x^2-y^2}$	A_g	$E_{x^2-y^2}$
T	T_{1g} or T_{2g}	$t_{2g} e_g^o$	d_{xy}	B_{1g}	E_{xy}
T'	T_{1g} and T_{2g}	$t_{2g} e_g$	$d_{xy} d_{x^2-y^2}$	B_{1g}	$E_{x^2-y^2} + E_{xy}$

TABLE V.

Energy differences in units of B between the T_1 and T_2 levels of class T', and between the singlet levels which correspond to the triplet levels of T'.

	$S = 0$	1	3/2
d^2, d^8	4	12	—
d^3, d^7	—	—	12
d^4, d^6	−16	−8	—
d^5	—	—	−8

Indleveret til Selskabet den 7. maj 1965.
Færdig fra trykkeriet den 17. september 1965.

Matematisk-fysiske Meddelelser
udgivet af
Det Kongelige Danske Videnskabernes Selskab
Bind **34,** nr. 14

Mat. Fys. Medd. Dan. Vid. Selsk. **34,** no. 14 (1965)

INFLUENCE OF CRYSTAL LATTICE ON MOTION OF ENERGETIC CHARGED PARTICLES

BY

JENS LINDHARD

København 1965
Kommissionær: Ejnar Munksgaard

CONTENTS

Synopsis

The paper describes a theoretical approach to the problems of directional effects for energetic charged particles moving through solids. Introductory comments on some aspects of directional effects are given in § 1. The fundamental approximations of the description are stated in § 2, and the associated simple concept of a string of atoms is introduced. A transverse continuum potential is a natural consequence of the basic approximations. The limit of applicability of continuum potentials is given by a critical angle. At high particle energies the critical angle is of an especially simple type. The critical angle separates particles behaving essentially as in a random substance from particles which do not come close to e.g. strings, with corresponding strong reduction of most physical processes. A number of examples are discussed, and critical angles belonging to atomic planes, strings, and pairs are compared. Characteristic features of a quantal treatment are briefly sketched.

§ 3 treats basic statistical estimates in calculations of directional effects. As a function of transverse energy, $E_\perp$, the slowing-down is calculated for electronic and nuclear collisions. Multiple scattering, i.e. lack of conservation of transverse energy, is studied in § 4. The normal multiple scattering, due to nuclear collisions, is strongly reduced for low values of $E_\perp$.

The rate of physical processes depends on the external angle between a beam and a crystal. In § 5 it is found that in simple cases the average of such rates over direction gives the same result as in a random system. Similar rules hold for spatial averages.

In § 6 experiments on directional effects are discussed from a theoretical point of view. The main effects to be taken into account are summarized. The order of magnitude of dip minima is estimated. The possibilities are discussed of using as an experimental tool the shadow belonging to e.g. strings. A few comments are made on recent experiments connected with string effects.

A more detailed investigation of classical deflections by lattice atoms, and the limits of validity of continuum potentials, is given in Appendix A, where also critical angles of particle emission from perfect strings are estimated. In Appendix B quantal corrections to the classical description are studied, and it is found that—in contrast to the familiar case of single collisions—the corrections are small at high velocities.

PRINTED IN DENMARK
BIANCO LUNOS BOGTRYKKERI A/S

§ 1. Introduction

Measurements of range distributions and energy loss in single crystals have revealed directional effects, both for slow, heavy ions[1] and, more recently, for protons[2]. The first indications of directional effects for slow charged particles seem to be in observations on sputtering[3]. Further indications were found in digital computer studies[4] of simplified models of penetration through lattices at extremely low particle energies.

The purpose of the present paper is to show that a comprehensive theoretical analysis may be made of directional effects in penetration of charged particles through crystal lattices. This analysis leads to conditions for the occurrence of a peculiar effect, described as atomic string effect. The corresponding string approximation is a well-defined approximation procedure by means of which primary and secondary directional effects can be treated. It then turns out that directional phenomena provide an interesting tool for solid state investigations, mainly because lattice points can be distinguished by means of a shadow effect. The theoretical results were summarized briefly in a recent note[5], and experiments were started along these lines[7].

At this point may be mentioned the well-known fact that, as a consequence of lattice periodicity, interference patterns of waves can be observed for both electromagnetic radiations and massive particles of not too short wave length. However, directional effects of that kind are not the subject of the present discussion, where mainly shadow phenomena are treated, with classical mechanics as a starting-point. Usually, the wave lengths of incoming particles are required to be exceedingly small and incoherence prevails, so that interference patterns are absent.

The basic case of the present approximation method is the case of high particle momenta. The classical orbital description of directional effects, as used in the following, is simple in this limit. In this connection it is also important that the classical approximation in directional phenomena turns out to be the better the higher the particle momentum, in contrast to most collision problems, where quantum mechanics takes over at high energies.

In the following chapters it is merely intended to present the general theoretical framework, with emphasis on a few basic phenomena and supplemented by a number of examples which can elucidate crucial problems. Several aspects, like quantal effects and thermal vibrations, are treated only in a cursory manner and need further study. Other problems, like the details of slowing-down, are not treated fully, because they are of secondary importance to the crucial questions discussed here.

The present chapter contains comments on some aspects of directional effects. A few facts are mentioned concerning slowing-down of charged particles.

Random systems

Although the spatial structure of a medium must have some influence on slowing-down and scattering of charged particles, the effect is normally disregarded. Several approximations are contained in a disregard of structure. They may be characterized by three mutually connected assumptions: homogeneity, isotropy, and randomness of the medium. The first two assumptions are often contained in the last one. An anisotropy due to lattice structure can thus result from some kind of correlation between collisions.

Suppose, that a penetrating particle has a certain differential cross section for scattering by single atoms, that its collisions with atoms of the medium are separable and independent, and finally, that the atoms are randomly distributed in space, with random orientation. Obviously, the slowing-down process is then independent of direction; the probability distribution in energy loss and scattering angle depends only on the mass per cm^2 penetrated, and is to be computed in a familiar way from single collisions. This is essentially a gas picture, and may be called a random system—implying homogeneity, isotropy, and random collisions. However, it is important to realize that the approximation of a random system is not confined to randomly distributed atoms or molecules, but may also be applied to media with lattice structure. As an example, one would a priori expect that a polycrystalline substance in many respects can be regarded as a random system.

Governed and ungoverned motion

A single crystal is a typical example of a medium in which directional effects in stopping might appear, due to both inhomogeneity, anisotropy and lack of randomness. We may classify directional effects for charged particles

moving through single crystals, or other media, by two labels: 1) ungoverned motion, and 2) governed motion. By ungoverned motion is meant the approximation where the path of the particle may be assumed to be essentially unaffected by the structure of the substance. Governed motion means that the path deviates definitely from that in a random system, because the path is determined by the structure of the medium. Ungoverned motion will be found to show merely fluctuations in physical effects due to correlations, whereas governed motion leads to more fundamental changes in physical processes.

In both categories of directional effects we may further distinguish between those cases where a) both direction and position of path are involved, and those where b) only direction is involved.

Direction and position

If a particle can be assumed to move classically along a straight line through a thin single crystal, the direction of the line of motion is important, as well as its position in the lattice (dependence on position indicates inhomogeneity, on direction: anisotropy). Thus, assume that the path is parallel to a major axis in the lattice. If then it is in between the atoms, there is a reduction of all those physical effects which require a close collision between particle and atom. If the particle is very close to atomic positions there is an increase in these effects.

Now, on the one hand, one can hardly hit e.g. only the space between atoms in a lattice, since a beam of projectiles will be spread over a large area, and thus one fraction of the beam may pass between atoms, while another fraction passes close to atoms. On the other hand, the impinging beam can be rather well collimated in direction, and thus a fraction of projectiles moving in straight lines might conceivably keep away from atoms for considerable distances of penetration.

As an example, consider the energy losses suffered by a beam of particles moving through a thin crystal film, where the energy loss remains small compared to the particle energy. The energy loss by a particle to an atom may be assumed to be a function of the impact parameter only. However, if the particles have ungoverned motion, the average energy loss (but not the fluctuations) remains the same as in a random system. This result is evident, since the particle beam consists of parallel randomly distributed paths. An average of energy losses over randomly distributed parallel paths must give the same result as an average over randomly distributed atoms.

In the case of governed motion, the paths do not remain independent of the lattice, and the average energy loss is expected to deviate from that of a random system. In the following, we are interested in possible occurrence of governed motion in a lattice, where effects depend on both direction and position of particle path, and where e.g. averages over external position of the path are not in conformity with results for random systems.

Direction only

For comparison, we briefly consider effects concerned with direction only, i.e. not associated with position in space of the particle path. Such purely directional effects may be divided in two.

The first case can be indicated by an example. Suppose that the medium is a homogeneous plasma in a constant external magnetic field parallel to the z-axis. The energy dissipation by a particle is then independent of its localization in space, but depends on the angle between the direction of motion and the z-axis. This directional effect is a property of the medium, and subsists even though the particle moves approximately along a straight line.

The second case occurs e.g. for wave interference patterns due to lattice periodicity. Such effects require an extended wave, in sharp contrast to a classical localization of the particle within the lattice. As mentioned previously, we shall not here treat wave interference.

Channelling

The concept of channelling was introduced in recent papers on penetration in crystals, at first for slow ions[4) 1)] and later for swift protons. By channelling is meant that a particle path near the centre of channels along a major axis in a crystal may have a certain stability. Particles moving along channels are subject to periodic forces, mainly focusing and occasionally defocusing. If the forces are of harmonic type and the focusing force is preponderant, this leads to a familiar solution of the equations of motion. The transverse motion in a channel is roughly a long-wave oscillation, combined with a short-wave vibration with the lattice period. The long-wave motion has a constant amplitude and wave-length v/ω, where ω is the period of average transverse harmonic oscillation and v the particle velocity. If the amplitude is large, the oscillation no longer remains harmonic. Any kind of oscillation within a channel we describe as proper channelling. A theoretical treatment of channelling is given by Lehmann and Leibfried[8)]

in a special case. Studies of individual paths at low energies by means of digital computers were performed by ROBINSON and OEN[4], and by others.

It is worth while to indicate in a qualitative way the possible occurrence of channelling and its relation to other phenomena. Suppose that a particle moves along the centre line of a channel, with oscillations about the centre line. If the energy of oscillation exceeds the barrier to a neighbouring channel, the particle escapes readily from the channel. We can roughly estimate the barrier for such escape either from the harmonic force in the centre of the channel, or from direct estimates at the channel border line. We introduce a barrier energy for channels, E_c, presumably of order of 5 eV for protons, and depending on Z_1 and on the medium. Let ψ be the angle between particle motion and channel direction when the particle is at the channel axis. If the energy in the transverse motion, $E\sin^2\psi$, is larger than E_c, the ion can escape from the channel; we need not discuss details as to the probability of escape. Thus, we find a critical angle

$$\alpha_c = \left(\frac{E_c}{E}\right)^{1/2}, \tag{1.1}$$

where E is the energy of the particle. Only if the incident ion both has an angle less than α_c with the channel axis and also starts close to the channel axis, can its escape from the channel be disregarded and proper channelling take place. This corresponds to a solid angle for proper channelling,

$$\Omega_c \sim \pi \frac{E_c}{E} \quad . \tag{1.2}$$

Within this solid angle, channelling can occur with a finite probability. In a wide channel, where the atoms in the walls are relatively closely packed, the energy E_c—and thus the solid angle Ω_c—is expected to be larger than in a narrow channel.

One consequence of (1.1) and (1.2) is that the critical angle depends strongly on the energy of the particle, while its charge and mass do not appear directly in the formula. Still, the barrier E_c depends somewhat on the atomic numbers Z_1 and Z_2, and changes with lattice direction.

Already the above cursory considerations indicate that at high particle energies the probability of channelling is negligible. At low energies the probability becomes larger, although some effects have a disturbing influence (cf. e.g. (A.13)). However, the probability of remaining in one channel is

not of much physical importance, except for a special group of phenomena. In the following chapters we arrive at a more complete picture of the phenomena at high and low particle energies.

Electronic and nuclear stopping

There are two sources of energy loss by a charged particle[12]. Electronic stopping is due to electronic collisions, where the particle excites or ejects atomic electrons, with loss of energy. The corresponding momentum transfer is small because electrons are light particles. Nuclear stopping arises from nearly elastic collisions with atoms, with transfer of both energy and momentum. Deflections of a particle are thus due to nuclear collisions, where large forces and heavy masses are involved. This simple fact is of significance in problems of directional effects.

One may distinguish between several regions of velocity in normal uncorrelated slowing-down of a charged particle. First, at high particle velocities, electronic stopping is completely dominating, and nuclear stopping is $\sim 10^3$ times smaller. This limiting case applies for protons, or heavier ions, when $v > v_1 = Z_1^{2/3} v_0$, Z_1 being the atomic number of the particle, v its velocity, and $v_0 = e^2/\hbar$. A quantal perturbation treatment of the excitation of the atomic system may then be applied (Bethe-Bloch treatment), the stopping being proportional to Z_1^2 and decreasing approximately as v to a power between -1 and -2. Second, at velocities $v < v_1$, electronic stopping can still remain dominating and is nearly proportional to velocity[6) 13)].

Third, the slowing-down of heavy ions of low velocities is dominated by nuclear stopping. In random systems, nuclear stopping can dominate over the electron stopping when $\varepsilon < 10$, where ε is a dimensionless measure of energy, of Thomas-Fermi type[6)],

$$\varepsilon = \frac{a \cdot E}{Z_1 Z_2 e^2} \cdot \frac{M_2}{M_1 + M_2} . \tag{1.3}$$

In (1.3), the atomic number of the medium is Z_2, the atomic screening radius is $a = a_0 \cdot 0.8853 \cdot (Z_1^{2/3} + Z_2^{2/3})^{-1/2}$, and $E = M_1 v^2/2$ is the energy of the particle. The parameter ε is convenient in the description of nuclear collisions.

The stopping of charged particles illustrates the necessity of distinguishing between electronic and nuclear collisions, and between several velocity regions. In the present context the actual stopping is not of primary importance, as discussed in § 2, but it remains a significant secondary phenomenon.

§ 2. Foundations of Theory

In order to find the proper approximation procedure for the treatment of directional effects, we must distinguish between primary and secondary phenomena. The energy loss of a particle (e.g. slowing-down by electronic collisions) is a secondary phenomenon, since it is determined by the path, but does not by itself govern the path. The possible governing of the path must be due to deflections of the particle in collisions with atoms, and thus a deflection is a primary phenomenon. Because of this simple fact, we can immediately introduce four basic assumptions[5], leading to a consistent approximation procedure for the treatment of possible governed motion of particles.

First, the angles of scattering of the particle may be assumed to be small. Not only does this usually hold for fast heavy particles, but scattering by large angles would imply that the original direction is completely lost, as well as correlations associated with the direction. The scattering of the particle is due to nuclear collisions, where it interacts with the charge distribution of an atom as a whole, the collision being nearly elastic. If the angles of scattering in the laboratory system, φ, and in the centre-of-gravity system, Θ, are small, we find for an elastic collision,

$$\operatorname{tg}\varphi = \frac{M_2 \sin\Theta}{M_1 + M_2 \cos\Theta} \to \varphi \simeq \frac{M_2}{M_1 + M_2}\Theta, \quad \text{for} \quad \varphi < 1, \quad \Theta < 1, \tag{2.1}$$

where M_1 is the particle mass and M_2 the mass of the atom, initially at rest. If we are interested in the motion of the particle only, we may find the correct scattering angle, φ, from the potential between particle and atom, calculating as if the atoms were infinitely heavy. In fact, the classical formula for scattering at small angles is

$$M_1\varphi = M_0\Theta = -\frac{1}{v^2}\int_{-\infty}^{+\infty} dz \frac{\partial}{\partial p} V(\sqrt{z^2 + p^2}), \tag{2.1'}$$

where p is the impact parameter and $V(R)$ the potential between ion and atom at distance R. For the present purpose, the accuracy of the Thomas-Fermi potential between particle and atom is ample in most cases, and it leads to a simple comprehensive description. If the potential far away from an atom is needed, other estimates of potentials may be useful.

Second, since a collision demands that the particle comes close to the atom, strong correlations between collisions occur if the particle moves at a small angle with a row of atoms; if it passes close to one atom in the row, it must also pass close to the neighbouring atoms in the same row. This leads us to the concept of a string of atoms, characterized merely by the constant distance of separation, d, of atoms placed on a straight line. We describe this as the perfect string. In first approximation, collisions occur with one string at a time, string collisions being independent and uncorrelated. The physical importance of the string is emphasized by the fact that practically all physical processes caused by the particle, or influencing its path, demand that it comes close to the string. One exception is resonance excitation of atomic electrons, which may take place many lattice distances away from the particle, if it has a high velocity. The simplicity of the string approximation is partly due to the circumstance that the lattice structure does not enter, the only lattice parameter being the distance d between atoms in the string. Strings belonging to low index directions have a small value of d, and are the most pronounced ones. Correlations weaker than those of strings are expected for crystal planes, atomic pairs etc.

Third, classical orbital pictures may be used to a large extent. They may be applied in locating the particle in the lattice, because the wave length $\lambda\!\!\!^{-}$, is small. It is less obvious that classical orbital pictures may be used in describing collisions with e.g. strings of atoms. In fact, since individual collisions with atoms need quantal corrections either when the quantity $\varkappa = 2Z_1Z_2e^2/\hbar v$ is not large compared to unity, or when the impact parameter is large, the classical approximation might seem to be doubtful in several cases. However, contrary to such expectations the classical description of many successive collisions with atoms in a string does not become invalid at high velocities. The quantal corrections are discussed below, cf. Appendix B.

Fourth, the idealized case of a perfect lattice, and a perfect string, may be used as a first approximation. The most important deviations are vibrations of strings, i.e. thermal and zero point vibrations. Again, some of the effects of vibrations are reduced by successive collisions with many atoms in a string.

On the basis of the above four assumptions it is possible to construct, step by step, a theory of directional effects for energetic charged particles. The discussion of correlations and small angle deflections has led to the basic concept of a string of atoms. This concept is not to be considered as a fixed model, but rather as a starting-point for an approximation procedure

applicable to directional effects. In this sense there is an analogy to the ideal gas as a starting-point for descriptions of real gases, or an ideal lattice as a starting-point for solid state theory.

Transverse continuum potential of a string

In order to study the effect of correlated small angle deflections on the motion of a particle, we may at first introduce the continuum string approximation. The basis of the continuum approximation is to assume that many consecutive atoms contribute to the deflection of the orbit. Having found the particle orbits in the continuum approximation, we may next ascertain whether these orbits are actually determined by many collisions, i.e. we can find a condition for validity of the continuum picture. A discussion of the connection between continuum string and perfect string is given in Appendix A, where the combined effect of successive classical collisions is considered in some detail.

In the continuum approximation we introduce the average potential at a distance r from the string, i.e.

$$U(r) = \int_{-\infty}^{+\infty} \frac{dz}{d} V(\sqrt{z^2 + r^2}), \tag{2.2}$$

where $V(R)$ is the ion-atom potential and d the distance between atoms in the string. Although $U(r)$ is determined as an average potential belonging to a string, it is of interest to notice that $d \cdot U'(p)$ determines the scattering already in a single collision with an atom, according to (2.1′).

If R is not very much larger than a, the potential $V(R)$ is essentially of Thomas-Fermi type, and we may put

$$V(R) = \frac{Z_1 Z_2 e^2}{R} \varphi_0\left(\frac{R}{a}\right) \quad . \tag{2.3}$$

Here, a is the screening length of the ion-atom interaction, equal to* $a = a_0 \cdot 0.8853 \cdot (Z_1^{2/3} + Z_2^{2/3})^{-1/2}$, and $\varphi_0(R/a)$ is the Fermi function belonging to one isolated atom[6) 9)]. It is seen from (2.2) that, as a general rule, the variation of U with $1/r$ is by one power less than the variation of V with $1/r$. When (2.3) holds, we can write U as

* In the following it is often implicitly understood that $Z_1 \ll Z_2$, so that a is put equal to $a_0 \cdot 0.8853 \cdot Z_2^{-1/3}$.

$$U(r) = \frac{Z_1 Z_2 e^2}{d} \cdot \xi(r/a), \tag{2.4}$$

which formula is valid if the Thomas-Fermi type potential (2.3) applies.

A comparatively accurate estimate of $\xi(r/a)$, at moderate values of r/a, is given in ref. 10. For the present purpose we shall use somewhat simpler estimates. In order to get qualitative insight in the behaviour of ξ, i.e. of U, we note that $\varphi_0 \approx 1$ for $R/a \ll 1$, and according to (2.2) and (2.4) the function $\xi(r/a)$ must then increase logarithmically for small r, or

$$\xi\left(\frac{r}{a}\right) \approx 2 \log \frac{Ca}{r} \quad , \quad \text{for} \quad r < Ca, \tag{2.5}$$

where $2 \log C$ is a constant of integration, determined by the screening. An approximation somewhat better than (2.5), and applicable for all values of r, is given by the expression, in the following described as the standard potential,

$$\xi\left(\frac{r}{a}\right) = \log\left[\left(\frac{C \cdot a}{r}\right)^2 + 1\right]. \tag{2.6}$$

According to (2.6), $\xi \sim (Ca/r)^2$ for $r > Ca$. Even though (2.6) decreases rapidly for large r, it becomes less accurate when $r \gg a$. As a standard value for C we shall use $C = \sqrt{3}$, which gives a fairly good over-all fit. The best fit at small r/a would be obtained for a lower value of C, while large r/a would require a slightly higher value. Besides such estimates of $U(r)$ we shall sometimes consider the important atomic region where $R \sim a$ and $r \sim a$, so that V behaves as $\sim R^{-2}$, and $\xi(r/a)$ becomes $\xi \sim \pi a/2r$. The accuracy of the above approximations is indicated in reference 10.

The formula (2.6) corresponds to simple expressions for the density of electrons, $\varrho(R)$, and for the atomic potential $V(R)$ in (2.5), i.e.

$$\varrho(R) = \frac{3}{4\pi} Z_2 \frac{(Ca)^2}{(R^2 + (Ca)^2)^{5/2}} \quad , \tag{2.6'}$$

$$V(R) = Z_1 Z_2 e^2 \left\{ \frac{1}{R} - \frac{1}{(R^2 + C^2 a^2)^{1/2}} \right\}. \tag{2.6''}$$

The limitation of the standard atomic potential in (2.6) is clearly seen if we attempt to compute the average of the atomic radius squared, $\overline{R^2}$. This

quantity diverges logarithmically, according to (2.6′). However, this is usually not of importance in the present calculations.

Condition for continuum approximation and critical angles*

A qualitative condition for the continuum approximation is obtained if we demand that the scattering in the vicinity of the minimum distance of approach is due to many atoms. Thus, the collision time, Δt, multiplied by the velocity component parallel to the string $v\cos\psi \approx v$, must be large compared to d. The collision time is of order of $r_{\min}(l)/(v\sin\psi)$, where l is the impact parameter with the string, and $r_{\min}(l)$ the corresponding minimum distance of approach. The condition is thus

$$\Delta t \cdot v\cos\psi \simeq \frac{r_{\min}(l)}{\psi} > d. \tag{2.7}$$

Let us apply the condition (2.7) in its most restrictive form, so that we demand its fulfilment for $l = 0$, i.e. for $r_{\min}(0)$. The latter quantity is a function of ψ. For brevity we simply write $r_{\min}$ instead of $r_{\min}(l = 0, \psi)$. The minimum distance of approach is determined by

$$U(r_{\min}) = \frac{1}{2} M_1 v^2 \cdot \sin^2\psi. \tag{2.8}$$

It is seen that $r_{\min}$ increases rapidly as ψ decreases. According to (2.7), the critical angle is obtained by inserting $r_{\min} = d\cdot\psi$ in (2.8).

If the energy, $E = M_1 v^2/2$, is increased at fixed ψ, $r_{\min}$ in (2.8) tends to zero. We may therefore expect that at high energies (2.5) applies, so that the condition (2.7) together with (2.8) leads to

$$\frac{Ca}{\psi d} \cdot \exp\left\{-\frac{\psi^2 d}{2b}\right\} > 1,$$

where $b = Z_1 Z_2 e^2/E$ is the collision diameter belonging to laboratory system coordinates.

For ψ increasing from zero, the inequality is violated first by the rapid decrease of the exponential, provided $Ca/\psi d$ can remain large. Condition (2.7) therefore remains fulfilled if

$$\psi < \psi_1 = \sqrt{\frac{2b}{d}} = \sqrt{\frac{E_1}{E}}, \quad E_1 = \frac{2Z_1 Z_2 e^2}{d}, \tag{2.9}$$

* For a detailed treatment cf. Appendix A; in particular (A. 8), (A. 20) and (A. 21).

provided $Ca/\psi_1 d$ is larger than unity, i.e. approximately

$$\psi_1 \lesssim \frac{a}{d} \quad , \qquad \text{or} \qquad E > E' = 2Z_1 Z_2 e^2 \frac{d}{a^2} \quad , \tag{2.9'}$$

where $a/d \sim 20^{-1}$, so that the energy E' is several hundred times larger than E_1. According to (1.3), the condition (2.9') may also be stated as $\varepsilon > \varepsilon' = 2(d/a) \cdot M_2/(M_1 + M_2)$, and if $M_1 \lesssim M_2$ this corresponds to $\varepsilon \gtrsim 2d \cdot Z_2^{1/3} a_0^{-2}$.

If ψ fulfils the condition (2.9), the continuum potential (2.4) may be used and, accordingly, the particle cannot come closer than $\sim a$ to the centre of the string. Since E_1 is normally much larger than E_c in (1.1), the angle ψ_1 is large compared to the critical angle α_c for channelling. Therefore, in a well-defined high energy region given by (2.9'), where electronic stopping dominates, we may use the transverse potential (2.4), with a critical maximum angle $\propto \psi_1$, i.e. an effective maximum height of the transverse potential $\propto 2Z_1 Z_2 e^2/d$. In several respects, this maximum potential is remarkably simple. It is independent of the total energy of the particle and of the atomic screening radius a. It is a function of $Z_2 e/d$, the charge per unit length of the string.

At low energies, where (2.9') is no longer valid, we obtain an approximate expression for the critical angle by introducing (2.6) in (2.8) and (2.7). This leads to the condition

$$\psi < \psi_2 = \left(\frac{Ca}{d\sqrt{2}} \psi_1 \right)^{1/2} , \tag{2.10}$$

and since $C/\sqrt{2} \approx \sqrt{3}/\sqrt{2} \sim 1$, the critical angle ψ_2 applies when

$$\psi_1 > \frac{a}{d} \quad , \qquad \text{or} \qquad E < E', \tag{2.10'}$$

cf. (2.9'). An interesting consequence of (2.10) is that the potential energy barrier, obtained by squaring the right-hand side of (2.10) and multiplying by E, decreases proportionally to $E^{1/2}$, instead of remaining constant as in the high energy region. In contrast to ψ_1 in (2.9), the critical angle ψ_2 in (2.10) depends on the atomic radius a and on the behaviour of the screened atomic potential. For this reason, (2.10) is only a rough estimate and can hardly be expected to hold accurately at very low energies. In the following discussion we treat mainly the case of high energies, where (2.9) and (2.9')

apply. The other limit, (2.10), will only be discussed briefly, but in a general sense the following description applies also when (2.10) holds.

Already the result (2.9) gives a qualitative idea of the behaviour of a beam of particles moving through a lattice. If the initial angle ψ is less than $\sim \psi_1$, the continuum picture of the string applies, and there are separate repulsive collisions with strings, the particle leaving the strings at the same angle ψ as it had prior to the collision. Such particles hardly come close to atoms, and their angle ψ is not changed as it would be by normal multiple scattering. This may be called the aligned beam of particles, the condition being that $\psi < C'\psi_1$, where C' turns out to be of order of 1-2. For the aligned beam, the approximation of ungoverned motion, mentioned in § 1, can not be valid.

From the formula (2.5) for the continuum potential it might seem as if there were an infinitely high barrier at $r = 0$. However, firstly we have seen from (2.9) that the continuum picture is not quite applicable when $\psi \gtrsim \psi_1$ (cf. Appendix A for a more detailed computation of critical angles). Secondly, if we use a continuum picture already the thermal vibration of atoms would lead to a smearing of the potential near $r = 0$, with a maximum $\sim Z_1 Z_2 e^2 d^{-1} \log(C^2 a^2/\varrho^2)$, where ϱ is the amplitude of vibration, and the resulting maximum potential remains of the order of E_1. From both points of views, if $\psi > C'\psi_1$ the particle moves rather freely through the lattice, and may easily be scattered by atoms in the usual way. In most respects, the penetration phenomena are then as in a random system. We therefore denote this part of the beam as the random beam.

Classical Rutherford shadow behind one atom

A simple and illustrative phenomenon is the shadow behind a repulsive scattering centre in an external, parallel beam of particles. The scattering is assumed to be classical (cf. (B.4) and (B.5)), and we suppose that there is a screen perpendicular to the beam, at a distance d behind the scattering centre. This idealized experiment may be said to represent a pair of atoms, the scattering centre being one atom, the second atom being placed in the screen, so that we ask for the probability of hitting the second atom.

An example of nearly isolated atomic pairs is found e.g. for nearest neighbours in the diamond lattice, i.e. in the $\langle 1\ 1\ 1 \rangle$-direction. Such pairs may also be regarded as incomplete strings, with successively two occupied and to unoccupied sites. The pair effect can occur not merely in a monatomic substance like Si, but also in e.g. ZnS, where all S atoms are shielded by Zn atoms in one direction, and conversely in the opposite direction.

For simplicity, we consider merely Rutherford scattering, corresponding to impact parameters $p \lesssim a$. Let the scattering centre be placed on the z-axis, the beam being parallel to this axis. A particle with impact parameter p hits the screen at a distance r from the z-axis, and for small angles of deflection r is given by

$$r = p + \frac{b}{p} d, \tag{2.11}$$

where $b = Z_1 Z_2 e^2/E$. The distance r has a minimum, $r_{\min} = 2\sqrt{bd}$, for $p = \sqrt{bd}$. The shadow region therefore has a parabolic shape, as a function of the distance d, since its edge is at $r = r_{\min} \propto d^{1/2}$.

In order to hit the centre of the screen, we must tilt the beam by an angle $\psi_{\min} = 2\sqrt{b/d} = \psi_1\sqrt{2}$, where ψ_1 is given by (2.9). The intensity distribution on the screen is easily obtained from (2.11). Let $f(r)$ be the intensity on the screen, the external beam containing one particle per unit area. Then, for large r, $f(r)$ tends to unity, whereas $f(r) = 0$ for $r < r_{\min}$. The particles aiming at $r < r_{\min}$ are pushed just outside $r_{\min}$, where $f(r)$ has a peak. In fact,

$$f(r) = \begin{cases} 0, & r < r_{\min} \\ \dfrac{1}{2}\left[\left(1 - \dfrac{r_{\min}^2}{r^2}\right)^{1/2} + \left(1 - \dfrac{r_{\min}^2}{r^2}\right)^{-1/2}\right], & r > r_{\min}. \end{cases} \tag{2.12}$$

The sharp edge at $r = r_{\min}$ is blurred when quantal corrections are taken into account, the blurring remaining small only when $\varkappa = 2Z_1 Z_2 v_0/v$ is large compared to unity (cf. (2.29)).

The number of particles missing on the screen inside $r_{\min}$ is $\pi r_{\min}^2$. The number missing inside r is $\pi r^2 - \int_{r_{\min}}^{r} 2\pi r dr f(r) = \pi r^2(1 - (1 - r_{\min}^2/r^2)^{1/2})$. For large r this implies that only half the missing number is compensated in Rutherford scattering with $p \ll d$. It is easy to show that, for screened atomic fields, the full compensation occurs for r larger than a. In fact, when (2.6′) holds, a 75 per cent compensation is obtained for $r = Ca$. Thus, for fast particles obeying eq. (2.9′) the compensation is divided in two equal parts, one occurring ar $r \gtrsim 2(bd)^{1/2}$, or $\psi \gtrsim \psi_1\sqrt{2}$, and the other at $r \sim Ca$, or $\psi \sim Ca/d$.

The critical angle $\psi_{\min}$ for a pair of atoms is apparently quite similar to that of a perfect string. Still, there are differences of major importance.

If we tilt by an angle of e.g. $\psi_{\min}/2$, the nearest approach to the centre of the screen will be $r_{\min}/2 = \sqrt{bd}$, which distance is much smaller than the corresponding distance of approach to a perfect string, $\sim a$, if (2.9′) is valid. In fact, both for strings and atomic pairs we must assume validity of (2.9′), in order that Rutherford scattering remains responsible for the phenomenon. The atomic pair is therefore much less effective than the string in pushing particles away from the atom. Another difference between atomic pairs and strings is that the atomic pair is less classical because there is only one repulsive collision instead of many. However, the most important difference between atomic pairs and strings is the small multiple scattering in the latter case, as will be discussed below.

Atomic planes

Another case of interest is that of a plane of atoms. Consider a particle moving not in any major string direction, but still nearly parallel to a plane in a lattice. There must then be some correlation between collisions with atoms, although in a weaker and less well-defined manner than for a string. Accordingly, one may expect effects of atomic planes in penetration. Like in the case of atomic pairs it is of interest to find the comparative merits of planes and strings.

A plane can give rise to governed motion of a particle, if the orbit of the particle, as derived from the continuum potential, involves many collisions with atoms. We therefore evaluate first of all the potential of a continuum plane, as obtained by smearing the atoms evenly in the plane*. As a function of the numerical value, y, of the distance from the plane, the continuum potential is

$$Y(y) = N \cdot d_p \int_0^\infty 2\pi r dr \cdot V(\sqrt{y^2 + r^2}), \tag{2.13}$$

where $N \cdot d_p$ represents the average number of atoms per unit area of the plane, d_p being the distance between planes. The ion-atom potential $V(R)$ is given by (2.3). The potential $Y(y)$ is similar to the string potential (2.2), but lower by a factor $\sim 2a/d$, when $r \lesssim 2a$. Further, in the plane — i.e. for $y = 0$ — the potential (2.13) has a finite value,

$$Y(0) = N \cdot d_p \cdot \int_0^\infty 2\pi R dR V(R) = \pi Z_1 Z_2 e^2 \cdot N d_p \cdot \bar{R}, \tag{2.14}$$

* The perfect plane has no preferred direction. The atoms may be assumed to be distributed as a two-dimensional liquid or, in simple estimates, random gas.

where $\bar{R}$ is the average radius of the 'atom', $\bar{R} = Z_2^{-1} \int_0^\infty 4\pi\varrho(R) \cdot R^3 dR$. The LENZ-JENSEN model[9] leads to $\bar{R} = 2.68\, a$, whereas (2.6′) implies $\bar{R} = 2Ca$.

By means of the standard atomic potential (2.6′) a simple estimate is obtained for the potential $Y(y)$

$$Y(y) = 2\pi Z_1 Z_2 e^2 \cdot N d_p \cdot [(y^2 + C^2 a^2)^{1/2} - y], \tag{2.15}$$

which expression may be compared with the corresponding one for a string, (2.6).

The criterion for use of continuum potential for a plane is more involved than for a string. Let the particle, when far away from the plane, have an angle θ with it, i.e. transverse energy $E_\perp = E \cdot \theta^2$. Even though many atoms contribute to the deflection of a particle, there remains an uncertainty in the nearest approach $y_{\min}$ to the plane. In contrast to the case of a string, the particle will usually not be deflected by atoms directly below its orbit, but it may happen that there is an atom directly below the orbit at minimum approach. Let us therefore demand that in this eventuality the deflection in the single collision is smaller than φ. According to (2.15), i.e. for the standard atomic potential, $y_{\min}$ is given by

$$\theta^2 = 2\pi b \cdot N \cdot d_p \cdot [(y_{\min}^2 + C^2 a^2)^{1/2} - y_{\min}], \tag{2.16}$$

and we demand

$$\theta > \varphi = -\frac{d \cdot U'(y_{\min})}{2E} = b \cdot \frac{1}{y_{\min}} \frac{1}{1 + \dfrac{y_{\min}^2}{C^2 a^2}}, \tag{2.17}$$

where the expression on the right-hand side is derived from the standard atomic potential (2.6′). When combining (2.16) and (2.17) we find that they contain two dimensionless parameters, $\zeta = y_{\min}/Ca$ and $\alpha = E_p/E$, where

$$E_p = \frac{Z_1 Z_2 e^2}{2\pi C^3 a^3 N \cdot d_p} \sim Z_1 Z_2^2 \cdot 30\,\text{eV}. \tag{2.18}$$

The condition (2.17) is then equivalent to

$$\zeta^2 (1 + \zeta^2)^2 [(\zeta^2 + 1)^{1/2} - \zeta] > \alpha. \tag{2.19}$$

If we demand that $y_{\min} \approx a$, this leads to $E > 3E_p$. In point of fact, the inequality (2.19) shows, on the one hand, that the continuum potential hardly ever holds at distances small compared to a, even though the energy E is very large. On the other hand, even for quite low energies the potential applies down to distances comparable with the atomic radius, $\bar{R} \sim 2Ca$. In view of the comparatively slow variation of $Y(y)$ with y, we may then normally assume that the potential barrier of a plane is not higher than

$$Y_{\text{eff}} = Y(0)/2, \tag{2.20}$$

and for quite low values of E/E_p the barrier becomes somewhat lower. So far, we have discussed merely one of the conditions for a continuum description of planes. We supplement this insufficient discussion by the description of a plane as a string of strings.

Plane described as string of strings

The limits of applicability of a continuum description are less obvious for planes than for strings. Some aspects of the properties of planes are illustrated by the following idealized picture. A plane of atoms can be treated as a string of strings, if the angles with a major string are not very large compared to ψ_1. This case is of particular interest also for studies of the way in which string effects and plane effects join.

Suppose that the angle ψ with a set of parallel major strings is of order of the characteristic angle ψ_1, so that for a wide region of impact parameters, l, with strings, the strings can be considered as continuum strings. The deflection can then be described in terms of the two-dimensional motion in the plane perpendicular to the strings, i.e. the transverse motion. Strings are arranged in a regular lattice, so that a plane consists of a row of strings, i.e. it can be conceived as a string of continuum strings. The transverse motion has a velocity $v_\perp = v \cdot \psi$, and the deflection by a string is determined by U(r). If the angle of deflection $\varphi_\perp$ in the transverse motion is small, it is obtained easily from the integrated force, and the result can be expressed in terms of the previously calculated plane potential Y in (2.13),

$$\varphi_\perp = -\frac{d_s \cdot Y'(l)}{2E \cdot \psi^2} \quad , \tag{2.21}$$

where d_s is the distance between strings. It is seen from (2.13) that the product $d_s \cdot Y$ depends on lattice constants only through $d_s \cdot N \cdot d_p = d^{-1}$, where d is the atomic spacing in the strings.

We may at first discuss the shadow behind one string, in analogy to the way in which we treated the Rutherford shadow behind an atom. This enables us to study both the case of a pair of strings and the validity of the continuum plane approximation. Consider a particle with transverse motion in the positive x-direction, and impact parameter l with a string placed in the origin, $(x,y) = (0,0)$. According to (2.21), the particle hits the line $x = d_s$ at a distance y from the x-axis, where

$$y = l + \frac{d_s^2 Y'(l)}{2E \cdot \psi^2} \quad . \tag{2.22}$$

We may write $y = \Phi \cdot d_s$, and find from (2.22) the minimum angle $\Phi_{\min}$ at which the centre of a string may be hit, due to the shadow from the previous string,

$$\Phi_{\min} = \frac{3}{2}\left(\frac{\pi}{2}\frac{\psi_1^2}{\psi^2}\frac{C^2 a^2}{d_s^2}\right)^{1/3}, \qquad \text{if} \qquad \psi^2 \ll \psi_1^2 \frac{\pi \cdot d_s}{2Ca} \quad . \tag{2.23}$$

If the inequality in (2.23) is not fulfilled, estimates of $\Phi_{\min}$ are not quite well-defined, since for small impact parameters l the continuum string is no longer applicable. If the inequality is fulfilled, the angle $\psi\Phi_{\min}$ remains smaller than that belonging to the continuum plane potential. In fact, the effective potential energy corresponding to $\Phi_{\min}$ is

$$Y_\psi = E \cdot \psi^2 \Phi_{\min}^2 = Y(0) \cdot \frac{9}{4}\frac{1}{(4\pi)^{1/3}} \cdot \left(\frac{\psi^2}{\psi_1^2}\frac{Ca}{d_s}\right)^{1/3} . \tag{2.24}$$

Thus, the effect of a plane disappears gradually in the neighbourhood of a string direction. This means that a string can stand out distinctly within a plane. However, for strings of high index number, the barrier belonging to (2.9) or (2.10) may be less than the barrier of the plane, and such strings can be engulfed by the planar effect.

Comparison of transverse potentials

In three cases, i.e. for channels, strings and planes, we have estimated continuum potentials, and we have also treated the case of atomic pairs. At high particle energies, cf. (2.9′), the potential barriers for major strings (and atomic pairs) are of order of $4Z_1 Z_2 e^2/d \sim Z_1 Z_2 \cdot 20\,\text{eV}$, since $d \sim 5a_0$. The barriers of major planes are, cf. (2.20), $5Z_1 Z_2 e^2 N d_p a \sim 5 \cdot Z_1 Z_2^{2/3}\,\text{eV}$, and thus lower than those of strings by a factor of $\sim 4Z_2^{1/3}$, such that critical angles are less by $\sim 2Z_2^{1/6}$. The barrier for proper channelling, perhaps $\sim 5\,\text{eV}$ for protons, is considerably lower than the two others. When comparing effects of strings and planes, however, one must first of all bear in mind that the string potential decreases more rapidly with distance than does the plane potential; the two potentials become equal at distances of order of $d/2$. The rapid decrease of the string potential makes penetration to the centre of string atoms more sensitive to e.g. temperature vibrations of atoms,

as will be discussed below. Moreover, there is a difference between strings and planes, because in the former case the particle motion is two-dimensional, while in the latter it is one-dimensional. However, strings and planes have in common the division of a particle beam into an aligned part which does not penetrate the potential barriers, and a random part which does. The aligned beam remains at distances larger than $\sim a$ in both cases. In the two latter respects, atomic pairs differ from strings and planes.

Quantal shadow behind an atom

As a counterpart to the classical shadow behind an atom, we may finally consider the quantum mechanical shadow in the limit where quantal perturbation theory applies for single collisions. This will also indicate a characteristic feature of string effects in a wave picture. The essential point in the following calculation is that we are not concerned with the standard case of scattering theory, where the scattered wave is recorded at infinity.

As before, we consider a scattering centre located at the origin, with potential $V(\vec{R})$, where $\vec{R} = (x, y, z)$. At a distance d behind the centre is placed a screen, i.e. with coordinates $\vec{R}' = (x', y', z' = d)$. The incoming particle has a wave function $\exp(ikz)$, where $k = M_1 v/\hbar$. Scattering angles are assumed to be small. The range, a, of the potential is small compared to the atomic spacing d. In first order perturbation theory, the wave function $\psi(\vec{R}')$ becomes

$$\psi(\vec{R}') = e^{ikd} - \frac{M_1}{2\pi\hbar^2}\int \frac{e^{ik|\vec{R}-\vec{R}'|}}{|\vec{R}-\vec{R}'|} V(\vec{R}) e^{ikz} d^3R. \tag{2.25}$$

Since all coordinates in the x and y directions are small compared to d, we find by series development of $|\vec{R}-\vec{R}'|$, and performing the integration over z,

$$\psi(\vec{R}') = e^{ikd}\left[1 - \frac{M_1}{2\pi\hbar^2}\int dx \int dy U(r) e^{\frac{ik}{2d}\{(x-x')^2+(y-y')^2\}}\right], \tag{2.26}$$

where $U(r)$ is given by (2.2) and (2.4).

At this stage it is essential to notice that the exponential in the integrand is a rapidly oscillating function. In fact, since U contains the screening length a, the exponential varies rapidly if

$$\frac{a^2}{\lambda \cdot d} \gg 1. \tag{2.27}$$

For $Z_2 \gg Z_1$ and with $d \approx 5a_0$, the inequality (2.27) is equivalent to

$$\frac{M_1}{m} \cdot \frac{v}{v_0} \cdot \frac{1}{5Z_2^{2/3}} \gg 1, \tag{2.27'}$$

and therefore the condition (2.27) is easily fulfilled for heavy particles. Another way of expressing (2.27') is to say that the momentum of the particle, $M_1 v$, should be very large compared to the average momentum, $mv_0 Z_2^{2/3}$, of an electron in the Thomas-Fermi atom. We conclude that even in the quantal perturbation treatment there is a considerable localization of path in analogy to the classical treatment. This is because the distance d between atoms is not large, in the sense stated by (2.27).

The results obtained in (2.26) and (2.27) show that, in a general quantal treatment, the contributions to the wave function at a certain point in space are due to scattering by atomic fields within a narrow cone opposite to the direction of motion. The disregard of all atomic fields except those within the cone (or e.g. the string), is equivalent to the basic assumptions on page 9ff.

We introduce (2.4) in (2.26),

$$|\psi(\vec{R'})|^2 = \left|1 - \frac{\varkappa}{4\pi} \int\int \frac{dx\,dy}{\lambda\!\!\!^{-} d} \xi\left(\frac{r}{a}\right) e^{\frac{i}{2\lambda\!\!\!^{-} d}[(x-x')^2 + (y-y')^2]}\right|^2, \tag{2.28}$$

where $r^2 = x^2 + y^2$. Suppose that $x' = y' = 0$, and apply the estimate (2.6) for $\xi(r/a)$. Then, for low values of $\varkappa$ and when (2.27) holds,

$$|\psi(0,d)|^2 \cong \left|1 - \frac{\varkappa}{2}\left(\frac{\pi}{2} + i\log\left(\frac{a^2 C^2 \gamma}{2\lambda\!\!\!^{-} d}\right)\right)\right|^2 \sim 1 - \frac{\varkappa\pi}{2}, \tag{2.29}$$

where γ is Euler's constant. The right-hand side is the limit for small $\varkappa$ of a familiar result belonging to a pure Coulomb field, $|\psi(0,d)|^2 = \pi\varkappa[\exp(\pi\varkappa) - 1]^{-1}$. For attractive fields we may here regard $\varkappa$ as a negative quantity, and obtain an increase in intensity behind the scattering centre.

§ 3. Statistical Treatment and Energy Loss

The previous chapter was concerned with basic problems and with the accessibility of different regions in a crystal lattice. In order to study in more detail the total behaviour of a beam of particles in a crystal lattice, we may, as a first approximation, apply the simple continuum picture of strings (and planes).

The continuum picture implies conservation of the velocity component parallel to the string. The motion may therefore be studied completely in terms of its projection on a plane perpendicular to the string. In this transverse motion, the velocity far from a string is $v_\perp = v\sin\psi \cong v\psi$, and the corresponding transverse energy is $E_\perp = E\cdot\sin^2\psi \simeq E\cdot\psi^2$. The potential is $U(r)$, and we shall use several of the approximate formulae for $U(r)$ introduced in § 2.

Available phase space in transverse motion

The use of statistical mechanical estimates is a powerful alternative to detailed studies of separate successive collisions with strings. We shall at first consider statistical estimates of particularly simple type. We use the continuum picture, and we need consider only the transverse motion; all angles ψ can be assumed to be small. For fixed values of velocity v and transverse energy $E_\perp$, we then ask for the two-dimensional probability distribution in a total potential $U_{\text{tot}} = \sum_i U(\vec{r} - \vec{r}_i)$, where U is given by (2.4), and $\vec{r}_i = (x_i, y_i)$ is the position of the i'th string of atoms. Evidently, we

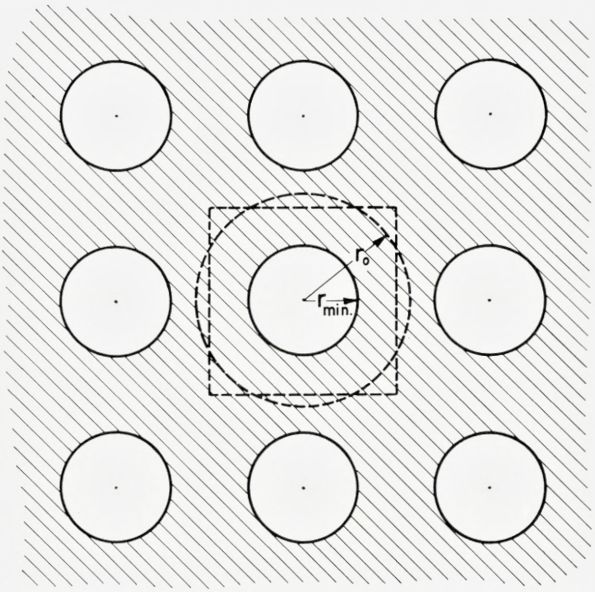

Fig. 1. Transverse plane of strings for simplest cubic lattice. The square indicates unit cell, and the dashed circle with radius r_0 is approximate unit cell. Shaded area outside circles with radius $r_{\min}$ illustrates accessible portion of the plane for a given transverse energy. There is uniform probability distribution in shaded area according to two-dimensional continuum picture.

may usually confine the treatment to one unit cell in the two-dimensional $\vec{r}$-plane, containing one string. For most purposes, we can assume that the unit cell is a circle around the string, with radius r_0, such that its area is $\pi r_0^2 = (N \cdot d)^{-1}$. We often disregard the potential due to neighbouring strings, so that the potential becomes simply $U_{\text{tot}} \approx U(r)$; this approximation applies if the transverse energy is not exceedingly low.

The beam of particles has some initial probability distribution, e.g. corresponding to a given direction in $p_\perp$-space. As a function of time t, or depth of penetration $z = vt$, the distribution will be $P(\vec{p}_\perp, \vec{r}, t)$. There will be a trend towards statistical equilibrium in the transverse phase space. Let us consider the equilibrium distribution within a transverse energy shell. We introduce the available momentum space as a function of $\vec{r}$, when the transverse energy is between $E_\perp$ and $E_\perp + dE_\perp$. Since the volume in two-dimensional momentum space is proportional to $dE_\perp$, the equilibrium probability distribution becomes

$$P_0(E_\perp, \vec{r}) = \begin{cases} \dfrac{1}{A}, & E_\perp > U_{\text{tot}}(\vec{r}), \\ 0, & E_\perp < U_{\text{tot}}(\vec{r}), \end{cases} \tag{3.1}$$

where the constant A is the accessible area in a unit cell with total area $A_0 = N^{-1} d^{-1}$. When the accessible portion of the unit cell is large, or $A \approx A_0$, we can simply disregard the overlapping of string potentials. This leads to $P_0 = 1/A \simeq 1/A_0$, and $U_{\text{tot}}(\vec{r}) = U(r)$, where r is the distance from a string.

One-dimensional distribution

It is interesting to notice the extreme simplicity of the probability distribution in two-dimensional space, i.e. (3.1), as compared to both one- and three-dimensional spaces. Thus, the one-dimensional equilibrium on an energy shell, corresponding to continuum planes, becomes

$$P_0(E_\perp, y) = \begin{cases} \dfrac{C}{d_p} \left(\dfrac{E_\perp}{E_\perp - Y(y)} \right)^{1/2}, & E_\perp > Y(y), \\ 0, & E_\perp < Y(y), \end{cases} \tag{3.2}$$

where d_p is the distance between planes and C a normalization constant. In the one-dimensional motion the particles stay with maximum probability at the edges of forbidden regions, where the velocity is lowest. The formula (3.2) has several consequences different from those of (3.1). Thus, when $E_\perp$ is large, higher than $Y_{\max}$, all values of y are allowed, but the particle still feels the potential—in contrast to (3.1)—and stays with increased probability near the planes, where Y is highest.

Trend towards equilibrium on transverse energy shell

Having studied the equilibrium distribution on an energy shell in the transverse motion, we may next estimate how quickly the equilibrium distribution is attained. A measure of this is the change of average transverse momentum, $\langle \vec{p}_\perp \rangle$. Suppose that strings can be considered a good approximation. It is easily shown that

$$\langle \vec{p}_\perp \rangle = \langle \vec{p}_\perp \rangle_0 \cdot \exp(-z/\lambda_\perp), \tag{3.3}$$

where $\langle \rangle_0$ denotes initial averages for $z = 0$, and where the mean free path length $\lambda_\perp$ of the particle is

$$\frac{1}{\lambda_\perp} = N \cdot d \cdot \sin\psi \int_{-\infty}^{+\infty} dl \cdot (1 - \cos\varphi(l)), \tag{3.4}$$

$\varphi(l)$ being the scattering angle of the transverse motion as a function of impact parameter with the string. It is to be noted that $\lambda_\perp \cdot \sin\psi$ is the so-called transport mean free path of the transverse motion, i.e. on the average the particle moves $\lambda_\perp \cdot \sin\psi$ in the transverse plane, in the direction of $\langle \vec{p}_\perp \rangle_0$.

If we assume that the minimum distance of approach exceeds $\sim a$, and the approximation $\xi = \pi a/(2r)$ is used for the string potential in (2.4), we get by a simple computation a direct estimate of $\lambda_\perp$,

$$\frac{1}{\lambda_\perp} = \frac{\pi^2}{4} \cdot N \cdot d \cdot a \frac{\psi_1^2}{\psi} \quad , \quad \text{for} \quad \xi\left(\frac{r}{a}\right) = \frac{\pi a}{2r} \quad . \tag{3.5}$$

Therefore, when $\psi < \psi_1$ the mean free path $\lambda_\perp$ is less than $1/(Nda\psi_1)$, the latter quantity being of order of 1000 atomic layers or less. After an energy loss of perhaps 1-10 keV, a proton attains equalization of distribution within the transverse energy shell.

The results (3.4) and (3.5) are based on random collisions for the transverse motion in the two-dimensional lattice of strings. However, as discussed in § 2, p. 19, this lattice contains strings of strings, or planes. When the direction of $\vec{p}_\perp$ is not far from a plane direction, there is again a reduction of scattering, but now in the two-dimensional motion. In this limit, continuum planes are applicable and the primary equalization of the distribution is in the one-dimensional motion, leading to the equilibrium described by (3.2). The mean free path for the one-dimensional equalization must be of order

of $\lambda_p \sim d_p/\varphi$, where φ is the angle between $\vec{v}$ and the plane. At this stage we need not treat further such questions of more detailed kind.

The quick scattering in azimuthal angle indicates that an assumption of statistical equilibrium on a transverse energy shell is often a fair approximation. Moreover, suppose that experimental conditions are such that initially an average is actually performed around a string direction, i.e. with respect to azimuthal angle. We then start from equalization on the transverse energy shell, which distribution has stable symmetry in the continuum picture.

Basic statistical averages over transverse motion

These results justify, so far, the use of (3.1). As a consequence of (3.1), we can for any function f, depending on $\vec{p}_\perp$ and $\vec{r}$, obtain first its average on an energy shell

$$f(E_\perp) = \frac{1}{A}\int dx \int dy \; f(\vec{p}_\perp, \vec{r}), \tag{3.6}$$

or, equivalently, for not too low $E_\perp$,

$$f(E_\perp) = \frac{1}{\pi(r_0^2 - r_{\min}^2)} \int_{r_{\min}}^{r_0} 2\pi r dr \; f(p_\perp, r), \tag{3.6'}$$

where $f(p_\perp, r)$ is the average of $f(\vec{p}_\perp, \vec{r})$ over angles, and $r_{\min}$ is determined by $E_\perp$ through the relation $U(r_{\min}) = E_\perp$. The formula (3.6′) is utilized repeatedly in the following. If $r_{\min}^2 \ll r_0^2$, the normalization factor is $(\pi r_0^2)^{-1} = N \cdot d$, and the upper limit in the integration may often be replaced by ∞.

When the transverse energy is so low that the motion is confined to small unconnected areas (proper channelling), the integration in (3.6) can be approximately within an ellipse or circle around minimum of potential, and with area A.

Second, we can determine the final average f of $f(E_\perp)$ over the probability distribution in ψ, i.e.

$$\langle f \rangle = \int g(E_\perp) f(E_\perp) dE_\perp, \tag{3.7}$$

where $g(E_\perp)$ is the probability density per unit transverse energy.

The function $g(E_\perp)$ will change with penetration depth, because of multiple scattering, i.e. lack of conservation of transverse energy. Multiple scattering is treated in § 4. Before doing that, we find further properties be-

longing to particles with a given transverse energy. In fact, we have so far assumed that the total energy of a particle is conserved. We must therefore estimate the nuclear and electronic stopping for a particle of given transverse energy.

Statistical estimate of nuclear stopping

When the particle passes one atom at a distance r, and has a small angle of deflection φ, one obtains directly in terms of $U(r)$ defined in (2.2), cf. also (2.1′),

$$\varphi = -\frac{d \cdot U'(r)}{2E}, \tag{3.8}$$

and therefore the energy transfer in this elastic collision is

$$T_n = \frac{d^2}{2M_2 v^2}[U'(r)]^2. \tag{3.9}$$

For aligned particles with a given value of $E_\perp$, we may average (3.9) over the available part of the unit cell according to (3.6), and obtain

$$T_n(E_\perp) = \frac{d^2}{2M_2 v^2}\frac{1}{A}\int_A dx \int dy \sum_j U'^2(|\vec{r} - \vec{r}_j|), \tag{3.10}$$

where $\vec{r}_j$ are the transverse coordinates of strings. Since we normally do not consider extremely low transverse energies, we may introduce (3.6′) in (3.10), assuming $r_{\min}^2 \ll r_0^2$,

$$T_n(E_\perp) = \frac{\pi N \cdot d^3}{M_2 v^2}\int_{r_{\min}}^{\infty} r dr U'^2(r), \tag{3.10′}$$

where the usual upper limit of the integration, r_0, is more correctly replaced by ∞. The average energy loss in (3.10) and (3.10′) is equal to $T_n(E_\perp) = N \cdot d \cdot S_n(E_\perp)$, where $S_n(E_\perp)$ is the stopping cross section for a given value of $E_\perp$. The integration in (3.10′) may be performed explicitly and the result expressed in terms of $E_\perp$, if the standard atomic potential (2.6) is used.

The main contribution to the integral in (3.10′) is in the vicinity of the lower limit, $r_{\min}$. If $U(r)$ varies as $r^{-\nu}$ when $r \approx r_{\min}$, we get directly from (3.10′) the nuclear stopping as a function of transverse energy

$$S_n(E_\perp) = \frac{\pi \cdot \nu}{4} d^2 \frac{E_\perp^2}{E} \cdot \frac{M_1}{M_2} \quad , \tag{3.11}$$

because $U(r_{\min}) = E_\perp$. Since ν is nearly equal to 1 for $a < r_{\min} < 2a$, increasing slowly to values ~ 2 for $r_{\min} > 2a$, the value of ν in (3.11) is not very sensitive to the magnitude of $E_\perp^2$, and (3.11) gives a useful first estimate of the nuclear stopping. At the same time, the distribution in magnitude of the individual energy losses is also implicitly given by (3.10′). The stopping cross section (3.11) may be compared with the normal nuclear stopping in a random gas, cf. (4.2). When comparing with (4.2), (3.11) is found to imply that $L_n(E_\perp) = (\nu/2) \cdot (E_\perp / E\psi_1^2)^2$, which is much smaller than for normal nuclear stopping at high energies, where $L_n = \log(1.29\varepsilon) \sim 5$–$10$; it should be noted that (3.11) is applicable only for $E_\perp \lesssim E\psi_1^2$. In any case, for swift particles the nuclear stopping cross section S_n is quite small compared to electronic stopping S_e.

Nuclear energy loss in single collision with string

The above application of phase space in transverse motion resulted in statistical estimates, (3.10) and (3.11), of average nuclear stopping. However, it is also of interest to find the energy loss in an individual encounter between ion and string, characterized by the energy E of the particle, and its initial angle ψ and impact parameter l with the string.

The energy loss to one atom, at a distance r, is given by (3.9). In a string collision r is a certain function of time, $r = r(t)$. Integrating (3.9) over the orbit, we thus obtain the energy loss to the string, $\tau_n(l,\psi)$,

$$\tau_n(l,\psi) = \frac{d}{2M_2 v} \int_{-\infty}^{+\infty} U'^2(r(t))dt. \tag{3.12}$$

The integration in (3.12), containing the radial motion $r(t)$ as a function of time, is usually not simple, but may be readily performed if the potential $U(r)$ is proportional to r^{-1} or to r^{-2}. It can then also be verified that an integration of (3.12) over all impact parameters results in the stopping cross section (3.10′). In the present context we omit more detailed evaluations of type of (3.12), one reason being that except at exceedingly low energies the nuclear energy loss is negligible compared to electronic energy loss.

Electronic stopping

Even though we made only cursory estimates of nuclear stopping, that case can be treated in a comprehensive manner, and the accuracy may be easily improved. The electronic stopping is less simple because we must

distinguish between a number of different cases. Still, one qualitative expectation can be stated generally; at a fixed particle energy E, but decreasing $E_\perp$, the electronic stopping is expected to decrease more slowly than does nuclear stopping. The ratio between electronic stopping and nuclear stopping should therefore be higher in the aligned beam than in the random beam.

We study primarily the important case of electronic stopping at those high particle velocities—and low charge numbers Z_1—where the Bethe-Bloch formula applies. This formula may be written as

$$\frac{dE}{dR} = S_e \cdot N \cdot Z_2 = \frac{4\pi Z_1^2 e^4}{mv^2} Z_2 \cdot N \cdot L_e, \tag{3.13}$$

where N is the number of atoms per unit volume, and S_e the stopping cross section per electron. The factor L_e is approximately given by

$$L_e \cong \log \frac{2mv^2}{\mathrm{I}}, \tag{3.14}$$

provided the velocity is so high that $x = v^2/(v_0^2 Z_2) \gg 1$, and[13) 14)] $v/v_0 > Z_1^{2/3}$. The quantity I is the average excitation potential, $\mathrm{I} \approx \mathrm{I}_0 \cdot Z_2$, and $\mathrm{I}_0 \approx 10$ eV.

When (3.14) applies, one may divide collisions with electrons in two groups, the distant resonance collisions and the close collisions with large momentum transfers to electrons (cf. Bohr[12)]). Since the phenomena are largely of quantum mechanical type, one may not apply classical orbital pictures in every detail for collisions between an electron and the particle. The precise distinction between close and distant collisions is in terms of, respectively, large and small momentum transfers. However, one may distinguish between the particle being outside the electronic orbit, where only resonance collisions occur, and inside the orbit, where close collisions occur with a probability distribution given essentially by the Rutherford scattering law. In a qualitative way, it is well-known from the derivation of the Bethe formula[12) 15)], that for very fast particles the stopping is asymptotically contributed equally by close and distant collisions. This turns out to hold also in a precise manner (equipartition rule[16)]), at not too low particle velocities. A detailed discussion of the dependence of energy loss on the space track of a particle of arbitrary velocity requires a generalization of the usual description and will be published separately.

From these considerations it seems proper, for large x, to replace (3.13) by

$$\frac{dE}{dR}(\vec{R}) = S_e \cdot [(1-\alpha)NZ_2 + \alpha \cdot \varrho(\vec{R})], \tag{3.15}$$

where $\varrho(\vec{R})$ is the density of electrons at the point in space through which the particle moves, and where $\alpha \gtrsim 1/2$, α being the closer to $1/2$ the higher the value of $x = v^2/(v_0^2 Z_2)$. This result means directly that the stopping cross section for a swift particle penetrating a thin foil can at most be reduced by a factor $\approx 1/2$. As we shall see, it can also increase by a factor slightly above unity, cf. § 5.

The increase per path length in square fluctuation of energy loss, $d(\Delta E)^2/dR$, in the case where (3.13) applies, is proportional to $Z_2 N$. The fluctuation contribution is due to close collisions only. In the present case, this contribution must be obtained by replacing the average electron density $Z_2 N$ by $\varrho(\vec{r})$. This straggling contribution, as a function of $\vec{r}$, becomes (cf. Bohr[12])

$$\left(\frac{d(\Delta E)^2}{dR}\right)_e = 4\pi Z_1^2 e^4 \cdot \varrho(\vec{R}). \tag{3.16}$$

A somewhat similar formula[13] holds at velocities $v < v_0 Z_2^{1/2}$. According to (3.16), the straggling depends more strongly on ϱ than does the stopping cross section (3.15).

We consider statistical equilibrium at a certain transverse energy $E_\perp$, and introduce an effective charge number $Z_2^*(E_\perp)$ such that with $U(r_{\min}) = E_\perp$ the number of electrons per atom outside the distance $r_{\min}$ from the string is $Z_2^*(E_\perp)$. Averaging (3.15) by means of (3.6′), the electronic stopping cross section is found to be

$$S_e(E_\perp) = S_e \cdot \left[1 - \alpha + \alpha \frac{Z_2^*(E_\perp)}{Z_2}\right], \tag{3.17}$$

where S_e is given by (3.13). The ratio $Z_2^*(E_\perp)/Z_2$ is according to (3.22) and (3.6′),

$$\frac{Z_2^*(E_\perp)}{Z_2} = \frac{d \cdot r_{\min} \cdot U'(r_{\min})}{2 Z_1 Z_2 e^2}. \tag{3.18}$$

Thus, $Z_2^*(E_\perp)/Z_2$ is approximately equal to $\nu E_\perp/(E\psi_1^2)$, if $U(r) \propto r^{-\nu}$ near $r_{\min}$, cf. also (3.11). When the atomic model (2.6) is introduced in (3.18), the following simple formula is obtained

$$S_e(E_\perp) = S_e \cdot \left[1 - \alpha \exp\left(-\frac{2E_\perp}{E \cdot \psi_1^2}\right)\right]. \tag{3.19}$$

The formula (3.19) shows that the dip in electronic stopping is somewhat narrower in angle ψ than are string effects where penetration to the centre of strings is necessary. The direct significance of the characteristic angle ψ_1 is also clearly indicated. It is noteworthy that the atomic screening radius a does not enter, in spite of (3.19) being based on (2.6), where the screening radius is an important parameter. The formula (3.19) contains the usual error belonging to continuum potentials, i.e. the stopping does not rise above the normal stopping S_e when $E_\perp \gtrsim E\psi_1^2$, and compensation of the dip (cf. § 5) is not obtained. The error is not serious, however, because the rise above normal stopping is rather small.

The average straggling energy loss is immediately found from (3.16) and (3.6′),

$$\left(\frac{d(\Delta E)^2}{dR}\right)_e = 4\pi Z_1^2 e^4 N \cdot Z_2^*(E_\perp), \tag{3.20}$$

where $Z_2^*(E_\perp)$ may be replaced by the estimates in (3.18) or (3.19).

Electronic energy loss in single collision with string

The electronic energy loss, $\tau_e(l, \psi)$, in a single collision with a string, at impact parameter l and initial angle ψ, can also be derived on the basis of (3.13) and (3.15). But we disregard the resonance stopping, i.e. the first term in (3.15), since it takes place independently of a string collision. The energy loss in a single collision with an atom at impact parameter r is then, from the second term in (3.15),

$$T_e(r) = \frac{S_e}{2} \cdot d \cdot \varrho_s(r) = \frac{S_e}{2} \int_{-\infty}^{+\infty} dz \cdot \varrho(\sqrt{z^2 + r^2}), \tag{3.21}$$

where $\varrho(R)$ is the electron density in an atom, at a distance R from the nucleus, and where the electron density $\varrho_s(r)$ of the continuum string is

$$\varrho_s(r) = \frac{1}{4\pi Z_1 e^2} \frac{1}{r} \frac{d}{dr}(rU'(r)). \tag{3.22}$$

As an example, we choose again the approximation $U = Z_1 Z_2 e^2 \pi a/(2dr)$, and obtain

$$\varrho_s(r) \simeq \frac{Z_2 a}{8d} \frac{1}{r^3} \quad . \tag{3.23}$$

We next integrate (3.21) over the encounters with atoms along a string, using (3.23) and the hyperbolic orbit of an r^{-1}-potential. The electronic energy loss in one collision with a string becomes, at a transverse energy $E_\perp = E\psi^2$ and impact parameter l,

$$\tau_e(l,\psi) = \frac{S_e \cdot Z_2 \cdot a}{8d} \cdot \frac{1}{tg\psi} \cdot \frac{1}{l^2} \left(1 - \frac{b_\perp}{2l} \operatorname{arctg} \frac{2l}{b_\perp}\right), \tag{3.24}$$

where $b_\perp$ is defined by $U(b_\perp) = E_\perp$, i.e. $b_\perp = \pi a \psi_1^2/(4\psi^2)$. If we integrate (3.24) over all l, we obtain the formula (3.18), with $\nu = 1$.

In order to estimate the straggling in energy loss, we can compare the maximum energy loss in a string collision, i.e. $\tau_e(0,\psi)$ in (3.24), with the usual maximum energy transfer to an electron, $2mv^2$. The ratio $\tau_e/2mv^2$ can be large compared to unity. If in (3.13) we introduce $L \simeq 1.5 \cdot x^{1/2} = 1.5 \cdot (v^2/v_0^2 Z_2)^{1/2}$, which formula applies approximately when x is of order of 1[13], (3.24) leads to

$$\tau_e < \tau_e(0,\psi) \approx \frac{a_0}{a} \left(\frac{a_0}{d}\right)^{1/2} \cdot \left(\frac{M_1}{m}\right)^{1/2} Z_1^{3/2} \cdot 70\,\mathrm{eV}, \tag{3.25}$$

which would be ~ 3keV for protons. Since this is an upper limit to τ_e, the energy loss is normally divided into bits much smaller than (3.25), so that the straggling is small.

§ 4. Scattering of Aligned and Random Beams

We have seen that a beam of fast particles, having some probability distribution in direction, can be divided roughly in two parts. For angles less than ψ_1 (or ψ_2, at low energies) we are concerned with the aligned part of the beam, while angles large compared to ψ_1 constitute the random part of the beam. The part between $\sim \psi_1$ and $\sim$ twice ψ_1 is a transition region. In most respects, the two parts have a quite different behaviour. Thus, the aligned part was found to have a smaller stopping cross section $S(E_\perp)$ than has the random part. Moreover, in first approximation the two parts of the beam appear not to communicate at all. Consider an ion in the random part of the beam. It can easily collide with atoms and be scattered to other directions within the random beam. If it were to be scattered into the aligned beam, a comparatively close collision is required—i.e. impact parameters much smaller than a. However, when the ion subsequently emerges from essentially the centre of the string, it cannot easily become aligned, since ions in the aligned beam do not come closer to the string than $\sim a$. Scattering

from random beam to aligned beam therefore seems prohibited. Conversely, an ion in the aligned beam will in the continuum approximation keep a constant ψ far away from strings, i.e. a constant transverse energy $E_\perp$, changing merely its azimuthal angle in a more or less random manner. This indicates the difficulty of being scattered into the random beam.

It is therefore important to discuss those phenomena which may be responsible for transitions between aligned and random beam and for angular diffusion within the beams, i.e. lack of conservation of transverse energy. In the discussion we may distinguish between three groups of phenomena responsible for transitions between aligned and random beams.

The first group concerns deviations from the picture of parallel continuum strings, with a potential $U(r)$ or $U_{\text{tot}}(\vec{r})$, cf. (3.1). Deviations can be due to thermal vibrations, including zero-point vibrations of atoms, which implies that the force on the particle fluctuates; the effect of fluctuation of atomic positions will be studied in some detail. Deviations must also occur when there are defects and impurities in the lattice. Defects and impurities lead to important scattering effects, but are of variable size and can be quite small in pure and perfect crystals. A special kind of deviation arises from the periodicity of a perfect string, which gives fluctuations of the path as compared to the motion in a continuum potential $U(r)$. The periodicity of perfect strings normally gives rise to only a small scattering effect (cf. Appendix A).

The second kind of scattering is due to deviations from classical motion in a conservative force field. It is necessary to estimate the magnitude of quantum mechanical corrections to classical mechanical motion (cf. Appendix B). Moreover, a single collision between an ion and an atom is quasi-elastic, so that the force field is not strictly conservative. In first approximation, the deviations from elastic collisions are included in electronic stopping and the damping effect, cf. below.

The above two groups of phenomena lead to an average increase of $E_\perp$. A third effect may be singled out, especially because it tends to reduce $E_\perp$. Suppose that electronic stopping is dominating, and that the motion is in a continuum potential. Now, if the slowing-down force is directed against the motion and the energy loss is δE, the corresponding average change in $E_\perp$ turns out to be $\delta E_\perp \cong -\beta \cdot \delta E \cdot E_\perp / E$, where $\beta \sim 0.5 - 1$. Although small, this damping effect can in some cases compete even with multiple scattering. We may also compare the damping with the change of transverse potential barrier. At high energies E, the transverse barrier is constant, while at low energies it may decrease as $E^{1/2}$ during slowing-down, cf. (2.10′). The damping by itself thus exceeds the decrease of the barrier.

Multiple scattering

When discussing the changes in ψ, or $E_\perp$, along the particle paths, it is useful to consider at first the normal case of multiple scattering in a random system. Let ψ_x and ψ_y be the angles with the z-axis of the projection of the direction of motion on the $x-z$ and $y-z$ planes, respectively, so that $\vec{\psi} = (\psi_x, \psi_y)$ and $\psi = (\psi_x^2 + \psi_y^2)^{1/2}$. The average square fluctuation in angle is then $\Omega^2 = \langle(\vec{\psi} - \langle\vec{\psi}\rangle)^2\rangle$. We study the change of Ω^2 as a function of penetration depth. It is well known (cf. BOHR[12]) that the increase in average square fluctuation in angle, due to nuclear collisions, is approximately given by

$$(\delta\Omega^2)_n \simeq \frac{M_2}{M_1} \cdot \frac{(\delta E)_n}{E} = \frac{(\delta E)_e}{E} \cdot \frac{Z_2 m}{M_1} \cdot \frac{L_n}{L_e} \quad , \tag{4.1}$$

where[6]

$$\left(\frac{dE}{dR}\right)_n = \frac{4\pi Z_1^2 Z_2^2 e^4}{M_2 v^2} N \cdot L_n, \qquad L_n \simeq \log(1.29\,\varepsilon), \tag{4.2}$$

the reduced energy ε being given by (1.3). The formulae (4.2) and (4.1) apply for ε large compared to unity. When $\varepsilon \gtrsim 10^3$, it is seen that $L_n \sim 5 - 10$, so that L_n is not sensitive to the value of ε.

There is a similar increase in average square fluctuation in angle, due to electronic collisions, and derived from Rutherford scattering in close collisions between particle and atomic electrons,

$$(\delta\Omega^2)_e = \frac{m}{2 M_1 E} \cdot S_e \cdot \varrho(\vec{R}) \cdot \delta R. \tag{4.3}$$

In a random system, where the density of electrons $\varrho(\vec{R})$ is replaced by its average, NZ_2, the electronic contribution is much smaller than the nuclear one, (4.1), by a factor $\sim 2Z_2 L_n / L_e$. The formula (4.3) is valid only if v is larger than the electronic orbital velocities, or rather $x = v^2/v_0^2 Z_2 \gg 1$.

In the case of the random beam, where all nuclear collisions are permitted, we can apply formula (4.1), with neglect of the electronic contribution (4.3). We can also use (4.1)—both for the random and aligned beams—in the case of interstitials, impurities that break the symmetry, amorphous surface layers, etc. Then, N represents the density of scattering centres, Z_2 being their atomic number.

In the present context, it is appropriate to consider ψ_1 as a standard angle, also for a random system without string effects. We introduce the path length, l_{n,ψ_1}, for which the average square multiple scattering in nuclear

collisions (4.1), applicable for the random beam, becomes equal to ψ_1^2. Evidently,

$$l_{n,\psi_1} = \frac{2}{\pi N d^2 \cdot L_n \psi_1^2} \quad , \tag{4.4}$$

and the corresponding total energy loss of a random beam, or in a random system, is according to (3.13)

$$\delta E_{\psi_1} = \frac{2 Z_1 e^2}{d} \frac{L_e}{L_n} \cdot \frac{M_1}{m} \quad , \tag{4.5}$$

i.e. of the order of $Z_1 \cdot A_1 \cdot 10\,\mathrm{keV}$ in the case of swift particles, for which $L_e/L_n \sim 1/2$.

In connection with (4.4) and (4.5), one should also consider single scattering by angles larger than ψ_1. The mean free path for such single scattering is larger than (4.4) by a factor $2L_n \sim 10$. We may therefore often disregard single scattering, but for special purposes it becomes important, cf. (6.15).

Starting from an initially well-defined direction, e.g. corresponding to polar angle $\Psi = 0$, the distribution becomes approximately Gaussian,

$$P(\Psi) 2\pi \Psi d\Psi \simeq \exp\{-\Psi^2/\Omega^2\} 2\Psi d\Psi/\Omega^2, \tag{4.6}$$

where Ω^2 is obtained by integration of (4.1). The Gaussian is a consequence of many small scattering processes. For large Ψ the actual distribution has a tail decreasing more slowly than (4.6), and due to large angle single scattering. The approximation of WILLIAMS and BOHR[12) 17)] may be applied. If (4.3) is not negligible, it must be added to (4.1), and (4.3) contributes to the Gaussian only—not to the tail.

Consider next particles in the aligned beam. We may at first estimate the contribution to multiple scattering from electronic collisions. In analogy to (4.4), we introduce the path length l_{e,ψ_1}, for which $(\delta\Omega^2)_e$ becomes equal to ψ_1^2. Averaging (4.3) according to (3.6′), we obtain

$$l_{e,\psi_1} = \frac{4 Z_2}{\pi N d^2 L_e \psi_1^2} \cdot \frac{Z_2}{Z_2^*(E_\perp)} \quad . \tag{4.7}$$

The factor $Z_2/Z_2^*(E_\perp)$ is given by (3.18) or (3.19), and tends to unity for the random beam, while for the aligned beam it becomes large when $\psi \to 0$. The path length l_{e,ψ_1} is larger than l_{n,ψ_1} in (4.4), by a factor of at least $2Z_2$.

The strong multiple scattering (4.1) for a random system disappears completely for the aligned beam colliding with continuum strings, i.e. when conservation of transverse energy applies. In § 3 it was found that part of the multiple scattering reappears as a quick trend towards uniform distribution on the transverse energy shell, cf. (3.4). Another part reappears due to deviations from perfect strings. Thus, suppose that in one transverse atomic plane there is a deviation $\delta\vec{K}(\vec{r})$ from the usual transverse force $\vec{K} = -\operatorname{grad} U(\vec{r})$. This gives a change in the transverse momentum $\vec{p}_\perp$, i.e. approximately

$$\delta\vec{p}_\perp = \frac{d}{v}\delta\vec{K}(\vec{r}). \tag{4.8}$$

When the square of this scattering is summed over the atoms along a string (or over successive transverse atomic planes), we obtain the change in average transverse energy, due to string imperfections, i.e. on the path length δR,

$$\delta\langle E_\perp\rangle = \sum \frac{(\delta\vec{p}_\perp)^2}{2M_1} = \frac{d}{4E}\cdot\langle\delta\vec{K}(\vec{r})^2\rangle\delta R, \tag{4.9}$$

where $\langle \ldots \rangle$ denotes an average over positions in transverse motion of the particle, i.e. (3.6) can be applied.

If the average square amplitude, ϱ^2, of the thermal vibrations (cf. (6.5)) may be considered as small, the corresponding force fluctuation becomes

$$\langle\delta\vec{K}(\vec{r})^2\rangle = \frac{1}{2}\varrho^2\langle K^2(r)r^{-2} + K'^2(r)\rangle, \tag{4.10}$$

in the case of axial symmetry. The total diffusion can be expressed in terms of the result (4.1) for a random system,

$$\delta\langle E_\perp\rangle = (\delta\Omega^2)_n \cdot E \cdot \gamma, \tag{4.11}$$

where the reduction factor $\gamma = \gamma_n(E_\perp, \varrho) + \gamma_e(E_\perp)$ is a sum of contributions from nuclear and electronic collisions. According to (4.9) and (4.10), the magnitude of γ_n becomes approximately

$$\gamma_n(E_\perp, \varrho) \approx \frac{1}{L_n}\cdot\frac{\varrho^2}{C^2a^2}\, e^{\frac{2E_\perp}{E\psi_1^2}}\left(1 - e^{-\frac{2E_\perp}{E\psi_1^2}}\right)^3, \tag{4.12}$$

if the standard atomic model (2.6) applies.

For comparison, we rewrite the electronic scattering contribution (4.7), introducing the standard atomic model by means of (3.19),

$$\gamma_e(E_\perp) = \frac{1}{L_n} \cdot \frac{L_e}{2Z_2} (1 - e^{-\frac{2E_\perp}{E\psi_1^2}}). \tag{4.12'}$$

Although (4.12) and (4.12') are merely cursory estimates, it is apparent that—in contrast to random systems—the electronic contribution γ_e may exceed γ_n, if $2E_\perp/E\psi_1^2$ is small, and Z_2 low. Note, however, that the damping effect, cf. p. 33, can dominate over (4.12') when $M_1\psi_1^2 > 2m$.

When the increase in average square angle is known, the corresponding diffusion equation becomes

$$\frac{\partial}{\partial z} g(\vec{p}_\perp, z) = \mathrm{div}_{\vec{p}_\perp} D(\vec{p}_\perp) \mathrm{grad}_{\vec{p}_\perp} g(\vec{p}_\perp, z), \tag{4.13}$$

where $g \cdot dp_{\perp,x} dp_{\perp,y}$ is the differential probability, measured e.g. at potential $U = 0$. Further, $z = vt$ is the distance of penetration. The diffusion constant, D, is determined by $\delta\langle E_\perp \rangle$, and for axial symmetry one finds

$$2D(p_\perp) + p_\perp D'(p_\perp) = M_1 \frac{\delta\langle E_\perp \rangle}{\delta R} \quad , \tag{4.14}$$

where the right-hand side is given by (4.11).

When the diffusion constant is known, the increase in square fluctuation of e.g. $p_\perp$ can be derived. In order to compare with the increase in $E_\perp$ we consider the quantity $\langle (p_\perp - \langle p_\perp \rangle)^2 \rangle / (2M_1)$, and obtain from (4.13), for initially well-defined $E_\perp$,

$$\frac{\delta\langle (p_\perp - \langle p_\perp \rangle)^2 \rangle}{2M_1 \cdot \delta R} = \frac{D(p_\perp)}{M_1} \quad . \tag{4.15}$$

If γ in (4.11) increases rapidly with $E_\perp$, the value of (4.15) is much less than $\delta\langle E_\perp \rangle / \delta R$. The smearing of the distribution by diffusion may then be disregarded, and the transverse energy remains well-defined, increasing steadily according to (4.9) or (4.11).

It can be of interest to solve the equations on the assumption of well-defined transverse energy. If the electronic contribution (4.12') can be disregarded, we obtain from (4.11), (4.12) and (4.4) the following change in $E_\perp$ on a finite path length δR,

$$\delta R \cdot \frac{4\varrho^2}{C^2 a^2 L_n} \cdot \frac{1}{l_{n,\psi_1}} = -\delta(1 - e^{-\frac{2E_\perp}{E\psi_1^2}})^{-2} \approx -\delta\left(\frac{E\psi_1^2}{2E_\perp}\right)^2, \tag{4.16}$$

where l_{n,ψ_1} is given by (4.4), and δ denotes the increase of the quantity in question. One interesting feature in (4.16) is not limited to this equation, but holds also for the more general diffusion based on (4.12); the path lengths for scattering are increased by a factor $\sim L_n a^2/\varrho^2$, as compared to (4.4), valid for random media. This result is essentially based on the validity of (4.10).

Single scattering

The reduction factor γ_n in (4.12) can become quite small. If the diffusion is sufficiently small, however, the dominant effect can be single scattering. By single scattering a particle may in one collision enter the random beam, or its fringes. Single scattering requires that the particle comes close to a nucleus, and the probability for single scattering is therefore proportional to the fraction of the total number of nuclei which may be hit by a particle with transverse energy $E_\perp$. This fraction turns out to be $\Pi_{\text{in}}(E_\perp) \approx P(r_{\min}(E_\perp))$, where $r_{\min}(E_\perp)$ is the minimum distance of approach to a string, and $P(r)$ the probability for a nucleus to be more than the distance r away from the string, cf. § 6. The effective cross section for single scattering is thus

$$d\sigma_{\text{eff}}(E_\perp) = d\sigma \cdot \Pi_{\text{in}}(E_\perp). \tag{4.17}$$

For a given penetration depth, (4.17) can be applied to angles of deflection larger than those belonging to the Gaussian peak of multiple scattering.

§ 5. Rules of Angular Averages and Compensation

Suppose that we are concerned with a definite physical effect, like the energy loss per cm., the number of K-shell excitations, or the number of (p, γ) reactions. For random systems the effect occurs at a definite rate, independently of direction. In a crystal, due to e.g. string effects, the rate may change drastically within small solid angles. In § 3 we estimated some changes of this kind in the approximation of transverse potentials. However, it can be difficult to carry out estimates to a high degree of accuracy at all angles. It is therefore appropriate to ask for rules which hold irrespective of the use of e.g. transverse continuum potentials. In particular, it is of interest to know in how far the average of an effect over all directions of incidence in a crystal is equal to that of a random system. If this is the case, we say that there is compensation of the directional effect in question.

At first we can disregard slowing-down of particles, i.e. we assume conservation of total energy. We are then concerned with particles moving in a fixed potential in three-dimensional space. We can here utilize two concepts from statistical mechanics, i.e. reversibility and microcanonical distribution. The idealized experiment of interest in the following is to consider an external beam of particles, represented by e.g. a point source at A, and to ask for the probability of hitting a certain point of space, B, in the neighbourhood of one atom. This probability is to be compared with the corresponding one when e.g. all atoms in the crystal, except the one in question, are removed or brought in disorder.

Rule of reversibility

The first useful result is that of reversibility. We need not enter on details, and shall disregard magnetic fields. Not only can the motion of a particle in its orbit from one point A outside the crystal to a point B inside the crystal be reversed according to mechanics, but also the transition probabilities for direct and reversed processes are equal, $P_{AB} = P_{BA}$, if the potentials at A and B are equal (cf. below). More definitely, suppose that at A is emitted ν particles per second per unit solid angle, in a direction towards B, and that the cross section at B is σ. The rate P_{AB} of direct processes is equal to the rate P_{BA} of reversed processes, for which emission at B is ν per unit solid angle and cross section at A is σ. This result may be regarded as a consequence of Liouville's theorem. By finding the angular distribution outside the crystal of particles emitted by atomic nuclei in strings in the crystal, we have then also obtained the probability of hitting nuclei by an external beam of particles. These results are not changed by multiple scattering, where the processes are reversible too.

Reversibility can be violated in some cases. In fact, if slowing-down on the path between A and B is so large as to influence the deflections on the way, it may not be possible to reverse the path, neither for potential motion nor for multiple scattering effects.

Rule of angular averages

In order to obtain the second rule, i.e. the rule of simple angular averages, we introduce the probability P of a particle of energy E being at a space point, $\vec{R}$, inside the crystal. The probability is measured relative to that without a crystal. Let the initial state be a particle beam of given uniform intensity, and a direction specified by angles ϑ, φ. The probability is

then a function of ϑ and φ, $P = P(\vartheta, \varphi, \vec{R})$. It should be noted that P also depends on other variables, especially on the energy E, as well as on the type of particle (Z_1, A_1), and on the medium (Z_2, lattice structure). If we average $P(\vartheta, \varphi, \vec{R})$ over all directions, and denote the average as $P(\vec{R})$, we obtain

$$P(\vec{R}) = \frac{1}{4\pi} \int P(\vartheta, \varphi, \vec{R}) \sin \vartheta d\vartheta d\varphi. \tag{5.1}$$

An average over external angles is equivalent to imposing on the system an external statistical equilibrium. The average can therefore be estimated from statistical equilibria, e.g. a microcanonical ensemble for one particle. For this purpose we introduce the particle-lattice potential $V_l(\vec{R})$ at the space point $\vec{R}$. If R is close to one atom, $V_l(\vec{R})$ should only include the potential from the other atoms, because we compare e.g. with the corresponding probability of coming near the atom in empty space (or in a random substance). Without considering details, we can state than $V_l(R)$ must be quite small, perhaps of order of few eV for protons, like E_e in (1.1), and thus usually much lower than the transverse potential $U(r)$. Since the available volume in momentum space is proportional to $pdE = \sqrt{\{2M_1(E - V_l(\vec{R})\}}dE$, the average value of the probability $P(\vartheta, \varphi, \vec{R})$ is approximately

$$P(\vec{R}) \simeq \left(\frac{E - V_l(\vec{R})}{E} \right)^{1/2} \simeq 1, \tag{5.2}$$

where the deviation of P from unity can be disregarded, being approximately equal to $V_l/2E$. Now, probabilities, intensities or fluxes may differ by $[E - V_l(\vec{R})]/E$ to a power between perhaps -1 and $+1$, but such factors are quite close to unity, so that even without detailed estimates we may state that averages of type of (5.1) are equal to unity.

This leads to the rule of angular averages for energy conservation: Any quantity Q, depending linearly on $P(\vartheta, \varphi, \vec{R})$, has the same angular average as in a random system. By a random system is meant a system with the same density, but without directional effects, for instance because of lack of structure. Examples of quantities obeying the simple rule are electronic stopping, e.g. (3.15), and nuclear stopping, (3.10), at a fixed energy E. We may formulate the rule of angular averages as follows. If Q is given by

$$\left.\begin{aligned} Q(\vartheta,\varphi) &= a + \int b(\vec{R})P(\vartheta,\varphi,\vec{R})d^3R, \\ \text{the average of } Q \text{ becomes, according to (5.1) and (5.2),} & \\ \langle Q(\vartheta,\varphi)\rangle &= \frac{1}{4\pi}\int d\Omega \cdot Q(\vartheta,\varphi) = a + \int b(\vec{R})d^3R. \end{aligned}\right\} \quad (5.3)$$

Both in (5.3) and in (5.1) it is often possible to limit the average to a solid angle Ω small compared to 4π. In fact, suppose that at the borderlines of a solid angle Ω the particles are not deflected into or away from this solid angle, by deflections due to strings or planes. The separate average over Ω must then also fulfill (5.3).

If we apply the result of reversibility, the rule of angular averages can also be used for particles coming from any space point $\vec{R}$ in the lattice and arriving at a point outside the lattice. In this case the rule is quite evident, even without use of reversibility and (5.3). In fact, imagine that atomic nuclei in the lattice emit α-particles, which process occurs at a fixed rate per unit solid angle. The α-particles are deflected away from string directions, and exhibit a certain angular distribution when emerging from the crystal. But, evidently, on a large sphere surrounding the crystal, all particles will be collected, independently of their possible deflections within the crystal. Moreover, if we collect within a relatively small solid angle around a string direction, the angular width still being large compared to string deflection, the number collected is the same as if the string were not there. Thus, the angular distribution has a complete compensation of the dip, characteristic of quantities linear in $P(\vartheta,\varphi,\vec{R})$. A similar problem was discussed in § 2, in connection with the classical shadow behind an atom.

Limitations of rule of angular averages

When we are concerned with definite physical observations, like those mentioned in the beginning of this section, the simple rule does not always apply, because in actual fact energy conservation is violated in slowing-down and the measured quantities may be strongly dependent on energy. By and large, physical effects depending on slowing-down will not obey the rule of angular averages. It can be useful to consider a few examples.

First, a basic quantity is the range of a particle. The stopping cross section $S(E_\perp,E)$, at a definite energy E, is linear in P and follows the rule of averages. The range, however, is of type of $\int dR = \int dE/(N\cdot S(E_\perp,E))$. It is

therefore not linear in P, and does not follow the rule. In fact, deviations can be quite large. In two cases will deviations from the rule become small. If $S(E_\perp) \approx S$, the latter being the stopping cross section for random slowing-down, we have $S(E_\perp)^{-1} \cong S^{-1} \cdot (2 - S(E_\perp)/S)$, which is linear in P. Moreover, in a polycrystalline medium where the size δR of each crystal corresponds to $\delta E = \delta R \cdot (S(E_\perp)N) \ll E$, the range will be as in a random system.

Second, an instructive example is afforded by a (p,γ) reaction for protons passing through a crystal. The reaction occurs at a definite energy E_0, and has a width Γ, very small compared to E_0. Suppose that Γ nevertheless remains so large that an energy loss $\sim \Gamma$ is obtained only by penetration of many atomic layers. The number ν of reactions is then proportional to $\nu \propto P(\psi,\vec{R}_n)/S_e(\psi)$, where $P(\psi,\vec{R}_n)$ indicates the probability of hitting a nucleus. Since the ratio P/S_e is not linear in P, its average over all directions need not correspond to a random system, and (5.3) does not apply. However, the probability of hitting an atomic nucleus may be essentially zero, except when $E_\perp$ is large. Since $S_e(E_\perp)$ has a rather narrow dip, cf. (3.19), we may have $S_e(E_\perp) \approx S_e = \text{const.}$, in the region where P is different from zero, in which case the compensation belonging to (5.3) is approximately obtained.

As indicated by these examples, there is a large number of combinations of effects which may influence the angular averages, when slowing-down comes into play. Therefore, a thin single crystal foil, where the energy loss remains small, is one of the few examples where physical effects can obey (5.3) in a straightforward manner.

In measurements of angular dependence of effects in the neighbourhood of strings and planes, the compensation in (5.3) is usually of interest in a qualitative way only. In other cases, e.g. if nuclear cross sections are to be measured with high accuracy in solids, the applicability of (5.3) can be of direct importance.

Rule of spatial averages

The previous averages were concerned with angles, but also averages over space give rise to interesting rules. Suppose that an external beam has a fixed direction given by (ϑ,φ), e.g. close to a string direction, and consider a nuclear process with a constant, energy independent cross section. The rate of the process depends on the position of the nucleus in the lattice. Now, if the probability density of the distribution of nuclei is constant in a

transverse plane, the process has for these nuclei the same rate as in a random substance, simply because every particle must pass through some point of the transverse plane. Thus, for a fixed value of z, less than the penetration depth of every particle,

$$\langle P(\vartheta,\varphi,\vec{R})\rangle_{xy} \equiv \frac{1}{A_0}\int\int_{A_0} dxdy\, P(\vartheta,\varphi,\vec{R}) = 1, \tag{5.4}$$

where P is the previously mentioned probability, normalized to unity for a random system. Any linear function $Q = \mathrm{a} + b \cdot P(\vartheta,\varphi,\vec{R})$ has the average $\langle Q\rangle_{xy} = a + b$. Therefore, if—for fixed external direction ϑ,φ—there is a dip in reaction rate when the atomic position is at a string, there must be a rise above normal yield at positions in between strings. However, the area outside strings is much larger than the effective area of a string; the increase in rate is then quite small, of order of $Nd \cdot \pi a^2$. A somewhat larger effect would occur for planes. Still, because of the smallness of these changes, reaction rates may then instead be dominated by secondary string phenomena, like electronic stopping, cf. § 6.

§ 6. Idealized Experiments and Comments on Measurements

When discussing experiments—both idealized and actual experiments—it is instructive to bear in mind that, at low angles of incidence, particles are prevented from coming closer than $\sim a$ to the centre of strings (or planes). This indicates, firstly, experimental tools that may be chosen. In fact, there is a possibility of utilizing any physical process requiring that the particle is less than the distance a from the atomic nucleus (nuclear reactions, Coulomb excitation, inner shell excitation, wide angle Rutherford scattering, emission of charged particles from radioactive nuclei). Secondly, measurements of this kind give direct information about paths of particles in the lattice and their scattering, and hence enables one to study the important primary phenomena, which govern the particle motion, cf. p. 9. Thirdly, by means of the shielding inside $\sim a$ one is able to pin atomic positions with an accuracy $< a$ in the vicinity of lattice sites, so that e.g. a method of observing defects and positions of impurity atoms is available.

It is easy to visualize many further applications, but it seems proper to demonstrate first the way in which theory and experiments can cope with the primary task sketched above. When that is done, a quantitative basis

is obtained for estimating in how far the more complicated applications may be realized. In the present context, however, we shall merely discuss briefly a few aspects of the primary task.

Three stages in particle motion

The fate of particles on their way from an external source to e.g. an atomic nucleus in a crystal may be divided into three successive stages. These three stages appear in the opposite order for the reversed process of a particle coming from a nucleus and arriving at a detector outside the crystal. A calculation of the probability of a direct process is often equivalent to an estimate of the reverse process, cf. § 5.

A particle beam has an initial angular spread before entering the crystal surface. Let the initial distribution be $P(E\psi_e^2)d(E\psi_e^2)$, where ψ_e is the external angle with strings. It can be convenient to include in this spread the multiple scattering due to impurity layers in front of the crystal surface. It should be remembered that the angular distribution from scattering by a thin layer consists of a narrow Gaussian peak and a tail due to single scattering.

Consider particles arriving at the crystal surface at a definite angle ψ_e with a string (or a plane). The first stage is then the transition from immediately outside to immediately inside the crystal surface. We may introduce a transmission factor,

$$T = T(E_\perp, E\psi_e^2),$$

such that $T \cdot dE_\perp$ is the differential probability of transverse energy between $E_\perp$ and $E_\perp + dE_\perp$, when the external angle is ψ_e. In the continuum description we get, if $U_{\text{tot}}(\vec{r}) \approx U(r)$,

$$T(E_\perp, E\psi_e^2) = \int_0^{r_0} \frac{2rdr}{r_0^2}\, \delta(E_\perp - E\psi_e^2 - U(r)), \tag{6.1}$$

because, at the point $\vec{r}$, the transverse energy becomes $E\psi_e^2 + U(r)$. In this way, the initial distribution $g(E_\perp, z = 0)$ can be obtained,

$$g(E_\perp, 0) = \int P(E\psi_e^2)d(E\psi_e^2)T(E_\perp, E\psi_e^2), \tag{6.2}$$

where the particle energy is E.

In (6.1) is assumed axial symmetry; the general formula corresponding to (6.1) is a normalized integration over the unit cell. Therefore, in the corresponding estimate for planes, the right-hand side of (6.1) is replaced by

$$\int_0^{d_p/2} \frac{2dy}{d_p}\,\delta(E_\perp - E\psi_e^2 - Y(y)),$$

where d_p is the distance between planes, ψ_e the angle with the plane, and $Y(y)$ the continuum plane potential. In (6.1) the direction of the transverse motion is disregarded and we shall omit estimates of e.g. $g(\vec{p}_\perp, \vec{r}, z = 0)$.

The second stage consists in the passage through the crystal from the surface to depth z. During this stage there is multiple scattering, i.e. a redistribution of transverse energy in a manner somewhat similar to diffusion. The redistribution depends strongly on the value of $E_\perp/E\psi_1^2$, cf. § 4. At the same time, the particles are subject to slowing-down, so that the energy E decreases. The slowing-down also depends on $E_\perp/E\psi_1^2$, cf. § 3. Accordingly, a redistribution factor R is obtained, giving the probability of energy E' and transverse energy $E'_\perp$, at depth z, if their values are E and $E_\perp$ at the surface, i.e.

$$R = R(E', E'_\perp, z; E, E_\perp, 0),$$

where $R(E', E'_\perp, 0; E, E_\perp, 0) = \delta(E' - E)\delta(E'_\perp - E_\perp)$. Usually, one can either disregard energy loss as compared to diffusion, or disregard diffusion and include only energy loss. This leads to considerable simplification in R. In some cases we can assume that both E and $E_\perp$ change smoothly, without fluctuations, as functions of depth, so that R is a δ-function in both E' and $E'_\perp$.

When R is known, we can estimate the probability $g(E', E'_\perp, z)dE'dE'_\perp$ of energy in the interval dE' and transverse energy in the interval $dE'_\perp$,

$$g(E', E'_\perp, z) = \int dE_\perp\, g(E_\perp, 0) R(E', E'_\perp, z; E, E_\perp, 0). \tag{6.3}$$

The third stage is the occurrence of the actual physical process, a nuclear reaction for instance. In processes of this kind, the particle essentially must penetrate to the centre of atoms, and the probability $\Pi_{\text{in}}(E_\perp)$ for this will be discussed in some detail. If $\Pi_{\text{in}}(E_\perp)$ is known, and the cross section for the process in question is σ, the effective cross section σ_{eff} at depth z becomes

$$\sigma_{\text{eff}}(z) = \int dE' \int dE'_\perp\, g(E', E'_\perp, z) \Pi_{\text{in}}(E'_\perp) \sigma(E'). \tag{6.4}$$

Cross sections $\sigma(E')$ for nuclear reactions can be of resonance type in the energy E'.

We refrain from discussing further the general case of superposition of the three stages mentioned. Instead, a few basic examples will be treated after the estimates of $\Pi(E_\perp)$.

Particle emission from string atoms and $\Pi(E_\perp)$

Several characteristics of basic phenomena in the string effect are illustrated by the following idealized experiment. A fast, positively charged particle leaves a nucleus by a process independent of lattice properties, e.g. an α-decay. The nucleus has some probability distribution in space. The first question to be solved is the probability $\Pi_{\text{out}}(E_\perp)dE_\perp$ of transverse energy between $E_\perp$ and $E_\perp + dE_\perp$.

We note that $\Pi_{\text{in}}(E_\perp) = \xi \cdot \Pi_{\text{out}}(E_\perp)$ is the probability of the opposite process as described by (6.4), where ξ is a constant accounting for available space—or phase space—in the two opposite processes. In fact, in the continuum description ξ^{-1} is the fraction of the area of the transverse plane accessible to the particle, i.e. $\xi^{-1} = 1 - r_{\min}^2(E_\perp)/r_0^2$, and thus ξ is normally close to unity. The subsequent fate of the particle, as determined by multiple scattering and emergence through surface, can be treated separately, the former being determined by (6.3) and the latter by reversal of (6.2).

Suppose that the atomic nucleus is in the neighbourhood of an atomic position in a perfect string, with probability distribution $dP(r)$, where r is the distance from the string axis. The distribution in z-direction may be disregarded. For simplicity, a Gaussian type distribution will be used as an example in the following, i.e.

$$dP = e^{-\frac{r^2}{\varrho^2}} 2r dr \cdot \alpha/\varrho^2, \tag{6.5}$$

where r is the distance from the perfect string, and α is a normalization constant, $\alpha = \{1 - \exp(-r_0^2/\varrho^2)\}^{-1}$, i.e. $\alpha \approx 1$ if ϱ^2 is small compared to $r_0^2 = 1/(\pi N \cdot d)$. The distribution (6.5) might roughly represent zero-point and thermal vibrations of an atom with respect to its neighbours. If ϱ is large, (6.5) corresponds to a uniform distribution within the unit cell. It can therefore represent cases other than vibrations. The calculations of several effects, cf. (4.10) and (6.13), involve merely the average square vibration of an atom, ϱ^2, and not the probability distribution as such. At low temperatures, ϱ^2 is determined by zero-point vibrations of lattice atoms, while at high temperatures it increases proportionally to temperature.

We ask for the initial distribution in transverse energy $\Pi_{\text{out}}(E_\perp)$, of particles emitted into the lattice from an atom close to a lattice site. Consider

the approximation in Appendix A, where a transverse potential $U(r)$ may be used, and $E_\perp$ is to be registered at the planes half-way between atoms. A particle initially at a distance r from the string, moving at an angle φ with the string and azimuthal angle ϑ, will be a distance r^* away from the string when it arrives at the half-way plane, where $r^{*2} = r^2 + (\varphi d/2)^2 + r\varphi d \cdot \cos\vartheta$. Therefore,

$$\Pi_{\text{out}}(E_\perp) = \int_{r=0}^{r_0} dP(r) \int d(E\varphi^2) \int_0^{2\pi} \frac{d\vartheta}{2\pi} \cdot \delta(E_\perp - U(r^*) - E\varphi^2), \tag{6.6}$$

and for planes an analogous formula holds.

If $\varphi d/2$ is small compared to the range ϱ of the distribution, we may put $r^* = r$, and (6.6) becomes

$$\Pi_{\text{out}}(E_\perp) = \int dP(r) \Big|_{U(r) < E_\perp}. \tag{6.7}$$

Although (6.7) implies a dip quite similar to that in (6.6) for low values of $E_\perp$, the magnitude of (6.7) apparently cannot exceed unity, in contrast to (6.6). The shoulder of the distribution at $E_\perp \sim E\psi_1^2$ is therefore absent in the approximation (6.7).

By means of (6.7), (6.5) and the standard potential (2.6) a definite expression for Π_{out} is obtained

$$\Pi_{\text{out}}(E_\perp) = \exp\left\{-\frac{C^2 a^2}{\varrho^2}\left(e^{\frac{2E_\perp}{E\psi_1^2}} - 1\right)^{-1}\right\} - \exp\left\{-\frac{r_0^2}{\varrho^2}\right\}, \tag{6.8}$$

where it is assumed that $\varrho \ll r_0$, i.e. $\alpha \approx 1$. When $E_\perp \to U(r_0)$, the expression in (6.8) tends to zero. However, the value of $\Pi_{\text{out}}(E_\perp \approx 0)$ is sensitive to the atomic potential, and to the behaviour of the probability distribution (6.5). The number of particles emerging from the crystal surface, at angles close to zero with the string, may therefore be strongly influenced by multiple scattering, etc.

In view of the variability of the maximum dip, it can be of interest to look for quantities less sensitive to multiple scattering. From (6.7) and (6.8) approximate estimates of the width of the dip in $\Pi(E_\perp)$ may be easily obtained, but a precise definition of the width is less simple. However, the integrated dip is more well-defined. Since the dip from unity is $1 - \Pi_{\text{out}}(E_\perp)$, we may integrate over positive values of this quantity. When (6.7) is introduced, we obtain an integrated dip

$$\left.\begin{aligned} \Omega(\varrho) &= \int (1 - \Pi_{\text{out}}(E_\perp))2\pi \sin\psi d\psi = \frac{\pi}{E}\int_0 (1 - \Pi_{\text{out}}(E_\perp))dE_\perp = \\ &= \frac{\pi\alpha}{E}\int_0^{r_0^2} \frac{d(r^2)}{\varrho^2} e^{-\frac{r^2}{\varrho^2}} U(r). \end{aligned}\right\} \tag{6.9}$$

When ϱ is large compared to a, but small compared to r_0, we find by partial integration,

$$\Omega(r_0 \gg \varrho \gg a) = \frac{1}{\varrho^2 d \cdot E}\int 4\pi R^2 dR\, V(R) = \frac{Z_1 Z_2 e^2}{\varrho^2 d \cdot E}\pi\frac{2}{3}\overline{R^2}, \tag{6.10}$$

where $\overline{R^2} = Z_2^{-1}\int_0^\infty 4\pi R^4 dR\varrho(R)$ is the average square radius of the atom per electron. In the LENZ-JENSEN description[9] the average square radius becomes $\overline{R^2} \simeq 15a^2$, which result agrees well with measurements as well as with the HARTREE treatment. For ϱ large compared to a, we may thus put

$$\Omega(\varrho) \simeq \pi \cdot \frac{\psi_1^2}{2} \cdot 10a^2/\varrho^2. \tag{6.11}$$

In the opposite limit of ϱ small compared to a we find readily, from (2.5),

$$\Omega(\varrho < a) = \pi \cdot \frac{\psi_1^2}{2}\log\left(\frac{C^2a^2}{\varrho^2}\gamma\right), \tag{6.11'}$$

where $\gamma = 1.78$ is Euler's constant. A qualitative estimate, applicable for all values of ϱ, is therefore

$$\Omega \simeq \pi \cdot \frac{\psi_1^2}{2}\log\frac{\gamma C^2a^2 + \varrho^2}{\varrho^2} \quad . \tag{6.12}$$

The formula (6.12), giving the dip as a function of transverse energy for $\varrho \ll r_0$, should in this case also give approximately the dip outside the crystal, if multiple scattering can be neglected. However, when ϱ in (6.9) becomes large compared to r_0, there is a uniform probability distribution $dP(r)$ in the unit cell, $r < r_0$. The effects of exit from the surface are then most important, and according to the discussion in § 5, there is no dip outside the crystal. It so happens that (6.12) has the value zero in this limit, and in this sense represents better the external than the internal angular distribution. There is, however, a serious drawback in the formulae (6.7) – (6.12). A continuum potential has been used, and thus compensating shoulders are disregarded. It would be more correct to use (6.6) and apply the formulae in Appendix A, according to which the potential energy is to be measured at the planes half-way between atoms.

The equation (6.12) can be used in two ways. From knowledge of ϱ, the value Ω can be found approximately; from measurements of Ω, the value of ϱ^2 can be estimated qualitatively. Apart from such estimates, it is seen that Ω is proportional to $\psi_1^2 = 2Z_1Z_2e^2/d \cdot E$.

Lowest minimum yield

The minimum yield of e.g. nuclear reactions at a given depth corresponds to external angle $\psi_e = 0$. The lowest value χ of the minimum occurs at low depth, where the multiple scattering is small. If we disregard the multiple scattering, we find from (6.1) and (6.4) that there always remains a yield from thermal vibrations. If the continuum description applies, we obtain from (6.7) and (6.1) the first contribution χ_1 to the total χ,

$$\chi_1 = N \cdot d \cdot \pi \varrho^2, \tag{6.13}$$

where ϱ^2 is the average square amplitude of atomic vibrations with respect to the string. It is noteworthy that (6.13) does not depend on the probability distribution, i.e. (6.5) need not apply. The magnitude of χ_1 is often $\chi_1 \lesssim 10^{-2}$, when $d \sim 3$Å.

For several reasons, the effective lowest minimum can be higher than the above value. Particles in the exterior beam, which hit within $\sim a$ from the centre of a string, obtain transverse energy $\sim E \cdot \psi_1^2$, and they may after very little multiple scattering be able to hit the centre of atoms; the path length in question is $\lesssim l_{n,\psi_1}$ in (4.4). This leads to the next, and less well-defined contribution to χ,

$$\chi_2 \cong N \cdot d \cdot \pi a^2. \tag{6.14}$$

In the case of major strings, i.e. for $d \sim 3 \cdot 10^{-8}$ cm, the magnitude of χ_2 varies between ~ 0.03 in the lighter substances and ~ 0.005 in heavy substances. For planes, we roughly find $\chi_2 \sim 2a/d_p$.

The result (6.14) corresponds to the high energy case (2.9′). At low energies, or large values of d, there is a well-defined increase in the fractional area χ_2 corresponding to transverse energy above the barrier. According to (2.10) or (A.21) one obtains $\chi_2 \cong \pi N \cdot d^2 a \psi_1$, when ψ_1 is large compared to a/d.

It may be noted that the atoms at the surface can react directly with the particle. The effective number of layers, of thickness d, giving full contribution is ξ, where $\xi > 1$. Measurements confined to the first 10-50 layers cannot therefore yield very strong dips, and a certain amount of multiple scattering must always be included in the measurements.

Although a classical orbit remains outside the centre of atoms in a perfect string, there is a quantal penetration. However, particles with the

same value of Z_1/E have the same characteristic angle ψ_1, but their wave length decreases proportionally to $(M_1E)^{-1/2} \propto (M_1Z_1)^{-1/2}$. The quantal penetration probability is in this sense an independent quantity which can be made quite small.

The presence of amorphous impurity layers on the surface of the crystal need not cause large multiple scattering. Still, effects of single scattering cannot be disregarded in the present context. Let the number per cm^2 of the i'th atomic species be ν_i, while its collision diameter with the particle is b_i. The fraction of particles deflected by an angle larger than Θ, in single scattering, is then

$$\sum_i \nu_i \cdot \pi b_i^2 \cdot \Theta^{-2},$$

where it is assumed that Θ is so large that Rutherford scattering applies. If the particles originally have zero angle with a string direction, we have directly obtained a tail of the distribution in transverse energy, and the contribution χ_3 to χ is obtained,

$$\chi_3 = \sum_i \nu_i \pi b_i^2 \cdot E \int_0^\infty \frac{dE_\perp}{E_\perp^2} \Pi(E_\perp). \tag{6.15}$$

The integral in (6.15) may be evaluated by means of (6.6) or (6.7). At high particle energies and for $\varrho < a$ we may assume, crudely, that $\Pi \sim 0$ for $E_\perp < E\psi_1^2$, and $\Pi \sim 1$ for $E_\perp > E\psi_1^2$, leading to $\chi_3 \sim \psi_1^{-2} \Sigma \nu_i \pi b_i^2$. This result is interesting in several respects. The value of χ_3 can exceed χ_1 or χ_2, if there is a substantial surface layer of not too low atomic number. It is also seen that at high particle energies both χ_1, χ_2 and χ_3 may be proportional to the spacing d between atoms in the string. It is therefore expected that the minimum yield, when small, increases with d in a simple manner.

In any case, if measured dips are in the neighbourhood of the minima quoted above, it seems possible to study in detail the effects of multiple scattering, etc., as discussed in the beginning of this chapter.

Comments on experiments

Although detailed comparisons with experiments would be out of place, it may be proper to comment briefly on some measurements directly connected with the theory. We do this in the spirit of the introductory remarks in this chapter (p. 43), selecting primary directional effects.

In the exploratory measurements on (p,γ) reactions in Al and Si at

~ 400 keV, BØGH, DAVIES and NIELSEN[7] observed the expected reduction in yield in string directions. The yield is proportional to $\Pi(E_\perp)/S_e(E_\perp)$, the probability distribution in $E_\perp$ depending on external angle. The observed reduction by a factor ~ 5 was large enough to be promising[5], partly because the disturbing influence of electronic stopping could then be disregarded, and partly because it seemed comparatively easy to develop further this tool of solid state observations. The measurements are apparently, as to purpose and result, different from those of THOMPSON[19].

In continued measurements, also effects of planes were clearly seen, and higher proton energies were used[20]. In connection with (p,γ) reactions, with rate $\propto S_e^{-1}(E_\perp)$, it may be mentioned that they might also be used for identifying interstitials, where peaks in yield, instead of dips, should appear for atoms outside strings when $\psi_e < \psi_1$ (cf. p. 43 and (3.19)).

The measurements by DOMEIJ and BJÖRKQVIST[18] are of particularly simple and informative kind. The angular distributions of α-particles, emitted by heavy ions stopped in W, showed dips by a factor ~ 4 and angular widths in agreement with (2.9). It could be concluded that most, if not all, ions ended up in lattice positions. In more detailed measurements, including changes of temperature, it should be possible to verify positions of ions in the lattice and even to check vibrations (cf. also (6.9)).

Observations utilizing wide angle Rutherford scattering would seem to provide a promising and versatile tool, because of the large cross sections, and the free choice of Z_1, Z_2 and E[5]. The measurements by BØGH and UGGERHØJ[22] of Rutherford scattering for 400 keV protons in Ta and with energy analysis of the emerging protons, provide the most definite and detailed information obtained so far. Strings of both low and high index numbers are clearly seen. The angular widths as functions of d and E are in accord with (2.9) and (2.10), and dips approach the lower limits (cf. p. 49 and ref. 5). An effect of planes is seen as a background of the dominating string dips. It may be added, as an example, that Rutherford scattering can be used for determining positions of impurity atoms, in lattice sites or in interstitial positions.

As to other processes requiring that the particle comes close to the nucleus, preliminary measurements of inner atomic shell excitation by ~ 100 keV protons have been performed by BRANDT et al.[21], but in the interpretation the repulsion by atomic strings was not taken into account.

As regards secondary directional effects (cf. p. 9), the most prominent one is slowing-down. For fast protons, the most accurate observations were performed by ERGINSOY, WEGNER and GIBSON[11]. These measurements

clearly reveal effects of planes and strings. The energy loss is found to be reduced by a factor of at most ~ 2, in rough agreement with (3.15). The wide distribution in energy loss is not to be accounted for as usual straggling, which becomes quite small according to (3.20), but in terms of the statistics of the two first stages in particle motion mentioned on p. 44 ff.

Numerous careful experimental studies on penetration by heavy ions in the keV region have been performed, especially by DAVIES and co-workers (e.g. refs. 1 and 23), and by LUTZ and SIZMANN[24].

Acknowledgments

I am particularly indebted to VIBEKE NIELSEN for collaboration and suggestions, to her and PHILIP LERVIG for enthusiastic criticism, and to SUSANN TOLDI for untiring help in the preparation of this manuscript.

It has been a great pleasure to co-operate with KARL OVE NIELSEN, who also kindly enforced publication of this work, with E. BØGH, J. A. DAVIES and E. EILERTSEN, and with J. U. ANDERSEN and E. UGGERHØJ as well as other members of the institute.

I am much indebted to I. BERGSTRÖM, B. DOMEIJ, C. ERGINSOY, W. M. GIBSON and O. S. OEN for discussions and communication of experimental results prior to publication.

Appendix A

Classical Scattering by Perfect String and Continuum Potential

The accuracy of the continuum string approximation may be assessed approximately within classical mechanics. Besides classical mechanics, the calculations in this appendix are based on the perfect string, i.e. atoms placed on a straight line with constant spacing d, and are easily generalized to a perfect lattice.

The first circumstance to be noted is the strict conservation of angular momentum with respect to the string. We shall at first discuss only the case of zero angular momentum. This is the least favourable case for conservation of transverse energy, because the particle penetrates the closest to the string.

Let atoms be placed on the z-axis, at $z = 0, \pm d, \pm 2d, \ldots$ It is convenient to introduce the planes half-way between atoms, $z = \pm d/2, \pm 3d/2, \ldots$, and measure transverse coordinates (x, y) at these planes. The distance

from the string is $r = (x^2+y^2)^{1/2}$, and the motion is assumed to be in a plane containing the string (cf. above). We want to find the accuracy with which transverse energy is conserved between the two planes, the a-plane where $z_a = -d/2$, and the b-plane where $z_b = +d/2$. In the a-plane the distance from z-axis is r_a and the angle with the z-axis is ψ_a, and in the b-plane distance and angle are r_b and ψ_b. At $z = 0$, where the deflection

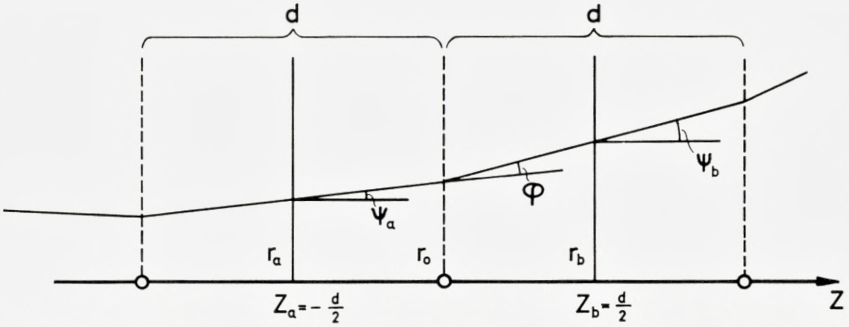

Fig. 2. Classical deflections of particle by perfect string, with coordinates recorded at half-way planes, cf. text.

occurs, the distance from the axis is r_0. Then, $r_b = r_0 + \psi_b \cdot d/2$, and $r_a = r_0 - \psi_a \cdot d/2$. The deflection at r_0 becomes, cf. (2.1′),

$$\varphi = \psi_b - \psi_a = -\frac{d \cdot U'(r_0)}{2E}; \tag{A.1}$$

r_0 and $r_b - r_a$ are given by

$$r_0 = \frac{r_a + r_b}{2} - \varphi\frac{d}{4}; \quad r_b - r_a = \frac{d}{2}(\psi_a + \psi_b). \tag{A.2}$$

We here disregard terms of relative magnitude $(\psi_a + \psi_b)^2/2$ in r_0, and of relative magnitude $\varphi r_0/d$ in $r_b - r_a$.

From these relations we may find the degree of conservation of transverse energy, retaining only powers of ψ less than ψ^4; the latter limitation is implicitly contained in the small angle approximation for ψ. We tentatively introduce transverse energies $E_\perp(r_a)$ and $E_\perp(r_b)$,

$$E_\perp(r_a) = E \cdot \psi_a^2 + W(r_a), \quad E_\perp(r_b) = E \cdot \psi_b^2 + W(r_b), \tag{A.3}$$

and ask whether a transverse energy of this kind can be approximately conserved, i.e.

$$E_\perp(r_a) = E_\perp(r_b). \tag{A.4}$$

If (A.4) holds, it is easy to calculate the angle of emergence ψ from the string, since $E \cdot \psi^2 = E_\perp$. An over-all validity of the continuum approximation would mean that the conservation in (A.3) holds not merely at the half-way planes, but is also accurate at other values of z.

Consider the difference between $E_\perp(r_a)$ and $E_\perp(r_b)$ in (A.3), and eliminate ψ_a and ψ_b by means of (A.1),

$$E_\perp(r_b) - E_\perp(r_a) = W(r_b) - W(r_a) - (r_b - r_a) \cdot U'(r_0). \tag{A.5}$$

Since (A.2) is an implicit equation for r_0, i.e.

$$r_0 = \frac{r_a + r_b}{2} + \frac{d^2}{8E} U'(r_0), \tag{A.6}$$

r_0 and $U'(r_0)$ are only functions of the sum $r_a + r_b$, in the present approximation. The mean distance $(r_a + r_b)/2$ is, for brevity, denoted as r, and we may ask for the connection between differential changes in r and r_0. From (A.6) is obtained

$$dr = dr_0 \left[1 - \frac{d^2}{8E} U''(r_0) \right]. \tag{A.7}$$

If r_0 initially is large, and then decreases, the two terms dr and dr_0 remain approximately equal, until the term in brackets in (A.7) becomes zero. Thereupon, r increases rapidly as r_0 tends to zero. It is therefore appropriate to require

$$E > \frac{d^2}{8} U''(r_{\min}), \tag{A.8}$$

in order that the transverse motion can be described by a continuum potential; in (A.8) the minimum distance of approach to the string is $r_{\min} = r_{\min}(E_\perp)$ for transverse energy $E_\perp$. The criterion (A.8) is closely equivalent to those in (2.9), (2.10), or (2.7).

In order to find W, we expand in (A.5),

$$W(r_b) - W(r_a) = (r_b - r_a) \cdot W'(r) + \frac{1}{24} (r_b - r_a)^3 \cdot W'''(r) + \ldots . \tag{A.9}$$

Assuming $r - r_0$ to be small, we also find

$$U'(r_0) = U'(r) + U''(r) \cdot \frac{d^2}{8E} U'(r) + \ldots . \tag{A.10}$$

As a result of this, we find that if the last term in (A.9) is disregarded, (A.5) becomes equal to zero when the potential $W(r)$ is given by

$$W(r) = U(r) + \frac{d^2}{16E}[U'(r)]^2 + \ldots . \tag{A.11}$$

However, it is easily verified that the condition (A.8) demands that the second term in (A.11) remains small compared to the first one. We may therefore identify $W(r)$ with the continuum potential $U(r)$. Nevertheless, the second term in (A.11) may be given a simple physical interpretation, accounting approximately for single scattering, albeit in an incomplete manner, cf. below.

We omitted the last term in (A.9). Since we need only a crude estimate, we may by means of this term find an upper limit to the lack of conservation of transverse energy in a collision with a string. In fact, suppose that this term represents twice the uncertainty in energy conservation when going from z_a to z_b. Suppose even that the uncertainties add. The total uncertainty in transverse energy after a string collision must be less than this sum. We write the sum as an integral, where we can put $(r_b - r_a)^2 = d^2 \cdot \psi_r^2 = d^2(E_\perp - U(r))/E$, as well as $W(r) = U(r)$,

$$\left.\begin{aligned} \delta E_\perp \to \int_{r_{\min}}^{\infty} \frac{d^2}{24E}\{E_\perp - U(r)\}\, U'''(r)dr = \frac{d^2 U'(r_{\min})^2}{48E} = \\ = \frac{d^2}{48E} E_\perp^2 \cdot \frac{v^2}{r_{\min}^2} \quad , \end{aligned}\right\} \tag{A.12}$$

where v is the effective power of $U(r)$, $v = -d\log U(r)/d\log r$. The right-hand side becomes comparable to $E_\perp$ only if $E_\perp > E\psi_1^2$, as was to be expected. Moreover, the right-hand side decreases as $E_\perp$ to a power between 3 and 4, since $v \sim 1-2$. It is therefore seen that transverse energy conservation must be accurately fulfilled, if $E_\perp$ is not large. We conclude that the conservation of transverse energy, as expressed by (A.4), is a good approximation, and that deviations from it must be due to e. g. atomic vibrations.

In connection with (A.3), (A.4) and (A.11) may also be noted the special case of a harmonic oscillator potential. Then, the higher derivatives of U vanish, and an exact solution is obtained. In fact, suppose that $U_{\text{tot}}(\vec{r}) = Cr^2/2$. The general two-dimensional motion obeys the equations (A.5) and (A.6), which may be solved to give

$$E\psi_a^2 + \frac{1}{2} C r_a^2 \frac{1}{1 - \dfrac{d^2 C}{8E}} = E\psi_b^2 + \frac{1}{2} C r_b^2 \frac{1}{1 - \dfrac{d^2 C}{8E}} \quad . \tag{A.13}$$

One must therefore require that $E > d^2 C/8$, in order that the motion does not diverge. This criterion coincides with (A.8). If the potential is not confined to the transverse plane of atoms, the critical energy is slightly reduced.

In the above, transverse energy $E_\perp$ was shown to be conserved. However, the particle energy E in the laboratory system was unchanged during the collision, i. e. the recoil energy of the atom was disregarded. We may briefly show that, even when the latter effect is included, $E_\perp$ may normally be taken to be conserved in a collision. To this end, consider an elastic collision, so that particle energy after the collision is $E - T_n$, where T_n is given by (3.9). The change of energy implies in itself a reduction of transverse energy, $\delta E_{\perp,1} = - T_n \cdot \psi_r^2$. Moreover, when there is transfer of energy and of angular momentum, the outgoing particle path is shifted outwards by an amount δr, cf. reference 10,

$$\delta r \simeq \frac{T_n}{E} \left(\frac{U(r)}{r \cdot U'(r)} + \frac{1}{2} \right) r \quad ;$$

the corresponding change of $E_\perp$ in the collision is $\delta E_{\perp,2} = \delta r \cdot U'(r)$. The total change is then $\delta E_{\perp,1} + \delta E_{\perp,2}$. Suppose next that $U \propto r^{-\nu}$, and find the statistical average of $\delta E_\perp$ for strings, according to (3.6). A simple calculation then shows that, for $r_{\min} \ll r_0$,

$$\frac{\langle \delta E_\perp \rangle}{E_\perp} = - \frac{\nu - 1}{3} \frac{\langle T_n \rangle}{E} \quad . \tag{A.14}$$

Therefore, $E_\perp$ is conserved quite accurately if $0 < \nu < 2$, cf. standard potential (2.6). For this reason, and since electronic stopping normally dominates over nuclear stopping—especially when $E_\perp$ is small—we may often disregard the change in $E_\perp$ due to elastic nuclear collisions in a perfect lattice. The change in $E_\perp$ during penetration is then usually due to electronic stopping, and to the other effects mentioned in § 4.

General equations of motion

As an alternative to the above estimates we treat a somewhat different approach, associated with variational principles in dynamics and useful for numerical estimates. For this purpose we record the distance r_j at $z = j \cdot d$, where j is an integer. Since the basic equation of deflection is

$$\frac{r_{j+1} - 2r_j + r_{j-1}}{d} = \varphi_j = - \frac{d \cdot U'(r_j)}{2E}, \tag{A.15}$$

we may form the sum

$$\sum L_j = \sum_{j=n+1}^{m} \left\{ E \cdot \frac{(r_j - r_{j-1})^2}{d^2} - U(r_j) \right\}, \tag{A.16}$$

and the orbit for given values of coordinates r_n and r_m is determined by variation of all r_j, $j = n+1, \ldots, m-1$, with a stationary value of (A.16).

So far, the deflection was assumed to occur in the plane $z = z_j$, the force being an approximate δ-function. At large distances from strings this is not quite correct. It is easy to introduce the smoothly varying force in the present formulation. In fact, let $V_{\text{tot}}(\vec{r}, z)$ be the total potential in the lattice. Then, the orbit from $(\vec{r}_1, z_1)$ to $(\vec{r}_2, z_2)$ is determined by the variational principle

$$\delta \int_{z_1}^{z_2} L(\vec{w}(z), \vec{r}(z), z) dz = 0, \quad \vec{r}(z_1) = \vec{r}_1, \quad \vec{r}(z_2) = \vec{r}_2, \tag{A.17}$$

where

$$L(\vec{w}(z), \vec{r}(z), z) = \frac{1}{2} M_1 \vec{w}^2(z) - V_{\text{tot}}(\vec{r}(z), z), \quad \vec{w}(z) = v \frac{d}{dz} \vec{r}(z),$$

and all angles are assumed to be small, i.e. $w \ll v$. The Lagrangian formulations (A.16) and (A.17) may be turned into Hamiltonian equations, but owing to the explicit dependence of L on z, i.e. on the time variable, one does not obtain the normal simple conservation of energy.

Emission of particle from atom in perfect string

On the basis of the approximate conservation of transverse energy $E_\perp$ in (A.4), we can discuss the emission of a particle from the centre of an atom in a string. It is of interest to find both the minimum angle and the angular distribution. It should be remembered, though, that this will not represent too well the actual emission from an atom in a lattice, because we disregard the vibrations of atoms, and in some cases quantal corrections should be included. However, we do obtain an alternative estimate of the validity of the continuum string picture.

The particle is emitted from the point $r = 0$, $z = 0$, at an angle Φ. Its total energy, $E_\perp = E \cdot \psi^2$, is then given by (A.3) and (A.11), where the energy is recorded at $z = d/2$, i.e. $r_b = d\Phi/2$, $\psi_b = \Phi$, and where we assume $W(r) = U(r)$,

$$E\psi^2 = E \cdot \Phi^2 + U(\Phi d/2). \tag{A.18}$$

Since emission probability is proportional to differential solid angle $\approx 2\pi\Phi d\Phi$, the probability distribution in angle ψ is also contained in (A.18). If the second term in (A.11) is included, we must add $W_2 = Ed^2 \cdot U'^2(\Phi d/2) \cdot (4E)^{-2}$ on the right-hand side of (A.18).

In order to obtain quantitative estimates, we introduce the standard potential (2.6), and (A.18) becomes

$$\psi^2 = \Phi^2 + \frac{\psi_1^2}{2} \log\left(\frac{4C^2a^2}{d^2 \cdot \Phi^2} + 1\right), \tag{A.19}$$

the additional term being $W_2 = \psi_1^4(2\Phi)^{-2}(1 + \Phi^2 d^2/4C^2a^2)^{-2}$.

It is interesting to compare the terms in (A.18) and (A.19) with the corresponding ones in scattering by a single atom, cf. p. 15 ff. In scattering by a single atom, with the same notation as in (A.18), one obtains

$$\psi^2 = \left(\Phi - \frac{d}{2E} U'(\Phi d)\right)^2 = \Phi^2 - \frac{\Phi d}{E} \cdot U'(\Phi d) + \frac{d^2}{4E^2} U'^2(\Phi d),$$

where the first term equals that in (A.19), whereas the second term tends to ψ_1^2 for low values of Φ. The third term dominates when Φ is small, and is similar to W_2 for $\Phi \to 0$. However, if $\psi_1 > a/d$, the third term can become $\sim W_2/16$. This indicates the ambiguity belonging to W_2. In the following we disregard W_2, primarily because its inclusion would not affect much the estimates of critical angles.

Returning to (A.19), we can estimate the minimum, $\psi_{\min}$, of the angle of emission, ψ. The minimum is obtained for

$$\Phi^2 = -\frac{2C^2a^2}{d^2} + \left[\left(\frac{2C^2a^2}{d^2}\right)^2 + \psi_1^2 \frac{2C^2a^2}{d^2}\right]^{1/2}.$$

It is convenient to distinguish between two limiting cases. Suppose that ψ_1 is small compared to a/d. Then

$$\psi_{\min} = \psi_1 \cdot \left[\log \frac{\alpha Ca}{\psi_1 d}\right]^{1/2}, \quad \text{for} \quad \psi_1 < \frac{a}{d}, \tag{A.20}$$

where $\alpha = 2^{3/2}\exp(1/2)$. The coefficient of ψ_1 is of order of 1.5-2, and is nearly independent of E and ψ_1, if ψ_1 is small.

At lower energies, where $\psi_1 > a/d$, we find from (A.19) the minimum angle

$$\psi_{\min} = 2\left(\frac{\psi_1}{\sqrt{2}} \frac{Ca}{d}\right)^{1/2} = 2\psi_2, \quad \text{for} \quad \psi_1 > \frac{a}{d}. \tag{A.21}$$

There is a smooth transition between the limiting cases (A.20) and (A.21). These two formulae are in good agreement with the qualitative considerations in § 2, cf. (2.9) and (2.10). It should be added that in the low energy region, where increasingly large impact parameters become important, the standard potential (2.6), as well as (A.21), should not be considered as accurate estimates.

In the formula (A.21), where angles are large, hardly more than the first atom contributes much to the deflection near the critical angle. It is noteworthy that in spite of the simplified transverse potential description used here, the critical angle (A.21) is 14 per cent above the corresponding precise result obtained for scattering by one atom only, at a distance d. This gives a justification of the use of transverse continuum potentials in one limit.

Appendix B

Quantal Corrections to Classical Description

The following discussion is divided in three sections, of which the two first are meant as a preamble to the third. The first section, Single Collisions, concerns a familiar case of scattering, where a classical description is the more accurate the lower the velocity. The second section, Continuum String, illustrates that if the continuum picture were completely valid, the transverse motion of particles would be essentially classical. The third section, Perfect String, aims at an estimate of the quantal correction to classical deflection by an actual string. It is shown that, in contrast to other collision problems, the classical description is the better the higher the velocity of the particle.

Single Collision

In a single collision the condition for a classical treatment is determined by essentially two lengths, the wave length $\lambda\!\!\!^{-}$ of the relative motion and $L_f = [\vartheta'(p)]^{-1}$, i.e. the focal length of the classical scattering, $\vartheta(p)$ being the deflection for impact parameter p. The total uncertainty, $\delta\vartheta$, in scattering angle can be obtained in a way analogous to that used by Bohr[12]. We assume that the angle $\vartheta(p)$ is small, and thus determined by (2.1′). With a wave packet of width δr there are two contributions to $\delta\vartheta$, one from diffraction and one from classical uncertainty in position, i.e.

$$(\delta\vartheta)^2 = \frac{\lambda\!\!\!^{-2}}{4(\delta r)^2} + (\delta r)^2 \cdot \big(\vartheta'(p)\big)^2. \tag{B.1}$$

The minimum value of (B.1) is obtained for $(\delta r)^2 = \lambda\!\!\!^{-}/(2\vartheta'(p))$, and becomes

$$(\delta\vartheta)^2 = \lambda\!\!\!^{-} \cdot \vartheta'(p). \tag{B.2}$$

In order to obtain a well-defined orbit, we may demand $(\delta\vartheta)^2 < \vartheta^2$, or

$$\lambda\!\!\!^{-} \frac{d}{dp}\left(\frac{1}{\vartheta(p)}\right) < 1, \tag{B.3}$$

which formula in the case of Rutherford scattering, $\vartheta = b/p$, leads to the inequality of Bohr[12]

$$\varkappa = \frac{2Z_1Z_2e^2}{\hbar v} > 1. \tag{B.4}$$

For the screened field of the standard atomic potential, (2.6″), the condition (B.3) and the scattering formula (2.1′) give the somewhat stronger condition

$$\varkappa > 1 + \frac{3p^2}{C^2a^2} \sim 1 + \frac{p^2}{a^2} \quad . \tag{B.5}$$

The above formulae apply for the relative motion, where $\lambda\!\!\!^{-} = \hbar/M_0v$, and $\vartheta(p)$ is the deflection in the centre of gravity system. However, it may be shown that the results also apply in the laboratory system, if (2.1) is fulfilled, i.e. with $\lambda\!\!\!^{-} = \hbar/M_1v$ and $\vartheta(p)$ the deflection in the laboratory system. This leads to a slight change in (B.1) and (B.2), since M_0 is replaced by M_1. However, (B.3), (B.4) and (B.5) remain unchanged, because the particle masses do not enter in these formulae, cf. (2.1′).

It should be strongly emphasized that (B.3), and similar conditions for the use of classical mechanics, are conditional and not absolute statements of limitations of classical estimates. Thus, (B.3) comes into play only if one desires a well-defined angle of deflection at very large distances from the scattering centre, in one-body or two-body scattering.

Continuum string

Let us assume that the continuum approximation is valid. We may then ask for the quantal correction to classical transverse motion. This is a quite straightforward problem, since both classically and in quantum mechanics there is conservation of transverse energy. As a simple example, we consider a string potential $U(r) = Z_1Z_2e^2\pi a/(2dr)$, and a particle with trans-

verse energy $E_\perp$. The Bohr condition (B.4) applied to the transverse motion with initial velocity $v_\perp = v\psi$, and initial energy $E_\perp = E\psi^2$, becomes

$$\varkappa_\perp = \varkappa \cdot \frac{\pi a}{2d} \cdot \frac{1}{\psi} > 1. \tag{B.6}$$

Since $\psi < \psi_1$, we find that $\varkappa_\perp$ is always larger than (we put $a \sim a_0 Z_2^{-1/3}$)

$$\varkappa_\perp \gtrsim \frac{\pi}{2}\left(\frac{M_1}{m}\right)^{1/2}\left(Z_1 Z_2^{1/3} \cdot \frac{a_0}{d}\right)^{1/2}. \tag{B.7}$$

The right-hand side in (B.7) is independent of energy E, and is certainly large compared to unity if M_1 is large compared to the electron mass m. In the general case of string deflection the formulae (2.21), (2.15) and (B.3) show that a classical description is applicable if $\lambda\!\!\!^{-}_\perp \ll a$. The essential point is that quantal tunnelling to the centre of a continuum string does not occur. The treatment can be extended, e.g. to continuum planes, but for the present purpose this is hardly necessary.

The following curious transformation from perfect string to continuum string may be illustrative. We start from a perfect string of atoms with spacing d. We imagine that each atom is cut in two equal parts, by a cut perpendicular to the string, retaining the electron distances from the string. The halves are placed with constant spacing $d/2$. Next, we cut each half in two, the spacing becoming $d/4$. This process can be continued, the string approaching more and more a true continuum string. On the one hand, consider an isolated collision between the moving particle and the fraction of an atom remaining at the n'th stage. The Born approximation will take over and be the more accurate, the higher the stage, and orbital pictures of the deflection fail completely (cf. the previous section). On the other hand, the continuum description of the particle motion gets more and more accurate as the cutting proceeds, and the estimates in the present section become relevant. In point of fact, the motion becomes rather classical. But in any case, the use of a continuum description is not determined by the isolated scattering by single entities; the decisive parameter is the length of the time interval d/v, between successive collisions, as will appear from the following section, and from (2.27).

Perfect string

When considering quantal corrections to the classical treatment of a set of successive collisions, we must compare the relative magnitude of a number of quantities. We can introduce five basic quantities of this kind, i.e.

$$\lambda\!\!\!^{-}, \quad L_f = [\vartheta'(r)]^{-1}, \quad a, \quad d, \quad L_{\text{coll}}, \tag{B.8}$$

where the first three parameters belong to single collisions too, whereas d is the distance between successive collisions, and $L_{\text{coll}} = v \cdot \Delta t$, cf. (2.7), the effective collision length with one string, combined of many separate atomic collisions. It is apparent that $L_{\text{coll}} > d \gg a$, and in the type of collisions considered here we also have $\lambda\!\!\!^{-} \ll d$.

Besides the above lengths, we are concerned with others, partly constructed from those in (B.8). Thus, if a wave-packet is formed in the transverse motion, of width δr, the wave-packet does not spread essentially on a path length $L_w = (\delta r)^2/\lambda\!\!\!^{-}$. We want to choose the size $(\delta r)^2$ of wave-packets, i.e. L_w, in an optimal way. A crucial question is whether L_w is large or small compared to d, the distance between successive collisions. Let us tentatively suppose that d could be large compared to L_w; we would then have a set of randomly adding fluctuations. In the i'th collision the angular fluctuation is analogous to (B.1),

$$(\delta\vartheta)_i^2 = \frac{\lambda\!\!\!^{-2}}{4(\delta r)_i^2} + (\delta r)_i^2 \vartheta'^2(r_i), \tag{B.9}$$

i.e. at minimum

$$(\delta r)_i^2 = \lambda\!\!\!^{-}/2\vartheta'(r_i), \quad (\delta\vartheta)_i^2 = \lambda\!\!\!^{-}\vartheta'(r_i), \tag{B.10}$$

and totally the angular fluctuation would become

$$(\delta\vartheta)^2 = \lambda\!\!\!^{-} \sum_i \vartheta'(r_i). \tag{B.11}$$

However, in this derivation we assumed that $d > L_{w,i}$, where $L_{w,i} = 1/2\vartheta'(r_i)$ according to (B.10). Since $\vartheta'(r_i) \approx \vartheta(r_i)/r_i$, this implies that $d > r_i/\vartheta_i$, which is in direct contradiction to the basic condition (2.7), requiring that several collisions take part in the repulsion of a particle, i.e. $L_{\text{coll}} > d$. We must therefore assume that $L_w \gtrsim d$, and can conclude that (B.11) does not apply. The conclusion that the wave-packets in consecutive collisions are not independent is in agreement with the inequalities (2.27), (2.27′).

Disregarding the assumptions leading to (B.11), we must then consider a wave-packet which approximately retains its width during the whole set of collisions. If the width is δr, the total contribution to angular dispersion from diffraction becomes $(\delta\vartheta)^2_{\text{diffr.}} = \lambda\!\!\!^{-2}/4(\delta r)^2$, which may be compared with the corresponding term $\Sigma\lambda\!\!\!^{-2}/4(\delta r)_i^2$ in (B.9), (B.10). As to the total uncertainty in deflection of the particle by the successive force fields, we assume that there is a lack of coherence between successive collisions. If they were completely coherent, the uncertainty in total deflection would

disappear when transverse energy is conserved. In order to get a slight overestimate of the uncertainty, we assume incoherence between successive terms, i.e. totally

$$(\delta\vartheta)^2 = \frac{\lambda\!\!\!^{-2}}{4(\delta r)^2} + (\delta r)^2 \sum_i \vartheta'^2(r_i), \tag{B.12}$$

leading to

$$(\delta\vartheta)^2 = \lambda\!\!\!^{-} \cdot [\sum_i \vartheta'^2(r_i)]^{1/2}, \tag{B.13}$$

and

$$(\delta r)^2 = \frac{\lambda\!\!\!^{-}}{2} [\sum_i \vartheta'^2(r_i)]^{-1/2}. \tag{B.14}$$

According to (B.13) and (B.14), both $(\delta\vartheta)^2$ and $(\delta r)^2$ become smaller than the corresponding expressions (B.11) and (B.10) belonging to completely independent wave packets. Since $\vartheta'^2(r_i)$ decreases strongly with increasing r_i, it can for large $E_\perp$ be permissible to include in (B.14) only the effect of the closest collision.

If we evaluate the summation in (B.13) as an integral, i.e. in the continuum approximation, we find

$$(\delta\vartheta)^2 = \lambda\!\!\!^{-} \cdot \frac{d^{1/2}}{2E} \left\{ \int_{-\infty}^{+\infty} dz U''^2(r(z)) \right\}^{1/2}, \tag{B.15}$$

where $r(z)$ is the distance from the string as a function of the coordinate z measured along the string. The integral in the brackets depends only on $E_\perp$ and on the impact parameter l in the transverse motion, but not on d. Therefore, (B.15) tends to zero for $d \to 0$, as it should do for continuum strings, in contrast to (B.11).

If (B.15) is multiplied by E, it represents the change in transverse energy in one collision. Let us consider a particle at different energies E, but in each case with the same transverse energy $E_\perp$. According to (B.15) its increase in transverse energy, by fluctuations due to quantal corrections, will then be proportional to the wave length $\lambda\!\!\!^{-}$ of its translatory motion. The quantal corrections to classical description therefore decrease with increasing velocity v.

A more detailed discussion of quantal effects will be published shortly, in collaboration with Ph. Lervig and V. Nielsen.

References

1) G. R. Piercy, F. Brown, J. A. Davies and M. McCargo, Phys. Rev. Lett. **10**, 399 (1963).
2) G. Dearnley, I.E.E.E. Trans. Nucl. Sci. NS11 (1964); R. S. Nelson and M. W. Thompson, Phil. Mag. **8**, 1677 (1963).
3) G. K. Wehner, Advances in Electronics **7**, 239 (1955); cf. also P. K. Rol, J. M. Fluit, F. P. Viehböck and M. de Jong, Proc. 4th Conf. on Ionization Phenomena in Gases, Uppsala, North-Holland Publ. Co., p. 257 (1959).
4) M. T. Robinson and O. S. Oen, Appl. Phys. Lett. **2**, 30, (1963), Phys. Rev. **132**, 2385 (1963).
5) J. Lindhard, Phys. Lett. **12**, 126 (1964).
6) J. Lindhard, M. Scharff and H. E. Schiøtt, Mat. Fys. Medd. Dan. Vid. Selsk. **33**, no. 14 (1963).
7) E. Bøgh, J. A. Davies and K. O. Nielsen, Phys. Lett. **12**, 129 (1964).
8) C. Lehmann and G. Leibfried, Journ. Appl. Phys. **34**, 2821 (1963).
9) P. Gombás, Die statistische Theorie des Atoms. Springer Verlag, Wien, 1949.
10) J. Lindhard, V. Nielsen and M. Scharff, Notes on Atomic Collisions I and IV, to be published.
11) C. Erginsoy, H. Wegner and W. Gibson, Phys. Rev. Lett. **13**, 530 (1964).
12) N. Bohr, Mat. Fys. Medd. Dan. Vid. Selsk. **18**, no. 8 (1948).
13) J. Lindhard and M. Scharff, Mat. Fys. Medd. Dan. Vid. Selsk. **27**, no. 15 (1953).
14) U. Fano, Ann. Rev. Nucl. Sci. **13**, 1 (1963); cf. also Studies in Penetration of Charged Particles in Matter, NAS-NRC Publ. no. 1133 (1964), p. 1 and p. 287.
15) H. A. Bethe, Ann. Physik **5**, 325 (1930).
16) J. Lindhard and Aa. Winther, Mat. Fys. Medd. Dan. Vid. Selsk. **34**, no. 4 (1964).
17) E. J. Williams, Proc. Roy. Soc. London *A***125**, 420 (1929).
18) B. Domeij and K. Björkqvist, Phys. Lett. **14**, 127 (1965).
19) M. W. Thompson, Phys. Rev. Lett. **13**, 756 (1964).
20) J. U. Andersen, J. A. Davies and K. O. Nielsen, to be published.
21) W. Brandt, J. M. Khan, D. L. Potter, R. D. Worley and H. P. Smith, Phys. Rev. Lett. **14**, 42 (1964).
22) E. Bøgh and E. Uggerhøj, Phys. Lett. **17**, 116 (1965), to be published.
23) J. A. Davies, L. Eriksson and P. Jespersgaard, to be published.
24) H. Lutz and R. Sizmann, Phys. Lett. **5**, 113 (1963).

Indleveret til Selskabet den 5. juli 1965.
Færdig fra trykkeriet den 29. november 1965.

Matematisk-fysiske Meddelelser
udgivet af
Det Kongelige Danske Videnskabernes Selskab
Bind **34,** nr. 15

Mat. Fys. Medd. Dan. Vid. Selsk. **34,** no. 15 (1966)

A SIMPLE NONBINARY SCATTERING MODEL APPLICABLE TO ATOMIC COLLISIONS IN CRYSTALS AT LOW ENERGIES

BY

HANS HENRIK ANDERSEN

AND

PETER SIGMUND

København 1966
Kommissionær: Ejnar Munksgaard

Synopsis

This paper presents the solution of a special scattering problem which may be important in the theory of slowing-down of atomic particles in crystals. A projectile moves along the center axis of a regular ring of n equal atoms which are free and do not interact with each other. The interaction between the projectile and each ring atom is described by a Born-Mayer potential, and the scattering is assumed to be elastic and governed by the classical equations of motion. Because of symmetry, the problem can be reduced to plane motion of a particle in a potential of elliptic symmetry. The elliptic force field is approximated by a spherical one, which is dependent on the initial conditions of the individual scattering problem. For the spherical symmetrical potential, scattering angles and related quantitites have been tabulated, but simple analytical approximations can be used too. As a result, one obtains the asymptotic velocities of the ring atoms as well as the energy loss of the projectile. Furthermore, it can be decided whether the projectile is reflected by the ring. Both the feasibility of assumptions specifying the problem and the validity of different approximations made in the transformation from the elliptic to the spherical potential are investigated. Special attention is paid to proper definitions of collision time and collision length which are important in collisions in crystals. Limitations to classical scattering arising from the uncertainty principle prove to be more serious than assumed previously. Inelastic contributions to the energy loss can easily be included. The oscillator forces binding lattice atoms turn out to influence the scattering process only at very small energies. The validity of the so-called momentum approximation and a related perturbation method are also investigated.

PRINTED IN DENMARK
BIANCO LUNOS BOGTRYKKERI A-S

CONTENTS

§ 1. Introduction

The slowing-down of an atom in a crystal is a many-body problem. The concept of mean free path, governing collisions in gases, is much less significant in solids because of the high density of scattering centres. The mean free path for elastic collisions with appreciable relative energy transfer is comparable to the interatomic distance except for energies considerably up in the keV region, dependent on mass and atomic number of projectiles and substance atoms involved. At these high energies, the majority of collisions are soft ones, so that perturbation methods may be successful. At low energies all collisions are more or less hard ones, so that the perturbation approach breaks down. As a consequence of the mean free path being so small, correlations between successive collisions, due to the regular lattice structure cannot be neglected in low energy collision theory.

Two main lattice structure effects on slowing-down have been proposed. Ion bombardment of single crystals parallel to low-indexed directions might result in almost completely suppressing close collisions by keeping projectiles a certain minimum distance away from lattice rows and planes (channelling). The experiments are usually done at energies from 1 keV up to several MeV, so that a theoretical treatment can make use of perturbation methods. But, for interpretation of range distributions and especially the so-called "super tails" it is important to investigate the slowing-down mechanism at the low energy end, to know whether the projectiles come to rest at lattice sites or interstitial positions, and, finally, whether they create defects or not. From this, one might also get information on possible diffusion following the slowing-down process.

It has furthermore been proposed that lattice geometry causes a high probability of nearly head-on (replacement) collisions for knock-on atoms. It seems difficult to verify this effect experimentally, but a great variety of sputtering and radiation damage phenomena are explained in a plausible way

by assuming it to exist. According to computer simulations of slowing-down, low energy knock-on atoms act preferably by exciting collision sequences along close-packed directions without travelling far away from their starting positions.

The characteristic difficulties of a many-body problem arise as soon as a collision is neither soft nor a pure two-body event. But the many-body problem might be simplified in special cases. Both in collision sequences and channelling *almost symmetrical* orbits between and parallel to lattice rows are supposed to have an appreciable statistical weight within certain energy intervals. Therefore, calculations of *perfectly symmetric* motion might answer some of the questions raised above.

This paper presents the treatment of a simple model. A set of lattice rows is resolved into symmetric rings; the projectile moves along their common symmetry axis, and its *interaction with one ring of atoms is considered to be the basic event*. Under certain simplifying assumptions it is possible to reduce this problem to scattering of one particle in a fixed force field, which can be solved approximately.

The accuracy of approximations as well as the limitations of classical elastic scattering and the applicability to collisions in crystals are examined. The main uncertainty entering the model is the interatomic potential. The repulsive Born-Mayer potential is used throughout the paper, mainly because of simplicity and for comparison with other investigations. As far as possible, the results are discussed without specifying potential constants too strictly.

The model gives rather definite answers on the break-down of perturbation theory and the maximum elastic energy transfer. Furthermore, it is possible to define a collision length in order to estimate the overlap between successive events. Finally, some suggestions are made about the approximate treatment of non-symmetric many-body collisions.

The present paper contains the general theory. It deals with the specification of the model and some direct consequences (§ 2); several methods of reduction to spherical scattering are examined in § 3; general results such as transferred energies and scattering angles are discussed in § 4, both numerically and analytically; this chapter also deals with the concept of collision length as well as the validity of approximations made in § 3; the last chapter is dedicated to the question of applicability of the model to collisions in crystals and to a discussion of quantum corrections and inelasticity. Applications to channelling and collision sequences will be contained in a forth-coming paper.

§ 2. The Model

2.1 Basic definitions

The dynamics of the following system (ANDERSEN & SIGMUND, 1965 a) will be investigated:

1) n atoms $i = 1 \ldots n$ of mass m_1, neither bound by external forces nor interacting with each other, form initially a regular ring with radius L.
2) A projectile of mass m_0 moving on the ring axis with an initial velocity $\vec{v}_0$ (Fig. 1) interacts with the ring atoms via some repulsive potential

$$V(r_{0i}) = V(|\vec{r}_0 - \vec{r}_i|). \tag{2.1.1}$$

In applications only Born-Mayer interaction

$$V(r) = Ae^{-r/a} \tag{2.1.2}$$

will be used.
3) The collision is treated by classical mechanics.

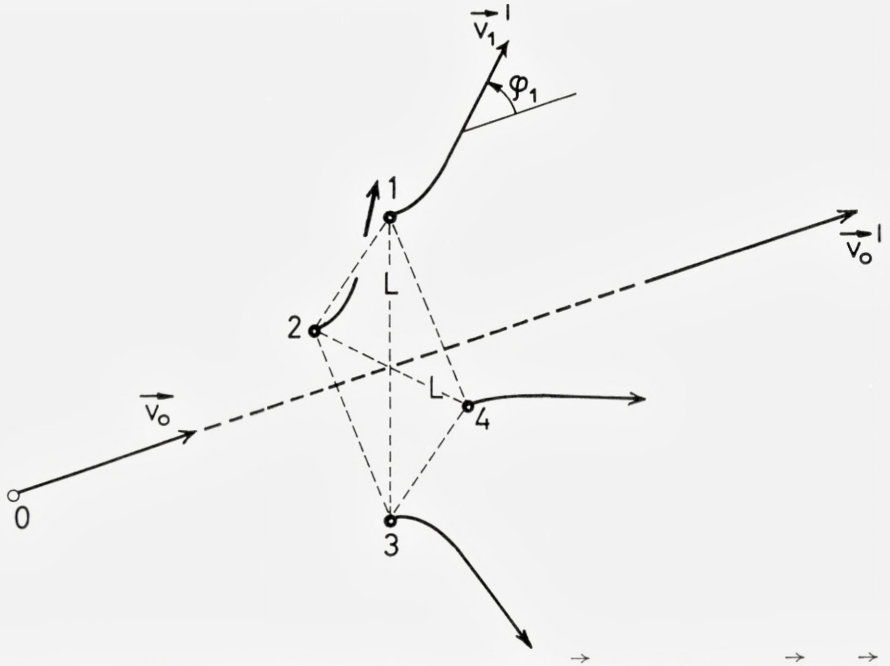

Fig. 1. Projectile 0 interacting with a ring of $n = 4$ atoms. $\vec{v}_0$ = initial velocity. $\vec{v}_0'$ and $\vec{v}_1'$ final velocities of projectile and ring particle 1.

Due to the symmetrical initial conditions the projectile will keep on moving on the ring axis, and ring atoms perform identical motions in planes made up by the axis and their initial positions (Fig. 1). Quantities of interest are:

i) the total energy loss ΔE of the projectile to the ring,
ii) the asymptotic orbits and energies of ring particles,
iii) the energy limit below which the projectile will be reflected by the ring, and
iv) the collision time and corresponding path length.

The feasibility of the assumptions involved in 1)–3) will be examined in later sections of this paper. The validity of assumption 1) depends on the role of binding forces (sect. 5.3). The significance of Born-Mayer repulsion and the choice of constants A, a is discussed in a separate paper (Andersen & Sigmund, 1965 b). Quantum mechanical limitations and inelastic effects are mentioned in sects. 5.1 and 5.2.

In applications to collisions in crystals, the ring radius L will be at least one half nearest neighbour distance ($L \gtrsim 1$Å), n may take the values 2, 3, and 4, a is supposed to be slightly smaller than one half Bohr-radius ($a \sim 0.2$Å), while A varies over a wide range of energies in the keV region, dependent on the atoms involved. Initial energies of interest range from about 10 eV up to 10 keV.

2.2 The perturbation approach

If the energy loss ΔE is very small compared to the initial energy E_0 of the projectile, ΔE can be calculated by first order perturbation theory (momentum approximation; for brevity: MA)

$$\Delta E = n \cdot \frac{1}{2m_1} \left(\int_{-\infty}^{\infty} \frac{dx_0}{v_0} \operatorname{grad}_\perp V(r_{01}) \right)^2, \tag{2.2.1}$$

where $\operatorname{grad}_\perp$ indicates the component of the force perpendicular to the orbit of the projectile. This orbit is assumed to be a straight line, while particle 1 is considered as being fixed during the collision.

For Born-Mayer interaction (2.1.2) one gets (Brinkmann, 1954)

$$\Delta E = n \cdot \frac{m_0}{m_1} \frac{A^2}{E_0} \left[\frac{L}{a} K_0 \left(\frac{L}{a} \right) \right]^2. \tag{2.2.2}$$

The function $K_0(\xi)$ is a modified Hankel function with the asymptotic expansion (JAHNKE et al., 1960)

$$K_0(\xi) \sim \sqrt{\frac{\pi}{2\xi}}\, e^{-\xi} \quad \text{for large } \xi. \tag{2.2.3}$$

According to the previous section,

$$\xi = L/a \gtrsim 5. \tag{2.2.4}$$

For these arguments the expansion (2.2.3) approximates K_0 with an accuracy better than 3 pct.

At small energies ΔE becomes large according to (2.2.2), so this approach must break down. In order to estimate the applicability of (2.2.2) we note that ΔE cannot be greater than either the initial energy E_0 or the height of the potential barrier at the ring center, so

$$\Delta E \leqq E_0 \tag{2.2.5}$$

and

$$\Delta E \leqq nAe^{-L/A}. \tag{2.2.6}$$

E_0 must be much greater than the limiting energies defined by (2.2.5) and (2.2.6). Inserting (2.2.2) and (2.2.3) we obtain

$$E_0 \gg \left(\frac{\pi}{2}\, n\, \frac{m_0}{m_1}\, \frac{L}{a}\right)^{1/2} Ae^{-L/a} \tag{2.2.5'}$$

and

$$E_0 \gg \frac{\pi}{2}\, \frac{m_0}{m_1}\, \frac{L}{a}\, Ae^{-L/a} \tag{2.2.6'}$$

as necessary conditions for the MA to be a good approximation.

For not too different masses, the two conditions are essentially equivalent. If $m_0 \gg m_1$, (2.2.6′) is the stronger one.

LEHMANN & LEIBFRIED (1963) have derived a criterion of the same type by comparing second and first order contributions in the perturbation series for the scattering angle of merely two particles:

$$E_0 \gg \frac{1}{\sqrt{2}} \left(1 + \frac{m_0}{m_1}\right) \frac{L}{a}\, Ae^{-L/a}. \tag{2.2.7}$$

(2.2.7) is equivalent to (2.2.6′) for $m_0 \gtrsim m_1$. It is easily seen that in our case (2.2.7) cannot be the appropriate criterion as soon as $m_0 \ll m_1$; the perturbation approach is reasonable if

i) the ring particles only move a small distance away during the collision, and
ii) the deflection of the projectile is small.

The latter condition is ideally fulfilled in the ring collision, while a corresponding two-particle event with $m_0 \ll m_1$ might result in a considerable deflection of the projectile. Hence, (2.2.7) will underestimate the applicability of the MA.

Numerically, the typical limits vary from some tens of eV up to several keV, because of the strong dependence on L and on the atoms involved.

Standard scattering theory is easily carried out beyond the MA, when one deals with pure two-body collisions. Also for our model some quantities of interest may be estimated using two-body scattering theory, but this must be expected to be a poor approach to the problem[1]. A comparison to the more accurate evaluation will be made in sect. 4.6.

2.3 Conservation laws

An accurate treatment is simplified by stating the conservation laws governing our system.

The asymptotic velocities $\vec{v}_i'$ of different ring atoms (Fig. 1) and their angles φ_i with the $\vec{v}_0$-axis are equal because of symmetry:

$$|\vec{v}_i'| = v_i' = v_1'; \quad \varphi_i = \varphi_1, \tag{2.3.1}$$

where

$$\cos \varphi_i = \frac{(\vec{v}_i' \cdot \vec{v}_0)}{v_i' v_0}. \tag{2.3.2}$$

Hence, momentum and energy conservation yield

$$m_0 v_0 = m_0 v_0' + n \cdot m_1 v_1' \cos \varphi_1, \tag{2.3.3}$$

$$\frac{m_0}{2} v_0^2 = \frac{m_0}{2} v_0'^2 + n \cdot \frac{m_1}{2} v_1'^2, \tag{2.3.4}$$

$\vec{v}_0'$ being the asymptotic velocity of the projectile.

Conservation of angular and transverse momentum has been fully taken into account by stating the symmetry of the orbits.

[1] Sometimes, especially in computer calculations, the interaction is cut off at a certain distance in order to ensure the two-body nature of collisions. It is obvious that this procedure might give rise to peculiar multiple scattering effects when applied to an almost symmetric ring collision (Robinson and Oen, 1963). The completely symmetric case cannot be simplified in this way.

(2.3.3) and (2.3.4) lead to the relative energy transfer to one ring atom,

$$\Delta E_1 = \frac{m_1}{2} v_1'^2 = \frac{4 \frac{m_1}{m_0} \cos^2 \varphi_1}{\left(1 + n \frac{m_1}{m_0} \cos^2 \varphi_1\right)^2} E_0 . \tag{2.3.5}$$

The total energy loss to the ring is given by

$$\Delta E = E_0 - E_0' = n \cdot \Delta E_1 , \tag{2.3.6}$$

where E_0' is the asymptotic projectile energy; the asymptotic velocity becomes

$$v_0' = \frac{1 - n \frac{m_1}{m_0} \cos^2 \varphi_1}{1 + n \frac{m_1}{m_0} \cos^2 \varphi_1} v_0 .$$

The particle is reflected by the ring if v_0'/v_0 is negative, i. e.

$$\cos \varphi_1 > \sqrt{m_0/n m_1} . \tag{2.3.7}$$

The reverse relation to (2.3.7) does not necessarily involve that the projectile really penetrates the ring, as the ring particles have a velocity component in the forward direction. However, in many applications this component is relatively small.

Most of the quantities of interest have thus been expressed by the angle φ_1. Clearly, φ_1 is governed by the interatomic potential.

2.4 Transformation to relative coordinates

Convenient coordinates describing the internal state of the system are the ring radius and the distance of the projectile from the ring center. Let us consider the motion in a plane formed by $\vec{v}_0$ and $\vec{v}_1'$ and choose $\vec{v}_0$ as the x-axis (Fig. 2). Then,

$$\vec{r}_0 = (x_0, 0); \quad \vec{r}_1 = (x_1, y_1) . \tag{2.4.1}$$

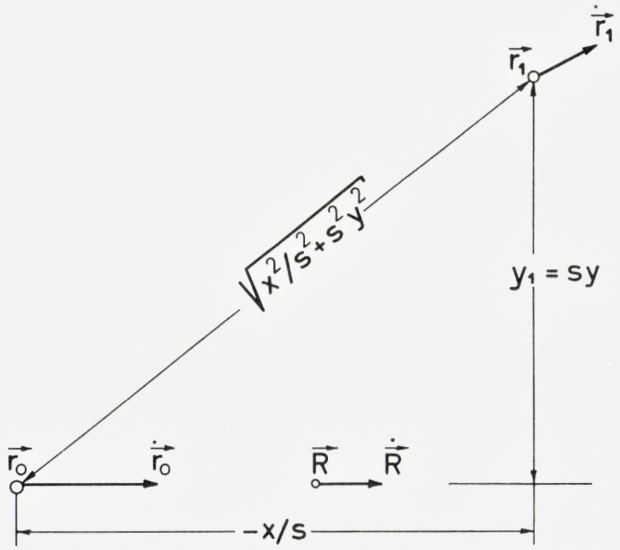

Fig. 2. Definition of relative coordinates x, y. $\vec{r}_0, \dot{\vec{r}}_0, \vec{r}_1, \dot{\vec{r}}_1$: position and velocity of projectile and *one* ring atom. $\vec{R}, \dot{\vec{R}}$: position and velocity of center-of-mass.

The center-of-mass moves along the x-axis, so

$$\vec{R} = (X, O); \quad X = \frac{m_0}{M} x_0 + n \cdot \frac{m_1}{M} x_1, \tag{2.4.2}$$

where M is the total mass:

$$M = m_0 + n m_1. \tag{2.4.3}$$

Furthermore, we define relative coordinates

$$x = s \cdot (x_0 - x_1); \quad y = y_1/s, \tag{2.4.4}$$

so that

$$x_0 = X + n \frac{m_1}{M} \cdot \frac{x}{s}; \quad x_1 = X - \frac{m_0}{M} \frac{x}{s}; \quad y_1 = sy. \tag{2.4.5}$$

In (2.4.4) we have introduced a scaling factor s. This is necessary in order to make the reduced mass isotropic. The kinetic energy

$$E_{\text{kin}} = \frac{m_0}{2}\dot{x}_0^2 + n \cdot \frac{m_1}{2}(\dot{x}_1^2 + \dot{y}_1^2)$$

becomes in the new coordinates (2.4.5)

$$E_{\text{kin}} = \frac{M}{2}\dot{X}^2 + n \cdot \frac{m_1}{2}\left(\frac{m_0}{M}\frac{\dot{x}^2}{s^2} + s^2\dot{y}^2\right).$$

This simplifies to

$$E_{\text{kin}} = \frac{M}{2}\dot{X}^2 + n\frac{m_1}{2}s^2(\dot{x}^2 + \dot{y}^2), \tag{2.4.6}$$

if we choose

$$s^4 = m_0/M = \frac{m_0}{m_0 + nm_1} < 1. \tag{2.4.7}$$

The total potential energy becomes, according to (2.1.1) and Fig. 2,

$$\Phi(x, y) = \sum_i V(r_{0i}) = nV(r_{01}) = nV\left(\sqrt{x^2/s^2 + s^2y^2}\right). \tag{2.4.8}$$

So, in the reduced scattering problem the force field has elliptical symmetry. If the projectile comes in from infinity we get the initial conditions

$$x(t = -\infty) = -\infty;$$

$$p = y(-\infty) = \frac{1}{s}y_1(-\infty) = L/s, \tag{2.4.9}$$

$$v_r = \dot{x}(-\infty) = sv_0, \tag{2.4.10}$$

$$E_r = n\frac{m_1}{2}s^2(\dot{x}^2 + \dot{y}^2)\Big|_{t=-\infty} = \frac{nm_1}{M}E_0, \tag{2.4.11}$$

where we have made use of (2.4.4), (2.4.6) and (2.4.7). The quantities p, v_r and E_r are the impact parameter, relative velocity and relative energy defining the reduced scattering problem (Fig. 3).

The relation between scattering angle ϑ in the reduced system (Fig. 3) and φ_1 is found in the following way:

$$\operatorname{tg}\varphi_1 = \frac{\dot{y}_1}{\dot{x}_1}\Big|_{t=\infty} = \frac{s^2v_0\sin\vartheta}{s^4v_0 - s^4v_0\cos\vartheta} = \frac{1}{s^2}\operatorname{ctg}\vartheta/2. \tag{2.4.12}$$

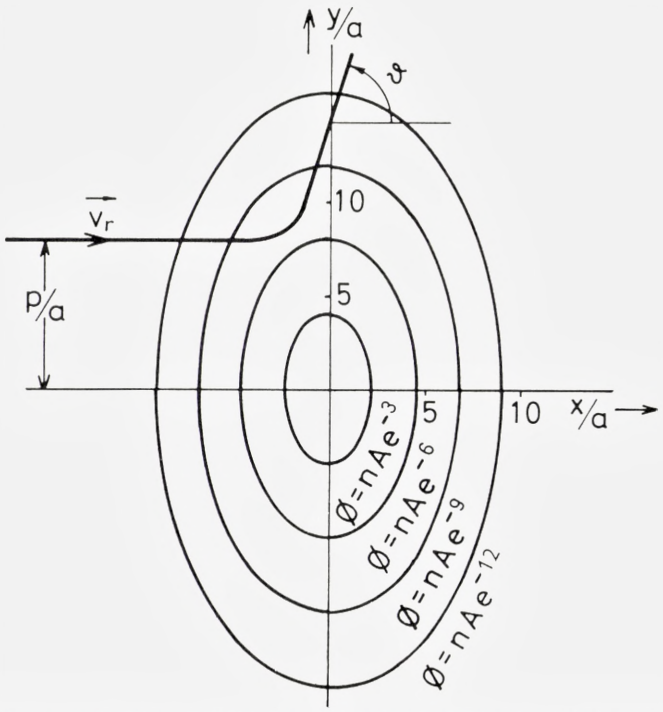

Fig. 3. The reduced scattering problem for Born-Mayer interaction. Successive equipotential lines differ by a factor of $e^{\pm 3}$. Quantitative details correspond to an example discussed in sect. 4.3 (Fig. 7).

Here we have used (2.4.5), (2.4.2) and (2.4.10). Inserting (2.4.12) into (2.3.5) we obtain the energy loss (2.3.6):

$$\Delta E = 4\frac{nm_1}{M} E_0 \cdot \sin^2\frac{\vartheta}{2}\left(1 - \frac{nm_1}{M}\sin^2\vartheta/2\right). \tag{2.4.13}$$

The condition (2.3.7) for reflection reads

$$\sin^2\vartheta/2 > \frac{M}{2nm_1}. \tag{2.4.14}$$

The projectile penetrates the ring if $\vartheta < \pi/2$, i. e.

$$\sin^2\vartheta/2 < 1/2. \tag{2.4.15}$$

In the intermediate interval,

$$\frac{1}{2} < \sin^2 \vartheta/2 < \frac{1}{2} \cdot \frac{M}{nm_1}, \tag{2.4.16}$$

the projectile moves asymptotically in the forward direction, but behind the centre of the ring.

§ 3. Reduction to Spherical Symmetry

3.1 General remarks

The reduced scattering problem is simple, but nontrivial because of the elliptical symmetry of the potential $\Phi(x,y)$. As angular momentum is not conserved, the scattering angle ϑ and related quantities cannot be expressed by integrals as in standard scattering theory. In order to calculate only the orbit of the scattered particle, it would be most convenient to start at Jacobi's principle, which states that

$$\delta \int_1^2 \sqrt{E_r - \Phi(x,y)}\, ds = 0; \tag{3.1.1}$$

where $y = y(x)$ has to be varied between two fixed points 1 and 2 in the x,y-plane, and ds is the line element

$$ds = \sqrt{1 + (dy/dx)^2}\, dx.$$

(3.1.1) is equivalent to a differential equation for $y = y(x)$:

$$\frac{1}{2} \cdot \frac{1}{E_r - \Phi} \left(\frac{\partial \Phi}{\partial y} - y' \frac{\partial \Phi}{\partial x} \right) + \frac{y''}{1 + y'^2} = 0. \tag{3.1.2}$$

Several standard procedures have been examined in order to solve (3.1.1) or (3.1.2). Most of them are rather specific for the spherical case. The only systematic approach, which was found to have some success, is the perturbation series expansion of (3.1.2). The first two terms are evaluated in Appendix A. But, as was stated by Lehmann and Leibfried (1963) for spherically symmetric interaction, the perturbation series has in general a finite radius of convergence, and higher than first order perturbations do hardly improve the scattering formula.

Instead of calculating approximate orbits in the exact field, one can also calculate exact orbits for an approximate field. The method is widely used in scattering theory and has the advantage that the limit of applicability may easily be found by comparing "true" and approximate forces.

As long as $m_0 \gtrsim m_1$, the excentricity of the potential lines is moderate. The proportion between major and minor axis: $\frac{1}{s^2} = \sqrt{1 + nm_1/m_0}$ becomes $\lesssim 2.5$. We shall mainly concentrate our attention on the case $m_0 \gtrsim m_1$, as in the opposite case, $m_0 \ll m_1$, the MA remains valid down to sufficiently low energies, given by (2.2.5′). Furthermore, deflections in strongly varying Born-Mayer fields will take place in a rather small region in space. Hence, in the case $m_0 \gtrsim m_1$ it is expected to be an excellent approximation to replace $\Phi(x,y)$ by a potential of *spherical symmetry* which is similar to Φ in a certain critical region. This critical region should be centered around that point where the scattered particle achieves its highest potential energy. Unfortunately, it is not possible to find this point in a straightforward manner when p and E_r are given.

Therefore, two complementary matching methods are discussed, which we call close collision approximation (CCA) and distant collision approximation (DCA). In both cases the center of a spherical potential is found from the radius of curvature of a certain equipotential line. CCA and DCA will be seen to cover the whole curve $\vartheta(p)$ for $o \leq p \leq \infty$ for given E_r with a good accuracy. As small impact parameters p do not occur in applications, the DCA will be the more important approach.

3.2 Close collision approximation

Figure 4 shows the orbit of a particle in an almost central collision. The closest distance of approach $R(p)$ will be approximately equal to $R(p = 0) = R_0$, which is given by

$$\Phi(-R_0, 0) = E_r. \tag{3.2.1}$$

The radius of curvature of the equipotential line in $(-R_0, 0)$ is, according to (2.4.8), given by

$$\varrho = \frac{(R_0/s^2)^2}{R_0} = \frac{R_0}{s^4}. \tag{3.2.2}$$

Hence, the centre of the CCA potential will be at

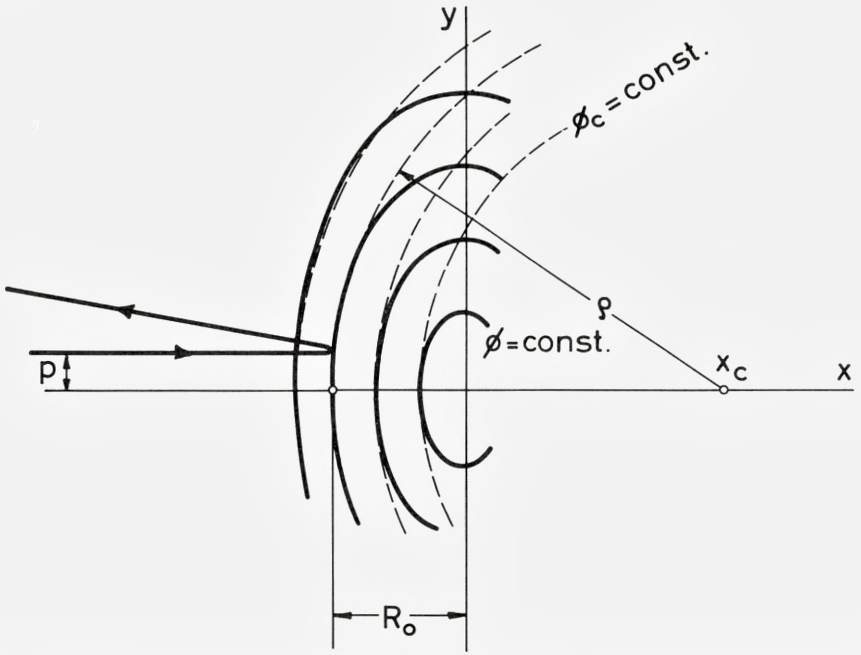

Fig. 4. Construction of the CCA potential Φ_C (schematically). For small p only the potential near $(-R_0, 0)$ causes deflection. x_C is the center of curvature to the potential line through this point.

$$x_C = -R_0 + \varrho = R_0\left(\frac{1}{s^4} - 1\right). \tag{3.2.3}$$

The CCA potential Φ_C is then constructed in such a way that

$$\Phi_C(x,y) = \Phi(x,y) \quad \text{for} \quad y = 0, \quad x \leq 0. \tag{3.2.4}$$

For the BM potential (2.1.2), $\Phi(x,y)$ is given by

$$\Phi(x,y) = nA \exp\left(-\frac{1}{a}\sqrt{x^2/s^2 + y^2 \cdot s^2}\right), \tag{3.2.5}$$

so that

$$\Phi_C(x,y) = nAe^{x_C/sa} \cdot e^{-r'/sa}, \tag{3.2.6}$$

where r' is the distance between (x,y) and $(x_C, 0)$. Hence, the scattering angle in the CCA may be expressed by that for a spherically symmetric potential

$$\Phi_C(r') = A_C e^{-r'/a_C}, \tag{3.2.7}$$

with

$$a_C = sa; \quad A_C = nAe^{x_C/sa} = E_r\left(\frac{nA}{E_r}\right)^{1/s^4}, \tag{3.2.8}$$

where we have made use of (3.2.1) and (3.2.3). Obviously, Φ_C yields the exact solution for the central collision. The validity of this approach at finite impact parameters will be investigated in sects. 4.3 and 4.5.

3.3 Distant collision approximation

In distant collisions, where ϑ is small, the scattering will essentially take place near the point $(0,p)$. We can therefore choose the center of curvature of the potential line through this point as symmetry center of another matching potential Φ_D, as indicated in Fig. 5. The radius of curvature ϱ is given by

$$\varrho = \frac{(ps^2)^2}{p} = ps^4, \tag{3.3.1}$$

and the symmetry center has the ordinate

$$y_D = p - \varrho = p(1 - s^4). \tag{3.3.2}$$

Φ_D is chosen so that

$$\Phi_D(x,y) = \Phi(x,y) \quad \text{for} \quad x = 0, \quad y \geq y_D. \tag{3.3.3}$$

Using (3.2.5), we get

$$\Phi_D = n \cdot A \cdot e^{-\frac{sy_D}{a}} \cdot e^{-\frac{sr'}{a}},$$

where r' is now the distance between (x,y) and $(0,y_D)$. Hence, the DCA potential is given by

$$\Phi_D(r') = A_D e^{-r'/a_D}, \tag{3.3.4}$$

where

$$a_D = \frac{a}{s} \tag{3.3.5}$$

and

$$A_D = n \cdot A \cdot e^{-\frac{sy_D}{a}} = nAe^{-\frac{sp}{a}(1-s^4)}. \tag{3.3.6}$$

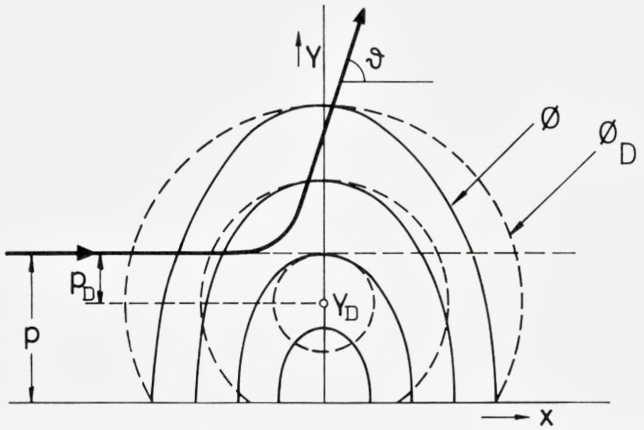

Fig. 5. Construction of the DCA potential Φ_D. For small scattering angle ϑ mainly the potential near $(0, p)$ causes deflection. y_D is the center of curvature of the potential line through this point. Quantitative details correspond to the example discussed in sect. 4.3 (Fig. 7).

Contrary to the CCA we also get a new impact parameter in the DCA. Instead of p we have (Fig. 5)

$$p_D = \varrho = ps^4. \tag{3.3.7}$$

The scattering angle is determined by the two proportions

$$\frac{p_D}{a_D} = s^4 \cdot \frac{L}{a}; \quad \frac{E_r}{A_D} = \frac{m_1}{M} \frac{E_0}{A} e^{\frac{L}{a} \cdot \frac{nm_1}{M}}. \tag{3.3.8}$$

Deriving (3.3.8) we have used (2.4.9), (2.4.11) and (2.4.7).

Also the applicability of this approach will be examined in sections 4.3 and 4.5.

3.4 Constant velocity approximation

A much simpler reduction to spherical scattering is found in the case $m_0 \gg nm_1$, where the projectile moves nearly uniformly independent of the interaction potential. In this case it seems reasonable to go over to a system moving with velocity v_0 and to consider the projectile as a fixed scattering center in this system. As the ring particles are independent of each other, they are scattered individually by an angle α (Fig. 6), which can be cal-

culated from the *true* Born-Mayer potential as interaction, impact parameter L and energy

$$E' = \frac{m_1}{m_0} E_0 . \tag{3.4.1}$$

In the laboratory system, particle 1 has, after the collision, velocity components

$$\left.\begin{aligned} v'_{1x} &= v_0(1 - \cos\alpha) \\ v'_{1y} &= v_0 \sin\alpha , \end{aligned}\right\} \tag{3.4.2}$$

corresponding to a scattering angle φ_1 given by

$$\operatorname{tg}\varphi_1 = \frac{\sin\alpha}{1-\cos\alpha} = \operatorname{ctg}\alpha/2 , \tag{3.4.3}$$

and an energy

$$\Delta E_1 = 4\frac{m_1}{m_0} E_0 \cdot \sin^2\alpha/2 . \tag{3.4.4}$$

An approach of this kind has been used by WEIJSENFELD (1964) in the theory of assisted focusing collision sequences. The essential difference to the MA is that the ring particles are not considered to be fixed during the collision. They are free to move away, while the projectile is restricted in its transversal motion. This approach, which we call constant velocity approximation (CVA), is a perturbation approach in the sense that the deflection of the ring particles is determined by the zero order motion of the projectile. The approximation does, however, not involve an expansion in powers of the interaction potential. It will turn out in sect. 4.3 that the quality of the CVA is surprisingly good, even for lighter projectiles.

When m_0 is of the order of nm_1, the CVA violates the conservation laws. Weijsenfeld avoided this by assuming only the y-component v'_{1y} to be determined by (3.4.2), while the x-component is found from energy and momentum conservation. However, for not too large energy transfers the two formulations are essentially equivalent, as the ring particles move almost perpendicularly to $\vec{v}_0$. The straightforward formulation of the Weijsenfeld approach gives an energy transfer

$$\Delta E_1 = 4\frac{m_1}{m_0} E_0 \sin^2\alpha/2\left(1 + 2n\frac{m_1}{m_0}\sin^4\frac{\alpha}{2} + \ldots\right) \tag{3.4.5}$$

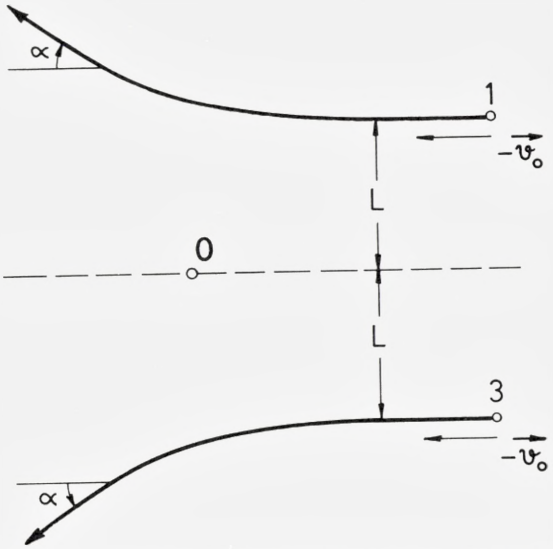

Fig. 6. Constant velocity approximation. The situation in Fig. 1 is considered from a system moving with $\vec{v}_0$. The projectile 0 is assumed to be at rest in this system throughout the collision.

which differs from (3.4.4) only by a correction term of fourth order in $\sin \alpha/2$, which is negligible. We prefer to use the CVA, as it is much simpler than Weijsenfeld's original approach. As it will turn out in sect. 4.3, the CVA may even be valid if ΔE_1 is not negligible compared to E_0.

§ 4. Application to Born-Mayer Interaction

4.1 Accurate scattering angles

We have now found three possibilities of reducing the original problem of finding φ_1 to that of calculating the scattering angle

$$\vartheta(E',p') = \pi - \int_{r'_m}^{\infty} \frac{2p'dr'/r'^2}{\sqrt{1 - \Phi'(r')/E' - (p'/r')^2}}, \tag{4.1.1}$$

for some spherical Born-Mayer potential

$$\Phi'(r') = A'e^{-r'/a'}. \tag{4.1.2}$$

E' and p' indicate relative energy and impact parameter in any of the three spherical scattering problems. r'_m is the distance of closest approach defined by the zero of the square root in (4.1.1).

The integral (4.1.1) has been tabulated by Robinson (1963) for $0.005 \leq E'/A' \leq 1$ and p'/a' ranging from zero up to such values where the accuracy of the MA is sufficiently good. The tables provide enough points to cover all cases of interest in applications as far as concerns the DCA, which is the approximation mostly used later on. Therefore, in plotting ΔE vs. E_0, uncertainties from the evaluation of (4.1.1) can be assumed to be negligible within the range of validity of the DCA.

For those cases where the tables do not provide data one has to use analytical approximations. A list of references has been given in an earlier paper (Sigmund & Vajda, 1964). We only mention two formulae, the most accurate one given by Heinrich (1964):

$$\sin \vartheta/2 = \frac{1}{1 + 2/\vartheta_1}, \tag{4.1.3}$$

where

$$\vartheta_1 = \frac{A'}{E'} \cdot \frac{r_m'^3}{a' p'^2} K_0(r'_m/a'). \tag{4.1.4}$$

It is seen by expansion that (4.1.3) gives the correct result at small angles. Furthermore, $\vartheta(p' = 0) = \pi$, as it must be. Within the whole range of the numerical tables the accuracy of (4.1.3) is better than 4 pct. The disadvantage of this formula is that r'_m is defined by a transcendental equation, so one has to use p' and r'_m as independent variables and calculate E'.

At large angles the following formula has proved to be a good approximation (Sigmund & Vajda, 1964):

$$\sin^2 \vartheta/2 = \frac{1 - \left(\frac{p'}{R'_0}\right)^2 \left(1 - \frac{a'}{R'_0}\right)^2}{1 + 4 \frac{a'}{R'_0} \cdot \left(\frac{p'}{R'_0}\right)^2}, \tag{4.1.5}$$

where R'_0 is the head-on radius defined by

$$\frac{R'_0}{a'} = \ln \frac{A'}{E'}. \tag{4.1.6}$$

(4.1.5) is based on the matching method of Leibfried & Oen (1962).

4.2 A simple analytical approximation

For qualitative considerations the above mentioned scattering formulae are too complex. If one is not interested in a high accuracy, an extremely simple approximation may be found as follows. The potential (4.1.2) is matched by a cut-off Coulomb potential:

$$\Phi_M(r') = \begin{cases} C\left(\frac{c}{r'} - 1\right) \ldots\ldots\ldots & r' < c \\ 0 \qquad\qquad \ldots\ldots\ldots & r' \geq c. \end{cases} \tag{4.2.1}$$

The constants C and c are chosen so that the potentials agree in value and slope at $r' = p'$:

$$\Phi_M(p') = \Phi'(p') \quad \text{and} \quad \frac{d}{dp'}\Phi_M(p') = \frac{d}{dp'}\Phi'(p'). \tag{4.2.2}$$

This matching method is similar to those by Leibfried & Oen (1962) and Lehmann & Robinson (1964); Leibfried and Oen fulfilled the conditions (4.2.2) in $r' = R_0'$ instead of $r' = p'$, and Lehmann and Robinson matched in $r' = r_m'$. For the very central collision ($p' \ll R_0'$) our matching procedure is expected to break down.

Potential (4.2.1) yields, according to Leibfried and Oen,

$$\sin^2\frac{\vartheta}{2} = \frac{1 - (p'/c)^2}{1 + \left(\frac{p'}{c}\right)^2 \cdot \frac{4E'}{C}\left(\frac{E'}{C} + 1\right)} \quad \text{for} \quad p' < c.$$

From (4.2.2),

$$c = \frac{p'^2}{p' - a'}; \quad C = A' e^{-p'/a'}\left(\frac{p'}{a'} - 1\right),$$

so

$$\sin^2\frac{\vartheta}{2} = \frac{2\frac{p'}{a'} - 1}{\left(\frac{p'}{a'} + 2\frac{E'}{A'}e^{p'/a'}\right)^2 - 4\frac{E'}{A'}e^{p'/a'}}, \tag{4.2.3}$$

We shall mainly apply (4.2.3) in connection with the DCA. According to (3.3.8), we have

$$\frac{p_D}{a_D} = s^4 \cdot \frac{L}{a} \gtrsim \frac{1}{5} \cdot 5 = 1 \quad \text{for} \quad m_0 \gtrsim m_1,$$

when we use the numerical estimates of sects. 2.1 and 3.1. Comparison with the numerical tables shows that the accuracy of (4.2.3) is better than 10 pct. for $p'/a' \gtrsim 1.5$. For the very lowest values of p_D/a_D one has to use more careful estimates. Clearly, (4.2.3) becomes wrong for $p' < a'$. Inserting (3.3.8) in (4.2.3) we obtain

DCA:
$$\sin^2 \frac{\vartheta}{2} = \frac{2 \frac{m_0}{M} \frac{L}{a} - 1}{\left(\frac{m_0}{M} \frac{L}{a} + 2 \frac{m_1}{M} \frac{E_0}{A} e^{L/a} \right)^2 - 4 \frac{m_1}{M} \frac{E_0}{A} e_{L/a}}. \tag{4.2.4}$$

4.3 General results

In order to give an impression of the applicability of the different approximation methods we discuss an example. Fig. 7 shows $\sin \vartheta/2$ as a function of L/a for $n = 2$; $m_0 = m_1$; $E_0/A = 4.45_{10}-3$. For the copper potential of Gibson et al. (1960),

$$A = 22.5 \text{ keV}; \quad a = .196 \text{ Å} \quad \text{for} \quad \text{Cu}, \tag{4.3.1}$$

this corresponds to $E_0 = 100$ eV. The calculations were done in the following way:

CCA: Parameters from (3.2.8), $\sin \vartheta/2$ a) from (4.1.3), b) from (4.1.5) (4.3.2)

DCA: Parameters from (3.3.8), $\sin \vartheta/2$ from numerical tables (Robinson, 1963) (4.3.3)

MA: $\vartheta = (\text{tg}\vartheta)^{(1)}$ from (A. 8) (4.3.4)

CVA: ϑ from (2.4.12), where φ_1 is given by (3.4.3) and α is taken from the numerical tables. (4.3.5)

As the CVA has no connection to the elliptical scattering problem, the reduced scattering angle ϑ introduced by (4.3.5) has only formal significance. It is plotted in Fig. 7 in order to show the direction of discrepancies.

We know that the CCA and MA are correct at, respectively, small and large impact parameters. Fig. 7 indicates that the DCA not only yields the

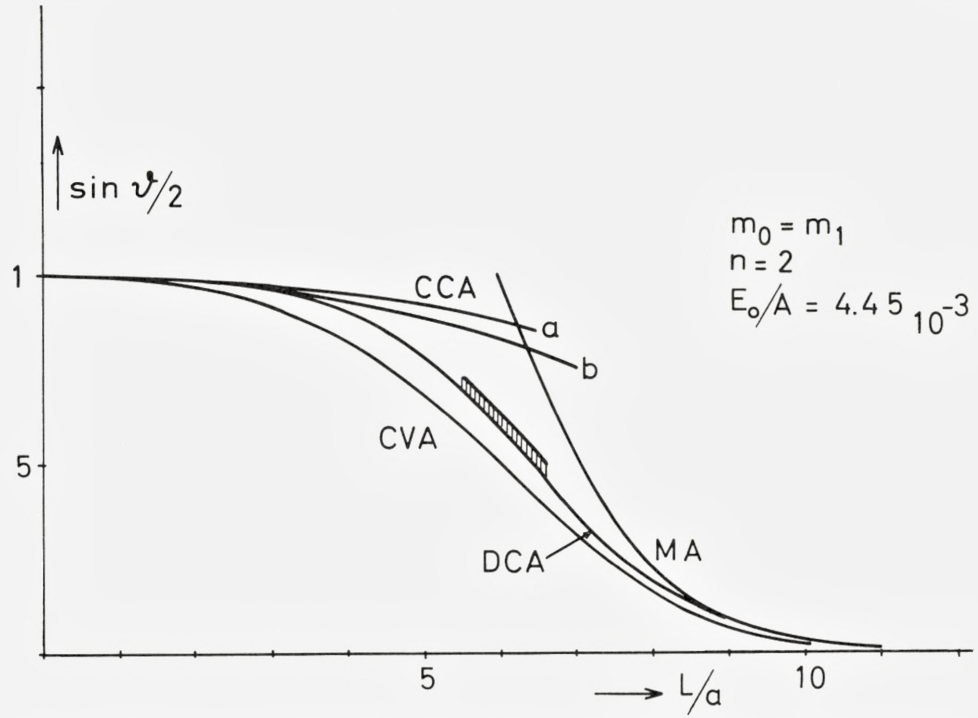

Fig. 7. Comparison of scattering angles in the reduced system, obtained by different approximations discussed in § 3. $\vartheta(p)$ passes probably through the shaded area in the region where the approximations differ most drastically (sect. 4.5).

asymptotic behaviour in these extremal cases (in Fig. 7: $L/a \lesssim 3$ and $L/a \gtrsim 8$), but also represents a plausible interpolation in the region where the discrepancy between the four curves is greatest (in Fig. 7: $5 \lesssim L/a \lesssim 7$). We note that it is just this interval of L/a which is extremely important in applications.

It will be shown in sect. 4.5 that the DCA slightly underestimates ϑ and that the correct ϑ-curve most probably lies in the shaded region.

We note that $s^4 = 1/3$ in this example. For s^4 closer to 1, the quality of the DCA is expected to be better, as this approach yields the exact solution for $s^4 = 1$. Let us, therefore, look at another example, where s^4 is much smaller.

In applications we are mainly interested in the dependence of ΔE on E_0 at a fixed ring radius L. ΔE is found from (2.4.13). We consider the case (Fig. 8)

$$n = 2; \quad \frac{m_0}{m_1} = \frac{20}{64}; \quad \frac{L}{a} = 6.5; \quad A = 10.1 \text{ keV}, \tag{4.3.6}$$

where $s^4 = 0.135$. (4.3.6) might represent a neon ion interacting with two nearest neighbour atoms in a copper crystal under the assumption that (4.3.1) properly describes the interaction between copper atoms (ANDERSEN & SIGMUND, 1965 b).

It appears that ΔE is reasonably approximated by the DCA over the whole range of energies E_0. This curve agrees with the MA at high energies ($E_0 \gtrsim 100$ eV), it goes through a maximum somewhat smaller than the potential barrier (30 eV) so that condition (2.2.6) is fulfilled. Below the maximum ΔE approaches the straight line $\Delta E = E_0$ corresponding to total stopping, and at still smaller energies the curve bends away from $\Delta E = E_0$, corresponding to reflection (2.3.7). Only at very low energies ($E_0 \ll 10$ eV) does DCA agree with CCA.

The CVA appears to be a poor approach in this case, which is due to the small mass ratio $m_0/nm_1 = 0.156$. On the other hand, the MA appears to be valid almost down to $E_0 = 50$ eV. Because of their big masses, the ring atoms can be considered as remaining at their lattice sites during the collision, so that condition i) in sect. 2.2 is fulfilled.

An analytical evaluation is possible for not too small projectile masses ($m_0 \gtrsim nm_1/2$). We insert the simple formula (4.2.4) into (2.4.13). Exact determination of the maximum of ΔE would be rather complicated because of the last factor in (2.4.13). Fortunately, this is slowly varying and close to 1 near the maximum as will be seen. If we neglect it for the determination of the maximum we obtain by differentiation

$$E_0(\max) = \frac{m_0}{2m_1} \cdot \frac{L}{a} A e^{-L/a}. \tag{4.3.7}$$

The energy transfer at $E_0(\max)$ becomes then

$$\Delta E(\max) \approx \Delta E\big(E_0(\max)\big) = nAe^{-L/a}\left(1 - \frac{nm_1}{2m_0}\frac{a}{L}\right). \tag{4.3.8}$$

(4.3.8) states that a heavy projectile ($m_0 \gg m_1$) is able to dissolve the ring almost completely during the collision, i. e. to transform the potential barrier $nAe^{-L/a}$ into kinetic energy of ring atoms.

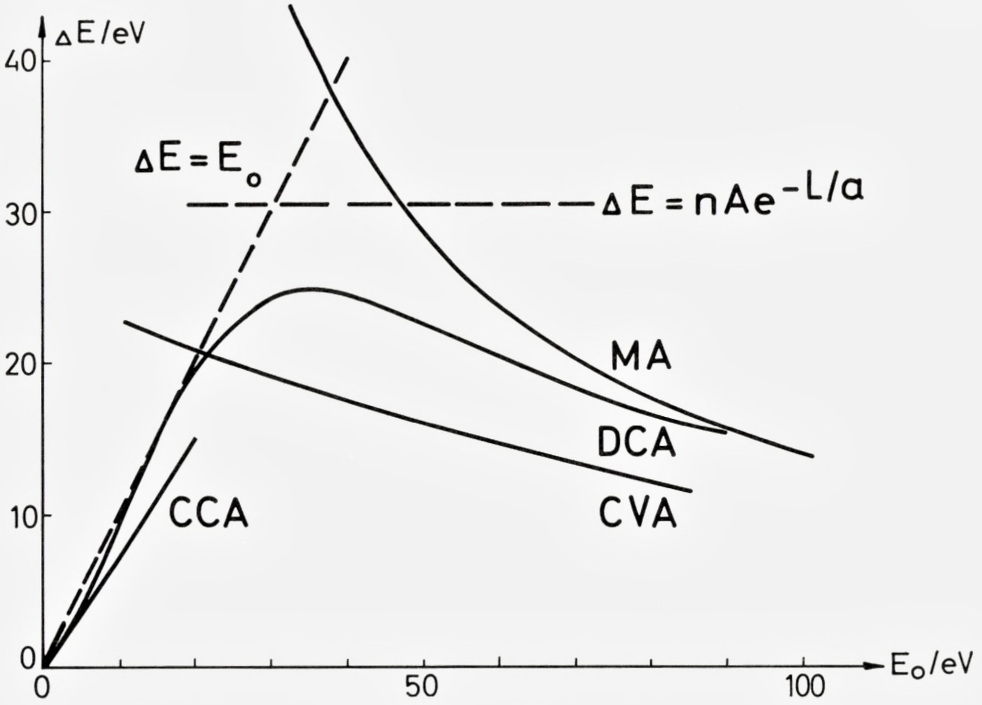

Fig. 8. ΔE vs. E_0 for $n = 2$; $\frac{m_0}{m_1} = \frac{20}{64}$; $s^4 = 0.135$, $L/a = 6.5$; $A = 10.1$ keV (Ne in Cu).

As soon as the term $\frac{nm_1}{2m_0}\frac{a}{L}$ becomes comparable to 1 (if $m_1 \gg m_0$), $\Delta E(\max)$ will be greater than (4.3.8) but, of course, smaller than the potential barrier. A more accurate analytical determination is, however, doubtful in view of the approximate character of the scattering formula (4.2.3). The error in (4.3.8) is by comparison to correct evaluation of the DCA found to be smaller than 25 pct. for $s^4 > .25$.

The complete function $\Delta E(E_0)$ becomes

$$\Delta E = nAe^{-L/a}\frac{4\xi(1-\beta/2)}{(1+\xi)^2 - 2\beta\xi}\left(1 - \frac{nm_1}{M}\frac{\beta(1-\beta)}{(1+\xi)^2 - 2\beta\xi}\right), \qquad (4.3.9.)$$

where

$$\xi = E_0/E_0(\max); \quad \beta = \frac{M}{m_0}\frac{a}{L}. \qquad (4.3.10)$$

Especially for $m_0 \gg m_1$, $\beta \ll 1$ so

$$\Delta E \approx nAe^{-L/a} \frac{4\xi}{(1+\xi)^2} \quad \text{for} \quad \xi \gtrsim 1. \tag{4.3.11}$$

This is a very important formula as it covers a region where the MA overestimates ΔE strongly. Inserting (4.3.7) into (2.2.2) and using (2.2.3) one would obtain

$$\text{MA:} \qquad \Delta E\big(E_0(\max)\big) = \pi nAe^{-L/a}, \tag{4.3.12}$$

which differs from (4.3.8) by a factor of π. It is characteristic for the case $m_0 \gg m_1$ that the maximum of ΔE is extremely broad. According to (4.3.11), ΔE drops to $\Delta E(\max)/2$ at $\xi = 5.8$. It should be mentioned that (4.3.11), within the mentioned accuracy of about 25 pct., also describes ΔE for $E_0 < E_0(\max)$.

While the MA fails completely for heavy projectile masses, $m_0 \gg m_1$, the CVA is supposed to be a good approximation. Evaluating (3.4.4) by use of (4.2.3) we obtain

$$\text{CVA:} \quad \Delta E = n\Delta E_1 = nAe^{-L/a} \frac{4\left(1 - \dfrac{a}{2L}\right)\xi}{(1+\xi)^2 - 2\xi\dfrac{a}{L}} \quad \text{for} \quad m_0 \gg m_1. \tag{4.3.13}$$

For $m_0 \gg m_1$, one gets $\beta \approx a/L$, so (4.3.13) agrees with (4.3.9), apart from the last factor in (4.3.9), which is small for $\xi > 1$.

The discussion of laboratory scattering angles is postponed to sect. 4.6. Here we examine the question whether the projectile will be reflected. At first we note that the condition (2.4.14) cannot be fulfilled as soon as

$$M \geq 2nm_1 \quad \text{or} \quad m_0 \geq nm_1. \tag{4.3.14}$$

This means that a heavy projectile penetrating a series of concentric rings of free, light atoms along their common axis will never be stopped completely. In a crystal, of course, the binding of ring atoms and thermal scattering will prevent this kind of "hyperchannelling". For $m_0 \leq nm_1$, the projectile will be reflected if its energy is smaller than a certain limiting energy E_{refl} corresponding to a critical scattering angle (2.4.14)

$$\sin^2 \vartheta_{\text{refl}}/2 = \frac{1}{2}\left(1 + \frac{m_0}{nm_1}\right), \tag{4.3.15}$$

$\vartheta_{\mathrm{refl}}$ is always greater than $\pi/2$. For these angles the Born-Mayer scattering law is well approximated by (4.1.5). Inserting (3.2.8) and (3.3.8) into (4.1.5) and neglecting $a'/R_0' \ll 1$ we obtain

$$\text{CCA:}\quad E_{\mathrm{refl}} \approx nA\left(1+\frac{m_0}{nm_1}\right)\exp\left(-\frac{L}{a}\sqrt{\frac{2nm_1m_0}{n^2m_1^2-m_0^2}}\right). \tag{4.3.16}$$

$$\text{DCA:}\quad E_{\mathrm{refl}} \approx nA\left(1+\frac{m_0}{nm_1}\right)\exp\left(-\frac{L}{a}\left(\frac{nm_1}{M}+\frac{m_0}{M}\sqrt{\frac{2nm_1}{nm_1-m_0}}\right)\right). \tag{4.3.17}$$

For $m_0 \ll nm_1$, (4.3.17) gives the expected result

$$E_{\mathrm{refl}} \approx nAe^{-L/a}, \tag{4.3.18}$$

namely, the potential barrier. $\vartheta_{\mathrm{refl}}$ is about $\pi/2$ in this case, so the CCA is not expected to give reliable ϑ-values.

For $m_0 \approx nm_1$, where $\vartheta_{\mathrm{refl}} \approx \pi$, the CCA yields

$$E_{\mathrm{refl}} \approx 2nA\exp\left(-\frac{L}{a}\sqrt{\frac{m_0}{nm_1-m_0}}\right). \tag{4.3.19}$$

This energy might become very small, hence the validity of (4.3.19) is limited again because of the role of binding forces (sect. 5.3).

The condition (2.4.15) for penetration is only evaluated in the DCA. Analogous to (4.3.17) one obtains

$$\text{DCA:}\quad E_{\mathrm{pen}} = nA\left(1+\frac{m_0}{nm_1}\right)\exp\left(-\frac{L}{a}\left(\frac{nm_1}{M}+\sqrt{2}\,\frac{m_0}{M}\right)\right). \tag{4.3.20}$$

Obviously, for $m_0 \ll m_1$,

$$E_{\mathrm{pen}} = nAe^{-L/a}, \tag{4.3.21}$$

as it must be.

4.4 Collision Length and Time Integral

The concept of collision length, which is a path length travelled during the collision, is needed both for the problem of overlap between successive impacts, the role of binding forces (sect. 5.3) and the validity of matching potentials (next section). The fundamental formulae will be derived in this section.

Let us start by considering a reduced system with fixed, spherical Born-Mayer potential and use the notations from sect. 4.1.

Within the limits of the MA, the flying particle (m' = mass, v' = velocity) transfers the total momentum

$$\Delta p = \frac{2A'}{v'} \cdot \sqrt{\frac{\pi p'}{2 a'}}\, e^{-p'/a'}, \quad \text{for} \quad \frac{p'}{a'} \gg 1, \tag{4.4.1}$$

to the scattering center. We define a collision time $\Delta\tau'$ by the relation

$$\Delta p = F_{\max} \cdot \Delta\tau', \tag{4.4.2}$$

where $F_{\max}$ represents the force acting at the closest approach, i. e.

$$F_{\max} = \frac{A'}{a'} e^{-p'/a'} \tag{4.4.3}$$

for a particle moving on a straight line. Comparing (4.4.1), (4.4.2) and (4.4.3) we have to choose

$$\Delta\tau' = \frac{1}{v'} \sqrt{2\pi a' p'}. \tag{4.4.3}$$

This corresponds to a collision length

$$\Lambda' = \sqrt{2\pi a' p'}. \tag{4.4.4}$$

It is characteristic for the rapidly decreasing Born-Mayer potential that Λ' is relatively small. Seen from the scattering center, the interaction takes place within an angle (Fig. 9) $\Lambda'/p' = \sqrt{2\pi a'/p'}$ going to zero for $p' \gg a'$. For comparison we mention that the corresponding angle for the Coulomb potential is 90° for large p'. The potential at the end of the collision length is given by

$$\Phi'_{\text{end}} = A' \exp\left(- \frac{1}{a'} \sqrt{p'^2 + (\Lambda'/2)^2} \right) \approx A' e^{-p'/a'} \cdot e^{-\pi/4} \tag{4.4.5}$$

for $p'/a' \gg 1$, which is less than half of the potential in the closest approach.

So far, we required the MA to be valid. Let us now keep p' fixed and lower the energy so that we arrive at appreciable scattering angles, where the MA breaks down. As a first approximation, Λ' being defined as the real path length travelled during the collision remains independent of

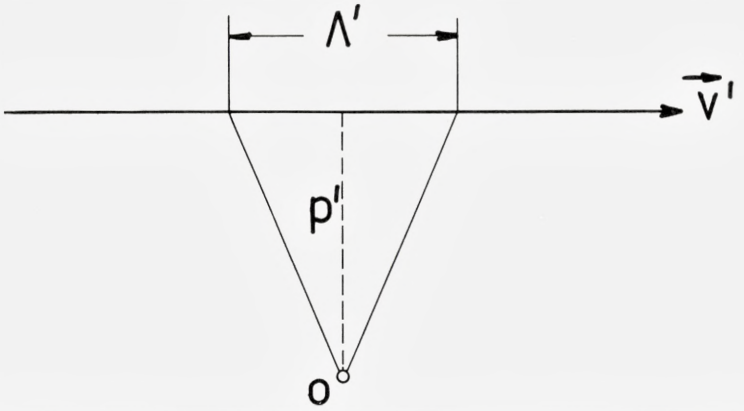

Fig. 9. The collision length Λ'. 0: scattering center. p': impact parameter. v': relative velocity.

energy; perhaps it will slightly decrease, since the particle is scattered away from the force field. Thus, we suppose that the relation

$$\Lambda' \lesssim \sqrt{2\pi a' p'} \tag{4.4.6}$$

should be valid even for large angle scattering.

Let us verify this by considering the opposite case, where p' is small. For $p' = 0$, one can solve the equation of motion exactly (LEHMANN & LEIBFRIED, 1961) with the result

$$\dot{r}' = v' \tanh \frac{v' t}{2a'}. \tag{4.4.7}$$

The velocity $\dot{r}'$ is zero in the closest approach ($t = 0$). From (4.4.7) we get a collision time

$$\Delta\tau' = 4a'/v' \tag{4.4.8}$$

and a corresponding path length

$$\Lambda' \approx 2a' \quad \text{for} \quad p' \approx 0, \tag{4.4.9}$$

as (4.4.7) represents, roughly, a uniformly accelerated motion within $|t| < 2a'/v'$.

Comparing the collision lengths (4.4.4) and (4.4.9) we find the unequality (4.4.6) being fulfilled, except for impact parameters $p'/a' < 2/\pi$, while a comparison of the corresponding collision times (4.4.3) and (4.4.8) gives discrepancies already at $p'/a' < 8/\pi$. So we conclude that Λ' is a well-

defined quantity, which for all impact parameters under consideration ($p'/a' \gtrsim 1$) may be majorized by (4.4.6).

We want to apply this result to our collision model within the range of applicability of the DCA. The corresponding path lengths in the elliptical potential can easily be found from the definitions in sect. 3.3, but the relation to laboratory quantities involves the so-called time integral. This quantity, which connects relative and centre-of-mass motion, is usually (LEHMANN & LEIBFRIED, 1961) derived for two-particle collisions but can easily be generalized to our situation. This is done in Appendix B. The coordinate system is chosen so that the origin is the initial ring center, and the time scale is such that the closest approach happens at $t = 0$. For $t \gg 0$, i. e. after the interaction, relative and center-of-mass motion obey the following equations:

$$\text{(B. 12)}: \quad r'(t) = \sqrt{p_D^2 + (sv_0 t + \tau_D)^2}. \tag{4.4.10}$$

$$\text{(B. 3) \& (B. 8)}: \quad X(t) = s^4 (v_0 t - \tau_D/s). \tag{4.4.11}$$

The time integral τ_D is given by (B. 9) and has been tabulated by ROBINSON (1963). The position of the projectile at $t = 0$ as well as the complete asymptotic motions $x_0(t)$, $x_1(t)$, $y_1(t)$ are listed in (B. 11) and (B. 14).

Finally, we are interested in the actual collision time $\Delta\tau$ corresponding to the path length (4.4.6). For not too large angles ($\vartheta < \pi/2$), $\Delta' = 2\,\overline{P_0 Q'}$ (Fig. 13 in appendix B) will approximately be equal to $2\overline{QQ'}$. Applying the cosine relation on the triangle $\overline{0QQ'}$ and inserting (4.4.10) and (4.4.4), we obtain

$$\Delta\tau = \frac{1}{sv_0}\left(\sqrt{2\pi a_D p_D} + 2p_D \operatorname{tg}\vartheta/2 - 2\tau_D\right). \tag{4.4.12}$$

For $\vartheta = 0$, τ_D goes to zero, so that $\Delta\tau$ goes over into $\Delta\tau'$ (4.4.3), as it must be. At finite angles, $\Delta\tau$ is greater than $\Delta\tau'$.

4.5 Validity of Approximations.

In this section we discuss the applicability of our four approximations within the model defined in 2.1. The limitations of the model itself will then be mentioned in the subsequent chapter.

In the following we assume scattering angles for a spherical potential to be given exactly, for example from Robinson's tables, so that the only approximative step consists in reduction to spherical symmetry. We shall first discuss the different approximations in terms of the reduced scattering angle ϑ.

From the construction we know that
i) the CCA yields the exact result for $\vartheta \approx \pi$. Furthermore from Appendix A,
ii) the MA is asymptotically exact for high energies (small ϑ).

Following the examples from sect. 4.3 we suggest:
I) The DCA is a good overall approximation.
II) For $s^4 \ll 1$ the validity of the MA is much better than in the corresponding two-particle collision.
III) For $s^4 \approx 1$, also the CVA is an excellent approximation

I. DCA. We first show that DCA and MA agree at high energies. Using the perturbation expansion

$$\vartheta = \frac{A_D}{E_r} \cdot \frac{p_D}{a_D} K_0(p_D/a_D) \approx \frac{A_D}{E_r} \cdot \sqrt{\frac{\pi}{2} \frac{p_D}{a_D}}\, e^{-p_D/a_D}, \tag{4.5.1}$$

and inserting (3.3.8) one obtains

$$\text{DCA:}\ \vartheta = \sqrt{\frac{Mm_0}{m_1^2}} \frac{A}{E_0} \sqrt{\frac{\pi}{2} \frac{L}{a}}\, e^{-L/a}. \tag{4.5.2}$$

For the MA we obtain from (A.7)

$$\text{MA:}\ \vartheta = ns^2 \frac{A}{E_r} \cdot \frac{sp}{a} K_0(sp/a) \approx \sqrt{\frac{Mm_0}{m_1^2}} \frac{A}{E_0} \sqrt{\frac{\pi}{2} \frac{L}{a}}\, e^{-L/a}, \tag{4.5.3}$$

in perfect agreement with (4.5.2). The second step in (4.5.1) using (2.2.3) is not exact as soon as p_D/a_D is not large ($s^4 \ll 1$). Numerically, ϑ_{DCA} is 10 pct. smaller than ϑ_{MA} at $p_D/a_D = 1$ and large E_0.

Next, we compare DCA and CCA at large ϑ. A convenient scattering formula near $\vartheta = \pi$ is found by expanding (4.1.5)

$$\cos \vartheta/2 = \frac{p'}{R_0'}(1 + a'/R_0'), \quad \text{for} \quad \vartheta \approx \pi, \tag{4.5.4}$$

where R_0' is defined in (4.1.6). Inserting (3.2.8) and (3.3.8) and neglecting a'/R_0' in (4.5.4) for low energy we get

$$\text{CCA:}\ \cos \vartheta/2 = \frac{s^2 L/a}{ln(MA/m_1E_0)}, \tag{4.5.5}$$

$$\text{DCA:}\ \cos \vartheta/2 = \frac{s^4 L/a}{ln(MA/m_1E_0) - \dfrac{nm_1}{M} L/a}. \tag{4.5.6}$$

Obviously, the two expansions only agree for $L/a \to 0$ and $s^4 = 1$. Otherwise both numerator and denominator in (4.5.6) are smaller than in (4.5.5) so that the numerical difference is not too big.

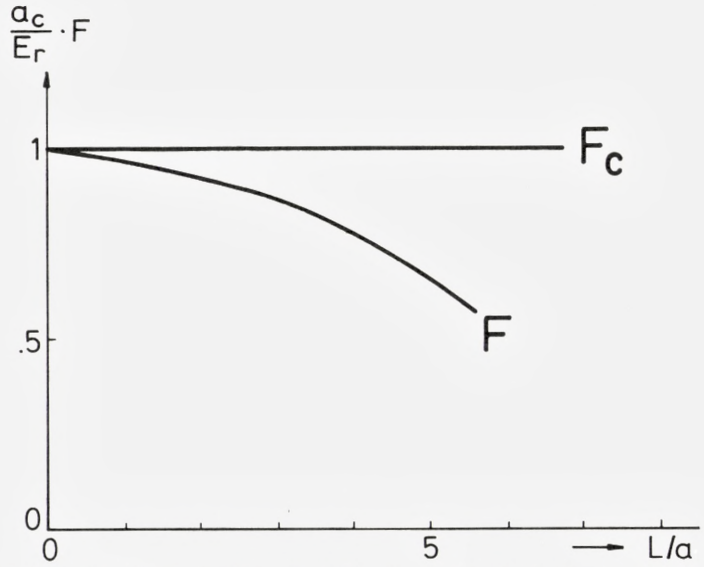

Fig. 10a. Magnitude of force in CCA. F = real force, F_C = CCA force.

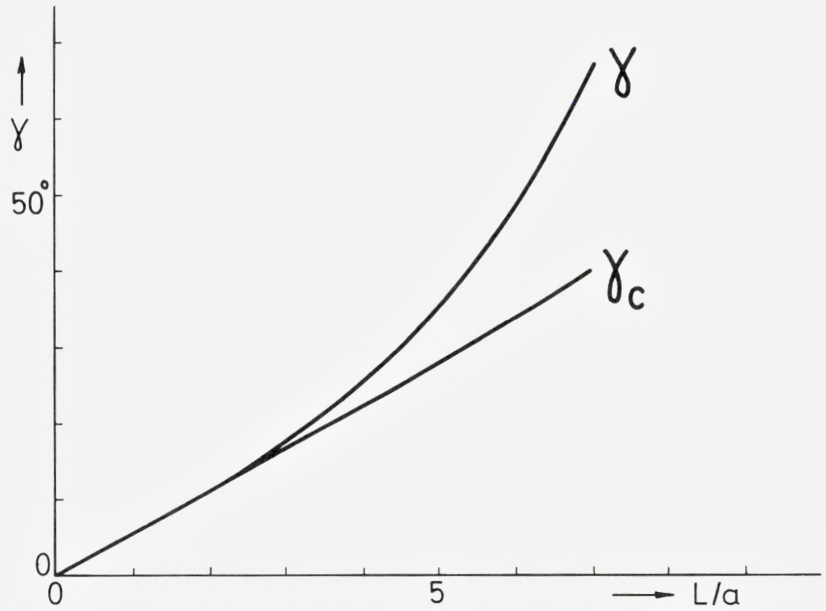

Fig. 10b. Angle of forces to the negative x-axis in CCA, γ = angle of the real force, γ_C = angle of the CCA force.

Fig. 10a–d. Comparison of real and approximate forces in the closest approach, for the example discussed in sect. 4.3 (Fig. 7); $s^4 = 1/3$, $E_0/A = 4.45_{10}{}^{-3}$.

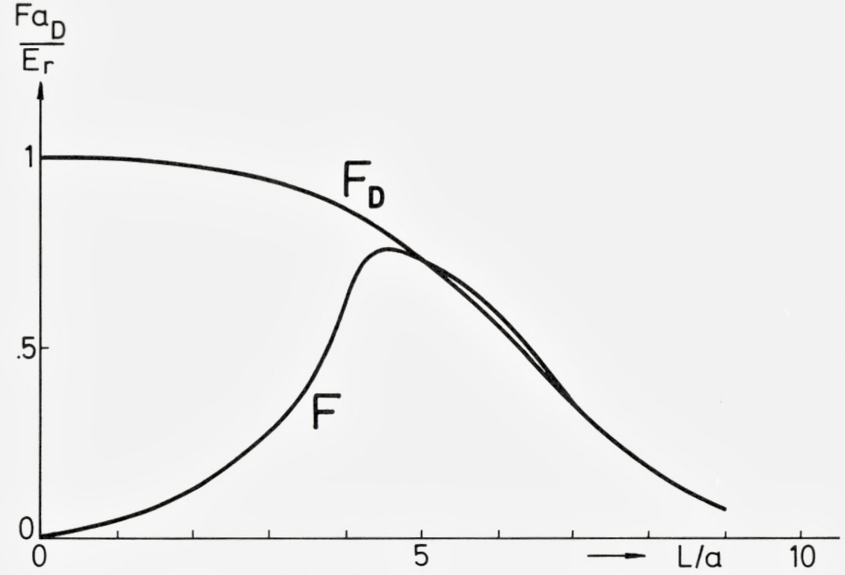

Fig. 10c. Magnitude of forces in DCA. F = real force, F_D = DCA force.

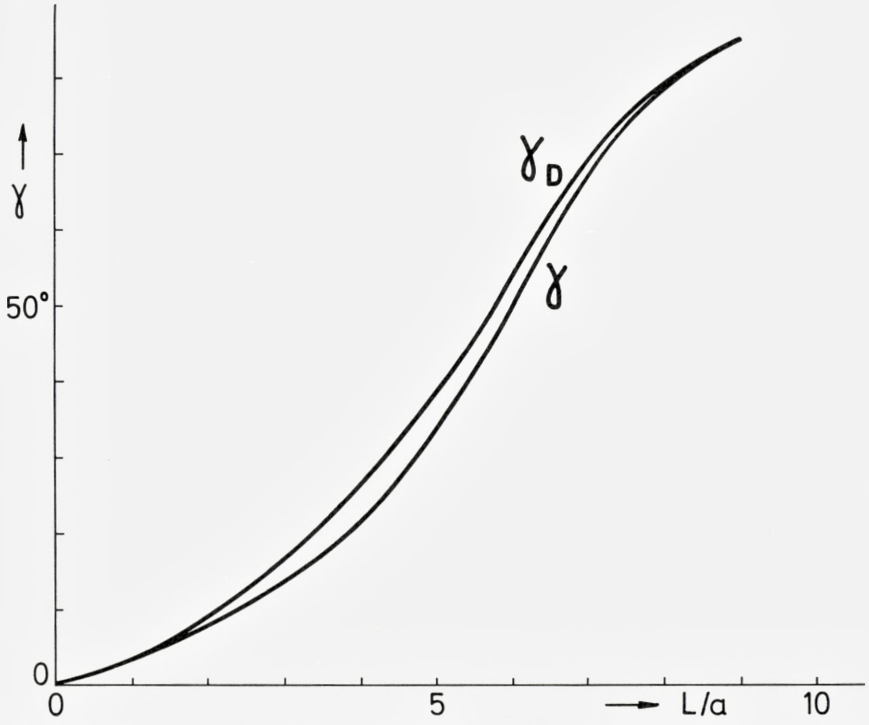

Fig. 10d. Angle of force to the negative x-axis in DCA. γ = angle of real force, γ_D = angle of DCA force.

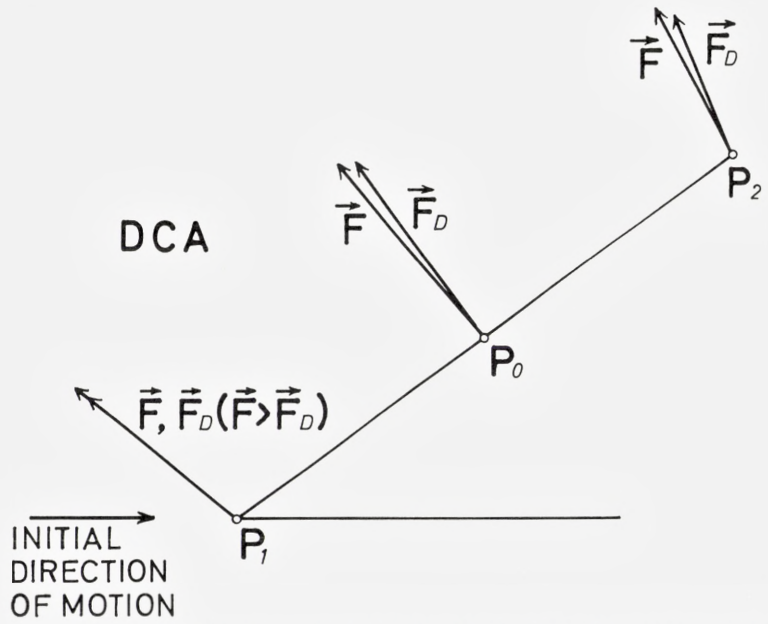

Fig. 11. Comparison of forces in three characteristic points within the collision length (see Fig. 13). $L/a = 6$; $s^4 = 1/3$; $E_0/A = 4.45_{10}{}^{-3}$.

At intermediate scattering angles both CCA and MA are suspect. To estimate the accuracy of the DCA we compare the actual, elliptic force field with the spherical one from the DCA in that region where deflection takes place, i. e. within the collision length. The most important point is, of course, the closest approach r'_m. In Fig. 10a–d we have plotted magnitude F and angle γ (measured with respect to the negative x-direction) of the real force $\vec{F}$ and the approximate forces $\vec{F}_C$ and $\vec{F}_D$ in the closest approach as calculated respectively by the CCA and the DCA. Fig. 10d shows that the direction of the force is very well approximated by the DCA at all impact parameters. The magnitude (Fig. 10c) is only correct at $L/a \gtrsim 5$, while it is drastically overestimated by the DCA at small L. This is immediately evident from the construction of the potential Φ_D (Fig. 5). The scattering angle ϑ is not affected very much by this discrepancy, but other quantities must be, for example the closest approach itself as well as time integral and collision length.

Figs. 10a and 10b show that the CCA force deviates considerably from the real force already at rather small values of L/a. This might explain the rather limited range of applicability of the CCA in Fig. 8. It means also that eq. (4.3.17) will in most cases be more adequate to determine E_{refl} than (4.3.16) or (4.3.19).

In order to estimate the accuracy of the DCA scattering angle at $L/a \approx 6$ we note that the errors of γ_D and F_D are around 5 pct., while the discrepancies of γ_C and F_C (Fig. 10a and b) are very large. Furthermore, the direction of the discre-

pancies indicates that the DCA underestimates ϑ, while CCA clearly overestimates. Hence, one would suppose that the DCA angle is about 5 pct. too small under the assumption that these relations are qualitatively the same within the whole collision length.

To be sure about this, we have also calculated the forces in two other points within the collision length, namely the points P_1 and P_2 from Fig. 13. It is easy to see that the length $\overline{P_1P_2}$ is not much smaller than Λ as defined by (4.4.4). The forces are shown in Fig. 11 for the case $L/a = 6$. P_0 is the closest approach (Fig. 13). Clearly, the discrepancies in P_1 and P_2 are not greater than in P_0.

We note that the validity of the DCA force field rapidly decreases, just as $\vartheta > \pi/2$. This seems evident from the construction of the potential (Fig. 5), as the particle is deflected far away from that point where we have matched the potential. We consider this result to be more general and assume in the following the DCA to be an accurate description of our model for $\vartheta \lesssim \pi/2$, except for $s^4 < 0.1$, where the error in ϑ might exceed 10 pct. At $\vartheta > \pi/2$, the scattering angle itself might be well approximated, but other quantities should be considered with care.

II. MA. We now investigate the error which is made by evaluating the DCA scattering angle by the MA. According to (4.5.2) and (4.5.3) this is equivalent to treating the original problem by the perturbation approach, for $s^4 > 0.1$.

Following LEHMANN & LEIBFRIED (1963), the error can be estimated from the proportion of second and first order contributions in the perturbation series

$$\vartheta = \vartheta^{(1)} + \vartheta^{(2)} + \ldots \tag{4.5.7}$$

to be

$$\left|\frac{\vartheta^{(2)}}{\vartheta^{(1)}}\right| = \frac{A_D}{E_r} \frac{\dfrac{p_D}{a_D} K_1\left(2\dfrac{p_D}{a_D}\right) - \dfrac{3}{2} K_0\left(\dfrac{p_D}{a_D}\right)}{K_0(p_D/a_D)} \approx \frac{A_D}{E_r} \cdot \frac{1}{\sqrt{2}} e^{-p_D/a_D}\left(\frac{p_D}{a_D} - 1.19\right). \tag{4.5.8}$$

In the second step we used the asymptotic expansion of the Hankel functions K_0 and K_1 (JAHNKE et al., 1960). Inserting (3.3.8) we get

$$\left|\frac{\vartheta^{(2)}}{\vartheta^{(1)}}\right| = \left(\frac{m_0}{m_1} + n\right) \frac{A}{E_0} \left(\frac{m_0}{M}\frac{L}{a} - 1.19\right) \frac{1}{\sqrt{2}} e^{-L/a}. \tag{4.5.9}$$

For the pure two-particle collision one would obtain

$$\left|\frac{\vartheta^{(2)'}}{\vartheta^{(1)'}}\right| = \left(\frac{m_0}{m_1} + 1\right) \frac{A}{E_0} \left(\frac{L}{a} - 1.19\right) \frac{1}{\sqrt{2}} e^{-L/a}. \tag{4.5.10}$$

Obviously, (4.5.9) and (4.5.10) are only equivalent for $m_0 \gg m_1$. Already for $m_0 \approx m_1$ there is a considerable difference, and for $m_0 \ll m_1$ one gets

$$\left|\frac{\vartheta^{(2)}}{\vartheta^{(1)}}\right| \approx \frac{A}{E_0} \left(\frac{m_0}{m_1}\frac{L}{a} - \frac{1.19}{n}\right) \frac{1}{\sqrt{2}} e^{-L/a}; \quad m_0 \ll m_1 \tag{4.5.9'}$$

instead of

$$\left|\frac{\vartheta^{(2)'}}{\vartheta^{(1)'}}\right| \approx \frac{A}{E_0}\left(\frac{L}{a} - 1.19\right)\frac{1}{\sqrt{2}}\, e^{-L/a} \tag{4.5.10'}$$

for the two-particle collision. For the example illustrated in Fig. 8 the error in the energy loss, which is twice the error in angle, is predicted to be

$$\frac{\delta(\Delta E)}{\Delta E} \leq \frac{31\ \text{eV}}{E_0} \tag{4.5.11}$$

by (4.5.9'), while (4.5.10') yields $114\ \text{eV}/E_0$. Comparison to Fig. 8 shows that the actual discrepancy between MA and DCA is even smaller than (4.5.11), as long as $E_0 > E_0(\max)$.

III. CVA.

We show that CVA and MA agree at high energies. Starting at (3.4.4) we obtain

$$\Delta E = n\Delta E_1 \approx \frac{m_1}{m_0} E_0 \cdot \alpha^2 = n\frac{m_0}{m_1}\frac{A^2}{E_0}\cdot\frac{\pi}{2}\frac{L}{a}\, e^{-2L/a}, \tag{4.5.12}$$

in agreement with (2.2.2), if only $L/a \gg 1$. This asymptotic behaviour is independent of the mass ratio, contrary to the DCA, which means that in the case $s^4 \ll 1$ the CVA is asymptotically exact, but a bad approximation at finite E_0, while the opposite holds for the DCA.

At $m_0 \gg m_1$, both DCA and CVA have the right asymptotic behaviour. In order to find the deviations at smaller energies, we consider the second order momentum approximation. Expanding both ϑ(DCA) and α(CVA) as well as the expressions for the energy loss (2.4.13) and (3.4.4) in powers of A, we obtain to the second order

$$\frac{\Delta E(\text{DCA})}{\Delta E(\text{CVA})} = \frac{1 + 2\vartheta^{(2)}/\vartheta^{(1)}}{1 + 2\alpha^{(2)}/\alpha^{(1)}} \approx 1 + 2\left(\frac{\vartheta^{(2)}}{\vartheta^{(1)}} - \frac{\alpha^{(2)}}{\alpha^{(1)}}\right). \tag{4.5.13}$$

$\vartheta^{(2)}/\vartheta^{(1)}$ is given in (4.5.9) apart from the sign: $\dfrac{\vartheta^{(2)}}{\vartheta^{(1)}} < 0$. $\alpha^{(2)}/\alpha^{(1)}$ is easily found using the definitions in sect. (3.4), so we obtain

$$\frac{\Delta E(\text{DCA})}{\Delta E(\text{CVA})} = 1 + 1.19\sqrt{2}\,\frac{nAe^{-L/a}}{E_0}, \quad \text{for large } E_0. \tag{4.5.14}$$

(4.5.14) is independent of the mass ratio but only correct for $\dfrac{m_0}{M}\dfrac{L}{a} \gg 1$. It is seen that the CVA underestimates ΔE, which is to be expected, as the CVA underestimates the collision time.

For numerical estimates one should remember that (4.5.14) is only valid within the radius of convergence of the perturbation series.

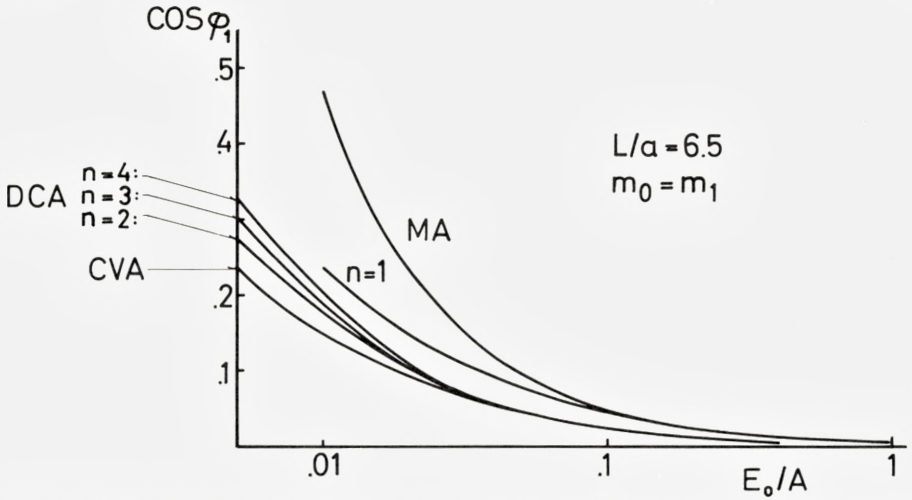

Fig. 12a. Starting angle φ_1 of ring particle 1 as a function of projectile energy for different numbers of ring atoms (n = 2, 3, 4), compared to n = 1 (pure two-particle scattering), MA and CVA.

4.6 Angular relations

It would be of considerable interest also to investigate many-body scattering events which are not as symmetrical as the model discussed until now. It is immediately evident that most of the techniques applied in the present paper are rather specific for the symmetric ring collision and cannot be generalized in a straightforward manner.

If we confine ourselves to distant collisions it will always be reasonable to apply the MA above some well-defined limiting energy. At low energies, it will often happen that the path of the projectile may be well approximated by a straight line, even if the relative energy transfer to atoms surrounding the path is not small, just because of the stabilizing effect of an assembly of scattering centers. In these cases, it seems most reasonable to apply the CVA in order to calculate the transferred energy, rather than to resolve all interactions into two-body events and treat these by familiar scattering theory.

Applying the CVA to a given scattering problem, one obtains energies and directions of motion for all the struck particles. From that, using conservation laws, one might also get the total energy and momentum change of the projectile. This procedure has been used by WEIJSENFELD (1964) in the theory of assisted focusing collision sequences. The validity of the approach has not been estimated.

From our model, it is only possible to estimate the accuracy of the CVA in the completely symmetrical case, where the assumptions underlying the CVA are best satisfied. As to the calculation of transferred energies, this has been done in the preceding section. In order to see that the situation is quite analogous with respect to angular relations, we just discuss an example. In Fig. 12a, we have plotted the cosine of the starting angle φ_1 of ring particle 1 for different approximations and various numbers of ring atoms. The CVA claims that φ_1 is independent of n. Within the DCA, the angle φ_1 appears to be almost identical for n = 2, 3 and 4.

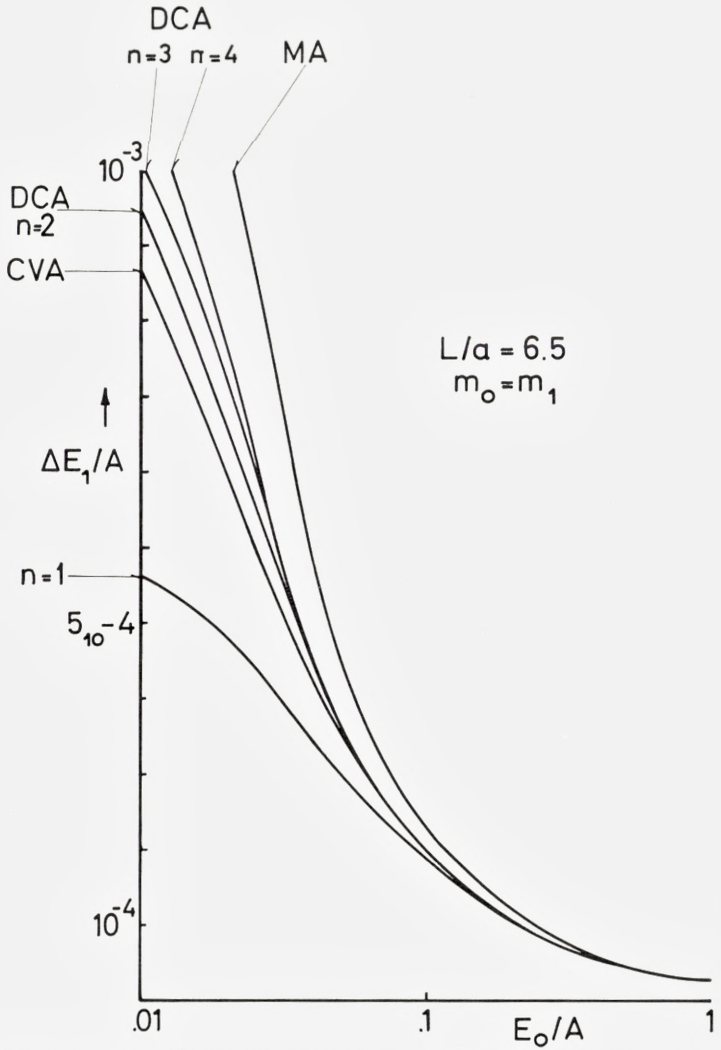

Fig. 12b. Energy transfer ΔE_1 to one ring atom corresponding to the angles in Fig. 12a.

In the energy region where the MA fails completely, the scattering angle calculated from the assumption of pure two-particle scattering ("$n = 1$") appears still to be a satisfactory approximation[1]. This is not the case if one considers the energy

[1] Note that for large E

$$\cos\varphi_1\Big|_{\text{2-body}} = \left(1 + \frac{m_1}{m_0}\right)\cos\varphi_{1\,\text{CVA}},$$

due to the violation of momentum conservation in x-direction. In applications, this discrepancy is unimportant.

ΔE_1 transferred to one ring atom (Fig. 12b). Here, the two-particle approach fails completely. One might suppose that the relations between the different approaches as indicated in Fig. 12a and b are more general, but a detailed investigation is outside the scope of this paper.

§ 5. Limitations of the Model

5.1 Validity of classical scattering

A detailed investigation of the limitations of classical scattering due to the uncertainty principle would require a wave packet description of our model. This requires in turn some knowledge of the classical orbits in the case of deviations from perfect symmetry which are not considered in this paper.

In order to get a feeling for the magnitude of quantum corrections to our model, we estimate the accuracy of ΔE_1 and ΔE only in the special case of a heavy projectile ($m_0 \gg m_1$) and small energy transfer, where the main uncertainty arises from localizing the ring particles, so that the projectile may be considered to have well-defined position and momentum.

The uncertainty in the scattering angle α of one ring particle in a system moving with velocity v_0 (Fig. 6) is calculated by the method of Bohr (1948) modified for Born-Mayer scattering. Assuming

$$\partial\alpha/\partial L \approx -\alpha/a, \tag{5.1.1}$$

one obtains the relative uncertainty

$$\frac{\delta\alpha}{\alpha} = \sqrt{\frac{\lambda\!\!\!^{-}_1}{a\alpha}}, \tag{5.1.2}$$

where

$$\lambda\!\!\!^{-}_1 = \frac{\hbar}{m_1 v_0}. \tag{5.1.3}$$

As α determines the energy transfer, we obtain from (3.4.4)

$$\frac{\delta(\Delta E_1)}{\Delta E_1} = 2\frac{\delta\alpha}{\alpha} = \left[\frac{8\hbar^2}{a^2 m_1 \Delta E_1}\right]^{1/4} \tag{5.1.4}$$

for the relative uncertainty in ΔE_1.

Finally, since the different ring particles are independent of each other, the uncertainty in the total energy loss ΔE is given by

$$\frac{\delta(\Delta E)}{\Delta E} = n^{-1/2} \cdot \frac{\delta(\Delta E_1)}{\Delta E_1} = n^{-1/4} \cdot \left(\frac{8\hbar^2}{a^2 m_1 \Delta E} \right)^{1/4}. \tag{5.1.5}$$

Assuming $a = 0.2$ Å one obtains from (5.1.5)

$$\frac{\delta(\Delta E)}{\Delta E} = \left(\frac{0.8\text{eV}}{n A_1 \Delta E} \right)^{1/4}, \tag{5.1.6}$$

where A_1 is the mass number. As the energy at which the fraction (5.1.6) becomes comparable to 1 usually lies in the range of validity of the MA, one might suppose that the classical approach should be successful below this limit, also at energies where the MA breaks down.

The relations (5.1.4) and (5.1.5) remain qualitatively correct even for $m_0 \lesssim m_1$, as long as the energy loss is small. But in the energy region where the projectile can be reflected, these considerations might be insufficient.

One should mention that the limiting energies calculated by Lehmann & Leibfried (1963) are considerably higher than those arising from (5.1.4) or related equations. This is due to the fact that the criterion of Williams (1945) used by these authors in the case of screened potentials is only a necessary condition for the applicability of classical orbit pictures.

5.2 Inelasticity

Due to ionization and excitation of electrons the collisions in a crystal are not perfectly elastic. It has often been assumed that a certain ionization threshold energy E_I exists below which inelastic effects should be negligible. It seems well-established that such a general threshold in the sense of a cut-off energy does not exist. Nevertheless, there might be a characteristic energy separating those regions, where, respectively, elastic and inelastic effects dominate, but this energy will in general depend in a sensitive way on the considered effect.

In this paper we are concerned with particle velocities much smaller than $e^2/\hbar$, so that dipole resonance excitation will not take place (Bohr, 1948). One only deals with close Coulomb encounters of the projectile with the electrons of the crystal. Seitz (1949) assumed that these will not lead to excitation if the maximum energy transfer is smaller than the Fermi energy in a metal or the ionization energy in an insulator. The theory for stopping of charged particles in an electron gas (Lindhard, 1954) does not confirm this statement. The stopping power turns out to be proportional to velocity:

$$\left(\frac{dE}{dx} \right)_e = \text{const} \cdot v, \tag{5.2.1}$$

the proportionality constant depending on the charge of the projectile and the density of the electron gas. Within the limits of applicability of the Thomas-Fermi

model eq. (5.2.1) should also be valid for non-uniform electron gases as they occur in solids and, especially, in metals.

As electronic stopping acts only as a minor correction on the orbit of the projectile, it seems to be a reasonable approximation to treat the collision as being elastic and to add the inelastic contribution later on, provided the proportionality constant in (5.2.1) can be calculated. Electronic stopping may be dominating at energies considerably below the ionization limit, especially in channelled motion.

5.3 Effect of binding forces

In our scattering model it is an essential assumption that the ring atoms are not bound by external forces or interact with one another. In a crystal, however, the atoms are bound to their lattice sites by oscillator forces, as a first approximation.

It has been shown by BOHR (1913, 1948) that oscillator forces can be neglected in collision problems if the collision time $\Delta\tau$ obeys the condition

$$\omega_1 \Delta\tau < 1, \tag{5.3.1}$$

where ω_1 is the oscillator frequency of the struck particle. Eq. (5.3.1) defines an adiabatic limit. For $\omega_1 \Delta\tau > 1$, the energy loss is overestimated by assuming free scattering.

As the collision time increases with decreasing energy, our description can only be correct above some limiting energy which turns out to be quite small.

For $\Delta\tau$ we use, for not too small s^4 and $\vartheta \ll \pi/2$, the first term in (4.4.12), so

$$(\Delta\tau)^2 \approx \frac{2\pi a_D p_D}{(sv_0)^2} = \frac{2\pi a L}{v_0^2}. \tag{5.3.2}$$

The frequency ω_1 is conveniently found from the coupling constants of the lattice by assuming all atoms fixed except 1. If we only take nearest neighbour interaction into account, we get

$$\text{for the FCC lattice: } m_1\omega_1^2 \approx 4(\alpha + 2\beta) \tag{5.3.3}$$

$$\text{and for the BCC lattice: } m_1\omega_1^2 \approx 8\alpha, \tag{5.3.4}$$

where α and β are coupling constants in the notation of LEIBFRIED (1955). Hence, (5.3.1) reads

$$\left.\begin{aligned} & 4\pi \frac{m_0}{m_1} \frac{aL(\alpha + 2\beta)}{E_0} < 1 \quad \text{for FCC lattice,} \\ \text{and} \quad & \\ & 8\pi \frac{m_0}{m_1} \frac{aL\alpha}{E_0} < 1 \quad \text{for BCC lattice.} \end{aligned}\right\} \tag{5.3.5}$$

As an example, we discuss the ⟨100⟩ focuson in Cu considered by WEIJSENFELD (1964). Here, we have (JACOBSEN, 1955)

$$\alpha = .30 \text{ eV/Å}^2; \quad \beta = .54 \text{ eV/Å}^2. \tag{5.3.6}$$

For $L/a = 10$, $a = .2$ Å and $m_0 = m_1$ we obtain

$$\omega_1 \Delta\tau = \left(\frac{7 \text{ eV}}{E_0}\right)^{1/2}, \tag{5.3.7}$$

so that the condition (5.3.1) is fulfilled at $E_0 > 7$ eV. As this energy is of the order of the potential barrier, the energy limits for reflection and penetration, as defined in (4.3.16) etc., will suffer some modifications. The ΔE vs. E_0 curves around and above $E_0(\max)$ will not be affected.

Appendix A

Perturbation Expansion

Eq. (3.1.2) can in principle be solved by a perturbation series

$$y(x) = y^{(0)}(x) + y^{(1)}(x) + \ldots . \tag{A 1}$$

in powers of the potential, Φ. We write (3.1.2) in the form

$$\frac{1}{2}(\Phi_y - y'\Phi_x)(1 + y'^2) + (E_r - \Phi)y'' = 0. \tag{A 2}$$

Φ_x and Φ_y indicating partial derivatives. The zero order term yields

$$E_r y^{(0)\prime\prime}(x) = 0; \quad y^{(0)\prime}(x) = \text{const.} = 0; \quad y^{(0)}(x) = \text{const.} = p; \tag{A 3}$$

Collecting first order terms we obtain

$$\frac{1}{2}\Phi_y(x,p) + E_r y^{(1)\prime\prime} = 0$$

or, using (2.4.8)

$$y^{(1)\prime\prime} = -\frac{nps^2}{2E_r}\,\frac{V'(\sqrt{x^2/s^2+s^2p^2})}{\sqrt{x^2/s^2+s^2p^2}}\,. \tag{A4}$$

where V' is the derivative of V with respect to the argument.

The scattering angle ϑ (fig. 3) in first order is given by

$$(\mathrm{tg}\,\vartheta)^{(1)} = y^{(1)\prime}(x=\infty) = \int_{-\infty}^{+\infty} dx\, y^{(1)\prime\prime}(x)$$

$$= -\frac{nps^3}{E_r}\int_{sp}^{\infty}\frac{V'(\eta)d\eta}{\sqrt{\eta^2-s^2p^2}}\,, \tag{A5}$$

where we have made the substitution

$$x^2/s^2 + s^2p^2 = \eta^2. \tag{A6}$$

For Born-Mayer interaction

$$V(\eta) = Ae^{-\eta/a} \tag{A7}$$

(A5) yields

$$(\mathrm{tg}\,\vartheta)^{(1)} = ns^2\cdot\frac{A}{E_r}\cdot\frac{sp}{a}\,K_0(sp/a). \tag{A8}$$

For small $\vartheta^{(1)}$, we write

$$(\mathrm{tg}\,\vartheta)^{(1)} \approx \vartheta^{(1)} \approx 2\sin\vartheta^{(1)}/2,$$

so (2.4.13) reads

$$\Delta E \approx 4\frac{nm_1}{M}E_0(\vartheta^{(1)}/2)^2 \approx n\frac{m_0}{m_1}\frac{A^2}{E_0}\left[\frac{L}{a}K_0\left(\frac{L}{a}\right)\right]^2, \tag{A9}$$

where we have used (2.4.9), (2.4.11) and (2.4.7). Eq. (A9) agrees with (2.2.2), as it must be.

Collecting second order terms in (A2) we obtain

$$\frac{1}{2}y^{(1)}\Phi_{yy}(x,p) - \frac{1}{2}y^{(1)\prime}\Phi_x(x,p) - y^{(1)\prime\prime}\Phi(x,p) + y^{(2)\prime\prime}E_r = 0$$

or, after partial integration,

$$(\mathrm{tg}\,\vartheta)^{(2)} = y^{(2)\prime}(\infty) = -\frac{1}{2E_r}\int_{-\infty}^{\infty} dx\, y^{(1)}(x)\,(\Phi_{yy}(x,p) - \Phi_{xx}(x,p)). \tag{A10}$$

As explained in sect. 3.1, there is no need to evaluate (A10) explicitly.

Appendix B

The time integral

Let the laboratory coordinates (2.4.1) satisfy the initial conditions

$$x_0(t_0) = \xi_0 < 0; \quad x_1(t_0) = 0; \quad y_1(t_0) = L \tag{B1}$$

and

$$\dot{x}_0(t_0) = v_0; \quad \dot{x}_1(t_0) = \dot{y}_1(t_0) = 0. \tag{B2}$$

From the definition (2.4.2) we get immediately the center-of-mass motion

$$X(t) = X(t_0) + \dot{X}(t_0)(t - t_0) = \frac{m_0}{M}\left(\xi_0 + v(t - t_0)\right). \tag{B3}$$

For the relative coordinates x, y (2.4.4) we obtain

$$\left.\begin{aligned} x(t_0) &= s\xi_0; \quad y(t_0) = L/s = p \\ \dot{x}(t_0) &= sv_0; \quad \dot{y}(t_0) = 0. \end{aligned}\right\} \tag{B4}$$

Integration of the equations of motion is possible for spherical potentials. Hence, we go over into the coordinate system (x', y') defined by the DCA, where (Fig. 5)

$$x' = x; \quad y' = y - y_D = y - p(1 - s^4). \tag{B5}$$

Here,

$$\left.\begin{aligned} x'(t_0) &= s\xi_0; \quad y'(t_0) = s^4 p = p_D \\ \dot{x}'(t_0) &= sv_0; \quad \dot{y}'(t_0) = 0. \end{aligned}\right\} \tag{B6}$$

With the potential $\Phi_D(r')$ from (3.3.4) we get

$$\frac{dr'}{dt} = \pm sv_0\left(1 - \frac{\Phi_D(r')}{E_r} - \frac{p_D^2}{r'^2}\right)^{1/2} \quad \text{for} \quad t \gtrless 0, \tag{B7}$$

where $r'^2 = x'^2 + y'^2$.

The closest approach is assumed at $t = 0$. Hence, $t_0 < 0$. Integration from t_0 to $t = 0$, assuming that the potential energy at $t = t_0$ is negligible, yields

$$sv_0 t_0 = \tau_D + x'(t_0) = \tau_D + s \cdot \xi_0, \quad \text{for} \quad t_0 \ll 0. \tag{B8}$$

Here τ_D is the "time integral"

$$\tau_D = (r_m'^2 - p_D^2)^{1/2} - \int_{r_m'}^{\infty} dr' \left\{\left(1 - \frac{\Phi_D(r')}{E_r} - \frac{p_D^2}{r'^2}\right)^{-1/2} - \left(1 - \frac{p_D^2}{r'^2}\right)^{-1/2}\right\}, \tag{B9}$$

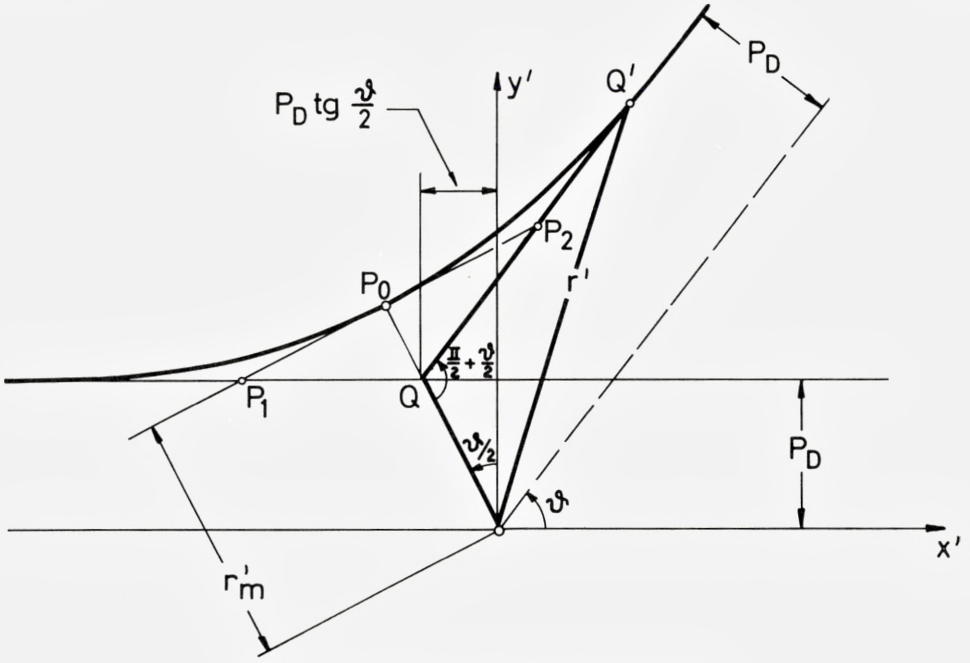

Fig. 13. Asymptotic orbits in reduced system.

which has been tabulated by ROBINSON (1963), and r'_m is the closest approach. From (B3) and (B8) we get the position of the centre-of-mass at $t = 0$:

$$X(0) = s^4(\xi_0 - v_0 t_0) = -s^3\tau_D. \tag{B10}$$

As

$$x'(0) = -r'_m \sin \vartheta/2,$$

the position of the projectile at the time of closest approach becomes

$$x_0(0) = X(0) + (1 - s^4)\frac{1}{s}x'(0) = -s^3\tau_D - (1 - s^4)\frac{r'_m}{s}\sin \vartheta/2, \tag{B11}$$

where use has been made of (2.4.5). Furthermore, for $t \gg 0$, we get in the same way as (B8)

$$sv_0 t = -\tau_D + \sqrt{r'^2 - p_D^2}; \quad \text{for} \quad t \gg 0. \tag{B12}$$

This relation governs the asymptotic orbits. We have (Fig. 13) for $t \gg 0$

$$y' = x' \operatorname{tg} \vartheta + \frac{p_D}{\cos \vartheta},$$

and x' and y' can be expressed by r':

$$\left.\begin{aligned} x' &= -p_D \sin \vartheta + \cos \vartheta \cdot \sqrt{r'^2 - p_D^2} \\ y' &= p_D \cos \vartheta + \sin \vartheta \sqrt{r'^2 - p_D^2}. \end{aligned}\right\} \qquad \text{(B13)}$$

Using eqs. (2.4.5), (B12) and (B13) one obtains

$$\left.\begin{aligned} x_0(t) &= (v_0 t + \tau_D/s)\left(1 - 2\frac{nm_1}{M}\sin^2 \vartheta/2\right) - s^3\left(2\tau_D + \frac{nm_1}{M} p \sin \vartheta\right); \\ x_1(t) &= (v_0 t + \tau_D/s) \cdot 2\frac{m_0}{M}\sin^2 \vartheta/2 - s^3\left(2\tau_D - \frac{m_0}{M} p \sin \vartheta\right); \\ y_1(t) &= (v_0 t + \tau_D/s) \cdot s^2 \sin \vartheta + sp\left(1 - 2\frac{m_0}{M}\sin^2 \vartheta/2\right), \end{aligned}\right\} \qquad \text{(B14)}$$

for $t \gg 0$.

Acknowledgments

The main part of this work has been done at Strandkrogen, Fakse Ladeplads. The fruitful research atmosphere provided by Pia and Nina Sigmund and Agnete Andersen is gratefully acknowledged.

Many points have been clarified in discussions with our colleagues at Aarhus and Risö. Our sincere thanks are to professor Jens Lindhard for many critical remarks and for introducing to us the problems discussed in sections 5.1 and 5.2, and to Mrs. V. Nielsen for critically reading the paper.

We acknowledge the careful assistance of Miss Susann Toldi in the preparation of various versions of the manuscript.

Part of this work was supported by a NATO fellowship provided by Deutscher Akademischer Austauschdienst (PS) and a fellowship from the Technical University of Copenhagen (HHA).

Hans Henrik Andersen
Physics Department
Atomic Energy Commission
Research Establishment Risø
Roskilde, Denmark.

Peter Sigmund
Institute of Physics, University of Aarhus
Aarhus, Denmark.

Present adress:
Institut für Reaktorwerkstoffe
Kernforschungsanlage
Jülich, Germany.

References

H. H. Andersen – P. Sigmund, 1965 a: Phys. Lett. **15**, 237.
1965 b: Risö Report No. 103.
N. Bohr, 1913: Phil. Mag. (6) **25**, 10.
1948: Mat. Fys. Medd. Dan. Vid. Selsk. **18**, no. 8.
J. A. Brinkmann, 1954: J. Appl. Phys. **25**, 961.
J. B. Gibson – A. N. Goland – M. Milgram – G. H. Vineyard, 1960: Phys. Rev. **120**, 1229.
D. Heinrich, 1964: Ann. Phys. **13**, 284.
E. H. Jacobsen, 1955: Phys. Rev. **97**, 654.
E. Jahnke – F. Emde – F. Lösch, 1960: Tafeln höherer Funktionen, Stuttgart.
G. Leibfried, 1955: Handbuch der Physik, Bd. VII/1 (Springer Verlag).
G. Leibfried – O. S. Oen, 1962: J. Appl. Phys. **33**, 2257.
C. Lehmann – G. Leibfried, 1961: Z. Phys. **162**, 203.
1963: Z. Phys. **172**, 465.
C. Lehmann – M. T. Robinson, 1964: Phys. Rev. **134** A, 37.
J. Lindhard, 1954: Mat. Fys. Medd. Dan. Vid. Selsk. **28**, no. 8.
M. T. Robinson, 1963: ORNL-3493.
M. T. Robinson – O. S. Oen, 1963: Phys. Rev. **132**, 2385.
F. Seitz, 1949: Disc. Far. Soc. **5**, 271.
P. Sigmund – P. Vajda, 1964: Risö Report No. 84.
C. H. Weijsenfeld, 1964: preprint to be published.
E. J. Williams, 1945: Rev. Mod. Phys. **17**, 217.

Indleveret til Selskabet den 17. august 1965.
Færdig fra trykkeriet den 3. marts 1966.

Matematisk-fysiske Meddelelser
udgivet af
Det Kongelige Danske Videnskabernes Selskab
Bind **34,** nr. 16

Mat. Fys. Medd. Dan. Vid. Selsk. **34,** no. 16 (1966)

HYDROGEN-BURNING MODELS FOR STARS IN THE HORIZONTAL BRANCH OF GLOBULAR CLUSTERS

BY

JØRGEN OTZEN PETERSEN

København 1966
Kommissionær: Munksgaard

Synopsis

The problem of the structure of stars in the horizontal branch of globular clusters is discussed, and hydrogen-burning models, assumed to be mixed by the helium flash, are studied in detail in order to investigate whether such model sequences can provide an accurate description of the observed properties of horizontal branch stars.

It is shown that homogeneous models with reasonable masses and chemical compositions correspond satisfactorily to the hottest stars of the observed horizontal branches, but in the later, fast stages their evolutionary tracks fall more than one magnitude above the horizontal branch region. Models containing an outer zone of the original chemical composition are shown to be placed along the horizontal branch, the position being determined by the mass fraction of the outer zone. Also their evolutionary tracks will in general fall above the branch when the fast evolution after the hydrogen burning in the central region starts. Hence, according to this interpretation the horizontal branch is not an evolutionary sequence, but rather a main-sequence-like phenomenon.

The model sequences are compared with observed colour-magnitude diagrams for M5 and M15, and it is concluded that such sequences can explain several features of the observed diagrams very satisfactorily. It is emphasized that the time scale for the evolution agrees reasonably well with the empirical value determined by SANDAGE for M3.

These results may be understood if the helium flash gives rise to mixing of the stars, and this mixing is more violent for stars poor in metal than for stars rich in metal. Finally a few other predictions based on this picture of the evolution of horizontal branch stars are mentioned.

PRINTED IN DENMARK
BIANCO LUNOS BOGTRYKKERI A/S

1. Introduction

Investigations of the evolution of population II stars have given a very satisfactory explanation of the observed main-sequences and red giant-sequences of globular clusters (HOYLE and SCHWARZSCHILD 1955, KIPPENHAHN, TEMESVARY, and BIERMANN 1958, HOYLE 1959, DEMARQUE and GEISLER 1963). The observed properties of stars in the horizontal branches of globular clusters, on the other hand, are not understood in a corresponding convincing way. For instance, it seems that the empirically determined time scale (SANDAGE 1957) is considerably longer than the time scale of helium-burning model sequences (HAYASHI, HOSHI, and SUGIMOTO 1962, NISHIDA and SUGIMOTO 1962), and the observed characteristic differences between colour-magnitude diagrams of globular clusters with different content of heavy elements have not been explained in detail.

The interpretation of the horizontal branches as loci for helium-burning sequences is based on the results of SCHWARZSCHILD and HÄRM (1962), HÄRM and SCHWARZSCHILD (1964), HAYASHI, HOSHI, and SUGIMOTO (1962), and SUGIMOTO (1964), suggesting a helium-burning stage to follow after the red giant stage.

If stars, however, are mixed by the helium flash we might expect that the subsequent evolutionary phase, with hydrogen burning in the core, would last considerably longer than the helium-burning phase following a helium flash without mixing.

We shall here first discuss the general problem of the structure of horizontal branch stars; we shall then consider models which are assumed to be mixed by the helium flash, and investigate whether such hydrogen-burning models can provide a reasonable interpretation of the horizontal branch stars, especially if it is possible to understand the observed colour-magnitude diagrams of globular clusters assuming mixing.

In Section 2 a summary of the observational results important for our investigation is given, and in Section 3 the possible structures of horizontal branch models are discussed. The last Sections, 4 and 5, contain the com-

puted evolutionary sequences and comparisons with observed colour-magnitude diagrams, together with a discussion of the results. The computational technique is briefly described in an appendix.

2. Observational Material

Colour-Magnitude Diagrams

Discussions of colour-magnitude diagrams of globular clusters have been offered by many authors. An important result of comparisons of clusters with different contents of heavy elements is that several characteristic properties are found to vary systematically with the strength of metal lines (Sandage 1953, Arp 1955, Sandage and Wallerstein 1960, Wildey 1961). The following Table 1 shows a summary of observational results important for a discussion of horizontal branch stars, for some of the well-observed clusters.

Table 1.

Catalogue no.		Composition		M_V	Age (10^9 years)	Percentage of		
NGC	Messier	$[M/H]$	Morgan type			Blue	RR Lyrae	Yellow
6341	92		I			88	10	2
7078	15		I	1.0		65	25	10
7089	2	−2.3	II	1.0	24	94	4	2
5272	3	−1.6	II	1.0	24	36	37	27
6205	13	−1.4	III	0.3	19	97	3	0
5904	5	−1.3	II	0.8	22	50	30	20
6254	10		IV			91	0	9
6171			V			3	5	92
6356		−0.3	VI			0	0	100
104	47 Tuc			1.0		0	2	98

The objects are arranged according to increasing content of heavy elements as given by $[M/H]$, defined by Wallerstein and Carlson (1960) as the logarithm of the metals-to-hydrogen ratio minus the same quantity in the sun. Besides the values of $[M/H]$ (from Arp 1962a) the Morgan type of the clusters (Morgan 1959) are given. M_V is the absolute magnitude for the RR Lyrae stars as given by Sandage (1962a), and the ages are those obtained by Arp (1962a) by means of the method given by Sandage (1962b). Cor-

rections to the B and V magnitudes for interstellar reddening are probably important (ARP 1962c), causing corrections of the values of M_V and the ages. It seems likely that the ages mentioned are systematically too large, not only because of reddening corrections, but also because recent evolutionary sequences using accurate formulae for the energy-generation rates of hydrogen-burning processes indicate smaller ages than earlier sequences based on the approximate temperature-power law $e_{pp} \approx T^4$ (DEMARQUE and LARSON 1964).

Following WOOLF (1964) we shall call stars in a horizontal branch, with higher temperatures than the RR Lyrae stars, "blue" stars of the horizontal branch and stars with lower temperatures than the RR Lyrae stars correspondingly "yellow" stars. The last three columns of Table 1 give the distribution of the horizontal branch stars in the three groups estimated from published colour-magnitude diagrams (ARP 1955, SANDAGE and WALLERSTEIN 1960, WILDEY 1961, WOOLF 1964).

The clusters can clearly be divided into three groups: Group 1 with $[M/H] < -2$, Group 2 with $[M/H] \simeq -1.5$ and Group 3 having a more normal population I chemical composition. As shown by SANDAGE and WALLERSTEIN (1960), the quantity ΔV (the difference in visual magnitude between the horizontal branch and the giant branch of a cluster read at $(B-V)_0 = +1.4$), the periods of the RR Lyrae stars and some characteristic properties of the horizontal branch are all well-correlated with the metal abundance. Of special interest for our investigation is the distribution of stars along the horizontal branch.

Group 1 with very weak metal lines have most of the horizontal branch stars situated in the blue part of the horizontal branch, while the clusters in Group 2 with weak metal lines show a more uniform distribution of the stars between the three parts of the horizontal branch, and Group 3 clusters with strong metal lines have practically all their horizontal branch stars placed in the yellow part of the branch.

The general rules described, however, are violated by several clusters, exceptions being especially conspicuous for M10 and M13. They have both practically all stars placed in the blue part of their horizontal branches, even though they belong to Group 2 and M10 has no RR Lyrae stars at all. Furthermore, a closer inspection of the colour-magnitude diagrams shows that many clusters display special individual features. Therefore differences in metal content is probably not the only reason for the observed differences between the three cluster groups. Other important causes could be found in the hydrogen content and the distribution of hydrogen throughout the

stars, or in different masses for the horizontal branch stars in different clusters. In this connection SANDAGE and WALLERSTEIN mention that the abnormal distribution of the stars in M13 may be due to higher masses of the horizontal branch stars in M13, compared with the other clusters. M13 is the youngest of the clusters considered here and therefore probably contains the most massive stars.

Lifetime of Evolutionary Stages

SANDAGE (1957) has applied a semiempirical method, utilizing observed luminosity functions and colour-magnitude diagrams and assumptions for the absolute magnitude of RR Lyrae stars to determine: the evolutionary tracks for stars in the clusters M67 and M3, the time scale of the evolution, and the fraction of hydrogen exhausted at each evolutionary stage. Of special interest for us is the time taken to evolve along the horizontal branch which for M3 was found to be 2.3×10^8 years, the RR Lyrae stage lasting about one third of this time. Further, the analysis indicated that the stars in M3 have burned nearly all their hydrogen supply at the top of the red giant branch just before the horizontal branch stage starts. On the other hand, the stars in M67 were found to have used only about half of their hydrogen supply at the top of the red giant branch.

The basis of SANDAGE's analysis was SCHÖNBERG-CHANDRASEKHAR models (1942) for the early evolution. WOOLF (1962) studied the evolutionary tracks in M3 using the same method, but a model sequence by HOYLE (1959) for the early evolution. WOOLF found the same time for evolution along the horizontal branch as SANDAGE, 2.3×10^8 years, but emphasized an apparent discrepancy: The stars seemed to emit more energy in the computed lifetime than burning of nuclear fuel could supply. As mentioned above, reliable ages of globular clusters probably cannot be given yet; first a satisfactory agreement between the observed colour-magnitude diagrams and the computed evolutionary sequences must be accomplished. Therefore the estimate of the lifetime of the horizontal branch stage is still considerably uncertain.

Mass Loss

Small differences in mass between different types of cluster stars can be determined from observations of differences in distribution of the types, provided that equipartition of energy between all stars in the cluster has been reached by gravitational interaction. Since heavier stars evolve faster

than less massive, we should expect the most evolved stars of a cluster to be concentrated near the cluster center, and since horizontal branch stars probably correspond to a later evolutionary phase than red giants do, we should expect the horizontal branch stars to be the most concentrated group of stars in globular clusters.

OORT and VAN HERK (1959) and WOOLF (1964) studied the concentration of stellar groups in the globular clusters M3, M5, M15 and ω Centauri, and found the above-mentioned expectations not to be fulfilled. OORT and VAN HERK found the RR Lyrae stars less concentrated than the red giants and WOOLF showed that the degree of concentration in M3 decreases in the following order:

(a) red giants
(b) blue stars of the horizontal branch
(c) RR Lyrae stars
(d) yellow stars of the horizontal branch.

These results can be interpreted as due to mass loss taking place between the red giant stage and the horizontal branch stage. The quantitative analysis showed that the mass loss is about 20 % of the total mass.

WOOLF proposed the following evolutionary scheme in order to understand the observations. A mixing was assumed at the top of the red giant branch, quickly transferring the star to the blue end point of the horizontal branch, and afterwards a slow evolution through the blue part of the horizontal branch, the RR Lyrae region, and the second giant branch somewhat above the red giant branch was supposed. The observed concentrations of the four stellar types can then be understood if mass loss of about 20 % occurs in the later part of the red giant phase, or, as preferred by WOOLF, at the RR Lyrae stage. After the massloss equipartition of energy will be established on a time scale not very different from the time scale for the evolution along the horizontal branch, giving rise to the observed differences in concentration of the stellar types.

3. Structure of Models for Horizontal Branch Stars

Helium-Burning Sequences

The first model sequence constructed in order to explain the horizontal branches of globular clusters was published by HOYLE and SCHWARZSCHILD (1955). The models, assumed to result from a helium flash, were built on a helium core containing about half the total mass (1.2 $M_\odot$) and an envelope

rich in hydrogen, with the original chemical composition. They were found to burn helium in a small convective core and hydrogen in a thin shell, and HOYLE and SCHWARZSCHILD showed that the gradual conversion of hydrogen to helium in the shell could explain an evolution from right to left in the colour-magnitude diagram somewhat above the horizontal branch.

However, as already stated by HOYLE and SCHWARZSCHILD, this idea is hardly realistic, because the helium burning at the center of the star will proceed much faster than the hydrogen burning in the shell. When the helium in the convective core is exhausted, the central temperature will rise and further nuclear burnings will start, quickly resulting in models with more complicated central regions than those considered by HOYLE and SCHWARZSCHILD. This will probably result in evolutionary tracks more complicated than the simple evolution from right to left in the colour-magnitude diagram.

The most promising attempt known to the author, of constructing an evolutionary sequence for the horizontal branch is due to HAYASHI, HOSHI, and SUGIMOTO (1962). They treated the evolution of a population II star of mass 0.7 $M_\odot$ in the helium-burning phase. The model consisted of a helium core with 76 % of the total mass and an outer envelope with the original chemical composition $X = 0.90$, $Y = 0.10$, $Z = 0.001$. In the first evolutionary phase helium was found to burn in a small convective core, and in the following phase the helium burning proceeds in a shell surrounding a core consisting of carbon and oxygen. The evolution was followed through most of the horizontal branch from left to right up to the tip of the second giant branch somewhat above the red giant branch, where, according to the computations, 90 % of the helium core were converted into carbon and oxygen. HAYASHI, HOSHI, and SUGIMOTO could correlate the length of the red giant phase, the horizontal branch phase, and the phase where the star moved through the second giant branch, respectively, with the relative numbers of stars observed in the corresponding regions of the colour-luminosity diagram of M 5 by ARP (1962 b). The comparison turned out to be quite satisfactory.

The length of the horizontal branch phase according to this evolutionary sequence is 3×10^7 years, while SANDAGE, as mentioned above, for M 3 determined the same quantity at 2.3×10^8 years; and it does not seem likely that this value should be in error by one order of magnitude.

Also the investigations of NISHIDA and SUGIMOTO (1962) showed that helium-burning sequences for the horizontal branch seem to give rather short time scales. They computed evolutionary sequences for population II stars of mass 1.2 $M_\odot$ with an inner helium region containing about 50 %

of the total mass and an envelope rich in hydrogen, and showed that the stage in which helium was burned in a small convective core would last 2.3×10^7 years and could correspond to the RR Lyrae stars.

However, both the evolutionary sequences and the comparison with observations are still so uncertain that it seems quite possible that further investigations could show that sequences burning helium at the centre of the stars were able to describe the horizontal branch stage. The serious problem of the too short time scale may be solved if a considerable part of the hydrogen content could be burned in models with energy production in two regions.

Mass and Chemical Composition

A major difficulty in the construction of evolutionary sequences for the horizontal branch is that the parameters determining the structure of the first model are little known.

For the mass of the heaviest stars in globular clusters 1.2 $M_\odot$ has often been used. But, as mentioned above, some clusters (M 13, for instance) may be younger than the average, hence containing more massive stars; and, on the other hand, a mass loss of about 20 % may occur between the red giant stage and the horizontal branch stage. Probably 1.5 $M_\odot$ will be an upper limit and 0.7 $M_\odot$ a lower limit for the masses.

The chemical composition also presents serious uncertainties. Theoretical evolutionary tracks show that the helium core contains about half of the mass when the helium flash starts for population II stars, and somewhat less (40 %) for population I stars (Hayashi, Hoshi, and Sugimoto 1962), while, according to the method of semiempirical evolutionary tracks (Sandage 1957), practically all the hydrogen should be converted into helium for the stars in M 3 before the flash starts. If mass loss occurs, it seems likely that the mass which escapes, is nearly pure hydrogen from the outer layers, thus mass loss is also reducing the hydrogen content. For the average hydrogen content X of horizontal branch stars we can therefore assume $X < 0.50$.

Before the helium flash is finished, a few per cent. of the mass of the star are probably burned to carbon, and if hydrogen somehow mixes into the hot central regions several nuclear processes will occur (Wallerstein and Greenstein 1964). These processes may give rise to a chemical composition of the horizontal branch stars, which neither corresponds to usual population II stars nor to population I stars. Wallerstein and Greenstein for two CH stars poor in metal, HD 26 and HD 201626, found a high carbon-

to-iron ratio and an excess of Ba, La, Ce, and Nd with respect to Fe with factors about 20, which they interpreted as the result of a helium flash followed by neutron addition to the iron-peak elements, caused by a mixing of a small amount of hydrogen into the edge of the hot core of the star. Afterwards a convective mixing of the edge of the core with the envelope was postulated to transport the resulting nuclei to the surface of the star.

For the average content of elements heavier than helium Z it therefore seems reasonable to assume $Z < 0.05$, remembering that the chemical composition of horizontal branch stars may be abnormal.

Mixing

The structure of a horizontal branch star will, however, depend much more on the distribution of hydrogen throughout the star than on the exact mass-value or the average chemical composition. If hydrogen is mixed into the central region by the helium flash, the structure and evolution of the star will be very different from the case where no mixing occurs, the star then being in a hydrogen-burning main-sequence-like stage instead of a helium-burning one. Therefore the question of mixing by the helium flash is important.

Härm and Schwarzschild (1964) investigated this question by detailed computations by means of the Henyey method. The evolution of three stellar models, differing in mass and chemical composition, was followed through the helium flash. The convective core round the centre was found to grow until, in the cooling stage after the peak of the flash, it extended to 99 % of the helium core. But it never reached the layers rich in hydrogen, so these computations indicated that mixing by the helium flash will not occur. However, Härm and Schwarzschild emphasized that in view of the narrowness of the margin by which the convective helium core missed the hydrogen layers, and in view of the fact that a number of physical items were not yet properly taken into account, they had to conclude that no decisive answer to the question of mixing by the helium flash could be given. Three crucial assumptions were made: The adiabatic approximation for the temperature gradient in the convective core was used, also in the phases around the peak of the flash, infinite conductivity was assumed in the degenerate region, and hydrodynamic effects were neglected in all phases.

The influence of these complications was considered by Sugimoto (1964), who attempted an extraction of the essential features of the physical processes by a more general investigation, using reasonable simplifications

in order to reduce the computational work. With respect to mixing, SUGIMOTO's results were almost identical with those already described. The convective core was found to extend to 99% of the mass of the helium core in the cooling phase, but failed to reach the envelope rich in hydrogen. Hydrodynamic effects caused a core more massive than 0.7 $M_\odot$ to explode, but cores as massive as this probably do not occur; and the effect of finite efficiency of convective heat transport, investigated by means of the mixing length theory was also shown to cause an explosion of the core, if α, the mixing length in units of pressure scale height, was taken to be less than 0.2. It is, however, by no means evident that the mixing length theory provides a realistic description of the energy-transport mechanisms under these extreme conditions.

The processes involved in the helium flash seem to be so complicated that realistic theoretical computations probably will not be obtained in the near future. In this connection we should like to mention the recent discovery (SCHWARZSCHILD and HÄRM 1965) that instabilities may occur in certain models. Furthermore, it seems likely that a fast rotation of the dense core might develop while the contraction proceeds just prior to the helium flash.

Besides the possible role of the helium flash for mixing, such an effect could also, at least theoretically, be caused by the outer convective zone, the question being whether this zone will extend into the helium core.

SCHWARZSCHILD and SELBERG (1962) have published a detailed model for a population II star of mass 1.3 $M_\odot$ just prior to the flash, and this model shows that convection stops before the helium core is reached. HAYASHI, HOSHI, and SUGIMOTO (1962) also arrived at the conclusion that the outer convective zone does not cause mixing before the flash. And when the surface temperature of the star increases after the flash, it seems improbable that the outer convective zone should move downwards.

Observationally, as stressed by WOOLF (1964), mixing would be indicated if determinations of element abundances for horizontal branch stars showed helium and carbon enrichment. As mentioned above, WALLERSTEIN and GREENSTEIN found carbon enrichment for two CH stars poor in metal, but because observed colours and magnitudes $(B-V, M_V) \simeq (1^m, 0^m)$ will place the CH stars somewhat to the right of the horizontal branches in globular clusters, there is no clear relationship between them and horizontal branch stars.

Let us consider a star with a certain mass and chemical composition before the helium flash. Its hydrogen content X as a function of relative mass $q = M(r)/M$ has approximately the form shown in Figure 1 a. We shall now

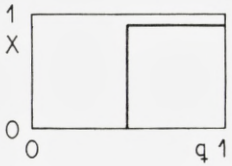

Fig. 1 a. – Sketch of hydrogen content X as a function of relative mass q before the helium flash.

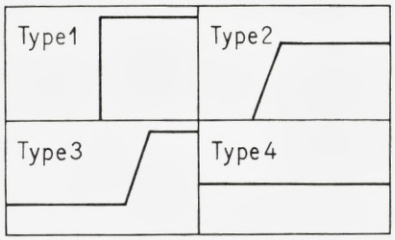

Fig. 1 b – $X(q)$ for 4 possible model-types after the helium flash.

classify the different possibilities for models after the helium flash according to the mixing type, and distinguish between four main types. For each type the function $X(q)$ is sketched in Figure 1 b. We do not, of course, know the exact shape of the curve $X(q)$ in the region of varying X in the mixing types 2 and 3; but this will not cause serious difficulties in our discussion.

Type 1: *No mixing.*

Models of Type 1 have been investigated by HOYLE and SCHWARZSCHILD (1955), HAYASHI, HOSHI, and SUGIMOTO (1962) and by NISHIDA and SUGIMOTO (1962), as mentioned in the first part of this section.

Type 2: *Partial mixing from the surface.*

This type of models might be produced if the outer convective zone reaches the helium core. As this seems an unrealistic possibility, and because the properties of this kind of models must be very similar to those of Type 1 models, we shall not consider Type 2 any further.

Type 3: *Partial mixing from the centre.*

Type 3 models will appear if the central convective core reaches the layers rich in hydrogen, mixing not being effective enough in transporting helium to the surface-layers. It is well-known that models with low hydrogen concentration in the inner regions and envelopes rich in hydrogen have larger radii than main-sequence stars. Table 1 shows that horizontal branch stars in clusters with high Z-values all have rather large radii; most of them are yellow and very few blue. Therefore one might suspect that stars in clusters rich in metal after a helium flash would appear as Type 3 stars, and it might be interesting to investigate whether the evolution of Type 3 stars will explain the colour-magnitude diagrams observed for clusters with high metal content.

Type 4: Complete mixing.

This type has been suggested by WOOLF (1964). Such homogeneous stars will start their evolution near the usual main-sequence, but they will, of course, have an unusually high luminosity for their mass ($X < 0.5$).

Using EDDINGTON's mass-luminosity relation

$$L = CM^{5.5}(\mu\beta)^{7.5}R^{-0.5}$$

we can easily estimate the absolute bolometric magnitudes. If we consider two stars with the same mass, but different hydrogen content, we find, neglecting the dependence on the radius R and assuming for the relative gas pressure $\beta = 1$, which will be good approximations here,

$$\Delta M_{\mathrm{bol}} = -2.5 \log \frac{L'}{L} \simeq -2.5 \log \left(\frac{\mu'}{\mu}\right)^{7.5} \simeq -19 \log \frac{2X + 0.75\ Y}{2X' + 0.75\ Y'}$$

Let us compare the horizontal branch models with "normal" population II main-sequence stars of mass $1.2\ M_\odot$, hydrogen content $X = 0.90$ and $M_{\mathrm{bol}} \simeq 4^m$. For $X = 0.20$ the formula gives: $\Delta M_{\mathrm{bol}} = -5^m.0$ and for $X = 0.30$: $\Delta M_{\mathrm{bol}} = -3^m.8$. Hence our horizontal branch models will have $M_{\mathrm{bol}} \simeq 0^m$ and will thus start their evolution near the left terminal point of the horizontal branch.

In the globular clusters poor in metal most stars are found in the blue part of the horizontal branch (Table 1). Therefore it is tempting to assume that the stars of these clusters are all completely mixed by the helium flash and evolve along the horizontal branch from left to right as proposed by WOOLF.

In the next section the evolution of Types 3 and 4 models will be considered in detail.

4. Model Sequences

The technique used in the computations is essentially the one developed by REIZ and PETERSEN (1964); it is briefly described in the Appendix.

Reddening and Blanketing Corrections

The evolutionary tracks will be compared with the observations of globular cluster stars by ARP (1955). Later ARP (1962b) gave a very detailed analysis of the colour-magnitude diagram of M 5, extending the earlier results. M 5, being poor in metal by a factor of 17 relative to the sun, belongs to the Group 2 clusters. Besides M 5 we shall especially consider M 15

as a representative of the Group 1 clusters extremely poor in metal, because the colour-magnitude diagram for M 15 shows some very characteristic features: The blue part of the horizontal branch is very narrow, and about $0^m.7$ below its blue terminal point a separate group of stars is located.

By means of the relations between $B-V$, $B.C.$ and T_e given by D. L. Harris (1963) the theoretical evolutionary tracks in the $(\log T_e, M_{\mathrm{bol}})$ diagram can be transformed into tracks in the colour-magnitude diagram for Hyades-like stars. As usual the intrinsic magnitudes obtained in this way will be denoted by $(B-V)_c$ and V_c.

The observed magnitudes, however, will in general need corrections for interstellar reddening and blanketing effects before a comparison with theoretical results is possible.

Reddening corrections of magnitudes of globular cluster stars have been a rather unsafe undertaking based on doubtful assumptions. Probably the best thing which can be done is, as proposed by Arp (1962c), to use the reddening laws:

$$E_{B-V} = 0.058 \operatorname{cosec} b, \quad A_V = 3.0\, E_{B-V}$$

for clusters with not too low galactic latitudes. Then we find for M 5: $E_{B-V} = 0.08$, $A_V = 0.24$ and for M 15: $E_{B-V} = 0.12$, $A_V = 0.36$.

Let us consider a globular cluster star and a Hyadeslike star with the same radius and luminosity, in other words with the same T_e. The much greater strength of metallic absorption lines in the atmosphere of the Hyades-like star will cause different distributions of the emergent radiation in the U, B, and V bands in the two stars. For main-sequence stars the metallic absorption lines block more light in B wavelengths than in V, and still more in U.

Wildey, E. M. Burbidge, Sandage, and G. R. Burbidge (1962) have published corrections $\Delta(B-V)$, $\Delta(U-B)$ and ΔV for these blanketing effects. The blanketing corrections must be applied to the observed $(B-V, V)$ values to give the corresponding $((B-V)_c, V_c)$, which are needed for a comparison with the theoretical evolutionary tracks.

The table, however, can only be used for main-sequence stars and only for $0.30 < B-V < 0.80$, thus this reduction is necessarily rather uncertain for horizontal branch stars with $B-V \simeq 0$. But for the main-sequence stars in M 5 Arp determined the blanketing corrections $\Delta(B-V) = 0.16$, $\Delta V = -0.08$ in the region $0.44 < B-V < 0.64$, and it seems likely that the corrections will decrease with higher temperature. Because the reddening correction for M 5 is 0.08, it is reasonable for M 5 to use: $(B-V)_c = B-V$ in the blue part of

the horizontal branch and $(B-V)_c = B-V+0.08$ in the yellow part. Furthermore, $\Delta V = -0.08$ will be adopted. By means of these relations we can determine the absolute magnitudes in B_c and V_c for the observed stars in M 5, when M_V for the RR Lyrae stars are known; and for this quantity we shall adopt the value 0.2 obtained by taking reddening corrections into account, according to the cosec reddening law (ARP 1962c).

For M 15 the situation is somewhat more complicated, partly because the observations (ARP 1955) were given in the (CI, m_{pv}) system, and partly because even less is known about reddening and blanketing effects here than for M 5. Comparing ARP's tables for M 5 in the (CI, m_{pv}) system and the same transformed to the ($B-V$, V) system (ARP 1962b) it is seen that the following relations are valid within a few hundredths of a magnitude. For the blue part of the horizontal branch: $B-V = CI$, $V = m_{pv}+0.20-0.5\,CI$ and for the yellow part: $B-V = CI+0.10$, $V = m_{pv}+0.12$. As both reddening corrections and blanketing corrections in $B-V$ for M 15 are a few hundredths of a magnitude larger than for M 5 their combined effect will be nearly the same for the two clusters, and we can use for M 15: $(B-V)_c = CI$ in the blue part of the horizontal branch and $(B-V)_c = CI+0.18$ in the yellow part. With the above-mentioned reddening correction for M 15 $A_V = 0.36$ and an estimated blanketing correction $\Delta V = -0.11$ we get: $V_c = m_{pv}-0.27+0.5\,CI$ in the blue part, and $V_c = m_{pv}-0.35$ in the yellow part of the horizontal branch.

This procedure clearly is not entirely satisfactory. A reliable comparison of colour-magnitude diagrams with evolutionary sequences probably cannot be made before the B and V magnitudes can be directly determined from sufficiently accurate model atmospheres computed for the specific models of the evolutionary sequences.

Homogeneous Models

We shall first consider completely homogeneous models, Type 4, and investigate the evolution of three stars with the following masses and chemical compositions:

Model-sequence	$M/M_\odot$	X	Y	Z
h1	1.0	0.200	0.799	0.001
h2	1.2	0.300	0.699	0.001
h3	1.3	0.300	0.699	0.001

TABLE 2. Evolutionary tracks of homogeneous models.

Series	Age (10^6 years)	M_{bol}	log T_e	$(B-V)_c$	M_{Vc}	Series	Age (10^6 years)	M_{bol}	log T_e	$(B-V)_c$	M_{Vc}
h1	0	0.52	4.230	−0.17	2.00		60	−0.05	4.226	−0.17	1.40
	20	0.44	4.230	−0.17	1.92		80	−0.16	4.222	−0.16	1.27
	35	0.37	4.229	−0.17	1.84		85	−0.20	4.222	−0.16	1.23
	50	0.30	4.229	−0.17	1.77		90	−0.22	4.222	−0.16	1.21
	60	0.24	4.230	−0.17	1.72		95	−0.26	4.225	−0.17	1.19
	67	0.19	4.233	−0.17	1.69		98	−0.30	4.230	−0.17	1.18
	71	0.15	4.238	−0.18	1.68						
	73	0.13	4.243	−0.18	1.69	h4	0	1.41	4.033	0.00	1.81
	75	0.10	4.251	−0.19	1.72		20	1.38	4.031	0.00	1.77
	76	0.08	4.260	−0.19	1.76		40	1.35	4.028	0.00	1.73
	76.4	0.05	4.267	−0.20	1.78		60	1.31	4.026	0.01	1.68
	76.6	0.03	4.273	−0.20	1.80		80	1.27	4.024	0.01	1.64
	76.7	0.00	4.278	−0.20	1.80		100	1.22	4.024	0.01	1.59
	76.8	−0.10	4.282	−0.20	1.73		108	1.19	4.026	0.01	1.56
	76.85	−0.17	4.283	−0.21	1.66		114	1.15	4.031	0.00	1.54
	76.92	−0.24	4.279	−0.20	1.57		118	1.11	4.037	−0.01	1.52
	77.5	−0.25	4.281	−0.20	1.57		121	1.06	4.046	−0.02	1.51
	78.0	−0.27	4.281	−0.20	1.55		123	0.99	4.058	−0.03	1.49
	78.5	−0.28	4.281	−0.20	1.54						
	80.0	−0.32	4.281	−0.20	1.50	h5	0	1.06	4,037	−0.01	1.47
	82.0	−0.37	4.282	−0.20	1.46		20	1.04	4.034	0.00	1.44
	84	−0.42	4.283	−0.21	1.41		80	0.96	4.025	0.01	1.33
	88	−0.55	4.286	−0.21	1.30		110	0.91	4.019	0.02	1.26
	92	−0.74	4.284	−0.21	1.10		130	0.87	4.015	0.02	1.20
	94	−0.96	4.269	−0.20	0.78		150	0.81	4.016	0.02	1.15
							160	0.76	4.022	0.01	1.12
h2	0	0.51	4.210	−0.16	1.86		165	0.69	4.034	0.00	1.09
	20	0.45	4.209	−0.16	1.79		167	0.63	4.047	−0.02	1.08
	40	0.38	4.207	−0.15	1.71		168	0.41	4.057	−0.03	0.90
	60	0.31	4.205	−0.15	1.63		169	0.40	4.057	−0.03	0.89
	75	0.26	4.204	−0.15	1.57		171	0.39	4.057	−0.03	0.88
	90	0.20	4.201	−0.15	1.49		175	0.36	4.056	−0.03	0.85
	100	0.15	4,201	−0.15	1.44		180	0.32	4.055	−0.02	0.81
							185	0.28	4.054	−0.02	0.76
h3	0	0.19	4.232	−0.17	1.68		193	0.21	4.052	−0.02	0.68
	20	0.11	4.231	−0.17	1.60		200	0.14	4.047	−0.02	0.59
	40	0.04	4.228	−0.17	1.51		207	0.04	4.039	−0.01	0.46

TABLE 3. Characteristics of sequence h1.

Age (10^6 years)	X_c	q_c	f_c	$\log R/R_\odot$	$\log L/L_\odot$	$\log T_c$	$\log \varrho_c$
0	0.200	0.214	0.977	−0.118	1.637	7.454	2.106
20	0.160	0.204	0.980	−0.101	1.668	7.464	2.119
35	0.125	0.193	0.980	−0.086	1.696	7.473	2.131
60	0.058	0.173	0.977	−0.062	1.747	7.497	2.182
67	0.035	0.167	0.972	−0.057	1.769	7.511	2.215
71	0.021	0.161	0.962	−0.059	1.784	7.525	2.249
73	0.014	0.159	0.949	−0.064	1.793	7.535	2.279
75	0.007	0.157	0.911	−0.077	1.804	7.552	2.331
76	0.0035	0.150	0.851	−0.090	1.812	7.567	2.375
76.4	0.0020	0.128	0.748	−0.099	1.822	7.578	2.415
76.6	0.0013	0.108	0.622	−0.106	1.833	7.586	2.456
76.7	0.0009	0.088	0.493	−0.109	1.845	7.590	2.493
76.8	0.0005	0.043	0.187	−0.099	1.884	7.583	2.585
76.85	0.0003	0.016	0.047	−0.084	1.913	7.566	2.679
76.92	0.0001	0	0	−0.063	1.941	7.508	2.830
77.5		0.016		−0.065	1.943	7.478	2.889
78.0		0.030		−0.062	1.950	7.475	2.908
78.5		0.050		−0.059	1.955	7.474	2.922
80.0		0.080		−0.052	1.971	7.471	2.958
82		0.100		−0.044	1.991	7.473	2.994
84		0.120		−0.037	2.011	7.476	3.033
88		0.143		−0.015	2.063	7.483	3.136
92		0.193		0.026	2.140	7.492	3.344
94		0.224		0.099	2.226	7.507	3.666

in order to get an idea of the question how changes in mass and hydrogen content influence the evolutionary tracks. As expected from the analysis of Section 3, the three models start their evolution near the main-sequence band and in the bluest region of the observed horizontal branches. They all have a convective core containing 21 % of the total mass, and at the first evolutionary stage with hydrogen burning in the slowly receding core, the evolution is proceeding in nearly the same way as the well-known evolution of heavy population I stars. The effective temperature T_e, however, decreases very little.

The evolution of the less massive star was studied also at the following stage, where the luminosity is supplied by hydrogen burning in a shell, until a helium core containing 22 % of the mass had developed, while the computations for the heavier models only covered the "main-sequence" phase. The results are given in Tables 2 and 3, and shown in a ($\log T_e$, M_{bol})

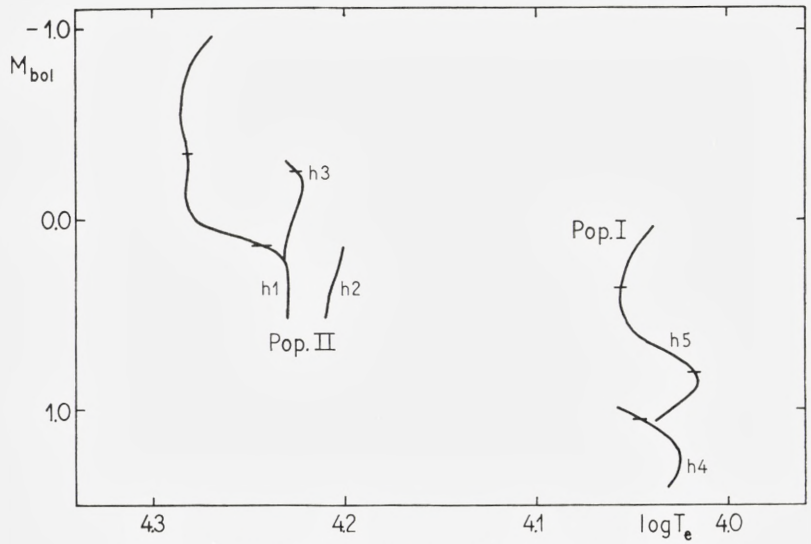

Figure 2. – Evolutionary tracks of homogeneous models.

diagram in Figure 2, where similar tracks for population I stars, which will be discussed below, are also drawn.

In order to facilitate the comparison with observations we shall distinguish between three parts of the evolutionary sequence for the sequence h 1, Table 2. In Part 1, lasting 73×10^6 years, the luminosity increases from $M_{bol} = 0.52$ to $M_{bol} = 0.13$, while T_e is nearly constantly $T_e \simeq 17000^0$. Part 2 is a very fast evolutionary phase, corresponding to the development of a small helium core round the centre. In 7×10^6 years the luminosity rises by 0.5, while T_e increases to 19000^0. The evolution in Part 3, lasting 14×10^6 years, is also fast, though not so fast as in Part 2, and the energy is now produced in a hydrogen-burning shell round the inert helium core. While the mass fraction of the helium core q_c grows from 0.08 to 0.22, the luminosity increases by 0.6 , T_e being first nearly constant. Only in the last models of the computed sequence, for $q_c > 0.20$ the evolutionary track in the colour-magnitude diagram turns towards lower temperatures. In Figure 2 the three parts of the sequence are indicated.

Using the tables of Harris we find that this evolutionary track starts at $((B-V)_c, M_{Vc}) = (-0.17, 2.0)$. At the first stage it moves about 0.4 upwards while the hydrogen is burned in the convective core. During the following fast evolution the luminosity increases from $M_{Vc} = 1.7$ to $M_{Vc} = 0.8$ with nearly constant $(B-V)_c \simeq -0.20$.

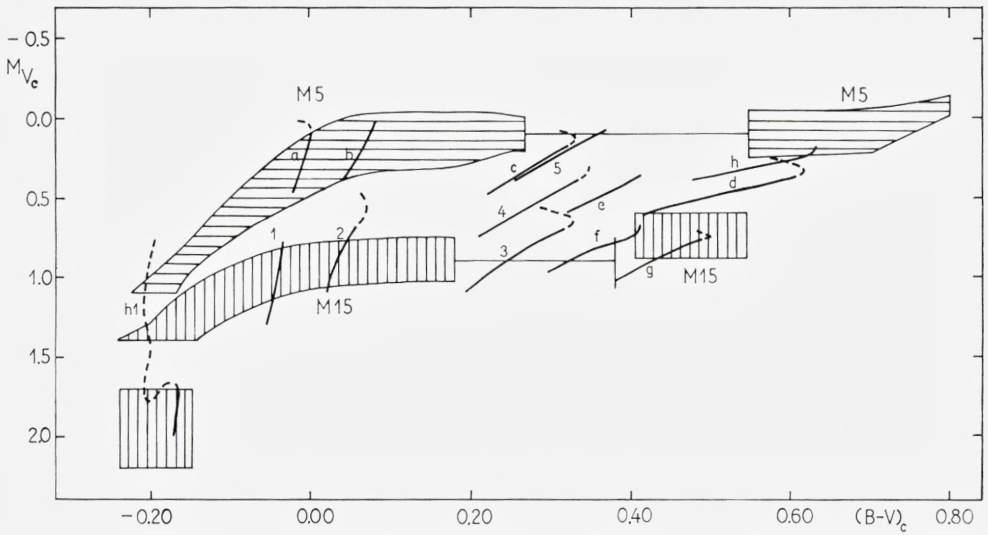

Figure 3. – Comparison of the evolutionary tracks with ARP's observations. The vertically, respectively horizontally, hatched regions are richly populated in M15 and M5. The dashed part of the tracks correspond to fast stages in the evolution.

The evolution following the stages given here must be fast, and probably the evolutionary track will move upwards and to the right in the colour-magnitude diagram. Even if M_{bol} did not change from -1.0 (model age 94×10^6 years) M_{Vc} would rise to -0.1 for $(B-V)_c = -0.1$ and to -0.6 for $(B-V)_c = 0.0$, simply because *B.C.* in this region of the diagram changes strongly with $(B-V)_c$. The star will then move to the right in the diagram, 1–2 magnitudes above the horizontal branch.

Part 1 of the evolutionary track till age 73×10^6 years corresponds nicely to the groups of stars observed in M2 and M15 with $CI \simeq -0.20$ and $m_{pv} \simeq 16.7$ These groups are evidently separated from the rest of the horizontal branch by a gap; they and the rest of the horizontal branch do not form a continuous sequence. From ARP's diagram it is seen that the group can be described by means of a slow evolution, during which the luminosity increases by half a magnitude (corresponding to a rise from $m_{pv} = 16.9$ to 16.4 at $CI = -0.20$). If we use SANDAGE's value (Table 1) for M_V for the RR Lyrae stars in M15: $M_V = 1.0$ or $M_{Vc} = 0.9$, it is seen that most of the stars in the group belonging to M15 cluster round a vertical line with $(B-V)_c = -0.20$ from $M_{Vc} = 2.2$ to 1.7. The theoretical track corresponds to a line with $(B-V)_c = -0.17$ from $M_{Vc} = 2.0$ to 1.6. In Figure 3 the $((B-V)_c, V_c)$ diagram is sketched for M15 and M5 by means of ARP's colour-magnitude diagrams and the

above-mentioned transformation formulae, and computed evolutionary tracks are drawn.

It may be fortuitous that the values of the quantities derived from observations and from the theoretical computations for the separate group of stars in M15 are almost identical, because both the theoretically and the observationally determined data are rather uncertain. In particular, knowledge of the accurate mass value and chemical composition for the stars of the group is lacking, and the absolute magnitudes are based on the little known magnitude of the RR Lyrae stars. But it is satisfactory that we can understand the group separated from the rest of the horizontal branch, the gap being caused by the second very fast phase of evolution following the hydrogen exhaustion at the centre of the stars.

M10 and M92 are in many respects similar to M2 and M15. Therefore we should expect also these clusters to have a separate group of completely mixed stars. As ARP's diagrams show, this is not the case, although many stars are found in the region where we should look for these groups. This may be understood as a result of larger variations in mass and chemical composition of the stars in M10 and M92, a necessary condition for the appearence of a well-separated group clearly being that all stars in the group must have very nearly the same mass and chemical composition (immediately after the helium flash). Perhaps also a smaller mass for the group stars than for the rest of the horizontal branch stars is necessary to explain the separation.

As mentioned above, the star of 1 $M_\odot$ in the late evolutionary phase with its energy produced in a thin shell surrounding an inert helium core, will move quickly to the right in the colour-magnitude diagram 1–2 magnitudes above the horizontal branch. Therefore, we should expect a few stars in this region of the diagrams of M2, M10, M15, and M92, and we find, in fact, a few of them in each cluster.

The globular clusters with relatively high metal content have few or no blue stars in the horizontal branch; hence they include no completely homogeneous stars. In order to investigate this matter more quantitatively, two evolutionary sequences for extreme population I stars with the following parameters were computed:

Model-sequence	$M/M_\odot$	X	Y	Z
h4	1.0	0.200	0.756	0.044
h5	1.3	0.301	0.655	0.044

The evolutionary tracks, displayed in Figure 2, show general properties very similar to those mentioned above for the extreme population II models: After a slow phase with hydrogen burning in the central regions follows a fast phase with an energy-producing shell round a growing helium core. The model of 1.3 $M_\odot$ was followed until the core contained about 16 % of the total mass. In the slow phase (lasting 110×10^6 years for the less massive and 155×10^6 years for the heavier star) we found:

$$4.037 > \log T_e > 4.015; \quad 0.76 < M_{\mathrm{bol}} < 1.41$$

or

$$0.00 < (B-V)_c < 0.02 \quad \text{and} \quad 1.1 < M_{Vc} < 1.8.$$

As the globular cluster NGC 6356 (Sandage and Wallerstein 1960) has no stars bluer than $(B-V)_c \simeq 0.25$, and 47 Tuc (Tifft 1963) apart from two RR Lyrae stars and one extremely blue star contains none bluer than $(B-V)_c \simeq 0.60$, we can conclude that these clusters do not contain homogeneous horizontal branch stars. Even extreme population I stars of this kind would have $(B-V)_c \simeq 0.00$.

On the other hand the rich galactic cluster M 67 has a horizontal branch extending into the blue region (Eggen and Sandage 1964). At its blue end three stars are found with $(B-V)_0 \simeq 0.05$ and $10.5 < V_0 < 11.1$. As blanketing effects for M 67 are very small and its distance modulus is determined very accurately: $(m-M)_0 = 9.38$, we can safely conclude that the three blue stars are placed at $(B-V)_c \simeq 0.05$ and have $1.1 < M_{Vc} < 1.8$. This is exactly the region corresponding to the slow phases of the computed evolutionary sequences for the population I stars of 1.0 and 1.3 solar masses. Of course, this is no crucial test of our assumptions; it shows, however, that the blue part of the horizontal branch in M 67 can be explained by completely mixed models of reasonable masses and chemical compositions. It is emphasized that we do not understand the reason why the horizontal branch of M 67 differs so noticeably from the horizontal branches of globular clusters rich in metal.

Partially Mixed Models

The homogeneous models just considered will not evolve along the horizontal branch from left to right. Hence, if our interpretation of horizontal branches as loci for hydrogen-burning sequences is correct, most horizontal branch stars must correspond to inhomogeneous models of Type 3 (cf. Section 3), and thus contain more hydrogen in the outer layers than in the central regions.

TABLE 4. Evolutionary tracks of partially mixed sequences.

Series	Age (10^6 years)	M_{bol}	$\log T_e$	$(B-V)_c$	M_{Vc}	Series	Age (10^6 years)	M_{bol}	$\log T_e$	$(B-V)_c$	M_{Vc}
1	0	0.67	4.087	−0.06	1.30		60	0.45	3.876	0.29	0.53
	20	0.62	4.085	−0.05	1.24		70	0.41	3.870	0.30	0.49
	40	0.56	4.082	−0.05	1.16		80	0.38	3.864	0.32	0.45
	60	0.51	4.078	−0.05	1.09		90	0.33	3.858	0.33	0.40
	80	0.43	4.074	−0.04	1.00		97	0.29	3.854	0.34	0.35
	100	0.37	4.070	−0.04	0.92						
	110	0.33	4.067	−0.04	0.87	5	0	0.29	3.890	0.25	0.39
	115	0.30	4.067	−0.04	0.84		10	0.24	3.883	0.27	0.33
	120	0.28	4.066	−0.04	0.81		20	0.20	3.874	0.29	0.28
	125	0.26	4.066	−0.04	0.79		24.84	0.17	3.869	0.31	0.24
							28.5	0.15	3.867	0.31	0.22
2	0	0.74	4.015	0.02	1.08		35	0.13	3.863	0.32	0.20
	20	0.69	4.011	0.03	1.01		42	0.10	3.856	0.33	0.17
	40	0.63	4.007	0.03	0.94		49	0.06	3.850	0.36	0.12
	60	0.58	4.004	0.04	0.88		54	0.02	3.844	0.37	0.08
	80	0.52	3.997	0.05	0.80						
	95	0.47	3.992	0.05	0.73	*a*	0	0.00	4.053	−0.02	0.48
	110	0.41	3.987	0.06	0.66		10	−0.06	4.050	−0.02	0.40
	120	0.38	3.984	0.07	0.62		20	−0.12	4.045	−0.01	0.32
	130	0.32	3.981	0.07	0.55		30	−0.18	4.040	−0.01	0.24
	136	0.29	3.983	0.07	0.53		38	−0.24	4.036	0.00	0.17
							43	−0.28	4.034	0.00	0.12
3	0	0.98	3.916	0.19	1.10		47	−0.32	4.033	0.00	0.08
	30	0.92	3.908	0.21	1.03		51	−0.35	4.034	0.00	0.05
	60	0.85	3.899	0.23	0.95		53	−0.37	4.037	0.00	0.04
	90	0.78	3.889	0.26	0.87		54.2	−0.39	4.040	−0.01	0.03
	105	0.73	3.881	0.28	0.82		55	−0.41	4.043	−0.01	0.03
	115	0.71	3.877	0.29	0.79						
	125	0.68	3.873	0.29	0.76	*b*	0	0.11	4.001	0.04	0.40
	141.33	0.62	3.864	0.32	0.69		10	0.06	3.996	0.05	0.33
	149	0.60	3.862	0.32	0.67		20	0.01	3.991	0.06	0.27
	155	0.58	3.860	0.33	0.65		30	−0.05	3.985	0.06	0.19
	159	0.56	3.861	0.33	0.63		38	−0.10	3.980	0.07	0.13
	162	0.54	3.862	0.32	0.61		45	−0.15	3.976	0.08	0.07
	165	0.52	3.865	0.32	0.59		50	−0.19	3.973	0.08	0.03
	167	0.50	3.869	0.31	0.57						
	168.5	0.48	3.875	0.29	0.56	*c*	0	0.38	3.904	0.22	0.49
							10	0.33	3.898	0.23	0.43
4	0	0.64	3.907	0.21	0.75		20	0.29	3.891	0.25	0.39
	20	0.58	3.898	0.23	0.68		30	0.25	3.883	0.27	0.34
	40	0.52	3.888	0.26	0.61		38	0.21	3.877	0.28	0.29

TABLE 4 (continued).

Series	Age (10^6 years)	M_{bol}	log T_e	$(B-V)_c$	M_{Vc}
	45	0.18	3.872	0.30	0.26
	51	0.15	3.867	0.31	0.22
	55	0.13	3.865	0.32	0.20
	59	0.10	3.863	0.32	0.17
	62	0.08	3.861	0.33	0.15
	65	0.05	3.861	0.33	0.12
	67	0.04	3.862	0.32	0.11
	69	0.01	3.866	0.31	0.08
d	0	0.57	3.828	0.41	0.62
	10	0.54	3.820	0.44	0.59
	25	0.49	3.809	0.47	0.53
	35	0.45	3.800	0.49	0.50
	45	0.41	3.790	0.53	0.46
	52	0.38	3.785	0.55	0.44
	59	0.35	3.778	0.58	0.41
	64	0.33	3.774	0.59	0.39
	68	0.30	3.770	0.60	0.37
	72	0.28	3.766	0.62	0.35
	75	0.26	3.765	0.62	0.33
	77	0.25	3.766	0.62	0.32
	79	0.22	3.774	0.59	0.28
	80	0.20	3.777	0.58	0.26
e	0	0.52	3.863	0.32	0.59
	10	0.48	3.856	0.34	0.55
	20	0.44	3.848	0.36	0.50
	30	0.40	3.841	0.38	0.46
	37	0.37	3.836	0.39	0.42
	42	0.34	3.833	0.40	0.39
	46	0.32	3.832	0.40	0.37
	50	0.30	3.831	0.41	0.35
f	0	0.88	3.871	0.30	0.96
	20	0.83	3.862	0.32	0.90
	40	0.78	3.852	0.35	0.84
	55	0.74	3.844	0.37	0.80
	65	0.71	3.838	0.39	0.76
	73	0.69	3.834	0.40	0.74
	78	0.67	3.831	0.41	0.72
	83	0.65	3.828	0.41	0.70
	87	0.63	3.828	0.41	0.68
	89	0.62	3.828	0.41	0.67
	91	0.61	3.828	0.41	0.66
g	0	0.97	3.841	0.38	1.03
	20	0.92	3.833	0.40	0.97
	35	0.88	3.826	0.42	0.93
	45	0.86	3.822	0.43	0.91
	55	0.83	3.818	0.44	0.87
	65	0.80	3.816	0.45	0.84
	73	0.78	3.813	0.46	0.82
	80	0.76	3.809	0.47	0.80
	85	0.74	3.806	0.47	0.78
	90	0.72	3.801	0.49	0.76
	94	0.71	3.799	0.50	0.76
	97	0.69	3.800	0.49	0.73
	99	0.67	3.801	0.49	0.71
h	0	0.35	3.806	0.48	0.39
	10	0.31	3.797	0.51	0.36
	18	0.27	3.788	0.54	0.32
	24	0.24	3.782	0.56	0.30
	29	0.22	3.779	0.57	0.28
	33	0.20	3.774	0.59	0.26
	37	0.17	3.768	0.61	0.24
	40	0.16	3.765	0.62	0.23
	42.5	0.14	3.763	0.63	0.22
	44.5	0.13	3.763	0.63	0.21
	46.3	0.11	3.762	0.63	0.19

TABLE 5. Characteristics of five partially mixed series.

Series	Age (10^6 years)	X_c	q_c	f_c	$\log R/R_\odot$	$\log L/L_\odot$	$\log T_c$	$\log \varrho_c$
1	0	0.300	0.215	0.978	0.138	1.573	7.402	1.958
	20	0.271	0.205	0.978	0.153	1.596	7.407	1.962
	40	0.240	0.195	0.979	0.171	1.619	7.413	1.968
	60	0.204	0.182	0.979	0.188	1.641	7.419	1.977
	80	0.165	0.171	0.980	0.212	1.670	7.428	1.988
	100	0.120	0.161	0.980	0.233	1.697	7.439	2.009
	110	0.094	0.154	0.980	0.246	1.713	7.447	2.024
	115	0.080	0.150	0.979	0.252	1.722	7.451	2.035
	120	0.066	0.145	0.977	0.257	1.731	7.457	2.048
	125	0.051	0.141	0.975	0.262	1.741	7.464	2.067
3	0	0.300	0.193	0.972	0.417	1.450	7.394	1.998
	30	0.264	0.182	0.973	0.446	1.475	7.400	2.005
	60	0.224	0.170	0.974	0.477	1.503	7.407	2.014
	90	0.178	0.157	0.974	0.512	1.532	7.416	2.027
	105	0.151	0.151	0.976	0.537	1.552	7.423	2.037
	115	0.132	0.145	0.975	0.551	1.561	7.427	2.046
	125	0.112	0.142	0.976	0.565	1.572	7.432	2.058
	141.33	0.077	0.135	0.975	0.593	1.595	7.444	2.083
	149	0.058	0.130	0.972	0.602	1.603	7.452	2.102
	155	0.043	0.126	0.970	0.611	1.613	7.460	2.123
	159	0.033	0.122	0.966	0.613	1.619	7.467	2.143
	162	0.025	0.119	0.959	0.614	1.625	7.474	2.163
	165	0.016	0.114	0.944	0.612	1.634	7.484	2.192
	167	0.0103	0.110	0.920	0.608	1.642	7.495	2.224
	168.5	0.0057	0.102	0.867	0.600	1.652	7.508	2.266
a	0	0.200	0.224	0.992	0.338	1.843	7.433	1.913
	10	0.174	0.214	0.991	0.358	1.866	7.438	1.918
	20	0.144	0.210	0.991	0.379	1.890	7.445	1.927
	30	0.113	0.197	0.990	0.402	1.915	7.454	1.939
	38	0.085	0.187	0.990	0.422	1.940	7.463	1.955
	43	0.066	0.180	0.989	0.434	1.955	7.471	1.971
	47	0.049	0.173	0.987	0.444	1.970	7.479	1.990
	51	0.031	0.166	0.981	0.448	1.984	7.492	2.021
	53	0.021	0.161	0.975	0.448	1.993	7.501	2.047
	54.2	0.015	0.158	0.966	0.445	2.000	7.510	2.070
	55	0.0107	0.156	0.954	0.441	2.006	7.518	2.092
c	0	0.200	0.198	0.989	0.563	1.693	7.422	1.963
	10	0.179	0.191	0.989	0.584	1.710	7.426	1.967
	20	0.157	0.183	0.989	0.607	1.727	7.431	1.974

TABLE 5 (continued).

Series	Age (10^6 years)	X_c	q_c	f_c	$\log R/R_\odot$	$\log L/L_\odot$	$\log T_c$	$\log \varrho_c$
	30	0.133	0.177	0.989	0.630	1.745	7.437	1.983
	38	0.112	0.174	0.988	0.650	1.759	7.442	1.993
	45	0.092	0.167	0.988	0.666	1.772	7.448	2.005
	51	0.075	0.160	0.987	0.682	1.785	7.454	2.018
	55	0.062	0.156	0.986	0.690	1.792	7.460	2.030
	59	0.049	0.153	0.984	0.700	1.803	7.466	2.046
	62	0.038	0.149	0.981	0.708	1.812	7.472	2.061
	65	0.028	0.145	0.977	0.714	1.822	7.481	2.083
	67	0.020	0.141	0.970	0.715	1.829	7.489	2.104
	69	0.012	0.135	0.951	0.711	1.838	7.500	2.139
g	0	0.200	0.162	0.982	0.570	1.457	7.406	2.041
	20	0.171	0.154	0.982	0.598	1.477	7.412	2.050
	35	0.146	0.147	0.982	0.617	1.490	7.417	2.060
	45	0.129	0.143	0.982	0.631	1.501	7.421	2.068
	55	0.111	0.138	0.982	0.644	1.511	7.426	2.078
	65	0.092	0.135	0.981	0.654	1.523	7.431	2.090
	73	0.075	0.133	0.981	0.665	1.532	7.437	2.103
	80	0.061	0.129	0.979	0.676	1.541	7.443	2.118
	85	0.049	0.125	0.978	0.686	1.548	7.448	2.131
	90	0.038	0.122	0.974	0.699	1.553	7.454	2.150
	94	0.028	0.118	0.971	0.706	1.561	7.462	2.169
	97	0.021	0.115	0.964	0.708	1.568	7.469	2.190
	99	0.016	0.112	0.950	0.709	1.574	7.476	2.211

In order to investigate the evolution of such inhomogeneous models we shall construct evolutionary sequences for the mass $M = 1.2\ M_\odot$ and the content of heavy elements $Z = 0.005$. The outer zone, which contains at least $1\,\%$ of the total mass, has the following chemical composition:

$$X = 0.900, \qquad Y = 0.095, \qquad Z = 0.005.$$

The hydrogen content X as a function of relative mass q for the first model of the sequences computed is shown in Figures 4 and 5, and the evolutionary tracks are drawn in the $((B-V)_c, V_c)$ diagram in Figure 3. Additional relevant information about the properties of the sequences is given in Tables 4 and 5.

The series 1–5 consist of two homogeneous zones. 1–3 have $1\,\%$, $5\,\%$,

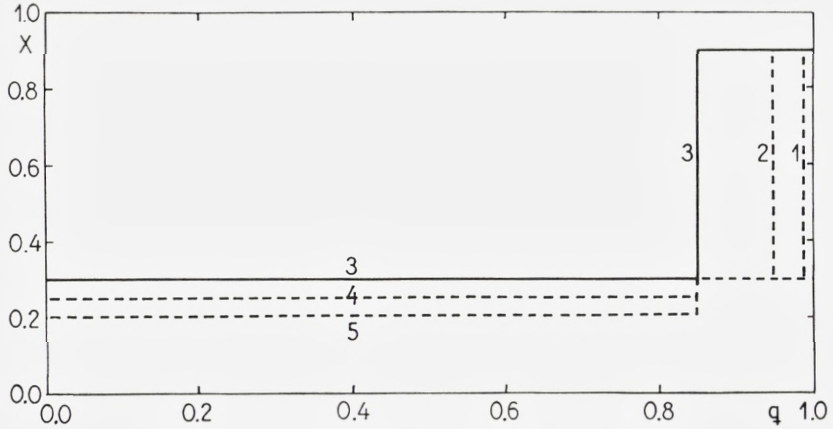

Figure 4. – $X(q)$ for the first model of the series 1–5.

and 15 %, respectively, of the mass in the outer zone, and an inner zone with the composition:

$$X = 0.300, \qquad Y = 0.695, \qquad Z = 0.005.$$

As was to be expected, the radius of the models was found to increase and the luminosity to decrease in the order 1, 2, 3. The series 3, 4, 5 all have an outer zone containing 15 % of the mass, and the hydrogen content X of the inner zone is in the order 0.30, 0.25, and 0.20. As was to be expected, the luminosity was found to increase in the order 3, 4, 5.

It does not seem quite realistic to assume a sudden jump in $X(q)$ at a certain relative mass. Therefore, we shall consider the model sequences a, b, c, d, e, f, g, and h (cf. Figure 5), with a smoother transition of X between the two zones. Their evolutionary tracks, however, have the same general characteristics as the tracks of the models consisting of two homogeneous zones. For instance, it is found that the sequences 5 and c are very similar. It is also seen that the only difference between the models is that in sequence c the hydrogen is somewhat less concentrated to the outer layers than in sequence 5.

The tracks h1, 1, 2, 3, f, and g pass through the region occupied by M15 in Figure 3. It should be emphasized that this circumstance by no means proves that the stars in M15 have precisely the properties of the corresponding models, even if the interpretation of the horizontal branch as a hydrogen-burning sequence is realistic. First, due to the uncertainty in the absolute magnitude of the RR Lyrae stars, the location of M15 in the

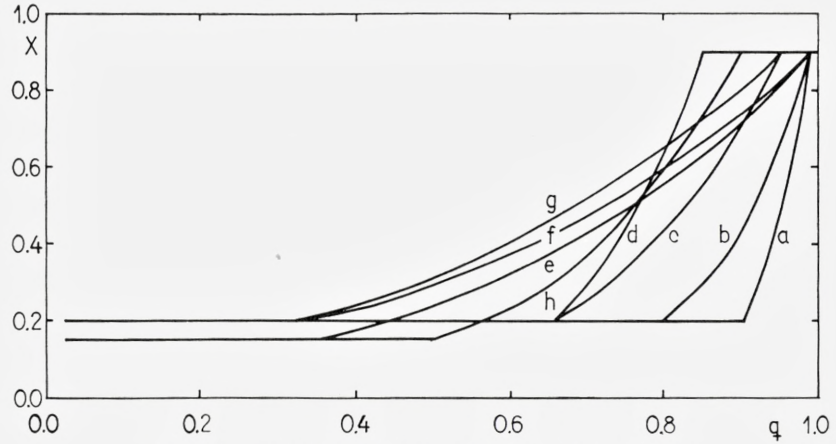

Figure 5. – $X(q)$ for the first model of the series a–h.

diagram is open to discussion, and secondly, it is possible that models with different masses and different distributions of the hydrogen can fall in the same region of the colour-magnitude diagram.

5. Discussion

Figure 3 shows that the computed model sequences fall within a region of the colour-magnitude diagram occupied by the observed horizontal branches of globular clusters. Therefore, our models might be realistic models for horizontal branch stars. But whether such sequences can provide a detailed description of the observed diagrams, or not, is a more difficult question.

From the series 1–3 we should expect a width of at least six tenths of a magnitude, corresponding to an increase in luminosity for such objects of the same amount during the first slow phase of evolution with hydrogen conversion in a convective core. This luminosity increase is clearly a characteristic feature of models containing 30 % of hydrogen in an inner homogeneous zone. The subsequent models show that the growth of luminosity in the slow phase decreases with diminishing hydrogen content. For $X = 0.25$ we find $\Delta M_V \simeq 0.4$ and for $X = 0.20$ $\Delta M_V \simeq 0.3$. To describe horizontal branches as narrow as observed in M15, therefore, a rather small X-value must be assumed. The width $\Delta M_V \simeq 0.3$ for $X = 0.20$ is clearly a minimum width, which will only be present in a cluster if all the horizontal branch

stars in the cluster have very nearly the same mass. A broader sequence does not necessarily imply a higher hydrogen content; variations in mass and chemical composition may produce the same effect.

All the partially mixed sequences investigated here have the same mass 1.2 $M_\odot$. If a larger mass is assumed, the sequences will become more luminous and of a somewhat higher temperature. Also the content of heavy elements Z was the same for all the sequences, 0.005. As is well-known, lower Z-values give higher temperatures and somewhat higher luminosities. However, there seems to be no reason to investigate in detail how changes in mass and chemical composition will affect this case, as the sequences already computed cover the region where horizontal branch stars are found, and as differences in mixing have a much stronger effect than small differences in mass and chemical composition.

The time scale for the horizontal branch phase according to these evolutionary sequences is about 150×10^6 years for series 1–3, while, for the more luminous series which contain only 20 % hydrogen in the central region, about 70×10^6 years were found. This is less than the time scale 230×10^6 years determined by Sandage for M 3, but considerably more than the time scale for helium-burning sequences.

As described in Section 2, differences in concentration of blue stars, RR Lyrae and yellow stars in the horizontal branches suggest a mass loss by the helium flash or at the RR Lyrae stage, and an evolution from the left to the right along the horizontal branch. Generally, the computed tracks run from left to right, but they also extend upwards in the diagrams, and no evolution from the blue end to the red end of the branch is predicted. It therefore seems that the observed differences in distribution of different groups of stars cannot directly be explained by our theory in the same way as done by Woolf (1964).

In Section 2 we mentioned (Table 1, the right-hand columns) the observed differences in stellar content among globular clusters of varying abundances of heavy elements. We can now describe these differences by means of the model sequences. In the clusters with very low content of metal, $[M/H] = -2.3$, nearly all stars are found to the left of the RR Lyrae gap. According to our interpretation, the models which fall in this region are either homogeneous or partially mixed with less than about 15 % of the mass in the outer zone with the original chemical composition. The typical clusters of Group 2 with $[M/H] \simeq -1.5$ have a considerable fraction of their horizontal branch stars in the yellow part of the branch, i.e. they contain fewer completely mixed stars than Group 1 clusters, but many stars

with an outer zone containing 15% of the mass or more. Finally, in the clusters with strong metal lines, only yellow horizontal branch stars are found, all having a considerable fraction of the mass in the outer zone.

The question why these differences occur, is outside the scope of the present investigations. But provided that the interpretation of horizontal branches as hydrogen-burning sequences is correct, we can understand the observed horizontal branches of globular clusters by the simple assumption that the mixing by the helium flash is most violent for extreme population II stars. The degree of mixing must depend on the content of heavy elements in such a way that stars with negligible content of heavy elements are mostly completely mixed, while intermediate population II stars in most cases only become partially mixed, and the stars of nearly normal population I composition always contain a considerable fraction of the mass in an outer unmixed zone.

Without doubt the mixing will also depend on the mass of the star. But as it seems likely that the mass of horizontal branch stars in all globular clusters are nearly the same, this dependence might be very little conspicuous. However, in this connection it is worth mentioning that the rather young cluster M13 contains very few yellow horizontal branch stars even if it belongs to Group 2 ($[M/H] = -1.4$). This might be due to slightly larger masses in M13 than in the other clusters.

Finally, we shall mention a few possible observational tests of the theoretical picture developed.

By an investigation of the pulsations of the models placed in the RR Lyrae gap it is possible to determine the dependence of the pulsation periods on the observed $(B-V)$ values, and a comparison with the detailed observations for M3 (Roberts and Sandage 1955) can be carried out. By means of determinations of detailed element abundances it is in principle possible to distinguish between the following three possible schemes for the horizontal branch evolution:

(1) Helium burning without mixing
(2) The scheme proposed by Woolf (1964)
(3) The scheme discussed here.

According to (1) the abundances determined for a horizontal branch star should be the same as those determined for other stars in the same cluster. According to (2), as described by Woolf, helium and carbon enrichment

will be observed in the yellow part of the horizontal branches, while according to (3), helium and carbon enrichment should be found for stars in the blue part of the horizontal branches, but not in the yellow part.

Appendix: Computational Technique

The computer programme, written in GIER-ALGOL language, is essentially the same as the one described by Reiz and Petersen (1964), in particular the fitting procedure and the handling of the opacity tables are not altered. However, a more complicated technique must be used in dealing with the atmosphere and the outer zone, as some of the models have effective temperatures so low that the outer convective zone cannot be neglected.

The functions $\ln P$, $\ln T$, $q = M(r)/M$, $f = L(r)/L$ are obtained by means of integration of the four basic differential equations from the surface of the star to a pre-assigned fitting-point and from the centre to the fitting-point. The method of integration and the fitting-procedure are exactly as described by Reiz and Petersen.

For the rate of energy generation by hydrogen-burning nuclear reactions, the formulae given by Reeves (1965) are used directly, and the energy release ε_g due to changes of the stellar structure with time is computed according to the formula (cf. Schwarzschild 1958):

$$\varepsilon_g = -\frac{3}{2}\varrho^{2/3}\frac{\partial}{\partial t}(p\varrho^{-5/3}).$$

However, it turns out that this term in the expression for the energy-generation rate has very little influence on the evolution of the models considered here, even in the fast evolutionary stage following the hydrogen exhaustion at the centre.

The opacity tables for the mixtures with $Z = 0.005$ and $X = 0.00$, 0.30, 0.60, and 0.90, respectively, were computed at the Institute for Space Studies, New York, and made available to the Copenhagen Observatory by B. Strömgren, while the tables for the mixtures $Z = 0.001$, $X = 0.00$ and 0.90, $Z = 0.044$, $X = 0.00$ and 0.602, published (after the present computations were performed) by Cox, Stewart, and Eilers (1965) were made available by R. Kippenhahn. Both sets of tables have been computed according to the method used by Cox (1965). For intermediate X-values linear interpolation in the sets of tables is used to compute the opacities. The small

uncertainties in the opacity values have very little influence in investigations in which, as in the present case, only moderate accuracy is attempted.

In order to reduce computing time, the integrations from the outside of the star to the fitting-point are not started at the atmospheres. By means of tables for the outer zones, computed by means of a separate programme, it is possible to use one of the three values for the relative mass $q = 0.99$, 0.95, or 0.85 as starting value for the inward integrations. At these q-values, the values of the corresponding relative radius x, $\ln T$, and $\ln \varrho$ are calculated by interpolation in the tables stored in the computer. By this method the very time-consuming integrations through the outer layers are replaced by fast interpolation in previously computed tables, and thus it is possible to start the inward integrations deep inside the star.

The tables for the outer layers have to be computed in a grid in the ($\log R/R_\odot$, $\log L/L_\odot$) plane, sufficiently narrow to allow accurate interpolation. It was found that second-order interpolation in a grid with intervals equal to 0.10 in the parameters $\log R/R_\odot$ and $\log L/L_\odot$ was entirely satisfactory for the sequences computed here; in fact the variations in the tables were often very nearly linear.

The integrations through the atmosphere and the outer layers, where ionization of hydrogen and helium must be taken into account in detail and non-adiabatic convection zones may occur, are performed by a procedure very similar to the method used by Baker and Kippenhahn (1962) and Baker (1963). In the present case, however, the influence of the radiation on the ionization is very slight and has therefore been disregarded.

If we use $\ln P$ as independent variable in the outer zone, the differential equations for $x = r/R$, $q = M(r)/M$ and $\ln T$ become:

$$\left.\begin{aligned} \frac{dx}{d\ln P} &= -\frac{Rx^2P}{GMq\varrho} \\ \frac{dq}{d\ln P} &= \frac{4\pi R^3}{M} x^2 \varrho \frac{dx}{d\ln P} \\ \frac{d\ln T}{d\ln P} &= \nabla \end{aligned}\right\} \quad (1)$$

In non-adiabatic convection zones the gradient ∇ is computed from the mixing-length theory of Böhm-Vitense (1958) by the method described by Baker (1963). The equation for ∇

$$(\nabla - \nabla_{\mathrm{ad}}) - (\nabla_R - \nabla_{\mathrm{ad}}) + \frac{9}{8U}\left(\sqrt{\nabla - \nabla_{\mathrm{ad}} + U^2} - U\right)^3 = 0 \tag{2}$$

with

$$U = \frac{12\sigma T^3}{C_p \varrho^2 \varkappa l}\left(\frac{8\mu}{RTQ}\right)^{1/2} \tag{3}$$

is solved by the following method described by Reiz (1964). Defining ξ by

$$\nabla - \nabla_{\mathrm{ad}} = \xi^2 + 2U\xi, \tag{4}$$

which implies

$$\nabla - \nabla_R = -\frac{9}{8U}\xi^3,$$

we get by means of (2)

$$\xi^3 + \frac{8U}{9}\xi^2 + \frac{16U^2}{9}\xi - (\nabla_R - \nabla_{\mathrm{ad}})\frac{8U}{9} = 0. \tag{5}$$

Equation (5) has one positive root $\xi = \xi_0$, which is determined by a simple Newton-iteration. For

$$f(\xi) = \xi^3 + \frac{8U}{9}\xi^2 + \frac{16U^2}{9}\xi - (\nabla_R - \nabla_{\mathrm{ad}})\frac{8U}{9}$$

we have

$$\frac{df}{d\xi} = 3\xi^2 + \frac{16U}{9}\xi + \frac{16U^2}{9}.$$

A good approximation to ξ_0 is always available. Near the boundaries of a convective zone $\xi_0 \simeq 0$, and inside a zone the value of ξ_0 from the previous integration step can be used as an approximate solution. Applying this method, it was found that 2–3 iterations were sufficient for securing a relative accuracy of 10^{-4} in ξ_0.

The integrations through the outer zones are performed by Merson's modified Runge-Kutta method (Merson 1958), which allows a prescribed accuracy in the integrated functions to be achieved by a minimum number of integration steps. The first part of the calculation of the derivatives consists in solving the Saha-equations for the ionizations of hydrogen and helium. This is done by a simple iterative procedure for E, the average number of free electrons per atom (cf. Baker and Kippenhahn (1962), Appendix A). However, at higher temperatures ($T > 10^6$ ^0K) the usual ap-

proximation: to replace the partition functions by their first term, is not permissible; effectively complete ionization occurs. In the computations we have simply assumed complete ionization for $T > 10^6$ ^0K, and the errors introduced in the model atmospheres by this procedure are negligible for the models considered here. After the ionization degrees have been determined, the density ϱ can be obtained from the equation of state, and ∇_R and ∇_{ad} can be found. If convection occurs, the root ξ_0 of (5) is determined as described, and ∇ is found by means of (4). Then the derivatives can be obtained from the formulae (1).

The computation of one outer zone, including output of x, $\log T$ and $\log \varrho$ for the relative mass-values q equal to 0.99, 0.95, and 0.85, requires about 5 minutes on the GIER-computer. It may be mentioned here that all the evolutionary sequences of partially mixed models described in Section 4, were computed by means of one table for outer zones containing results from 63 envelopes. The total computing time for this table was about 5 hours, which, however, is less than 10 per cent. of the time used for the computation of the evolutionary sequences.

Acknowledgements

The author wishes to thank Professor B. Strömgren and Professor R. Kippenhahn for making the opacity tables available, and to express his sincere gratitude to Professor A. Reiz for advice and support at several stages of the work, especially for many valuable comments on the manuscript. Also it is a pleasure to thank Mr. H. E. Jørgensen for many discussions, Mr. P. M. Hejlesen for computational assistance and Miss B. Hindkjær for her careful typing of the manuscript. The calculations have been carried out with the aid of the GIER computer made available to the Copenhagen Observatory by the Carlsberg Foundation.

Copenhagen University Observatory.

References

Arp, H. C., 1955, A. J. **60**, 317.
— 1962a, IAU Symposium, No. 15, 42.
— 1962b, Ap. J. **135**, 311.
— 1962c, Ap. J. **135**, 971.
Baker, N., and Kippenhahn, R., 1962, Zs. f. Ap. **54**, 114.
— 1963, Tables of Convective Stellar Envelope Models, Institute for Space Studies, New York.
Böhm-Vitense, E., 1958, Zs. f. Ap. **46**, 108.
Cox, A. N., 1965, Stars and Stellar Systems, Vol. 8, ed. L. H. Aller and D. B. McLaughlin (Chicago, Univ. of Chicago Press).
— Stewart, J. N., and Eilers, D. D., 1965. Ap. J. Suppl. **11**, 1.
Demarque, P. R., and Geisler, J. E., 1963, Ap. J. **137**, 1102.
— and Larson, R. B., 1964, Ap. J. **140**, 544.
Eggen, O. J., and Sandage, A. R., 1964, Ap. J. **140**, 130.
Harris III, D. L., 1963, Stars and Stellar Systems, Vol. 3, ed. K. Aa. Strand (Chicago, Univ. of Chicago Press).
Hayashi, C., Hoshi, R., and Sugimoto, D., 1962, Prog. Theoret. Phys. Suppl. **22**.
Hoyle, F., and Schwarzschild, M., 1955, Ap. J. Suppl. **2**, 1.
— 1959, M. N. **119**, 124.
Härm, R., and Schwarzschild, M., 1964, Ap. J. **139**, 594.
Kippenhahn, R., Temesvary, St., and Biermann, L., 1958, Zs. f. Ap. **46**, 257.
Lance, G. N., 1960, Numerical Methods for High Speed Computers (London, Iliffe and Sons Ltd.).
Merson, R. H., 1958, Unpublished, quoted in Lance (1960).
Morgan, W. W., 1959, A. J. **64**, 432.
Nishida, M., and Sugimoto, D., 1962, Prog. Theoret. Phys. **27**, 145.
Oort, J. H., and v. Herk, G., 1959, B. A. N. **14**, 299.
Reeves, H., 1965, Stars and Stellar Systems, Vol. 8, ed. L. H. Aller and D. B. McLaughlin (Chicago, Univ. of Chicago Press).
Reiz, A., 1964, Private communication.
— and Petersen, J. O., 1964, Publ. og mindre Medd. fra Københavns Observatorium, Nr. 182.
Roberts, M., and Sandage, A. R., 1955, A. J. **60**, 185.
Sandage, A. R., 1953, A. J. **58**, 61.
— 1957, Ap. J. **126**, 326.
— 1962a, IAU Symposium, No. 15, 359.
— 1962b, Ap. J. **135**, 349.
— and Wallerstein, G., 1960, Ap. J. **131**, 598.

Schwarzschild, M., 1958, The Structure and Evolution of the Stars (Princeton N. J., Princeton Univ. Press.)
— and Selberg, H., 1962, Ap. J. **136**, 150.
— and Härm, R., 1962, Ap. J. **136**, 158.
— and Härm, R., 1965, Ap. J. **142**, 855.
Schönberg, M., and Chandrasekhar, S., 1942, Ap. J. **96**, 161.
Sugimoto, D., 1964, Prog. Theoret. Phys. **32**, 703.
Tifft, W. G., 1963, M. N. **126**, 209.
Wallerstein, G., and Carlson, M., 1960. Ap. J. **132**, 276.
— and Greenstein, J. L., 1964, Ap. J. **139**, 1163.
Wildey, R. L., 1961, Ap. J. **133**, 430.
— Burbidge, E. M., Sandage, A. R., and Burbidge, G. R., 1962, Ap. J. **135**, 94.
Woolf, N. J., 1962, A. J. **67**, 286.
— 1964, Ap. J. **139**, 1081.

Indleveret til Selskabet den 26. november 1965.
Færdig fra trykkeriet den 25. april 1966.

MATEMATISK-FYSISKE
MEDDELELSER

UDGIVET AF

DET KGL. DANSKE VIDENSKABERNES SELSKAB

BIND 34

KØBENHAVN
KOMMISSIONÆR: MUNKSGAARD
1963—66

INDHOLD